Transactions of the ASME®

FLUIDS ENGINEERING DIVISION
Technical Editor
DEMETRI P. TELIONIS (1999)
Executive Secretary
PAT WHITE (1999)
Assistant to the Editor
N. W. SCHAEFFLER
Calendar Editor
M. F. ACKERSON

Associate Technical Editors
P. R. BANDYOPADHYAY (1998)
S. BANERJEE (1999)
P. W. BEARMAN (1998)
P. BRADSHAW (2000)
M. S. CRAMER (1998)
M. N. DHAUBHADEL (1999)
J. K. EATON (1998)
G. ERLEBACHER (2000)
J. A. C. HUMPHREY (1998)
F. HUSSAIN (1998)
J. KATZ (1998)
C. L. MERKLE (2000)
B. SCHIAVELLO (1999)
P. M. SOCKOL (1998)
M. SOMMERFELD (1999)
M. S. TRIANTAFYLLOU (1998)
F. K. WASDEN (2000)
D. R. WILLIAMS (2000)

BOARD ON COMMUNICATIONS
Chairman and Vice-President
R. K. SHAH

OFFICERS OF THE ASME
President, **W. M. PHILLIPS**
Exec. Director
D. L. BELDEN
Treasurer
J. A. MASON

PUBLISHING STAFF
Managing Director, Engineering
CHARLES W. BEARDSLEY
Director, Technical Publishing
PHILIP DI VIETRO
Managing Editor, Technical Publishing
CYNTHIA B. CLARK
Managing Editor, Transactions
CORNELIA MONAHAN
Production Assistant
MARISOL ANDINO

Transactions of the ASME, Journal of Fluids Engineering (ISSN 0098-2202) is published quarterly (Mar., June, Sept., Dec.) for $205.00 per year by The American Society of Mechanical Engineers, Three Park Avenue, New York, NY 10016. Periodicals postage paid at New York, NY and additional mailing offices. POSTMASTER: Send address changes to Transactions of the ASME, Journal of Fluids Engineering, c/o THE AMERICAN SOCIETY OF MECHANICAL ENGINEERS, 22 Law Drive, Box 2300, Fairfield, NJ 07007-2300.

CHANGES OF ADDRESS must be received at Society headquarters seven weeks before they are to be effective. Please send old label and new address.

PRICES: To members, $40.00, annually: to nonmembers, $205.00. Add $40.00 for postage to countries outside the United States and Canada.

STATEMENT from By-Laws. The Society shall not be responsible for statements or opinions advanced in papers or . . . printed in its publications (B7.1, Par. 3).

COPYRIGHT © **1998** by The American Society of Mechanical Engineers. Authorization to photocopy material for internal or personal use under circumstances not falling within the fair use provisions of the Copyright Act is granted by ASME to libraries and other users registered with the Copyright Clearance Center (CCC). Transactional Reporting Service provided that the base fee of $3.00 per article is paid directly to CCC, 27 Congress St., Salem, MA 01970. Request for special permission or bulk copying should be addressed to Reprints/Permission Department.

INDEXED by Applied Mechanics Reviews and Engineering Information, Inc. Canadian Goods & Services Tax Registration #126148048.

Journal of Fluids Engineering

Published Quarterly by The American Society of Mechanical Engineers

VOLUME 120 • NUMBER 3 • SEPTEMBER 1998

Technical Papers

(Contents continued on p. 487)

This journal is printed on acid-free paper, which exceeds the ANSI Z39.48-1992 specification for permanence of paper and library materials. ∞™

♻ 85% recycled content, including 10% post-consumer fibers.

Downloaded 03 Jun 2010 to 171.66.16.159. Redistribution subject to ASME license or copyright; see http://www.asme.org/terms/Terms_Use.cfm

(Contents continued)

Technical Briefs

Announcements and Special Notices

Journal of Fluids Engineering

Technical Forum

Questions in Fluid Mechanics: Natural Tree-Shaped Flows

By Adrian Bejan[1]†

The Hardest Questions. Last January, at a historic event that brought together biologists and engineers who see common ground in how living systems are built and function, Professor Trefethen (1998) reminded us to ask unanswered questions for which not even we know the answers. He also warned us that to formulate such questions is a very difficult task, and I agree. The difficulty is due to a subtlety, which I want to discuss in the first part of this column.

There is great diversity not only in topics but also in the way we formulate questions. I can imagine two extremes in which to formulate questions is easy. In one extreme, we may ask questions about areas in which we are completely ignorant. These are the questions for which even we, the speakers, have no hope. If we all proceed in this direction, our destination is the Tower of Babel. The very act of speaking (asking questions) requires the use of words to which the speaker attaches at least some understanding.

In the other extreme, we may ask questions for which the answers are well known. We do this routinely when we formulate problems for students in introductory courses. In this extreme we teach to the new generations the disciplines that are required by the profession. The beginner is well advised not to linger too much along this path, because too much discipline is poison to the individual's innate creativity.

The hardest questions are in between. They are the most likely to move the boulders that mark the frontier of knowledge. When we speak we are ignorant, but we also know ''just enough'' to be able to open our mouths intelligently. These valuable questions are triggered by hunches, or feelings of ''aha!'' Hunches occur when we meditate in isolation, or when we catch a glimpse of a development in a field where its importance is not recognized—a gemstone among the pebbles of the river bottom, seen by fish.

The fluid mechanics questions formulated in this column are driven by such a hunch—the accident that two years ago I was busy designing cooling systems for miniature electronic packages. I found that when the generated heat flows from a finite-size volume to one point, and when I have two conductive materials at my disposal (one with high conductivity, and the other with low conductivity), then the optimal heat flow path designed by me is a tree. Every single geometric feature of this structure is the result of a unique deterministic priniciple: the minimization of flow resistance subject to volume constraints (Bejan, 1997a, b).

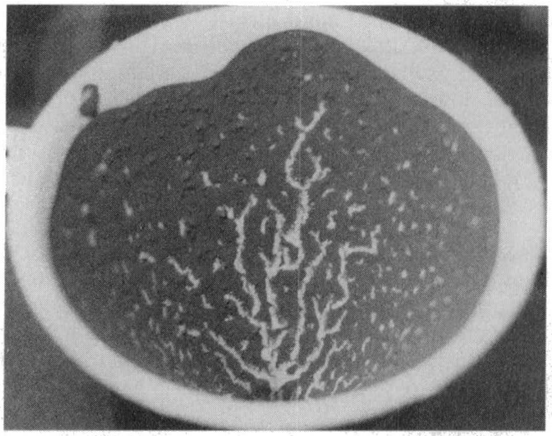

Fig. 1 The formation of the smallest rivers in the drainage basin of a funnel coated with unfiltered coffee sediment. The funnel was held vertically upward, and the photograph was taken at an angle, from above and the side. Note the marriage of shapeless flow (disorganization, diffusion) and flow with tree shape and structure (organization, streams) at the smallest, finite scale. Trees form all around the funnel, and are visible from above (Bejan, 1997b).

Why Are Tree Networks Everywhere in Nature? It is an undisputed fact that natural volume-to-point (or point-to-volume) flows have a common internal tree structure. Channels, or streams fill the volume partially, and the channels that are closer to the root point are thicker. The interstitial spaces are bathed by a flow with relatively high resistance (diffusion), which touches every point of the infinity of points that make up the volume. The tree structure unites the animate with the inanimate: lungs, river basins (Fig. 1), vascularized tissues, river deltas, neural dendrites, lightning, botanical trees and roots, dendritic crystals, the nerves of leaves, urban growth patterns and bacterial colonies. There are billions and billions of tree images in nature. What law is responsible for this permanent occurrence?

Why Cannot Channels Be Smaller Than a Characteristic Size? A common feature of natural trees is that the channels cannot be smaller than a certain length scale, which is why the channels fill the volume only partially. The smallest length scale is a characteristic of the flow medium, e.g., the alveolus in the

---

[1] Duke University, Department of Mechanical Engineering and Materials Science, Box 90300, Durham, NC 27708-0300.

† In memory of my mother Marioara Bejan (1914–1998), Pharmacist.

lung, the smallest capillary in the tissue, the smallest needle of the snowflake and the smallest rivulet (you may watch the development of the smallest rivers in your own coffee grounds, e.g., Fig. 1).

This question is extremely important today as the fractal geometry movement is promoting the idea that natural tree networks are fractal objects. They are not, because according to Mandelbrot's (1982) definition a fractal is an object generated by repeating *ad infinitum* an algorithm based on postulated similarity rules. The infinite sequence of stages of branching or coalescence is famously missing from natural tree systems. By Mandelbrot's own definition, and contrary to his claim in physics, the geometry of nature is not fractal. The fractal algorithm manipulator is forced to interrupt the sequence after only a few steps (the inner cutoff), so that we may be able to *see* the drawing. If natural structures were truly fractal, "we would be seeing nothing but blurred images and shades of gray" (Bejan, 1997b, p. 765). Similar words have appeared more recently in *Science* (Avnir et al., 1998). Why is the inner cutoff a necessary move in the descriptive (not predictive) graphic technique called fractal geometry?

Why Bifurcation (Pairing), and Why Does This Rule Break Down at Small Length Scales? Another striking feature of natural tree flows is the bifurcation, dichotomy, or pairing exhibited by the thicker channels. This rule—the integer 2—breaks down in the direction of smaller scales, such that the number of branches per branching stage increases (e.g., alveoli, the thinnest capillaries, pine needles on the smallest branch). Is the number of branches the result of an optimization process?

Is the Geometric Form of Nature the Result of the Constrained Minimization of Flow Resistance? The tree network is one of the three geometric forms of natural flow systems. The other two are the round cross-section (e.g., bronchial tubes, blood vessels, earth worms, underground caves) and the cross-section of rivers, which resembles a segment of circle. These cross-sectional shapes have been predicted successfully by minimizing the flow resistance subject to fixed volume (total cross-sectional area). Is the same principle responsible for the natural tree structures and all the features questioned in the preceding paragraphs?

Is the Same Optimization Principle Responsible for Turbulence? The common features of natural tree networks may hold additional meaning for fluid mechanicists. The coexistence of organized stream flow (channels) with disorganized molecular motion (diffusion) at the smallest macroscopic length scale reminds us of the elementary building block of turbulent flow fields: the smallest eddy. That in natural tree structures streams cannot be smaller than a characteristic length scale reminds us again of the smallest eddy. The finite sequence of stages (branching, or coalescence) that define the tree and fill the space reminds us of the transitions, cascades and ladders of turbulence.

To start questioning the origin of turbulence along the lines indicated in this column is highly appropriate. Classical fluid mechanics asks (correctly) why a shear flow does not remain laminar forever. The equivalent question for trees is why the volume-to-point flow is not always effected by a single flow mechanism—diffusion—with a quasi-radial flow pattern. The tree question of why dendritic patterns are seen only when flow systems are large and fast enough, becomes the turbulence question of why diffusion ceases to be the only mechanism when the shear flow becomes sufficiently thick and fast.

References

Avnir, D., Biham, O., Lidar, D. and Malcai, O., 1998, "Is the Geometry of Nature Fractal," *Science*, Vol. 279, 2 Jan., pp. 39–40.

Bejan, A., 1997a, "Constructal-Theory Network of Conducting Paths for Cooling a Heat Generating Volume," *International Journal of Heat and Mass Transfer*, Vol. 40, pp. 799–816.

Bejan, A., 1997b, *Advanced Engineering Thermodynamics*, Second Edition, Wiley, New York.

Mandelbrot, B. B., 1982, *The Fractal Geometry of Nature*, Freeman, New York.

Trefethen, L., 1998, Comments during the International Conference on Plants, Animals and Their Environments: An Integrative Perspective, Santa Barbara, CA, Jan. 12–16.

Journal of Fluids Engineering

Industry Perspectives

A Design Method for High-Speed Propulsor Blades[1]

Ki-Han Kim.[2] The authors presented a practical application of a new approach for marine propeller design that was first proposed by Mishima and Kinnas (1997). The new method for designing cavitating propellers could potentially change the traditional marine propeller design paradigm. The traditional propeller design philosophy is to design a propeller that performs optimally in the circumferentially uniform, but radially varying, flow in the subcavitating condition (Greeley and Kerwin, 1982). The cavitation aspects are considered empirically in the design stage by changing the geometric parameters, such as skew and chord distributions. In the new approach, Mishima and Kinnas developed a numerical optimization method for designing propeller blade sections that optimally operate in the cavitating condition in a spatially nonuniform flow. Since cavitation is unavoidable in high-speed ships and boats, it is prudent to consider the cavitation as part of the design parameters.

The authors further improved the versatility of the original method by expanding the design parameters, such as the nonlinear skew and the minimum pressure in wetted part of the blade, for optimization constraints. The main engine of the CAVOPT-3D code is the cavitating propeller analysis code, HPUF-3AL. HPUF-3AL is an unsteady lifting-surface code that was originally developed by Lee (1979) and improved by many researchers over the years. The performance of a propeller designed by the new method will be dependent upon the accuracy of the HPUF-3AL code.

Although this method has not yet been widely adopted for actual marine propeller designs, primarily due to the marine community's conservative culture, there is great potential for industry to adopt this method for design of high speed propellers for which cavitation is unavoidable.

References

Mishima, S., and S. Kinnas, 1997, "Application of a Numerical Optimization Technique to the Design of Cavitating Propellers in Non-Uniform Flow," *Journal of Ship Research,* Vol. 41.

Greeley, D., and J. E. Kerwin, 1982, "Numerical Methods for Propeller Design and Analysis in Steady Flow," *Transactions, SNAME,* Vol. 90.

Lee, C.-S., 1979, "Prediction of Steady and Unsteady Performance of Marine Propellers with or without Cavitation by Numerical Lifting-Surface Theory," Ph.D. thesis, M.I.T. Department of Ocean Engineering.

---

[1] By P. E. Griffin and S. A. Kinnas published in this issue pp. 556-562.

[2] Senior Hydrodynamicist, Naval Surface Warfare Center, Carderock Division, 9500 MacArthur Blvd., W. Bethesda, MD 20817.

A Numerical Methodology to Predict Exhaust Plumes of Propulsion Nozzles[1]

Marco Caporicci.[2] In view of the possible development of reusable space transportation systems, the European Space Agency (ESA) is funding vehicle system studies and the development of new technologies required by this new generation of launchers.

In the framework of the development of new propulsion systems, the availability of accurate numerical methods has shown to be crucial to obtain detailed information on the flow behaviour in the propulsive ducts. In many cases these very sophisticated tools require so long computational times, that their use becomes impractical for design purposes or for initial performance evaluations. In these cases the introduction of some approximation is welcome, if it gives the possibility to obtain initial estimates with reduced effort and provides a sufficient level of accuracy.

This paper represents an interesting example of development of such approaches. In particular, it provides a contribution to the simplification of the treatment of problems featuring a mixing between two jets with different thermodynamic characteristics.

The numerical prediction of the flow behavior in such conditions would require the use of very complex codes. Indeed, the flow is characterized by a mixing of two gases with different chemical composition and the use of a chemical nonequilibrium model is necessary to achieve detailed predictions. Moreover, the flow in the mixing layer is turbulent and accurate turbulent models as well as suitable grids, refined in the zone of interaction of the two jets, are required. Nevertheless, in many cases the practical goal of the study is to get indications on the flow structure or to provide preliminary evaluations of the performance of the propulsive device, whereas there is no interest in the knowledge of the details of the local flow structure, except for what affects the above issues.

The main contribution of the approach presented in this paper, which makes it interesting from the point of view of practical applications, is the possibility to allow a substantial reduction of the computational time required for the numerical solution, without deterioration of the accuracy, at least as far the performance parameters are concerned. Indeed, the idea of replacing the mixing layer by a contact discontinuity surface does eliminate the major causes of the computational burden, while preserving the representation of the main physical aspects of the

---

[1] By F. Nasuti, R. Niccoli, and M. Onofri published in this same issue pp. 563-569.

[2] Future Programmes and Tech. Coordinator, Directorate of Launchers, European Space Agency, 75738 Paris, France.

phenomena. Moreover, the large number of analytical and experimental validations presented, show the robustness and versatility of the proposed technique.

The method has been recently applied by the authors of this paper in a study performed in the framework of the ESA Future European Space Transportation Investigations Programme (FESTIP), that concerns the analysis of the flow behavior in advanced configurations of modular plug nozzles exhausting on a central spike. In particular, the variation of the nozzle performance caused by the change of the ratio of the pressure at module exit and the ambient pressure was studied. In fact, as this ratio changes along the flight trajectory, the slope of the boundary between external flow and jet exhausted from a primary module changes as well, generating a different flow structure and consequently different nozzle efficiency. The zone of interaction between the propulsive jet and the external flow was simulated by a contact discontinuity surface and numerically treated by an advanced version of a fitting technique, as proposed in the paper. The method was able to provide fast response and accurate solutions, despite the possible irregular profiles of the jet.

Applications of similar approaches were also successfully carried out in the framework of previous ESA studies. As an example, during the European Launcher Investigation and Technology Effort (ELITE) Programme, a study was carried out to assess the efficiency of a nozzle film cooling concept, using the cooling exhaust gas of the turbopump exhaust gases (TEG) injected tangentially in the divergent section of the nozzle. Predictions of the mixing layer generated by the main flow and TEG injection were carried out by simulating the interaction of the two streams by a contact surface. The study intended also to evaluate if the nozzle performance would increase, as a secondary effect of the TEG injection.

Also in this case the results obtained were very satisfactory when compared to those obtained by more sophisticated and time-consuming methods.

Turbulent Flow Past an Array of Bluff Bodies Aligned Along the Channel Axis[1]

Jen-Ming Hsu.[2] The authors are the first to investigate the periodic turbulent flow in a channel with a detached rib array experimentally and numerically. The results obtained in this article are very valuable to both heat exchanger and air conditioning technologies. The measured mean flow data as well as the turbulent fluctuation quantities discussed by the authors can be a benchmark for CFD researchers in the above related industries.

In regard to the discussion of the difference between experimental data and computational results, the authors have suggested that a low-Reynolds number turbulence model can be used to improve the predictions near the rib corners. The low-Re number turbulence model is normally more accurate than the high Re number turbulence model when the large separation exists in the flow. The proposed improvement for prediction is very positive for further investigation. They also point out the crucial role played by a complete set of inlet flow conditions, including detailed profiles of mean and turbulent quantities, in affecting the computational results; however, experimentalists often fail to provide such a set of data. The further suggestion is to look into the increase of grid in both streamwise and transverse directions and to compare the difference of the fluctuation quantities instead of axial mean velocity profile. The resolution to the fluctuation quantities requires a higher grid density. Also, performing flow visualization to compare with the computed flow patterns shown in Fig. 14(*a*) will be a useful aid in understanding the flow characteristics past the rib array. The three-dimensional effect will also be more clearly revealed from flow visualization experiment. Future works on the spectrum of flow unsteadiness and heat transfer measurements are encouraged.

---

[1] By T. M. Liou and S. H. Chen published in this issue pp. 520-530.

[2] Manager, Energy Research Lab., Power Research Institute, Taiwan Power Company, 84 Ta-An Rd., Shu-Lin, Taipei, Taiwan.

Three-Dimensional Laminar Flow in a Rotating Multiple-Pass Square Channel With Sharp 180-Deg Turns[1]

Jen-Ming Hsu.[2] Taiwan Power Company (TPC) is the sole electric power company and one of the largest turbine users in Taiwan ROC. For keeping the whole system's operation in high performance, TPC spent some 60 million U.S. dollars in research and development activities annually in a few years. The paper presented by Prof. Hwang and his colleague is part of the results of the project sponsored by TPC, which dealt with the rotating return flow cooling system. The return flow cooling system investigated in this paper is based on the first stage rotor blades of turboengines, such as, Simens V84.2, etc., which is used as the first buckets to cope with a noticeable rise in firing temperature.

To assure the reliability as well as the thermal efficiency of the turboengines, cooling of the turbine blade is one of the major research topics that we are currently supporting. This paper is a carefully planned study of flow and pressure losses in a rotating return flow passage. The significant contribution of this paper is to provide a good understanding of the wall frictions in the radially rotating channel. In addition, the information of the pressure losses within the rotating sharp turns is also very important to the design of the cooling flow system. As we know, it is still difficult at present to acquire experimental friction-loss data in a rotating return flow passage, and no experimental data of this kind are available yet. This paper has proposed an innovative way for solving the problem by making a modification on a reasonable geometrical domain. This simple model provides a straightforward approach to help understand the rotation effect on pressure drop characteristics in return flow passages.

I am impressed with their contribution and encourage them to include higher Reynolds number in their future works, which would be more representative of the actual turbomachinery operating conditions.

Ali H. Hadid.[3] The paper entitled "Three-Dimensional Laminar Flow in a Rotating Multi-Pass Square Channel With Sharp 180-Deg Turns," authored by Jenn-Jiang Hwang and Dong-Yuo Lai highlights notable aspects of laminar flow in a rotating duct with 180 deg turns. The emphasis of the paper on laminar flow somehow restricts its relevance to industry. The authors, however, nicely combine numerical and experimental techniques to describe the strong effects of rotation induced Coriolis forces on the secondary flow and flow stability at low Reynolds numbers. As such, the results of the paper are useful to further our understanding of the basic physics of rotating flows which can be a useful tool to study the impact of second-

---

[1] By Jenn-Jiang Hwang and Dong-Yuo Hai published in this issue pp. 488-495.

[2] Manager, Energy Research Lab., Power Research Institute, Taiwan Power Company, 84 Ta-An Road, Shu-Lin, Taipei, Taiwan.

[3] Senior Engineering Specialist, The Boeing Company, Rocketdyne Propulsion and Power, Canoga Park, CA 91309.

ary flows under rotation in multistage turbomachinery applications. However, for industrial applications in general and propulsion and power in particular emphasis should be placed on turbulent and transitional flows which are common occurrences. For example, transition flows in ducts of jet engines and turbulent flows in rotating cooling passages of gas turbine blades are important.

Supersonic Jet Noise Reductions Predicted With Increased Jet Spreading Rate[1]

Patrick M. Hurdle.[2] During the 1960s through the mid 1970s considerable research was conducted to reduce noise from subsonic jets. Many of the concepts developed during this time were implemented by the Civil Aviation Industry and resulted in a reduction of the noise from commercial jet aircraft. This was one of the elements responsible for the significant growth of commercial aviation. In the early 1970s, with U. S. Government support, efforts were started to develop a supersonic transport aircraft. These efforts were terminated partly due to the problem of noise and sonic boom. Within the last few years there has been renewed interest in developing a Supersonic Civil Transport in order to further advance commercial aviation. To make this a reality, problems due to noise and sonic boom will have to be mitigated. As in the case of subsonic jets, this will be accomplished by using concepts that are presently being developed from ongoing research, such as the work described in this paper. This paper derives a simplified model, as compared to numerical calculations based on the full Navier-Stokes equation, to predict changes in the far field directivity peak level based on the mixing layer spreading rate. This model should greatly assist in the prediction and interpretation of future experiments conducted to measure the effects of enhanced mixing on noise reduction from supersonic jets.

Thonse R. S (Srini) Bhat.[3] Noise of all aircrafts is a big concern due to environmental reasons. This is especially true for the supersonic jets exhausting from the propulsion systems of high speed civil transport airplanes. As a result, the efforts at reducing noise, supersonic jet noise in this case, becomes very important. This paper discusses one such effort on reducing supersonic jet noise by increasing the jet spreading rate.

This paper predicts the reduction in supersonic jet noise with enhanced mixing (at fixed jet operating conditions) for single, supersonic, axisymmetric jets. The mixing noise is assumed to be dominated by the large-scale structures in the shear layer and these structures are modeled as linear superposition of instability waves. The noise radiated to far field is determined based on the axial growth and decay of the instability wave. This approach has been well established. The attractive feature of this approach is that it is relatively simple to implement and is not computationally intensive.

The contribution of this study is in the application of the instability wave model to investigate the effects of increased jet spreading rate on jet noise. The results presented are very encouraging and show a potential of achieving substantial noise reductions through enhanced mixing at fixed jet operating conditions. However, the model has certain limitations. First of all, it has been assumed that the initial amplitude of the wave does not change with spreading rate of the jet. This assumption may not be valid and needs further investigation. Second, this study does not consider the effects of increased jet spreading rate on the performance of the engines. One of the main constraints in applying noise reduction concepts to industrial problems is the impact on performance. So, further work is needed to investigate if there is any performance loss due to enhanced mixing before this concept can be applied on aircraft engines.

---

[1] By M. D. Dahl and P. J. Morris published in this issue pp. 471-476.

[2] Boeing Technical Fellow, The Boeing Company, Rocketdyne Propulsion and Power, 6633 Canoga Avenue, MS I831, P.O. Box 7922, Canoga Park, CA 91309-7922.

[3] Boeing Commercial Airplane Group, Noise Engineering Technology, P.O. Box 3707, MS 67-ML, Seattle, WA 98124-2207.

Perspective: Flow at High Reynolds Number and Over Rough Surfaces—Achilles Heel of CFD

V. C. Patel
Iowa Institute of Hydraulic Research and
Department of Mechanical Engineering,
The University of Iowa,
Iowa City, IA 52242

The law of the wall and related correlations underpin much of current computational fluid dynamics (CFD) software, either directly through use of so-called wall functions or indirectly in near-wall turbulence models. The correlations for near-wall flow become crucial in solution of two problems of great practical importance, namely, in prediction of flow at high Reynolds numbers and in modeling the effects of surface roughness. Although the two problems may appear vastly different from a physical point of view, they share common numerical features. Some results from the 'super-pipe' experiment at Princeton University are analyzed along with those of previous experiments on the boundary layer on an axisymmetric body to identify features of near-wall flow at high Reynolds numbers that are useful in modeling. The study is complemented by a review of some computations in simple and complex flows to reveal the strengths and weaknesses of turbulence models used in modern CFD methods. Similarly, principal results of classical experiments on the effects of sand-grain roughness are reviewed, along with various models proposed to account for these effects in numerical solutions. Models that claim to resolve the near-wall flow are applied to the flow in rough-wall pipes and channels to illustrate their power and limitations. The need for further laboratory and numerical experiments is clarified as a result of this study.

Introduction

Methods of computational fluid dynamics (CFD) place no a priori limit on the Reynolds number at which they may be applied. At least this is the impression that is conveyed by the proponents of CFD. The limitations are quite easily revealed, however. These limitations arise from those of the numerical algorithm and those inherent in the physical model. While this paper is focused on the latter, namely, the component that addresses the physics of the flow at high Reynolds numbers, it is difficult to entirely divorce the numerical factors. Table 1, adapted from Dolphin (1997) and Coder and Flechner (1991), shows that the Reynolds number in ship hydrodynamics applications covers a range wider than that found in most other branches of fluids engineering. In principle, CFD models should be applicable to this entire range, eliminating or diminishing the need for model tests at low Reynolds numbers and extrapolations to full scale. Similar comments apply to other applications. Yet, there are very few attempts made to apply and evaluate CFD at the upper end of this Reynolds number range.

The connection between Reynolds number and surface roughness is made quite early in one's education in fluid mechanics through the Moody diagram for friction factor in smooth and rough pipes. In fact, to many practicing engineers, this would have the authority of gospel, with much of the background forgotten. It is sobering to ponder the meager theoretical and empirical basis for this generally accepted truth, one on which is built a large part of fluids engineering practice.

Flow over a rough surface occurs in diverse situations, including atmospheric wind over terrain of varying roughness and water flow over a river bed in the natural environment, and flow past man-made surfaces, such as those of airplanes, ships, turbomachinery, heat exchangers, and piping systems, to name only a few. Surface roughness affects, in addition to the flow itself, the transport of heat and mass in the atmosphere, and transport of sediment in rivers. In other applications, it affects resistance (or drag) and heat transfer. In all cases, the principal effect of roughness is a change in the velocity and turbulence distributions near the surface. As the type and relative size of roughness varies widely from one application to another, it might be expected that the problem of determining the effect of roughness in these diverse fields of fluids engineering would be treated in different ways. While a cursory review of the literature in each of these fields might suggest just such a situation, in reality, all of these fields rely on an empirical framework and a rather narrow database, both of which were established from observations in what are now regarded as classical experiments in pipes and boundary layers. Subsequent experiments and correlations have sought to relate different types of roughness in different fields to the results of these classical experiments. Thus, for example, there is considerable work which attempts to relate the regular roughness geometry used for heat-transfer enhancement, and similarly, corrosion and fouling roughness encountered in ships, to sand-grain roughness employed in the classical experiments. Similar efforts have been made with respect to terrain roughness in the atmospheric boundary layer, and bedform and gravel roughness in hydraulics. Application of CFD to flow over rough walls is limited by a database that pertains to steady two-dimensional or axisymmetric flow in which there exists substantial balance between turbulence production and dissipation.

A Bit of Religion—Textbook Results

Fluids engineering textbooks show that the Moody diagram, reproduced here in Fig. 1, is principally based on the experiments of Colebrook and White (1937) in pipes roughened with

---

Contributed by the Fluids Engineering Division for publication in the JOURNAL OF FLUIDS ENGINEERING. Manuscript received by the Fluids Engineering Division April 17, 1998; revised manuscript received June 26, 1998. Associate Technical Editor: P. Bradshaw.

Table 1 Reynolds numbers of ships, adapted from Dolphin (1997) and Coder and Flechner (1991)

Ship type	Ship name	Length ft	Velocity knots	Reynolds number Re × 10^6
Aircraft Carrier	Nimitz	1,040	30	4,117
Battleship	Iowa	887	35	4,097
Passenger Liner	United States	990	28	3,658
Crude Oil tanker	Mobil Magnolia	1,063	15	2,104
Frigate	O.H. Perry	445	29	1,703
Submarine	Ohio	560	20	1,478
Heavy Lift Transport	Mighty Servant 3	591	14	1,092
Attack Submarine	Los Angeles	360	20	950
Ferry	John F Kennedy	285	15	564
Mine Warfare	Avenger	224	14	414
Tug	Valerie F.	138	15	273
12-m Yacht	Stars & Stripes	47	15	93

sand grains, and the existence of the law of the wall, which is formally written

$$u^+ = F(y^+, k_s^+) \tag{1}$$

where

$$u^+ = u/u_\tau, \quad y^+ = u_\tau y/\nu, \quad k_s^+ = u_\tau k_s/\nu, \quad u_\tau = \sqrt{\tau_w/\rho} \tag{2}$$

u is the velocity at a distance y from the wall, k_s is the equivalent sand grain roughness height, ν is the kinematic viscosity of the fluid, and u_τ is the friction velocity defined by the wall shear stress τ_w and the fluid density ρ. The function F in Eq. (1) includes the sublayer, the buffer layer, and the logarithmic layer in which, for a "hydrodynamically smooth" surface,

$$u^+ = \frac{1}{\kappa} \ln y^+ + B \tag{3}$$

where $\kappa = 0.418$ and $B = 5.45$ are constants. Values of k_s^+ below which the surface is hydrodynamically smooth, and beyond which lies the transitional regime, vary from 2.25 to 5 (Bradshaw, 1998). The smooth-wall constants quoted here are those recommended by the author (Patel, 1965) on the basis of Preston tube calibrations although other pairs of values are equally well accepted. However, in one recent book on turbulence modeling the Karman constant κ takes values ranging from 0.4 to 0.435, depending on the turbulence model being described, without any discussion, or consideration for B. Indeed, it has been suggested by some that an international convention may be needed to secure agreement on a fixed pair.

If Eq. (1) is assumed to approximate the velocity distribution throughout the pipe, ignoring departures from it in the sublayer and the buffer layer near the wall, and in the core of the pipe, its integration leads to

$$\frac{1}{\sqrt{f}} = 2.0 \log (\mathrm{Re}\sqrt{f}) - 0.8 \tag{4}$$

where f and Re are, respectively, the friction factor and Reynolds number, defined by

$$f = 8\tau_w/\rho V^2 = 8(u_\tau/V)^2, \quad \mathrm{Re} = Vd/\nu \tag{5}$$

d being the pipe diameter and V the average velocity. The constants in Eq. (4) were adjusted to secure agreement with Nikuradse's data. This is *Prandtl's universal law of friction for smooth pipes* (Schlichting, 1968, equation 20.30). Schlichting goes on to say "*From its derivation it is clear that it may be extrapolated to arbitrarily large Reynolds numbers, and it may be stated that measurements with higher Reynolds numbers are, therefore, not required.*"

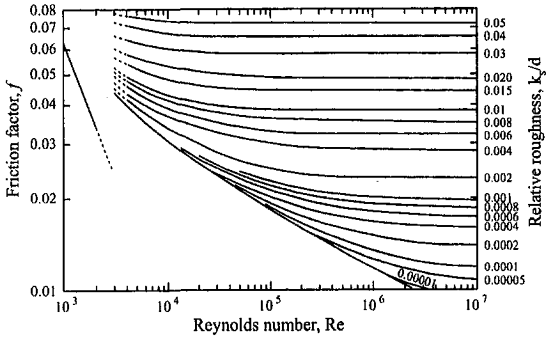

Fig. 1 Friction factor in pipe flow, Moody diagram

The long-accepted universality of Eqs. (3) and (4) has been challenged by Barenblatt et al. (1997), who employ similarity arguments and asymptotic methods to obtain, in place of the logarithmic law, Eq. (3), a power law

$$u^+ = Cy^{+^\alpha} = \left[\frac{1}{\sqrt{3}} \ln \mathrm{Re} + \frac{5}{2}\right] y^{+^{3/2 \ln \mathrm{Re}}} \tag{6}$$

in which the dependence of the "constants" on the Reynolds number was again determined by recourse to Nikuradse's data. Integration of Eq. (6) across the pipe then leads to the corresponding friction formula

$$\left(\frac{f}{8}\right)^{2(1+\alpha)} = \frac{e^{3/2}(\sqrt{3} + 5\alpha)}{2^\alpha \alpha(1 + \alpha)(2 + \alpha)}, \quad \alpha = \frac{3}{2 \ln \mathrm{Re}} \tag{7}$$

which the authors claim agreed with Nikuradse's friction data without further adjustment of constants. According to Barenblatt et al. (1997), the logarithmic law results from assumptions of *complete similarity* while the power law is the result of assuming *incomplete similarity,* which admits Reynolds number dependence of the constants in the logarithmic law.

It is not the intent here to explore the differences between the two results, for they are still subject of considerable disagreement among researchers (see, for example, Zagarola, Perry and Smits, 1997; Barenblatt and Chorin, 1998; and Smits and Zagarola, 1998). They are presented here only to illustrate the critical role the classical experimental data of Nikuradse continue to play in determining the effects of Reynolds number. It is important here to point out that the highest Reynolds number in these experiments was 3.4 × 10^6, whereas extrapolations of friction formulas to much higher values are of interest, particularly in ship hydrodynamics (see Table 1).

The literature on roughness follows similar lines. It is not surprising that the continuing discussion about the logarithmic versus power laws also involves the possible role of surface roughness with increasing Reynolds numbers. The data of Nikuradse (1932) with uniform sand-grain roughness, Colebrook and White (1937) (see also Moody, 1944) with nonuniform sand, Schlichting (1936) with distributed regular roughness elements, Moore (1951) with regularly spaced transverse ribs, and Hama (1954) with wire-mesh roughness are most often used to show that the effect of roughness is observed in the logarithmic law:

$$u^+ = \frac{1}{\kappa} \ln y^+ + B - \Delta B \tag{8}$$

where ΔB, the so-called roughness characterization function, depends not only on the size but also the type of roughness (see Fig. 2 adapted from Clauser, 1956). For uniform sand grain roughness, White (1991) suggests a curve-fit

$$\Delta B = \frac{1}{\kappa} \ln (1 + 0.3k_s^+) \tag{9}$$

Integration of Eq. (8) with correlations such as (9) leads to the friction formula for pipes with rough walls (see White, 1991)

$$\frac{1}{\sqrt{f}} = 2.0 \log \left(\frac{\mathrm{Re}\sqrt{f}}{1 + 0.1 \frac{k_s}{d} \mathrm{Re}\sqrt{f}} \right) - 0.8 \tag{10}$$

However, the Moody diagram is based on the correlation formula of Colebrook:

$$\frac{1}{\sqrt{f}} = -2.0 \log \left(\frac{k_s/d}{3.7} + \frac{2.51}{\mathrm{Re}\sqrt{f}} \right) \tag{11}$$

For large roughness, in the fully-rough regime ($k_s^+ > 60$), substitution of Eq. (9) in (8) gives

$$u^+ = \frac{1}{\kappa} \ln \frac{y}{k_s} + 8.5 \tag{12}$$

independent of viscosity, and therefore Reynolds number. The constant in this formula corresponds to Nikuradse's values of $\kappa = 0.4$ and B = 5.5.

Fluids textbooks also describe extensions of these results to predict the drag of smooth and rough flat plates, although in this case the logarithmic law of the wall has to be supplemented by corrections for the outer, velocity-defect layer. The above summary of classical textbook material is presented to remind us of the basis on which modern CFD relies for predictions at high Reynolds numbers and on rough walls, not only for simple canonical flows, such as pipes, channels and flat-plate boundary layers, but also very complex and practical flows.

Flow at High Reynolds Numbers

Pipe Flow. Nikuradse's data extended to Re = 3.4×10^6 for smooth pipes, and only to 10^6 for rough pipes, but the derivation of the friction formulas in the form of Eqs. (4), (10), and (11) has led to their extrapolations to far greater values, as is evident from most plots of Moody diagrams and flat-plate resistance in textbooks. As already noted, the validity of the logarithmic law, which underpins the friction formulas, has been questioned in recent years and data from the recent 'super-pipe' experiments performed at Princeton University (Zagarola, 1996; Zagarola and Smits, 1997) have been used by both sides to support their claims.

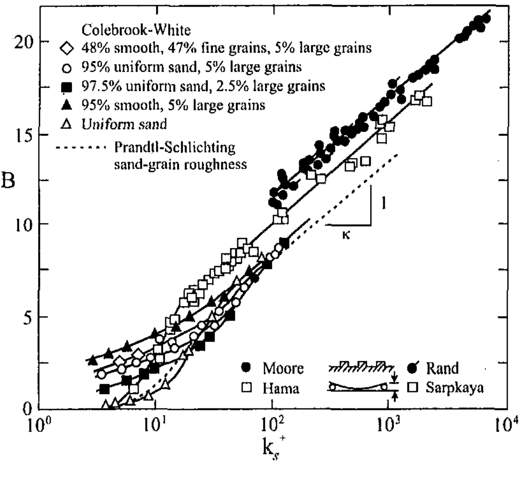

Fig. 2 Roughness characterization function, adapted from Clauser (1956)

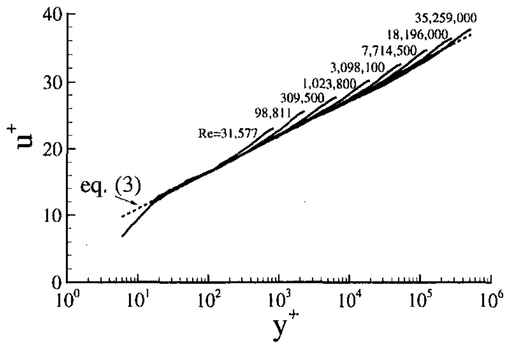

Fig. 3 Velocity profiles in Princeton super-pipe experiment, Zagarola (1996)

The Princeton data are plotted in traditional format in Fig. 3. They indicate that there is no a priori reason to discard the logarithmic law, especially if it is viewed as no more than an experimental correlation of near-wall velocity profiles. Smits and Zagarola (1998) recommend $\kappa = 0.436 \pm 0.002$ and $B = 6.15 \pm 0.12$ to provide a better fit to the data at Re $> 10^6$ (some of which lie below the dashed line in Fig. 3). The data are plotted in a different format in Fig. 4 to better reveal the logarithmic region. Now it is seen that the logarithmic region grows with increasing Reynolds number with respect to the upper limit of y^+. Any change in the lower limit cannot be established, however, as accurate measurements very close to the wall are difficult. From Figure 4, a case can be made to increase κ at high Re, as recommended by Smits and Zagarola, and even to make it a function of Re, as suggested by Barenblatt et al. (1997). Regardless of the position one takes on this issue, the increasing range of validity of the logarithmic law with increasing Reynolds number in terms of wall coordinates is good news for CFD methods that use wall functions. On the other hand, not having a consensus on the constants in a widely employed correlation, the logarithmic law, has unknown effects on the results of CFD calculations.

It is natural to first inquire whether modern CFD is able to reproduce this information before looking at more complex flows. Fully developed flow in a pipe is a very simple calculation for any modern CFD method because it requires no inputs other than the Reynolds number. Invariance in the axial direction can be exploited and grid refinement of any order can be used to ensure solutions that are insensitive to grid density. For turbulence models that do not explicitly use the logarithmic law, i.e., wall functions, these calculations provide a very direct test of the models.

Constantinescu and Patel (1998) performed calculations for flow in a smooth pipe over the Reynolds number range of the Princeton experiments with a numerical method developed for very complex three-dimensional flows. These calculations were made with two state-of-the-art, two-equation, near-wall turbulence models, namely, a two-layer k-ϵ model (Chen and Patel, 1988) and two versions of the k-ω model (Wilcox, 1991). These models solve the equations up to the wall, imposing the no-slip condition, and therefore are not directly coupled to the logarithmic law. They are also representative of the most commonly used models in CFD methods designed for complex flow.

Table 2 compares the friction factors predicted with two turbulence models with values obtained from the Moody diagram [Eq. (11) with $k_s = 0$] and measured in the Princeton experi-

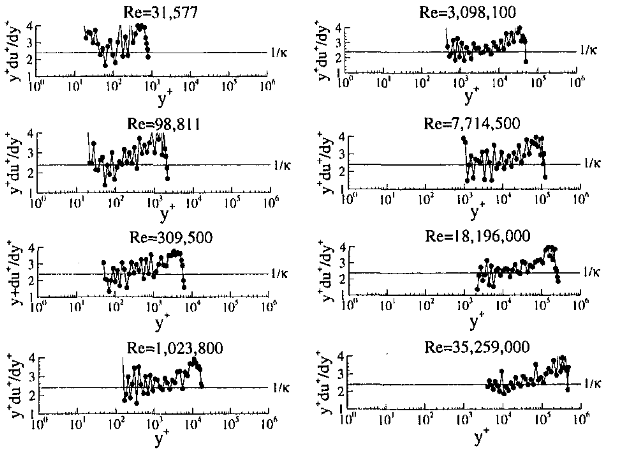

Fig. 4 Princeton super-pipe data plotted to reveal the logarithmic region

ments. The fact that the measured values fall increasingly above those of the Moody diagram with increasing Reynolds number, by as much as 5 percent at the highest value, might suggest a roughness effect. On the other hand, it is found that the agreement between the experiments and CFD solutions improves with increasing Reynolds number, the difference at the highest Reynolds number being around 1 percent.

To explore this further, it is necessary to examine the velocity profiles, which are plotted in Fig. 5. The data show a region of agreement with the logarithmic law at all Reynolds numbers, with no hint of a roughness effect (which would have resulted in a downward shift of the data). Also evident is the increasing range of y^+ in which the logarithmic law applies. The two CFD calculations differ from each other and from the data in important respects. The k-ϵ model shows better agreement with the data and faithfully reproduces the increasing logarithmic region, while the k-ω model agrees with the data only at the higher Reynolds numbers, which is somewhat surprising because it is the "low Reynolds number" version of the model that was used here. The difference between the two models at low Reynolds numbers, and particularly in the buffer layer, may have significant consequences in some applications. Even though the data in this region may be subject to probe interference errors, they tend to favor the k-ϵ model calculations. Finally, it is significant that neither model predicts the observed wake component of the velocity profile. In fact, the models show no wake component at the lower Reynolds numbers, and underpredict its magnitude at the higher Reynolds numbers.

An anonymous reviewer of this paper was inspired to make calculations using the near-wall k-ϵ turbulence model of Jones and Launder (1977). Friction factors in excellent agreement with the Moody values were obtained over the entire range of Reynolds numbers, and the calculated profiles showed a wake component at low as well as high Reynolds numbers. These results are clearly at variance with those of Table 2. Disagreements of this type and magnitude are not uncommon in modern CFD, but the fact that they occur in such a simple flow undermines confidence in CFD. Such disagreements will continue to provide ammunition to skeptics of CFD until their sources are revealed and corrected by careful scrutiny of the numerical and physical contents of the calculations.

Table 2 *Friction factor in a smooth pipe*

Re	100f Moody, Eq. (4)	100f experiments	100f k-ϵ model	100f Low Re k-ω mode
31,577	2.321	2.324	2.654	2.691
98,811	1.803	1.802	1.938	1.975
1,023,800	1.160	1.182	1.180	1.185
4,420,300	0.915	0.948	0.936	0.950
29,927,000	0.695	0.731	0.736	0.741

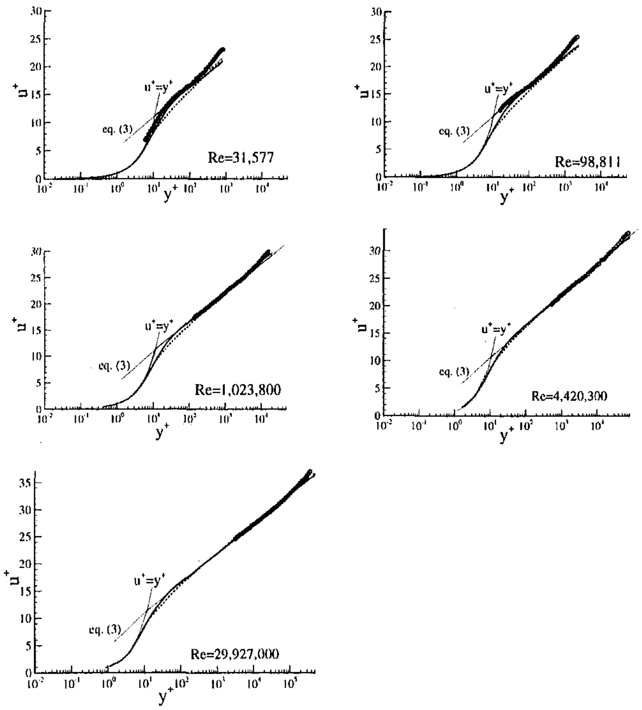

Fig. 5 Velocity profiles in pipe flow over a range of Reynolds numbers Symbols: experiment; solid line: two-layer k-ϵ model; broken line: low-Re k-ω model

Flat-Plate Boundary Layer. Friction formulas for flat plates have been of great interest in ship hydrodynamics for their importance in the prediction of frictional resistance of ships by extrapolation of model results to full scale. Dolphin (1997) recently calculated the total resistance (integrated friction) coefficient of a smooth plate as a function of Reynolds number based on plate velocity and length. The calculations were performed with a well-established CFD code, which uses the eddy-viscosity model of Baldwin and Lomax (1978). Due care was given to grid spacing and convergence. Figure 6 compares these CFD results with the Prandtl-Schlichting formula, which Schlichting (1968) claims *is valid in the whole range of Reynolds numbers up to Re = 10^9*, and the generally accepted correlation line of the International Towing Tank Conference (ITTC). The rather small difference between the ITTC line and the Prandtl-Schlichting formula for Re > 10^6 is not surprising as both are based on the same physics. The larger differences at the lower Reynolds numbers arise from an empirical adjustment of the ITTC line to secure better correlation between model and full-scale ship resistance data. Be that as it may,

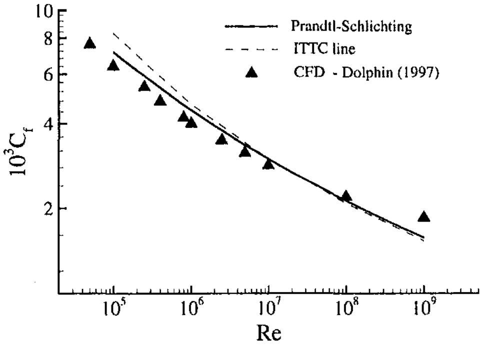

Fig. 6 Frictional resistance of flat plates

there is a very significant difference between these two formulas and results of modern CFD over the entire range of Reynolds numbers. At the highest Reynolds number of 10^9, the CFD calculation gives a value more than 10 percent higher than that of the classical resistance formula and the ITTC line.

Figure 7 shows the calculated velocity profiles in wall coordinates. As in pipe flow, the logarithmic portion, which is well reproduced, occupies an increasing range of y^+ as the Reynolds number increases. The differences in the friction coefficient are all the more surprising because the CFD model embodies the same well known and generally accepted correlation on which the earlier formulas are based. There are a number of factors which could contribute to the observed differences, including *transition location, and leading and trailing-edge effects, at the* lower Reynolds numbers, and constants in the logarithmic law and correlations for the outer (velocity-defect layer) over the entire range. Nevertheless, the differences at the higher Reynolds numbers are particularly worrisome if CFD is to bridge the gap between experiments and full scale.

Boundary Layer on a Body of Revolution. The next example is that of the boundary layer on a body of revolution. Ju and Patel (1991) describe calculations of the flow on a submarine-like body for which data were obtained by Coder (1982, 1988) from experiments in the Twelve Foot Pressurized (TFP) wind tunnel at the NASA Ames Research Center and the National Transonic Facility (NTF) at the NASA Langley Research Center. Measurements were limited to surface pressures and velocity magnitudes (Q) in the boundary layer. The estimated uncertainty in the velocity measurements ranged from 3.1 to 0.6 percent from the lowest (1.2×10^7) to the highest (1.046×10^9) Reynolds number, based on tunnel velocity, U_o, and body length, L (about 6 m). The calculations were made with the k-ϵ model, but with wall functions, applying equation (3) at the two inner-most grid points close to the wall (see Patel, Chen and Ju, 1988, for details of this two-point wall-functions approach).

The data are plotted in Fig. 8 using the friction velocity quoted by Coder for the measurements and the calculated friction velocity for the numerical solutions. Equation (3) is also shown. It is clear that, (*a*) the numerical solutions are consistent with the logarithmic law used to provide the boundary conditions; (*b*) there is excellent agreement between the calculations and data at the higher Reynolds numbers; (*c*) at the lower Reynolds numbers, either the measured velocities are too low or the friction velocities of Coder are too high; and (*d*) most importantly for the present purposes, the logarithmic law is valid for increasing values of y^+ as the Reynolds number increases. With regard to the last point, we note that in the numerical solutions at the highest Reynolds number, the innermost grid point was located at y^+ around 1400.

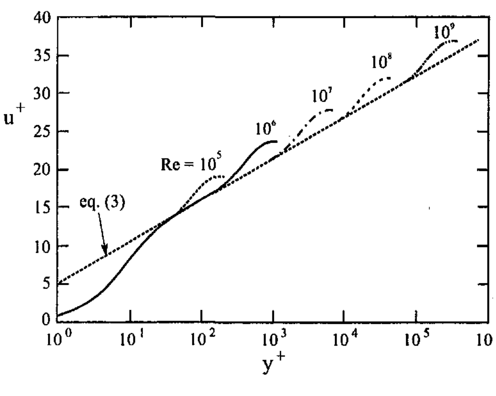

Fig. 7 Calculated velocity profiles in flat-plate boundary layer, Dolphin (1997)

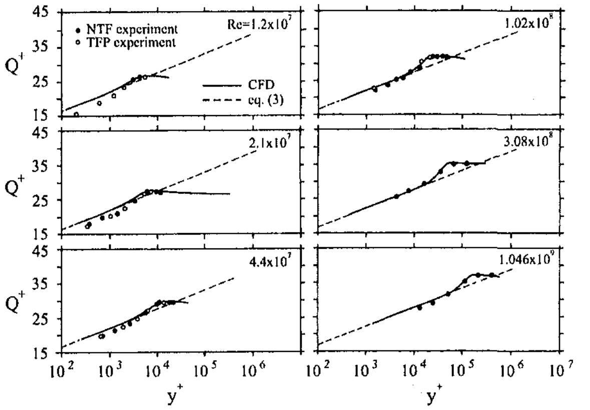

Fig. 8 Velocity measurements on a body of revolution, Ju and Patel (1991)

The data of Coder did not extend to the region near the body stern where pressure gradient and transverse surface curvature effects become dominant. The comparisons between CFD predictions and experiment were confined to the boundary layer on the parallel middle body where both these effects are negligible, and the flow is quite similar to that on a flat plate. The difference between these calculations and those of Dolphin discussed above lies in the turbulence model and the treatment of the wall boundary conditions.

Ship Boundary Layer and Wake. The design of a ship propeller requires knowledge of the velocity field at the transverse section where the propeller is to be installed. This is an example of a complex three-dimensional flow developing rapidly from a thin boundary layer toward an unconstrained wake under the influence of strong longitudinal and transverse pressure gradients. Information on the "nominal wake" (in the absence of the propeller) at full-scale is usually obtained by measurements on models and extrapolations (or scaling) to the prototype. Reviews by Tanaka et al. (1984) and Tanaka (1988) indicate that methods to predict scale effects in this manner are based on well known correlations for two- and three-dimensional turbulent boundary-layers or those of two-dimensional and axisymmetric wakes, or combinations of these flows.

To test the potential of modern CFD to address the scaling problem, Ju and Patel (1991) applied the numerical method of Patel, Chen and Ju (1988) to calculate the flow over the stern of a laboratory research ship hull known as the HSVA Tanker over a range of Reynolds numbers up to 5×10^9. These calculations employed the k-ϵ model with two-point wall-functions, with corrections for pressure gradients and flow three-dimensionality, and were possible only by exploiting the observation that the law of the wall applies to larger values of y^+ as the Reynolds number increases. Although this ship was never built, quite extensive data were gathered from model tests and used to evaluate CFD models at international workshops (Larsson, Patel and Dyne, 1991; Kodama, 1994). To evaluate the scaling methods, Ju and Patel regarded the velocity field calculated at the lowest Reynolds number as the model-scale information, applied two representative scaling methods to estimate the velocity field at the highest Reynolds number, assumed to represent the full-scale ship, and compared them with the CFD calculation at that Reynolds number. Only typical results of this exercise are presented here.

Figure 9 shows contours of axial velocity (U/U_o) in the propeller plane at two Reynolds numbers, namely, Re = 5×10^6 representing model scale, and Re = 5×10^9 representing full scale, U_o being the ship velocity, and L the ship length. The shrinkage in the region of viscous flow is evident but the reduction is not as large as might be expected simply on the

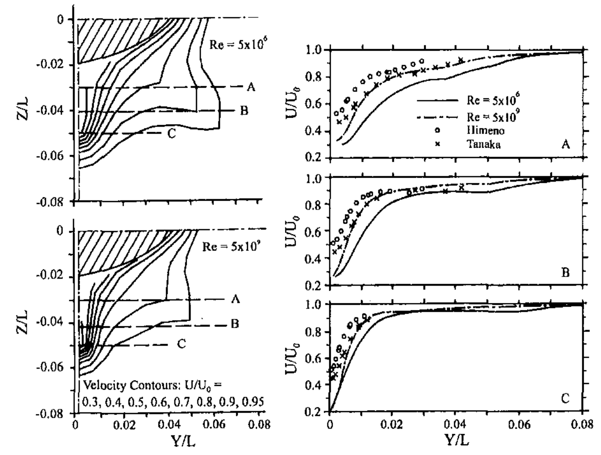

Fig. 9 Reynolds-number scaling of velocity distribution in the propeller plane of a ship hull, (*a*) Contours of axial velocity; (*b*) velocity profiles along lines *A*, *B*, and *C*, Ju and Patel (1991)

basis of boundary layer theory. In fact, this is a central difficulty of the problem and one that only CFD might answer. Figure 9(*a*) also shows the local hull section, and three horizontal lines along which the velocity profiles are compared in Fig. 9(*b*). The profiles at the two Reynolds numbers (indicated by lines) were calculated by CFD. Comparing the profile for Re $= 5 \times 10^9$ with those predicted by the two scaling relations (symbols) indicates that neither relation gives good agreement with CFD. A particularly noteworthy feature is that both relations grossly overestimate the velocities in the wake centerplane. Although these comparisons are made in locations and conditions that are most favorable to the scaling relations employed, the results clearly illustrate the limitations of simple formulas based only on boundary-layer and wake concepts.

Law of the Wall in Complex Flows. The high Reynolds number calculations for pipe flow and flat-plate boundary layers provided a test of the turbulence models insofar as they could reproduce the law of the wall. The calculations of the flow on the ship hull at large Reynolds numbers, on the other hand, were made possible only by directly employing the law of the wall with corrections for pressure gradients and three dimensionality. A number of previous studies have challenged the validity of the law of the wall in complex flows, while others have sought to establish its limits. Since many CFD models rely on this law, either directly or indirectly, it is useful to present an example that clarifies the limitations in a relatively straightforward manner.

Consider the flow in a long, straight, two-dimensional channel followed by a section with a wavy wall on one side, as sketched in Fig. 10. There exist comprehensive experimental data on flow in such channels over a range of wave amplitude and Reynolds number. It is found that changes in these parameters lead to different flow regimes, including that with separated flow in the wave troughs. Here it suffices to discuss calculations made by Patel, Chon and Yoon (1991) corresponding to the experiments of Kuzan (1986) with $2a/\lambda = 0.20$, Re = 8,160, where λ and a are the wavelength and amplitude, respectively, and Re is the channel Reynolds number based on the mean velocity, U_o, and channel height, H. Experiments as well as calculations indicate that the flow becomes spatially periodic rather quickly, establishing almost fully-periodic conditions by the second or third wave. The numerical method was similar to that employed for the other calculations described above. The two-layer k-ϵ turbulence model of Chen and Patel (1988) was employed with the first grid point at $y^+ = 0.01$.

Spatial periodicity implies that it is necessary to calculate the flow over only one wave by prescribing periodic boundary conditions, upstream and downstream, with the Reynolds number (or the mean pressure gradient, or discharge) and wave geometry as the only inputs. In this respect this is an excellent test of CFD models designed for flows with significant pressure gradients and surface curvatures. Although the calculations did not employ the spatial periodicity, the results presented here are in that region.

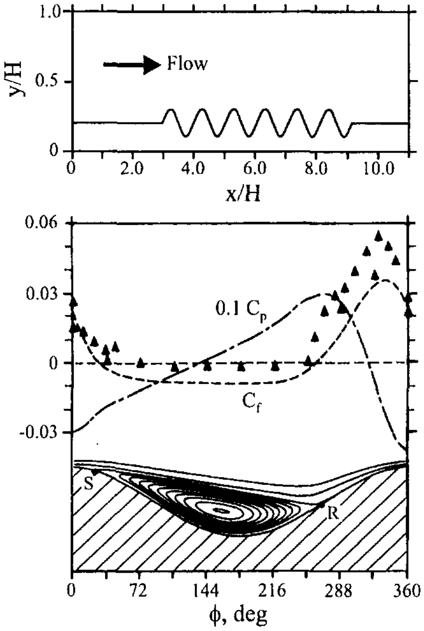

Fig. 10 Pressure and friction coefficients, and streamlines, in a channel with a wavy wall, Symbols: measured friction coefficient; lines: calculations, Patel et al. (1991)

The distributions of pressure and friction coefficients, defined in the conventional way using the mean velocity in the channel, over one wave are shown in Fig. 10, along with the wave profile, the calculated streamlines, and the separation (S) and reattachment (R) points. Figure 11 shows linear and logarithmic plots of the velocity profiles at five stations one-fifth of a wavelength apart, beginning with the wave crest labeled $\phi = 0$. Although the measurements extended to the opposite flat wall the logarithmic plots are shown only on the wavy-wall side up to the velocity maximum, with the friction velocity based on the magnitude of the local wall shear stress, because it is negative in separated flow. The logarithmic plots of the calculated and

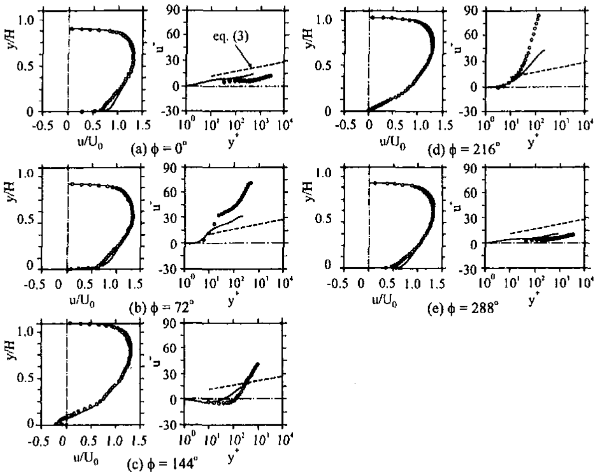

Fig. 11 Velocity profiles at various positions along the wavy wall, Symbols: experiment; solid line: two-layer k-ϵ model; broken line: log law, Eq. (3), Patel et al. (1991)

measured velocity profiles were made using the calculated and measured local friction velocities, respectively. This format provides the most direct comparison between predictions and measurements with respect to the near-wall velocity distribution. It is clear that the standard logarithmic law, Eq. (3), is simply not applicable even where the flow is attached. The calculations, which do not rely explicitly on the logarithmic law, mimic the breakdown of the logarithmic law indicated by the data but there remain significant differences between the calculations and the data. It is interesting to note that much of the disagreement in the near wall region, and in the friction distributions, cannot be discerned from linear plots of the velocity profiles, which is frequently all that is presented when CFD results are compared with experiment.

Lessons. A common element of all of the high Reynolds number calculations discussed above is that they all required very fine grids to obtain converged, steady-state solutions. For the simpler pipe and flat-plate boundary layer flows this did not present a big computational challenge, and solutions could be obtained with very fine grids and with turbulence models designed to resolve the near-wall flow including the sublayer. In fact, even the axisymmetric body calculations could have been made in this way although the results presented here were obtained with wall functions. The ship calculations, on the other hand, were certainly not possible at the time they were made without using wall functions and, in particular, exploiting the observed increased region of validity of the logarithmic law in terms of y^+. In fact, calculations with near-wall turbulence models at such high Reynolds numbers for this, and similar complex three-dimensional flows, have yet to be demonstrated. While this aspect of the problem of CFD at high Reynolds numbers may be viewed by some as largely a numerical one, to be overcome with a sufficiently fine grid and robust algorithm, successful solutions may prove prohibitively expensive, if not elusive.

The second, and perhaps more critical aspect of CFD at high Reynolds numbers concerns the physics, which enters through the turbulence model and the assumptions, explicit or implicit, about the near-wall flow. In this respect the results are not particularly encouraging. The recent high Reynolds number flow experiments tend to favor continued use of the logarithmic law and the friction formulas based on it, vindicating Schlichting, but the disagreement between the flat-plate resistance formulas derived from it and CFD calculations essentially using the same information through the turbulence model is a cause for concern. Some further adjustment of constants may be required to bring the two in agreement over the entire range of Reynolds numbers but the basis for making such adjustments is not at all clear. The flow in a channel with a wavy wall illustrated the breakdown of the law of the wall in the presence of strong pressure gradients and flow separation. This calls into question the use of wall functions, which is quite prevalent for even more complex flows. This example also reveals the shortcomings of near-wall turbulence models in current use even though they are to be preferred over wall functions.

The third aspect of the problem concerns calibration and validation of CFD codes at high Reynolds numbers. It is rather surprising that few investigators, if any, have taken the time to revisit the flows upon which rests much of the CFD edifice. The flow in a pipe, a flat-plate boundary layer, and a channel with wavy walls, are just examples of very simple flows, from a CFD perspective, from which much can still be learnt about CFD codes. This is also true of surface roughness.

Flow Over Rough Surfaces

Models for Flow Over Rough Walls. There are several different levels at which models of roughness are made, apart from the classical analysis in which equation (8) is integrated to derive friction formulas for pipes in the Moody diagram, and similar results for channels and flat plates.

Rotta (1962) proposed a simple modification to the well-known van Driest (1956) formula for mixing length to account for roughness by adding a shift Δy^+ to the distance from the wall and making it a function of the equivalent sand-grain roughness height k_s^+. Cebeci and Chang (1978) used this model to perform some of the earliest numerical calculations of boundary layers on rough walls. The model of Rotta, along with several others, were reviewed by Granville (1985) to relate the van Driest damping function, and the distributions of mixing length and eddy viscosity, to the roughness function ΔB of equation (8). In a recent paper, Krogstad (1991) has suggested yet another version of the mixing-length model for sand grain roughness. The various mixing-length models differ in the manner in which the effect of roughness is introduced, ranging from a shift in the wall distance (effectively specifying a non-zero mixing length at the wall) to introduction of roughness-dependent damping functions in formulas of the van Driest type. Unfortunately, these models cannot be readily generalized to apply to flows with separation, and to three-dimensional flows.

In the wall-functions approach to modeling roughness, equations of continuity and momentum, along with turbulence-model equations, are solved only in the region $y^+ > y_m^+$ and all boundary conditions are specified at y_m^+, usually located in the logarithmic region, where equation (8) applies. The boundary conditions needed to solve the equations depend on the turbulence model. In the k-ϵ model, for example, the wall functions most commonly used are

$$u^+ = \frac{1}{\kappa} \ln (Ey^+), \quad E = \exp\{\kappa(B - \Delta B)\},$$

$$k^+ = \frac{1}{\sqrt{C_\mu}}, \quad \epsilon^+ = \frac{1}{\kappa y^+} \tag{13}$$

which admit no direct effect on the turbulence parameters. The wall-functions approach relies on the validity of Eq. (8), the limitations of which were discussed above in the absence of roughness.

Another way to account for surface roughness, especially regular arrays of discrete three-dimensional elements, such as cones, spheres, etc., is to introduce a form drag term into the momentum equation and take into account the blockage effect of the roughness elements on the near-wall flow. Among such approaches are those of Christoph and Pletcher (1983), who added a sink term to the momentum equation for the form drag and employed a variant of the mixing-length model including roughness effect, and Taylor et al. (1985), who modified the continuity and momentum equations to account for the blockage effect of the roughness array, added a form drag term to the momentum equations, and employed the standard smooth-wall mixing-length formula of van Driest. Aupoix (1988) derived similar modifications with formal volume averages, and Glikson and Aupoix (1996) have extended it to k-ϵ and k-ω models. An advantage of these discrete element models is that they attempt to make a direct connection between the roughness geometry and roughness effect, and do not rely on a single length scale k_s^+ to characterize the roughness. Such models are not immediately applicable to sand grain or similar random roughness, however.

Yet another level of modeling involves modification of smooth-wall turbulence-model equations to treat rough walls. Mixing-length and eddy-viscosity models discussed in the previous section also could be included in this category to the extent that they are sometimes used in combination with turbulence-model equations, as in the k-ϵ model. On a somewhat different level, however, are models that explicitly account for roughness effects through additional terms in the turbulence-model equations, or modifications in model constants or func-

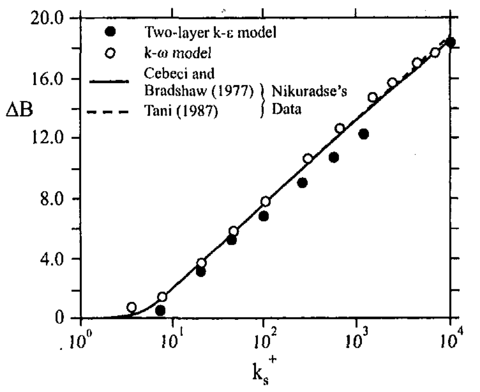

Fig. 12 Roughness function for sand-grain roughness calculated with two turbulence models, Patel et al. (1991)

tions. A model that falls in this category is the k-ω model of Wilcox (1993), in which the same equations are employed for smooth and rough surfaces but the effect of roughness is accounted for through the boundary conditions at the wall.

Almost all applications of the familiar k-ϵ model to rough walls have employed the wall-functions approach. On the other hand, for smooth walls, a great deal of effort has been devoted to abandon the wall functions and use the so-called low-Reynolds-number or near-wall models (see, for example, Patel, Rodi and Scheuerer, 1985). None of these consider the possibility of including surface roughness. An alternative to near-wall extensions of the k-ϵ model is to use the two-layer approach in which the near-wall flow is resolved by a one-equation model and the flow beyond the wall layer by the standard two-equation model. Patel and Yoon (1995) attempted an extension of the model of Chen and Patel (1988) to incorporate Rotta's (1962) suggestion on roughness effect on the length scale in the wall region.

In summary, it is found that modeling of the flow near a rough surface, and particularly that between the logarithmic layer and the effective location of the wall, where the no-slip condition applies in some average sense, has not received much attention. This is so particularly in the context of applications to complex flows with separation and reattachment, where the logarithmic law and the associated wall-function approach lose their validity. In the selection of a turbulence model for rough surfaces, two factors are critical: (a) the model should be capable of describing the three roughness regimes, namely, hydrodynamically smooth, transitional, and full-rough surfaces, and (b) it should be possible to apply the model to describe separated flows. In the following sections, some examples are presented to assess the current situation.

Channel and Pipe Flows. Figure 12, reproduced from Patel and Yoon (1995), shows the results of calculations of fully-developed flow in a straight channel with classical sand-grain roughness of uniform size. The roughness size k_s^+ was varied to capture the range that is usually plotted in the Moody diagram. The roughness function ΔB determined from the calculated velocity profiles is shown along with the correlation of Cebeci and Bradshaw (1977) of Nikuradse's data, and Tani's (1987) re-evaluation of the same data. It is found that the k-ω model gives an almost perfect match with the correlation for k_s^+ as large as 10^4, much larger than the limit of 400 imposed by Wilcox. The extended two-layer k-ϵ model, while providing the correct trends, underestimates the roughness effect, and the discrepancy appears to grow with increasing roughness. Not surprisingly, these observations were confirmed by comparison of the calculated friction coefficients with analytically derived values. Obviously further refinements would be needed in the two-layer model to match the performance of the k-ω model.

Constantinescu and Patel (1998) recently performed similar k-ω model calculations for flow in a pipe. From the results summarized in Table 3 it is seen that the maximum difference between the calculated friction factor and that read from the Moody diagram is about 4%, as is the difference in the roughness function.

The calculations with increasing roughness required increasingly finer grids. From the calculated velocity profiles shown in Fig. 13 it appears that the buffer layer is predicted in addition to the shifted logarithmic region even for the largest roughness. However, with increasing roughness this modeled buffer layer and parts of the logarithmic layer lie well inside the roughness height, $y^+ < k_s^+$. While the turbulence model requires finer grids to resolve the increasing velocity gradient near the wall, the model itself loses realism and, at best, the results represent some sort of an average of the flow within the roughness elements. Nevertheless, the fact that this model may be employed without change for more complex flows, including separation, as already demonstrated for smooth walls, is a boon to CFD. In other words, it may be more appropriate than the wall functions of Eq. (13).

Asymmetric Channel Flow With Different Types of Roughness—Ice-Covered Channels. Ice cover formation on a river or a channel is a common wintertime event in the northern environment. When a floating cover develops, an open channel becomes closed, with different roughness on the top and bottom boundaries. Roughness of the ice surface in contact with the water varies over wide limits. The roughness on the channel bottom also changes as the ice cover develops. For a given flow rate and channel-bed slope, the water depth is increased due to the resistance added by the ice cover and this, in turn, affects sediment transport rates and bed forms.

Parthasarathy and Muste (1994) conducted experiments to simulate the flow in ice-covered channels. The experiments were performed in a hydraulic flume with recirculating water and sediment. The sediment was uniform sand with a mean diameter of 1.3 mm and the flow conditions were selected such that the bed remained flat, without ripples or dunes. The flow in the open channel flow was measured as a reference case. Floating covers, in the form of plywood sheets with different roughness characteristics were then added on the free surface to simulate free-floating ice covers. In each case, with the bed slope and discharge fixed at the open-channel values, the flow depth was adjusted to reestablish uniform flow conditions. The added resistance required increased flow depth to pass the same discharge. Simulated ice covers with three types of roughness were used. In one, the surface of the plywood in contact with the water was painted and this served as the smooth cover. In the second, a 2-mm thick wire mesh was stapled to the plywood surface. In the third, and largest roughness, wooden strips of 8.9-mm height and 13-mm width were glued to the plywood surface at interval 50.2 mm to obtain a regular pattern of transverse ribs. A two-component LDV was used to measure the

Table 3 Pipe flow at Re = 1,020,000 with standard k-ω model

Wall	$100k_s/d$	Calculated $100f$	Moody $100f$	Difference in f %	Calculated ΔB	Experiment ΔB	Difference in ΔB %	k_s^+
Smooth	0.0025	1.231	1.182	4.08				1
Rough	0.125	2.130	2.108	1.04	6.78	6.62	2.38	65
Rough	0.250	2.540	2.500	1.60	8.35	8.53	−2.11	145
Rough	0.500	2.953	3.050	−3.23	9.95	10.36	−3.98	310

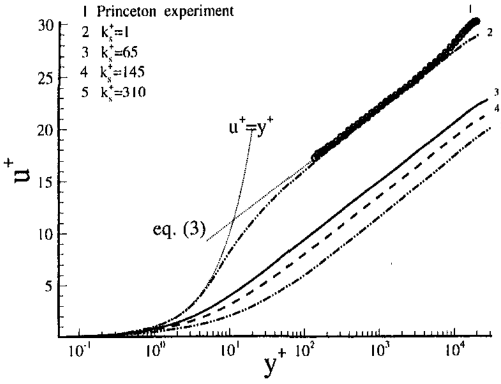

Fig. 13 Velocity profiles in a pipe with different sand-grain roughness at Re = 1,020,000, Constantinescu and Patel (1998)

mean and fluctuating velocity components along and normal to the flow direction at the center of the channel.

Yoon et al. (1997) made calculations for these flows using the standard k-ω model. For each type of roughness, the equivalent sand-grain roughness k_s^+ was determined from known empirical correlations. Figure 14 shows the velocity and Reynolds shear-stress profiles in the four experiments. Table 4 shows the friction coefficient C_f on the two walls and the their sum. Here, H is the channel height and U_o is the mean velocity. The friction coefficient is based on the mean velocity. It is clear that agreement between the calculations and experiments deteriorates with increasing roughness, but the predictions follow the observed trends. The implications of these results for channel hydraulics are discussed by Yoon et al.

Flow Over a Sand Dune—Flow With Separation and Reattachment. Consider turbulent open channel flow of constant mean depth over a train of fixed, two-dimensional dunes, identical in size and shape. Mierlo and De Ruiter (1988) conducted experiments in such a flow in a water flume with 33 identical, sand-plastered concrete dunes installed on the flume bottom. The dune profile is shown in Fig. 15. A layer of sand grains of nearly uniform size was glued over the concrete dunes. As in the wavy-wall channel, calculations for this case could be made over one dune assuming spatial periodicity of the flow.

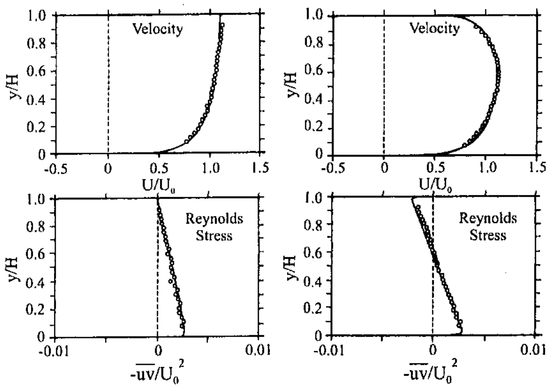

(a) Open channel (b) Smooth cover

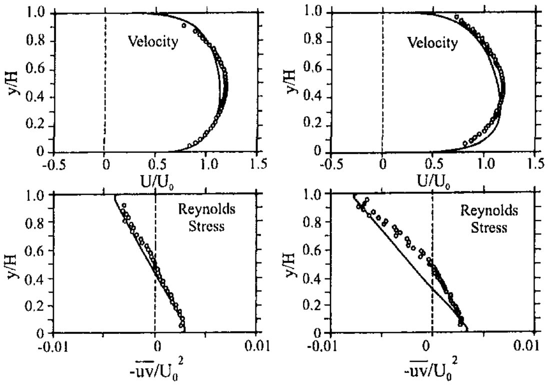

(c) Wire-mesh cover (d) Rib roughness on cover

Fig. 14 Velocity and Reynolds shear stress profiles in channels with different roughness Symbols: experiment; solid lines: calculations, Yoon et al. (1996)

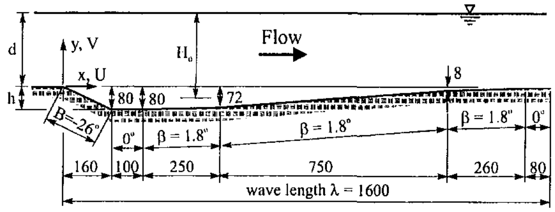

Fig. 15 Sand dune geometry, Meirlo and Ruiter (1988)

Details of the calculations and comparisons with experiments are described in Yoon and Patel (1996). Here it is of interest to present the results of their parametric study in which the dune height h and wavelength λ were varied. The resistance coefficient and its friction and pressure components are shown in Fig. 16 as functions of the dune steepness parameter h/λ. The numerical model shows a slight decrease in frictional resistance but a marked increase of pressure resistance with increasing dune steepness. These trends are to be expected as the size of the separation region in the dune trough increases with dune height and there is diminished contribution of friction in the presence of an enlarged back-flow region. Figure 16 also shows the resistance components calculated with the formula of Engelund (1966, 1967). The results are rather surprising. It is observed that this formula predicts a gradual increase in frictional resistance with increasing dune steepness, but it over estimates the magnitude by as much as a factor of three. The over prediction of the frictional component is most likely due to the use of a pipe-flow based logarithmic formula, which ignores the presence of flow separation and associated regions of negative and low friction. For the pressure component, Engelund's formula predicts much smaller values. The discrepancies in the two components counteract somewhat to yield an increase of total resistance with dune steepness as indicated by the numerical model. However, Engelund's formula underestimates the total resistance by as much as a factor of two.

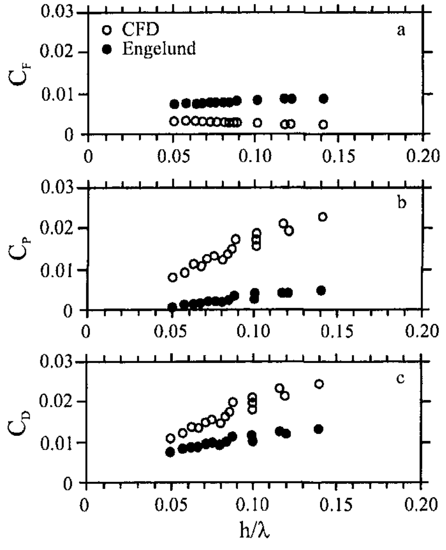

Fig. 16 Resistance components in dune-bed open channels, (*a*) Frictional resistance; (*b*) pressure resistance; (*c*) total resistance, Yoon and Patel (1996)

Table 4 Friction coefficients in channels with different wall roughness

		Experiment			Calculation		
Type of cover	Roughness k_s^+/H	C_f bottom	C_f top	C_f total	C_f bottom	C_f top	C_f total
Open	—	0.00551	0	0.00551	0.00577	0	0.00577
Smooth	0	0.00621	0.00427	0.01048	0.00643	0.00488	0.01131
Wire Mesh	0.0163	0.00712	0.00776	0.01488	0.00682	0.00869	0.01551
Ribs	0.0963	0.01014	0.01493	0.02507	0.00771	0.01620	0.02391

The reasons for the differences between the predictions of the numerical model and those of this well known semi-empirical formula are not clear. The numerical model is based on an idealized two-dimensional flow over fixed two-dimensional dunes of regular shape, while empirical formulas are developed from data taken in laboratory flumes and natural channels, in the presence of sediment and three-dimensional movable bed forms of varying heights and wavelengths. However, the observed differences in magnitudes, and particularly the trends, of the resistance components with varying dune steepness are rather large and may have important consequences in the prediction of stage-discharge relations of natural channels with dunes.

Lessons. The example calculations of flow over rough surfaces presented here were all made at typical laboratory Reynolds numbers. As already noted, increasing roughness requires finer grids to numerically resolve the near-wall flow, but this does not imply that the physics of the flow in that region is better represented or is resolved with greater accuracy. On the contrary, this is an artifact of the model equations, and whether the results represent any form of an average of the flow within the roughness elements remains speculative. The reproduction of the empirical roughness function correlation by the k-ω model is not surprising because it was based on those correlations. In the context of CFD its performance is encouraging to the extent that it may be used in place of the wall functions for complex flows. This was demonstrated by the calculations of the flow over sand dunes. However, the calculations for even the simplest flows reveal serious deficiencies in modeling the effect of wall roughness.

Most of the examples of rough-wall flows presented above involved relatively large roughness, with the resulting flow in the fully rough regime. This regime is of interest in hydraulics, atmospheric flows, and many industrial applications. It is quite well known that most roughness encountered in these situations cannot be characterized by an equivalent sand-grain height, k_s^+. This limits the usefulness of the available models. There is even greater difficulty in the characterization of airplane and ship roughness, which mostly lies in the transitional regime. In analyzing ship-hull roughness, for example, Grigson (1992) distinguishes between two types of roughness: an imperfectly smooth surface, in which the elements of the roughness have a small height to spacing ratio and are themselves streamlines; and a severely rough surface, where the elements are closely spaced drag producing protrusions. There is, to be sure, a whole range of roughness types between these extremes. Analysis of ship hull data shows the roughness function ΔB to depend on these differences in texture, in addition to the roughness height. Clearly, these issues are not addressed in the roughness models being used in CFD.

Conclusions

A common numerical difficulty of applying CFD to flows at increasing Reynolds numbers and on rough walls is the resolution of the increasing gradients of velocity and turbulence parameters within a layer of diminishing thickness. This has tended to favor the use of wall functions even though they are known to fail in complex flows. It is unlikely that this practice will be abandoned without further progress in near-wall modeling, because resolution of the near-wall flow with existing models is prohibitively expensive, especially at high Reynolds numbers and on rough walls.

It is clear that much of our knowledge on flows at high Reynolds numbers and on rough walls is derived from empirical correlations, such as the law of the wall, established several decades ago at low Reynolds numbers and in simple flows. A few recent experiments at high Reynolds numbers have tended to confirm the established correlations in those simple flows on smooth walls. CFD methods continue to rely on these correlations, and extrapolations are routinely made to much more complex flows without direct verification or justification although there exists sufficient evidence to doubt their universality. In fact, calculations are rarely made for even simple flows to recheck the accuracy of the solutions or the realism of the simulations. As shown here, calculations for flow in pipes and flat-plate boundary layers reveal much about the limitations of numerical schemes and turbulence models embodied in modern CFD codes, and should be routinely made.

Much effort has been expended over the years in diverse fields to relate specific types of roughness to the classical roughness that led to the empirical database, but systematic study of roughness effects in complex flows has been lacking. Most applications of CFD to rough walls have used wall functions in spite of their proven limitations. Recent applications of the k-ω model show that it mimics the known effects of roughness rather well, and may be employed in complex flows, but there remains a need to make fresh approaches to this old problem.

The increasing use of CFD in fluids engineering should encourage establishment of an experimental database beyond the canonical flows to include more complex flows, and to develop fresh strategies to model flow over rough surfaces. For example, combination of experimental investigations with DNS and LES solutions with various types of roughness might yield better parameterizations for use in conventional Reynolds-averaged models. Fitting numerical grids to individual roughness elements at any level of modeling does not seem very practical. A more pragmatic but rational approach would be to study the physics of the near-wall flow over different types of roughness to develop models that admit roughness texture as well as size as controlling parameters.

Acknowledgments

I owe much to a generation of graduate students and postdoctoral associates for the work that is quoted herein. Their identity is revealed by the co-authorship of papers in the list of references. Cui Jie helped reproduce some of the figures for this publication. I thank the reviewer who provided new results of pipe-flow calculations that served to reinforce observations that are easily overlooked. I am also grateful to the following individuals for their comments and suggestions on the first draft: P. Bandyopadhyay, P. Bradshaw, D. H. Choi, C. Grigson, A. Gyr, P-A. Krogstad, Y-T. Lee, A. Muller, K. R. Sreenivasan, and A. J. Smits.

Postscript

This is neither a review nor a research paper in the traditional sense. Soon after I was informed that I had been chosen to receive the 1997 ASME Fluids Engineering Award, I was approached by the organizers of the Summer Meeting of the Fluids Engineering Division in Vancouver to give a talk on a subject of my choice. I was told that this was the first time the award winner was subjected to this task. As they could not be persuaded to withhold this honor for the next award winner, I agreed to make a presentation with a title that described some threads running through the work of some of my recent graduate students and postdoctoral associates. A written version was not intended as much of the material was already in print. Soon after the lecture, however, Demetri Telionis requested a written version for possible publication in this journal after some sort of a friendly communal review. So, this is not a review, in-depth or cursory, of either Reynolds number or roughness effects, nor is it a review of CFD methods or turbulence models. It is, instead, a perspective drawn from observations made over a number of years from studies of fluid flow problems in diverse applications. The reader would therefore find a somewhat unusual mix of topics, which I hope would demonstrate the ubiquity of the problems that come to mind from the title of the paper. Some elaboration on the material presented in the talk at Vancouver has occurred in response to comments from readers of the first draft.

References

Aupoix, B., 1994, "Modelling of Boundary Layer Flows over Rough Surfaces," Fifth European Turbulence Conference, Siena, Italy, July 5–8.

Barenblatt, G. I., and Chorin, A. J., 1998, "Scaling of the Intermediate Region in Wall-Bounded Turbulence: The Power Law," *Physics of Fluids,* Vol. 10, pp. 1043–1044.

Barenblatt, G. I., Chorin, A. J., and Prostokishin, V. M., 1997, "Scaling Laws for Fully Developed Turbulent Flow in Pipes," *Applied Mechanics Reviews,* Vol. 50, pp. 413–429.

Baldwin, B. S., and Lomax, H., 1978, "Thin-Layer Approximation and Algebraic Model for Separated Turbulent Flows," AIAA Paper 78-257.

Bradshaw, P., 1998, A Note on "Critical Roughness Height" and "Transitional Roughness", in preparation.

Cebeci, T., and Bradshaw, P., 1977, *Momentum Transfer in Boundary Layers,* Hemisphere Publishing Corporation.

Cebeci, T., and Chang, K. C., 1978, "Calculation of Incompressible Rough-Wall Boundary-Layer Flows," *AIAA Journal,* Vol. 16, pp. 730–735.

Chen, H. C., and Patel, V. C., 1988, "Near-Wall Turbulence Models for Complex Flows Including Separation," *AIAA Journal,* Vol. 26, pp. 641–648.

Christoph, G. H., and Pletcher, R. H., 1983, "Prediction of Rough-Wall Skin Friction and Heat Transfer," *AIAA Journal,* Vol. 21, pp. 509–515.

Clauser, F. H., 1956, "The Turbulent Boundary Layer," *Advances in Applied Mechanics,* Vol. 4, Academic Press, NY, pp. 1–51.

Coder, D. W., 1982, "Reynolds Number Scaling of Velocities in Axisymmetric Turbulent Boundary Layers," *Proceedings of the 14th ONR Symposium on Naval Hydrodynamics,* Ann Arbor, MI.

Constantinescu, S. G., and Patel, V. C., 1998, "Numerical Simulation of Flow in Pump Bays Using Near-Wall Turbulence Models," Iowa Institute of Hydraulic Research, University of Iowa, IA, IIHR Report No. 394, 276 p.

Coder, D. W., 1988a, "Mean Velocities in the Turbulent Boundary Layer Flow of an Appended Body of Revolution for Reynolds Numbers from 20 Million to 1000 Million," *Proc. 17th ONR Sym. Naval Hydrodynamics,* The Hague, Netherlands.

Colebrook, C. F., and White, C. M., 1937, "Experiments with Fluid-Friction in Roughened Pipes," *Proceedings of the Royal Society,* Vol. A161, pp. 367–381.

Dolphin, G. W., 1997, "Evaluation of Computational Fluid Dynamics for a Flat Plate and Axisymmetric Body from Model- to Full-Scale Reynolds Numbers," M.S. thesis, University of Iowa, Iowa City, IA.

Engelund, F., 1966, "Hydraulic Resistance of Alluvial Streams," *Journal of Hydraulic Engineering,* Vol. 92, pp. 315–327.

Engelund, F., 1967, "Hydraulic Resistance of Alluvial Streams," *Journal of Hydraulic Engineering,* Vol. 93, pp. 287–296.

Glikson, F., and Aupoix, B., 1996, "Modelling of Compressible Boundary Layer Flows over Rough Surfaces," *3rd International Symposium on Turbulence Modelling and Measurements,* Crete, Greece, May 27–29.

Granville, P. S., 1985, "Mixing-Length Formulations for Turbulent Boundary Layers over Arbitrarily Rough Surfaces," *Journal of Ship Research,* Vol. 29, pp. 223–233.

Grigson, C., 1992, "Drag Losses of New Ships Caused by Hull Finish," *Journal of Ship Research,* Vol. 36, pp. 182–196.

Hama, F. R., 1954, "Boundary Layer Characteristics for Smooth and Rough Surfaces," *Transactions of the Society of Naval Architects and Marine Engineers,* Vol. 62, pp. 333–358.

Jones, W. P., and Launder, B. E., 1973, "The Calculation of Low Reynolds Number Phenomena with a Two-Equation Turbulence Model," *International Journal of Heat and Mass Transfer,* Vol. 16, pp. 1119–1120.

Ju, S., and Patel, V. C., 1991, "Stern Flows at Full-Scale Reynolds Numbers," *Journal of Ship Research,* Vol. 35, pp. 101–113.

Kodama, Y. (Ed), 1994, "Proceedings of CFD Workshop Tokyo 1994," Ship Research Institute, Tokyo, Japan, 2 vols.

Krogstad, P., 1991, "Modification of the van Driest Damping Function to Include the Effects of Surface Roughness," *AIAA Journal,* Vol. 29, pp. 888–894.

Kuzan, K. D., 1986, "Velocity Measurements for Turbulent Separated and Near Separated Flow over Solids Wave," Ph.D. thesis, University of Illinois, Urbana, IL.

Larsson, L., Patel, V. C., and Dyne, G. (Eds.), 1991, "Proceedings of 1990 SSPA-CTH-IIHR Workshop on Ship Viscous Flow," Flowtech International, Gothenburg, Sweden, Report No. 2.

Mierlo, M. C. L. M., and de Ruiter, J. C. C., 1988, "Turbulence Measurements above Artificial Dunes," Delft Hydraulics Laboratory, Delft, The Netherlands, Report Q789.

Moody, L. F., 1944, "Friction Factors for Pipe Flow," *Trans. ASME,* Vol. 66, pp. 671–684.

Moore, W. F., 1951, "An Experimental Investigation of the Boundary-Layer Development along a Rough Surface," Ph.D. dissertation, University of Iowa, Iowa City, IA.

Nikuradse, J., 1932, "Gesetzmaessigkeiten der Turbulenten Stroemung in Glatten Rohren," *VDI Forschungheft,* No. 356.

Parthasarathy, R. N., and Muste, M., 1994, "Velocity Measurements in Asymmetric Turbulent Channel Flows," *Journal of Hydraulic Engineering,* Vol. 120, pp. 1000–1020.

Patel, V. C., 1965, "Calibration of the Preston Tube and Limitation on Its Use in Pressure Gradients," *Journal of Fluid Mechanics,* Vol. 23, pp. 185–208.

Patel, V. C., Chen, H. C., and Ju, S., 1988, "Ship Stern and Wake Flows: Solutions of the Fully-Elliptic Reynolds-Averaged Navier-Stokes Equations and Comparisons with Experiments," Iowa Institute of Hydraulic Research, University of Iowa, IA, IIHR Report No. 323, 261 p.

Patel, V. C., Chon, J. T., and Yoon, J. Y., 1991, "Turbulent Flow in a Channel with a Wavy Wall," ASME JOURNAL OF FLUIDS ENGINEERING, Vol. 113, pp. 579–586.

Patel, V. C., Rodi, W., and Scheuerer, G., 1985, "Turbulence Models for Near-Wall and Low Reynolds Number Flows: A Review," *AIAA Journal,* Vol. 23, pp. 1308–1319.

Patel, V. C., and Yoon, J. Y., 1995, "Application of Turbulence Models to Separated Flow over Rough Surfaces," ASME JOURNAL OF FLUIDS ENGINEERING, Vol. 117, pp. 234–241.

Rotta, J., 1962, "Turbulent Boundary Layers in Incompressible Flow," *Progress in Aerospace Science,* Oxford, UK, Vol. 2, pp. 73–82.

Schlichting, H., 1936, "Experimentelle Untersuchungen zum Rauhigkeitsproblem," *Ingenieur-Archiv.,* Vol. 7, pp. 1–34; also, NACA TM 823 (1937).

Schlichting, H., 1968, *Boundary Layer Theory,* 6th Ed., McGraw Hill, New York, NY.

Smits, A. J., and Zagarola, M. V., 1998, "Response to "Scaling of the Intermediate Region in Wall-Bounded Turbulence: The Power Law," *Physics of Fluids,* Vol. 10, pp. 1045–1046.

Tanaka, I., 1988, "Three-Dimensional Ship Boundary Layer and Wake," *Advances in Applied Mechanics,* Vol. 26, pp. 311–359.

Tanaka, I., Suzuki, T., Himeno, Y., Takahei, T., Tsuda, T., Sakao, M., Yamazaki, Y., Kasahara, M., and Takagi, M., 1984, "Investigation of Scale Effects on Wake Distribution using Geosim Models," *J. Kansai Society of Naval Architects,* Japan, Vol. 192, pp. 103–120.

Tani, I., 1987, "Turbulent Boundary Layer Development over Rough Surfaces," *Perspectives in Turbulence Studies,* H. U. Meier and P. Bradshaw, eds., Springer.

Taylor, R. P., Coleman, H. W., and Hodge, B. K., 1985, "Prediction of Turbulent Rough-Wall Skin Friction Using a Discrete Element Approach," ASME JOURNAL OF FLUIDS ENGINEERING, Vol. 107, pp. 251–257.

van Driest, E. R., 1956, "On Turbulent Flow Near a Wall," *Journal of Aeronautical Sciences,* Vol. 23, pp. 1007–1011, 1036.

White, F. M., 1991, *Viscous Fluid Flow,* McGraw Hill, New York, NY, pp. 426–428

Wilcox, D. C., 1993, *Turbulence Modeling for CFD,* DCW Industries Inc., La Canada, CA.

Yoon, J. Y., and Patel, V. C., 1996, "Numerical Model of Turbulent Flow over Sand Dune," *Journal of Hydraulic Engineering,* Vol. 122, pp. 10–18.

Yoon, J. Y., Patel, V. C., and Ettema, R., 1996, "Numerical Model for Flow in Ice-Covered Channel," *Journal of Hydraulic Engineering,* Vol. 122, pp. 19–26.

Zagarola, M. V., 1996, "Mean Flow Scaling of Turbulent Pipe Flow," Ph.D. thesis, Princeton University, NJ.

Zagarola, M. V., and Smits, A. J., 1997, "Scaling of Mean Velocity Profile for Turbulent Pipe Flow," *Physical Review Letters,* Vol. 78, pp. 239–242.

Zagarola, M. V., Perry, A. E., and Smits, A. J., 1997, "Log Laws or Power Laws: the Scaling in the Overlap Region," *Physics of Fluids,* Vol. 9, pp. 2094–2100.

K. K. Brown
Principal Engineer,
Space America, Inc.,
Huntsville, AL 35824

H. W. Coleman
Eminent Scholar in Propulsion
and Professor,
Propulsion Research Center,
Department of Mechanical and
Aerospace Engineering,
University of Alabama in Huntsville,
Huntsville, AL 35899

W. Glenn Steele
Giles Distinguished Professor and Head,
Department of Mechanical Engineering,
Mississippi State University
Mississippi State, MI 39762

A Methodology for Determining Experimental Uncertainties in Regressions

A methodology to determine the experimental uncertainties associated with regressions is presented. When a regression model is used to represent experimental information, the uncertainty associated with the model is affected by random, systematic, and correlated systematic uncertainties associated with the experimental data. The key to the proper estimation of the uncertainty associated with a regression is a careful, comprehensive accounting of systematic and correlated systematic uncertainties. The methodology presented in this article is developed by applying uncertainty propagation techniques to the linear regression analysis equations. The effectiveness of this approach was investigated and proven using Monte Carlo simulations. The application of that methodology to the calibration of a venturi flowmeter and its subsequent use to determine flowrate in a test is demonstrated. It is shown that the previously accepted way of accounting for the contribution of discharge coefficient uncertainty to the overall flowrate uncertainty does not correctly account for all uncertainty sources, and the appropriate approach is developed, discussed, and demonstrated.

1 Introduction

When experimental information is represented by a regression, the regression model will have an associated uncertainty due to the uncertainty in the original experimental program. An uncertainty is an estimate of an error whose value is unknown. The uncertainty U of a quantity gives the $\pm U$ interval around the measured or predicted value of the quantity that will contain the true, but unknown, value of the quantity 95 times out of 100. Uncertainties are usually divided into two categories: random (or precision) uncertainties and systematic (or bias) uncertainties. Since measured variables can share identical bias error sources, correlated systematic uncertainties can occur and must be considered in analyses. Previously there has been no accepted methodology to assess the uncertainty of a regression when the regression variables contain random, systematic, and correlated systematic experimental uncertainties.

Consider the general case where a test is conducted on a hardware component. The data are plotted and a linear regression is used to determine the best fit of a curve through the data. (Note that the term *linear* regression means the regression coefficients $a_0, a_1, \ldots, a_n$ are not functions of the X variable, and not that the relationship between X and Y is linear.) Since the data are obtained experimentally, both X and Y will have experimental uncertainties and these uncertainties will be made up of systematic (bias) and random (precision) uncertainties. A linear regression is then performed on the (X, Y) data and the general form of the regression is

$$Y(X) = a_0 + a_1X + a_2X^2 + \ldots + a_nX^n \tag{1}$$

This polynomial equation is then used to represent the performance of the hardware. The original data and its uncertainty are usually forgotten in subsequent use. This model will not predict the *true* performance of the hardware because of the experimental uncertainties; thus the uncertainty associated with the regression is needed to provide the interval within which the *true* performance can be expected, at a given level of confidence. This article presents a methodology to assess the uncertainty associated with regressions when the regression variables contain random, systematic, and correlated systematic uncertainties. A more detailed discussion is provided in Brown (1996).

Obviously, an additional error is introduced if the wrong regression model is used, for example, if a third-order regression model is used and the true relationship is first order. This is the classical problem of incorrectly fitting the data, overfitting or underfitting. *The error introduced by choice of an inappropriate regression model is not addressed in this article.* It is assumed in the techniques presented that the correct model is being used and the only uncertainties in the regression model are those due to the uncertainties in the original experimental information.

The methodology presented in this article is an extension of accepted uncertainty propagation techniques (Coleman and Steele, 1995) as applied to the linear regression equations. The effectiveness of this new methodology was evaluated using Monte Carlo-type simulations. The following sections discuss uncertainty aspects of regression models, results of the Monte Carlo simulation evaluation of the methodology, and some observations on reporting the uncertainty associated with regressions. The final section of this article demonstrates the application of this methodology to the determination of the uncertainty in a venturi flowmeter measurement.

Categories of Regression Uncertainty. This methodology is developed to cover the types of situations commonly encountered in engineering for which regressions are used. Three primary categories can be defined based upon how the regression information is being used. The first category is when the regression coefficients are the primary interest. The second category is when the regression model is used to provide a value for the Y variable. And the third category is when the (X_i, Y_i) data points are not measured quantities, but are functions of other variables. This third category can include both of the other two categories, with the uncertainty associated with either the regression coefficients or the regression value of Y being of interest.

The key to the proper estimation of the uncertainty associated with a regression is a careful, comprehensive accounting of

---

Contributed by the Fluids Engineering Division for publication in the JOURNAL OF FLUIDS ENGINEERING. Manuscript received by the Fluids Engineering Division January 7, 1997; revised manuscript received May 2, 1998. Associate Technical Editor: J. A. C. Humphrey.

systematic and correlated systematic uncertainties. Correlated systematic uncertainties will be present and must be properly accounted for when the (X_i, Y_i) and the (X_{i+1}, Y_{i+1}) data pairs have systematic uncertainties from the same source. The examples presented below demonstrate some ways in which correlated systematic uncertainties can be present and must be properly accounted for.

Uncertainty in Coefficients. The general expression for a straight-line regression is

$$Y(X) = mX + c \tag{2}$$

where m is the slope of the line and c is the y-intercept. In some experiments these coefficients are the desired information. An example is the stress-strain relationship for a linearly elastic material

$$\sigma = E\epsilon \tag{3}$$

where the stress, σ, is linearly proportional to the strain, ϵ, by Young's modulus, E. Young's modulus for a material is determined by measuring the elongation of the material for an applied load, calculating the normal stress and strain, and determining the slope of the line in the linearly elastic region. Since the stress and strain are determined experimentally they will have experimental uncertainties, and thus the experimental value of Young's modulus will have an associated uncertainty.

Uncertainty in Y From Regression Model. Often, the uncertainty associated with a value determined using the regression model, Eq. (1) or (2), is desired. One would obtain a regression model for a given set of (X_i, Y_i) data, then use that regression model to obtain a Y value at a measured or specified X. The nature of the data and the usage of the data determines how the uncertainty estimate is determined, such as

- some or all (X_i, Y_i) data pairs from different experiments
- all (X_i, Y_i) data pairs from same experiment
- new X from same apparatus
- new X from different apparatus
- new X with no uncertainty

It is instructive to discuss an example of each of these situations.

Suppose heat transfer coefficient data sets from various facilities were combined as a single data set, with each facility contributing data over a slightly different range, and a regression model generated. The random and systematic uncertainties for each test apparatus are different. If the systematic uncertainties for the (X_i, Y_i) data and the (X_{i+1}, Y_{i+1}) data are obtained from the same apparatus and thus share the same error sources, their systematic uncertainties will be correlated. However, if they are from different apparati and do not share any error sources they will not be correlated. The uncertainty associated with the regression model must properly account for the correlation of the systematic uncertainties.

The calibration of a thermocouple is an example where all of the data could come from the same experiment. A calibration curve for the thermocouple would be generated by measuring an applied temperature and an output voltage, both of which contain uncertainties. The calibration curve could have the form

$$T = mE + c \tag{4}$$

where m and c are the regression coefficients determined from the (E_i, T_i) calibration data. When the thermocouple is then used in an experiment, a new voltage, E_{new}, is obtained. The new temperature is then found using the calibration curve

$$T_{\text{new}} = mE_{\text{new}} + c \tag{5}$$

The uncertainty in T_{new} includes the uncertainty in the calibration curve as well as the uncertainty in the voltage measurement, E_{new}. If the same voltmeter is used in the experiment as was used in the calibration, the systematic uncertainty from the new voltage measurement will be correlated with the systematic uncertainty of each E_i used in finding the regression and appropriate correlation terms are needed. If a different voltmeter is used to measure the new voltage, the systematic uncertainty of E_{new} will not be correlated with the systematic uncertainties of the E_i.

When a regression is used to represent a set of data and that regression is then used in an analysis, often the new X value is postulated and can be considered to have no uncertainty. An example would be pumping power, P, versus pump speed, N, for a centrifugal pump. The regression might have the form

$$P = a(N)^b \tag{6}$$

If an analyst uses this expression to obtain a value of power at a postulated value of N, then the uncertainty in N could be considered to be zero.

(X_i, Y_i) Variables Are Functions. Another common situation is when the (X_i, Y_i) variables used in the regression are not the measured data, but are each functions of several measured variables. The Young's modulus determination discussed previously is a typical example. Neither the stress nor strain is measured directly. The stress is calculated from measurement of the applied force with a load cell and measurement of the cross-sectional area. The data reduction equation for stress is

$$\sigma = \frac{CV_{lc}}{V_i A} \tag{7}$$

where C is the calibration constant, V_{lc} is the load cell voltage, V_i is the excitation voltage, and A is the cross-sectional area. The strain is determined using a strain gage, and the data reduction equation is

$$\epsilon = \frac{2V_{br}}{GV_i} \tag{8}$$

where V_{br} is the bridge voltage, G is the gage factor, and again V_i is the excitation voltage. The regression coefficient representing Young's modulus is thus a function of the variables C, V_{lc}, V_i, V_{br}, A, and G. In instances where error sources are shared between different variables, as would exist if all of the voltages are measured with the same voltmeter, additional terms in the uncertainty propagation expression are necessary to properly account for the correlated systematic uncertainties.

2 Uncertainty Analysis Background

Only a brief overview of the methodology to obtain uncertainty estimates and how they propagate through a given data reduction equation is given here. The reader is referred to Coleman and Steele (1989, 1995) for a detailed discussion of uncertainty analysis techniques.

In nearly all experiments, the measured values of different variables are combined using a data reduction equation (DRE) to form some desired result. A general representation of a data reduction equation is

$$r = r(X_1, X_2, \ldots, X_J) \tag{9}$$

where r is the experimental result determined from J measured variables X_i. Equations (7) and (8) are examples. Each of the measured variables contains systematic errors and random errors. These errors in the measured values then propagate through the data reduction equation, thereby generating the systematic and random errors in the experimental result, r.

If the "large sample assumption" is made (Coleman and Steele, 1995), then the 95 percent confidence expression for U_r becomes

$$U_r^2 = \sum_{i=1}^{J}\left(\frac{\partial r}{\partial X_i}\right)^2 B_i^2 + 2\sum_{i=1}^{J-1}\sum_{k=i+1}^{J}\left(\frac{\partial r}{\partial X_i}\right)\left(\frac{\partial r}{\partial X_k}\right)B_{ik} + \sum_{i=1}^{J}\left(\frac{\partial r}{\partial X_i}\right)^2 P_i^2 + 2\sum_{i=1}^{J-1}\sum_{k=i+1}^{J}\left(\frac{\partial r}{\partial X_i}\right)\left(\frac{\partial r}{\partial X_k}\right)P_{ik} \qquad (10)$$

with the bias limit (systematic uncertainty) estimate for each X_i variable determined as the root sum square combination of its elemental systematic uncertainties

$$B_i = \left[\sum_{j=1}^{M} (B_i)_j^2\right]^{1/2} = [(B_i)_1^2 + (B_i)_2^2 + \ldots + (B_i)_M^2]^{1/2} \qquad (11)$$

and where B_{ik}, the 95 percent confidence estimate of the covariance appropriate for the bias errors in X_i and X_k, is determined from

$$B_{ik} = \sum_{\alpha=1}^{L} (B_i)_\alpha (B_k)_\alpha \qquad (12)$$

where variables X_i and X_k share L identical error sources. The P_i are the precision limit (random uncertainty) estimates for each X_i variable. A more detailed discussion of the covariance approximation is given in Brown (1996) and Brown et al. (1996). Typically, correlated random uncertainties have been neglected so that the P_{ik}'s in Eq. (10) are taken as zero, and that is assumed in the work reported here.

3 Linear Regression Uncertainty

Linear regression analysis is based upon minimizing the sum of the squares of the Y-deviations between the line and the data points, commonly known as the method of least squares. Linear regression analysis can be divided into three broad categories: straight line regressions, polynomial regressions, and multivariate regressions. Multivariate regressions will not be discussed in this article. Straight-line regressions, also called first-order regressions or simple linear regressions, are a commonly used form. It is often recommended that if the data are not inherently linear that a transformation be used to try to obtain a linear relationship (Seber, 1977, Montgomery and Peck, 1992). Exponential functions and power law functions, for example, can be transformed to linear functions by appropriate logarithmic transformations. Reciprocal transformations are also very useful in linearizing a nonlinear function. If a suitable transformation cannot be found, a polynomial regression is then often used.

In using the basic regression models with typical engineering data, some of the underlying assumptions used in the statistical development of the regression models are violated. The underlying assumptions assume that the errors "(1) are unbiased; (2) have constant variance; (3) are uncorrelated, and (4) are normally distributed" (Seber, 1977). In a typical experimental program the first three assumptions will usually be violated. Assumption 1 is violated when systematic uncertainties are present. Since the uncertainty can be a function of the value of the reading, the standard deviation of the data can vary and violate assumption 2. If the systematic uncertainties in two different data points arise from the same error source, the uncertainties are correlated, thus violating assumption 3. Violation of these assumptions does not preclude using linear regression analysis to obtain a model for the data. However, violating these assumptions means that simple statistical inferences, such as classical statistical estimates of 95 percent confidence uncertainty intervals, cannot be relied upon. Linear regression texts, such as Seber (1977), Montgomery and Peck (1992), Draper and Smith (1981), and Neter et al. (1989) provide methods to deal with some of the individual assumption violations.

These statistical methods cannot accommodate the simultaneous violation of these assumptions, as is encountered when experimental data has several systematic uncertainty sources. The statistical confidence intervals are estimated based upon the difference between the data and the regression, the residual error. However, these confidence intervals assume all of the errors are observed in the dependent variables, the Y variables. If errors are present in the independent variables, the X variables, it is assumed their effect is observed in the Y variables. Montgomery and Peck (1992) and Seber (1977) discuss techniques to obtain regressions when the X measurements have error; however, these do not provide the associated confidence intervals.

Uncertainty in Coefficients—First-Order Regressions. The development of the equations to calculate m and c can be found in numerous statistics and regression books (Seber, 1977, Montgomery and Peck, 1992, and Natrella 1963, for example) and only the equations are presented here. For $N(X_i, Y_i)$ data pairs, the slope, m, is determined from

$$m = \frac{N\sum_{i=1}^{N} X_iY_i - \sum_{i=1}^{N} X_i \sum_{i=1}^{N} Y_i}{N\sum_{i=1}^{N} (X_i^2) - \left(\sum_{i=1}^{N} X_i\right)^2} \qquad (13)$$

and the intercept is determined from

$$c = \frac{\sum_{i=1}^{N} (X_i^2) \sum_{i=1}^{N} Y_i - \sum_{i=1}^{N} X_i \sum_{i=1}^{N} (X_iY_i)}{N\sum_{i=1}^{N} (X_i^2) - \left(\sum_{i=1}^{N} X_i\right)^2} \qquad (14)$$

Considering Eqs. (19) and (20) to be data reduction equations of the form

$$m = m(X_1, X_2, \ldots, X_N, Y_1, Y_2, \ldots, Y_N) \qquad (15)$$

and

$$c = c(X_1, X_2, \ldots, X_N, Y_1, Y_2, \ldots, Y_N) \qquad (16)$$

and applying the uncertainty analysis equations, the most general form of the expression for the uncertainty in the slope is

$$U_m^2 = \sum_{i=1}^{N}\left(\frac{\partial m}{\partial Y_i}\right)^2 P_{Y_i}^2 + \sum_{i=1}^{N}\left(\frac{\partial m}{\partial X_i}\right)^2 P_{X_i}^2 + \sum_{i=1}^{N}\left(\frac{\partial m}{\partial Y_i}\right)^2 B_{Y_i}^2 + 2\sum_{i=1}^{N-1}\sum_{k=i+1}^{N}\left(\frac{\partial m}{\partial Y_i}\right)\left(\frac{\partial m}{\partial Y_k}\right)B_{Y_iY_k} + \sum_{i=1}^{N}\left(\frac{\partial m}{\partial X_i}\right)^2 B_{X_i}^2 + 2\sum_{i=1}^{N-1}\sum_{k=i+1}^{N}\left(\frac{\partial m}{\partial X_i}\right)\left(\frac{\partial m}{\partial X_k}\right)B_{X_iX_k} + 2\sum_{i=1}^{N}\sum_{k=1}^{N}\left(\frac{\partial m}{\partial X_i}\right)\left(\frac{\partial m}{\partial Y_k}\right)B_{X_iY_k} \qquad (17)$$

where P_{Y_i} is the random uncertainty for the Y_i variable, P_{X_i} is the random uncertainty for the X_i variable, B_{Y_i} is the systematic uncertainty for the Y_i variable, B_{X_i} is the systematic uncertainty for the X_i variable, $B_{Y_iY_k}$ is the covariance estimator for the correlated systematic uncertainties in the Y_i and Y_k variables, $B_{X_iX_k}$ is the covariance estimator for correlated systematic uncertainties in the X_i and X_k variables, and $B_{X_iY_i}$ is the covariance estimator for the correlated systematic uncertainties between X_i and Y_i.

A similar expression for the uncertainty in the intercept is

$$U_c^2 = \sum_{i=1}^{N}\left(\frac{\partial c}{\partial Y_i}\right)^2 P_{Y_i}^2 + \sum_{i=1}^{N}\left(\frac{\partial c}{\partial X_i}\right)^2 P_{X_i}^2 + \sum_{i=1}^{N}\left(\frac{\partial c}{\partial Y_i}\right)^2 B_{Y_i}^2 + 2\sum_{i=1}^{N-1}\sum_{k=i+1}^{N}\left(\frac{\partial c}{\partial Y_i}\right)\left(\frac{\partial c}{\partial Y_k}\right)B_{Y_iY_k} + \sum_{i=1}^{N}\left(\frac{\partial c}{\partial X_i}\right)^2 B_{X_i}^2$$

$$+ 2\sum_{i=1}^{N-1}\sum_{k=i+1}^{N}\left(\frac{\partial c}{\partial X_i}\right)\left(\frac{\partial c}{\partial X_k}\right)B_{X_iX_k}$$

$$+ 2\sum_{i=1}^{N}\sum_{k=1}^{N}\left(\frac{\partial c}{\partial X_i}\right)\left(\frac{\partial c}{\partial Y_k}\right)B_{X_iY_k} \quad (18)$$

These equations show the most general form of the expressions for the uncertainty in the slope and intercept, allowing for correlation of bias errors among the different X's, among the different Y's and also among the X's and Y's. If none of the systematic error sources are common between the X variables and the Y variables, the last term of Eqs. (17) and (18), the X-Y covariance estimator, is zero.

The partial derivatives can be determined analytically or numerically. The Monte Carlo simulations discussed in this article used central-difference partial derivatives and double-precision arithmetic to reduce numerical truncation errors.

Uncertainty in Y From Regression Model—First-Order Regression. The expression for the uncertainty in the Y determined from the regression model at a measured or specified value of X is found by substituting Eqs. (13) and (14) into

$$Y(X_{\text{new}}) = mX_{\text{new}} + c \quad (19)$$

and applying Eq. (10) to obtain the uncertainty in Y as

$$U_Y^2 = \sum_{i=1}^{N}\left(\frac{\partial Y}{\partial Y_i}\right)^2 P_{Y_i}^2 + \sum_{i=1}^{N}\left(\frac{\partial Y}{\partial X_i}\right)^2 P_{X_i}^2 + \sum_{i=1}^{N}\left(\frac{\partial Y}{\partial Y_i}\right)^2 B_{Y_i}^2$$

$$+ 2\sum_{i=1}^{N-1}\sum_{k=i+1}^{N}\left(\frac{\partial Y}{\partial Y_i}\right)\left(\frac{\partial Y}{\partial Y_k}\right)B_{Y_iY_k} + \sum_{i=1}^{N}\left(\frac{\partial Y}{\partial X_i}\right)^2 B_{X_i}^2$$

$$+ 2\sum_{i=1}^{N-1}\sum_{k=i+1}^{N}\left(\frac{\partial Y}{\partial X_i}\right)\left(\frac{\partial Y}{\partial X_k}\right)B_{X_iX_k}$$

$$+ 2\sum_{i=1}^{N}\sum_{k=1}^{N}\left(\frac{\partial Y}{\partial X_i}\right)\left(\frac{\partial Y}{\partial Y_k}\right)B_{X_iY_k} + \left(\frac{\partial Y}{\partial X_{\text{new}}}\right)^2 B_{X_{\text{new}}}^2$$

$$+ \left(\frac{\partial Y}{\partial X_{\text{new}}}\right)^2 P_{X_{\text{new}}}^2 + 2\sum_{i=1}^{N}\left(\frac{\partial Y}{\partial X_{\text{new}}}\right)\left(\frac{\partial Y}{\partial X_i}\right)B_{X_{\text{new}}X_i}$$

$$+ 2\sum_{i=1}^{N}\left(\frac{\partial Y}{\partial X_{\text{new}}}\right)\left(\frac{\partial Y}{\partial Y_i}\right)B_{X_{\text{new}}Y_i} \quad (20)$$

The first seven terms on the right hand side (RHS) of Eq. (20) account for uncertainties from the (X_i, Y_i) data pairs. The eighth and ninth terms account for the systematic and random uncertainties for the new X. The tenth term is included if the new X variable is measured with the same apparatus as that used to measure the original X variables. The last term is included if error sources are common between the new X and the original Y_i variables.

If an analysis is being conducted using a Y value determined using Eq. (19) and it is postulated that the X value being used in the regression model has no uncertainty, then terms 8 through 11 on the RHS of Eq. (20) are omitted.

Higher-Order Regressions. The general expression for an nth order polynomial regression model is

$$Y(X_{\text{new}}) = a_0 + a_1 X_{\text{new}} + a_2 X_{\text{new}}^2 \ldots + a_n X_{\text{new}}^n \quad (21)$$

where the regression coefficients, a_i, are determined with a least squares fit by minimizing the Chi-square function, χ^2. The numerical least squares regression method used in this work utilizes orthogonal polynomials and a singular decomposition solution routine and is described in Press et al. (1986). The expression for the uncertainty in a value found using the polynomial regression model is the same as Eq. (20) with Y defined by Eq. (21). The complexity of the polynomial regression determination usually makes analytical determination of the partial derivatives prohibitive.

X and Y as Functional Relations. In many, if not most instances, the test results will be expressed in terms of functional relations, often dimensionless. In these cases, the measured variables will not be the X's and Y's used in the regression. Examples of common functional relations are Reynolds number, flow coefficient, turbine efficiency, specific fuel consumption, etc. For example, in the experimental determination of the pressure distribution on the surface of a cylinder in cross-flow, the results are usually presented as pressure coefficient versus angular position θ. The pressure coefficient is

$$C_P = \frac{P - P_\infty}{q_\infty} \quad (22)$$

where P is the local pressure, P_∞ is the freestream pressure, and q_∞ is the dynamic pressure. The Y_i variables used in the regression model are the determined pressure coefficient values and are functions of the three measured variables

$$Y_i = C_{p,i} = f(P_i, P_{\infty,i} q_{\infty,i}) \quad (23)$$

and the X_i variables are the angular positions θ_i. If the pressures are measured with separate transducers that were calibrated against the same standard, the systematic uncertainties from the calibration will be correlated and must be properly taken into account. Equations (17), (18), and (20) apply in such cases, with Y (in this case C_p) taken as the dependent function for the regression and the X_i's and Y_i's replaced by the full set of measured variables (in this case the P_i's, $P_{\infty,i}$'s, $q_{\infty,i}$'s, and θ_i's, assuming no uncertainty in the new value of θ.)

In general, for an experiment with n sets of J measured variables, the regression model can be viewed as being a function of the J variables, such as

$$Y(X_{\text{new}}, X_i, Y_i) = f(\text{VAR1}_i, \text{VAR2}_i, \ldots, \text{VAR}J_i) \quad (24)$$

where the function X_i is made up of some of the variables and the function Y_i is made up of some of the variables, such as

$$X_i = f(\text{VAR1}_i, \text{VAR2}_i, \ldots, \text{VAR}K_i, \ldots) \quad (25)$$

and

$$Y_i = f(\ldots, \text{VAR}K_i, (\text{VAR}K + 1)_i, \ldots, \text{VAR}J_i) \quad (26)$$

and X_{new} is the new value of the independent variable in the regression. The general expression for the uncertainty in the value determined from the regression model becomes

$$U_Y^2 = \sum_{i=1}^{n}\sum_{j=1}^{J}\left(\frac{\partial Y}{\partial \text{VAR}j_i}\right)^2 P_{\text{VAR}j_i}^2 + \sum_{i=1}^{n}\sum_{j=1}^{J}\left(\frac{\partial Y}{\partial \text{VAR}j_i}\right)^2 B_{\text{VAR}j_i}^2$$

$$+ 2\sum_{i=1}^{n-1}\sum_{k=i+1}^{n}\sum_{j=1}^{J}\left(\frac{\partial Y}{\partial \text{VAR}j_i}\right)\left(\frac{\partial Y}{\partial \text{VAR}j_k}\right)B_{\text{VAR}j_i\text{VAR}j_k}$$

$$+ 2\sum_{i=1}^{n}\sum_{k=1}^{n}\sum_{j=1}^{J-1}\sum_{l=j+1}^{J}\left(\frac{\partial Y}{\partial \text{VAR}j_i}\right)\left(\frac{\partial Y}{\partial \text{VAR}l_k}\right)B_{\text{VAR}j_i\text{VAR}l_k}$$

$$+ \sum_{j=1}^{J}\left(\frac{\partial Y}{\partial\ \text{VAR}\ j_{\text{new}}}\right)^2 P_{\text{VAR}j_{\text{new}}}^2$$

$$+ \sum_{j=1}^{J}\left(\frac{\partial Y}{\partial \text{VAR}j_{\text{new}}}\right)^2 B_{\text{VAR}j_{\text{new}}}^2$$

$$+ 2 \sum_{i=1}^{n} \sum_{j=1}^{J} \left(\frac{\partial Y}{\partial \mathrm{VAR}j_{\mathrm{new}}} \right) \left(\frac{\partial Y}{\partial \mathrm{VAR}j_i} \right) B_{\mathrm{VAR}j_{\mathrm{new}}} B_{\mathrm{VAR}j_i}$$

$$+ 2 \sum_{i=1}^{n} \sum_{j=1}^{J-1} \sum_{l=j+1}^{J} \left(\frac{\partial Y}{\partial \mathrm{VAR}j_{\mathrm{new}}} \right) \left(\frac{\partial Y}{\partial \mathrm{VAR}l_i} \right) B_{\mathrm{VAR}j_{\mathrm{new}}} B_{\mathrm{VAR}l_i} \qquad (27)$$

where the third RHS term accounts for correlated systematic uncertainty sources within each variable and the fourth RHS term accounts for systematic uncertainty sources common between variables. Similar expressions for the uncertainty in the slope and intercept are readily obtained. Since the X_i and Y_i variables used to determine the regression model are now functional relations, the determination of the partial derivatives becomes more complex and should probably be performed numerically.

Linearizing transformations are often used to transform nonlinear functions to linear functions. For example, an exponential function is a linear function in semi-logarithmic space. The uncertainty associated with the regression model can be estimated using the techniques discussed above where the functional relationships, as expressed in Eqs. (25) and (26), are logarithmic functions. Again, the complexity introduced by the transformation usually makes analytical determination of the partial derivatives prohibitive.

4 Evaluation of Methodology Using Monte Carlo Simulations

For uncertainty in coefficients, Monte Carlo simulations were performed for the first-order regression case and included investigations of the effect of sample size and the type of dominant uncertainty. A portion of the results were presented earlier in Brown et al. (1995). For uncertainty in the Y value determined from the regression model, simulations were performed for first through sixth-order regressions and included investigations of the effects of type of dominant uncertainty and of both "percent of full scale" and "percent of reading" type uncertainties. Cases in which the regression variables were themselves functions were simulated for first, third, and fourth-order cases. Results of all simulations showed that the new methodology provides the appropriate uncertainty intervals.

Also investigated were confidence intervals calculated using previously proposed regression uncertainty methods: (1) a typical traditional statistical method (Natrella, 1963) that does not consider systematic uncertainties, and (2) a method proposed by Price (1993) that uses a root-sum-square combination of a random uncertainty and a systematic uncertainty for each point along a curvefit, or "X-Y plot" in Price's nomenclature. More discussion of the classical statistical confidence intervals can be found in Seber (1977), Montgomery and Peck (1992), and similar linear regression texts. Since space prohibits detailed presentation of these methods, the reader is referred to Brown (1996) for a more complete discussion. Similarly, the results of only a few of the simulations are presented here, and the reader is referred to Brown (1996) for more complete discussion of the cases investigated.

Monte Carlo Simulation Procedure. The methodology for assessing the uncertainty in linear regressions was evaluated using Monte Carlo simulations. Monte Carlo simulations are often used in uncertainty analysis to determine the effectiveness of a particular uncertainty model (for example, Brown et al., 1996). As used in this work, a Monte Carlo simulation is a numerical simulation of an experiment. Experimental data are generated by randomly sampling predefined error distribution populations and adding these errors to a predefined *true* value.

The Monte Carlo simulations were conducted in the following manner. "*True*" values for data from a chosen relationship were defined. The word *true* is emphasized to indicate that it represents the actual physical quantity of the variable if it could be measured without any bias error or precision error, which is always an unobtainable value. The two-sigma (2 standard deviation or 95 percent confidence) systematic uncertainties and random uncertainties for each variable were then specified. The errors in each variable were assumed to come from normally distributed error populations with the specified standard deviations. A random value for each bias error and precision error was found from a Gaussian random deviate generator subroutine using the specified standard deviations. In the cases in this study, the bias errors for all data points for each variable were assumed to be from the same source (simulating that all data was taken with the same apparatus), and were assigned the same random deviate within each iteration. In some cases the bias errors were a fixed amount and in some cases they were percent-of-reading type errors. Precision errors were obtained by sampling the precision error populations such that independent random deviates for each variable were obtained. The individual error values, bias errors, and precision errors were then summed and added to the *true* value to obtain a data point with errors from the specified error populations. For each iteration, these data points were then used in the linear least squares equations to obtain the regression coefficients and the regression model.

Using a first-order case as an example, uncertainty intervals (at 95 percent confidence) for the m, c, and Y (at each X_i point) were calculated from the uncertainty propagation analysis equations for m, c, and Y. A $\pm U_m$ interval was placed around the slope coefficient value, m, and if the true value of the slope was found to be within the interval a counter was incremented. A similar procedure was used for the intercept and for the Y value from the regression model. This procedure was repeated 10,000 times and the percent coverage, defined as the fraction of times the true result was within the estimated uncertainty interval, was determined. The percent coverage was used to judge the effectiveness of the uncertainty propagation equation. If 95 percent confidence uncertainty estimates for each of the elemental uncertainties are used in the regression uncertainty propagation equation, the percent coverage should be 95 percent to demonstrate that the methodology works.

Also calculated for each simulation was the uncertainty ratio, defined as the ratio of the average of the uncertainty intervals from the 10,000 iterations divided by the true 95 percent confidence interval. The true 95 percent uncertainties are calculated as two times the sample standard deviations, S_m, S_c, and S_Y, from the 10,000 samples of the regression coefficients and Y's. The sample standard deviations from the 10,000 sample population can be expected to be good representations of the actual standard deviations of the infinite population with the elemental uncertainty sources as defined. An uncertainty ratio of or near unity shows that the uncertainty methodology works for the particular case, with values greater than one meaning an overprediction and values less than one meaning an underprediction.

Results of Simulations.

Uncertainty in Regression Coefficients—First Order. As presented in Brown et al. (1995), the effect of sample size was studied by varying the number of X variable setpoints and the number of Y measurements taken at each X setpoint. Using the new methodology with its "large sample" assumption (taking $t = 2$ as in Eq. (16)), it was shown that the coverage obtained is 94 percent or greater when the number of data points used in the regression is about 25 or more, and that even when as few as 10 or so data points are used in the regression a greater than 92 percent coverage is obtained. As discussed in Coleman and Steele (1995), the difference between 92 and 95 percent coverage is essentially irrelevant in a practical engineering sense

Table 1 First-order regression simulation results—dominant systematic uncertainties

$B_{X1} = 2.5$ $B_{X2} = 2.5\%$ $P_X = 0.1$
$B_{Y1} = 2.5$ $B_{Y2} = 2.5\%$ $P_Y = 0.1$ $B_{X3} = B_{Y3} = 2.5$

	Uncertainty propagation			Classical statistics		
pt	U_Y(avg)	Cov (%)	Ratio	U_Y(avg)	Cov (%)	Ratio
1	4.58	95.4	0.99	0.15	3.9	0.02
2	4.81	95.3	0.99	0.11	2.5	0.02
3	5.06	95.4	0.99	0.09	1.8	0.01
4	5.32	95.3	0.99	0.11	2.3	0.02
5	5.59	95.4	0.99	0.15	3.0	0.02
	U(avg)	Cov (%)	Ratio	tS(avg)	Cov (%)	Ratio
m	0.036	95.6	1.01	0.005	21.1	0.13
c	3.56	95.3	0.99	0.47	20.2	0.13

since estimates of the systematic and random uncertainties cannot consistently be made to that level of certainty.

Other simulations were performed in which the "correct" random uncertainties and systematic uncertainties were used in the propagation equations. Such cases assume that the correct random uncertainties have been estimated based upon prior information and experience with the test apparatus, so that the simulations evaluate the methodology only. (This assumption is made in all of the simulations discussed in the rest of this article.) Results for uncertainties in slope and intercept are shown for two cases in Tables 1 and 2.

For first-order regressions, when the systematic uncertainties are a fixed value, or "percent of full scale," then the systematic uncertainties are the same value for each data pair and the linear least squares line through the data simply translates vertically or horizontally from the true line. The value of the slope remains the same and there is no systematic uncertainty in the slope. The value of the intercept will change and will accordingly have a systematic uncertainty. When the systematic uncertainties are of a "percent of reading" nature, so that the systematic uncertainty is a function of the magnitude of the variable, the slope *will* have an associated nonzero systematic uncertainty.

Uncertainty in Y Value From Regression Model—First Order. The uncertainty associated with a Y value calculated from the regression model is determined using Eq. (20). For the Monte Carlo simulation, the *true* relationship for the 1st order regression simulations was defined by the equation

$$Y = X + 10 \tag{28}$$

Five points along this line were defined as the *true* data in the Monte Carlo simulations. In each simulation the average uncertainty, the percent coverage, and the uncertainty ratio were calculated and used to compare the regression uncertainty methodology results to the classical statistical results and to the results using Price's method.

Table 2 Polynomial simulation results—dominant systematic uncertainties

$B_{X1} = 0.0$ $B_{X2} = 0\%$ $P_X = 2.5$
$B_{Y1} = 0.0$ $B_{Y2} = 0\%$ $P_Y = 2.5$ $B_{X3} = B_{Y3} = 0$

	Uncertainty propagation			Classical statistics		
pt	U_Y(avg)	Cov (%)	Ratio	U_Y (avg)	Cov (%)	Ratio
1	2.74	95.6	1.00	3.15	95	1.46
2	1.96	95.3	1.00	2.25	94.8	1.46
3	1.59	95.3	1.00	1.84	94.6	1.46
4	1.98	95.4	1.00	2.28	94.9	1.46
5	2.76	95.4	1.00	3.17	94.8	1.46
	U(avg)	Cov (%)	Ratio	tS(avg)	Cov (%)	Ratio
m	0.112	95.4	1.01	0.163	94.9	1.48
c	11.31	95.5	1.01	16.5	94.8	1.47

Three different types of simulations were investigated. First were simulations where the systematic uncertainties were much greater than the precision uncertainties and where all of the systematic uncertainties were correlated within the X's and within the Y's, including an error source correlated between the X's and the Y's. Second were simulations where the systematic uncertainties were the same value as the random uncertainties, and the systematic uncertainties are correlated within the X's and within the Y's, but not correlated between the X's and the Y's. The third type of simulations included only random uncertainties.

Table 1 shows results for the case for dominant systematic uncertainties. The new methodology provides the appropriate (approximately 95 percent) coverage for the predicted value and the regression coefficients, while the classical statistical method severely underestimates the uncertainty. For the case with dominant random uncertainties, Table 2 presents the simulation results and shows that both methods provide the desired coverage. The classical statistical method overpredicts the uncertainty interval by almost 50 percent, however. This is a result of using a small sample size (5 data points) for the simulation. While the uncertainty propagation methodology assumes the precision limits are large sample estimates, the classical statistical method does not. When simulations were performed with increasingly larger sample sizes the uncertainty ratio obtained for the statistical confidence interval approached unity, as expected. For the case of comparable magnitude systematic and random uncertainties, the results (not presented here) showed that the new methodology provides the appropriate coverage and the statistical method does not.

Higher-Order Regressions. Higher-order regression models were also simulated with the Monte Carlo technique. In the example discussed here, seven data points along a curve defined by

$$Y(X) = -300 + 10{*}X - 0.05{*}X^2 \tag{29}$$

were chosen to represent the *true* data. Three systematic error sources were defined, as well as a precision error source for each variable. The first systematic error source affects only the X measurements, the second systematic error source affects only the Y measurements, and the third systematic error source affects both the X and Y measurements.

Table 3 shows results for a simulation performed with dominant systematic uncertainties. Bias sources 1 and 2 were assigned the same value and bias source 3—common to both X and Y—was assigned a larger value. Random uncertainties much smaller than the systematic uncertainties were assigned to the X and Y variables. The results indicate the appropriate

Table 3 First-order regression simulation results—dominant random uncertainties

$B_{X1} = 1.0$ $P_X = 0.0$
$B_{Y1} = 1.0$ $P_Y = 0.0$ $B_{X2} = B_{Y2} = 3.0$

	Uncertainty propagation			Price method		
Pt	U_Y(avg)	Cov (%)	Ratio	U_Y(avg)	Cov (%)	Ratio
1	5.25	95.2	1.01	8.52	99.9	1.63
2	2.37	95.5	1.01	5.71	100.0	2.43
3	1.49	96.4	1.04	4.49	100.0	3.13
4	1.91	96.1	1.01	3.56	99.8	1.89
5	3.17	95.1	1.00	3.20	96.1	1.01
6	4.64	95.0	1.00	3.56	87.9	0.77
7	6.16	95.2	1.00	4.49	85.4	0.73

uncertainty intervals are obtained with the uncertainty propagation method while Price's method provides inconsistent results. Similar conclusions were also evident in the results of a simulation performed with dominant precision uncertainties. Overall, the simulations showed that Price's method does not provide the correct uncertainty intervals for first-order linear regressions when a systematic error source is common to both the independent and dependent variables and it does not provide the appropriate uncertainty intervals for higher order regressions.

Many different simulations were performed with higher-order polynomials to investigate the robustness of the regression uncertainty methodology. Simulations with higher-order polynomials and polynomials with smaller and larger curvature were simulated, and the proposed methodology provided the appropriate uncertainty intervals. As would be expected, in regions of greater curvature more points were necessary to avoid underfitting or overfitting the data.

5 Reporting Regression Uncertainties

After the uncertainty associated with a regression has been calculated, it should be documented clearly and concisely so it can be easily used. Figure 1 shows a set of (X, Y) data, the first-order regression model for that data set, and the associated uncertainty interval determined using Eq. (20). It would usually be very useful to have not only the regression model, but also an equation giving $U_Y(X)$. While Eq. (20) gives such information, it requires having the entire (X_i, Y_i) data set as input each time a calculation of U_Y is made for a new X value. Since this is cumbersome and inconvenient, the authors propose that a set of (X, U) points be calculated using Eq. (20) and a regression be performed using these points to produce an expression for $U_{Y\text{-regress}}(X)$, which is used as explained below to calculate $U_Y(X)$ at a given X value.

The procedure that should be used is as follows. If the X_{new} to be used in Eq. (1)

$$Y(X) = a_0 + a_1X + a_2X^2 + \ldots + a_nX^n \tag{1}$$

has no uncertainty, then Eq. (20)—with terms 8–11 on the RHS set equal to zero—is used over the desired X range to produce the (X, U) data set to be curvefit to produce $U_Y(X)$.

If the X_{new} to be used in Eq. (1) is from the same apparatus as produced the (X_i, Y_i) data set, then all of the terms in Eq. (20) must be considered. However, the $P^2_{X_{\text{new}}}$ term will often be larger during the test than during the more well-controlled calibration. This can be taken into account by assigning the same systematic uncertainty components that were in the X_i data to the X_{new}'s used in Eq. (20) to produce the (X, U) points to curvefit, but with the $P^2_{X_{\text{new}}}$ term in Eq. (20) set equal to zero. The resulting (X, U) points are then curvefit to yield $U_{Y\text{-regress}}(X)$. When an X_{new} is used in Eq. (1), the uncertainty U_Y in the Y determined from the regression is then calculated as

$$(U_Y)^2 = U^2_{Y\text{-regress}} + \left(\frac{\partial Y}{\partial X_{\text{new}}}\right)^2 P^2_{X_{\text{new}}} \tag{30}$$

If the X_{new} to be used in Eq. (1) is from a different apparatus than that which produced the (X_i, Y_i) data set, then terms 10 and 11 on the RHS of Eq. (20) will be zero. This situation would be encountered if a thermocouple calibration curve was determined but then another voltmeter was used in testing than that which produced the original (T_i, E_i) data set. Equation (20)—with terms 8–11 on the RHS set equal to zero—is used over the desired X range to calculate a set of (X, U) points that are then curvefit to produce a $U_{Y\text{-regress}}(X)$ expression. When an X_{new} is used in Eq. (1), the uncertainty U_Y in the predicted Y is then calculated using

$$(U_Y)^2 = U^2_{Y\text{-regress}} + \left(\frac{\partial Y}{\partial X_{\text{new}}}\right)^2 [B^2_{X_{\text{new}}} + P^2_{X_{\text{new}}}] \tag{31}$$

The contribution of $U_{Y\text{-regress}}$ to U_Y in Eqs. (30) and (31) is purely a systematic uncertainty, since all random uncertainties are fossilized once the regression is performed. It should be noted that the lowest order curvefit that provides an acceptable fit for the regression uncertainty should be used to represent that uncertainty.

6 Venturi Flowmeter Application

This section discusses the application of the regression uncertainty methodology to the calibration of a venturi flowmeter and its subsequent use to determine water flowrate in a test. It is shown that previous ways of accounting for the contribution of discharge coefficient uncertainty to the overall flowrate uncertainty do not correctly account for all uncertainty sources, and the appropriate approach is presented and discussed.

Venturi flowmeters are often used to measure fluid flow because of their simplicity, durability, and lack of moving parts. They are part of a class of flowmeters known as differential pressure producers since a pressure drop across a region in the meter is produced, and this pressure differential is used to determine the flowrate through the meter. The one-dimensional model for the volumetric flowrate through a venturi flowmeter is

$$Q_{\text{Th}} = \frac{A_2}{\sqrt{1 - \left(\frac{A_2}{A_1}\right)^2}} \sqrt{2\frac{(P_1 - P_2)}{\rho}} \tag{32}$$

(Bean, 1971). If the pressure drop measured between taps 1 and 2 is used to calculate the "head" of the flowing fluid

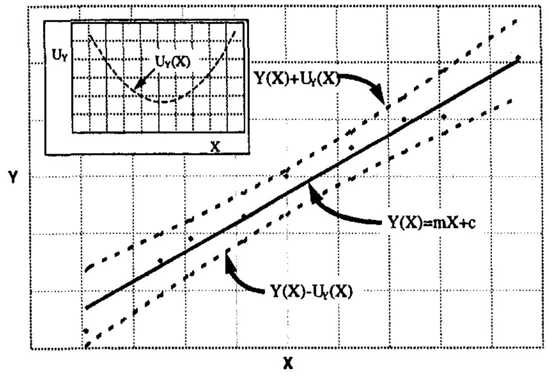

Fig. 1 Expressing regression uncertainty intervals

$$h = \frac{P_1 - P_2}{\rho g} \tag{33}$$

and the ratio of the venturi throat diameter, d, to the venturi inlet diameter, D, is denoted as

$$\beta = \frac{d}{D} \tag{34}$$

then the 1-D flowrate can be expressed as

$$Q_{\mathrm{Th}} = Kd^2 \sqrt{\frac{h}{1 - \beta^4}} \tag{35}$$

where K is a constant.

The actual flowrate will never equal the theoretical flowrate, and the venturi must be calibrated against a reference meter. The discharge coefficient, C_d, is defined as the flowrate through the standard divided by the theoretical flowrate

$$C_d = \frac{Q_{\mathrm{std}}}{Q_{\mathrm{Th}}} = \frac{Q_{\mathrm{std}}}{Kd^2 \sqrt{\dfrac{h}{1 - \beta^4}}} \tag{36}$$

Often a venturi flowmeter is calibrated over a range of flowrates and the discharge coefficient is written as a function of Reynolds number defined at the venturi throat

$$\mathrm{Re} = \frac{Vd}{v} = \frac{4Q}{\pi d v} \tag{37}$$

In this work, a first-order regression model

$$C_d(\mathrm{Re}) = a_0 + a_1 \,\mathrm{Re} \tag{38}$$

is determined from the $N(\mathrm{Re}(i),\ C_d(i))$ data points produced in the calibration.

When the venturi flowmeter is used in a test, the flowrate is determined from

$$Q = C_d(\mathrm{Re}_{\mathrm{new}}) K d^2 \sqrt{\frac{h_{\mathrm{new}}}{1 - \left(\dfrac{d}{D}\right)^4}} \tag{39}$$

or, substituting Eqs. (37) and (38) into (39)

$$Q = \frac{a_0 K d^2 \sqrt{\dfrac{h_{\mathrm{new}}}{1 - \left(\dfrac{d}{D}\right)^4}}}{1 - \dfrac{4 a_1 K d}{\pi v_{\mathrm{new}}} \sqrt{\dfrac{h_{\mathrm{new}}}{1 - \left(\dfrac{d}{D}\right)^4}}} \tag{40}$$

Since the variables d, D, and possibly v_{new} and h_{new} in Eqs. (39) and (40) share identical systematic error sources with the same variables in the $(\mathrm{Re}(i),\ C_d(i))$ data points used in the regression that produced the a_0 and a_1 coefficients, the estimate of the uncertainty in Q should include correlated systematic uncertainty terms to take this into account. This has not previously been done and will be discussed further in a following section.

Note that the kinematic viscosity, v_{new}, appearing in $\mathrm{Re}_{\mathrm{new}}$ will be different than the $v(i)$ used in determining $\mathrm{Re}(i)$ if the venturi is calibrated with a different fluid than being measured during the test. In such cases, since the systematic uncertainties do not arise from the same source no correlation terms are needed.

Experimental Apparatus. A calibration apparatus was assembled to calibrate the 2 in. diameter venturi flowmeter. A variable speed pump pumped water through the flowmeters, the flowrate was measured with the reference flowmeter, and the differential pressure produced by the venturi flowmeter was recorded. The flowmeter used as the calibration standard was a $1\text{-}\frac{1}{2}$ in. diameter turbine-type flowmeter. This flowmeter was used because it was available and was installed in the water tunnel facility being used. The differential pressure was measured with a differential pressure transducer that required a 12 Vdc excitation voltage and produced a millivolt output proportional to the pressure difference between the two ports on the transducer.

Pressure Transducer Calibration and Uncertainty. The transducer was calibrated by applying a water column to each port of the transducer and recording the output voltage as the height of the water column on one side was increased. The first-order regression representing the calibration data points was determined as

$$h = 2.2624 V_o - 0.42334 \tag{41}$$

(with h in (inches H_2O) and V_0 in (mV)). The uncertainty associated with the h-value determined from this transducer calibration curve was assessed using Eq. (20) (where in this case $Y = h$ and $X = V_0$).

No error sources were shared between the measured differential pressure and the measured transducer output voltage, so all B_{XY} terms were zero. Since a random uncertainty estimate for X_{new} based upon the transducer calibration data might not be representative of the random uncertainty in X_{new} encountered when the transducer is used in a test to determine the flowrate through the venturi, the $P_{X_{\mathrm{new}}}$ term in Eq. (20) was omitted from the regression uncertainty and will be accounted for in the flowrate uncertainty. (This corresponds to the case in which Eq. (30) is used to determine U_Y.) This is a common situation since the calibration process is usually more well-controlled and provides more stable data than when the transducer is used in the actual experiment.

The uncertainty contribution for the value of h determined from the differential pressure transducer calibration regression then becomes

$$\begin{aligned} U^2_{h\text{-regress}} = {} & \sum_{i=1}^{N} \left(\frac{\partial h}{\partial h(i)}\right)^2 P^2_{h(i)} + \sum_{i=1}^{N} \left(\frac{\partial h}{\partial V_0(i)}\right)^2 P^2_{V_0(i)} \\ & + \sum_{i=1}^{N} \left(\frac{\partial h}{\partial h(i)}\right)^2 B^2_{h(i)} + 2 \sum_{i=1}^{N-1} \sum_{k=i+1}^{N} \left(\frac{\partial h}{\partial h(i)}\right) \\ & \times \left(\frac{\partial h}{\partial h(k)}\right) B_{h(i)h(k)} + \sum_{i=1}^{N} \left(\frac{\partial h}{\partial V_0(i)}\right)^2 B^2_{V_0(i)} \\ & + 2 \sum_{i=1}^{N-1} \sum_{k=i+1}^{N} \left(\frac{\partial h}{\partial V_0(i)}\right)\left(\frac{\partial h}{\partial V_0(k)}\right) B_{V_0(i)V_0(k)} \\ & + \left(\frac{\partial h}{\partial V_0(\mathrm{new})}\right)^2 B^2_{V_0(\mathrm{new})} \\ & + 2 \sum_{i=1}^{N} \left(\frac{\partial h}{\partial V_0(\mathrm{new})}\right)\left(\frac{\partial h}{\partial V_0(i)}\right) B_{V_0(\mathrm{new})V_0(i)} \end{aligned} \tag{42}$$

A systematic uncertainty of $\frac{1}{16}$ in. H_2O and a random uncertainty of $\frac{1}{8}$ in. H_2O were used as the uncertainty estimates for

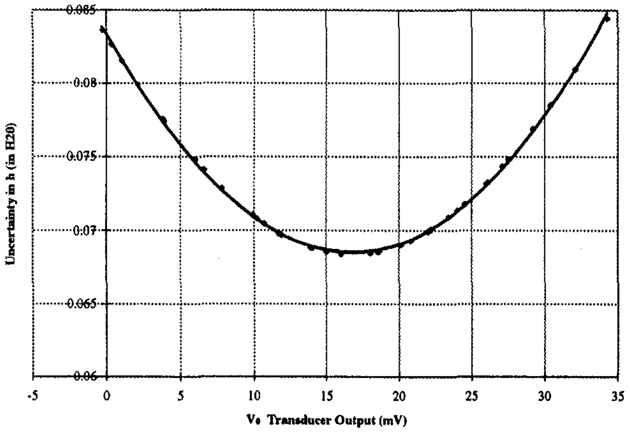

Fig. 2 Differential pressure transducer calibration curve uncertainty

the applied differential pressure. These estimates were based upon the accuracy and readability of the scale used to measure the heights of the water columns. A systematic uncertainty of 0.5 mV was estimated for the voltmeter based upon manufacturer's specifications. The uncertainty associated with the differential pressure transducer calibration curve was obtained from Eq. (42) and is shown as a function of the output voltage in Fig. 2. The second-order polynomial

$$U_{h\text{-regress}} = 5.28 \times 10^{-5} V_o^2 - 0.00177 V_o + 0.0833 \quad (43)$$

was fit to the uncertainty results and used to express the differential pressure uncertainty as a function of the transducer output voltage. As discussed previously, this expression does not include the contribution of the random uncertainty in the $V_0(\text{new})$ measured during the testing, so an equation similar to Eq. (30) must be used to estimate the overall U_h.

Venturi Discharge Coefficient and Its Uncertainty. As described earlier in this section, prior to this work all of the correlated uncertainty contributions have not been taken into account in estimating uncertainties in discharge coefficients or in estimating the flowrate uncertainties. In this subsection, the approach that has been used previously is shown and its deficiencies are discussed. In the next subsection, the new approach that properly accounts for all correlated uncertainty contributions will be demonstrated.

In the calibration experiment performed in this effort, the flowrate, Q_{std}, measured by the calibration standard flowmeter and the differential pressure produced by the venturi flowmeter were obtained at selected settings of the variable speed pump. Using Eqs. (36) and (37), obtaining the dimensions of the venturi from the manufacturer's drawings ($D = 2.125$ in., $d = 1.013$ in.) and a reference room temperature value for kinematic viscosity of water (1.08×10^{-5} ft^2/s), the Reynolds number and discharge coefficient for each data point were calculated.

The data set used to determine the regression model was obtained by averaging the Q_{std} and h data taken at each pump speed setting. The ($\text{Re}(i)$, $C_d(i)$) data set was fit with a first-order regression model that yielded

$$C_d = 0.991 - 1.21 \times 10^{-7}\ \text{Re} \quad (44)$$

Recalling Eqs. (36) and (37), the C_d predicted by this expression is actually a function of the variables $Q_{\text{std}}(i)$, $h(i)$, $\upsilon(i)$, d, and D and can be written functionally as

$$C_d = f\{Q_{\text{std}}(i), h(i), \upsilon(i), d, D\} \quad (45)$$

The expression for the uncertainty associated with a predicted value from the discharge coefficient regression model is obtained by applying Eq. (27) to Eq. (45), yielding

$$\begin{aligned} U^2_{C_d\text{-regress}} = {} & \sum_{i=1}^{N} \left(\frac{\partial C_d}{\partial Q_{\text{std}}(i)}\right)^2 P^2_{Q_{\text{std}}}(i) + \sum_{i=1}^{N} \left(\frac{\partial C_d}{\partial Q_{\text{std}}(i)}\right)^2 B^2_{Q_{\text{std}}}(i) \\ & + 2\sum_{i=1}^{N-1}\sum_{k=i+1}^{N} \left(\frac{\partial C_d}{\partial Q_{\text{std}}(i)}\right)\left(\frac{\partial C_d}{\partial Q_{\text{std}}(k)}\right) B_{Q_{\text{std},i}Q_{\text{std},k}} \\ & + \sum_{i=1}^{N} \left(\frac{\partial C_d}{\partial h(i)}\right)^2 [B_h^2(i) + P_h^2(i)] \\ & + 2\sum_{i=1}^{N-1}\sum_{k=i+1}^{N} \left(\frac{\partial C_d}{\partial h(i)}\right)\left(\frac{\partial C_d}{\partial h(k)}\right) B_{h_i h_k} \\ & + \sum_{i=1}^{N} \left(\frac{\partial C_d}{\partial \upsilon(i)}\right)^2 B_\upsilon^2(i) \\ & + 2\sum_{i=1}^{N-1}\sum_{k=i+1}^{N} \left(\frac{\partial C_d}{\partial \upsilon(i)}\right)\left(\frac{\partial C_d}{\partial \upsilon(k)}\right) B_{\upsilon_i \upsilon_k} \\ & + \left(\frac{\partial C_d}{\partial d}\right)^2 B_d^2 + \left(\frac{\partial C_d}{\partial D}\right)^2 B_D^2 \end{aligned} \quad (46)$$

The $B_h(i)$ in Eq. (46) is given by Eq. (42) since all uncertainty contributions to Eq. (42) are fossilized when it is used. The $P_h(i)$ in Eq. (46) is found by applying the uncertainty propagation equation to Eq. (41). Remember also that Eq. (46) includes no contributions from the uncertainties in Re_{new} when Eq. (44) is used.

The uncertainties estimated for the venturi discharge coefficient variables are shown in Table 4. The calibration flowmeter has an uncertainty quoted by the manufacturer of 1.0 percent of reading, and this value is used as the systematic uncertainty in Eq. (46). The calibration flowmeter random uncertainty was estimated based upon variation observed during the testing. When the differential pressure transducer calibration curve, Eq. (41), is used during the venturi calibration testing, the transducer uncertainty as determined by Eq. (43) is considered a fossilized systematic uncertainty. The uncertainty estimates for the venturi inlet and throat dimensions are based upon the machining tolerances noted on the venturi manufacturer's data sheet. A systematic uncertainty of approximately 0.5 percent of reading is assigned to the kinematic viscosity to account for the uncertainty in the original experimental viscosity data used. (An argument could be made for a larger estimate of B_υ.)

The uncertainty in discharge coefficient given by Eq. (46) was modeled as a function of Reynolds number with a second-order regression

$$\begin{aligned} & U_{C_d\text{-regress}}(\text{Re}) \\ & \quad = 1.38 \times 10^{-12}\ \text{Re}^2 - 3.46 \times 10^{-7}\ \text{Re} + 0.0333 \end{aligned} \quad (47)$$

and is shown along with the discharge coefficient data and regression model in Fig. 3.

Also shown on Fig. 3 are the uncertainty intervals for the individual (Re, C_d) data points. The discharge coefficient uncertainty for each individual data point was determined by applying the uncertainty propagation equations to Eq. (36) to obtain

Table 4 Uncertainties for Venturi calibration

Source	Systematic	Random
Turbine meter	1% of *Rdg*	0.5 gpm
Differential Pressure Transducer	Eq. (43)	$(\partial h/\partial V_o)^2 \times (P_{V_o})^2$
Venturi throat Dia.	0.005″	0.0
Venturi inlet dia.	0.005″	0.0
Kinematic Viscosity	5.0 E-8	0.0

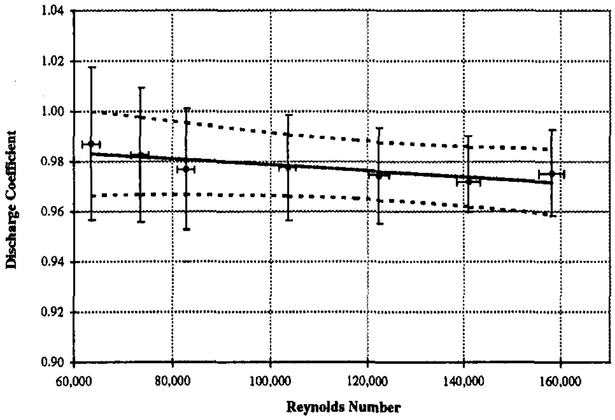

Fig. 3 Discharge coefficient vs. Reynolds number, averaged data

$$U_{C_d}^2 = \left(\frac{\partial C_d}{\partial Q_{\text{std}}}\right)^2 P_{Q_{\text{std}}}^2 + \left(\frac{\partial C_d}{\partial Q_{\text{std}}}\right)^2 B_{Q_{\text{std}}}^2 + \left(\frac{\partial C_d}{\partial h}\right)^2 B_h^2 + \left(\frac{\partial C_d}{\partial d}\right)^2 B_d^2 + \left(\frac{\partial C_d}{\partial D}\right)^2 B_D^2 \quad (48)$$

and the Reynolds number uncertainty was similarly determined as

$$U_{\text{Re}}^2 = \left(\frac{\partial \text{Re}}{\partial Q_{\text{std}}}\right)^2 P_{Q_{\text{std}}}^2 + \left(\frac{\partial \text{Re}}{\partial Q_{\text{std}}}\right)^2 B_{Q_{\text{std}}}^2 + \left(\frac{\partial \text{Re}}{\partial d}\right)^2 B_d^2 + \left(\frac{\partial \text{Re}}{\partial \upsilon}\right)^2 B_\upsilon^2 \quad (49)$$

It is observed in Fig. 3 that the discharge coefficient uncertainty for individual data points is larger than the uncertainty associated with the discharge coefficient regression model at the same Re. This is reasonable, since the regression uncertainty interval at a given Re point includes information from the N data points used in the regression, while the uncertainty interval for a single data point at that Re includes information from that point only.

The uncertainty in C_d (given by Eq. (47) or Eq. (48)) is not as useful as has been previously supposed. When C_d is used in Eq. (39) or a_0 and a_1 are used in Eq. (40) to determine Q in an experiment, U_{Cd} or U_{a0} and U_{a1} contain(s) components that are correlated with the systematic uncertainties in the values of d, D, and possibly υ_{new} and h_{new} in Eq. (39) or Eq. (40). These additional correlation terms are difficult (or impossible) to formulate correctly, and the authors recommend a new approach described in the following section.

Flowrate and Its Uncertainty in a Test. As stated in the previous section, it is difficult to propagate properly the discharge coefficient uncertainty to obtain the uncertainty associated with a flowrate determination because of correlated systematic uncertainties. This section demonstrates how the uncertainty associated with the venturi flowmeter calibration can be determined and how it can be reported in a form which properly expresses the uncertainty associated with the flowrate determination.

When the venturi flowmeter is used in a test, the flowrate is calculated using Eq. (39) or Eq. (40). A seemingly straightforward method to determine the flowrate uncertainty would be to apply the uncertainty propagation equations to Eq. (39) to obtain the uncertainty expression

$$U_Q^2 = \left(\frac{\partial Q}{\partial C_d}\right)^2 B_{C_d}^2 + \left(\frac{\partial Q}{\partial d}\right)^2 B_d^2 + \left(\frac{\partial Q}{\partial D}\right)^2 B_D^2 + \left(\frac{\partial Q}{\partial \upsilon_{\text{new}}}\right)^2 (B_{\upsilon_{\text{new}}}^2) + \left(\frac{\partial Q}{\partial h_{\text{new}}}\right)^2 (B_{h_{\text{new}}}^2 + P_{h_{\text{new}}}^2) + \left\{\begin{matrix}\text{correlation terms between } C_d \text{ and } d,\ C_d \text{ and } D, \\ C_d \text{ and } h_{\text{new}}, \text{ and } C_d \text{ and } \text{V}_{\text{new}}\end{matrix}\right\} \quad (50)$$

or an equivalent expression with a_0 and a_1 appearing instead of C_d if Eq. (40) is used. The correlation terms have not previously been considered in analyses estimating the contribution of the discharge coefficient uncertainty to the overall flowrate uncertainty. Even if one wanted to consider them, their evaluation is difficult, if not impossible. The correlated systematic uncertainty effects must be taken into account, however, since some of the variables in Eq. (39) or Eq. (40) are the same variables in the (Re(i), $C_d(i)$) data set used in finding the discharge coefficient regression model (Eq. (38) or Eq. (44)). The same values for the throat and inlet diameters, d and D, are used in Eq. (39) (or (40)) as were used in the determination of the discharge coefficient regression. If the same differential pressure transducer is used in the test to determine the flowrate as was used during the calibration, or if a different transducer that has common systematic uncertainty sources with the calibration transducer is used to measure the differential pressure, appropriate correlation terms must be included. Similarly, if the value of kinematic viscosity has common systematic uncertainty sources with the values used during the discharge coefficient determination the appropriate correlated systematic uncertainty terms must be included.

The authors recommend a new approach rather than that of Eq. (50). Recognizing that the flowrate is the result desired from the venturi during a test and that it is a function of the variables used to obtain the discharge coefficient regression as well as the variables measured in the test, the expression for Q can be represented functionally as

$$Q = f\{C_d(Q_{\text{std}}(i), h(i), \upsilon(i), d, D), h_{\text{new}}, \upsilon_{\text{new}}\} \quad (51)$$

where C_d is the regression expression Eq. (38) or (44), but with the regression coefficients replaced by expressions similar to those given by Eqs. (13) and (14). The uncertainty propagation equations can be applied directly to Eq. (51) to produce an expression for $U_{Q\text{-regress}}$.

The equation for $U_{Q\text{-regress}}$ can be written with the information known at the time of the venturi calibration and prior to the test; however, one must be careful to properly consider what systematic and random uncertainty information will only be known after the test has been conducted. If the same differential pressure transducer is used in the test as was used in the calibration and if the systematic uncertainty for the test value of kinematic viscosity is known, the only uncertainty not known prior to the test is the random uncertainty for the differential pressure measurements. Thus $U_{Q\text{-regress}}$ can be calculated as in Eq. (52)

$$U_{Q\text{-regress}}^2 = \sum_{i=1}^{N}\left(\frac{\partial Q}{\partial Q_{\text{std}}(i)}\right)^2 P_{Q_{\text{std}}}^2(i) + \sum_{i=1}^{N}\left(\frac{\partial Q}{\partial h(i)}\right)^2 P_h^2(i) + \sum_{i=1}^{N}\left(\frac{\partial Q}{\partial Q_{\text{std}}(i)}\right)^2 B_{Q_{\text{std}}}^2(i) + 2\sum_{i=1}^{N-1}\sum_{k=i+1}^{N}\left(\frac{\partial Q}{\partial Q_{\text{std}}(i)}\right)\left(\frac{\partial Q}{\partial Q_{\text{std}}(k)}\right) B_{Q_{\text{std},i}Q_{\text{std},k}}$$

$$
+ \sum_{i=1}^{N} \left(\frac{\partial Q}{\partial h(i)}\right)^2 B_h^2(i) + 2 \sum_{i=1}^{N-1} \sum_{k=i+1}^{N} \left(\frac{\partial Q}{\partial h(i)}\right)
$$

$$
\times \left(\frac{\partial Q}{\partial h(k)}\right) B_{h_i h_k} + \sum_{i=1}^{N} \left(\frac{\partial Q}{\partial \upsilon(i)}\right)^2 B_\upsilon^2(i)
$$

$$
+ 2 \sum_{i=1}^{N-1} \sum_{k=i+1}^{N} \left(\frac{\partial Q}{\partial \upsilon(i)}\right)\left(\frac{\partial Q}{\partial \upsilon(k)}\right) B_{\upsilon_i \upsilon_k}
$$

$$
+ \left(\frac{\partial Q}{\partial d}\right)^2 B_d^2 + \left(\frac{\partial Q}{\partial D}\right)^2 B_D^2 + \left(\frac{\partial Q}{\partial h_{\text{new}}}\right)^2 B_{h_{\text{new}}}^2
$$

$$
+ 2 \sum_{i=1}^{N} \left(\frac{\partial Q}{\partial h(i)}\right)\left(\frac{\partial Q}{\partial h_{\text{new}}}\right) B_{h(i)h_{\text{new}}} + \left(\frac{\partial Q}{\partial \upsilon_{\text{new}}}\right)^2 B_{\upsilon_{\text{new}}}^2
$$

$$
+ 2 \sum_{i=1}^{N} \left(\frac{\partial Q}{\partial \upsilon(i)}\right)\left(\frac{\partial Q}{\partial \upsilon_{\text{new}}}\right) B_{\upsilon(i)\upsilon_{\text{new}}} \quad (52)
$$

and where

$$
U_Q^2 = U_{Q\text{-regress}}^2 + \left(\frac{\partial Q}{\partial h_{\text{new}}}\right)^2 P_{h_{\text{new}}}^2 \quad (53)
$$

and

$$
P_{h_{\text{new}}}^2 = \left(\frac{\partial Q}{\partial V_{0,\text{new}}}\right)^2 P_{V_{0,\text{new}}}^2 \quad (54)
$$

The first ten terms on the RHS of Eq. (52) propagate the uncertainties associated with the venturi calibration into the flowrate uncertainty. The remaining four terms of Eq. (52) propagate the uncertainties associated with the ''new'' variables when Eq. (40) is used to determine Q.

The effects of B_d and B_D in Eq. (52) deserve discussion. If the same values of d and D are used in the calibration and in Eq. (40), then the $(\partial Q / \partial d)$ and $(\partial Q / \partial D)$ factors in terms nine and ten on the RHS of Eq. (52) are zero. Thus, the uncertainties in d and D contribute nothing to the uncertainty in Q—they have been ''calibrated out.'' This makes sense if one realizes that using a value of d that is too large by a factor of two would not change anything as long as exactly the same value is used in the calibration and in determining Q using Eq. (40).

If the throat diameter d of the venturi changes (perhaps as a result of abrasion or erosion) and a different value of d is used in Eq. (40) than in the calibration, that d should be treated as a different variable (perhaps labeled d_{new}) than the d used in the calibration. In that case, the $\partial Q / \partial d$ factor in term nine on the RHS of Eq. (52) will no longer be zero, and an additional term, $[(\partial Q / \partial d_{\text{new}})^2 (B_{d\text{new}})^2]$, must be added to Eq. (52).

The kinematic viscosity terms in Eq. (52) also deserve discussion. If the same fluid is used in the calibration as in the test and if it has a constant kinematic viscosity and systematic uncertainty, then the uncertainty in the kinematic viscosity has no effect on the uncertainty in Q. For this case, the four terms for kinematic viscosity in Eq. (52) add to zero.

The uncertainty $U_{Q\text{-regress}}$ determined after the calibration, as calculated using Eq. (52) and as a function of Reynolds number, is shown in Fig. 4. A regression was performed using the set of (Re, $U_{Q\text{-regress}}$) points to give

$$
U_{Q\text{-regress}} = 5 \times 10^{-16}\,\text{Re}_{\text{new}}^3 - 1 \times 10^{-10}\,\text{Re}_{\text{new}}^2 + 2 \times 10^{-5}\,\text{Re}_{\text{new}} - 0.1162 \quad (55)
$$

where $U_{Q\text{-regress}}$ is in gpm.

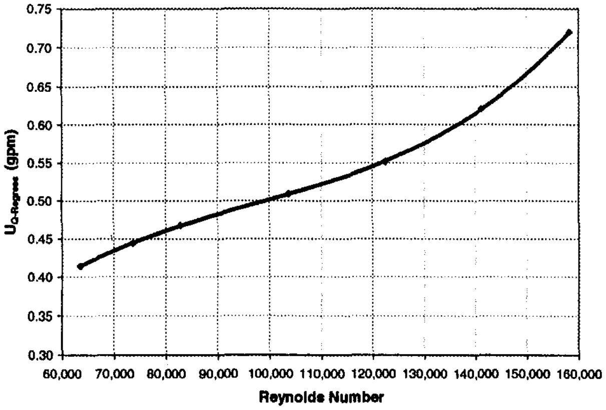

Fig. 4 Uncertainty in venturi flowrate as a function of Reynolds number

If the pressure transducer used during the test is not the same pressure transducer as was used during the calibration, and does not share any common systematic uncertainty sources, the systematic uncertainty term for the new transducer and the $B_{h(i)h\text{new}}$ term should be set equal to zero in Eq. (52), producing a new expression similar to Eq. (55). For the case where the test fluid kinematic viscosity systematic uncertainty is known, the resulting expression for the uncertainty in flowrate would then be

$$
U_Q^2 = U_{Q\text{-regress}}^2 + \left(\frac{\partial Q}{\partial h_{\text{new}}}\right)^2 P_{h_{\text{new}}}^2 + \left(\frac{\partial Q}{\partial h_{\text{new}}}\right)^2 B_{h_{\text{new}}}^2 \quad (56)
$$

The regression giving $U_{Q\text{-regress}}$ (Eq. (55) or a similar one) should be reported along with either Eq. (53) or (56), as appropriate.

7 Summary

A new methodology for assessing the uncertainty associated with linear regressions is presented. This methodology is based upon the propagation of experimental uncertainties, and it was found that the key to the proper estimation of the uncertainty associated with regressions is a careful, comprehensive accounting of random, systematic, and correlated systematic uncertainties. Using Monte Carlo simulations, it was shown that the new regression uncertainty methodology provides the appropriate uncertainty intervals for first-order regression coefficients and predicted values from first-order and nth-order linear regressions. The Monte Carlo simulations indicated that the classical statistical confidence intervals cannot account for systematic and correlated systematic uncertainties. The simulations also showed that Price's method does not provide the correct uncertainty intervals for first-order linear regressions when a systematic error source is common to both the independent and dependent variables and it does not provide the appropriate uncertainty interval for higher-order regressions.

The methodology for assessing the uncertainty associated with regressions was demonstrated for the calibration of a venturi flowmeter and its subsequent use to determine flowrate in a test. It was shown that the previously accepted way of accounting for the contribution of discharge coefficient uncertainty to the overall flowrate uncertainty does not correctly account for all uncertainty sources, and the appropriate approach was developed, discussed, and demonstrated.

The authors also proposed an approach to reporting regression uncertainty using another regression to represent $U_Y(X)$, thus avoiding carrying the entire (X_i, Y_i) data set to compute a $U_Y(X_{\text{new}})$ each time an uncertainty is desired at an X_{new}.

Acknowledgments

The first two authors acknowledge the support of NASA Marshall Space Flight Center (contract NAS8-38609 D.O. 140) during a portion of this effort. The first author also acknowledges support from the 1995 AFOSR Graduate Summer Research Program and Arnold Engineering Development Center.

References

Bean, Howard S. (ed.), 1971, *Fluid Meters: Their Theory and Application,* 6th ed., American Society of Mechanical Engineers, New York.

Brown, Kendall K., Coleman, Hugh W., and Steele, W. Glenn, 1995, ''Estimating Uncertainty Intervals for Linear Regression,'' AIAA Paper 95-0796, 33rd Aerospace Sciences Meeting and Exhibit.

Brown, Kendall K., 1996, ''Assessment of the Experimental Uncertainty Associated with Regressions,'' Ph.D. dissertation, University of Alabama in Huntsville, Huntsville, AL.

Brown, Kendall K., Coleman, Hugh W., Steele, W. G., and Taylor, Robert P., 1996, ''Evaluation of Correlated Bias Error Effects in Experimental Uncertainty Analysis,'' *AIAA Journal,* Vol. 34, No. 5.

Coleman, Hugh W., and Steele, W. Glenn, 1995, ''Engineering Application of Experimental Uncertainty Analysis,'' *AIAA Journal,* Vol. 33, No. 10.

Coleman, Hugh W., and Steele, W. Glenn, 1989, *Experimentation and Uncertainty Analysis for Engineers,* Wiley, New York.

Draper, N. R., and Smith, H., 1981, *Applied Regression Analysis,* 2nd ed., Wiley, New York.

Montgomery, Douglas C., and Peck, Elizabeth A., 1992, *Introduction to Linear Regression Analysis,* 2nd Ed., Wiley, New York.

Natrella, M. G., 1963, *Experimental Statistics,* NBS Handbook 91, National Bureau of Standards, United States Department of Commerce.

Neter, John, Wasserman, William, and Kutner, Michael H., 1989, *Applied Linear Regression Models,* 2nd ed., Irwin, Homewood, IL.

Press, William H., Flannery, Brian P., Teukolsky, and Vetterling, William T., 1986, *Numerical Recipes: The Art of Scientific Computing,* Cambridge University Press, Cambridge.

Price, Mark L., 1993, ''Uncertainty of Derived Results on X-Y Plots,'' ISA Technical Paper 93-107, *Proceedings of the 39th International Instrumentation Symposium,* Instrument Society of America.

Seber, G. A. F., 1977, *Linear Regression Analysis,* Wiley, New York.

A Wall-Distance-Free k-ϵ Model With Enhanced Near-Wall Treatment

U. Goldberg
Senior Scientist.

O. Peroomian
Scientist.

S. Chakravarthy
Chief Scientist.

Metacomp Technologies, Inc.,
650 Hampshire Road, No. 200,
Westlake Village, CA 91361

This paper evaluates a wall-distance-free low-Re k-ϵ turbulence closure model which incorporates an extra source term in the ϵ transport equation designed to increase the level of ϵ in nonequilibrium flow regions, thus reducing the kinetic energy and length scale magnitudes to improve prediction of adverse pressure gradient flows, including those involving separated flows regions. Two such cases are used here to test the model: one in the low speed flow regime, the other a supersonic one. Comparisons with experimental data and with an earlier version of the k-ϵ model, as well as with a variant of the k-ω model (both also wall-distance-free) reveal that the proposed model enables improved prediction of adverse pressure gradient flows relative to more traditional k-ϵ models.

1 Introduction

It has been established over the years that the k-ϵ model, while performing fairly well in free shear flows, does not work satisfactorily in wall-bounded flows, especially under adverse pressure gradient conditions. The extent of reversed flow regions is underpredicted, and large spurious post-reattachment peaks in heat transfer and skin friction are commonly predicted (Launder, 1988). These result from the inadequacy of the modelled ϵ equation. Near-wall functions, commonly employed to render the model applicable to low-Re flow regions, do not overcome this inadequacy (Launder, 1988).

An early attempt to improve the behaviour of ϵ under nonequilibrium flow conditions was made by Yap (1987) who added a term to the ϵ equation which acts, in nonequilibrium flows, to reduce the departure of the turbulence length scale from its local equilibrium level. Yap showed much improved predictive quality of the k-ϵ model in separated flows as a result of including this extra term. Unfortunately, his proposition involves explicit wall distance which is ambiguous in all but the simplest topologies. Besides, it is not at all evident that wall distance bears a relationship to the structure of turbulence (Launder, 1988). In an attempt to eliminate this shortcoming in the Yap correction, Ince (see, Launder, 1988) proposed a term involving length scale gradient such that it acts to raise ϵ near walls with attendant reduction in k and l, the turbulence length scale. This approach is evaluated in the present work and is found inadequate. Instead, a proposal is made for a term which involves turbulence time scale gradient in conjunction with a realizable velocity scale. The merits of this approach are discussed in the following sections.

An important attribute of the model is time scale realizability enforcement. This means that the turbulence time scale is not permitted to become less than the corresponding Kolmogorov micro-scale. This has been proposed earlier by Durbin (1991) and by Goldberg (1991). One significant outcome of enforcing time scale realizability is the automatic asymptotic consistency of the ϵ transport equation at walls, without the need to involve ad hoc near-wall damping functions, prevalent in many low-Re k-ϵ models such as the Lam-Bremhorst model (Lam and Bremhorst, 1981). This also enables a simple boundary condition for ϵ at walls. In contrast, the k-ω model uses $\omega \equiv \epsilon/k$ as the length-scale-determining variable, which is singular at walls since ϵ/k is not the correct inverse time scale there. This requires a special treatment which leads to a cumbersome and grid-dependent wall boundary condition for ω (see Wilcox, 1993 and Section 3).

The formulation of the proposed model is wall-distance-free, tensorially invariant and frame-indifferent, thus applicable to arbitrary topologies and moving boundaries. The model is usable in conjunction with solvers based on either unstructured or structured book-keeping, executed on any computer architecture, including massively parallel processors.

This paper evaluates flow cases involving separation, which is of interest to both aerodynamic and turbomachinery applications. It is shown that the proposed k-ϵ model predicts the supersonic flow case better than a typical low-Re k-ϵ model does, with respect to the skin friction profile.

2 Highlights of the Numerical Approach

A Navier-Stokes solver for either compressive or incompressive flows was used in the present work. The solver features a second-order Total Variation Diminishing (TVD) discretization based on a multi-dimensional interpolation framework. This framework is utilized also for the viscous terms. A Roe Riemann solver is used to provide proper signal propagation physics. Further details regarding the numerical methodology can be found in Chakravarthy et al. (1996), Peroomian et al. (1997), Peroomian et al. (1998).

3 Proposed Turbulence Model Formulation

Reynolds stresses are related to the mean strain through the Boussinesq model:

$$-\rho\overline{u_i u_j} = \mu_t(U_{i,j} + U_{j,i} - \tfrac{2}{3}U_{k,k}\delta_{ij}) - \tfrac{2}{3}\rho k\delta_{ij} \qquad (1)$$

where the eddy-viscosity field is given by

$$\mu_t = C_\mu f_\mu \rho k^2/\epsilon \qquad (2)$$

Here f_μ is a damping function discussed later, and k and ϵ, the turbulence kinetic energy and its dissipation rate, respectively, are determined by the following transport equations.

$$\frac{\partial(\rho k)}{\partial t} + \frac{\partial}{\partial x_j}(U_j\rho k) = \frac{\partial}{\partial x_j}\left[\left(\mu + \frac{\mu_t}{\sigma_k}\right)\frac{\partial k}{\partial x_j}\right] + P_k - \rho\epsilon \qquad (3)$$

Contributed by the Fluids Engineering Division for publication in the JOURNAL OF FLUIDS ENGINEERING. Manuscript received by the Fluids Engineering Division June 21, 1997; revised manuscript received April 21, 1998. Associate Technical Editor: M. M. Sindir.

$$\frac{\partial(\rho\epsilon)}{\partial t} + \frac{\partial}{\partial x_j}(U_j\rho\epsilon) = \frac{\partial}{\partial x_j}\left[\left(\mu + \frac{\mu_t}{\sigma_\epsilon}\right)\frac{\partial\epsilon}{\partial x_j}\right] + (C_{\epsilon 1}P_k - C_{\epsilon 2}\rho\epsilon + E)T_t^{-1} \quad (4)$$

P_k is the turbulence production, $-\rho\overline{u_iu_j}U_{i,j}$, modeled in terms of the Boussinesq concept (1):

$$P_k = \left[\mu_t\left(\frac{\partial U_i}{\partial x_j} + \frac{\partial U_j}{\partial x_i} - \frac{2}{3}\frac{\partial U_k}{\partial x_k}\delta_{ij}\right) - \frac{2}{3}\rho k\delta_{ij}\right]\frac{\partial U_i}{\partial x_j} \quad (5)$$

In the above, U_i are the Cartesian mean velocity components, x_i are the corresponding coordinates, ρ is density, and μ and μ_t are the molecular and eddy dynamic viscosities, respectively. The constants appearing in these transport equations are given below.

The following realizable time scale is used here:

$$T_t = \frac{k}{\epsilon}\max\{1, \xi^{-1}\} \quad (6)$$

where $\xi \equiv \sqrt{R_t}/C_\tau$, $R_t \equiv \rho k^2/(\mu\epsilon)$ is the turbulence Reynolds number, and C_τ is a constant. This time scale is k/ϵ at large R_t (hence large ξ) but becomes proportional to the Kolmogorov scale, $C_\tau\sqrt{\nu/\epsilon}$, for $R_t \ll 1$. This scale was applied in earlier work by Durbin (1991) and by Goldberg (1991) and Goldberg and Apsley (1997). The latter reference includes full details about this time scale. Note that its inclusion in the ϵ equation guarantees near-wall asymptotic consistency of that equation without resorting to ad hoc damping functions found in Lam and Bremhorst (1981), for example.

The damping function, f_μ, is based on the fact that in near-wall regions the proper velocity scale (see Durbin, 1991) is $\sqrt{v^2}$, not $\sqrt{k}$, and the time scale is the realizable one, given in Eq. (6). Full details on the derivation of f_μ are given in Goldberg and Apsley (1997). The final form is

$$f_\mu = \frac{1 - e^{-A_\mu R_t}}{1 - e^{-\sqrt{R_t}}}\max\{1, \xi^{-1}\} \quad (7)$$

where A_μ is a constant. Note that $f_\mu \to A_\mu C_\tau$ as $R_t \to 0$. This type of near-wall limit was also adopted by Durbin (1991), arguing that $\mu_t \sim y^4$, rather than y^3, is acceptable since $\mu_t \ll \mu$ there. It is also noted that outside shear layers the level of R_t may diminish, causing f_μ to become less than 1; however, in such flow regions the eddy-viscosity levels are usually low, therefore $f_\mu < 1$ should not impose a problem.

The extra source term, E, in the ϵ equation, is designed to increase the level of ϵ in nonequilibrium flow regions, thereby reducing the length scale and enabling improved prediction of adverse pressure gradient flows, including those involving backflow regions. Ince's proposal (see, Launder, 1988), corrected for time scale realizability, is as follows:

$$\Psi_l = \max\left\{\frac{\partial k}{\partial x_j}\frac{\partial l}{\partial x_j}, 0\right\} \quad (8)$$

$$E_l = A_{E_l}\rho\sqrt{\epsilon T_t}\Psi_l \quad (9)$$

where $l = k^{3/2}/\epsilon$, the turbulence length scale. As will be shown in the Results section, this proposal fails to produce correct behavior in shear layer edge regions and is, therefore, rejected. Instead, the following formulation is suggested in the new model:

$$\Psi = \max\left\{\frac{\partial k}{\partial x_j}\frac{\partial \tau}{\partial x_j}, 0\right\} \quad (10)$$

$$\mathcal{V} = \max\{k^{1/2}, (\nu\epsilon)^{1/4}\} \quad (11)$$

$$E = A_E\rho\mathcal{V}\sqrt{\epsilon T_t}\Psi \quad (12)$$

where $\tau = k/\epsilon$, the turbulence time scale. The extra source term is invoked only in near-wall regions, where $\Psi > 0$, increasing ϵ and thereby decreasing k and l. Note the realizable velocity scale, $\mathcal{V}$, used in the current proposal. Its presence limits the influence of E to a relatively small fraction of the boundary layer near walls, with a sharp cut-off further away. Ince's method does not have this feature, causing E to reappear in boundary layer edges (see flat plate case) which is undesirable behavior.

Finally, the model constants are $C_\mu = 0.09$, $C_{\epsilon 1} = 1.44$, $C_{\epsilon 2} = 1.92$, $\sigma_k = 1.0$, $\sigma_\epsilon = 1.3$, $C_\tau = \sqrt{2}$, $A_\mu = 0.01$, $A_E = 0.3$. The last two constants are determined by forcing correct prediction of the log-law constant (≈ 5.2) in near-wall flat-plate and channel flows.

The two transport equations, Eqs. (3) and (4), are subject to the following boundary conditions at solid walls. The kinetic energy of turbulence and its first normal-to-wall derivative vanish there. The former condition is implemented directly:

$$k_w = 0 \quad (13)$$

The boundary condition for ϵ is based on its near-wall asymptotic behavior ($y \to 0$):

$$\epsilon_w = 2\nu_1\frac{k_1}{y_1^2} \quad (14)$$

where "1" denotes the centroid of the first cell away from walls. This requires normal distance from a wall to the first internal nodes only, which is unambiguous and readily available, thus still preserving the local attribute of the model. This boundary condition implies that $(\partial k/\partial y)_w = 0$, satisfying the second condition for k implicitly. In contrast, ω of the k-ω model is singular at smooth walls and, therefore, a special treatment is necessary to implement a boundary condition for it. Wilcox (1993) suggests the following (BC 1):

$$\omega_w = 2500\frac{\mu_w}{\rho_w k_R^2}, \quad k_R^+ < 5 \quad (15)$$

It is important to make sure that $k_R^+ < 5$, or else the predicted skin friction will be wrong. However, to guarantee this limit requires knowledge of the friction velocity scale, u_τ, which is not known a priori. Thus iterative adjustment of k_R may be necessary, and even the final value is grid-dependent. This difficulty is completely avoided in the current k-ϵ model. Another proposal for ω_w (BC 2) is commonly used, see Krist et al. (1996):

$$\omega_w = 60\frac{\nu_1}{\beta y_1^2}, \quad \beta = 0.075 \quad (16)$$

The sensitivity of the k-ω model to these alternative boundary conditions will be demonstrated in the next section.

4 Results

In the following flow test cases the proposed model's performance is compared with experimental data as well as with the Goldberg-Apsley (GA) k-ϵ (Goldberg and Apsley, 1997) and the Wilcox k-ω (Wilcox, 1993) models, both also wall-distance-free. The former represents a model not particularly geared to handle adverse pressure gradient flows; the latter includes the cross-diffusion term proposed by Wilcox to eliminate the model's sensitivity to the freestream value of ω. See Wilcox (1993), p. 101, for details. The two k-ϵ models shown in the figures are labeled as follows: the GA model is denoted as k-ϵ GA, and the current proposal is labeled k-ϵ τ. The modified k-ω model is marked k-ω mod. All computations were performed on a 200 MHz Pentium Pro PC.

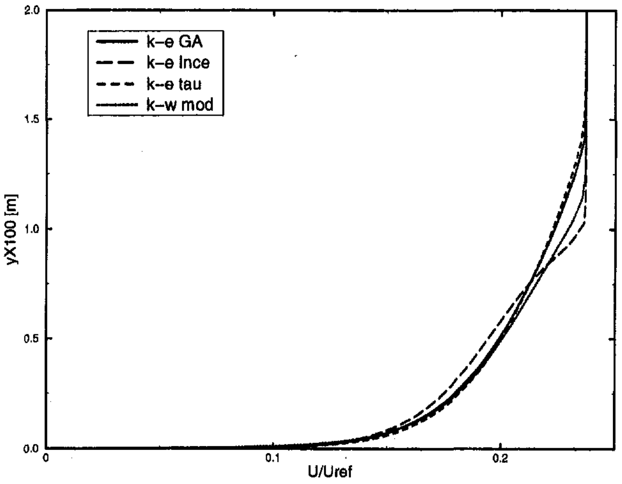

Fig. 1(*a*) Flat plate: streamwise velocity profiles, $M = 0.2$, $x = 0.8$ m

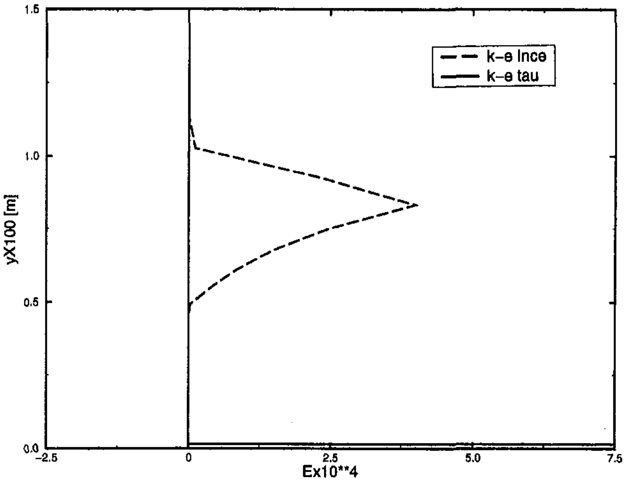

Fig. 1(*b*) Flat plate: *E* term profiles, $M = 0.2$, $x = 0.8$ m

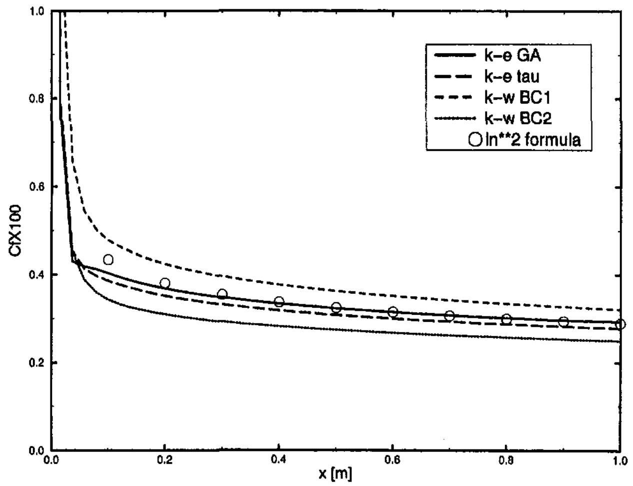

Fig. 1(*c*) Flat plate: skin friction distributions, $M = 0.2$

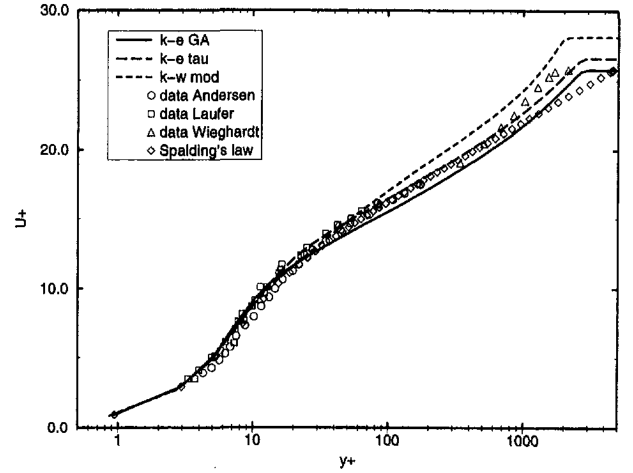

Fig. 1(*d*) Flat plate: velocity profiles in law-of-the-wall coordinates, $M = 0.2$, $x = 0.8$ m

4.1 Flow Over a Flat Plate. Mach 0.2 flow over a flat plate at Reynolds number 6×10^6 is computed on a 65×97 grid, with $y^+ \leq 1$ at first centroidal locations away from the wall. The plate leading edge is preceded by a section of free-stream flow parallel to it. The plate extends to one meter. Figure 1(*a*) shows velocity profiles at $x = 0.8$ m, including a prediction using Ince's proposal (Eqs. (8), (9)). While the k-ϵ GA and k-ϵ τ models predict practically the same profile, Ince's method leads to anomalous behavior toward the boundary layer edge, which affects the entire profile. The reason for this is seen in Fig. 1(*b*), where Ince's E term in the ϵ equation reappears in the shear layer edge region, increasing ϵ with attendant decrease in k and μ_t. This artificial suppression of the turbulence damages the entire flowfield prediction and is the reason for rejecting Ince's proposal.

Figure 1(*c*) shows skin friction profiles including two predictions by k-ω mod, one using BC 1 (Eq. (15)), the other BC 2 (Eq. (16)). The sensitivity of the model to ω_w is clearly demonstrated here. All subsequent predictions by this model use BC 2, which is easier to apply. The following formula (White, 1974, p. 498) was used to evaluate the predictions: $C_f \approx 0.455/(\ln^2 0.06\ \mathrm{Re}_x)$, considered one of the most accurate correlations available. The k-ϵ GA model is the closest to the formula while the k-ϵ τ model slightly underpredicts it.

Figure 1(*d*) is a replot of Fig. 1(*a*) using wall coordinates. The figure includes experimental data (Laufer, 1952; Andersen et al., 1972; Coles and Hirst, 1969) as well as Spalding's formula (Spalding, 1961). Based on these, the k-ϵ τ model predicts the law-of-the-wall best.

4.2 Low Speed Flow in a Channel With Slanted Step. A series of test cases involving two-dimensional channel flows with lower walls including a backward-facing step at various step angles was carried out by Ruck and Makiola (1993). The case used here for testing the model has a 45 deg step angle. The inflow velocity is 40.13 m/s, and the Reynolds number, based on channel height upstream of the step, is 64,000. The inflow velocity and turbulence kinetic energy profiles are based on the reported experimental profiles of U and u'. Neumann conditions are applied at the outflow boundary, located at $x/H = 50$, and nonslip conditions are imposed on the solid surfaces. A 150×100 grid size was used, with first internal node located below $y^+ = 1$.

The geometry and main flow features are seen in Fig. 2(*a*) which shows skin friction profiles predicted by the two k-ϵ and k-ω models. Figures 2(*b*–*e*) compare predictions with experimental data of velocity and normal Reynolds stress at two streamwise stations: one at the reattachment location, the other well downstream of it. The k-ϵ GA model predicts this flow best, capturing the reattachment location. However, it also predicts a post-reattachment peak in skin friction which the other two models avoid. The k-ϵ τ and k-ω models predict almost identical skin friction distributions, but the velocity and normal stress profiles are better predicted by the former.

A 225×150 grid was also employed and verified grid independence of the reported results, as seen in the figures. The shift in the results computed on the two grids is small even at

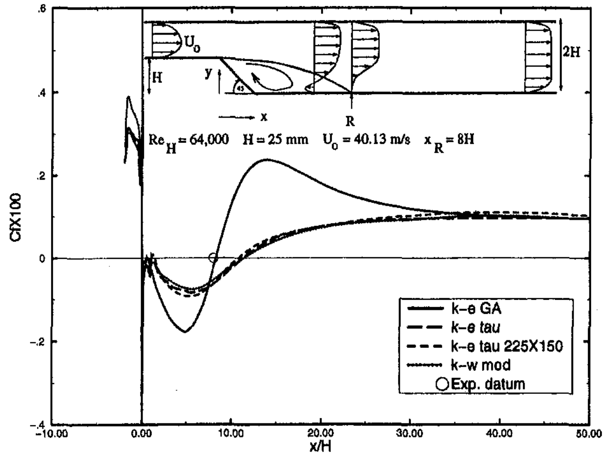

Fig. 2(a) 45 deg slanted backstep: skin friction profiles on the step-side wall, M = 0.1

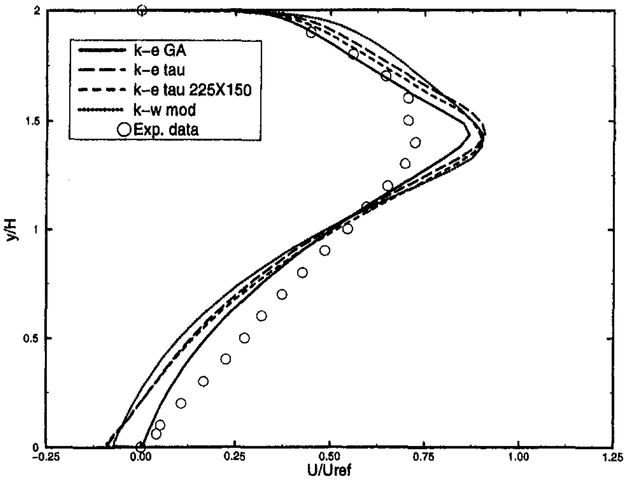

Fig. 2(b) 45 deg slanted backstep: streamwise velocity profiles at x/H = 8, M = 0.1

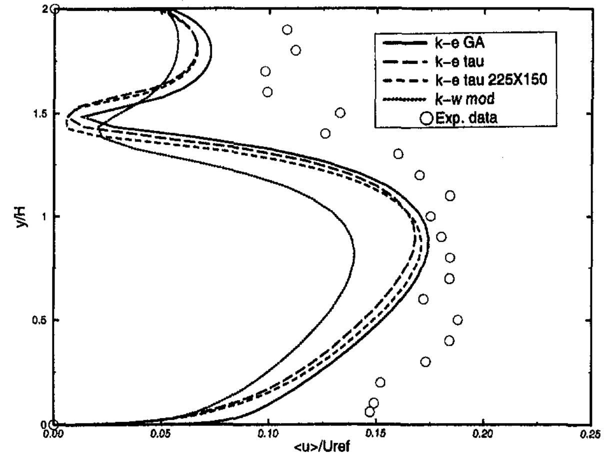

Fig. 2(c) 45 deg slanted backstep: normal Reynolds stress profiles at x/H = 8, M = 0.1

the Reynolds stress level. Solution convergence, based on skin friction history at x/H = 15, is shown in Fig. 2(f).

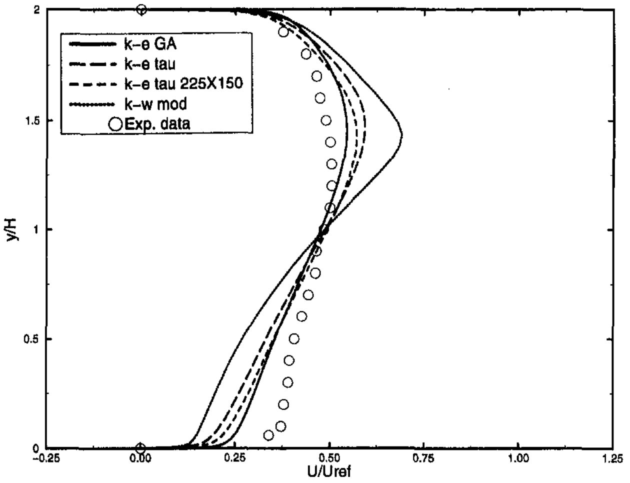

Fig. 2(d) 45 deg slanted backstep: streamwise velocity profiles at x/H = 15, M = 0.1

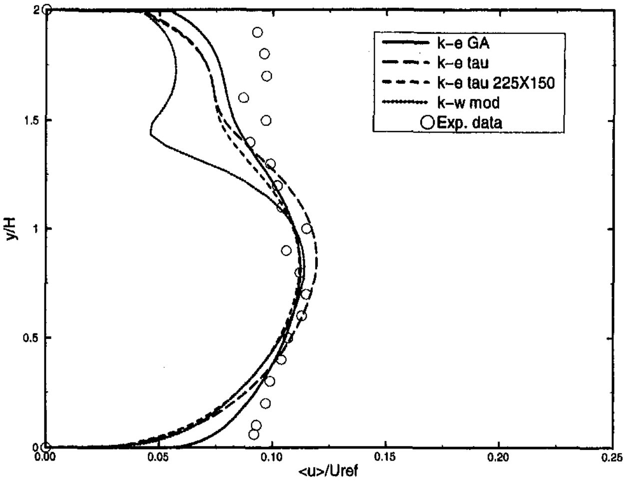

Fig. 2(e) 45 deg slanted backstep: normal Reynolds stress profiles at x/H = 15, M = 0.1

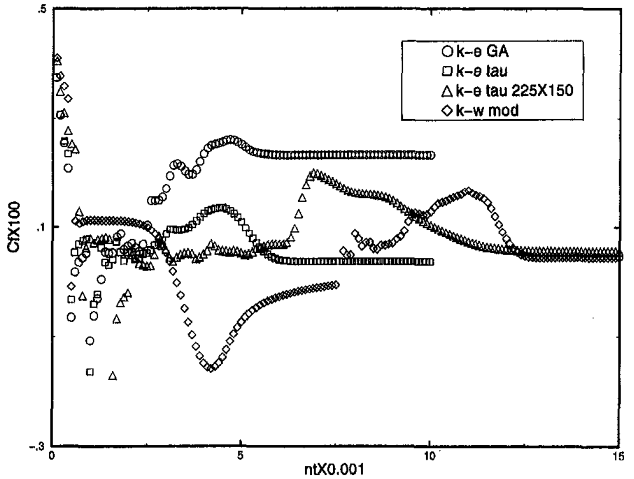

Fig. 2(f) 45 deg slanted backstep: solution convergence history, M = 0.1

4.3 Supersonic Flow Over a Compression Ramp. This is the supersonic two-dimensional flow over a 24 deg ramp measured by Settles (1979), with additional data by Dolling and Murphy (1983), and by Selig (1989). An oblique shock, impinging on the boundary layer ahead of the ramp corner (due to upstream influence), induces flow detachment, with subsequent reattachment onto the ramp surface. The origin of the (x, y) Cartesian coordinate system is located at the corner, with directions along and normal to the upstream flat plate, respectively. These coordinates are scaled by the boundary layer thickness upstream of the shock, δ_0. Wall pressure (p_w) is scaled by the upstream inflow pressure (p_∞). The computation was

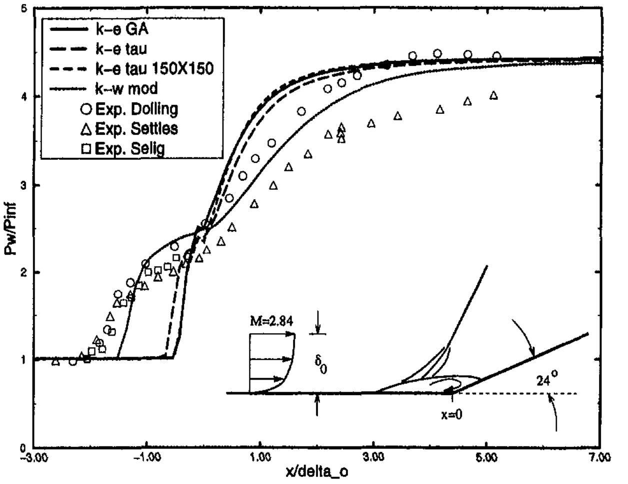

Fig. 3(*a*) Compression ramp: surface pressure distribution, 2D 24 deg ramp, *M* = 2.84

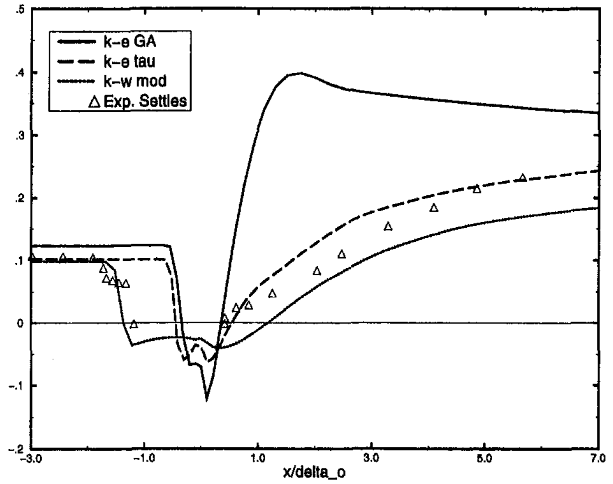

Fig. 3(*b*) Compression ramp: skin friction distribution, 2D 24 deg ramp, *M* = 2.84

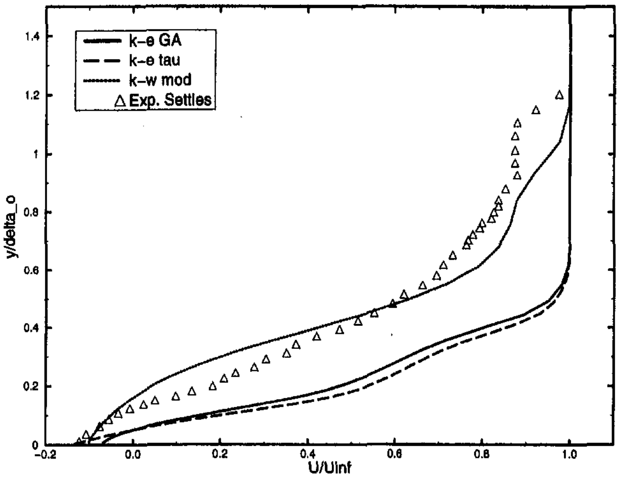

Fig. 3(*c*) Compression ramp: streamwise velocity profile at ramp corner, 2D 24 deg ramp, *M* = 2.84

done on two grids: a 99 × 99 and a 150 × 150 mesh, both with at least 8 cells inside the viscous sublayer, first centroidal point off the wall being at $y^+ < 1$. The grids were clustered in the x direction too, with $(\Delta x)_{\min} = 0.1\delta_0$, located at the ramp corner. The smaller grid was recommended in the ETMA workshop on evaluation of turbulence models for compressive flows (Loyau and Vandromme, 1994).

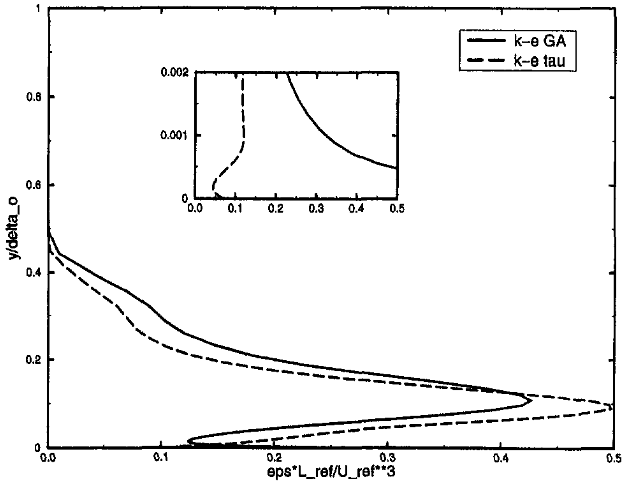

Fig. 3(*d*) Compression ramp: ϵ profiles at ramp corner, 2D 24 deg ramp, *M* = 2.84

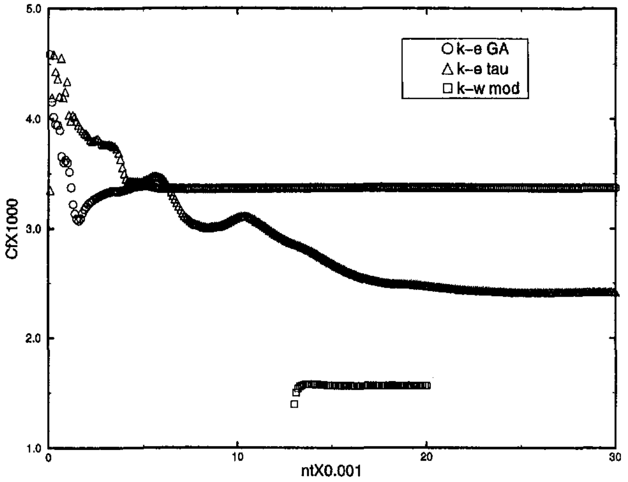

Fig. 3(*e*) Compression ramp: solution convergence history, 2D 24 deg ramp, *M* = 2.84

Numerical predictions of this case are known to be strongly dependent on inflow conditions (Loyau and Vandromme, 1994). The inflow Mach number was 2.84; $Re_\infty = 7.3 \times 10^7$/m; total temperature 262 K; and static pressure 24 kPa. Wall temperature was 276 K but adiabatic conditions were assumed, according to the experimental report (Settles et al., 1979). The measured upstream boundary layer thickness, $\delta_0 = 0.023$ m, was located at $x/\delta_0 = -3.0$. The computational inflow was placed at $x/\delta_0 = -21.7$ and a compressive equilibrium turbulent boundary layer (wake strength parameter $\Pi = 0.55$) of thickness $\delta_{in}/\delta_0 = 0.6$ was imposed to enable matching the measured boundary layer upstream of the strong interaction region. k_∞ was set corresponding to a freestream turbulence level $T' = 0.8$ percent, and ϵ_∞ was set to a level that imposed freestream eddy viscosity on the order of the molecular one. The inflow profiles of k and ϵ were the following:

$$k = \min\left\{\frac{0.1}{\sqrt{C_\mu}}, 0.035y^+\right\}y^+u_\tau^2, \quad y^+ \le 10$$

$$k = \max\left\{k_\infty, \frac{u_\tau^2}{\sqrt{C_\mu}}\left(1 - \frac{y^+ - 10}{390}\right)\right\}, \quad y^+ > 10$$

$$l_i = 200y^+$$

$$l_\infty = C_\mu^{3/4}\frac{k_\infty^{3/2}}{\epsilon_\infty}$$

$$l_o = \min\{\kappa y(1 - e^{-y^+/27}), l_\infty\}$$

$$l = \min\{l_i, l_o\}$$

$$\epsilon = C_\mu^{3/4}\frac{k^{3/2}}{l}$$

where $y^+ = y\rho u_\tau/\mu$ and the friction velocity $u_\tau = \sqrt{(\tau/\rho)_w}$.

Figures 3(*a–d*) show predictions and data comparisons of surface pressure, skin friction, corner velocity profiles, and corner ϵ profiles. A sketch, showing the geometry and main flow features, is included in Fig. 3(*a*). As observed in this figure, the fine grid results are slightly shifted relative to the 99 × 99 mesh solution, but further grid refinement did not change the predictions. All reported k-ϵ τ model results are on the fine grid.

The k-ω model clearly outperforms the two k-ϵ models in predicting this flow case. This is consistent with previous results reported in the literature, Wilcox (1990) and Marshall and Dolling (1992). Note, however, the greatly improved performance of the k-ϵ τ model over the k-ϵ GA model in predicting skin friction. The artificial post-reattachment peak, predicted by the latter (and by many other k-ϵ models (Launder, 1988) has been completely eliminated by the new model. In addition, the extent of flow separation has increased, although not to the magnitude predicted by the k-ω model. Note in Fig. 3(*d*) that the ϵ profiles predicted by both k-ϵ models feature a local maximum level at the wall, in qualitative agreement with DNS data (Mansour et al., 1988). As expected, the near-wall magnitude of ϵ predicted by the k-ϵ τ model is much reduced relative to that of the k-ϵ GA model due the E term in the former.

Figure 3(*e*) is a convergence history plot based on skin friction well downstream of flow reattachment.

5 Concluding Remarks

This paper proposed and evaluated a wall-distance-free low-Re k-ϵ model in which the ϵ transport equation includes an extra source term designed to increase the level of ϵ in nonequilibrium flow regions with attendant decrease in the kinetic energy and length scale magnitudes in order to improve predictive capability of flows with adverse pressure gradient. Comparing the performance of this model to that of a more traditional low-Re k-ϵ model showed a marked improvement in near-wall flow prediction, manifested in skin friction characteristics: the typical post-reattachment peak has been eliminated, and the extent of the reversed flow has increased. While the new model may still underestimate the size of the separation bubble, compared to predictions by Wilcox's k-ω model, it is not subject to ambiguity in regard to the wall boundary condition for ϵ, in contrast to that of ω, as demonstrated in the flat plate flow example.

The proposed k-ϵ model is tensorially invariant and frame-indifferent, applicable to arbitrary topologies and moving surfaces. It is suitable for flow solvers based on structured, unstructured or hybrid book-keeping, and usable on any computer architecture, including the increasingly popular massively parallel processors. It also proved numerically robust and easy to use. A nonlinear extension of the model will be considered to further enhance its performance.

References

Andersen, P. S., Kays, W. M., and Moffat, R. J., 1972, "The Turbulent Boundary Layer on a Porous Plate: an Experimental Study of the Fluid Mechanics for Adverse Free-Stream Pressure Gradients," Report No. HMT-15, Dept. Mech. Eng., *Stanford University*, CA.

Chakravarthy, S., Peroomian, O., and Sekar, B., 1996, "Some Internal Flow Applications of a Unified-Grid CFD Methodology," AIAA Paper 96-2926.

Coles, D. E., and Hirst, E. A., 1969, "Computation of Turbulent Boundary Layers," 1968 AFOSR-IFP-Stanford Conference, Vol. II, Stanford University, CA.

Dolling, D. S., and Murphy, M. T., 1983, "Unsteadiness of the Separation Shock Wave Structure in a Supersonic Compression Ramp Flowfield," *AIAA Journal*, Vol. 21, No. 12, pp. 1628–1634.

Durbin, P. A., 1991, "Near-Wall Turbulence Closure Modeling without 'Damping Functions'," *Theoretical and Computational Fluid Dynamics*, Vol. 3, pp. 1–13.

Goldberg, U. C., 1991, "Derivation and Testing of a One-Equation Model based on Two Time Scales," *AIAA Journal*, Vol. 29, pp. 1337–1340.

Goldberg, U., and Apsley, D., 1997, "A Wall-Distance-Free Low Re k-ϵ Turbulence Model," *Computer Methods in Applied Mechanics and Engineering*, Vol. 145, pp. 227–238.

Krist, S. L., Biedron, R. T., and Rumsey, C. L., 1996, *CFL3D User's Manual, Version 5.0*, NASA Langley Research Center, Hampton, VA.

Lam, C. K. G., and Bremhorst, K. A., 1981, "Modified Form of k-ϵ Model for Predicting Wall Turbulence," ASME JOURNAL OF FLUIDS ENGINEERING, Vol. 103, pp. 456–460.

Laufer, J., 1952, "The Structure of Turbulence in Fully Developed Pipe Flow," NACA TM 1174.

Launder, B. E., 1988, "On the Computation of Convective Heat Transfer in Complex Turbulent Flows," ASME *Journal of Heat Transfer*, Vol. 110, pp. 1112–1128.

Loyau, H., and Vandromme, D., 1994, "TC5 Workshop Synthesis," in *Proc. of ETMA Workshop*, UMIST, Manchester, U.K.

Mansour, N. N., Kim, J., and Moin, P., 1988, "Reynolds Stress and Dissipation Rate Budgets in Turbulent Channel Flow," *Journal of Fluid Mechanics*, Vol. 194, pp. 15–44.

Marshall, T. A., and Dolling, D. S., 1992, "Computation of Turbulent, Separated, Unswept Compression Ramp Interactions," *AIAA Journal*, Vol. 30, No. 8, pp. 2056–2065.

Peroomian, O., Chakravarthy, S., and Goldberg, U., 1997, "A 'Grid-Transparent' Methodology for CFD," AIAA Paper 97-07245.

Peroomian, O., Chakravarthy, S., Palaniswamy, S., and Goldberg, U., 1998, "Convergence Acceleration for Unified-Grid Formulation using Preconditioned Implicit Relaxation," AIAA Paper 98-0116.

Ruck, B., and Makiola, B., 1993, "Flow Separation over the Step with Inclined Walls," *Near-Wall Turbulent Flows*, R. M. C. So, C. G. Speziale, and B. E. Launder, eds., Elsevier, p. 999.

Selig, M. S., Andreopoulos, J., Muck, K. C., Dussauge, J. P., and Smits, A. J., 1989, "Turbulence Structure in a Shock Wave/Boundary Layer Interaction," *AIAA Journal*, Vol. 27, No. 7, pp. 862–869.

Settles, G. S., Fitzpatrick, T. J., and Bogdonoff, S. M., 1979, "Detailed Study of Attached and Separated Compression Corner Flowfields in High Reynolds Number Supersonic Flow," *AIAA Journal*, Vol. 17, No. 6, pp. 579–585.

Spalding, D. B., 1961, ASME *Journal of Applied Mechanics*, Vol. 28, p. 455.

White, F. M., 1974, *Viscous Fluid Flow*, McGraw-Hill, New York.

Wilcox, D. C., 1990, "Supersonic Compression-Corner Applications of a Multiscale Model for Turbulent Flows," *AIAA Journal*, Vol. 28, No. 7, pp. 1194–1198.

Wilcox, D. C., 1993, "Turbulence Modeling for CFD," DCW Industries, Inc., La Cañada, CA.

Yap, C., 1987, "Turbulent Heat and Momentum Transfer in Recirculating and Impinging Flows," Ph.D. thesis, Faculty of Technology, University of Manchester, United Kingdom.

High-Speed PIV Analysis Using Compressed Image Correlation

Douglas P. Hart
Associate Professor of
Mechanical Engineering,
Department of Mechanical Engineering,
Massachusetts Institute of Technology,
Cambridge, MA 02139-4307

With the development of Holographic PIV (HPIV) and PIV Cinematography (PIVC), the need for a computationally efficient algorithm capable of processing images at video rates has emerged. This paper presents one such algorithm, sparse array image correlation. This algorithm is based on the sparse format of image data—a format well suited to the storage of highly segmented images. It utilizes an image compression scheme that retains pixel values in high intensity gradient areas eliminating low information background regions. The remaining pixels are stored in sparse format along with their relative locations encoded into 32 bit words. The result is a highly reduced image data set that retains the original correlation information of the image. Compression ratios of 30:1 using this method are typical. As a result, far fewer memory calls and data entry comparisons are required to accurately determine tracer particle movement. In addition, by utilizing an error correlation function, pixel comparisons are made through single integer calculations eliminating time consuming multiplication and floating point arithmetic. Thus, this algorithm typically results in much higher correlation speeds and lower memory requirements than spectral and image shifting correlation algorithms. This paper describes the methodology of sparse array correlation as well as the speed, accuracy, and limitations of this unique algorithm. While the study presented here focuses on the process of correlating images stored in sparse format, the details of an image compression algorithm based on intensity gradient thresholding is presented and its effect on image correlation is discussed to elucidate the limitations and applicability of compression based PIV processing.

1 Introduction

Until recently, Particle Image Velocimetry, PIV, has been limited to applications in which two-dimensional, instantaneous velocity measurements are of interest. Most flows, however, are unsteady and three-dimensional in nature and thus, there has been a growing effort to develop three-dimensional velocity measurement techniques and techniques to quantitatively resolve unsteady flows. This effort has resulted in the development of Holographic PIV (HPIV) and PIV Cinematography (PIVC). Both these techniques are highly computationally intensive often requiring the determination of millions even tens of millions of vectors. With present software processing speeds, a single experimental run using HPIV or PIVC can take several hours of computer time to obtain results. Because of this, dedicated coprocessors are often utilized in these applications. These costly coprocessors, although significantly faster than present PC software processing, are still slower than desired. Ideally, one would like to process HPIV and PIVC images at a rate faster than they can be acquired. This negates the need to store the images requiring only that the results be stored. It also allows an investigator to observe PIVC results in near real-time and potentially use the information for system feedback control in much the same way LDV systems are now being used in industry.

At present, electronic imaging systems operate with pixel transfer rates on the order of 10 million pixels per second. At 8 bits per pixel, this is roughly twice the speed at which most PC's can stream uncompressed data to a hard disk. Even compressed by a factor of ten, more than one megabyte of storage is needed for each second of video signal. A typical statistical correlation with 64 × 64 pixel windows and 50 percent overlap requires more than 75 million multiplications and 225 million memory calls per second to process data at this rate—far faster than the capabilities of present PC technology. Fourier correlation techniques require significantly fewer operations but due to multiple memory calls and floating-point calculations, their processing requirements are still well beyond present PC capabilities for real time PIVC or video rate processing of HPIV images. Thus, if video rate PIV processing is to be achieved without the need for a dedicated coprocessor, an algorithm must be developed that significantly reduces the number of memory calls and arithmetic operations. This paper introduces one such algorithm, sparse array image correlation.

2 Methodology

Sparse array image correlation is based on storing and correlating a compressed data set that retains the particle displacement information from the original PIV image. By reducing coding and interpixel redundancy, far fewer memory calls and calculations must be made to correlate the image. PIV images typically contain significant data redundancy. Compression ratios of 30:1 or greater are normal. Thus, since the time required to correlate an image is proportional to the square of the number of data entries, significant gains in processing speed are possible.

Background. The simplest form of data reduction that can be made to a PIV image is to eliminate the low intensity pixels from the image file. Since the low intensity pixels contribute little information about particle displacement, their elimination has very little effect on the accuracy of the image correlation. Several high-speed algorithms have been developed based on this type of data reduction. The most recent of these algorithms is the one by Hatem and Aroussi (1995) in which a probability histogram of possible particle displacements is used to determine the velocity vector. Unlike Hatem and Aroussi's algorithm, sparse array image correlation relies on a true correlation of the image—it is not a particle tracking type algorithm and

---

Contributed by the Fluids Engineering Division for publication in the JOURNAL OF FLUIDS ENGINEERING. Manuscript received by the Fluids Engineering Division June 26, 1996; revised manuscript received May 4, 1998. Associate Technical Editor: J. Katz.

it does not rely on the binary (0, 1) representation of particles. The relative intensity difference between pixels is maintained despite the utilization of an image compression scheme. A more pertinent algorithm to the present algorithm is the one by Landreth and Adrian (1987) in which each section of an image is orthoganally compressed and the low intensity pixel combinations are eliminated from the data before it is correlated. Like the present algorithm, Landreth and Adrian's algorithm processes the data in a sparse format. This is the basic scheme by which the present algorithm correlates images. Unlike Landreth and Adrian's algorithm, however, both coding redundancy and interpixel redundancy are reduced during image preprocessing without decoupling the x and y correlations. The two-dimensional spatial relationship and the relative intensity variation between pixels are maintained. Significant speed is gained by encoding the remaining data specifically for 32-bit processing and utilizing an error correlation function to eliminate multiplication and division operations.

As with all correlation schemes that require preprocessing of images, a tradeoff is made between the time required to reduce the data set and the time required to correlate the reduced data set. The original intent of the sparse array image correlation algorithm was to process PIV images at video rates. Therefore, the algorithm presented here uses a relatively simple data compression scheme to facilitate the processing of a video signal as it is being downloaded from a CCD camera. This allows a data set from a previous frame to be analyzed at the same time the video data from a camera is being compressed. It is desired to perform both preprocessing and correlation of the images at roughly the same rate, $\frac{1}{30}$ of a second. The result is an image compression algorithm that is not necessarily optimized for data reduction but allows pipelining of the original image data set to reduce image preprocessing time and data transfer latency.

Image Compression. The first step in sparse array image correlation is to generate a data array that contains enough information to determine the displacement of particles in a PIV image or between two images in the case of cross-correlation. In order to facilitate processing, it is desired to retain the minimum amount of data to obtain a specified resolution in the final results. Unfortunately, it is difficult to determine a priori the exact information that is needed to achieve this. It can be shown, however, from the statistical correlation function,

$$\Phi_{\Delta i,\Delta j} = \frac{\sum_{m=1}^{M} \sum_{n=1}^{N} [I_{m+\Delta i,n+\Delta j} \cdot I_{m,n}]}{\sqrt{\sum_{m=1}^{M} \sum_{n=1}^{N} I^2_{m,n}} \cdot \sqrt{\sum_{m=1}^{M} \sum_{n=1}^{N} I^2_{m+\Delta i,n+\Delta j}}}$$

that pixels with high intensity contribute more to the overall value of the correlation coefficient than pixels of low intensity. This characteristic of the statistical correlation function adversely affects the ability to determine the subpixel displacement of tracer particles in a PIV image by unduly weighting the significance of high-intensity pixels. Much of the information contained in a PIV image that allows subpixel resolution of tracer particle movement resides in the intensity of pixels representing the edges of the particle images. It is not the level of pixel intensity in a PIV that allows the displacements to be determined through correlation. It is the relative change in intensity between the background and the tracer particle images that makes this possible. In much the same way two blank pieces of paper are aligned on a desk, image correlation relies on the change in intensity around the edges of the objects being aligned and not the featureless, low intensity gradient, regions. Thus, in principle, all pixels in low intensity gradient regions can be eliminated from a PIV image with only a slight loss in correlation information as long as the relative positions and intensities of the remaining pixels are maintained. Except for a small number of pixels representing tracer particles, PIV images are predominantly blank. Therefore, the data size necessary to determine tracer particle movement within PIV images can be significantly reduced with little or no loss in accuracy. This is the basis by which sparse array image correlation works. Eliminating pixels that have little effect on the determination of tracer particle movement reduces the data set representing a PIV image. The remaining pixel intensities are recorded in sparse format along with their relative positions. This sparse data set is then used to determine movements of the tracer particles in the fluid.

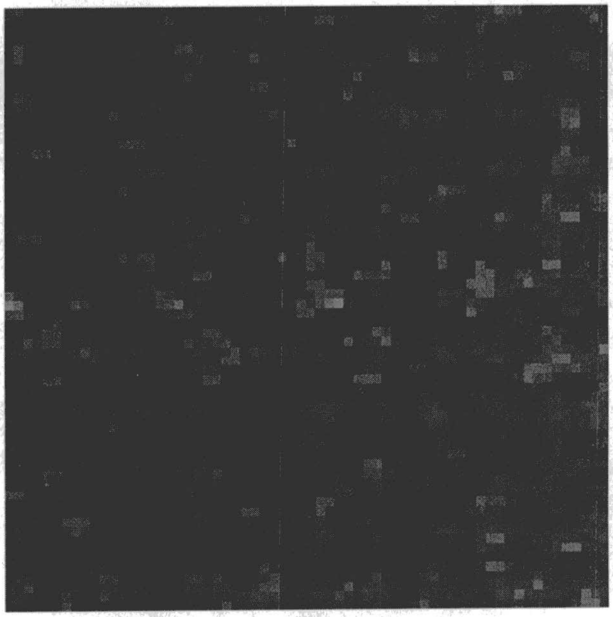
Fig. 1 Typical 64 × 64 pixel region of a PIV image

Segmentation. PIV images are strongly bimodal, composed of light particle images on a dark background, Fig. 1. It is, therefore, relatively easy to eliminate low intensity, background, pixels from the data. The simplest technique to accomplish this is to set a threshold level and retain only those pixels with intensities above the threshold. A relatively robust and accurate

Nomenclature

Φ = correlation function
β = characteristic image pixel size [m]
Δ = correlation search length [pixels]
Δs = imaged particle displacement [m]
Δt = time between image exposures [s]
Δi, Δj = difference in pixel image [pixels]
∇ = gradient operator
γ = image compression ratio
$\vec{v}$ = flow velocity [m/s]
D = particle image diameter [m]
G_∇ = relative flow divergence
I = pixel intensity
i, j = image coordinates [pixels]
m, n = data array indices
l = variable-length encoded data entry length [pixels]
M = image magnification [m/pixel]
M, N = interrogation image diameter [pixels]
u, v = pixel displacement in x and y directions [pixels]
x, y = pixel image coordinates [pixels]

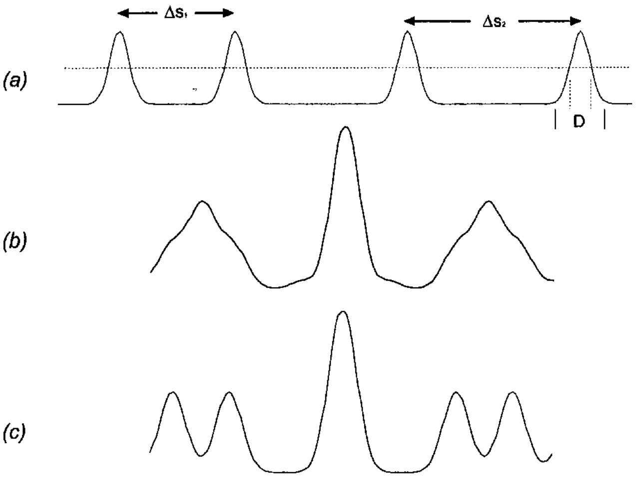

Fig. 2 Illustration of the effects flow divergence on correlation processing

technique for setting the appropriate threshold level is to perform a histogram concavity analysis (Rosenfield and De La Torre, 1982). A simpler and somewhat faster technique is to generate an intensity distribution curve that indicates the number of pixels with intensities above a specified level. Since the curve is an accumulation of pixel numbers, it is piecewise smooth, at least to the resolution of the CCD camera and thus, it is a simple matter to select a threshold level that corresponds to a specific slope on the curve. This technique is not as robust or accurate as the histogram concavity analysis but, because the pixel intensities in PIV images are so strongly bimodal, the precise threshold level is often not critical.

Several PIV and Particle Tracking Velocimetry (PTV) algorithms have been developed based on the intensity thresholding of images (Hart, 1996, and Hatem and Aroussi, 1995). While at first this appears to be a simple and robust way of reducing a PIV image, there are a number of difficulties with this method that makes it inappropriate for poor quality images. Consider a double exposed one-dimensional intensity plot of two tracer particles in a flow, Fig. 2(*a*). The intensity profile of the particle images appear Gaussian with a spot diameter that depends on the particle diameter, image magnification, imaged wave length, pixel size, focal length, and aperture of the camera recording the image. As illustrated by the distance traveled between exposures of the two tracer particles in this figure, Δs_1 and Δs_2, any gradient in the flow, $\nabla \tilde{v}$, over the observed region results in unequal displacements between the first and second exposures of the tracer particles. If $(\Delta s_1 - \Delta s_2)$ is small relative to the particle image spot diameter, D, then the peak correlation of the sub-window is an average of the displacements represented by the double exposure of the two particles, $(\Delta s_1 - \Delta s_2)/2$, Fig. 2(*b*). If, however $(\Delta s_1 - \Delta s_2)$ is large relative to D, then there exists no clear peak correlation, Fig. 2(*c*). Although algorithms exist that are highly robust to large local velocity gradients in the flow such as the spring model algorithm by Okamoto et al. (1995), in general, large velocity gradients result in an increase in spurious vectors. Thresholding an image has the effect of reducing the spot diameter of the particle images as illustrated by the dotted line in Fig. 2(*a*). Thus, thresholding can result in a loss in the information necessary to obtain average particle displacement information. Furthermore, most PIV images suffer from an inconsistency in the relative intensity between particle images. This is particularly true of images that are under exposed. In these cases, the information lost by thresholding to obtain significant data reduction can result in the loss of particle displacement information even for relatively small flow divergence.

A more robust, although slightly more computationally intensive, method of segmenting an image is to rely on the magnitude of the gradient in intensity of the pixels in the image. To reduce computational intensity, the magnitude of the intensity gradient can be approximated as the absolute value of the gradients in the x and y directions, $|\nabla I| \cong |\partial I/\partial x| + |\partial I/\partial y|$. To first order, $|\nabla I| \cong |I_{(i+1,j)} - I_{(i,j)}| + |I_{(i,j+1)} - I_{(i,j)}|$. An appropriate magnitude for the cutoff in the intensity gradient can then be selected in the same manner as it is done for intensity thresholding. Pixel intensities in regions where the gradient is sufficiently high are retained and the rest are discarded (assumed to have a value of zero). The result is the compression of an image where only the pixels around the edges of tracer particles are retained. The center of the particle images which have a low intensity gradient are discarded, Fig. 3. Because of this, intensity gradient segmentation of PIV images usually results in a smaller data set than images segmented by intensity thresholding. The gradient method of segmentation is the method of choice for most bimodal images (Gonzalez, Woods, 1993). It is, however, particularly well suited to the compression of images for correlation since it is the change in pixel intensities that allows subpixel particle displacements to be determined by correlation and not the average intensity of the particle images, Figs. 4 and 5.

Data Encryption. Once an image is compressed, it is stored with each pixel indices and intensity combined into a single 32-bit word. This reduces the number of memory calls that must be made when correlating. For example, **i** = 2, **j** = 2, **I** = 254 is stored as 00000000001000000000001011111110 binary = 2,097,918. By masking the bits, the values of **i**, **j**, and **I** can be extracted from this single entry in a few clock cycles of most processors.

Along with the sparse image array, an indices table is generated which contains the location in the sparse image array of the first entry representing a pixel combination in the next line of a PIV image. This line index array is used to jump to the next value of **j** in the sparse image array when a specified pixel separation is exceeded in the **i**th direction. When correlating large images, this index array significantly speeds processing.

Window Sorting. The reduction in the number of data entries in the PIV image data set by the elimination of pixels in regions with a low intensity gradient and the encoding of the remaining data greatly improves the speed at which correlation windows can be sorted from the data set. In addition, the line index array reduces the number of multiple entries into the sparse image array that must be made to extract the pixels located in a given correlation subwindow. Despite this, window sorting is a slow memory intensive task that requires considerable processing time. The present algorithm requires almost as much time to sort the correlation subwindows from the image data as it does to correlate the subwindows once they have been sorted.

Correlation window sorting in sparse array format is considerably more difficult than it is in an uncompressed format since the spacing of the data entries is image dependent. A simple

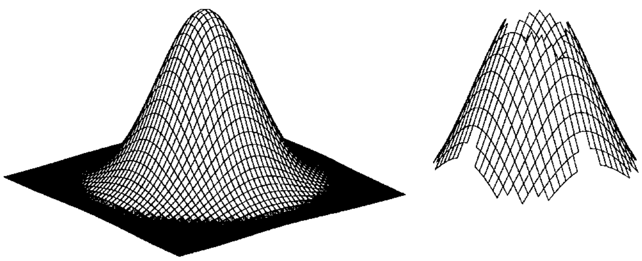

Fig. 3 Particle image intensity plot illustrating the effect of gradient pixel segmentation

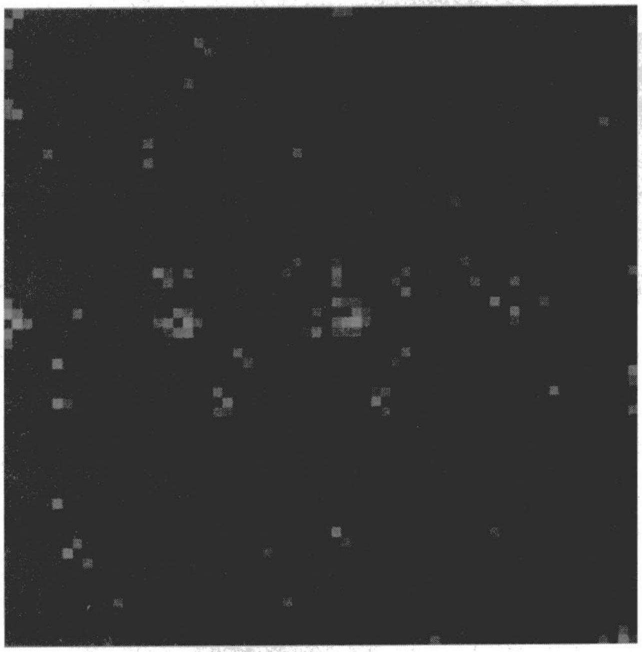

Fig. 4 Reconstructed image of figure 1 after 30:1 gradient level compression

block transfer as is commonly done in an uncompressed format cannot be done in the sparse array format. A solution to this is to generate the sparse array at the same time that the correlation windows are being extracted from the image. This technique works well, as long as there is no significant overlap of the correlation windows. If there is significant overlap, the number of redundant memory calls greatly slows processing. The most computationally efficient technique is to presort all of the correlation windows as the sparse array is generated. This technique requires a significant increase in memory storage depending on the overlap in the correlation windows. A 50 percent overlap results in a four times increase in memory storage. The 32-bit sparse array data encryption scheme, itself, requires four times the number of bits per pixel. Therefore, there is an increase in memory storage requirement by a factor of sixteen. Image compression, however, sufficiently reduces the number of data entries such that there is a net reduction in data storage by roughly a factor of four compared with storing the entire image in memory at one time. In addition, presorting the windows in this manner moves the processing time for window sorting from the basic correlation algorithm into the image-preprocessing algorithm. This allows more time for image correlation within the $\frac{1}{30}$ of a second video framing speed. Presorting the correlation subwindows at the same time the image is compressed is, therefore, the optimum solution in the majority of applications.

Search Length Selection. Processing speed can be further increased while, at the same time, reducing the odds of obtaining spurious correlation values by limiting the search for a maximum correlation. This is done by allowing the user to specify a maximum change in $\Delta\mathbf{i}$ and $\Delta\mathbf{j}$ based on knowledge of the image being correlated. An adaptive scheme can be used to narrow the correlation search—a scheme that predicts the range of correlation values to calculate based on previous calculations from subwindows of the same image. This procedure, however, is not particularly robust and can result in spurious errors in obtaining the maximum correlation. Because the sparse array correlation process is inherently very fast, adaptive schemes generally do not gain enough processing speed to warrant their use. It is sufficient to set a single value for the correlation range for an entire image.

Subwindow Correlation. By using the error correlation function rather than a statistical correlation function, image correlation can be carried out using integer addition and subtraction only. These are very fast operations for most microprocessors requiring only a few clock cycles. It is far faster to perform these calculations than to use a "look-up table" scheme to avoid 8-bit or 4-bit pixel multiplication. The use of the error correlation function, therefore, significantly improves processing speed over the more commonly used statistical correlation function. A detailed analysis of the error correlation function in comparison to the statistical correlation function is presented in a paper by Roth et al. (1995). It was shown that the error correlation function produces essentially the same results as the more computationally intensive statistical correlation function.

The error correlation function can be expressed as,

$$\Phi_{\Delta i,\Delta j} = \frac{\sum_{m=1}^{M}\sum_{n=1}^{N}\left[I_{m,n} + I_{m+\Delta i,n+\Delta j} - \left|I_{m,n} - I_{m+\Delta i,n+\Delta j}\right|\right]}{\sum_{m=1}^{M}\sum_{n=1}^{N}\left[I_{m,n} + I_{m+\Delta i,n+\Delta j}\right]}$$

such that,

$$\Phi_{\Delta i,\Delta j} = 1 - \frac{\sum_{m=1}^{M}\sum_{n=1}^{N}\left[\left|I_{m,n} - I_{m+\Delta i,n+\Delta j}\right|\right]}{\sum_{m=1}^{M}\sum_{n=1}^{N}\left[I_{m,n} + I_{m+\Delta i,n+\Delta j}\right]}$$

The value of this correlation function ranges from 1 when the images are perfectly correlated to 0 when there is no correlation between the images. Because it relies on the difference in pixel intensities, it does not unduly weight the significance of high-intensity pixels as does the statistical correlation function. Aside from being faster to calculate than the statistical correlation function, it has the added benefit of being easier to implement in hardware without the need for a microprocessor. The error correlation function, therefore, has potential for use in hardware based PIV systems.

Unlike the more common statistical correlation function, the error correlation function used in sparse array image correlation is not computed one entry at a time. The entire correlation table is constructed by summing entries as they are found while iterating through the sparse image array. When auto-correlating subwindows, each entry in the sparse image array is compared with the entries below it and a correlation approximation between the entries is added into the correct location in the correlation table based on the difference in $\mathbf{i}$ and $\mathbf{j}$ between the array entries. If the location is out of range of the specified search length in the $\mathbf{i}$th direction, the entry is ignored, and processing

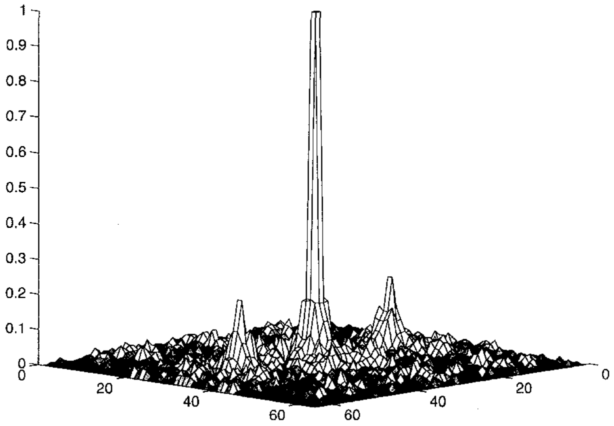

Fig. 5 Correlation table resulting from sparse array auto-correlation of the image in Fig. 4

continues with the next entry specified in the line index array. If the location is out of range in the jth direction, the entry is ignored and a new series of iterations are made starting with the next sparse image array entry. Because the sparse array is correlated from the top down, only the half of the correlation table representing the positive j direction is calculated. The auto-correlation of an image is symmetrical and thus, calculation of both halves of the correlation table is unnecessary.

Cross-correlation is accomplished by generating two sparse image arrays representing the two images being correlated. The entries of one array are then compared to all of the entries of the other array that are within the search length. Because the difference in array indices can be both positive and negative in the i and j directions, the entire nonsymmetrical correlation table is calculated.

Once the correlation table is complete, the table is searched for the maximum correlation value. A simple bilinear interpolation scheme is then used to determine the correlation maximum within subpixel resolution. Bilinear interpolation is ideal in this application since reducing the data set by image preprocessing and using the error correlation function results in a very steep, nearly linear, correlation peak.

3 Processing Speed

Computational Intensity. The computational intensity of sparse array image correlation is comparable to the better known statistical correlation technique except that the image data set is compressed in preprocessing. If the data set is reduced to a fraction, γ, of the original image data set, than the number of data comparisons that must be made, the computational intensity, is, $\frac{1}{2}\gamma\Delta^2(\gamma N^2 - 1) + \gamma N^2$ for sparse array auto-correlation and $\gamma^2\Delta^2N^2$ for cross-correlation. For PIV images where the particle seeding densities are high such that, $\gamma N^2 \gg 1$ and $\gamma\Delta^2 \gg 1$ then $\frac{1}{2}\gamma\Delta^2(\gamma N^2 - 1) + \gamma N^2$ is approximately equal to, $\frac{1}{2}\gamma^2\Delta^2N^2$. A typical PIV data set can be reduced by a factor of 30 such that $\gamma = \frac{1}{30}$. Thus, a typical 64×64-pixel correlation subwindow requires a little less than one thousand data comparisons to complete an auto-correlation with a search window of 20×20 pixels. During each comparison, three memory calls are made, one to retrieve a data entry to be compared with the data entry already in the processors register, one to retrieve the value of the correlation table entry, and one to place the comparison result in memory. Memory calls require a great deal more processing time than integer addition and subtraction so that the time for each data entry comparison is essentially the time it takes to make these memory calls (Hennessy and Patterson, 1990). PCI based systems can transfer over 60 Mbytes of data per second or about two million 32-bit data entries per second over the bus. By ordering data entries sequentially when extracting the correlation subwindows from the image data set, bus transfer rates of this speed can be achieved by block memory transfers. Thus, correlation speeds of 2000 vec./s are theoretically possible for typical PIV images under these conditions.

Speed Relative to Spectral FFT Correlation. FFT spectral correlation is known to be a computationally efficient method of PIV processing. It is accomplished by taking the two-dimensional Fourier transform of an image and multiplying it by the complex conjugate of the Fourier transform of another image (or the same image in the case of auto-correlation) before taking the inverse transform. The computational intensity of this method of image correlation is of order $N^2 \log(N)$. In comparison, sparse array image correlation is an N^2 algorithm for a fixed correlation search length, Δ. It is, therefore, faster than FFT spectral correlation as long as $(\Delta\gamma)^2$ is smaller than about $\log(N)$. At low compression ratios, $\gamma \cong 1$, FFT spectral correlation is far faster than sparse array correlation for any reasonable correlation search length. At compression ratios greater than $\Delta/2$, however, sparse array image correlation results in significant computational savings as is illustrated in Fig. 6 by plotting the computational intensity of FFT spectral correlation divided by the computational intensity of sparse array correlation for correlation windows of $N = 32$, 64, and 128.

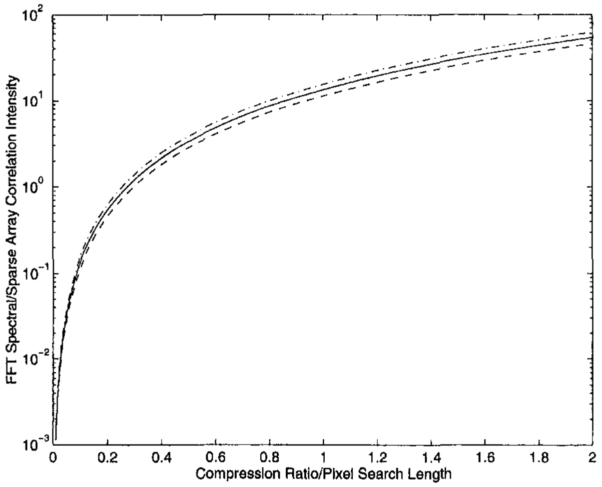

Fig. 6 Semi-log plot of the computational processing intensity of FFT spectral correlation relative to sparse array correlation as a function of the compression ratio divided by the search length for N = 32, 64, and 128

4 Accuracy and Robustness

The process of correlating images in sparse format using the algorithm presented here is independent of the method by which the image data set is generated. With no compression of the image, sparse array image correlation is identical to the more common statistical image shifting correlation method except for the use of the error correlation function. A comprehensive study of the error correlation function by Roth et al. showed that there exists no significant variation between the results from the error correlation function and that of the statistical correlation function (Roth et al., 1995). There is, thus, no reason to believe that the error correlation function is any more or less accurate than statistical or spectral correlation techniques. Any inaccuracy or lack of robustness in the present algorithm can be attributed entirely to the loss of data from image compression. The speed of sparse array image correlation, however, is strongly dependent on the reduction in the image data set through compression. Little is gained by using this algorithm if the data set remains unchanged. It is therefore necessary to address the problems associated with image compression to assess the limitations of the sparse array image correlation algorithm.

Velocity Gradient Affects. A method of determining the probability that a particular correlation is valid is to perform a nonparametric correlation and observe the peak correlation value relative to the mean. This method provides an indication of the probability that a particular correlation is valid. Unlike the more common parametric correlation processing used for PIV that provides information about the relative value of correlations within a particular subregion, nonparametric correlation can be used to compare the correlations from one subregion to the next. Nonparametric correlation can be accomplished by ranking the pixels in an image before correlation. Pixels with the same intensity are assigned an average of the rank they would receive if they had different values. Images with a poor rank correlation value relative to the mean are more likely to produce spurious vectors and to lack information needed to obtain accurate subpixel resolution. Thus, nonparametric correlation provides, in essence, a measure of the correlation signal to noise ratio.

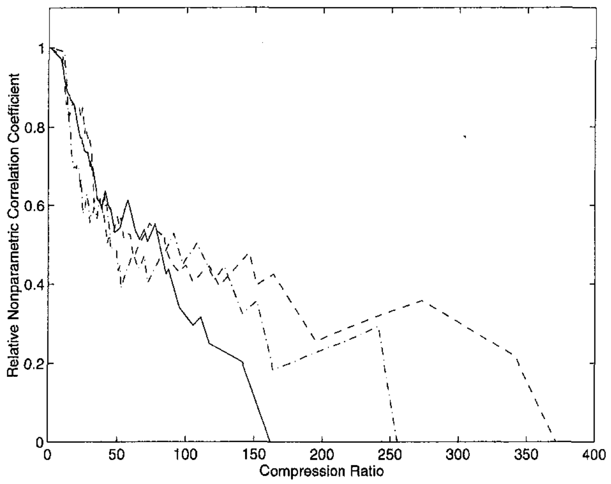

Fig. 7 Relative non-parametric correlation coefficient plotted as a function of intensity threshold image compression for $G_\nabla = 0, 1$, and 2

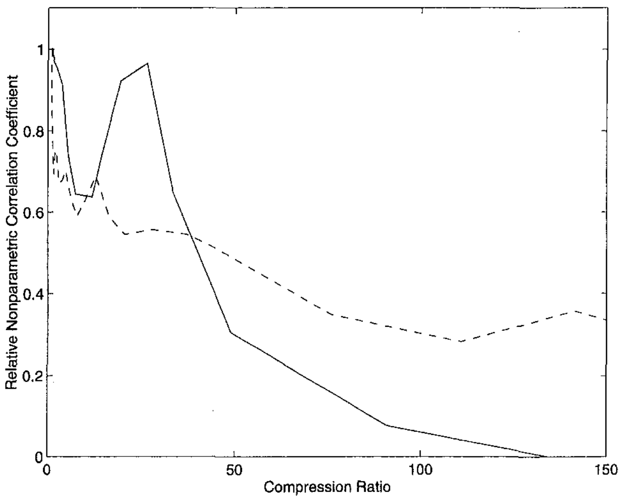

Fig. 8 Relative non-parametric correlation coefficient plotted as a function of intensity gradient image compression (dotted line) and intensity threshold compression (solid line) for the image in Fig. 1

As discussed in Section 2, the particle image diameters are important for resolving the average particle displacement in flows where there exist large gradients in the flow velocity. This is the factor which image compression affects the most. Other parameters such as seeding density, average flow velocity and relative correlation window size that influence all PIV correlation processing are unaffected. Using rank correlation, the effects of intensity threshold compression are plotted in Fig. 7 for several values of the ratio of the flow divergence to the particle image diameter based on the correlation window diameter, N, $G_\nabla = (M|\nabla \cdot \vec{v}\,|N\Delta t/D)$. For ideal PIV images where there exists no divergence in the flow, $G_\nabla = 0$, and no variation in peak image intensity, the compression ratio has little effect on the relative correlation of the image until a significant portion of the data of the tracer particle images are eliminated. These images can be compressed to a small fraction of their original size and retain enough correlation information to determine the subpixel displacement of the tracer particles. As shown in Fig. 7, images where G_∇ does not equal zero are affected to an increasingly greater extent by compression as G_∇ increases.

Intensity Variation Effects. Variations in intensity resulting from poor illumination and/or variations in particle characteristics severely affect the ability to extract particle displacement information from a PIV image using correlation. This is particularly true of auto-correlation processing, as there often exists a systematic intensity variation between the first and second exposures of the particle images. This type of intensity variation adversely affects both spectral correlation and compressed image correlation processing. It, however, limits the level to which an image can be compressed and thus has a much more pronounced effect on the speed and accuracy of compressed image correlation. Nonsystematic intensity variations, which result from differences in tracer particle characteristics and non-uniform illumination, affect both spectral correlation and compressed image correlation to roughly the same degree.

Consider the Gaussian intensity profile of a tracer particle image. This profile can be approximated by $I_r \cong I_o e^{-(4.3r/D)^2}$ where I_o is the peak intensity of a particle centered at (x_o, y_o) and r is the distance from the center. The magnitude of the gradient in intensity is then equal to $|\nabla I_r| \cong (37rI_o\beta/D^2)e^{-(4.3r/D)^2}$ where β is the characteristic size of a single pixel in the image. The maximum magnitude of the intensity gradient of a particle image occurs at a distance $r = D/4.3$ and has a value $|\nabla I_{r=D/4.3}| \cong 8.6(I_o\beta/D)$. If an intensity gradient threshold level is set above this value, all correlation information for this particle will be lost. Note, however, that the minimum particle diameter is roughly $D/2$ as long as the intensity gradient threshold level is set below $8.6(I_o\beta/D)$. This is not true of image segmentation based on intensity level thresholding where the particle image diameter approaches zero as the threshold level is increased. If there are significant variations in particle peak intensities within an image, however, then both methods of image segmentation adversely affect correlation although intensity thresholding to a somewhat less extent for the same compression ratio. This is illustrated in Fig. 8 by plotting the nonparametric correlation peak value obtained from Fig. 1 as a function of compression ratio for both gradient level compression and threshold compression. As illustrated in this figure, threshold intensity compression results in less information loss at low compression ratios. At higher compression ratios, however, gradient intensity compression results in less information loss. In many instances, image compression can greatly enhance the ability to obtain the correct correlation value by eliminating background information thus effectively improving the signal to noise ratio. This is clearly illustrated in Fig. 8 by a peak in the nonparametric correlation for threshold compression that occurs at a compression ratio near 30. This is an anomaly of this particular image indicating that the image contains significant correlated background noise below the threshold level at this compression ratio.

In practice, exposure levels are difficult to control and image-recording devices have limited intensity resolution. PIV images that have been over exposed have *tophat* particle image intensity profiles, Fig. 9. While this results in some information lose,

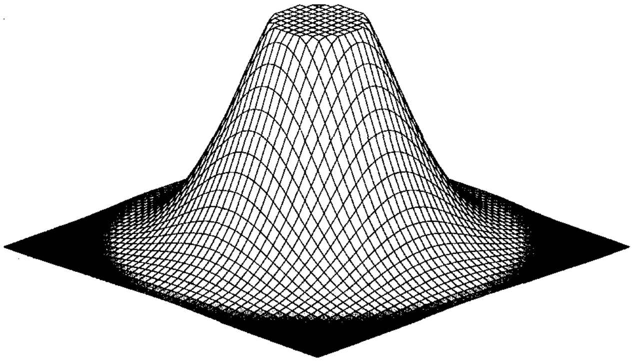

Fig. 9 Tophat profile of a particle image which has reached the saturation level of the image recording media

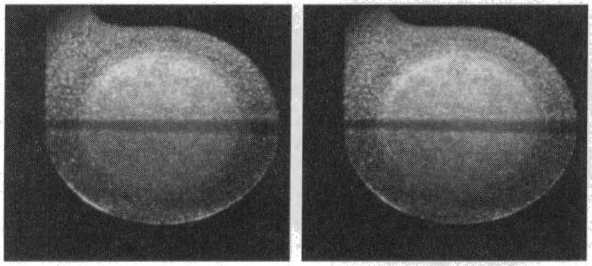

Fig. 10 Typical pair of PIV images recorded from a Cardio Assist Device, CAD

these images often correlate accurately for the same reason images compressed using intensity gradient thresholding correlate accurately—it is the change in intensity at the edges of the particle images that hold the information necessary for accurate correlation and not the low gradient regions near the center of the particle images. PIV images that are slightly over exposed are often better suited to intensity gradient compression rather than intensity threshold compression. This is because the saturated intensity regions of the particle images that contain little correlation information and have a low intensity gradient are eliminated from the data. Because intensity gradient image compression is more robust to variations in image exposure, it is generally a better choice for PIV image compression although it results in slightly more information loss at moderate compression ratios.

5 Experimental Demonstration

Variations in particle image intensity and size, correlated background noise, poor contrast, insufficient illumination and optical aberrations are only a few of the many factors that effect the quality of experimental images. For this reason, a comparison was made between spectral correlation and sparse array correlation based on the processing of experimentally obtained PIVC images of a highly unsteady vortical flow.

Images were used from the experimental measurement made of the flow inside a Cardio Assist Device, CAD. This device is used to aid the flow of blood in patients with weakened hearts. The flow in this device is highly unsteady and exhibits strong vortical flow formations (Huang et al., 1997). A frequency doubled Nd:YAG laser was used to illuminate a 10 cm × 10 cm area. The flow was seeded with 50 μm florescent particles. A Pulnex, TM-9701 512 × 486 pixel CCD camera, recorded PIVC images at 30 Hz. Typical images are shown in Fig. 10. Because of the curvature of the wall, all of the images exhibit significant variations in light intensity. These images were specifically chosen for comparison with the spectral correlation method because they exhibit features that are poorly suited to processing in sparse format. These features include significant local variation in illumination, large gradients in the flow velocity, heavy seeding densities, and very small tracer particle movement between images (less than 1 pixel on average) requiring accurate subpixel interpolation to resolve flow structures. Because of these features, the test images provide a means of illustrating the limitations of sparse array image correlation.

The experimental images were processed by cross-correlation using 64 × 64 pixel subwindows that overlapped by 50 percent in both the x and y directions. When compressed 30:1 with a maximum correlation search length of 32 pixels, the sparse array algorithm processed these images at roughly 300 vec./s on a Pentium 166 MHz computer with 16 Mbytes of memory. This was about sixty times faster than spectral correlation, which generated 5 vec./s on the same machine. An example of the output of both sparse array correlation and of spectral

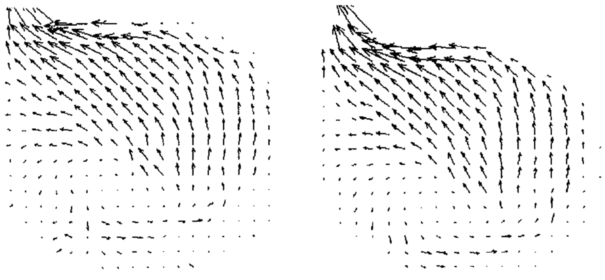

Fig. 11 Vector map obtained from sparse array cross-correlation of the images in Fig. 10 with a 30:1 compression ratio (left) and by spectral correlation (right)

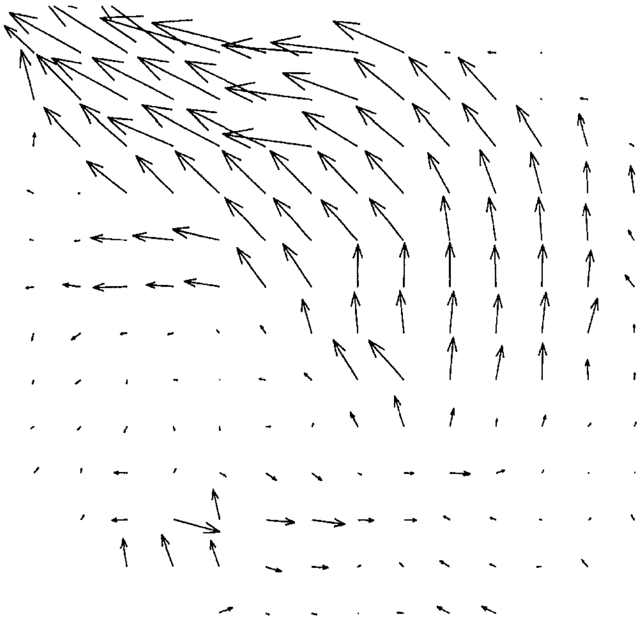

Fig. 12 Vector map obtained from sparse array cross-correlation of the images in Fig. 10 with a 100:1 compression ratio

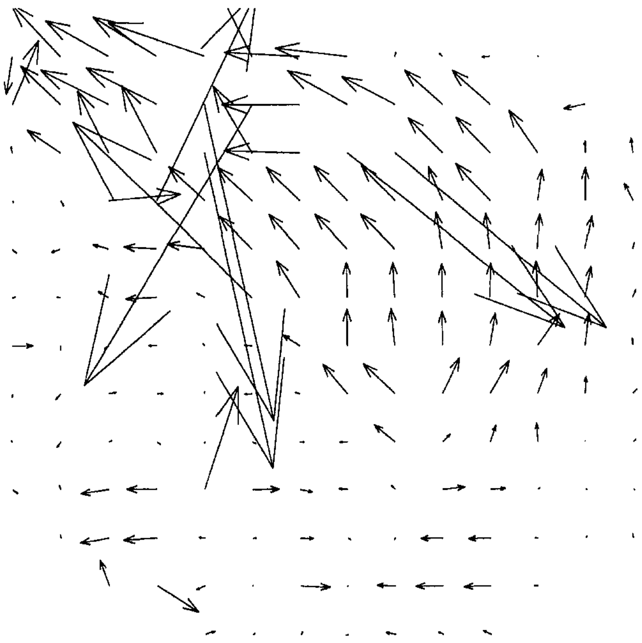

Fig. 13 Vector map obtained from sparse array cross-correlation of the images in Fig. 10 using a 200:1 compression ratio

correlation of the images in Fig. 10 is shown in Fig. 11. Sparse array correlation yielded results that were typically within 0.05 pixels of spectral correlation. No significant variation between the two correlation algorithms was observed with image compression ratios below 50:1. At higher compression ratios, 100:1, differences in the velocity profile in low velocity areas were observed, Fig. 12. These variations, on the order of 0.05 pixels, are the result of information loss due to compression. At much higher compression ratios, 200:1 and higher, sparse array image correlation generated significant spurious vectors near the wall of the test section and in other regions where high velocity gradients exist, Fig. 13. This behavior is consistent with the analysis discussed in Section 4. At these extremely high compression ratios, each vector represents the correlation of less than thirty pixels.

6 Summary and Conclusions

Sparse array image correlation is a technique by which PIV images can be accurately processed at high-speeds. It is based on the compression of images in which the number of data set entries containing tracer particle displacement information is reduced. Very high correlation speeds are obtained by encrypting the reduced data set into 32-bit integers and correlating the data entries using an error correlation function to eliminate multiplication, division and floating point arithmetic.

The maximum correlation value associated with sparse array image correlation is characterized by a steep peak that improves subpixel interpolation. The performance of this method of image correlation, however, is largely dependent on the level to which an image can be compressed without losing significant correlation information. Thus, the performance of this correlation method relative to the better known spectral correlation method is image dependent.

Through an analysis of the affects of flow divergence, tracer particle image diameter, and intensity variations, it was shown that typical PIV images can be highly compressed with no significant lose in correlation information. Characteristic limitations of sparse array image correlation were illustrated by comparing results from the spectral correlation of experimental images with the results from the sparse array correlation of the same images at varying levels of compression from 30:1 to 200:1. For applications requiring extremely high correlation speeds such as holographic particle image velocimetry (HPIV) and video rate particle image velocimetry cinematography (PIVC), sparse array image correlation appears to be a viable processing technique.

References

Adrian, R. J., 1986, "Multi-point Optical Measurement of Simultaneous Vectors in Unsteady Flow—a Review," *Int. J. Heat and Fluid Flow,* pp. 127–145.

Adrian, R. J., 1991, "Particle Imaging Techniques For Experimental Fluid Mechanics," *Annual Review of Fluid Mechanics,* Vol. 23, pp. 261–304.

Gonzalez, R. C., and Woods, R. E., 1993, *Digital Image Processing,* Addison-Wesley, Reading, MA, pp. 414–456.

Hatem, A. B., and Aroussi, A., 1995, "Processing of PIV Images," SAME/JSME and Laser Anemometry Conference and Exhibition, August 13–18, Hilton Head, SC, FED-Vol. 229, pp. 101–108.

Hennessy, J. L., and Patterson, D. A., 1990, *Computer Architecture—A Quantitative Approach,* Morgan Kaufmann Pub., San Mateo, CA.

Huang, H., Hart, D. P., and Kamm, R., 1997, "Quantified Flow Characteristics in a Model Cardiac Assist Device," ASME Summer Annual Meeting, Vancouver, B.C., Experimental Fluids Forum, pp. 1–6.

Landreth, C. C., and Adrian, R. J., 1987, "Image Compression Technique for evaluating Pulsed Laser Velocimetry Photographs having High particle Image Densities," FED-Vol. 49.

Okamoto, K., Hassan, Y. A., and Schmidl, W. D., 1995, "New Tracking Algorithm for Particle Image Velocimetry," *Experiments in Fluids,* pp. 342–347.

Rosenfeld, A., and De La Torre, P., 1983, "Histogram Concavity Analysis as an Aid in Threshold Selection," *IEEE Transactions on Systems, Man, and Cybernetics,* Vol. 13(3), pp. 231–235.

Roth, Hart, and Katz, 1995, "Feasibility of Using the L64720 Video Motion Estimation Processor (MEP) to increase Efficiency of Velocity Map Generation for Particle Image Velocimetry (PIV)," ASME/JSME Fluids Engineering and Laser Anemometry Conference, Hilton Head, SC, pp. 387–393.

Milo D. Dahl
Research Scientist,
NASA Lewis Research Center,
Cleveland, OH 44135

Philip J. Morris
Boeing Professor of Aerospace Engineering,
Penn State University,
University Park, PA 16802

Supersonic Jet Noise Reductions Predicted With Increased Jet Spreading Rate

In this paper, predictions are made of noise radiation from single, supersonic, axisymmetric jets. We examine the effects of changes in operating conditions and the effects of simulated enhanced mixing that would increase the spreading rate of the jet shear layer on radiated noise levels. The radiated noise in the downstream direction is dominated by mixing noise and, at higher speeds, it is well described by the instability wave noise radiation model. Further analysis with the model shows a relationship between changes in spreading rate due to enhanced mixing and changes in the far field radiated peak noise levels. The calculations predict that enhanced jet spreading results in a reduction of the radiated peak noise level.

1 Introduction

Recent interest in the development of a new High Speed Civil Transport has renewed research efforts to make the aircraft environmentally compatible. One issue is the level of noise generated by the supersonic jets exhausting from the propulsion systems. Supersonic jets are intense noise generators and means must be found to modify the noise generation process to reduce radiated noise levels in order for the aircraft to meet community noise regulations. A recent review by Seiner and Krejsa (1989) discusses the challenge of reducing supersonic jet noise associated with both mixing and shocks while maintaining acceptable propulsion system performance requirements. In this paper, we focus on the issue of mixing noise and the concept that the promotion of rapid mixing of the jet shear layer is an effective means of reducing radiated levels of mixing noise.

At present, the primary means of promoting enhanced jet shear layer spreading is either through acoustical or mechanical excitation. It is well known that subsonic jet mixing can easily be enhanced through acoustic excitation; but, for supersonic jets, acoustic excitation is much less effective (Lepicovsky et al., 1985). Mechanical means for promoting jet shear layer spreading were found to be more effective in supersonic jets than acoustic excitation. For example, Ahuja and Brown (1989) inserted small tabs into the jet flow at the lip of the nozzle exit. Alternatively, Gutmark et al. (1989) used nozzle shaping, such as elliptic and rectangular nozzles, to promote increased shear layer spreading. Experiments to measure the noise from supersonic jets with mechanical tabs have been performed by Ahuja (1993) and Kobayashi et al. (1993). In both studies, the jets contained shocks and for the most part the overall noise reduction was primarily due to the reduction of noise associated with shocks. However, the studies did show decreases in noise levels in the downstream direction where mixing noise dominates. Measurements of noise from perfectly expanded jets from elliptic nozzles (Seiner and Ponton, 1991) showed noise reductions compared to the equivalent axisymmetric jet. In this case, the results depended on the azimuthal angle.

The amount of experimental research on the effects of enhanced mixing on radiated jet noise has been much greater to date than analytical studies of the same problem. While there have been noise predictions for both supersonic axisymmetric and elliptic jets, noise predictions have not been made for supersonic jets with enhanced mixing. It is the purpose of this paper to make such predictions for single, supersonic, axisymmetric jets and evaluate the resulting noise reduction from simulated enhanced mixing that increases the spreading rate of the jet shear layer.

It is known that instability waves are the dominant source of mixing noise radiating into the downstream arc of a supersonic jet when the phase velocities of the instability waves or large scale turbulent structures are supersonic relative to ambient conditions (Tam, 1991). The analysis to predict the noise radiated to the far field is based on the determination of the axial growth and decay of the instability wave in the jet shear layer. In order to complete the analysis, the mean flow properties are needed. The next section describes the procedure used to determine the mean flow development of a jet that models the changes in spreading rate according to the operating conditions and simulates enhanced mixing. This is followed by a presentation of the instability wave noise generation model. The present model is preferable to a numerical simulation of the governing disturbance equations since the model equations enable us to derive a relationship between the changes in shear layer spreading rate and the changes in far field radiated peak noise levels. This relationship would be obscured if a numerical simulation was used. The final section shows how radiated noise is affected by changes in spreading rate due to changes in the operating conditions and shows how simulated enhanced mixing affects radiated noise. The analysis that predicts changes in radiated peak noise levels with enhanced mixing is also developed and the predicted changes are compared with results calculated using the full instability wave noise generation model.

2 Mean Flow

This section discusses the procedure used to determine the description of the mean flow development of a compressible, axisymmetric jet for inclusion in the instability wave noise generation model presented in Section 3. The jet flow is assumed to be perfectly expanded, thus the jet static pressure is matched to the ambient pressure. Often in the analysis of the mixing noise generation in single supersonic axisymmetric jets, the axial variation in the mean velocity profile is based on simple analytic functions with axially varying parameters. Tam and Burton (1984) used a generalized half-Gaussian function to describe the mean velocity at all axial locations with the centerline velocity, the potential core radius, and the jet shear layer half-width as the scaling parameters that varied with axial location. The axial variation of these parameters was determined by fitting equations to measured data. In supersonic jets where

---

Contributed by the Fluids Engineering Division for publication in the JOURNAL OF FLUIDS ENGINEERING. Manuscript received by the Fluids Engineering Division December 29, 1995; revised manuscript received April 10, 1998. Associate Technical Editor: M. M. Sindir.

temperature profiles are not easily measured, the Crocco-Busemann relation can be used to obtain mean density profiles. However, in order to use analytic functions to describe the mean flow for a variety of operating conditions where there is no measured data, the necessary axial variation in the scaling parameters must be predicted which requires a numerically generated mean flow.

A prediction scheme for the mean flow properties of a jet was developed with the capability to compute both single stream axisymmetric jets and dual stream coaxial jets as described in detail by Dahl and Morris (1997a). A set of compressible, Reynolds averaged, boundary layer equations with a modified mixing length model to determine the Reynolds stresses was used as the basis for the numerical mean flow analysis. Simplicity and robustness were emphasized in order to calculate the mean velocity and density. This led to the use of a simple turbulence model with a consequent high level of empiricism. To simulate the effects of enhanced mixing, the coefficient of the mixing length model is increased to provide a larger turbulent viscosity which causes the jet shear layer to spread faster. This turbulence model formulation is described next to show how the effects of velocity ratio, density ratio, and compressibility are included in the mean flow calculation. The numerically generated mean flow for a single jet is not used directly in the inviscid stability calculations but is used to derive the scaling parameters for a half-Gaussian function description of the velocity following the approach of Tam and Burton (1984). This allows easy calculation of the mean velocity, the mean density, and their derivatives along a contour in the complex plane when the numerical results exist only on the real axis. This contour is required to bypass a singularity that occurs in the inviscid stability equations during the course of the calculations for the instability wave when it is decaying or damped.

2.1 Turbulence Model. For the single jet, the Reynolds averaged equations contain a Reynolds stress term $-\bar{\rho}\overline{u'v'}$ and a heat flux term $-\bar{\rho}c_p\overline{v'T'}$ that are described by the following mixing-length model:

$$-\bar{\rho}\overline{u'v'} = \mu_T \frac{\partial \bar{u}}{\partial r} \tag{1}$$

and

$$-\bar{\rho}c_p\overline{v'T'} = \frac{c_p\mu_T}{\mathrm{Pr}_T}\frac{\partial \bar{T}}{\partial r} \tag{2}$$

where primes denote fluctuating variables and overbars denote mean variables. The turbulent viscosity μ_T is defined as

$$\mu_T = \bar{\rho}(\kappa C_1 C_2 l)^2\left|\frac{\partial \bar{u}}{\partial r}\right| \tag{3}$$

and the turbulent Prandtl number Pr_T is constant. The characteristic mixing length scale l is given by

$$l = \frac{\Delta\bar{u}}{|\partial\bar{u}/\partial r|_{\max}}, \tag{4}$$

where $\Delta\bar{u}$ is the velocity difference $\bar{u}_j - \bar{u}_\infty$ across the shear layer, and κ is a constant used to simulate the effects of enhanced mixing.

$$\begin{aligned} &\kappa = 1, \quad \text{no enhanced mixing} \\ &\kappa > 1, \quad \text{enhanced mixing} \end{aligned} \tag{5}$$

The factor C_1 is the incompressible part of the mixing length constant. It depends on the velocity ratio $r_u = U_\infty/U_j$ and the density ratio $s_\rho = \rho_\infty/\rho_j$. A calibration of C_1 was carried out for an incompressible jet over a range of expected r_u and s_ρ values resulting in a correlation for C_1 for $r_u < 1$

$$C_1(r_u, s_\rho) = \frac{A(r_u) + B(r_u)\sqrt{s_\rho} + C(r_u)s_\rho}{(1+\sqrt{s_\rho})(1 + r_u\sqrt{s_\rho})} \tag{6}$$

where

$$A(r_u) = (6.5919 + 11.918r_u - 4.1855r_u^2) \times 10^{-2},$$

$$B(r_u) = (10.880 - 2.3578r_u + 6.5642r_u^2) \times 10^{-2},$$

$$C(r_u) = (3.1013 + 16.420r_u - 5.8217r_u^2) \times 10^{-2}.$$

The C_2 factor is the compressible part of the mixing length constant. Its purpose is to decrease the growth of the shear layer as compressibility effects become important. It depends on a Mach number in a frame of reference convecting with the real phase speed of a growing disturbance in the shear layer. This convected Mach number M_c depends on the velocity ratio, the density ratio, and the Mach number of the jet,

$$M_c = M_j\frac{\sqrt{s_\rho}(1 - r_u)}{1 + \sqrt{s_\rho}}. \tag{7}$$

The resulting correlation equation for C_2 was found with C_1 taking on its value defined in equation (6).

$$C_2(M_c) = 1 + 0.4959[\exp(-1.4593M_c^2 + 0.0427M_c^3 - 0.3658M_c^4) - 1] \tag{8}$$

Thus, this model includes the effects of velocity ratio, density ratio, and compressibility in calculating a spreading jet shear layer and provides a means to simulate enhanced mixing.

2.2 Mean Flow Profiles. The velocity profiles generated by the numerical mean flow analysis were fitted by a half-Gaussian function for $r \geq h$,

$$\bar{u}(r, x) = \bar{u}_c(x)\exp\left[-(\ln 2)\left(\frac{r - h(x)}{b(x)}\right)^2\right], \tag{9}$$

where $\bar{u}_c$ is the centerline velocity, h is the potential core radius, and b is the shear layer half-width. For $h > 0$, then $\bar{u}(r, x) = \bar{u}_c(x)$ for $r < h$. The density profile is then found from the Crocco-Busemann relation

$$\frac{1}{\bar{\rho}} = -\frac{1}{2}\frac{\gamma - 1}{\gamma\bar{p}}(\bar{u} - \bar{u}_j)(\bar{u} - \bar{u}_\infty) + \frac{1}{\bar{\rho}_j}\frac{(\bar{u} - \bar{u}_\infty)}{(\bar{u}_j - \bar{u}_\infty)} + \frac{1}{\bar{\rho}_\infty}\frac{(\bar{u}_j - \bar{u})}{(\bar{u}_j - \bar{u}_\infty)}. \tag{10}$$

3 Instability Waves and Radiated Noise

It is well known that thin free shear layers containing an inflection point in the mean velocity profile are inherently unstable even in the absence of viscosity. An instability wave in the shear layer initially grows rapidly. As the shear layer grows, the wave growth rate decreases. Eventually, the shear layer is too thick to support unstable waves and the wave amplitude decreases until it disappears. This instability wave process is assumed to be governed by the linearized, inviscid, compressible equations of motion.

For slowly diverging jet flows, two solutions are created that apply to separate but overlapping regions. Following the approach of Tam and Burton (1984), the inner region, including the jet flow and the immediate region just outside the jet, has different length scales between the radial and the axial directions that leads to a multiple scales expansion of the governing equations. With the pressure disturbances represented as

$$p'(r,\theta,x,t)=\sum_{m=0}^{\infty}\delta_m(\epsilon)p_m(r,s)\times\exp\left[i\left(\frac{\phi(s)}{\epsilon}+n\theta-\omega t\right)\right],\qquad(11)$$

the lowest order set of equations may be reduced to

$$\frac{\partial^2 p_0}{\partial r^2}+\left[\frac{1}{r}+\frac{2\alpha}{\omega-\alpha\bar{u}}\frac{\partial\bar{u}}{\partial r}-\frac{1}{\bar{\rho}}\frac{\partial\bar{\rho}}{\partial r}\right]\frac{\partial p_0}{\partial r}+\left[\bar{\rho}M_j^2(\omega-\alpha\bar{u})^2-\frac{n^2}{r^2}-\alpha^2\right]p_0=0\qquad(12)$$

which is known as the compressible Rayleigh equation with variables normalized by the jet exit conditions of nozzle radius, velocity, and density. In Eq. (11), $\delta_m(\epsilon)$ are the gauge functions of the asymptotic expansion in the small parameter ϵ where $\delta_0(\epsilon)=1$, s is the slow variable to recognize the slow mean flow development in the axial direction $s=\epsilon x$, $\phi(s)$ is an axial phase function related to the axial wavenumber α by $d\phi/ds=\alpha(s)$, n is the azimuthal mode number, and ω is the radian frequency. For spatial instabilities, the frequency is real and the axial wavenumber is complex, $\alpha=\alpha_r+i\alpha_i$.

The solution to Eq. (12) is written as the sum of two general linearly independent solutions that are functions of r and s

$$p_0(r,s)=A_0(s)\zeta_1^n(r,s)+B_0(s)\zeta_2^n(r,s).\qquad(13)$$

As $r\to\infty$, the flow outside the jet becomes uniform and the solution to Eq. (12) may be written in the form

$$p_0=A_0H_n^{(1)}(i\lambda(\alpha)r)+B_0H_n^{(2)}(i\lambda(\alpha)r)\qquad(14)$$

where

$$\lambda(\alpha)=[\alpha^2-\bar{\rho}_\infty M_j^2(\omega-\alpha\bar{u}_\infty)^2]^{1/2}\qquad(15)$$

and $H_n^{(1)}$ and $H_n^{(2)}$ are nth-order Hankel functions of the first and second kind, respectively. Thus, for large r, Eq. (13) must tend to Eq. (14). As $r\to 0$, Eq. (13) must be finite.

In the outer region, which slightly overlaps the inner region, the governing equations control disturbances that are acoustic in nature. These disturbances have the same length scales in all directions; hence, all coordinates are treated equally. To create an outer solution in a form that allows it to be asymptotically matched to the inner solution, we use the axial coordinate $s=\epsilon x$ and the radial coordinate $\bar{r}=\epsilon r$. The solution is obtained from a Fourier transform of the outer region governing equations in the s direction. After considerable algebra, the lowest order outer solution is found to be

$$p(r,\theta,x,t)=\int_{-\infty}^{\infty}g(\eta)H_n^{(1)}(i\lambda(\eta)r)e^{i\eta x}e^{in\theta}e^{-i\omega t}d\eta\qquad(16)$$

where

$$g(\eta)=\frac{1}{2\pi}\int_{-\infty}^{\infty}\tilde{A}_0(\epsilon x)e^{i\phi(\epsilon x)/\epsilon}e^{-i\eta x}dx.\qquad(17)$$

The two solutions in the inner and the outer regions, represented in part by Eqs. (13) and (16), respectively, are matched asymptotically in an overlap region. To lowest order, we find that

$$A_0(s)=\tilde{A}_0(s)\quad\text{and}\quad B_0(s)=0.\qquad(18)$$

With the condition of finite value at $r=0$, equation (12) has become an eigenvalue problem with solutions only for certain values of α.

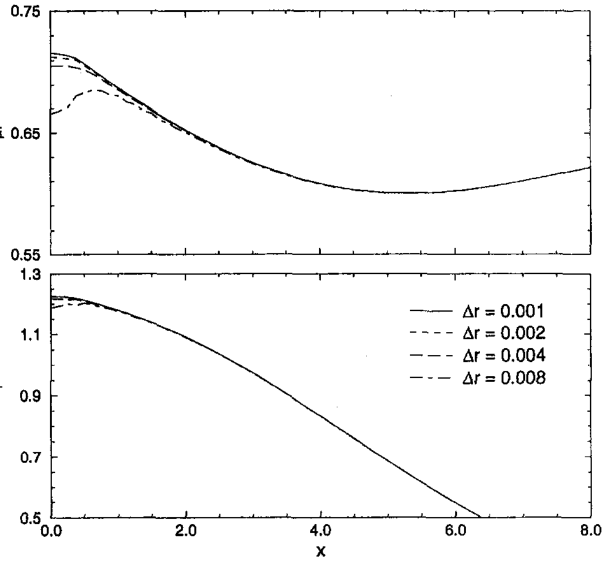

Fig. 1 Results for local growth rate, $-\alpha_i$, and phase velocity, c_{ph}, calculations at four different radial grid spacings. $n=1$; $fD_j/U_j=0.24$

Since the rate of spread of the jet is slow for high speed jets and ϵ is very small, $\tilde{A}_0(\epsilon x)$ in Eq. (17) is taken to be constant. Furthermore with $\alpha(x)$ found from the solution of Eq. (12) at every axial location, the axial phase function is found from $\phi(\epsilon x)/\epsilon=\int_0^x\alpha(\chi)d\chi$. *We can then solve for* $g(\eta)$ in Eq. (17), the Fourier transform of the instability wave. Subsequently the near field pressure disturbance is found from the inverse Fourier transform, Eq. (16). To obtain the pressure in the far field, Eq. (16), in spherical coordinates, is approximated by the method of stationary phase. The resulting sound power radiated per unit solid angle is

$$D(\psi)=\frac{1}{2}|p|^2R^2=2\frac{|g(\bar{\eta})|^2}{[1-M_\infty^2\sin^2\psi]}.\qquad(19)$$

The stationary point is given by

$$\bar{\eta}=\frac{\bar{\rho}_\infty^{1/2}M_j\omega\cos\psi}{(1-M_\infty^2)(1-M_\infty^2\sin^2\psi)^{1/2}}-\frac{\bar{\rho}_\infty M_j^2\bar{u}_\infty\omega}{1-M_\infty^2}\qquad(20)$$

and ψ is the polar angle.

A finite-difference approximation has been used to discretize Eq. (12) creating a system of equations that is second order accurate when the mean flow quantities are defined by Eqs. (9) and (10). The eigenvalue is found from the resulting diagonal matrix using a Newton-Raphson iteration for refinement. To assess the accuracy of the numerical calculations, the effect of the radial grid spacing on the calculated eigenvalue as a function of axial distance is shown in Fig. 1 for a Mach 2 jet. For the initially thin axisymmetric shear layer, the growth rate, $-\alpha_i$, and phase velocity, $c_{ph}=\omega/\alpha_r$, for the first helical mode at $fD_j/U_j=0.24$, where D_j is the jet exit diameter and U_j is the jet exit velocity, are underestimated if the grid resolution is insufficient. As the flow expands downstream and the shear layer gets thicker, the eigenvalue results converge to the same value. The ability to calculate the correct eigenvalue depends on the accurate representation of the derivatives of the pressure disturbance eigenfunction in Eq. (12). For the initial thin shear layer, the eigenfunction has rapid changes in its derivative values within the shear layer. With a course grid, these values are represented inaccurately. As the flow smooths out, the derivatives change more gradually and a numerical representation for the derivatives is obtained with sufficient accuracy on a course grid. Thus, a fine grid is initially required to obtain accurate representation of the eigenfunction derivatives within the thin shear layer.

Further details of this noise radiation prediction scheme and validation with measured data and other calculated results are given in Dahl and Morris (1997b).

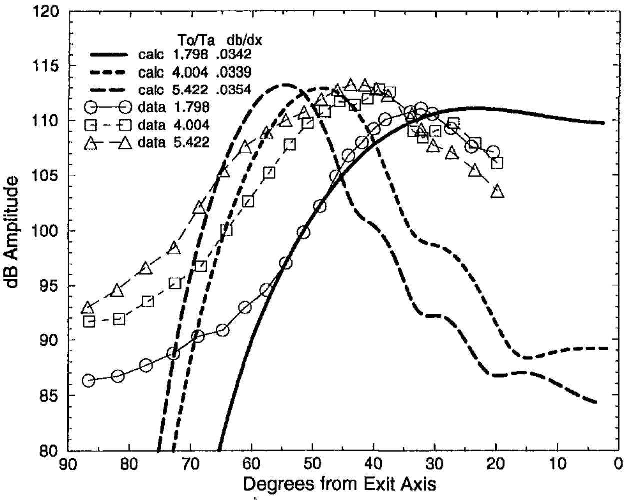

Fig. 2 Comparison of $M_j = 2$ jet calculations to measured far field noise data. $n = 1$, $fD_j/U_j = .11$

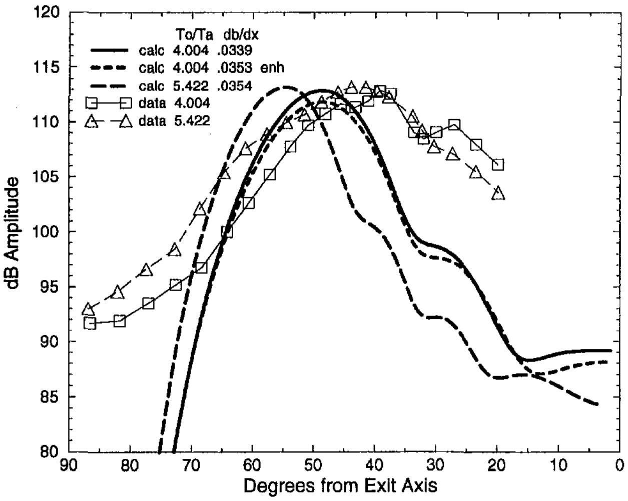

Fig. 3 Effects of operating conditions versus enhanced mixing on radiated noise, $M_j = 2$, $n = 1$, $fD_j/U_j = .11$

4 Predicted Sound

4.1 Variations in Operating Conditions. We first consider the changes in calculated noise due to changes in the operating conditions that naturally affect the jet spreading rate. Figure 2 shows a comparison between calculated and measured far field noise radiation patterns for three $M_j = 2$, hot jet cases given in Seiner et al. (1992). Both the measured and the calculated noise results are for a frequency corresponding to a Strouhal number fD_j/U_j of 0.11. The comparison is shown using the calculated first helical mode instability wave since this mode has the largest amplitude at this Strouhal number (see Seiner et al., 1993). The calculations are normalized to the measured peak level. As the figure indicates, the jet spreading rate $b' = db/dx$, where b is the jet shear layer half-width, is changing with the operating conditions. The measured results show that to increase the spreading rate by changing the operating conditions does not necessarily lead to a decrease in the radiated peak noise level. For example as the temperature ratio T_o/T_a increases from 4.004 to 5.422, the spreading rate increases from 0.0339 to 0.0354; but the measured far field peak levels increases slightly by 0.3 dB. In contrast, when the temperature ratio is lowered to 1.798 from 4.004, the spreading rate increases slightly to 0.0342 and the far field peak level decreases by 1.8 dB. The increase in jet temperature does increase the convected Mach number resulting in a shift of the measured noise radiation peak to larger angles. The measured noise levels show that at this Strouhal number this increase in jet temperature results in an increase in noise levels at higher angles to the jet axis and a decrease in noise levels at lower angles to the jet axis. The calculated results follow this trend. This paper is focussed primarily on the effects of jet spreading on far field peak noise levels and we will next show the effects of enhanced mixing on peak noise levels at fixed operating conditions.

4.2 Effects of Enhanced Mixing. To simulate enhanced mixing, κ in Eq. (3) is increased above 1. Using the two jets in Fig. 2 with $T_o/T_a = 4.004$, $b' = 0.0339$, and $T_o/T_a = 5.422$, $b' = 0.0354$, κ is increased for the cooler jet until the spreading rate is the same as the spreading rate of the hotter jet. Assuming that the initial amplitude of the instability wave remains unchanged, Fig. 3 shows the calculated far field radiated noise that results from increased mixing at fixed operating conditions. The radiated peak noise levels of the cooler jet are reduced and the directivity essentially unchanged. Even though the hotter jet has the same spreading rate as the cooler jet with enhanced mixing, the additional effects of increased temperature, increased velocity, and increased convected Mach number on the hotter jet result in an increased far field peak noise level and a change in directivity.

4.3 Predictions With Enhanced Mixing. The effects of simulated enhanced mixing as a function of spreading rate and Strouhal number for a hot, $M_j = 2$ jet are considered next. The choice of Strouhal number and stability mode is based on the results shown in Fig. 4. This figure shows the scaled maximum instability wave amplitude calculated from

$$A_{\max} = \exp\left(-\int_0^{x_c} \alpha_i \, dx\right) \approx \exp\left(-\frac{1}{b'}\int_0^{b_c} \alpha_i \, db\right) \qquad (21)$$

where $b \approx b'x$, $-\alpha_i$ is the local spatial growth rate, and x_c is the axial location at which $\alpha_i = 0$. Here it is assumed that the jet half-width grows linearly with axial distance based on the initial spreading rate. Calculated results are shown for three modes (the axisymmetric mode, $n = 0$, and two helical modes, $n = 1$ and 2) and five spreading rates (the normal spreading rate with $\kappa = 1$, $b' = 0.03818$, and four enhanced spreading rates at 0.125 intervals of κ). If Eq. (21) is rewritten as

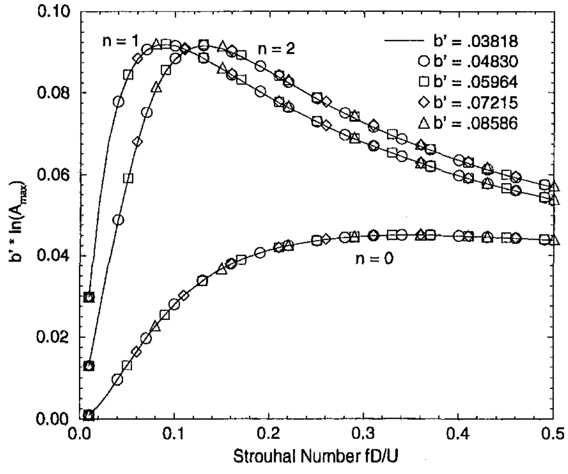

Fig. 4 Scaled maximum instability wave amplitude for a Mach 2 jet at five different spreading rates and three instability modes

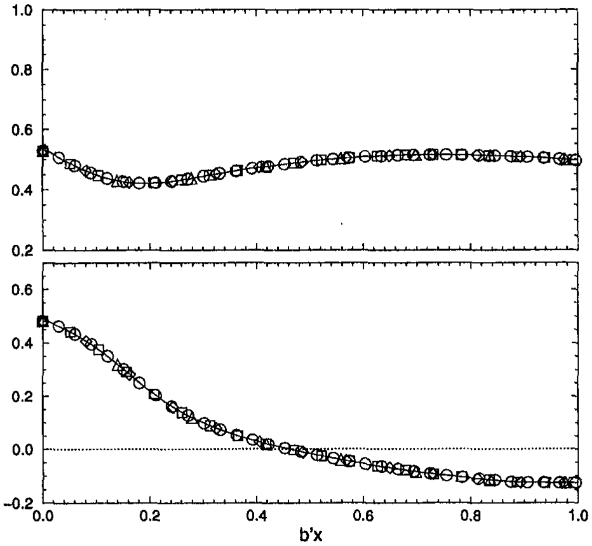

Fig. 5 Growth rate, $-\alpha_i$, and phase velocity, c_{ph}, as a function of the jet shear layer half-width. $n = 1$; $fD_j/U_j = 0.1$; see Fig. 4 for legend.

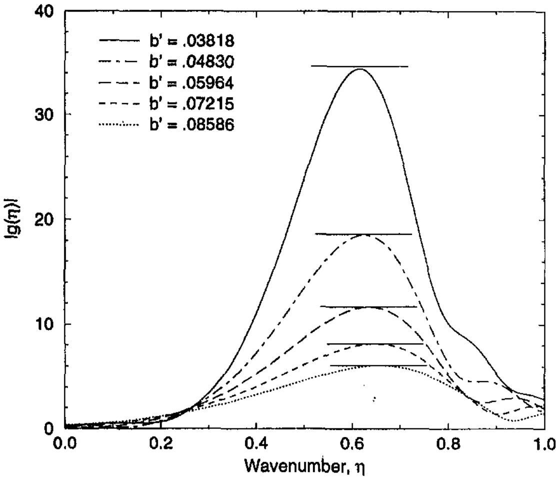

Fig. 6 Wavenumber spectra for instability waves defined by the stability characteristics shown in Fig. 5 calculated using Eq. (17). Short horizontal lines indicate the spectrum amplitude predicted by Eq. (23). $n = 1$; $fD_j/U_j = 0.1$.

$b' \ln (A_{\max}) = C_A$, then the maximum amplitudes as a function of Strouhal number for each mode are found to collapse to a single curve and, as a result, C_A is independent of the spreading rate. Since the $n = 1$ mode has the largest maximum amplitude, it is chosen for further study and the Strouhal numbers are chosen to be 0.1, near the peak noise Strouhal number, and 0.05, 0.2, and 0.4.

Figure 5 shows the local growth rates and phase velocities for the $n = 1$ mode at a Strouhal number of 0.1. The calculated results for the five different spreading rates are nearly equal at the axial locations where $b'x$ has the same value. Michalke (1984) has shown that the local stability characteristics of a compressible shear layer will scale with the shear layer thickness for a given Strouhal number and jet operating conditions. If only the shear layer width is allowed to increase, the local stability characteristics adjust to maintain this scaling with the shear layer thickness. In this case where the jet shear layer half-width b is nearly linear with x, constant local stability characteristics are moved toward the nozzle, decreasing x, as the spreading rate increases. This maintains the same growth rate and phase velocity for the same shear layer half-width. The same collapse of the growth rate and phase velocity curves with $b'x$ is also found for the other Strouhal numbers. Similar results are seen in the measured data from Moore (1977) where the data for growth rates and phase velocities of the axisymmetric mode collapsed to an approximate single curve when normalized for frequency at a fixed axial location. Here, the results are for a fixed frequency and show agreement as a function of the scaled axial location. Even though Fig. 5 shows that the local growth rates and phase velocities are equivalent for different spreading rates when the axial distance is scaled by the spreading rate, Fig. 3 shows a change in the far field peak noise level when the spreading rate is enhanced. Thus, we next show how this scaling of the local stability characteristics with spreading rate results in changes to the far field directivity peak noise level.

To use the results in Fig. 5, we approximate $g(\eta)$ in Eq. (17) by its asymptotic evaluation based on small spreading rates. Letting $s = \epsilon x \approx b'x$ and assuming $\tilde{A}_0(\epsilon x)$ to be constant and set to 1, the lowest order solution in terms of magnitude is

$$|g(\eta)| = \left[\frac{1}{2\pi b' |\alpha'(\bar{s})|}\right]^{1/2} \exp\left(-\frac{1}{b'}\int_0^{\bar{s}} \alpha_i \, ds\right) \quad (22)$$

where $\bar{s}$ is known as the saddle point in the asymptotic evaluation of the integral and $\alpha' = d\alpha/ds$. From Figs. 4 and 5, the terms in Eq. (22) involving α are constant for b' small; hence,

$$|g(\eta)| = b'^{-1/2} C_B \exp\left(\frac{1}{b'} C_A\right). \quad (23)$$

Since the saddle point $\bar{s}$ can be shown to lie near the location where $\alpha_i = 0$ then C_A can be approximated as the scaled maximum amplitude of the instability wave previously derived in Eq. (21) and shown in Fig. 4. Equation (23) then applies only to the peak of $|g(\eta)|$ as shown in Fig. 6 where C_B is calculated using an $|\alpha'|$ determined from the data shown in Fig. 5 at the point where $\alpha_i = 0$. The full wavenumber spectrum is calculated from Eq. (17). Using the normal spreading jet as a reference to eliminate the constant C_B, an equation for the change in far field directivity peak level is found using Eq. (19),

$$\begin{aligned} \Delta dB &= 10 \log D - 10 \log D_n \\ &= \frac{20}{\ln 10}\left[\frac{1}{2}\ln\frac{b_n'}{b'} + \frac{C_A}{b_n'}\left(1 - \frac{b_n'}{b'}\right)\right] \end{aligned} \quad (24)$$

where D_n and b_n' are the normal spreading jet far field directivity peak level and spreading rate, respectively. Figure 7 shows the agreement between the estimated peak level difference and the

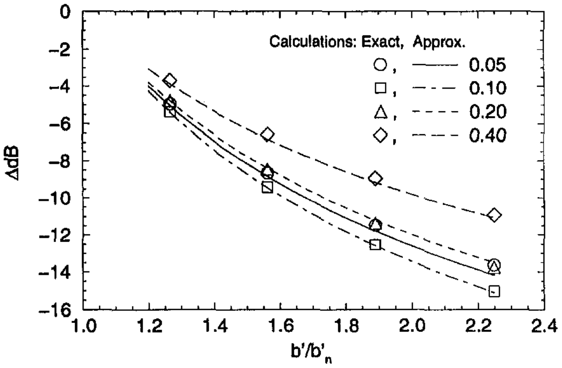

Fig. 7 Example noise reductions versus relative enhanced spreading rate as in ΔdB as a function of b'/b_n' in Eq. (24). $n = 1$, $M_j = 2$, $M_c = 1.3$. Symbols for full calculation. Lines for Eq. (24). $fD_j/U_j = 0.05$, 0.1, 0.2, and 0.4.

difference based on the full calculation. As the relative spreading rate increases, the relative peak far field noise level decreases. In addition, the amount of reduction depends on the maximum amplitude of the instability wave through C_A. The largest amplitude wave for the $n = 1$ mode with a Strouhal number of about 0.09 would have the largest reduction and the smaller amplitude waves at all the other Strouhal numbers have less reduction. It should be noted that substantial reductions in the peak noise levels may be achieved for relatively modest increases in jet spreading: 4 dB for a 20 percent increase in spreading rate. However, these reductions should be viewed in light of possible performance penalties that might be incurred for a given mixing enhancement method. The trends shown in Fig. 7 as the Strouhal number changes follow directly from the maximum amplitude plot in Fig. 4. The relative decrease in far field directivity peak level may also be predicted for other modes using Eq. (24). Since the peak of $|g(\eta)|$ must be radiated to the far field for Eq. (24) to apply, it then follows from the inversion of equation (20) that $\eta_{\text{peak}} \leq \bar{\rho}_\infty^{1/2} M_j \omega/(1 + M_\infty)$ (Dahl and Morris, 1997b), a condition that holds for all wavenumber components of the instability wave that radiate noise to the far field.

5 Summary

The instability wave noise generation model was used to predict the mixing noise radiated from supersonic axisymmetric jets and to study the effects of simulated enhanced mixing on changes in the radiated peak noise levels. The following results were found:

1. Changes in the jet operating conditions changed the jet shear layer spreading rate and the far field radiated noise levels. However, decreases in radiated peak noise levels did not necessarily occur when the spreading rate was increased in this case. Other factors such as jet temperature, velocity, and convected Mach number were more important to determining changes in noise levels.
2. Assuming a constant initial instability wave amplitude, increased spreading rate through enhanced mixing with the operating conditions held constant resulted in a decrease in peak radiated levels and no significant change in directivity.
3. The change in far field peak noise levels with spreading rate was shown to depend on the peak amplitude of the instability wave. As the peak amplitude changed with Strouhal number, the peak noise level changed. An equation was developed to predict the amount of change in the far field peak noise levels as both the Strouhal number and the spreading rate were changed.

References

Ahuja, K. K. and Brown, W. H., 1989, "Shear Flow Control by Mechanical Tabs," AIAA paper 89-0994.

Ahuja, K. K., 1993, "Mixing Enhancement and Jet Noise Reduction Through Tabs Plus Ejectors," AIAA paper 93-4347.

Dahl, M. D. and Morris, P. J., 1997a, "Noise from Supersonic Coaxial Jets, Part 1: Mean Flow Predictions," *Journal of Sound and Vibration*, Vol. 200, pp. 643–663.

Dahl, M. D., and Morris, P. J., 1997b, "Noise from Supersonic Coaxial Jets, Part 2: Normal Velocity Profile," *Journal of Sound and Vibration*, Vol. 200, pp. 665–699.

Gutmark, E., Schadow, K. C., and Wilson, K. J., 1989, "Noncircular Jet Dynamics in Supersonic Combustion," *Journal of Propulsion and Power*, Vol. 5, pp. 529–533.

Kobayashi, H., Oinuma, H., Sawamura, T., and Outa, E., 1993, "Effects of Tab Size on Supersonic Under-expanded Cold and Heated Jet Noise Suppression and Jet Thrust Loss," AIAA paper 93-4348.

Lepicovsky, J., Ahuja, K. K., Brown, W. H., and Burrin, R. H., 1985, "Coherent Large-Scale Structures in High Reynolds Number Supersonic Jets," NASA CR-3952.

Michalke, A., 1984, "Survey of Jet Instability Theory," *Progress in Aerospace Sciences*, Vol. 21, pp. 159–199.

Moore, C. J., 1977, "The Role of Shear-Layer Instability Waves in Jet Exhaust Noise," *Journal of Fluid Mechanics*, Vol. 80, pp. 321–367.

Seiner, J. M. and Krejsa, E. A., 1989, "Supersonic Jet Noise and the High Speed Civil Transport," AIAA paper 89-2358.

Seiner, J. M. and Ponton, M. K., 1991, "Supersonic Acoustic Source Mechanisms for Free Jets of Various Geometries," in *Combat Aircraft Noise*, AGARD-CP-512.

Seiner, J. M., Ponton, M. K., Jansen, B. J., and Lagen, N. T., 1992, "The Effects of Temperature on Supersonic Jet Noise Emission," DGLR/AIAA paper 92-02-046.

Seiner, J. M., Bhat, T. R. S., and Ponton, M. K., 1993, "Mach Wave Emission from a High Temperature Supersonic Jet," AIAA paper 93-0734.

Tam, C. K. W. and Burton, D. E., 1984, "Sound Generated by Instability Waves of Supersonic Flows. Part 2. Axisymmetric Jets," *Journal of Fluid Mechanics*, Vol. 138, pp. 273–295.

Tam, C. K. W., 1991, "Jet Noise Generated by Large-Scale Coherent Motion," *Aeroacoustics of Flight Vehicles: Theory and Practice Volume 1: Noise Sources*, NASA RP-1258, chapter 6.

Y. Sakakibara
Assistant,
Department of Industrial &
Mechanical Engineering,
Tokyo Denki University,
Ishizaka, Hatoyama-machi, Hiki-gun,
Saitama-ken 350-0394, Japan

J. Iwamoto
Professor,
Department of Mechanical Engineering,
Tokyo Denki University,
2-2 Nishiki-cho, Kanda, Chiyoda-ku,
Tokyo 101-8457, Japan

Numerical Study of Oscillation Mechanism in Underexpanded Jet Impinging on Plate

The mechanism of the oscillatory phenomena of an underexpanded jet impinging on a flat plate is studied numerically. Pressure changes generated in the flow field near the plate propagate radially in the surrounding region of the jet. The configuration of the jet boundary is changed by them and so, the waves forming the underexpanded jet are displaced when they are reflected from the jet boundary. And then, the pressure disturbances return to the region near the plate. Unsteady flow with repetition of growth and decay of the separation bubble on the plate is also found under certain conditions.

1 Introduction

When air exhausts from a convergent nozzle with a nozzle pressure ratio p_0/p_a (p_0: stagnation pressure of the jet, p_a: atmospheric pressure) that is higher than the critical pressure ratio $p_0/p_a \simeq 1.893$ in case of the air, the jet is underexpanded and a typical cell structure which consists of alternate expansive and compressive regions is formed in the jet. It is well known that, under certain conditions, the underexpanded jet impinging on a flat plate which is located perpendicularly downstream becomes unstable and oscillatory.

Powell (1994) experimentally studied unsteady behavior of a moderately underexpanded round jet impinging on two different plates, i.e., "small" and "large." The experiments performed were both acoustical measurement and photographic flow visualization: the frequency of the oscillation was measured and shadowgraph pictures were taken to yield information about the overall structure of the flow. He found that periodic oscillations of the jet occurred over a wide variation of the control parameters such as pressure ratio, plate size and nozzle-plate spacing and that such oscillations were accompanied by the radiation of the noise with discrete frequencies. In addition, the feedback mechanisms of the oscillation under each condition were analyzed experimentally.

For the small plate, which has the same diameter as that of the nozzle exit, Kashimura and Yasunobu (1991) studied the mechanism of the oscillation of the jet using the numerical flow visualization. The impinging jet on the large plate can be considered to be one of the simplified models of the supersonic jets for the industrial applications such as the assist gas of the laser cutting, the exhaust gas from the rocket engine, and so on. As reported by Powell (1994), the noise generated from the impinging jet is related to the oscillation of the jet and then, to solve the industrial problem caused by the noise, the mechanism of the oscillation should be made clear.

So, in this paper, unsteady behavior of the underexpanded jet impinging on the large flat plate is studied numerically and the mechanism of the oscillation is described.

2 Numerical Schemes

Figure 1 shows the computational model we used. A supersonic air jet exhausts from the circular nozzle with the radius of curvature $R = 20$ mm and the diameter of the nozzle exit $D = 10$ mm, and the jet impinges on the flat plate perpendicularly. The nozzle-plate spacing is l and the air flows radially on the plate after the impingement. The point P is the center of the plate and the pressure history during the oscillation of the jet is examined at this point.

The effects of the configuration of the sonic line where the flow velocity reaches the local speed of sound in the flow field are considered in our computations to obtain the boundary conditions at the nozzle exit. The velocity distribution on the nozzle exit plane is calculated using the equations by Kliegel and Levine (1969).

The axisymmetric Navier-Stokes equations are solved using the multigrid TVD-type scheme by Wiedermann and Iwamoto (1994). With Yee and Harten's upwind TVD-type scheme (Yee and Harten, 1987) and Yee's symmetric TVD-type scheme (Yee, 1987), they studied the effects of the limiter function on the steady solution of the Euler and Navier-Stokes equations and then, suggested that, in both schemes, a good shock resolution can be stably obtained using the general β-limiter which is mixed with Van Leer's limiter (Hirsch, 1988). Furthermore, adding a hybrid Runge-Kutta scheme and a multigrid scheme (Jameson, 1985) in time integration, a considerable improvement in the convergence rate can be achieved with just weakly effects on the solution in case of using the symmetric type scheme.

In this paper, the above second-order symmetric TVD-type scheme is applied for the spacial discretization and the hybrid five step Runge-Kutta scheme for time integration, which is proved to be well-adjusted to the requirements of multigrid convergence acceleration (Jameson, 1985). The multigrid scheme is used in the early steps of iteration to accelerate the propagation of the boundary conditions to the whole computational domain. When the oscillation phenomena of the jets are analyzed, the multigrid scheme was not used because the second-order accuracy in time was needed. CFL-coefficient used which determines the time step size Δt is 0.6 and, with such Δt, the good convergence of the solution was obtained stably in the case of the steady impinging jet and those numerical results agree well with those of experiment especially concerning the cell structure of the jet and the flow pattern near the impinged plate (Sakakibara and Iwamoto, 1993).

3 Results and Discussions

3.1 Optical Observations. Figure 2(a) shows the computed density and pressure contours of the impinging jet with $l/D = 2.6$ and the pressure ratio across the nozzle $p_0/p_a = 3.0$. The upper half of this figure shows the density contours and

---

Contributed by the Fluids Engineering Division for publication in the Journal of Fluids Engineering. Manuscript received by the Fluids Engineering Division December 11, 1995; revised manuscript received February 9, 1998. Associate Technical Editor: M. M. Sindir.

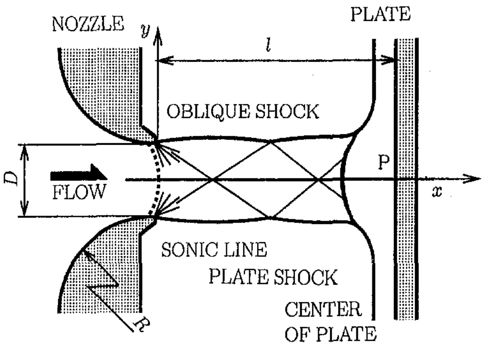

Fig. 1 Computational model

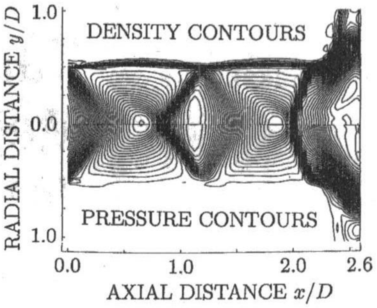

(a) l/D=2.6 (by Calculation)

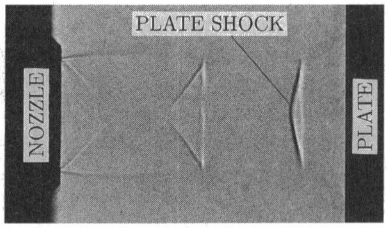

(b) l/D=2.6 (by Experiment)

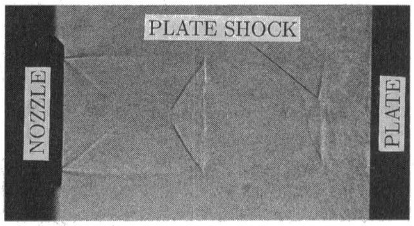

(c) l/D=2.8 (by Experiment)

Fig. 2 Impinging jets with $p_0/p_a = 3.0$

the lower half the pressure contours. Figure 2(b) shows the shadowgraph picture of the jet under the same condition of Fig. 2(a). Comparing these figures shows that an agreement is good as far as the location of the shock wave, the shape of the jet boundary and so on are concerned.

Figure 2(c) shows the shadowgraph picture of the jet with $l/D = 2.8$. In case of the nozzle-plate spacing $l/D = 2.6$ (Fig. 2(b)), the plate shock is clearly seen in the upper shadowgraph and the position and the configuration of the plate shock and the cell structure of the jet obtained by the computation is in good agreement with those of the shadowgraph.

For the shadowgraph picture with $l/D = 2.8$, the resolution of the shock becomes worse and the boundary of the wall jet on the plate is seen to be disturbed. These are considered to be caused by the oscillation of the shock and it has been found, in the experiment, that the jet becomes unsteady with the nozzle-plate spacings larger than $l/D = 2.8$.

As can be seen in the following, the oscillation occurs also in the computed result. Figure 2(c) shows flow field at a certain instant during the oscillation.

3.2 Computational Grid. A simple rectangular computational grid is used in this study. The grid points are clustered near the nozzle wall, the plate shock and the impinged flat plate in x-direction, and they are also clustered in the jet in y-direction.

Figure 3 shows the effects of the different grid size on the computed pressure distribution on the plate in case of the steady impinging jet ($l/D = 1.3$). The size of grid is smallest on the plate in the whole computational domain and Δx in this figure shows the grid spacing in x-direction at that point with $\Delta y/D \simeq 0.01$.

In this figure, the pressure distribution which is nondimensionalized by the atmospheric pressure p_a near the center of the plate ($y/D \simeq 0.0$) for $\Delta x/D \simeq 0.005$ seems to be almost the same as that for $\Delta x/D \simeq 0.01$. Furthermore, concerning the wave-like distribution generated by the repetition of the reflection of the expansion and compression waves between the wall-jet boundary and the plate (between $y/D \simeq 0.8$ and $y/D \simeq 1.6$), the pressure distributions with $\Delta x/D \simeq 0.01$ and $\Delta x/D \simeq 0.005$ are very similar with each other.

So, the computational grid with $\Delta x \simeq 0.01$ and $\Delta y \simeq 0.01$ can be considered to be suitable for the computations of the impinging jet.

3.3 Features of Flow Fields. Table 1 summarizes different flow patterns in the flow field near the plate for different nozzle-plate spacings at $p_0/p_a = 3.0$ obtained by the computations. It is found that the impinging jets oscillate with the spacings larger than $l/D = 2.3$ (see the second line in Table 1).

The third line shows the features of the pressure history at the center of the plate and the fourth line those of the results of FFT-analysis of the pressure oscillations shown in the third line. Between $l/D = 2.3$ and 2.7, except $l/D = 2.5$, the pressure oscillations with very small amplitudes are shown and, in this range of nozzle-plate spacings, the amplitudes become slightly larger with larger nozzle-plate spacings. The pressure oscillation becomes stronger between $l/D = 2.8$ and 2.9 and the growth of the amplitude is evident.

Dominant frequencies of the pressure oscillation are shown in the fifth line and, for the comparison with the experimental data, the frequency of oscillation obtained from noise measurement by Tamura and Iwamoto (1994) is shown in the sixth line.

Although the frequencies obtained by the computations are almost the medium values of the first and second dominant frequency of the noise, they have qualitatively the same tendency concerning the decrease of the frequency with increase of the nozzle-plate spacing between certain spacings and frequency "jump" between them. The frequency jumps between $l/d =$

Nomenclature

D = diameter of nozzle exit
l = nozzle-plate spacing
p = pressure
P = center of plate
p_0 = stagnation pressure of jet
p_a = atmospheric pressure
R = radius of curvature of nozzle wall
x, y = coordinate system

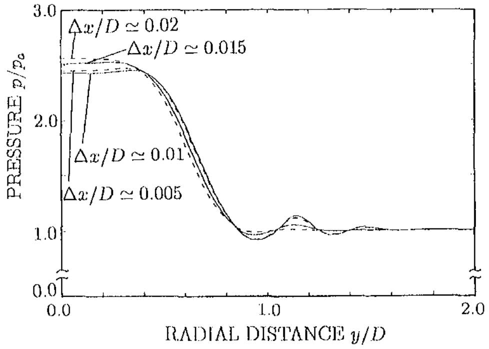

Fig. 3 Pressure distribution on plate (l/D = 1.3)

2.7 and 2.8 in case of the numerical result and it occurs between l/D = 2.6 and 2.7 experimentally.

That the number of the grid points in the ambient flow field is too small to resolve the propagation of the pressure changes like acoustic waves is considered to cause the difference of the frequency values between experiment and calculation and so, the quantitative agreement may be obtained with mesh refinement.

It is surmised from the shadowgraphs in Figs. 2(b) and 2(c) that the oscillation of the jet occurs with spacings larger than l/D = 2.8, while numerically it occurs with spacings larger than l/D = 2.3 as shown in Table 1. This inconsistency is due to the fact that the fluctuations of the jet boundary and the shock are too small to appear in the shadowgraph. Because the scales of the fluctuation of jet boundary and shock at the spacings between l/D = 2.3 and 2.7, except l/D = 2.5, are very small as well as the amplitudes of the pressure oscillations, the shock wave looks to stand still in the shadowgraph.

In case of the nozzle-plate spacing l/D = 2.5, a peculiar pattern of the pressure oscillation and the corresponding characteristic of the frequency are shown by the sketch in Table 1. This is considered to be caused by the repetition of the growth and the decay of the separation bubble formed in the jet near the plate and this will be discussed in Section 3.5.

The pressure oscillation for the nozzle-plate spacing l/D = 3.0 has many frequency components because, in the third line, the pattern of the pressure oscillation changes and the periodicity of the oscillation is lost.

These changes of the flow pattern are considered to be related to the position of the plate shock on the jet axis shown in the fifth line in Table 1. The flow is steady when the plate shock is located in the expansive region in the second cell on the jet axis. The oscillations with very small amplitudes occur when the oblique shock merges into the plate shock before it reaches the jet axis in the second cell and the amplitudes become large when the oblique shock is reflected from the jet axis upstream of the plate shock. Furthermore, when the plate shock stands in the expansive region of the third cell, the pattern of the oscillation changes as shown for l/D = 3.0 in Table 1.

In the bottom line of Table 1, it is shown that the separation bubble is generated in the region near the plate both in the steady and unsteady jet.

3.4 Mechanism of Flow Oscillation. As described above, the periodic pressure oscillation with the largest amplitude at the center of the plate occurs with a certain dominant frequency about 20 kHz when l/D = 2.9, so that the changes of the flow field with time can be seen clearly under this condition.

Figure 4(a) shows the pressure contours of the jet with the time-averaged pressure distribution for one cycle of the oscillation and Figs. 4(b) to 4(f) show a time sequence of the flow field represented by the pressure deviations from time-averaged pressure of the jet (Fig. 4(a)) during the oscillation. The bold lines in these figures represent the jet boundary and the plate shock, and the thin solid lines are the lines of the time-averaged pressure. Thus, the pressure is higher or lower than the averaged pressure across this solid line.

The pressure upstream and downstream of the plate shock alternately increases and decreases with time. The pressure at the center of the plate also changes so as to be in the same sense with that in the region upstream of the plate shock. These pressure changes which are shown by the dark and bright regions on the plate move radially on the plate with time and affect the surrounding air of the jet. These effects are shown in Figs. 4(b) to 4(f) as the radiation of the pressure waves from the impinging region into the surroundings of the jet. They can be seen to propagate toward the nozzle wall gradually and the configuration of the jet boundary is changed by them.

In the underexpanded jet, the expansion waves, which are generated at the nozzle rim, are reflected from the jet boundary as the compression waves and these compression waves merge into the oblique shock. Thereafter this oblique shock reaches the jet boundary and then, the expansion waves are reflected. This wave pattern forms the cell structure of the jet and so, in Fig. 4, it can be considered that these wave patterns are affected by the pressure waves in the surrounding region when the waves in the jet are reflected from the changed jet boundary described above. The disturbances come back to the impinging region and affect the plate shock. Even the supersonic flow just downstream of the nozzle exit is also affected with this mechanism by the disturbances generated in the impinging region downstream.

Because the above pressure waves which consist of the alternate positive and negative pressure deviations in the surrounding air of the jet are weakened by the viscosity as they propagate toward the nozzle wall, the changes of the configuration of the jet boundary become larger as further away from the nozzle. Accordingly, the amplitudes of the pressure oscillation of the jet with the nozzle-plate spacings between l/D = 2.3 and 2.7, except 2.5, become slightly larger with larger nozzle-plate spacings, although they are very small, because the location of the plate shock is also changed downstream. The frequency decreases with the increase in nozzle-plate spacing from about 37 kHz (for l/D = 2.3) to 27 kHz (for l/D = 2.7).

When the nozzle-plate spacings l/D = 2.8 and 2.9, the plate shock is located in the compressive region of the second cell and downstream of the oblique shock on the jet axis (see Table 1). This means that the oblique shock in the second cell reaches the jet boundary upstream of the plate shock and is reflected as the expansion waves. The effects of the changed jet boundary on the reflection of the oblique shock are considered to be stronger than those on the reflection of the expansion waves and then, comparing with the above cases with very small amplitudes of the pressure oscillations, the amplitudes for l/D = 2.8 and 2.9 become larger and their frequencies change from about 31 kHz to 30 kHz.

Another movement of the plate shock can be considered to be superposed on that at larger nozzle-plate spacings than this

Table 1 Flow fields for different nozzle-plate spacing (p_0/p_a = 3.0)

LEGEND

Com.=Computational results	Exp.=Experimental results (Tamura and Iwamoto(1994))	P.S.=Plate Shock
CR=Compressive Region		S.B.=Separation bubble
D.F.=Dominant Frequency	N.P.S=Nozzle-Plate Spacing	1(2,3)C=First(Second,Third) Cell
ER=Expansive Region	O.S.=Oblique Shock	

LINE													
1	N.P.S.(l/D)	1.3	2.0	2.1	2.2	2.3	2.4	2.5	2.6	2.7	2.8	2.9	3.0
2	Flow	Steady				Unsteady							
3	Pressure Oscillation	——				——			——		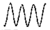		
4	Frequency	——											
6	D.F.(Com.) [kHz]	——				36	32	30	27.5	26.7	31	29.9	29 etc.
8	D.F.(Exp.) 1st [kHz] 2nd	no	29 22.1	26.5 20.6	25.3 19.8	25.3 51	19 42.6	18.5 42	17.9 45.5	21.8 44.5	21.1 43	20.4 41.5	19.9 39.5
7	Location of P.S. on Jet Axis	CR -1C	ER-2C			CR-2C (Upstream of O.S.)					CR-2C (Downstream of O.S.)		ER -3C
8	S.B.	○	——				○			——			

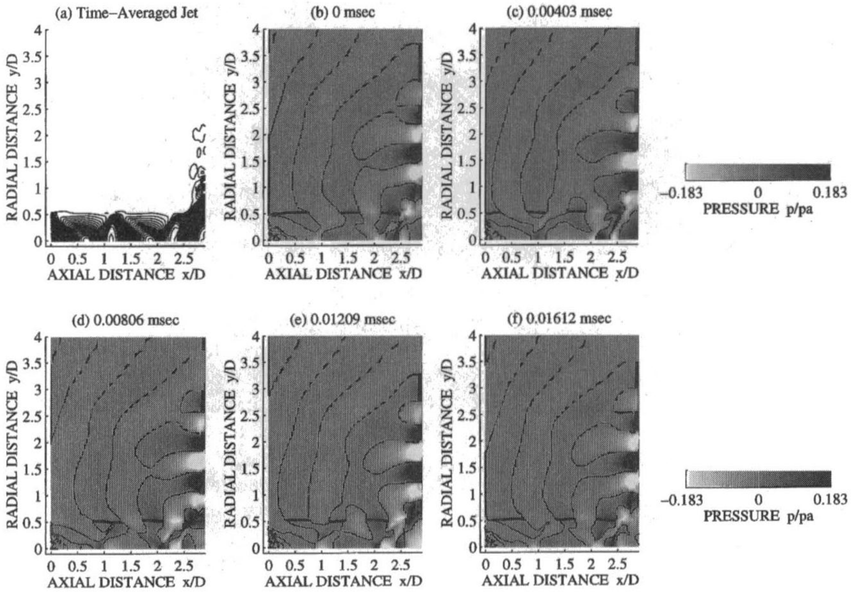
(a) Time–Averaged Jet (b) 0 msec (c) 0.00403 msec (d) 0.00806 msec (e) 0.01209 msec (f) 0.01612 msec

Fig. 4 Pressure deviations from time-averaged jet ($l/D = 2.9$)

because the plate shock is positioned in the compressive region of the third cell.

3.5 Flow Oscillation With Separation Bubble. When the underexpanded jet impinges on the plate, the separation bubble may form between the plate shock and the plate under certain nozzle-plate spacings both in the steady and unsteady flow field (see bottom line in Table 1). Authors have studied the necessary conditions for the generation of the separation bubble numerically using both the Euler- and Navier-Stokes-computations and found that the configuration of the plate shock is the most important factor for its generation (Sakakibara and Iwamoto, 1993).

When the plate shock is stronger near the jet axis than that in the region near the jet boundary, such as the case of the bow-type shock, the flow downstream of the shock becomes the shear flow and, as a result, the viscosity plays an important role in this region. Furthermore, the drop in stagnation pressure across the shock at the jet axis is large compared to the other part of the shock, and thus, the stagnation pressure at the center of the plate becomes low. Therefore, the air on the plate can be considered to flow from the surrounding region with higher stagnation pressure toward the center of the plate where the stagnation pressure is lower.

In the bottom line in Table 1, the ranges of the nozzle-plate spacing in which the circles are shown correspond to the jet with the bow-type plate shock, where the above description applies. The jet with $l/D = 1.3$ is steady and those with the spacings between $l/D = 2.4$ and 2.6 are unsteady. In the computational results the flow conditions for $l/D = 2.4$ and 2.6 are found to be similar to that for $l/D = 1.3$ in spite of the oscillatory behavior for $l/D = 2.4$ and 2.6 because the scales of the fluctuation of the jet boundaries and the shocks in the jet are very small, as well as the amplitudes of the pressure oscillation at the center of the plate. The size of the separation bubble changes little with time.

In case of the impinging jet with the spacing $l/D = 2.5$, a peculiar pattern of the pressure oscillation is obtained. Figure 5 shows the pressure history at the center of the plate. The abscissa is the time steps, where the physical time per unit time step corresponds to about 12.3 μs, and the ordinate is the pressure which is nondimensionalised by the atmospheric pressure. The remarkable pressure change is found to appear almost every 4200 time steps.

The density contours and the velocity vectors at each instant ① to ④ in Fig. 5 are shown in Fig. 6. The velocity vectors are shown in the enlarged area near the plate indicated in the diagram of the density contours.

At the instant ① the pressure at the center of the plate is decreasing and reaches the minimum value at ② as shown in Fig. 5. As can be seen in the density contours at ① and ② in Figs. 6, the location of the plate shock on the jet axis moves upstream and the vortex becomes larger with the comparatively larger velocity components in radial direction as time passes from ① to ②. After that, the pressure rapidly increases to the maximum value at ③ with the decay of the vortex and the movement of the plate shock toward the plate. Then, from ④ on, the separation bubble grows gradually and this continues until the next remarkable pressure change begins to occur at ①.

The decay of the separation bubble can be considered to be due to the movement of the plate shock; the shock moves downstream and pushes the vortex out of the impinging region radially on the plate. The disturbance caused by the pushed-out vortex propagates into the surrounding region of the jet in the manner shown in Fig. 5 and described in the previous section, and it can be considered to return to the impinging region after almost 4200 time steps.

4 Conclusions

The underexpanded impinging jet on the flat plate with the pressure ratio $p_0/p_a = 3.0$ is studied numerically using TVD-scheme. The oscillation of the jet is observed with larger nozzle-plate spacing than $l/D = 2.3$.

Noting the pressure deviations at each instant from the time-averaged pressure of the jet during the oscillation, the mechanism of oscillation is described; the pressure changes in the

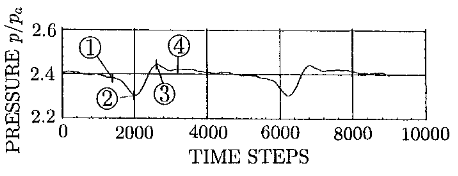

Fig. 5 Pressure history at center of plate ($l/D = 2.6$)

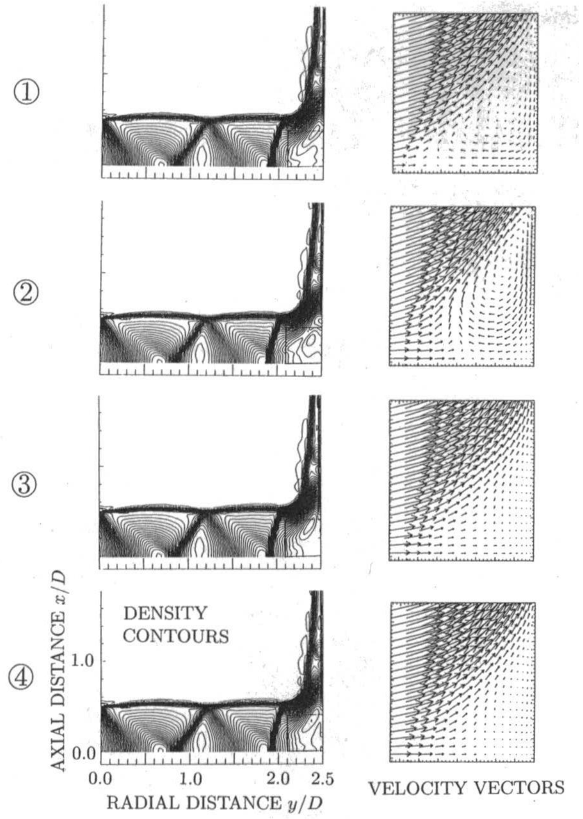

Fig. 6 Density contours and velocity vectors (l/D = 2.5)

impinging region propagate toward the nozzle through the surrounding region of the jet, the configuration of the jet boundary is changed slightly by this, the waves in the jet are also affected as they are reflected from such changed jet boundary and the disturbances return to the impinging region. At $l/D = 2.5$ the peculiar flow pattern with the repetition of the growth and the decay of the separation bubble is also obtained by the computation and the plate shock and the vortex are found to influence to one another according to such mechanism.

Acknowledgments

We would like to thank Dr. A. Wiedermann (Senior Research Engineer, Takasago R&D Center, Mitsubishi Heavy Industries, LTD) for the various comments and advice given to us in the present study and Mr. T. Nakamura (Graduate Student, Tokyo Denki University) for giving the shadowgraphs presented in this paper. Also, we thank Mr. S. Kitamura, Mr. K. Nakano (Graduate Students, Tokyo Denki University), and Mr. T. Abe (Undergraduate Student, Tokyo Denki University) for their help.

References

Hirsch, C., 1988, *Numerical Computation of Internal and External Flows,* Vol. 2, Wiley, pp. 536–556.

Jameson, A., 1985, "A Nonoscillatory Shock Capturing Scheme Using Flux Limited Dissipation," *Lectures in Applied Mathematics,* Vol. 22, pp. 345–370.

Kashimura, H., and Yasunobu, T., 1991, "Visualization of Self Induced Flow Oscillation in an Underexpanded Sonic Jet," *Journal of the Visualization Society of Japan,* Vol. 11, No. 2, pp. 31–34 (in Japanese).

Kliegel, J. R., and Levine, J. N., 1969, "Transonic Flow in Small Throat Radius of Curvature Nozzle," *AIAA Journal,* Vol. 7, No. 7, pp. 1375–1378.

Powell, A., 1994, "The Sound-producing Oscillations of Round Underexpanded Jets Impinging on Normal Plates," *Journal of Acoustical Society of America,* Vol. 83(2), pp. 515–533.

Sakakibara, Y., and Iwamoto, J., 1993, "Underexpanded Jet Impingement on a Flat Plate," *Conference Proceedings of Pacific International Conference on Aerospace Science and Technology,* Vol. III, pp. 1306–1312.

Tamura, S., and Iwamoto, J., 1994, "Study on the Noise Generated from Underexpanded Free and Impinging Jet," *Transactions of The Japan Society of Mechanical Engineers,* Vol. 60, No. 579, pp. 1–7 (in Japanese).

Wiedermann, A., and Iwamoto, J., 1994, "A multigrid TVD-type Scheme for Computing Inviscid and Viscous Flows," *International Journal of Computers & Fluids,* Vol. 23, No. 5, pp. 711–735.

Yee, H. C., 1987, "Construction of Explicit and Implicit Symmetric TVD Schemes and Their Applications," *Journal of Computational Physics,* Vol. 68, pp. 151–179.

Yee, H. C., and Harten, A., 1987, "Implicit TVD-schemes for hyperbolic conservation laws in curvilinear coordinates," *AIAA Journal,* Vol. 25, No. 2, pp. 266–274.

Thickness Variation of a Liquid Sheet Formed by Two Impinging Jets Using Holographic Interferometry

Y.-B. Shen
Graduate Student,
Mechanical Engineering Department,
University of Illinois at Chicago,
842 W. Taylor Street,
Chicago IL 60607

D. Poulikakos
Professor,
Institute of Energy Technology,
Laboratory of Thermodynamics in
Emerging Technologies, Swiss
Federal Institute of Technology (ETH),
Zurich 8032, Switzerland.
Fellow ASME

In the work presented in this paper a real time holographic interferometry technique is developed to measure instantaneously and nonintrusively the thickness distribution of a liquid sheet formed by the impingement of two liquid jets. The experimental results are compared with earlier largely unverified analytical predictions. It is shown that the assumption that the sheet thickness is inversely proportional to the radial distance from the impingement point is in principle good. The dependence of the theoretically obtained proportionality constant on the azimuthal angle, however, while exhibiting the same trend it also shows some quantitative differences. Reasons are given in the context of the work. In addition, a weak effect of the jet velocity on the proportionality constant is found to exist. In the theories no such effect was modeled. Finally, comparisons between theoretical and experimental isothickness contours show differences. Overall, there appears to be a justification for improved theoretical studies including effects such as that of gravitation.

1 Introduction

The atomization of liquids into gaseous surroundings has important applications exemplified by fuel injection and combustion, agriculture, food processing, pharmaceutics, materials manufacturing, and the chemical industry.

Because of its simplicity and effectiveness, impinging jet atomization is widely used in mixing processes and liquid propellant rocket engines. Its fundamental operating mechanism is schematically described in Fig. 1. Two coplanar jets are injected from two separate holes and impinge one upon the other at an impingement angle 2θ. At low impingement velocities they form a liquid sheet that is normal to the plane of the two jets. V_j is the jet velocity, and φ is the azimuthal angle on the plane of the spreading sheet.

With increasing jet velocity, the sheet in Fig. 1 undergoes the following regimes (Heidmann, 1957): closed rim (where the droplets are generated tangentially at the rim) periodic drop rim, open rim and, finally, fully developed regime (where the droplet generation starts practically at the impingement point). In practical rocket applications, the impinging jet atomizers operate in the fully developed regime. However, jet impingement at low velocity (closed rim regime) is relevant to the improving of our understanding of the relevant breakup mechanisms. Previous studies of impinging jet atomization can generally be classified into categories according to the above mentioned spray regimes. The present work focuses on low velocity impingement where a liquid sheet exists. For this reason as well as for brevity only representative earlier studies related to low speed impingement will be reviewed.

Taylor (1960) first studied the collision of two identical jets at an oblique angle in the low velocity range. In the study, Taylor applied laminar jets created by a pair of sharp-edge orifices of 2.27 mm in diameter to form impinging jet sprays at the close rim regime. The jet velocity was 3.63 m/s and the jet impingement angle 120 degrees. The Reynolds number of the jets is 6670, the Weber number is 330, and the Froude number is 727 (based on the jet diameter with a contraction coefficient of 0.66). He found that the impingement forms a liquid sheet whose ultimate shape is defined by the axisymmetric cardioid waves generated at the impaction of two jets. A liquid collection method was used in his study to estimate the edge thickness of the sheet formed by two low speed laminar jets colliding at an angle between 60 to 120 degrees. Taylor's measurements showed that the thickness of the sheet, h, is inversely proportional to the radius, r, which was measured from the impingement point. The relationship was expressed as

$$hr = K(\varphi, \theta) \tag{1}$$

where K is a constant that is independent of the jet velocity but dependent on the impingement angle 2θ and the azimuthal angle φ of the spreading sheet as defined in Fig. 1.

Hasson and Peck (1964) analyzed theoretically the thickness distribution of the sheet formed by two impinging jets. Their analysis (based on inviscid flow theory) assumed that the cross section of the jet in a plane parallel to the sheet is an ellipse, and mass and momentum are conserved between an angular element in the ellipse and the corresponding element in the liquid sheet. They concluded that the constant K is given by the following expression:

$$K = hr = \frac{R^2 \sin^3 \theta}{(1 - \cos \varphi \cos \theta)^2} \tag{2}$$

where R is the radius of the impinging jets.

Ibrahim and Przekwas (1991) obtained semi-empirical/theoretical expressions for the thickness and the shape of the liquid sheet at low Weber numbers (We < 500). They adopted the expression for the initial sheet thickness obtained by Naber and Reitz (1988) in their study of engine spray/wall impingement. This expression reads

$$h_i = \left[\frac{\beta R \sin \theta}{e^{\beta} - 1}\right] e^{\beta(1-\phi/\pi)} \tag{3}$$

where β is the constant determined from mass and momentum conservation. The thickness at any position, r, is expressed as

---

Contributed by the Fluids Engineering Division for publication in the JOURNAL OF FLUIDS ENGINEERING. Manuscript received by the Fluids Engineering Division July 2, 1997; revised manuscript received April 21, 1998. Associate Technical Editor: J. K. Eaton.

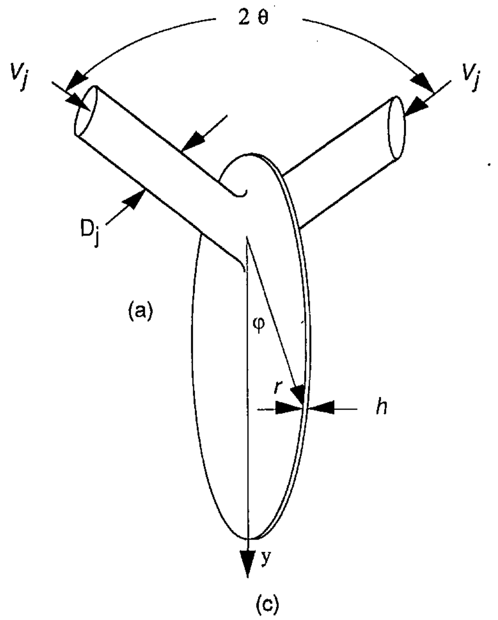

Fig. 1 Schematic of a liquid sheet formed by two impinging jets

$$h = \frac{R/\sin\theta}{r} h_i \tag{4}$$

From Eqs. (3) and (4), Ibrahim and Przekwas (1991) proposed that the thickness constant K is given by the following expression

$$K = hr = (R/\sin\theta)h_i = (R/\sin\theta)\left[\frac{\beta R \sin\theta}{e^{\beta} - 1}\right] e^{\beta(1-\phi/\pi)} \tag{5}$$

To predict the shape of the liquid sheet, they used Taylor's expression (1960) for the thickness at the edge of the sheet. Taylor showed that the form of cardioid waves which can remain at rest to form the edge of the liquid sheet is described by

$$h_e = \frac{2\sigma}{\rho_L U^2 \sin^2 \psi} \tag{6}$$

where ψ is the angle between the wave front and the radius vector and U is the sheet velocity. They developed an expression for ψ satisfying all boundary conditions in the form

$$\psi = \left(\frac{\pi}{2}\right) e^{\ln(2\theta/\pi)(1-\phi/\pi)} \tag{7}$$

The shape of the liquid sheet can be predicted by calculating the radial distance r_e between the edge of the sheet and the point of impact from Eq. (4) utilizing Eqs. (3), (6), and (7).

$$r_e = \frac{R}{\sin\theta} \frac{h_i}{h_e} \tag{8}$$

Both Hasson et al. (1964) and Ibrahim et al. (1991) compared their predictions with Taylor's experimental results and showed favorable agreements. Different coefficients of contraction were applied in their comparisons in order to estimate the jet radius based on the orifice dimension in Taylor's experiment. Hasson et al. (1964) applied a coefficient of contraction of 0.72, while Ibrahim et al. (1991) applied 0.64.

Kang et al. (1995) conducted experiments of water impinging jet sprays with 1.5 mm diameter jets in the velocity range of 1.5–3.5 m/s in order to verify the shape predictions of a spreading sheet. Good agreement was found between the experimental results of the shape of the rim of the liquid sheet and the theoretical prediction of Ibrahim and Przekwas (1991).

Ryan et al. (1995) studied experimentally the atomization characteristics of sheets formed by both laminar and turbulent impinging jets with jet Weber numbers range between 350 to 6600 and Reynolds numbers between 2800 to 26,000. At low jet velocities, the results were compared with theories in terms of sheet breakup length, droplet size and sheet shape. They noted the similarities of the shape between the experiments and the prediction by Ibrahim and Przekwas (1991).

In the work presented in this paper a real time holographic interferometry technique is developed to measure instantaneously and non-intrusively the thickness distribution of a liquid sheet formed by the impingement of two liquid jets. The experimental results are compared with earlier largely unverified analytical predictions.

2 Experimental Setup and Methodology

The impinging jet apparatus of Kang et al. (1995) was used to create the liquid sheet in this study as well. To this end only a brief summary of the apparatus is presented herein. Two precision glass tubes with a 1.53 mm inner diameter and a length to diameter ratio of 100 are used as the impinging-jet injectors and produce fully developed velocity profiles at their exit (jet orifice). The impingement angle was set to 120 degrees in this study. The pre-impingement length was set to 10 mm. The two impinging jets were adjusted precisely to assure that their axes were located in the same plane and the liquid sheet generated was perpendicular to the impinging jet plane and symmetric. The experimental apparatus allows for all needed fine adjustments (Kang et al., 1995).

A 59 percent by weight mixture of glycerine in water was chosen as the test fluid ($\mu = 10.25 \times 10^{-3}$ Ns/m^2, $\sigma = 68.7 \times 10^{-3}$ N/m and $\rho = 1136$ Kg/m^3). This mixture is very easy to produce and allows the easy formation of a liquid sheets. There is nothing unique about this solution and one can use a host of mixtures and pure liquids as working fluids. The mixture was stored in a liquid tank and pressurized by nitrogen gas to 0.68 Mpa (100 psi). Due to the pressurization, the liquid flowed from the storage tank to the injectors through a flowmeter (Cole-Parmer Instrument 32043-46). Subsequently, the flow was evenly divided between the two injectors by adjusting control valves located in each path. The injection velocity of the jets was determined with a flow meter.

The impinging jet apparatus was positioned in the optical path of the real-time holographic interferometry system mounted on a vibration-isolated optical bench as shown in Fig. 2. A laser beam emitted from a 20 mW He-Ne laser was first split into the reference and object beams by a cubic beamsplitter. The

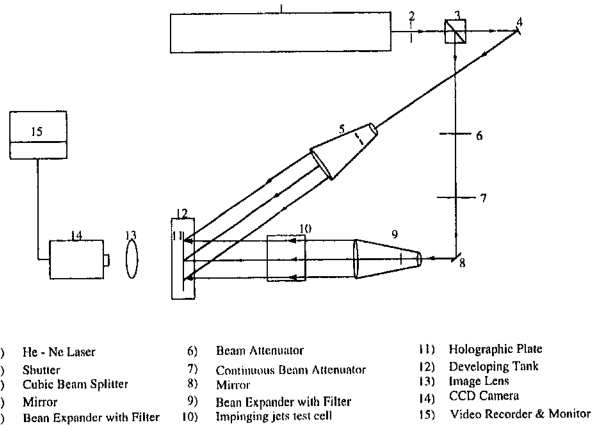

Fig. 2 Real time holographic interferometry system

reference beam was filtered, expanded and collimated to a uniform 50 mm diameter plane beam that illuminated the holographic plate with an incident angle of 40 degrees. The object beam was first attenuated by the variable beam splitter (Newport 50G00AV1) and then filtered and expanded to a 50 mm diameter plane beam. The object beam passed perpendicularly through the plane where the impinging jet sheet was formed. Both the object and reference beams are intercepted by the holographic plate, which was installed in the holder contained inside a real time developing tank (Newport Liquid Gate/Film plate holder/Processor) filled with water. This setup allowed for in-situ film development after fabricating a hologram.

To begin the experiment, one hologram was first fabricated under the condition that no liquid sheet was present. The holographic plate was then illuminated by the same reference beam used in the recording process and the recorded image was thus reconstructed. Next, the valve that controlled the flow of the impinging jets was opened and the liquid sheet was formed. The spreading sheet was continuously illuminated by the object beam as shown in the Fig. 2. As a result, the image of the spreading sheet was formed in the same location as the first image reconstructed by the reference beam. These two images were different in that in the second image the thin and transparent liquid sheet was present in the optical path.

Because of this change, optical interferometric fringes, which were formed from the interference between the real image and the earlier reconstructed image, appeared on the spreading sheet. A CCD camera and a video recording system were used to record these events in real time. The images of the liquid sheet containing the interferometric fringes were transferred to a Macintosh Quadra 800 computer equipped with Image Analyst (Automatrix Inc., 1992) software for image processing.

To calibrate the magnification rate of the system, a transparent precision ruler was placed in the plane where the spreading liquid sheet was formed. The image of the calibration ruler was then recorded. By measuring the image size, the actual magnification rate of the optical system was determined.

Interferometric Fringe Interpretation. According to holographic interferometric theory (Vest, 1979), at a location (r_0, φ_0) in the liquid sheet, the relationship between the refractive index n, the sheet thickness h_0, and the interferometric fringe can be expressed as:

$$h_0 \cdot dn = N_0 \cdot \lambda \tag{9}$$

where h_0 is the sheet thickness at the location of the fringe, dn is the difference of refractive indices between the glycerol solution (working fluid) and air, N_0 is the count number (order) of the fringe and λ is the wavelength of the He-Ne laser. Equation (9) shows that the interferometric fringes are generated in locations where the change of the optical path $h_0 \cdot dn$ is an integer multiple of the wavelength of the light source. The thickness difference between two locations "0" and "1" is

$$(h_1 - h_0) = \frac{(N_1 - N_0) \cdot \lambda}{dn} \tag{10}$$

Therefore, the sheet thickness difference between two locations can be determined directly from the experiments by counting the interferometric fringes under the condition that the refractive index of the liquid and the wavelength of the laser are known.

The refractive index of the water glycerol (59 percent weight percent) solution at room temperature was measured by an Abbe refractometer and was found to equal 1.399975 ± 0.000025. The refractive index of air is known to be 1.0 (Vest, 1979). In addition, the wavelength of the He-Ne laser is 632.8 nm.

Figure 3 shows an example of the detailed measurement procedure. First, an azimuthal angle coordinate grid was superimposed on the interferometric image at 10 degree intervals starting from the impingement point. Next, along each azimuthal angle, the first detectable fringe near the impingement point was chosen as the reference fringe. The location of the reference fringe depended on the azimuthal angle but it was within the range of 6 to 15 mm from the impingement point. Starting from the reference fringe, the number and the radius of the interferometric fringes up to a desired location were measured and the thickness obtained from Eq. (10).

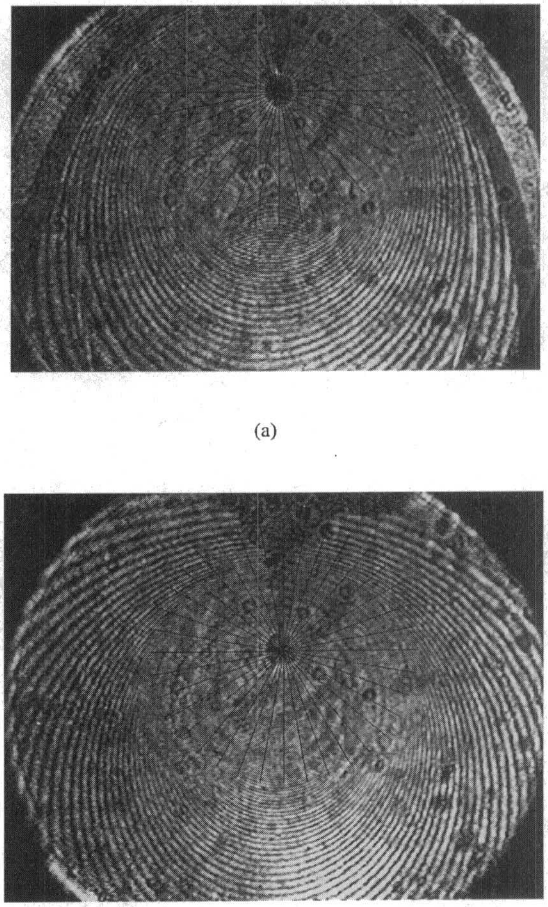
(a)

(b)

Fig. 3 Representative interferometric patterns on the spreading sheets formed by the impinging jets. The jet diameter is 1.33 mm, and the impingement angle = 120 deg: (*a*) jet velocity = 2.1 m/s, (*b*) jet velocity = 3.0 m/s.

3 Results and Discussion

At first, the experimental results aimed at testing the commonly used relation that the sheet thickness is inversely proportional to the radius with the proportionality constant $K(\varphi, \theta)$ independent of the jet velocity, Eqs. (1) and (2). Equation (2) can be rearranged in terms of the difference in thickness between two points

$$K = (h_2 - h_1)/(1/r_2 - 1/r_1) \tag{11}$$

In the experiment, the ratio of $(h_2 - h_1)/(1/r_2 - 1/r_1)$ was measured at different radial and angular positions on the sheet and the results are shown in Fig. 4. The jets have a Reynolds number of 354, Weber number of 126 and Froude number of 441. Clearly, at a fixed azimuthal angle, the ratio of $(h_2 - h_1)/(1/r_2 - 1/r_1)$ is a constant within acceptable accuracy and it is independent of the radial position. This constant has the largest value at an azimuthal angle of zero degrees and it decreases with an increase in the azimuthal angle. The relationship between Δh and $(1/r_0 - 1/r_i)$ is further illustrated in Fig. 5.

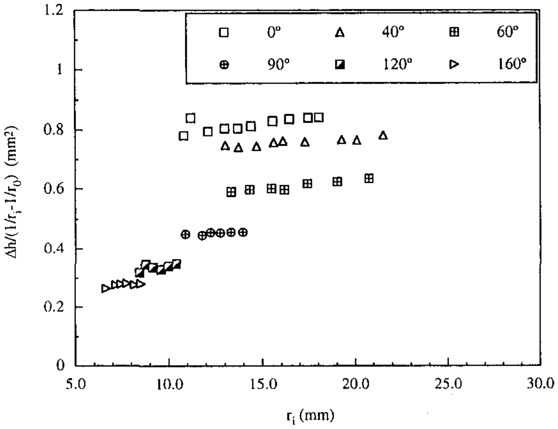

Fig. 4 *Dh*/(1/*ri* − 1/*r*0)) at various azimuthal angles and radius. The conditions of the experiment are: jet diameter 1.33 mm, jet velocity 2.4 m/s, and impingement angle 120 deg. Uncertainty 2%

The experimental results show that the thickness difference Δh is linearly proportional to $(1/r_0 - 1/r_i)$. From the results presented in Figs. 4 and 5, it is verified experimentally that for the spreading sheet generated by the impingement of two identical oblique jets, the ratio of Δh to $(1/r_0 - 1/r_i)$ can indeed be approximated as a constant at each fixed azimuthal angle as analytically shown by Hasson and Peck (1964).

The effect of jet velocity on the dimensionless thickness constant was also investigated in Fig. 6 for the jet velocity range from 2.1 to 3.0 m/s. The respective Reynolds number range is from 309 to 442, Weber number range from 100 to 192 and the Froude number range from 338 to 690. The sheet thickness constants were obtained from the average ratios of $\Delta h/(1/r_0 - 1/r_i)$ at different locations along each azimuthal angle. The thickness constant K was nondimensionalized with respect to the jet radius R^2. In the present study, the coefficient of contraction was determined experimentally to be 0.75. The results indicate that the sheet thickness constants do not change markedly as the jet velocity increases from 2.0 to 3.0 m/s. This underpins the independence of the thickness constant K from the jet velocity, to acceptable accuracy. However, there appears to be some velocity effect.

The experimental results of thickness constant are further compared with the results of previous studies. Figure 7 shows that the theoretical analysis of both Hasson and Peck (1964) and Ibrahim and Przekwas (1991) correctly predicted the trend of the sheet thickness constants as a function of the azimuthal angle. The analytical constants were obtained from Eq. (2) for Hasson and Peck's (1964) analysis and Eqs. (3) to (5) for Ibrahim and Przekwas's (1991) prediction. To plot Taylor's experimental results, the jet diameter was estimated by using a coefficient of contraction of 0.64 and an orifice diameter of 2.27 mm. The theoretical predictions agreed acceptably with Taylor's experimental results. The present measurements show the same trend but a weaker dependence of the dimensionless thickness constant on the azimuthal angle. A speculative explanation is that our experimental conditions differ from the idealized conditions of the theoretical studies. An additional discussion follows Fig. 8.

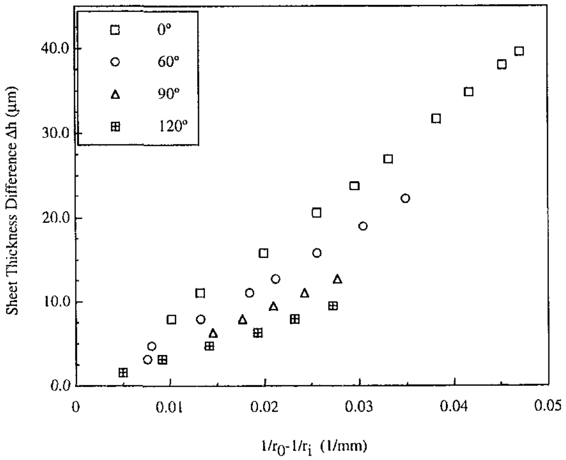

Fig. 5 Sheet thickness difference versus difference of the inverse radius at various azimuthal angles. The conditions of the experiments are: jet diameter 1.33 mm, jet velocity 2.4 m/s and impingement angle 120 deg. Uncertainty 2%

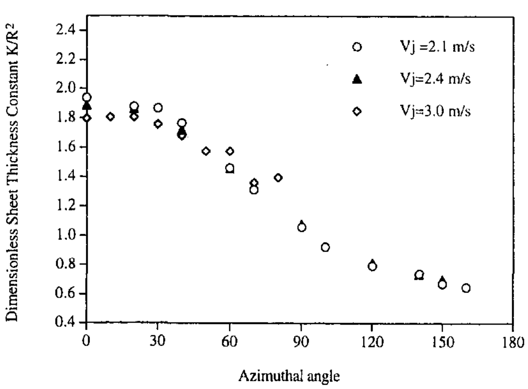

Fig. 6 Dimensionless sheet thickness constants at different velocities versus azimuthal angle. Jet diameter 1.33 mm and impingement angle 120 deg. Uncertainty 5%

Figure 8 compares the theoretical iso-thickness contours of the spreading sheet predicted by Hasson and Peck (1964) and Ibrahim and Przekwas (1991) with the experimental measurements. The contour of the present experiments was obtained directly by tracing one of the interferometric fringes, which physically represented the locations that have a certain thickness on the sheet. It was earlier in this section experimentally verified that the thickness at a certain point on the spreading sheet is inversely proportional to the corresponding radius from the impingement point at a specific azimuthal angle. Therefore, it is now possible to calculate the thickness of the spreading sheet at a contour from the experimental results with he help of Eq. (1). For the experimentally obtained isothickness contour plotted in Fig. 8, for example, the radial distance at 60 deg azimuthal

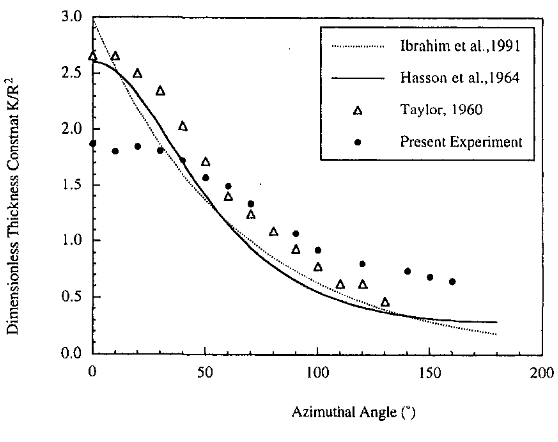

Fig. 7 Comparison of the measured thickness constants with previous studies. Uncertainty 8%

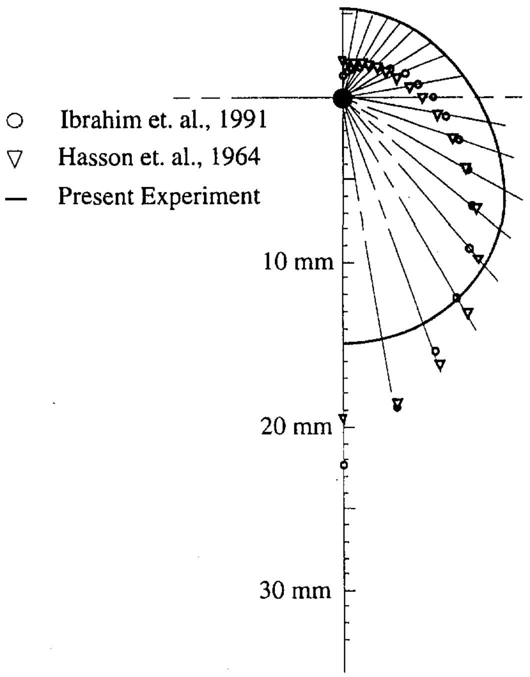

Fig. 8 Comparison of the experimental iso-thickness contour with existing analytical results at the location of the sheet thickness of 0.06 mm. Uncertainty 8%

angle was 11.36 mm and the dimensionless thickness constant was found to be 1.50 (Fig. 6). The sheet thickness was calculated from Eq. (1) and was found to be 0.06 mm. The theoretical contours corresponding to the thickness of 0.06 mm (for example) can be obtained from Eqs. (1) through (5).

The results in Fig. 8 show that for azimuthal angles greater than 40 deg, the predicted radius corresponding to a thickness of 0.06 mm is smaller than the experimentally obtained. On the other hand, at azimuthal angles of less than 40 deg, the predicted radius is significantly larger than the experimental radius. Gravitational effects may have contributed to the discrepancy between experiment and theory. In present experiment, the impinging jet sheet is formed in the plane parallel to the direction of gravitational acceleration. Gravity is one of the forces that affect the formation of the liquid sheet at low velocity. In the theory the gravatational effects were not considered. In Taylor's experiment, gravity is perpendicular to the impinging sheet and did not affect the formation of the sheet. It is worth noting that the Froude number based on the jet diameter and velocity of the experiments in Fig. 8 is $\mathrm{Fr} = V^2/(Dg) = 450$. This value implies that inertia is prevalent over gravity in the spreading process but does not totally exclude gravitational effects. As illustrated in Fig. 8, in the upstream region where the gravity tends to retard the movement, the liquid is likely to accumulate. The sheet thickness required more distance that theoretically predicted to reduce down to 0.06 mm. On the other hand, in the downstream region of the sheet where the gravity aids the spreading of the liquid sheet, the measurements showed that the liquid sheet required less distance than predicted to reach a thickness of 0.06 mm.

4 Uncertainty Estimation

There are two major sources of errors that contributed to the measurement uncertainty. The first was the measurement of the reflective index of the test liquid; the second source was the measurement of the distance r from the impingement point to the interferometric fringes in the image processing.

With reference to the former, the refractive index of the test fluid was measured by the Abbe refractometer (AGOTA type 3T) and was found to be 1.399975 ± 0.000025. Therefore, the relative measurement uncertainty was determined to be 0.04 percent. Also noted is the difference between the refractometer light source (sodium light source, $\lambda = 589.3$ nm) and the experiment (He-Ne laser, $\lambda = 623.8$ nm). The error introduced by the wavelength difference was estimated at 0.1 percent. Hence, the total uncertainty of refractive index measurement is the square root of the sum of the squares of each of the individual errors, which leads to the total error of 0.2 percent.

The uncertainty of distance measurements includes two sources. First, the magnification rate of the imaging system was calibrated by a transparent precision ruler with a 10 mm mark. The image of the mark was measured and the uncertainty was determined to be ±0.05 mm over 10 mm length, which is a 0.5 percent uncertainty. Second, in the measurement of the distance from the impingement point to the position of fringe of interest, there is an average of 0.1 mm uncertainty in locating the impingement point. This counts to an average of 0.7 percent of uncertainty to an average radial distance of 15 mm. Accounting these two error sources, the uncertainty of the distance measurement in the experiment is estimated to about 1.0 percent.

The length measurement also caused the uncertainty of determining the diameter of the jets. Measurements showed the jet diameter at the exit of the glass tubes is 1.33 mm. Consideing the uncertainty of ±0.05 mm in measurements, the relative error of the measured jet diameter is estimated to be 3 percent.

Other uncertainties of in the experiment include the determination of jet velocity and impingement angle. The jet velocity was determined by a calibrated flow meter (Cole-Parmer Instruments 32043-46). The uncertainty is about 0.1 m/s in the velocity range investigated. The impingement angle was set by two precision rotating plates with 1 degree resolution. The uncertainty is ±1 degree for half of the impingement angle (θ).

Counting all these error sources, the uncertainties of various measurements can be evaluated. In determining the relative thickness at two locations of the spreading sheet, only the uncertainty of refractive index was involved. Therefore, the error of relative thickness measurements is 0.2 percent. In determining the dimensional thickness constant $[dh/(1/r_0 - 1/r_1)]$, as in Figs. 4 and 5, and accounting for the additional uncertainty in the radial distance measurements, the total uncertainty adds up to be 1.5 percent. In Fig. 6, showing the dimensionless thickness constant $[dh/(1/r_0 - 1/r_1)]/R^2$ the uncertainty of the jet radius needs to be accounted. The result is approximately 5%.

The uncertainty of jet velocity measurements did not affect the above results. Neither did the error of the impingement angle. However, the uncertainty of impingement angle affects the calculation of the analytical thickness constants. At 1 degree uncertainty for half of the impingement angle (θ), the maximum uncertainty between the dimensionless thickness constant in Hasson and Peck (1964) and in the present experiment is 5 percent and between Ibrahim and Przekwas (1991) and the present experiment 3 percent.

Considering all the uncertainties of the measurements in Figs. 7 and 8, in which the comparison between the present work and previous predictions are made, the overall uncertainty is about 8 percent.

5 Conclusions

In this paper an experimental study was presented on the determination of the thickness distribution in a liquid sheet formed by two impinging jets. It was shown that utilizing real time holographic interferometry the thickness distribution of the sheet can be accurately obtained. The experimental results were utilized to test existing theories. It was shown that the assumption that the sheet thickness is inversely proportional to the radial distance from the impingement point is in principle good. The dependence of the theoretically obtained proportionality constant on the azimuthal angle, however, while exhibiting the same trend it also showed quantitative differences. Reasons were discussed in the previous section. In addition, a weak effect of the jet velocity on the proportionality constant was found to exist. In the theories no such effect was accounted for. Finally, comparisons between theoretical and experimental isothickness contours showed differences. Overall, there appears to be a justification for improved theoretical studies including effects such as that of gravitation.

Acknowledgment

The work reported in this paper was supported by AFOSR grant no. 95-1-0323.

References

Hasson, D., and Peck, R. E., 1964, "Thickness Distribution in a Sheet Formed by Impinging Jets," *AIChE Journal,* Vol. 10, pp. 752–754.

Heidmann, M. F., Priem, R. J., and Humphrey, J. C., 1957, "A Study of Sprays Formed by Two Impinging Jets," NASA TN-3835.

Ibrahim, E. A., and Przekwas, A. J., 1991, "Impinging Jet Atomization," *Physics of Fluids A,* Vol. 3, pp. 2981–2987.

Kang, B. S., Shen, Y. B., and Poulikakos, D., 1995, "Holographic Experiments in the Breakup Region of a Liquid Sheet Formed by Two Impinging Jets," *Atomization and Sprays,* Vol. 5, pp. 387–402.

Naber, J. D. and Reitz, R. D., 1988, "Modeling Engine Spray/Wall Impingement," SAE 880107.

Ryan, H. M., Anderson, W. E., Pal, S., and Santoro, R. J., 1995, "Atomization Characteristics of Impinging Liquid Jets," *J. Propulsion,* Vol. 11, pp. 135–145.

Taylor, G., 1960, "Formation of Thin Flat Sheets of Water," *Proceedings of Royal Society,* Series A, Vol. 259, pp. 1–16.

Vest, C. M., 1979, *Holographic Interferometry,* Wiley, NY.

Three-Dimensional Laminar Flow in a Rotating Multiple-Pass Square Channel With Sharp 180-Deg Turns

Jenn-Jiang Hwang
Professor.

Dong-Yuo Lai
Former Graduate Student.

Department of Mechanical Engineering,
Chung-Hua University, Hsinchu,
Taiwan 300

This paper presents a study of three-dimensional laminar flow in a rotating multiple-pass channel connected with 180-deg sharp bends. Fluid-flow fields are calculated for the entire domain via the Navier-Stokes equations through a finite-difference scheme. For closure of this elliptic-type problem, periodical fully developed conditions are employed between the entrance and exit of the two-pass module. Experiments for the stationary two-pass channel are conducted to validate the numerical procedure and data. The emphasis of the present prediction is on the rotating and through-flow rate effects on the fluid-flow and friction characteristics in the straight channel as well as in the turn region. It is found that the rotation-induced Coriolis force significantly raises the wall-friction losses in the straight channel. However, the head loss of the sharp turn is decreased with increasing rotation speed, because the flow discrepancy between the inlet and outlet of the sharp turn is less significant for the higher rotation speed. Moreover, overall pressure-drop penalty across the two-pass channel is found to be enhanced by the rotation speed as well as the duct through-flow rate.

Introduction

Studies of fluid flow in rotating ducts are significant for engineers because of their potential applications in industry. The internal cooling of turbine blade is a familiar example. In such a method, coolant air is routed through the passages within the airfoil to convectively remove the heat from the blade. The cooling passages in an actual turbine blade of a typical aero-engine are usually idealized as a multiple-pass serpentine-type channel. Inside a radially rotating multiple-pass channel, the flow structure is, of course, influenced by the presence of sharp 180-deg turns which results in flow separation and recirculation in the turnaround regions and flow redevelopment downstream of the 180-deg turns. In addition, the Coriolis force due to the radial rotation is nevertheless an important factor for affecting the flow behavior. Most early simulation works have only dealt with the flow either in a single-pass straight channel with radial rotation (Mori and Nakayama, 1968; Hart, 1971; Ito and Nanbu, 1972; Spezal and Thangam, 1983; Kheshgi and Scriven, 1985; Hwang and Jen, 1990; Iacovides and Launder, 1991) or in stationary multiple-pass channels connected by 180-deg turns (Metzger et al., 1984; Johnson and Launder, 1985. The numerical effort concerning the fluid-flow characteristics in rotating multiple-pass channels is rather sparse, which motivates the present study to predict the laminar fluid flow in a multiple-pass square channel with and without radial rotation. Although, the flow in the above-mentioned application would be turbulent in nature, the present work addresses the laminar case due to its relevancy to some practical applications (Hart, 1971; Spezal and Thangam, 1983) and fundamental interest.

The multiple-pass channel can be readily simulated as a straight entrance (radial-outward) channel followed by a number of periodic two-pass channels because the fully developed condition begins with the first turn of the multiple-pass channel (Yang et al., 1992). In the present work, emphasis is placed on a periodically fully developed situation, which assumes that the fluid-flow characteristics repeat themselves cyclically from the entrance of a two-pass channel to the next. The concepts and formulation previously used for periodic fully developed laminar flows in finned tubes (Patankar et al., 1977) are employed to resolve the problem described above. This treatment allows the calculation domain to be limited to the region across a two-pass channel (i.e., a combination of a radial-inward channel, an 180-deg sharp turn, and a radial-outward channel), and has an advantage of saving computation time and memory storage. Fluid flow in the entire domain is calculated from the three-dimensional Navier-Stokes equations through the well-known SIMPLER numerical scheme. The effects of flow Reynolds number and rotating speed on the fluid flow are examined. Typical developments of the cross flow along the streamwise direction of the two-pass channel are provided. The local friction factor distributions along the radial straight channel, as well as the pressure drops across the 180-deg sharp turn, are interesting and discussed. A comparison of the numerical results with the experimental data for stationary two-pass channels is also presented. It is believed that a substantial body of numerical data for detailed flow profiles, as done in this work, are highly valuable for checking and interpreting the experimental results of the heat transfer/performance in a rotating multiple-pass channel.

Theoretical Analysis

Governing Equations. Figure 1 shows a physical configuration of the periodic two-pass channel. The channel has a square cross section (1 *De* × 1 *De*) and 20 *De* in length. The main stream from the channel entrance turns 90-deg miter into the radial-inward straight channel, then turns sharply with a 180-deg bend to the radial-outward channel, and finally exits the channel through another 90-deg miter. This two-pass channel is to simulate the periodic region of a typical multiple-pass cooling passage of the turbine blade. The fluid-flow characteristics at the entrance and exit of this module should be identical via a

---

Contributed by the Fluids Engineering Division for publication in the JOURNAL OF FLUIDS ENGINEERING. Manuscript received by the Fluids Engineering Division March 12, 1997; revised manuscript received May 6, 1998. Associate Technical Editor: M. M. Sindir.

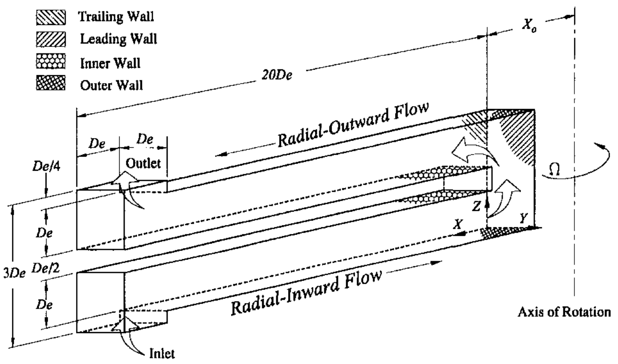

Fig. 1 Configuration, dimensions, and coordinate system of the present test model

suitable parameter reduction. The coordinate system and the denotation of each wall of the channel are shown in Fig. 1. The channel rotates at an angular speed Ω about the axis in parallel with the Z coordinate and normal to the main flow direction (X). To facilitate the analysis, the flow is assumed to be incompressible, steady, and constant property. In such a system, account is taken of the Coriolis and centrifugal forces, which appear as additional source terms in the momentum equations.

A comprehensive discussion of the periodically fully developed analysis is given by Patankar et al. (1977), and all details are not elaborated on here. Basically, all flow variables repeat cyclically over the length of the computational module. Thus,

$$\varphi(x, y, z) = \varphi(x, y, z + 3De) \qquad (1)$$

where φ could be any velocity component (u, v, w). As for the pressure, it can be decomposed as

$$p = -\beta z + p^* \qquad (2)$$

where p^* is cyclic (i.e., abides by above equation) while the term βz is related to the net pressure loss over the computation module. Practically, in a periodic analysis, the duct throughflow rate (i.e., Reynolds number) is not known a priori. Solution for a given flow rate number is achieved by iteratively updating the value of the global pressure gradient parameter, β, until convergence is reached. The corresponding dimensionless governing equations of continuity and momentum are:

$$\frac{\partial U}{\partial X} + \frac{\partial V}{\partial Y} + \frac{\partial W}{\partial Z} = 0 \qquad (3)$$

$$U\frac{\partial U}{\partial X} + V\frac{\partial U}{\partial Y} + W\frac{\partial U}{\partial Z} = -\frac{\partial P'}{\partial X} + \frac{1}{\mathrm{Re}}\left(\frac{\partial^2 U}{\partial X^2} + \frac{\partial^2 U}{\partial^1 Y^2} + \frac{\partial^2 U}{\partial^1 Z^2}\right)$$
$$+ 2\,\mathrm{Ro}V + (X + X_o)\,\mathrm{Ro}^2 \qquad (4)$$

$$U\frac{\partial V}{\partial X} + V\frac{\partial V}{\partial Y} + W\frac{\partial V}{\partial Z} = -\frac{\partial P'}{\partial Y}$$
$$+ \frac{1}{\mathrm{Re}}\left(\frac{\partial^2 V}{\partial X^2} + \frac{\partial^2 V}{\partial^1 Y^2} + \frac{\partial^2 V}{\partial^1 Z^2}\right) - 2\,\mathrm{Ro}U \qquad (5)$$

$$U\frac{\partial W}{\partial X} + V\frac{\partial W}{\partial Y} + W\frac{\partial W}{\partial Z} = -\frac{\partial P'}{\partial Z}$$
$$+ \frac{1}{\mathrm{Re}}\left(\frac{\partial^2 W}{\partial X^2} + \frac{\partial^2 W}{\partial^1 Y^2} + \frac{\partial^2 W}{\partial^1 Z^2}\right) - \beta' \qquad (6)$$

where $\mathrm{Re} = \overline{W}De/\nu$, $\mathrm{Ro} = \mathrm{Re}_\Omega/\mathrm{Re}$, and $\mathrm{Re}_\Omega = \Omega De^2/\nu$ The dimensionless variables chosen are:

$$X = x/De, \quad Y = y/De, \quad Z = z/De$$

$$U = u/\overline{W}, \quad V = v/\overline{W}, \quad W = w/\overline{W}$$

$$P' = p^*/(\rho\cdot\overline{W}^2), \quad \beta' = \beta\cdot De/(\rho\cdot\overline{W}^2)$$

The terms 2 RoV and 2 RoU on the right-hand side of Eqs. (4) and (5) are the Coriolis forces driving the flow in the Y and W directions, respectively. As already discussed, the fluid is assumed incompressible (density is assumed constant) and buoyancy effects caused by the density variety are neglected. Therefore, the centrifugal force, $(X + X_0)\,\mathrm{Ro}^2$ in Eq. (4), is uniform distributed on the YZ cross section and will be balanced with the hydrostatic pressure distribution. As a result, the pressure is interpreted as the modified pressure, and the centrifugal term appears only as an additional source term in the momentum equation, which does not affect the flow field. Once the centrifugal buoyancy is ignored, the distance from the axis of rotation to the two-pass module (X_o) is therefore irrelevant.

The no-slip conditions are applied on the channel wall, whereas periodic conditions are employed at the channel inlet

Nomenclature

C_p = local pressure coefficient, $(p - p_o)/(\rho\overline{W}^2/2)$
De = channel hydraulic diameter
f = friction factor, Eq. (7)
$\overline{f}$ = channel average friction factor, Eq. (9)
f_s = fully developed friction factor for the straight stationary channel
$f\mathrm{Re}$ = peripherally average friction parameter
K_t = loss coefficient of the sharp turn, $(p_{\mathrm{ent.}} - p_{\mathrm{ex.}})/(\rho\overline{W}^2/2)$
L_e = equivalent channel length
L_s = actual streamwise length of the two-pass channel
P, p = dimensionless and dimensional pressure
$p_{\mathrm{ent.}}$ = stagnation pressure at sharp-turn entrance, i.e., $p + \rho\overline{W}^2/2 + \rho x^2\Omega^2/2$
$p_{\mathrm{ex.}}$ = stagnation pressure at sharp-turn exit, i.e., $p + \rho\overline{W}^2/2 + \rho x^2\Omega^2/2$
p_o = wall static pressure at $X' = 0$
Re = Reynolds number, $\overline{W}\cdot De/\nu$
Re_Ω = Rotational Reynolds number, $\Omega\cdot De^2/\nu$
Ro = Rotation number, $\Omega\cdot De/\overline{W}$
U = dimensionless local velocity component in X direction
V = dimensionless local velocity component in Y direction
W = dimensionless local velocity component in Z direction
$\overline{W}$ = average velocity of the through-flow in the channel
u = local velocity component in X direction
v = local velocity component in Y direction
w = local velocity component in Z direction
X, Y, Z = dimensionless rectangular coordinate, see Fig. 1
X' = dimensionless axial coordinate, see Fig. 5
x, y, z = rectangular coordinate
β = pressure drop parameter, Eq. (2)
ν = kinematics viscosity
ρ = air density
τ_w = wall shear stress
Ω = angular velocity of rotation

Subscripts

s = smooth or stationary
w = wall

Superscripts

$*$ = periodicity
$-$ = average value

and outlet, i.e., $U(X, Y, Z) = U(X, Y, Z+3)$, $V(X, Y, Z) = V(X, Y, Z+3)$, and $W(X, Y, Z) = W(X, Y, Z+3)$

Flow Characteristics. After the velocity fields of the full-domain are obtained, the computations of the wall-averaged friction factors are practical interest. Following the conventional definitions, the wall-averaged friction factor along the radial-inward and -outward straight channels is written as

$$f = 2\bar{\tau}_w/(\rho \bar{W}^2) \qquad (7)$$

where $\bar{\tau}_w$ is the (spanwise) average wall shear stress and can be derived from the local derivative

$$f = 2(\partial \bar{W}/\partial n)_w/\mathrm{Re} \qquad (8)$$

The parameters for the present study are flow Reynolds numbers, Re = 300 to 2000, and the rotation number, Ro = 0 to 0.5. The channel aspect ratio is fixed at one.

Computational Details. The control-volume-based finite difference method described by Patankar (1977) is employed to solve the governing equations described above. The finite-differencing procedure ensures conservation of mass and momentum over each control volume. Velocity control volumes are staggered with respect to the main control volumes, and coupling of the pressure and velocity fields is treated via the SIMPLER (Patankar, 1980) pressure correction algorithm. In order to reduce numerical diffusion resulting from the existence of large cross-flow gradients and obliquity of the flow to the grid lines, the smooth hybrid central/skew upstream difference scheme (SCSUDS) is used for the diffusion and convective terms (Hwang and Lai, 1998). The set of the differential equations over the entire region of interest is solved by obtaining new values for any desired variables, taking into account the latest known estimated values of the variable from the neighboring nodes. One iteration process is complete when, in line-by-line technique, all lines in a direction have been accounted for. Because of the large variations in the source terms, under-relaxation is necessary for the dependent variables and the source terms to achieve convergence (Van Doormaal and Raithby, 1984). Line inversion iteration with typical under-relaxation values of 0.5 for the velocity terms and 0.7 for the pressure correction term are incorporated to the facilitated calculation. Solutions are considered converged at each test condition after two criteria are satisfied. First, the ratio of residual source (including mass and momentum) to the maximum flux across a control surface is required to be below 1.0×10^{-3}. Second, the iteration-to-iteration change is examined at every nodal location for all calculated values. However, to reduce the likelihood of false convergence related to small but persistent changes between successive iterations due to under-relaxation, examinations are implemented between iteration number I and I − 20. The change in computed value, when compared to the maximum value in the domain is required to be less than 5.0×10^{-6} for a solution to be considered converged. This comparison method do not eliminate the possibility of false convergence, but it did reduce it. Typically, the former criterion is to be later satisfied.

In this problem, most of the real action is found around the 180-deg turns and near all solid surfaces, and therefore, nodes are clustered in these regions in order to resolve the strong gradients present there. All computations are performed on 72 × 20 × 50 (X by Y by Z) grids in the present work. Additional runs for the coarser meshes, 60 × 15 × 40, and the finer meshes, 80 × 25 × 60, are taken for a check of grid independence. The parameters used to check the grid independence are the axial-velocity profile and the pressure-drop parameter. A comparison of the axial-velocity profiles at two selected axial stations (X = 1.0 and 10.0) in the radially outward channel among the three grid sizes at Ro = 0.1 and Re = 1000 is made in Fig. 2. The differences of U between two succeeding grids shown in this figure become small, confirming that the results are converging toward the grid-independence solution. Computations of the pressure-drop parameter (β) for the three grid sizes at Re = 300 and various Ro are given in Table 1. The results indicate the maximum change in β is less than 2.6 percent between the solutions of 72 × 20 × 50, and 80 × 25 × 60 grids. These changes are so small that the accuracy of the solutions on a 72 × 20 × 50 grids is deemed satisfactory. Numerical computation of the periodically fully developed flow is rendered difficult by the fact that no boundary information is available in the main flow direction along which the discritization coefficients are largest. Partly due to this reason, the code takes about 4000–5000 iterations for convergence. On Convex-3400, this translates to about 180 minutes of CPU time.

Experimental Apparatus

Figure 3 shows a schematic drawing of the experimental apparatus including a two-pass-channel flow system, the flow-visualization instrument and the static-pressure measurement system. Air from the laboratory is drawn into the two-pass channel through the flow straightener and a bell-like entrance by a 5 hp blower. The entire two-pass channel is made by Plexiglas®. It has a length of 80 cm and a 4-cm square cross section. The flow rate is measured by a flow meter situated at the downstream end of the test section. The smoke generated by the smoke generator is injected into the two-pass channel before the blower is turned on. The flow visualization is realized by a laser sheet which is constructed by passing a Helium-Neon laser beam (60 mW, Spectra Physics 120) through a rod of glass. A 35-mm single lens reflex camera is focused on the illuminated plane. Photographs of the flow are taken on Agfa film with a shutter speed of 1/1000 s. For the static-pressure measurement, as given in Fig. 3, 16 pressure taps are located along the centerline of the channel outer wall. Each tap is connected with the microdifferential transducer (Kyowa PDL-40B) with an accuracy up tp 0.1 percent. The pressure signal is subsequently amplified by a Kyowa WGA-200A amplifier and then is read for a digital readout. The flow visualization and the static-pressure measurement of the present study are based on the nonrotating condition.

Results and Discussion

Comparison With Experimental Results. Prior to discussing the predicted results in rotating channels, the validity of the present numerical procedure and the reliability of the present data are confirmed by comparing the prediction with

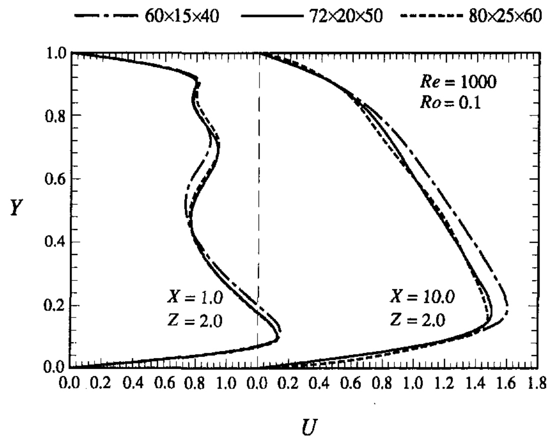

Fig. 2 Grid-independence test by using the axial-velocity profiles

Table 1 Grid-independence test by using the pressure-drop parameter

	Re	Ro	60 × 15 × 40	72 × 20 × 50	80 × 25 × 60	Relative error (%)		
		0.0	2.3041	2.1284	2.1022	9.48	1.24	—
β	300	0.1	2.7232	2.6216	2.5641	6.21	2.48	—
		0.5	3.1314	2.9539	2.8791	8.76	2.60	—

the experiments. Since rotating data are not available in the present work, the calculation is therefore compared with that in a stationary two-pass channel. Figures 4(a), (d), and (g) are the flow patterns of smoke-injection visualization on the YZ planes cutting across the axial stations $X = 0.25$ (i.e., in the sharp turn region), 1.0, and 2.0, respectively for Re = 300. The numerical results for the main-flow and cross-flow patterns at the corresponding stations are given in Figs. 4(b), (e) and (h), and (c), (f) and (h), respectively. The main flow is expressed by iso-speed contours of U, whereas the cross flow is represented by vectors composed by V and W components. At the station of the turn region ($X = 0.25$), both the experiment and the simulation reveal that two vortices exist around two upper concave corners of the channel. Moreover, the dense-smoke (bright) region in the visualized photo is coincident with the region of low main-flow velocity as given in Fig. 4(b). This is very reasonable because the region of the lower main-flow velocity could keep the smoke, whereas in the higher main-flow velocity region the smoke is easily blown off. Hence, the dark region is found in the central portion of the channel as given in Fig. 4(a).

At the outward station of straight channel entrance (i.e., the upper part of $X = 1.0$) as shown in Figs. 4(d) to (f), both the simulated and experimental results show two counter-rotating vortex-pairs circulating between inner and outer channel walls. The central vortex-pair, which circulates from the outer wall through the channel mid-plane and then returns back to the inner wall along the axes about $Y = 0.25$ and 0.75, is conjectured to be swirled by the rebounding flow from the outer wall. This rebounded flow is originated from the flow impingement on the outer wall by the separated flow from the channel divider. This phenomenon can be confirmed by the fact that main-flow has an M-shaped contour (please see the contour with the magnitude of $U = 0.95$) at this station, which implies that a large mount of the fluid close to the outer wall intends to flow toward the inner channel wall via channel center. The side-wall vortex pair may be due to the centrifugal inertia of the flow curvature around the turn region, which is obviously suppressed to the two side walls by the above-mentioned vortices. At the inward station of Fig. 4(d), the dense smoke region (bright) is again in coincident with the low main-flow velocity predicted (Fig. 4(e)).

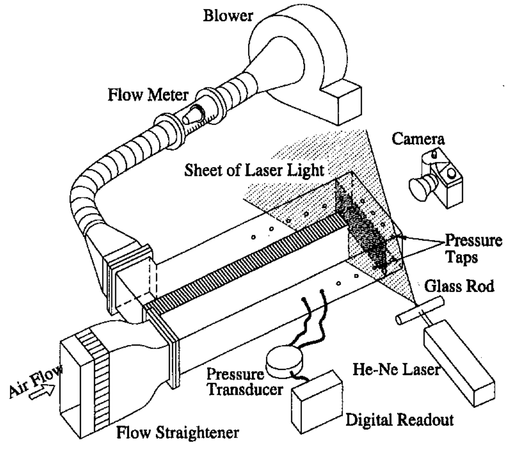

Fig. 3 Schematic drawing of the experimental apparatus

At the station $X = 2.0$ in the outward channel (upper half), the secondary flow patterns reveal that the side-wall vortex pair caused by the imbalance of the centrifugal inertia disappears, and the central-core vortex pair swirled by the rebounded flow still sustains near the inner wall. At the corresponding station of the inward channel, the high smoke density persists only near wall region due to the uniform distribution of the main-flow velocity in the core region.

Comparisons of the measured and predicted local pressure coefficients (C_p) on the outer wall along the channel centerline ($Y = 0.5$) for Re = 1000 and Ro = 0 are shown in Fig. 5. Here, the abscissa X' is the dimensionless streamwise coordinate originated from $X = 6.0$ on the outer wall of the radially inward channel. The circular symbols are the measured data while the dotted is the numerical results. As expected, notable pressure differences, both for the experiment and the prediction, exist between the entrance and exit of the sharp turn. In general, the computational local pressure coefficient distributions are in good agreement with the measured data. The satisfactory agreement in the above comparisons has confirmed that the present numerical procedure is adequate and the present numerical results are reliable.

Evolution of Secondary Flows. The evolutions of cross flows along the streamwise direction in the periodic two-pass channel on the rotating conditions of Ro = 0.1 and 0.5 are shown in Figs. 6(a) and (b), respectively. The flow Reynolds number is fixed at Re = 500. Carefully inspecting these figures, we can find that the cross-flow structures, regardless the flow direction, are largely alike between the radial-inward and radial-outward flow channels if the axial distance relative to the upstream sharp turn is the same. Therefore, the following discussion is focused on a common radial channel with outward flow. At the lower rotational speed (Ro = 0.1), due to the separated and swirled flows in the turnaround region, the entrance of the radial straight channel ($X = 1.0$) has a very strong cross-flow intensity and a rather complex cross-flow structure. Then, the Coriolis force starts acting the channel flow after the flow turn around the 180-deg bend. The interaction of these effects therefore results in the complex development of the vortices in the entrance region ($1.0 \leqq X \leqq 5.0$). As the fluid moves downstream, the entrance effects are gradually weaken, while the Coriolis force continuously acts on the channel flow, and has became the dominant of the flow field. It is obvious that the well-known counter-rotating vortex pair caused by Coriolis force, which circulates from the trailing (high-pressure) surface to the leading (low-pressure) surface along the side walls and returns back through the central core of the flow, starts appearing at the station of $X = 5.0$, and constitutes continuously downstream. Generally speaking, these counter-rotating vortices have fully established at the station $X = 12.5$ in which they are largely symmetric about the Y axis. Before encountering the 180-deg sharp turn, at the station of $X = 19.0$, the two vortices disappear totally. When the rotation number increases to Ro = 0.5, as given in Fig. 6(b), beside the primary vortex-pair, an additional vortex pair has obviously originated near the central portion of the high-pressure surface at about the station between $X = 10.0$, and 12.5.

Axial Velocity Profiles. The axial velocity profiles in the radial-outward flow channel along the centerline of $Z = 2.0$ at selections of $X = 2.0$ and 15.0 for Re = 500 are shown in Fig. 7. At the station of $X = 2.0$, the axial velocity profiles for the

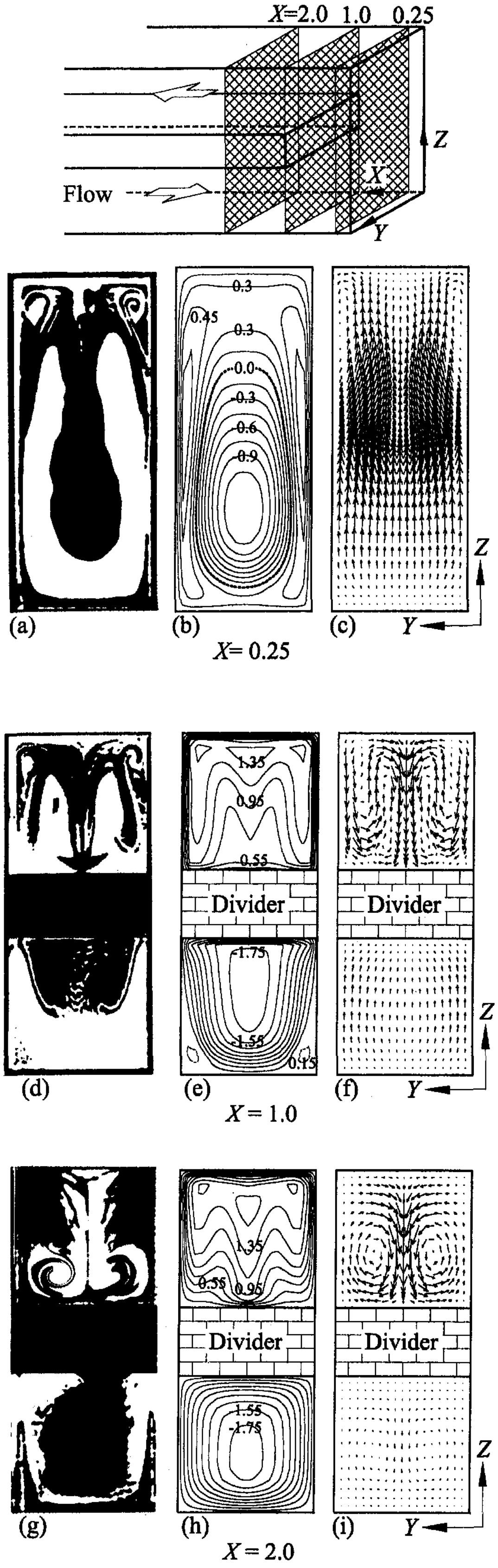

Fig. 4 Comparison of the numerical and experimental results for the stationary two-pass channel for Re = 300 (*a*) Smoke injection, *X* = 0.25, (*b*) axial-flow pattern (*U*), *X* = 0.25, Hwang and Lai (1998) (*c*) secondary-flow vectors (*V* by *W*), *X* = 0.25, Hwang and Lai (1998) (*d*) smoke injection, *X* = 1.0, (*e*) axial-flow pattern (*U*), *X* = 1.0, (*f*) secondary-flow vectors (*V* by *W*), *X* = 1.0, (*g*) smoke injection, *X* = 2.0, (*h*) axial-flow pattern (*U*), *X* = 2.0, (*i*) secondary-flow vectors (*V* by *W*), *X* = 0.25.

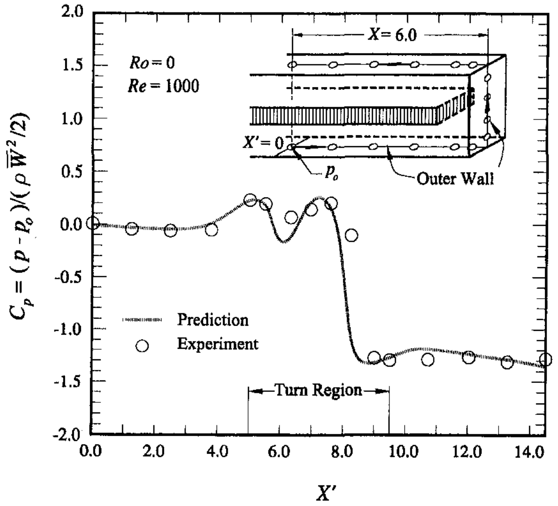

Fig. 5 Comparison of the local-pressure coefficient between the experimental and computational results at Re = 1000 and Ro = 0.1

stationary channel have two peaks values near the two channel walls due to the entrance effect of the 180-deg turn. In the rotating channels, the axial-velocity peak near the leading wall is significantly dismissed by the rotation speed and, clearly, the axial-velocity profile has been ruled by the Coriolis force for Ro = 0.5 at this station. This means that the entrance effect of the 180-deg sharp bend is relatively weaker in a higher rotating-speed channel. At the downstream station of $X = 15.0$, the axial velocities for the stationary channel, as well as the rotating channel, have been fully developed. At this station, the axial-velocity peak moves toward the trailing surface as Ro increases from 0 to 0.1 due to the enhancement of the primary vortex pair by the Coriolis force. When the rotation number further increases to Ro = 0.5, the peak value of the axial velocity obviously lays off and is deflected back toward the channel center. This is attributed to the presence of the secondary vortex pair near the high-pressure surface (Fig. 6).

Friction Factor Distribution Along the Radial Straight Channel. The friction losses in a rotating two-pass channel could be regarded as the sum of the major losses, due to the wall-friction effects in the radial straight channels, and the minor losses, due to 180-deg sharp-edge return bend. Here we consider the rotation effect on the major and minor losses, respectively, and subsequently, determine the effect of rotation on the total pressure-drop penalty in the entire two-pass channel.

Because of the large similarity of the fluid-flow mechanisms between the radial inward and outward flow channels, the friction factor in these two channels is, as expected, identical. Therefore only results of the radial—outward flow channel are presented and discussed. Figures 8 and 9, respectively, show the effects of the rotation number and Reynolds number on axial variations of $f \cdot \mathrm{Re}$, which is widely used to express the friction performance of the straight channels. The values taken on each channel wall are spanwise averages. The straight dashed line on each graph represents the well-known result of the fully developed laminar flow in a straight stationary channel, i.e., $f \cdot \mathrm{Re} = 14.2$.

As given in Fig. 8, the solid curves are the results in the stationary two-pass channel, which serve as a reference so that the effects of rotation may be examined by comparison. Except for the inner wall, the friction factors along the other three channel walls decrease monotonically along the axial direction, and approach the fully developed value. Along the inner wall the friction factor, however, begins with a local maximum, decreases steeply due to the flow reversal, then increases to a local maximum at about $X = 4.0$, and finally decreases downstream.

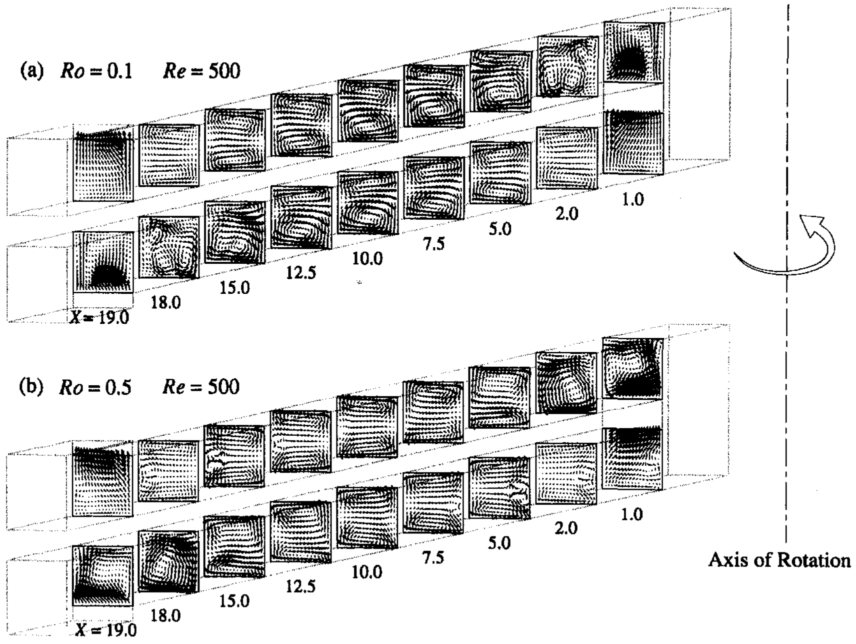

Fig. 6 Evolution of the cross flow (*V* by *W*) in the two-pass channel (*a*) Re = 500, Ro = 0.1, and (*b*) Re = 500, Ro = 0.5

The local maximum near $X = 4.0$ on the inner wall is attributed to the approach of the rebounded flow pushed back from the outer wall. As for the effect of rotation speed, the friction factor on the trailing wall is significantly larger than that on the stationary channel wall, and subsequently higher than that on the leading wall. A significant increase in $f\,\mathrm{Re}$ on the inner and outer walls due to the rotation is also found. It further shows that the friction factor is nearly independent on the rotation number for the leading wall, and is significantly intensified by the rotational speed on the trailing as well as the two side walls. Along the trailing surface, the variation of $f\,\mathrm{Re}$ with X for $\mathrm{Ro} \leq 0.2$ is monotonic and similar to that of nonrotating channel flow. The steep fall in $f\,\mathrm{Re}$ near the entrance region ceases earlier for the larger values of Ro due to the emergence and enhancement of the principal vortices caused by the Coriolis forces. In the case of the highest rotation number, i.e., $\mathrm{Ro} = 0.5$, the $f\,\mathrm{Re}$ curve on the trailing surface has two slight bumps near the regions of $X = 4.0$ and 11.0. The first bump is, of course, attributed to the initiation of the principal vortex pair, whereas the secondary vortex pair generated near the central high-pressure wall at about $X = 11.0$ (Fig. 6) arises the second one. As for the effect of the Reynolds number, as given in Fig. 9, the friction factor is enhanced by increasing the Reynolds number for the four walls of the radial straight channel.

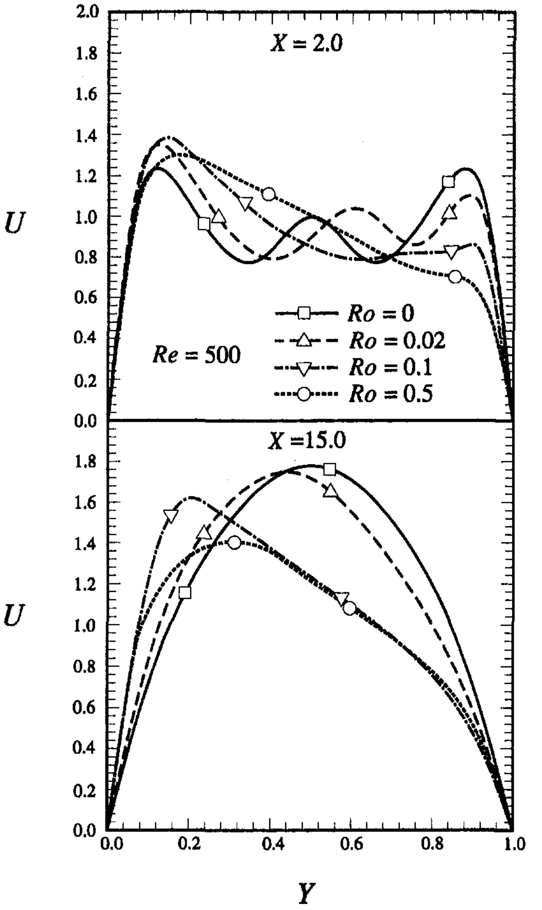

Fig. 7 Axial velocity profiles at the selected stations of *X* = 2.0, and 15.0 for the radial-outward flow channel

Pressure Drop of the Sharp Turn. In contrast to the wall-friction loss in radial straight channels, the pressure drop due to the sharp turn is commonly specified by the loss coefficient (or head loss), K_t, which is defined as $K_t = (p_{\mathrm{ent.}} - p_{\mathrm{ex.}})/(\rho \overline{W}^2/2)$, where $p_{\mathrm{ent.}}$ and $p_{\mathrm{ex.}}$ are the rotary stagnation pressure at the entrance and exit planes of the sharp turn, respectively. Figure 10 gives the rotational Reynolds number dependence of the loss coefficient of the sharp turn with various Reynolds numbers. The loss coefficient, as expected, decreases with increasing Reynolds number for both the stationary and rotating conditions. However, it is very surprising that at the same through-flow rate (Re) the loss coefficient for the rotating 180-deg turn is lower than that for the stationary one, and decreases with increasing the rotational speed. The reason may be explained as follows. In the stationary channel, the inlet conditions of the sharp turn should be fully developed with relatively uniform axial-velocity profiles and relatively small cross-flow intensities; while in the rotating channel, the flow has been largely disturbed by the rotation induced Coriolis force before entering the 180-deg turn. With the similar complexity of flow structure

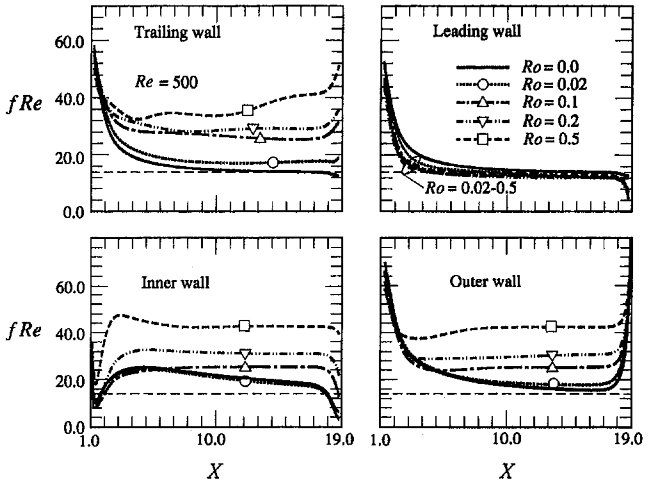

Fig. 8 Effect of the rotation number on the wall-averaged friction factor distributions along the radial-outward flow channel

at the sharp-turn outlet, the changes in the flow structure (including the axial and cross flows) between the inlet and outlet of the 180-deg sharp turn are relatively remarkable for the stationary channel as compared with those for the rotating channel, which is therefore the result of a higher pressure drop across the sharp turn.

Overall Pressure-Drop Penalty. In Eq. (2), β is introduced as the magnitude of the overall pressure gradient for a periodic two-pass channel. Therefore, the use of the value in Eq. (2) could lead to

$$\bar{f} \cdot \mathrm{Re} = 2\beta \cdot De^2/(\mu \bar{W}) \tag{9}$$

Figure 11 presents that variation $\bar{f} \cdot \mathrm{Re}$ with the rotational Reynolds number for various Reynolds number. It is seen that the stationary two-pass channel produces a greater friction loss than the fully developed flow through a single-pass channel of equal length (dashed line, $f_s\,\mathrm{Re} = 14.2$), which increases with the flow Reynolds number. The additional losses are mainly attributed to the separated flow around the turn as well as the swirling secondary flow that occurs because of the imbalance of the centrifugal inertia. The above effects is enhanced by the duct through-flow rate. When the two-pass channel is rotating, the secondary flow induced by the Coriolis force significantly enhances the wall-friction losses in the straight channel (Fig. 8). However, as given in Fig. 10, the pressure drop across the sharp-turn region is slightly decreased with increasing rotation speed. The combination of these two counteracting effects results in a slight increase in the overall pressure-drop penalty due to the increase of the rotation speed. The increased rate in $\bar{f} \cdot \mathrm{Re}$ due to rotation is slightly retarded by the duct through-flow rate. Note that the vertical coordinate on the right-hand side of this figure is the ratio of the equivalent length of the two-pass channel and the actual streamwise distance of this channel. It is seen that the equivalent length ratio increases with the flow Reynolds number as well as the rotational Reynolds number.

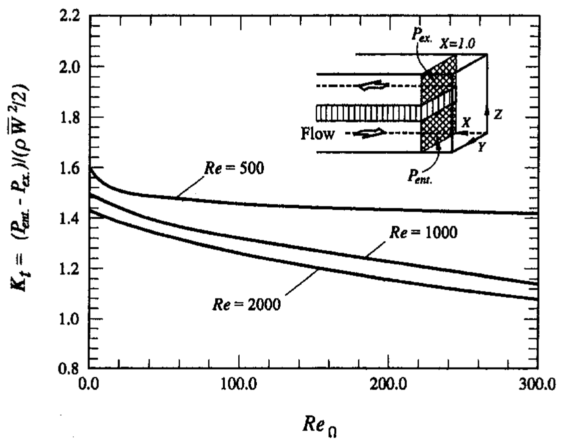

Fig. 10 Rotational Reynolds number dependence of loss coefficient in the 180-deg sharp turn for various Reynolds numbers

In general, a high value of $\bar{f} \cdot \mathrm{Re}$ represents a large pressure-drop penalty incurred in the two-pass channel. As far as thermal performance concern, if the resulting gain in heat transfer is not substantial, the large pressure drop should be regarded as unacceptable.

Concluding Remarks

The problem of three-dimensional laminar flow in a periodic two-pass channel with stationary and radially rotating conditions has been solved numerically. Owing to the presence of the 180-deg sharp turn, the numerical calculation of the present problem is elliptical in nature. Illustrations describing the flow-field characteristics are constructed for Re = 300–2000, and Ro = 0–0.5. Predictions of the flow pattern and wall-static-pressure distribution in the stationary two-pass channel are compared well with the experiments. The flow pattern changes along

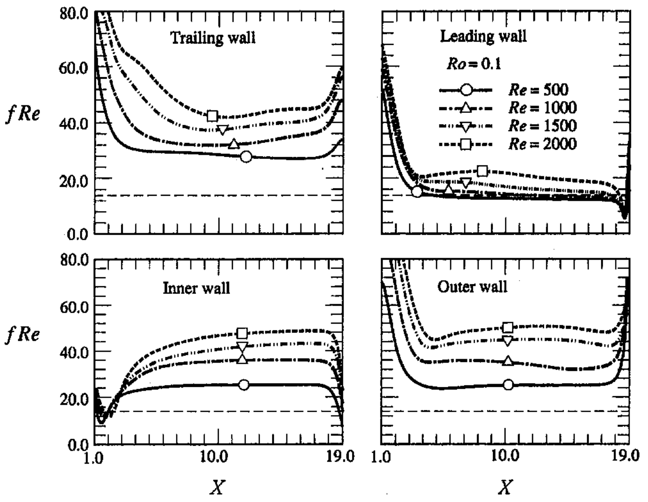

Fig. 9 Effect of the flow Reynolds number on the wall-averaged friction distributions along the radial-outward flow channel

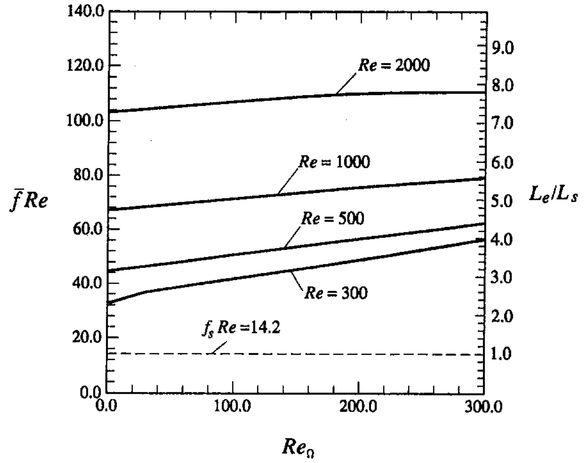

Fig. 11 Rotational Reynolds number dependence of total pressure drop across the two-pass channel for the various Reynolds numbers

the two-pass channel due to entrance effect of the 180-deg turn, including the flow separation as well as swirling flow due to the imbalance of centrifugal inertia caused by flow curvature, the effect rotational Coriolis force, and their interaction. In the radial straight channels, an increase in rotation number yields a significant increase in friction factor on the high-pressure as well as two-side walls, but slightly degrades the friction factor on the low-pressure wall. The Coriolis-force effect consequently raises the peripherally averaged friction factors of the radial straight channel. In the sharp turn region, however, the increase in the rotational Reynolds number causes a slight decrease in the loss coefficient (head loss) due to the less departure of the flow structure between the sharp-turn inlet and outlet for the higher rotational speed. The above counteracting effects cause a slight increase in the overall pressure-drop penalty in the two-pass channel due to the increase of rotation speed. Further efforts are needed to investigate the effect of the turbulence when the rotational speed and flow velocity are large.

Acknowledgments

Support for this work was provided by the Taiwan Power Company and the National Science Council of the Republic of China under contract No. NSC 87-TPC-E-216-002.

References

Hart, J. E., 1971, "Instability and Secondary Motion in Rotating Channel Flow," *Journal of Fluid Mechanics,* Vol. 45, pp. 337–395.

Hwang, G. J., and Jen, T. C., 1990, "Convective Heat Transfer in Rotating Isothermal Ducts," *International Journal Heat and Mass Transfer,* Vol. 33, pp. 1817–1828.

Hwang, J. J., and Lai, D. Y., 1998, "Three-Dimensional Mixed Convection in a Rotating Multiple-Pass Square Channel," *International Journal Heat and Mass Transfer,* Vol. 41, pp. 979–991.

Iacovides, H., and Launder, B. E., 1991, "Parametric and Numerical Study of Fully Developed Flow and Heat Transfer in a Rotating Rectangular Duct," ASME, *Journal of Turbomachinery,* Vol. 113, pp. 331–338.

Ito, H., and Nanbu, K., 1972, "Flow in Rotating Straight Pipes of Circular Cross-Section," ASME *Journal of Basic Eng.,* Vol. 94, pp. 261–270.

Johnson, R. W., and Launder, B. E., 1985, "Local Nusselt Number and Temperature Field in Turbulent Flow Through a Heated Square-Sectional U-Bend," *International Journal of Heat and Fluid Flow,* Vol. 6, pp. 171–180.

Kays, W., and Crawford, M., 1980, *Convective Heat and Mass Transfer,* McGraw-Hill, New York.

Kheshgi, H. S., and Scriven, L. E., 1985, "Viscous Flow Through a Rotating Square Channel," *Physics of Fluids,* Vol. 28, pp. 2968–1979.

Metzger, D. E., Plevich, C. W., and Fan, C. S., 1984, "Pressure Loss Though Sharp 180 Degree Turns in Smooth Rectangular Channels," ASME *Journal of Engineering for Gas Turbine and Power,* Vol. 106, pp. 667–681.

Mori, Y., and Nakayama, W., 1968, "Convection Heat transfer in Rotating Radial Circular Pipe (1st Report, Laminar Region)," *International Journal of Heat and Mass Transfer,* Vol. 11, pp. 1024–1040.

Patankar, S. V., Liou, L. H., and Sparrow, E. M., 1977, "Fully Developed Flow and Heat Transfer Ducts Having Periodic Variations of the Cross-Sectional Area," ASME, *Journal of Heat Transfer,* Vol. 99, pp. 180–186.

Patankar, S. V., 1980, *Numerical Heat Transfer and Fluid Flow,* Hemisphere, Washington, DC.

Spezal, C. G., and Thangam, S., 1983, "Numerical Study of Secondary Flow and Roll-Cell Instabilities in Rotating Channel Flow," *Journal of Fluid Mechanics,* Vol. 130, pp. 337–395.

Van Doormaal, J. P., and Raithby, G. D., 1992, "Enhancements of the SIMPLE Method for Predicting Incompressible Fluid Flows," *Numerical Heat Mass Transfer,* Part A, Vol. 7, pp. 147–163.

Yang, W. J., Zhang, N., and Chiou, J., 1992, "Local Heat Transfer in a Rotating Serpentine Flow Passage," ASME *Journal of Heat Transfer,* Vol. 114, pp. 354–361.

Methods to Set Up and Investigate Low Reynolds Number, Fully Developed Turbulent Plane Channel Flows

F. Durst
Professor and Head.

M. Fischer
Ph.D. Student.

J. Jovanović
Senior Research Scientist.

H. Kikura[1]
Postdoctoral Fellow.

Lehrstuhl für Strömungsmechanik,
Universität Erlangen-Nürnberg,
Cauerstr. 4, 91058 Erlangen, Germany

The tripping of fully developed turbulent plane channel flow was studied at low Reynolds number, yielding unique flow properties independent of the initial conditions. The LDA measuring technique was used to obtain reliable mean velocities, rms values of turbulent velocity fluctuations and skewness and flatness factors over the entire cross-section with emphasis on the near-wall region. The experimental results were compared with the data obtained from direct numerical simulations available in the literature. The analysis of the data indicates the important role of the upstream conditions on the flow development. It is shown that the fully developed turbulent state at low Reynolds number can be reached only by significant tripping of the flow at the inlet of the channel. Effects related to the finite size of the LDA measuring control volume and an inaccuracy in the estimation of the wall shear stress from near-wall velocity measurements are discussed in detail since these can yield systematic discrepancies between the measured and simulated results.

1 Introduction

Turbulence in a fully developed channel flow has been of great interest in modern fluid mechanics and numerous investigations have been carried out. Whereas in the past most of the investigations were carried out experimentally, in recent years an increasing number of papers have appeared that provide flow information based on numerical flow computations. In this respect the most recent publications of Kim et al. (1987), Kuroda et al. (1989), Gilbert and Kleiser (1991), Lyons et al. (1991), Antonia et al. (1992), and Kuroda et al. (1993) should be mentioned. The computational data of these authors correspond to relatively low Reynolds number flows, e.g., $R_{e_m} \simeq 3000-13800$ based on the bulk velocity ($\bar{U}_m$) and width (H) of the channel.

Considering the way in which the state of fully developed channel flow has been achieved in numerical fluid flow investigations, i.e., by imposing periodic inlet and outlet boundary conditions, raises questions regarding comparability of the numerically established turbulent flow field and the corresponding experimental fully developed channel flow. For example, there is firm experimental evidence which indicates that it is very difficult to achieve well-defined, fully developed turbulent flow independent of the initial conditions at low Reynolds numbers, $R_{e_m} < 10000$. This was first demonstrated by Nikuradse (1932), who used considerable size tripping plates at the entrance of the pipe in order to produce the fully developed flow state at low Reynolds numbers. Therefore, one can question whether the simulated flow properties at low Reynolds numbers are realistic enough to be directly compared with the experimentally measured data. This holds particularly for the higher order moments that describe the rare, intermittent events which affect the details of the probability density function.

For the above reason, it is desirable to perform verification measurements under well-controlled laboratory conditions and at approximately similar Reynolds numbers. By comparing the measured and simulated data, one can judge the capabilities of numerical techniques currently used in turbulence research to reproduce the experimental flow conditions. With this aim in mind, the authors have performed an extensive set of measurements in plane channel flow at low Reynolds numbers. In this paper, the emphasis is placed on the effects of the initial conditions on flow development and details of the measuring technique employed and signal interpretation, which can substantially influence the accuracy of the measured data.

2 Test Rig and LDA System

2.1 Channel Test Rig. To study low Reynolds number effects on fully developed plane channel flows, a water flow facility was set up which permitted mean velocities of up to 1.15 m/s to be obtained. Figure 1 shows schematically the test rig used for the present investigations. To drive the flow at a constant, pre-chosen flow rate, a total head tank was installed with a water head of approximately 6 m.

Experimental investigations were performed in the two-dimensional channel of dimensions $l \times b \times H = 1 \times 0.18 \times 0.01$ m. The channel test section was preceded by a rectangular contraction chamber (0.15×0.18 m). Upstream of the contraction, an 80 mm long honeycomb with 6 mm diameter cells was placed to improve flow uniformity. Downstream of the honeycomb, grids of 1 mm mesh size were installed to reduce the free-stream turbulence intensity. Two Plexiglas plates, spanning the whole length of the channel, were used as side-walls to allow optical access to the flow. The height of the channel was kept constant by using precise metal pieces between the base plates of the channel. As Fig. 2 indicates, the developing boundary layers were tripped by plates of variable heights l_t placed at the entrance of the channel. Addition of silicon carbide particles or milk was used for seeding the flow.

2.2 LDA Measuring System. For experimental investigations of near-wall turbulence we employed laser Doppler anemometry (LDA) in order to obtain reliable mean velocity and turbulence measurements. The LDA system consisted of a beam expander of expansion ratio 2.5 and a double Bragg cell unit

---

[1] Present address: Paul Scherrer Institut, CH-5232 Villigen PSI, Switzerland.

Contributed by the Fluids Engineering Division for publication in the JOURNAL OF FLUIDS ENGINEERING. Manuscript received by the Fluids Engineering Division May 14, 1997; revised manuscript received January 13, 1998. Associate Technical Editor: J. K. Eaton.

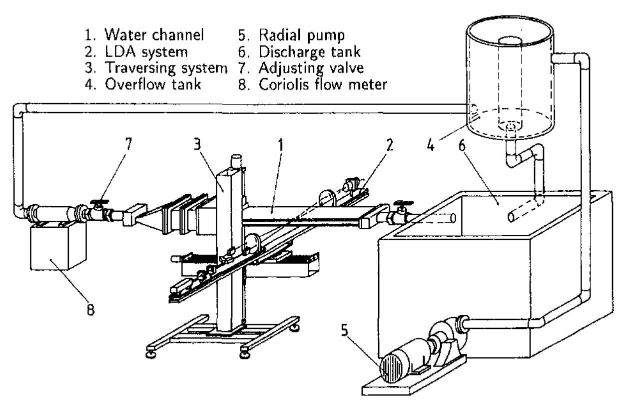

Fig. 1 Channel flow facility

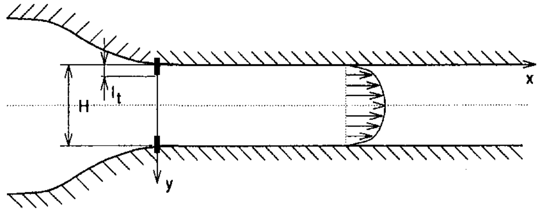

Fig. 2 Channel flow test section

together with an 8 mW He-Ne laser. A frequency shift of 0.5 MHz between the two Bragg cells was used. The focal length of the sending lens was 160 mm and the measuring control volume, based on the e^{-2} Gaussian intensity cut-off point, was about 80 μm in diameter and 520 μm in length. Light scattered in the forward direction was focused on a pin-hole of 75 μm diameter, which was located in front of an avalanche photodiode (APD).

The output signal of the APD was bandpass filtered between the frequency limits 0.3 and 2 MHz prior to processing the data. A TSI-1990 counter was employed for the measurement and it was operated in a single burst mode (with at least 32 cycles per burst) and a 1 percent comparison setting. The counter output was interfaced to a PC. The mean velocity and velocity fluctuations were computed using arrival time averaging to correct for velocity bias at the low data rates. Data rates of 5–100 Hz were typical, depending on the flow velocity. At every measuring point 20,000–40,000 samples were acquired to compute the mean velocity and turbulence properties. For the above-mentioned sample size, the relative statistical uncertainty in the measurements could be estimated to be ±0.2 percent for the mean velocity, ±1 percent for the turbulence intensity, and ±2 percent for the fourth-order moment.

3 Time Averaged Flow Measurements

When LDA measurements of time-averaged flow properties are carried out, it is the aim of the experiments to obtain local flow information directly comparable to the corresponding numerically predicted data. However, owing to the finite size of the LDA measuring control volume, local velocity information cannot be obtained directly. The measured turbulence properties show a dependence on the size of the measuring control volume and require the application of volume corrections, particularly for measurements near the channel walls. The spatial integration of LDA signals due to the finite size of the measuring control volume can be derived analytically to yield explicit relationships between measured mean quantities and true local flow properties. The procedure for correcting the LDA measurements is outlined in Section 3.1 and was applied at each measuring point in the flow.

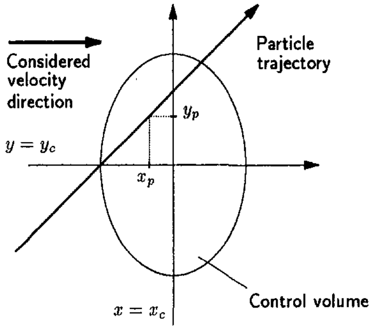

Fig. 3 Sketch of the LDA measuring control volume

The presentation of local flow quantities in fully developed plane channel flows in a general form requires the local wall shear velocity u_τ to be measured. Usually, u_τ is determined from the slope of the measured mean velocity profile in the viscous sublayer, assuming a linear velocity profile e.g.,

$$\tau_w = \mu\left(\frac{\partial \bar{U}}{\partial y}\right)_w, \quad u_\tau = \sqrt{\frac{\tau_w}{\rho}} \qquad (1)$$

However, the method based on the linear velocity assumption, as shown by Durst et al. (1996), has inherent problems since at low Reynolds numbers the velocity profile exhibits observable non-linearity near the wall. For this reason, estimates of u_τ using the linear slope technique are too low, yielding artificial shifts in the measured velocity data when scaled with respect to the wall variables. To overcome this difficulty, a novel method is introduced in Section 3.2 that allows accurate estimates of u_τ even when measurements cannot be taken down to the wall.

3.1 Influence of Effective Volume Size on Turbulence Measurements.

Several attempts to obtain the influence of the effective volume size of LDA systems on turbulence measurements have been described in the literature. Among the first publications in this field is the paper by Goldstein and Adrian (1971), followed by later work by Durst et al. (1992). In these papers the influence of the size of the LDA measuring volume on turbulence data was deduced from theoretical considerations, assuming that the detection of the instantaneous particle velocity is directly proportional to the distribution of the light intensity in the measuring control volume. Below we provide derivations for a seeded flow with particles of well-defined size and a measuring volume of elliptical shape.

Let us split the instantaneous velocity field $\underline{U}(t, \underline{x})$ into the mean velocity and instantaneous fluctuation:

$$\underline{U}(t, \underline{x}) = \underline{\bar{U}}(\underline{x}) + \underline{u}(\underline{x}, t) \qquad (2)$$

Owing to the small dimensions of the measuring control volume, we may expand the mean velocity and instantaneous fluctuation in a Taylor expansion:

$$\underline{\bar{U}}(\underline{x}) = \underline{\bar{U}}(\underline{x}_c) + \sum_{n=1}^{\infty} \frac{1}{n!}\left(\frac{\partial \underline{\bar{U}}(\underline{x})}{\partial x_i^n}\right)_{\underline{x}=\underline{x}_c} x_i^n \qquad (3)$$

$$\underline{u}(\underline{x}, t) = \underline{u}(\underline{x}_c, t) + \sum_{n=1}^{\infty} \frac{1}{n!}\left(\frac{\partial \underline{u}(\underline{x}, t)}{\partial x_i^n}\right)_{\underline{x}=\underline{x}_c} x_i^n \qquad (4)$$

At this point it is necessary to explain the general practice of LDA measurement. With systems of finite size measuring volume, velocity information obtained from one point in the flow corresponds to the average information taken over a trajectory through the control volume (see Fig. 3).

To simplify further analysis, we shall assume that the mean quantities $\bar{A}_{c_v}$ vary only in the y-direction and that these can be represented as averages over the time and LDA control volume (V)

$$\bar{A}_{c_v} = \lim_{T\to\infty} \frac{1}{T} \int_0^T \left\{ \frac{1}{V} \int_{c_v} A(\underline{x}, t) d\underline{x} \right\} dt \tag{5}$$

Using Eqs. (2)–(5) with $A(t, \underline{x}) = \underline{U}(t, \underline{x})$ and exchanging the time and space averaging in Eq. (5), we obtain an expression for the correction of mean velocity measurements:

$$\bar{U}_{c_v} = \bar{U}(y_c) + \frac{d_y^2}{32} \left(\frac{d^2\bar{U}}{dy^2} \right)_{\underline{x}=\underline{x}_c} + h.o.t. \tag{6}$$

Utilizing Eq. (2), the measured instantaneous fluctuation $u_{c_v}(t) = \underline{U}(t, \underline{x}) - \bar{U}_{c_v}$ across the LDA control volume can be written as

$$u_{c_v}(\underline{x}, t) = \sum_{n=1}^{\infty} \frac{1}{n!} \left(\frac{d\bar{U}(y)}{dy^n} \right)_{y=y_c} y^n + \underline{u}(\underline{x}_c, t) + \sum_{n=1}^{\infty} \frac{1}{n!} \left(\frac{\partial \underline{u}(x_c, y, z, t)}{\partial x^n_{i=2,3}} \right)_{\underline{x}=\underline{x}_c} x^n_{i=2,3} - \frac{d_y^2}{32} \left(\frac{d^2\bar{U}}{dy^2} \right)_{\underline{x}=\underline{x}_c} - h.o.t. \tag{7}$$

Using Eq. (5) with $A(\underline{x}, t) = u^2_{c_v}(\underline{x}, t)$ and truncating the expansion for $u_{c_v}(\underline{x}, t)$ to the second-order derivatives yields the correction equation for intensity measurements:

$$\overline{u^2_{c_v}} = \overline{u^2(\underline{x}_c)} + \frac{d_y^2}{16} \left(\frac{d\bar{U}}{dy} \right)^2_{\underline{x}=\underline{x}_c} + \frac{d_y^2}{32} \left(\frac{d^2\overline{u^2}}{dy^2} \right)_{\underline{x}=\underline{x}_c} + h.o.t. \tag{8}$$

where d_y is the minor axis of the control volume which is ellipsoidal in shape.

In an analogous way, we may obtain expressions for correcting the measured third- and fourth-order moments

$$\overline{u^3_{c_v}} = \overline{u^3(\underline{x}_c)} + \frac{1}{8} \left(\frac{d_y}{2} \right)^2 \left(\frac{d^2\overline{u^3}}{dy^2} \right)_{\underline{x}=\underline{x}_c} + \frac{3}{4} \left(\frac{d_y}{2} \right)^2 \left(\frac{d\bar{U}}{dy} \right)_{\underline{x}=\underline{x}_c} \left(\frac{d\overline{u^2}}{dy} \right)_{\underline{x}=\underline{x}_c} + h.o.t. \tag{9}$$

$$\overline{u^4_{c_v}} = \overline{u^4(\underline{x}_c)} + \frac{3}{2} \left(\frac{d_y}{2} \right)^2 \left(\frac{d\bar{U}}{dy} \right)^2_{\underline{x}=\underline{x}_c} \overline{u^2(\underline{x}_c)} + \left(\frac{d_y}{2} \right)^2 \left(\frac{d\overline{u^3}}{dy} \right)_{\underline{x}=\underline{x}_c} \left(\frac{d\bar{U}}{dy} \right)_{\underline{x}=\underline{x}_c} + \frac{1}{8} \left(\frac{d_y}{2} \right)^2 \left(\frac{d^2\overline{u^4}}{dy^2} \right)_{\underline{x}=\underline{x}_c} + h.o.t. \tag{10}$$

The analysis presented in Section 4.3 shows that the contribution of the mean velocity gradient to the volume corrections overweights the terms involving the gradients of the velocity correlations. For this reason, the terms containing variations of the mean velocity profile $\bar{U}$ were only retained when the above-derived corrections were applied to the measured data.

In the above considerations, we assumed that the effective LDA measuring volume is only dependent on the arrangement of the transmitting optical setup. However, simple experiments indicate that the volume size also depends on the employed receiving optics, photo-detector, signal processing electronics, scattering particles, etc.

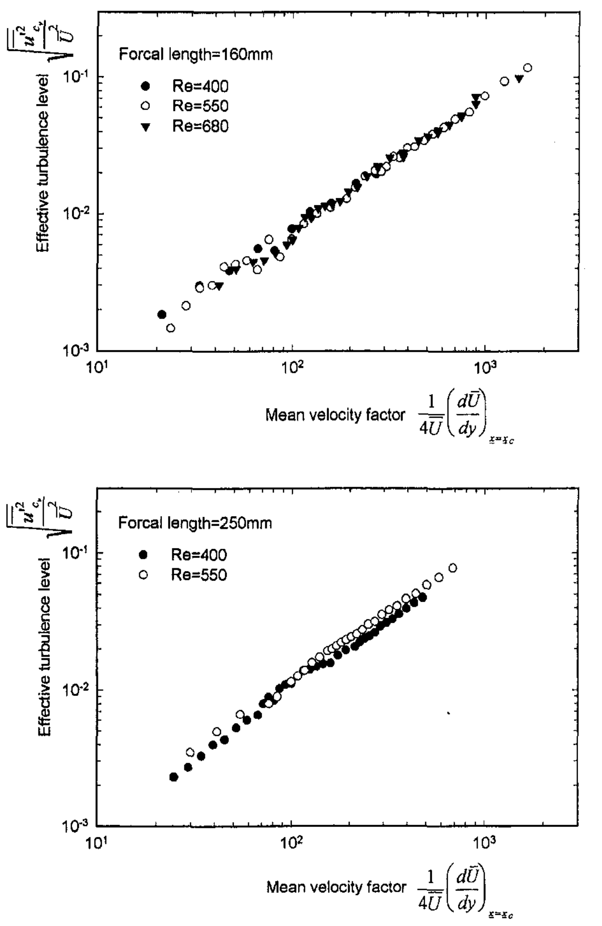

Fig. 4 Measurements of the length scale d_y in a laminar channel flow: (*a*) $f = 160$ mm, $d_y = 73.8$ μm ($R_e = 400$), $d_y = 72.5$ μm ($R_e = 550$), $d_y = 71.6$ μm ($R_e = 680$); (*b*) $f = 250$ mm, $d_y = 108$ μm ($R_e = 400$), $d_y = 117$ μm ($R_e = 500$). The estimated uncertainty in the measurements is ±4 percent.

For evaluation of the turbulent measurements near the wall, it is necessary to justify the particular choice of a length scale d_y. This can be achieved by performing measurements in a laminar flow with the same optical and electronic settings. Since in a laminar flow there are no turbulent fluctuations, Eqs. (8)–(10) may be written in the following form:

$$\overline{u^2_{c_v}} = \frac{d_y^2}{16} \left(\frac{d\bar{U}}{dy} \right)^2_{\underline{x}=\underline{x}_c} + h.o.t. \tag{11}$$

$$\overline{u^3_{c_v}} = \frac{3}{32} \left(\frac{d_y}{2} \right)^4 \left(\frac{d\bar{U}}{dy} \right)^2_{\underline{x}=\underline{x}_c} \left(\frac{d^2\bar{U}}{dy^2} \right)_{\underline{x}=\underline{x}_c} + h.o.t. \tag{12}$$

$$\overline{u^4_{c_v}} = \frac{1}{8} \left(\frac{d_y}{2} \right)^4 \left(\frac{d\bar{U}}{dy} \right)^4_{\underline{x}=\underline{x}_c} + h.o.t. \tag{13}$$

It can be seen that corrections given by Eqs. (12) and (13) consist entirely of the higher order terms.

From Eq. (11), it follows that the measured effective turbulence level is related to the mean velocity and its gradient as

$$\sqrt{\frac{\overline{u^2_{c_v}}}{\bar{U}^2}} = d_y \frac{1}{4\bar{U}} \left(\frac{d\bar{U}}{dy} \right)_{\underline{x}=\underline{x}_c} \tag{14}$$

Hence, it is possible to determine d_y in laminar channel flows from the slope of the straight line obtained by plotting $(\overline{u^2_{c_v}}/\bar{U}^2)^{1/2}$ against $(4\bar{U})^{-1}(d\bar{U}/dy)$. This is shown in Fig. 4

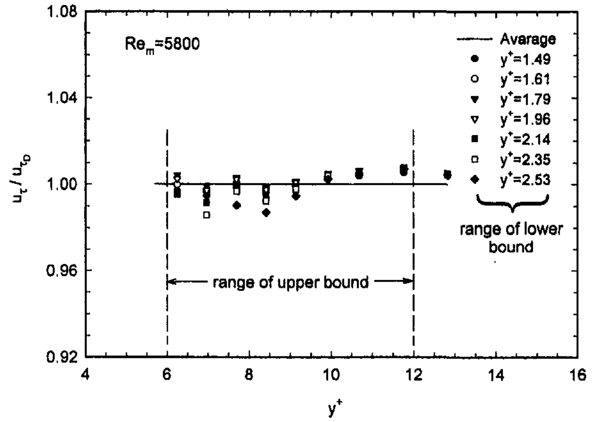

Fig. 5 Evaluation of the friction velocity using polynomial fitting method. The estimated uncertainty in the measurements is ±1 percent.

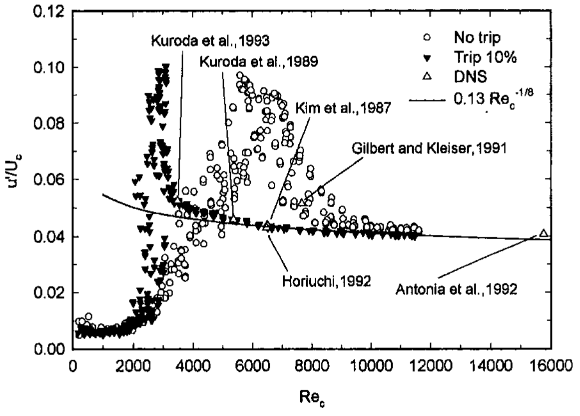

Fig. 6 Transition between the laminar and turbulent states at the channel centreline. The estimated statistical uncertainty in the measurements is ±1 percent.

for two different focal lengths of the transmitting optics and different Reynolds numbers. The results from Fig. 4 are in good agreement with the calculated dimensions of the measuring control volume based on the e^{-2} light intensity cut-off point but for different electronic settings this might change.

3.2 Determination of Wall Shear Stress. The wall shear velocity was evaluated using the polynomial fit of the mean velocity data in the viscous sublayer and the lower part of the buffer region:

$$\bar{U} = \frac{u_\tau^2}{\nu}(y - y_0) - \frac{1}{h\nu} u_\tau^2 (y - y_0)^2 + D(y - y_0)^4 + E(y - y_0)^5 \quad (15)$$

where D and E are constants. Such a fit was proposed by Durst et al. (1996) to obtain accurate shear stress information, even for higher Reynolds number flow. From the suggested fitting procedure, the friction velocity u_τ and the wall-distance correction y_0 were obtained simultaneously.

Figure 5 shows the estimated friction velocity normalized with that deduced from Dean's (1978) empirical correlation for the skin-friction coefficient. Various symbols indicate the lower bound of each fitted data range and the abscissa is the upper bound of the fitted range. The horizontal line represents the average friction velocity over all ranges considered. The method produced very consistent results for u_τ if the fitted data range was between $y^+ = 1-2$ for the lower bound and $y^+ = 6-12$ for the upper bound.

4 Experimental Results and Comparisons

4.1 Tripped Versus Nontripped Flow. Initial investigations were carried out to provide quantitative information on the details of the flow development into the fully developed state and to document how this changes with Reynolds number. Local measurements were performed at measuring points across the entire channel cross-section and at various measuring stations downstream of the tripping plates. These measurements verified that the flow reached its fully developed state close to the wall first and at the centreline last. Hence the state of fully developed turbulent, plane channel flow could be established most easily by local measurements along the centreline of the channel. Such measurements were performed for the "natural transition" of the flow from its laminar to its turbulent state and also for flow transition by applying different tripping levels.

Downstream from the tripping plates ($x/H = 80$), the centreline turbulence intensity is presented in Fig. 6 for a number of nontripped and a tripped flow cases. For data shown in this figure tripping was set by thin plates of 0.5 mm height. For Reynolds numbers $Re_{c} < 2000$ the flow remained laminar in character with about 0.7 percent turbulent intensity. For the nontripped case the increase in the Reynolds number was accompanied by a turbulent intensity increase which reaches a peak value of about 10 percent at $Re_{c} \approx 6000$. A further increase in Re_{c} was followed by slow decrease of the turbulent intensity which attained at $Re_{c} \approx 10{,}000-12{,}000$ the values typical for fully developed turbulent, plane channel flows. This set of experiments also revealed problems with obtaining the unique flow properties without tripping the flow. This is indicated by the large variations of the centreline turbulence intensity with Reynolds number obtained for repeated flow settings.

For a trip blockage ratio of 10 percent (defined as the ratio of the trip area to the cross-sectional area of the channel), transition from laminar to turbulent state is fairly rapid. Compared with the nontripped case, there is a considerable decrease in the Reynolds number at which the fully developed flow conditions are reached, $Re_{c} \approx 4000$. This result is in accord with the expectation that the trip enhances the turbulence and, in this way, reduces the length required for flow development. Comparison of the experimental with the corresponding numerical results clearly reveals the need to trip the flow. Only when tripping is applied is fully developed turbulent flow obtained at the downstream measuring location for low Reynolds numbers.

Figure 7 summarizes measurements of the centerline turbulence intensity carried out using the tripping plates of different heights. These results indicate that for the trip blockage ratios higher than 15 percent the flow characteristics remain indepen-

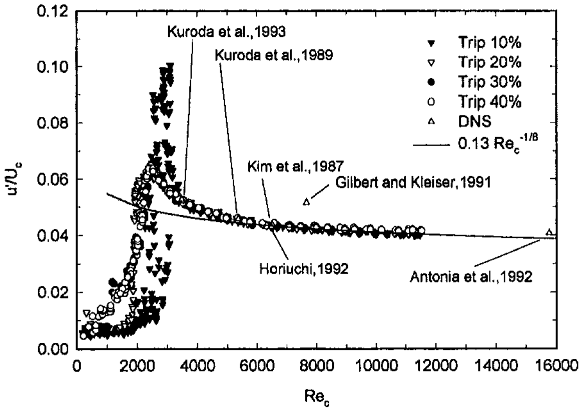

Fig. 7 Turbulence intensity at the channel centreline for different tripping levels. The statistical estimated uncertainty in the measurements is ±1 percent.

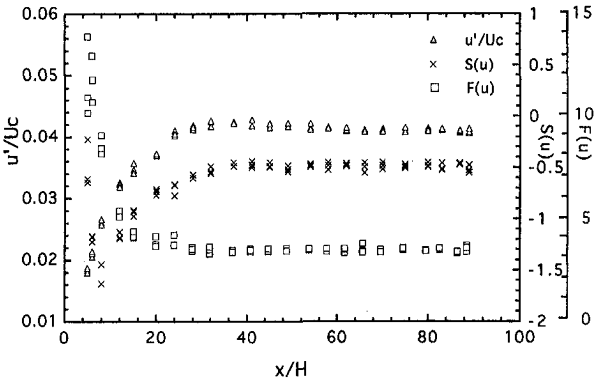

Fig. 8 Distribution of the turbulent intensity, skewness and flatness factors along the channel centreline. The estimated statistical uncertainty in the measurements is ±2 percent.

dent of the conditions at the channel entrance. This issue is especially important since it appears that only with appropriate tripping of the turbulence transition is it possible to achieve fully developed turbulent flow at low Reynolds numbers. These findings are in agreement with the results obtained by Nikuradse (1932), who also used tripping plates ($l_t/D = 0.2$) at the inlet of the pipe in order to promote turbulence and in this way to obtain fully developed turbulent flow at low Reynolds number, $R_{e_m} \simeq 3500$.

To document further the flow development measurements of the turbulent intensity, skewness and flatness factors were obtained along the channel centreline. The higher order moments are very sensitive indicators of the degree to which the flow is fully developed. Figure 8 shows the distributions of turbulence intensity, skewness and flatness factors measured along the channel centreline at $R_{e_m} = 10000$. These results clearly illustrate that the flow was fully developed at the nominal measuring station, i.e., for all distances from the inlet larger than 60 channel heights downstream. For this reason, all measurements were carried out at a streamwise station 71 channel heights downstream from the inlet. The measurements, which are reported here, correspond to low Reynolds numbers, $R_{e_m} =$ 2500, 3000, 4600, 5800, 6600, and 9800. The flow was tripped at the entrance of the channel with thin plates of 0.75 mm height giving a blockage ratio of 15 percent. Some typical parameters for each experiment are summarized in Table 1.

4.2 Mean Velocity Distributions. Figure 9 shows the mean velocity profiles as a function of the normalized distance y^+ from the wall, i.e., $u^+ = f(y^+)$:

$$\bar{U}^+ = \frac{\bar{U}}{u_\tau}; \quad y^+ = \frac{y u_\tau}{\nu}$$

To normalize the data, the friction velocity was used, which was determined from the proposed fitting method.

Mean velocity profiles exhibit universal behavior in the near-wall region and show a downward shift in the logarithmic region at low Reynolds numbers. This trend in the logarithmic region vanishes at $R_{e_m} > 5000$. Similar behavior was observed in the results of direct numerical simulations of turbulent channel flow that were summarized by Kasagi and Shikazono (1994). At $R_{e_m} = 5800$ the present experimental data are in very good agreement with the results of numerical simulations by Kim et al. (1987).

Table 1 Mean flow parameters.

U_c (m/s)	U_m (m/s)	U_c/U_m	Re_c	Re_m	Re_τ	$(C_f)_c$	$(C_f)_m$	u_τ(× cm/s)	$u_\tau/u_{\tau D}$	l_ν (mm)
0.301	0.250	1.203	3100	2500	87	0.00657	0.00952	1.727	0.9611	0.055
0.350	0.293	1.195	3500	3000	102	0.00668	0.00954	2.021	0.9810	0.048
0.536	0.459	1.166	5400	4600	149	0.00649	0.00885	3.051	1.0065	0.033
0.660	0.570	1.159	6700	5800	188	0.00626	0.00841	3.693	1.0006	0.027
0.762	0.658	1.158	7600	6600	209	0.00598	0.00802	4.167	0.9962	0.024
1.117	0.971	1.151	11300	9800	293	0.00542	0.00718	5.817	0.9910	0.017

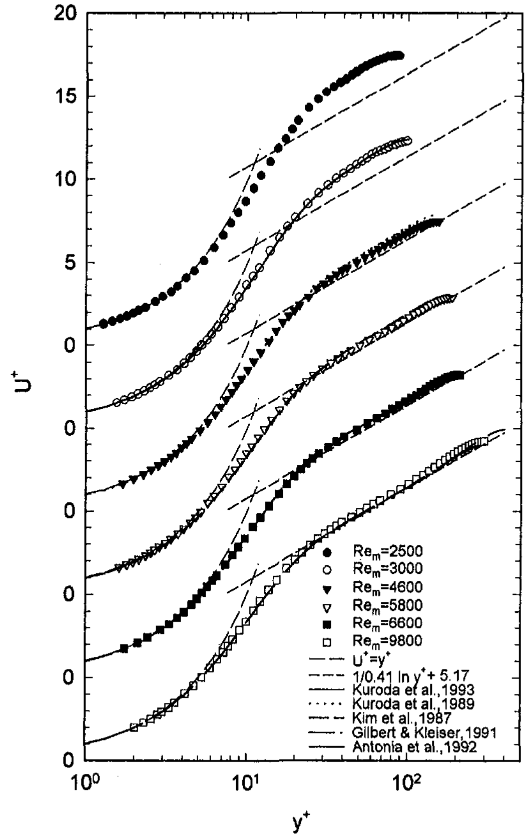

Fig. 9 Mean velocity profiles for different Reynolds numbers. The estimated statistical uncertainty in the measurements is ±0.2 percent.

4.3 Turbulence Intensity Measurements. Turbulence intensity measurements, normalized with the wall variables, are shown in Fig. 10. All sets of data presented indicate that intensity scales with the wall shear velocity starting from the wall up to the edge of the buffer region, $y^+ \approx 50$. The peak value of the intensity is located in the middle of the buffer region, $y^+ \approx 12$, and is approximately constant, $u'^+_{\max} \approx 2.55$, over the Reynolds number range investigated. This finding seems to be inconsistent with the corresponding numerical results, which

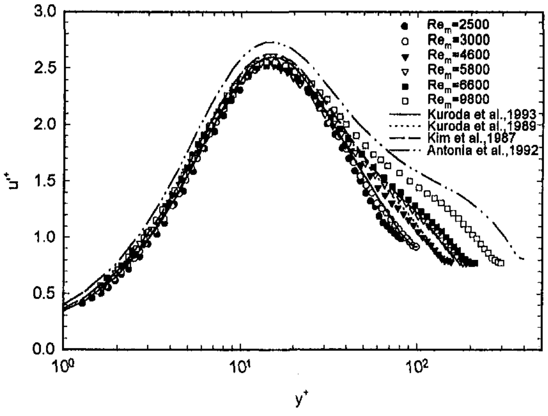

Fig. 10 Turbulence intensity profiles for different Reynolds numbers. The estimated statistical uncertainty in the measurements is ±1 percent.

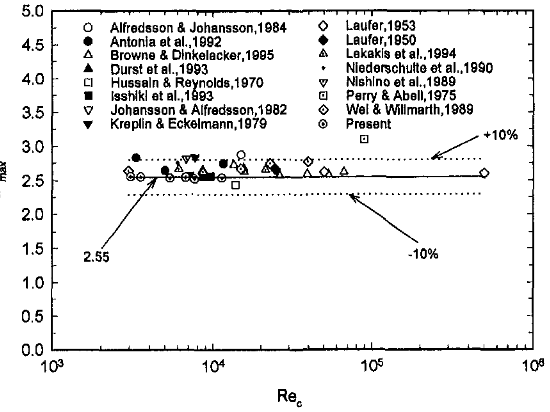

Fig. 11 Demonstration of inner scaling of the maximum turbulence intensity close to the wall. A summary of the existing data reproduced from different experimental studies. The estimated statistical uncertainty in the measurements is ±10 percent.

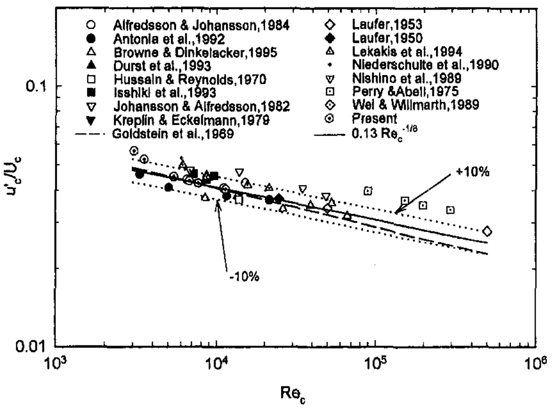

Fig. 13 Turbulence intensity at the channel centreline normalized by local mean velocity as a function of the Reynolds number. The estimated statistical uncertainty in the measurements is ±10 percent.

suggest a continuous increase in the peak value of intensity with increasing Reynolds number. This holds especially for the data of Antonia et al. (1992) obtained for $R_{e_m} = 13800$. The data for u'^+_{max} of other workers, shown in Fig. 11, obtained at much higher Reynolds numbers compared with those attained in the present study, clearly support the conjecture mentioned above.

It is interesting that the present experimental results and other published data, which are plotted in Fig. 12, indicate that turbulence intensity at the channel centreline scales with the wall friction velocity. This result, together with the skin friction equation for C_f, implies that the following relationship holds at the channel centerline:

$$\frac{u'_c}{U_c} \simeq 0.13 R_{e_c}^{-1/8} \tag{16}$$

For the data shown in Figs. 12 and 13 the estimated relative measuring error is about ±10 percent.

Figure 13 shows that the correlation given above agrees well with experimental and numerical data for $R_{e_c} \geq 4500$. This result also suggests that the friction velocity can be determined only from the intensity measurement at the channel centreline if the Reynolds number is large enough.

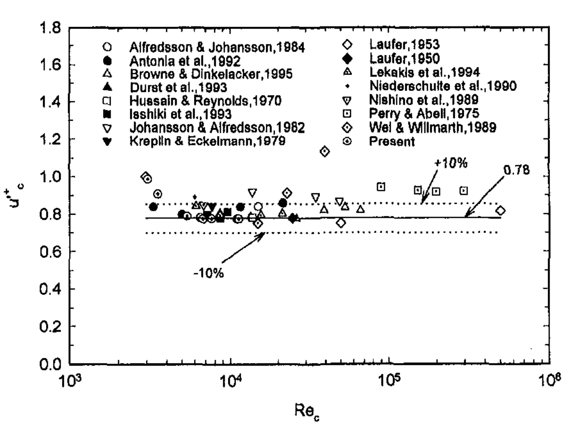

Fig. 12 Demonstration for the inner scaling of the centreline turbulence intensity. A summary of the existing data reproduced from different experimental studies. The estimated statistical uncertainty in the measurements is ±10 percent.

It is interesting to analyze the influence of Reynolds number on the limiting behavior of the turbulent intensity at the wall

$$\lim_{y\to 0}\frac{u'}{U} \tag{17}$$

since it can shed some light on the dynamics of turbulence in the near-wall region. Using the Taylor series expansion for the instantaneous velocity fluctuations near the wall:

$$\left.\begin{aligned} u &= a_1 y && + a_2 y^2 + \ldots \\ v &= && + b_2 y^2 + \ldots \\ w &= c_1 y && + c_2 y^2 + \ldots \end{aligned}\right\} \tag{18}$$

it can be shown that the turbulent dissipation rate at the wall is given by

$$(\epsilon)_{\rm wall} = \nu(\overline{a_1^2} + \overline{c_1^2}) \tag{19}$$

According to direct numerical simulations of turbulent channel flow, the streamwise velocity component accounts for about 75 percent of the dissipation rate at the wall (Kim et al., 1987; Antonia et al., 1992):

$$(\epsilon)_{\rm wall} \approx \nu\overline{a_1^2} \tag{20}$$

Thus, by measuring

$$(\overline{a_1^{+2}})^{1/2} = \lim_{y\to 0}\frac{u'}{U}, \quad a_1^+ = \frac{a_1\nu}{u_\tau^2} \tag{21}$$

it is possible to obtain an insight into the influence of Reynolds number on $(\epsilon)_{\rm wall}$.

In connection with the issue discussed above, it is important to estimate the accuracy of gradient-broadening correction on the limiting behavior of u'/U since the last term in Eq. (8) is not accessible by direct measurements. By normalizing Eq. (8) using the wall shear velocity u_τ and kinematic viscosity ν of the fluid, we obtain

$$\overline{u_{c_v}^{+2}} = \overline{u^{+2}(\underline{x}_c)} + \frac{d_y^{+2}}{16}\left(\frac{d\overline{U}^+}{dy^+}\right)^2 + \frac{d_y^{+2}}{32}\left(\frac{d^2\overline{u^{+2}}}{dy^{+2}}\right)_{\underline{x}=\underline{x}_c} + h.o.t. \tag{22}$$

Evaluating the above equation at the wall, $y = 0$, yields

$$(u'_{c_v})^+_{\rm wall} = \frac{d_y^+}{4}[1 + \overline{a_1^{+2}}]^{1/2} \tag{23}$$

Using Eq. (20), we may express the apparent intensity at the wall as

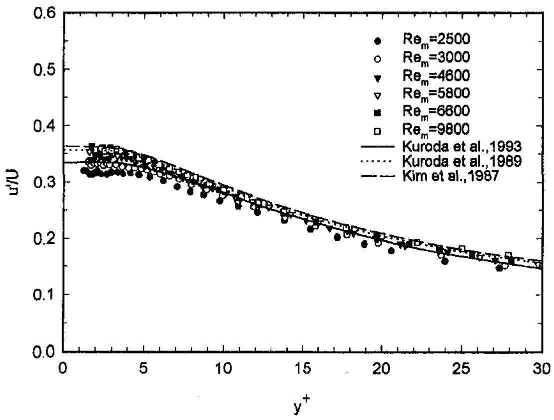

Fig. 14 Limiting behavior of the turbulence intensity near the wall at different Reynolds numbers. The estimated statistical uncertainty in the measurements is ±1 percent.

$$(u'_{c_v})^+_{\text{wall}} \approx \frac{d_y^+}{4}\,[1 + (\epsilon)^+_{\text{wall}}]^{1/2} \qquad (24)$$

Numerical databases, as compiled by Shih and Lumley (1993), indicate that ϵ^+_{wall} varies with Reynolds number in the range $(\epsilon)^+_{\text{wall}} = 0.16 - 0.22$. For $R_{e_m} = 3000{-}13800$, we may conclude from Eq. (24) that the term $d^2\overline{u^2}/dy^2$ in Eq. (8) contributes 7–10 percent to $(u'_{c_v})^+_{\text{wall}}$, resulting in a variation of about three percent with the Reynolds number.

Figure 14 shows the distributions of u'/U near the wall obtained at different Reynolds numbers. The results indicate an increase of 15 percent in the limiting behavior of turbulence intensity at the wall with increasing the Reynolds number. Figure 14 also shows that the trend in the experimental data is consistent with the results of direct numerical simulations. Since the measured trend is much higher than the trend resulting from truncation of the gradient-broadening correction given by Eq. (8), we believe that there is physical origin for the dependence of the dissipation rate at the wall on Reynolds number.

4.4 Skewness and Flatness Factors.

The present experimental investigations also involved measurements of higher order moments, the skewness and flatness factors

$$S = \frac{\overline{u^3}}{u'^3}, \quad F = \frac{\overline{u^4}}{u'^4} \qquad (25)$$

These quantities describe the details of the probability density function and in wall shear flows are significantly different from those for the Gaussian probability function. Only in homogeneous isotropic turbulence do the higher order moments attain the values $S = 0$ and $F = 3$ which are valid for the Gaussian distribution.

Distributions of the measured skewness and flatness factors are plotted in Fig. 15. Across the entire flow field the higher order moments exhibit highly non-Gaussian character. In particular, the non-Gaussian variations are pronounced in the near-wall region where the measured distributions show universal behavior. At the wall the skewness and flatness factor approach the limiting values of $S \simeq 1$ and $F \simeq 4.5$. In the buffer and logarithmic flow regions the distributions of the higher order moments are not universal and show a tendency for decreasing non-Gaussian variations with increasing Reynolds number.

5 Conclusion

Near-wall laser-Doppler measurements were performed in a turbulent channel flow in order to examine the influence of the upstream conditions on the flow development. The experimental results indicate that unique flow properties independent of the conditions at the entrance of the channel can be obtained at low Reynolds numbers only by sufficient tripping of the flow upstream of the measuring test station. For trip blockage ratios higher than 15 percent it was found that turbulence quantities remain independent of the upstream conditions. From the measured data, the minimum Reynolds number at which the flow could still be considered to be fully developed and turbulent is estimated to be $R_{e_c} \approx 3000$.

The experimental results for the mean velocity show a downward shift in the measured profiles across the logarithmic region with increasing Reynolds number. These observations are in agreement with the corresponding results of direct numerical simulations of turbulent channel flow.

The measured intensity profiles show, within the experimental uncertainty, that these scale with the inner variables close to the wall. The maximum intensity, which is located in the middle of the buffer region, scaled with u_τ is constant and independent of the Reynolds number. The universal scaling for the maximum intensity close to the wall, however, cannot be confirmed by the corresponding numerical results. Better agreement between the experimental and numerical results was obtained for the turbulence intensity at the channel centreline. Both sets of data indicate that the centreline intensity scales with the wall variables over a very wide range of Reynolds numbers.

The limiting values of the turbulence intensity extrapolated at the wall were found to increase with increasing Reynolds number. This trend in the experimental data agrees with the limiting behavior of $u'/\bar{U}$ deduced from numerical flow predictions.

JFE Data Bank Contribution

The data, which correspond to flow conditions given in Table 1, are available for the following quantities: $Y+$—normalized

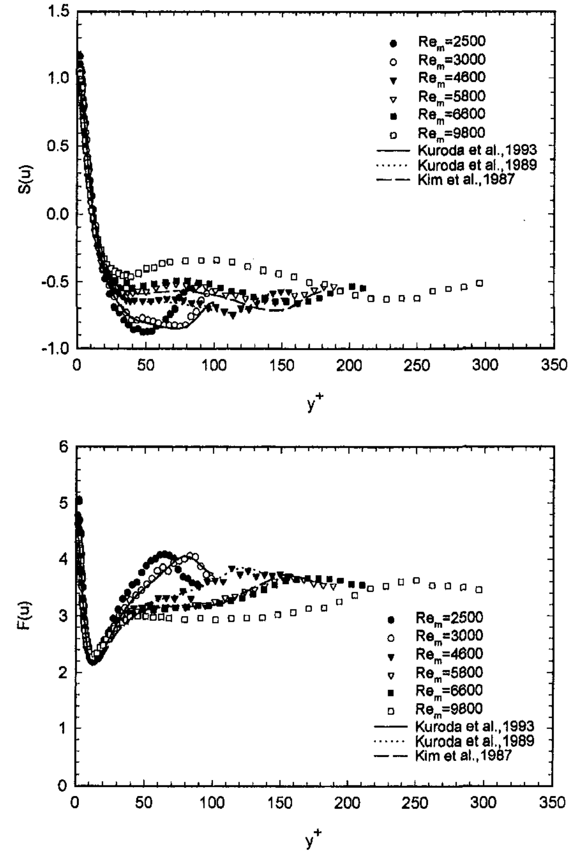

Fig. 15 Distribution of the higher-order moments for different Reynolds numbers: (*a*) skewness factor; (*b*) flatness factor. The estimated statistical uncertainty in the measurements is ±2 percent.

distance from the wall; $U+$—normalized mean velocity; $u'+$—normalized streamwise intensity; u'/U—streamwise intensity normalized by the local mean velocity; S,F—skewness and flatness factors of the streamwise velocity component.

Acknowledgments

This research received financial support through the Deutsche Forschungsgemeinschaft within the project Du 101/16-3. The authors greatefully acknowledge this support of their work. H. Kikura received support for his stay at LSTM-Erlangen through Japan Society for the Promotion of Science (JSPS).

References

Alfredsson, P. H., and Johansson, A. V., 1984, "On the Detection of Turbulence-Generating Events," *Journal of Fluid Mechanics*, Vol. 139, pp. 325–345.

Antonia, R. A., Teitel, M., Kim, J., and Browne, L. W. B., 1992, "Low-Reynolds Number Effects in a Fully Developed Channel Flow," *Journal of Fluid Mechanics*, Vol. 236, pp. 579–605.

Browne, W. B., and Dinkelacker, A., 1995, "Turbulent Pipe Flow: Pressures and Velocities," *Fluid Dynamics Research*, Vol. 15, pp. 177–204.

Dean, R. B., 1978, "Reynolds Number Dependence of Skin Friction and Other Bulk Flow Variables in Two-Dimensional Rectangular Duct Flow," ASME JOURNAL OF FLUIDS ENGINEERING, Vol. 100, pp. 215–223.

Durst, F., Martinuzzi, R., Sender, J., and Thevenin, D., 1992, "LDA Measurements of Mean Velocity, rms Value, and High-order Moments of Turbulence Intensity Fluctuations in Flow Fields with Strong Velocity Gradients," *Proceedings of 6th International Symposium on Applications of Laser Techniques to Fluid Mechanics*, Lisbon, Portugal, pp. 5.1.1–5.1.6.

Durst, F., Jovanovic, J., and Sender, J., 1993, "Detail Measurements of the Near Wall Region of Turbulent Pipe Flow," FED-Vol. 146, *Data for Validation of CFD Codes*, ASME, Book No. H00786, pp. 79–86.

Durst, F., Kikura, H., Lekakis, I., Jovanović, J., and Ye, Q.-Y., 1996, "Wall Shear Stress Determination from Near-Wall Mean Velocity Data in Turbulent Pipe and Channel Flows," *Experiments in Fluids*, Vol. 67, pp. 257–271.

Gilbert, N., and Kleiser, L., 1991, "Turbulence Model Testing with the Aid of Direct Numerical Simulation Results," *Proceedings of 8th Symposium on Turbulent Shear Flows*, TU of Munich, Germany, Sept. 9–11, pp. 26.1.1–26.1.6.

Goldstein, R. J., Adrian, R. J., and Kreid, D. K., 1969, "Turbulent and Transition Pipe Flow of Dilute Aqueous Solutions," *I&EC Fundamentals*, Vol. 8, pp. 489–502.

Goldstein, R. J., and Adrian, R. J., 1971, "Measurements of Fluid Velocity and Gradient using Laser-Doppler Techniques," *Review of Scientific Instruments*, Vol. 42, pp. 1317–1320.

Horiuchi, K., 1992, "Establishment of the DNS Database of Turbulent Transport Phenomena," Report Gants-in-Aid for Scientific Research, No. 02302043.

Hussain, K. M. F., and Reynolds, W. C., 1970, "The Mechanics of an Organized Wave in Turbulent Shear Flow," *Journal of Fluid Mechanics*, Vol. 41, pp. 241–258.

Isshiki, S., Obata, T., Kasagi, N., and Hirata, M., 1993, "An Experimental Study on Heat Transfer in a Pulsating Pipe Flow (1st Report, Time-Averaged Turbulent Characteristics)," *Transaction of JSME B*, Vol. 59, pp. 2245–2251, in Japanese.

Johansson, A. V., and Alfredsson, P. H., 1982, "On the Structure of Turbulent Channel Flow," *Journal of Fluid Mechanics*, Vol. 122, pp. 295–314.

Kasagi, N., and Shikazono, N., 1994, "Contribution of Direct Numerical Simulation to Understanding and Modeling Turbulent Transport," *Proceedings of Osborne Reynolds Centenary Symposium*, UMIST Manchester, England, May 24, pp. 1–27.

Kim, J., Moin, P., and Moser, R., 1987, "Turbulence Statistics in Fully Developed Channel Flow at Low Reynolds Number," *Journal of Fluid Mechanics*, Vol. 177, pp. 133–166.

Kreplin, H., and Eckelmann, H., 1979, "Behavior of Three Fluctuating Velocity Components in Wall Region," *Physics of Fluids*, Vol. 22, pp. 1233–1239.

Kuroda, A., Kasagi, N., and Hirata, M., 1989, "A direct numerical simulation of the fully developed turbulent channel flow," *Proceedings of International Symposium on Computational Fluid Dynamics*, Nagoya, pp. 1174–1179.

Kuroda, A., Kasagi, N., and Hirata, M., 1993, "Direct Numerical Simulation of the Turbulent Plane Couette-Poiseulle Flows: Effect of Mean Shear on the Near Wall Turbulence Structures," *Proceedings of 9th Symposium on Turbulent Shear Flows*, Kyoto, Japan, Aug. 16–18, pp. 8.4.1–8.4.6.

Laufer, J., 1950, "Investigation of Turbulent Flow in a Two-Dimensional Channel," NACA TN 2123.

Laufer, J., 1953, "The Structure of Turbulence in Fully Developed Pipe Flow," NACA TN 2954.

Lekakis, I., Durst, F., and Sender, J., 1994, "LDA Measurements in the Near-Wall Region of an Axisymmetric Sudden Expansion," *Proceedings of 7th International Symposium on Applications of Laser Techniques to Fluid Mechanics*, Lisbon, Portugal, July 11–14, pp. 13.6.1–13.6.8.

Lyons, S. L., Hanratty, T. J., and McLaughlin, J., 1991, "Large-Scale Computer Simulation of Fully Developed Turbulent Channel Flow with Heat Transfer," *International Journal of Numerical Methods in Fluids*, Vol. 13, pp. 999–1028.

Niederschulte, M. A., Adrian, R. J., and Hanratty, T. J., 1990, "Measurements of Turbulent Flow in a Channel at Low Reynolds Numbers," *Experiments in Fluids*, Vol. 9, pp. 222–230.

Nikuradse, J., 1932, "Gesetzmäßigkeiten der turbulenten Strömung in glatten Rohren," *Forschungsheft 356*, Ausgabe B Band 3, VDI-Verlag, Berlin, in German.

Nishino, K., and Kasagi, N., 1989, "Turbulence Statistics Measurement in a Two-Dimensional Channel Flow using Three-Dimensional Particle Tracking Velocimeter," *Proceedings of 7th Symposium on Turbulent Shear Flows*, Stanford, Aug. 21–25, pp. 22.1.1–22.1.6.

Shih, T.-H., and Lumley, J. L., 1993, "Kolmogorov Behavior of Near-Wall Turbulence and Its Application in Turbulence Modeling," *Proceedings of 9th Symposium on Turbulent Shear Flow*, Kyoto, Japan, Aug. 16–18, pp. 8.1.1–8.1.5.

Perry, A. E., and Abell, C. J., 1975, "Scaling Laws for Pipe-Flow Turbulence," *Journal of Fluid Mechanics*, Vol. 67, pp. 257–271.

Wei, T., and Willmarth, W. W., 1989, "Reynolds-Number Effects on the Structure of a Turbulent Channel Flow," *Journal of Fluid Mechanics*, Vol. 204, pp. 57–95.

Tong-Miin Liou
Professor.
Fellow ASME

Chih-Wen Kao
Graduate Student.

Shih-Hui Chen
Graduate Student.

Department of Power
Mechanical Engineering,
National Tsing Hua University,
Hsinchu, Taiwan 30043

Flowfield Investigation of the Effect of Rib Open Area Ratio in a Rectangular Duct

The spatially periodic turbulent fluid flows and friction in a rectangular passage of width-to-height ratio of 4:1 with perforated rectangular ribs mounted on one wall have been studied using laser Doppler velocimetry and pressure probing. The parameters fixed were rib height to duct hydraulic diameter ratio of 0.106, rib width-to-height ratio of 0.76, rib pitch-to-height ratio of 10, and Reynolds number of 2×10^4*, while the main parameter investigated was the rib open-area ratio* (β) *with values of 0%, 10%, 22%, 38%, and 44%. Two critical ranges of* β *and three characteristic flow regimes were identified, which provides useful references of practical tests of computational models. The results also showed that the dominant fluid dynamic factors responsible for the reported peak values of local Nusselt number distribution could be recognized. Moreover, the secondary-flow mean velocity components were found to be one to two orders of magnitude smaller than the bulk mean velocity.*

Introduction

In the cooling panels of a scramjet inlet (Chang and Mills, 1993), chemical reaction vessels and gas-cooled nuclear reactors, various types of bluff bodies are deliberately arranged on the passage walls to periodically disrupt the flow for attaining heat and mass transfer augmentation. Often, the disturbances are applied in an asymmetric manner. Previous heat transfer (Liou and Hwang, 1992) and fluid flow (Liou et al., 1993b) studies indicated that for duct flows with solid-type ribs attached on the walls, the heat transfer locally deteriorated immediately downstream of the ribs due to the presence of separated recirculation cells. To remove the local heat transfer deterioration in the rib-wall corners of the attached solid ribs, laser holographic interferometry (LHI) measurements in a rectangular duct with repeated perforated ribs attached on one wall (Fig. 1) have been performed (Hwang and Liou, 1994) and the results showed the elimination of the aforementioned heat transfer deterioration around the rib-wall corners and reduction of pressure loss by fluid flow through the rib perforations. The present paper focuses on the complementary turbulent fluid flow study.

Some relevant previous works are summarized in Table 1 where the ranges of parameters investigated, techniques used, and physical quantities measured are also listed for reference purpose. Among the previous studies of turbulent flows around perforated bluff bodies in a rectangular channel, Tanasawa et al. (1983) employed the resistance heating method and thermocouple technique to determine the heat transfer coefficients in a channel with turbulence promoters of fence-type, perforated plate-type, and slit plate-type symmetrically mounted on two opposite walls for rib open area ratio β (defined in Fig. 1) and Reynolds number Re ranging from 0 to 50 percent and 1.3×10^4 to 9×10^4, respectively. Results showed that surfaces with perforated plate-type turbulence promoters gave excellent performance under the same pumping power. Under the same flow conditions, Tanasawa et al. (1984) subsequently compared the thermal performance of plain rectangular rib-type, perforated rib-type, and half-perforated rib-type. They concluded that half-perforated rib-type turbulence promoters with perforations on the lower half of the rib gave better performance. Another important finding was that the local heat transfer coefficient decreased as a whole when fewer than two pairs of promoters were placed upstream. Ichimiya and Mitsushiro (1988) studied the effect of rib thickness, $W_r/H = 0.5$, 1, and 1.5, on the thermal performance and friction loss of flow in a rectangular duct with porous-type turbulence promoters arranged on one insulated wall placed opposite to the smooth heated wall for rib pitch-to-height ratio of $Pi/H = 3.5$, rib open area ratio of $\beta = 87.3$ percent, and Reynolds number of $\mathrm{Re} = 2.6 \times 10^4$ to 1.5×10^5. The thermocouple measured average Nusselt number and pressure tap measured average friction factor were, respectively, found to be augmented to about two to four times that of the smooth duct and reduced to one fourth to two thirds of that of the solid-type turbulence promoters. Nevertheless, no conclusive trend for thickness effect was reported. Ichimiya et al. (1991) further experimentally investigated the effects of a single porous-type roughness of $\beta = 87.3$ percent on the heat transfer and friction characteristics in a parallel plate duct. The porous-type roughness was applied to the insulated wall facing the heated smooth surface. Results showed that the thermal performance under the constant pumping power constraint is better in the laminar region than in the turbulent region. Yamada and Osaka (1992) conducted flow visualization and pressure measurements to study the effects of the aspect ratio and open-area ratio of the plate on the heat transfer characteristics of the flow over a rectangular perforated plate standing on a flat wall. Only one flow velocity ($U_b = 5$ m/s) was tested. They found that the critical open-area ratios for the presence of a recirculation behind the plate were between 32.5 and 48.5 percent. Recently, Hwang and Liou (1994) focused on the heat transfer enhancement in a channel containing perforated ribs. The experimental techniques employed were laser holographic interferometry and Pitot tube probing, and the parameters investigated were rib open-area ratio ($\beta = 0$ to 44 percent), rib pitch-to-height ratio ($Pi/H = 5$ to 10), and rib height-to-channel hydraulic diameter ratio ($H/De = 0.081$ to 0.162). An important finding they made was that the ribs with $\beta = 44$ percent gave the best thermal performance among the rib open area ratios investigated.

In the papers cited above, most studies of the flow past perforated or porous ribs have so far been related to heat transfer measurements and very few works relevant to velocity field measurements. The present work therefore focuses on the flow characteristics investigation. Moreover, previous qualitative ob-

---

Contributed by the Fluids Engineering Division for publication in the JOURNAL OF FLUIDS ENGINEERING. Manuscript received by the Fluids Engineering Division March 3, 1997; revised manuscript received May 5, 1998. Associate Technical Editor: S. Banerjee.

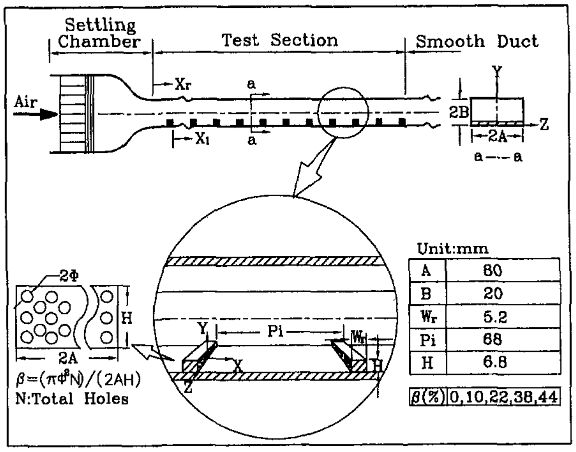

Fig. 1 Sketch of configuration, dimensions, and coordinate system of test section (Uncertainty in *H*: ±0.1 mm, in *Wr*: ±0.1 mm, in *A* and *B*: ±0.2 mm, in axial position: ±0.1 mm, in transverse position: ±0.1 mm, in spanwise position: ±0.1 mm)

Table 1 A list of relevant works

Year	Authors	Configuration	A/B	Pi/H	Wr/H	H/De	β	Re/Ub	Exp. Tech.	Meas. Quon.
1970	Castro		1.5	∞	0.038	0.028	0% ≀ 64.5%	25000 ≀ 90000	HW PT	P U
1984	Tanasawa et al.		3.3	9.9 14.4 31.6	0.075 0.109 0.240	0.036 0.079 0.117	0% ≀ 50%	13000 ≀ 90000	PT TC	P T
*1988	Ichimiya& Mitsushiro	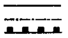	7.5	3.5	0.5 1 1.5	0.28	87.3%	26000 ≀ 150000	PT TC	P T
*1991	Ichimiya et al.		7.5	∞	1 1.5 3	0.14 ≀ 0.42	87.3%	1000 ≀ 28000	TC	T
1992	Yamada& Osaka		UN	∞	0.027	UN	0% ≀ 48.5%	5m/s	PT FV	P
1994	Hwang& Liou		4	5 10	0.5 1	0.081 0.162	0% ≀ 44%	10000 ≀ 50000	PT TC LHI	P T
1997	Present Study	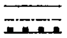	4	10	0.76	0.106	0% ≀ 44%	20000	PT LDV	P U

FV:Flow Visualization HW:Hot Wire LDV:Laser Doppler Velocimetry
LHI:Laser Holographic Interferometry P:Pressure PT:Pitot Tube/Pressure Transducer
T:Temperature TC:Thermocouple U:Velocity
UN:Unkown *:Porous Ribs Quan. : Quantities

servation of flow patterns was performed for a single perforated rib (Yamada and Osaka, 1992). In the present study nonintrusive laser-Doppler velocimetry measurements are thus undertaken for a perforated rib array mounted on one wall of a rectangular duct. The size of perforations is varied to examine its effect on the flow structures. In addition, the acquired fluid flow information can be complementary to our previous heat transfer study (Hwang and Liou, 1994). Some turbulence quantities related to turbulence modeling are also addressed.

Experimental Apparatus and Conditions

Apparatus. The overall experimental setup is shown in Fig. 2 and is similar to that described in Liou et al. (1993a). Please refer to this earlier paper for more detail. The LDV optics is a two-color four-beam two-component system. A 4-W argon-ion laser with 514.5 nm (green) and 488 nm (blue) lines provided the coherent light sources. Both forward and off-axis scattering configurations were used in the experiment; based on $1/e^2$ extent of light intensity, the former gave an ellipsoid probe volume of about 1.69 nm in length and 0.164 mm in diameter and the latter 0.74 mm in length and 0.164 mm in diameter inside the test section. The entire LDV system was mounted on a milling machine with four vibration-isolation mounts, allowing the probe volume to be positioned with 0.01 mm resolution. The light scattered from salt particles with a nominal 0.8 μm was collected into photomultiplier and subsequently downmixed to the appropriate frequency shift of 0.1 to 10 MHz. Then two counter processors with 1 ns resolution were used to process the Doppler signals and feed the digital outputs into a PC-586 for storage and analysis. Depending on the location of the probe volume in the flow, typical coincidence rates were between 500 and 3000 s^{-1} with a 50 μs coincidence window. In addition, pressure tapes were used for streamwise static pressure drop measurements.

Test Section. The test section was 1150 mm in length and 160 mm × 40 mm ($2A \times 2B$) in cross-sectional area, and made of 5-mm Plexiglas, as shown in Fig. 1. The corresponding hydraulic diameter of the test duct was 64 mm. The aluminum rectangular perforated ribs of size 5.2 mm × 6.8 mm ($W_r/H =$

Nomenclature

A = half width of channel (80 mm)
B = half height of channel (20 mm)
C_f = wall static pressure coefficient, $(P - P_0)/(0.5\rho U_b^2)$
De = duct hydraulic diameter, $4B/(1 + B/A)$ (64 mm)
d = normal distance from wall
f = (Darcy) friction factor
H = rib height (6.8 mm)
k = turbulent kinetic energy, $\frac{3}{4}(\overline{u^2} + \overline{v^2})$
L_R = length of primary recirculation zone, Fig. 8
N = total number of perforations drilled through the rib
$\overline{\mathrm{Nu}}$ = local Nusselt number
$\overline{\mathrm{Nu}}_s$ = average Nusselt number for the smooth duct (at the same mass flow rate)
P = pressure
Pi = rib pitch (68 mm)
Re = Reynolds number, $\rho U_b D_e/\mu_l$
S_p = stagnation point, Fig. 8
U = streamwise mean velocity
u = streamwise velocity fluctuation
u' = streamwise turbulence intensity, $(\overline{u^2})^{1/2}$
U_b = duct bulk mean velocity, 5.6 (m/s)
U_{mn} = maximum negative streamwise mean velocity
$-\overline{uv}$ = turbulent shear stress
V = transverse mean velocity
v = transverse velocity fluctuation
v' = transverse turbulence intensity, $(\overline{v^2})^{1/2}$
W = spanwise mean velocity
W_r = rib width (5.2 mm)
w = spanwise velocity fluctuation
w' = spanwise turbulence intensity, $(\overline{w^2})^{1/2}$
X = streamwise coordinate ($X = 0$ at each rib's rear edge, Fig. 1)
X_1 = streamwise coordinate ($X = 0$ at first rib's rear edge, Fig. 1)
X_J = effective jet length, Fig. 8
X_R = reattachment length, Fig. 8
X_r = streamwise coordinate ($X = 0$ at inlet reference, Fig. 1)
Y = transverse coordinate, Fig. 1
Z = spanwise coordinate, Fig. 1
β = open-area ratio of perforated rib, $(N\pi\phi^2)/(2AH)$
ϕ = the radius of perforation
ρ = air density
μ_l = laminar viscosity

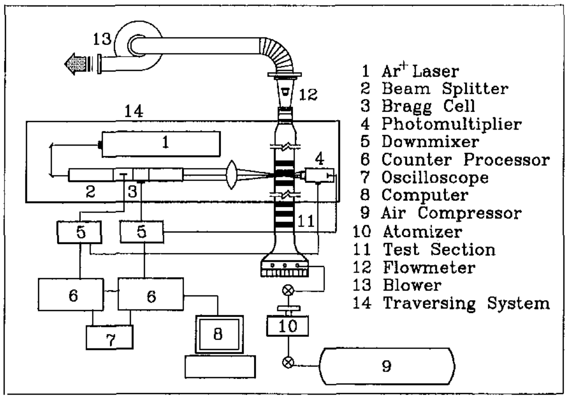

Fig. 2 Schematic drawing of overall experimental system

0.76 and $H/2B = 0.17$ or $H/De = 0.106$) were attached onto the bottom wall ($Y = 0$). The leading edge of the first rib was placed at 150 mm downstream of the bell-shaped 10:1 contraction ($X_r = 0$ in Fig. 1). There were 16 ribs in the rib array.

Experimental Conditions. The main parameter investigated was the rib open-area ratio β defined in Fig. 1 with values of 0, 10, 22, 38, and 44 percent. A photograph of these perforated ribs can be found in our previous heat transfer work (Hwang and Liou, 1994) in which the shape, location, and distribution of the holes are clearly displayed. It should be pointed out that the mass flow rate through the perforations may be a more appropriate parameter than β because entrance and exit effects through the perforations may be important, depending on the shape of the holes. Nevertheless, the parameter β has been adopted in all the previous studies on perforated ribs, as shown in Table 1. The adoption of β thus allows the comparison between the present work and previous studies to be made. As mentioned in the Introduction, Tanasawa et al. (1983) have also explored some effects of the shape, location, and distribution of the perforations. None of the previous studies was able to report the flow rate through the perforated ribs due to the experimental difficulty. In the current study, the laser beams could not be brought to sufficiently near the rib holes to allow the velocity measurements for determining the flow rate through the rib holes due to the blockage of laser beams by the rib itself. Measurements using particle image velocimetry are highly recommended for future study. The rib pitch-to-height ratio (Pi/H) and Reynolds number (Re) were fixed at 10 and 2×10^4, respectively. Re $= 2 \times 10^4$ corresponded to a bulk mean velocity of $U_b = 5.6$ m/s which was used to nondimensionalize the experimental results. At a sufficient distance downstream of the first rib, it is expected that the flow pattern will repeat itself from pitch to pitch, i.e., becomes spatially periodic. Along the central plane $Z/A = 0$, LDV measurements of periodically fully developed flow were obtained at 22 axial stations between the 11th and 12th ribs. At each station the measurements were made at 10 to 15 locations and could be brought as close as 0.6 mm from the wall.

Verification of the spatially periodic condition was performed by comparing profiles of mean velocity and fluctuating components between several consecutive pitches for $\beta = 44$ percent and Re $= 2 \times 10^4$. The repeatability was found to be within ±5.3 percent for both mean and fluctuating components. The spatially periodic condition can also be checked by examining the streamwise wall static pressure coefficient distribution, as shown in Fig. 3 for $\beta = 22$ and 44 percent. In the figure the first rib is located at $X_1/H = 0$ or $X_r/H = 10$ (Fig. 1) and the rib pitch-to-height ratio is $Pi/H = 10$. The locations of static pressure taps relative to the ribs are $X/H = 0.76$ and $X/H = 6.7$ in each pitch where the wall static pressures are local minimum and maximum, respectively. Notice that in the periodic region the pressure differences between X_1 and $X_1 + Pi$, $X_1 + Pi$ and $X_1 + 2Pi$, $X_1 + 2Pi$ and $X_1 + 3Pi$, . . . , etc., are identical. That is, if the pressure at points, X_1, $X_1 + Pi$, $X_1 + 2Pi$ and $X_1 + 3Pi$, . . . , are plotted, they will fall on a straight line. From Fig. 3 and the data for $\beta = 0$, 10, and 38 percent (not shown due to space limitation) one concludes that the pressure field attains spatially periodic condition after the third or fourth perforated rib.

There were typically 4096 realizations averaged at each measuring location. The statistical errors in the mean velocity and turbulence intensity were less than 1.6 and 2.5 percent, respectively, for a 95 percent confidence level. Representative values of other uncertainty estimates are noted in figure captions. More detailed uncertainty estimates and velocity bias correlations are included in Liou et al. (1990 and 1993a). For the range of atomizer pressure setting used, the saline solution was mixed to produce particles from 0.5 to 1.2 μm. This particle diameter range is able to follow turbulence frequencies exceeding 1 KHz (Durst et al., 1976).

Results and Discussion

Friction Factor. Although the ribbed duct augments heat transfer, the presence of ribs increases the pressure loss. It is therefore worthwhile to study how the friction factor varies with rib's open area ratio. The friction factor in the spatially periodic region of the ribbed duct can be expressed as $f = [(-\Delta P/\Delta X)\cdot D_e]/(\rho \cdot U_b^2/2)$ where $\Delta P/\Delta X$ is the axial pressure gradient evaluated by calculating the ratio of the pressure difference ΔP between corresponding points (pressure taps) of successive cycles to the rib pitch. Figure 4 shows the decrease of f with increasing β according to the functional form of $f = -0.183\beta^{0.525} + 0.3$. Quantitatively, the perforation of ribs can reduce the friction factor to about 60, 63, 72, and 82

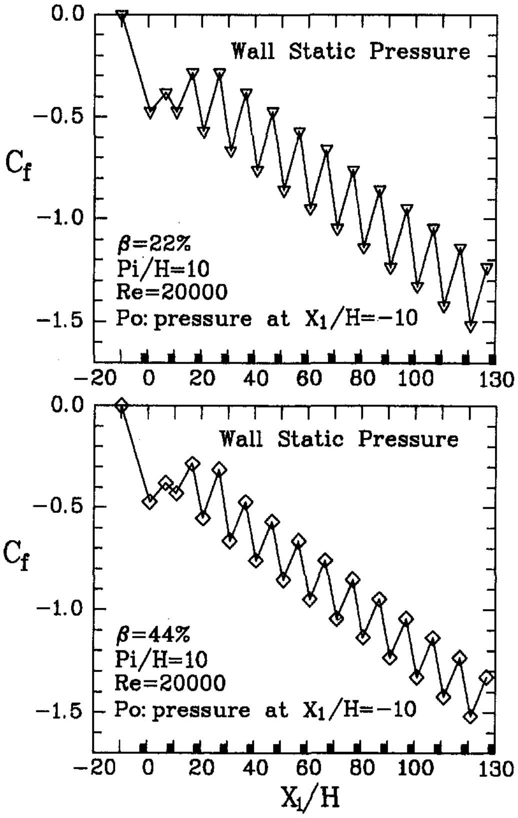

Fig. 3 Measured wall static pressure coefficient distributions for $\beta = 22$ and $\beta = 44$ percent (■: rib; Uncertainty in C_f: less than ±3.1 percent)

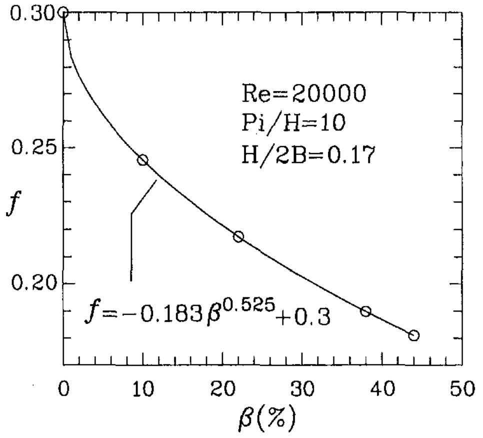

Fig. 4 Variation of friction factor with rib's open area ratio (Uncertainty in f: less than ±3.5 percent)

percent of that of corresponding solid-type ribs ($f = 0.3$ at $\beta = 0\%$) for $\beta = 44$, 38, 22, and 10 percent, respectively.

Flow Characteristics in Central Longitudinal Plane

Mean Flow Pattern. The longitudinal mean flow pattern for $\beta = 44\%$, (38 percent, 22 percent) and (10 percent, 0 percent) are presented in terms of velocity vectors in Fig. 5, Fig. 6, and Fig. 7, respectively. These figures reveal significant influence of the value of β on the mean flow pattern, especially the recirculating flow in the rib wake region and the corner vortex in front of the rib. In general, the core flow undergoes an acceleration during contracting into the region in between the rib top and upper duct wall and then expands downstream of the rib. The degree of flow contraction (or acceleration), i.e., the steepness of the vector angle around the rib top front corner, depends on the value of β. For $\beta = 44\%$, Fig. 5, a larger part of fluids located within a rib height distance from the bottom duct wall can flow through the rib perforations and emerge from the rib rear edge in the form of multi-jets (will be elaborated on in the later text), which results in the absence of corner vortex at the rib bottom front corner, and less flow contraction and expansion around the rib top front and rear corner, respectively.

The degree of flow bending during expansion process also depends on the value of β or the strength of aforementioned multi-jets. The multi-jets or the core flow separated from the rib top tends to be drawn down onto the wall by the Coanda effect, as depicted in Figs. 5 to 7. As β decreases from 44% (Fig. 5) to 38% (Fig. 6), the amount of fluids passing through rib perforations correspondingly decreases, hence not enough to provide the entrainment needs of the separated shear layer, and the Coanda effect becomes more significant. As a result, the flow bending increases to an extent such that the reattachment flow forms a small flow reversal region immediately upstream of the reattachment point $X_R/H = 3.4$. Comparing Fig. 6 with Fig. 5, one finds the presence of a critical range of rib open area ratio ($38\% < \beta_{c1} < 44\%$). Above β_{c1}, the Coanda effect only draws the expanding core flow and multi-jets slightly approaching the bottom duct wall, due to a sufficient amount of bleed air coming through rib perforations and providing the entrainment needs of the separated shear layer. Below β_{c1}, the Coanda effect makes the expanding core flow impinge upon the bottom duct wall and form a recirculating flow region, due to an insufficient entrainment of the separated shear layer. It should be pointed out that the critical rib open area ratio range, $38\% < \beta_{c1} < 44\%$, concluded by the present LDV measurements is somewhat narrower than $32.5\% < \beta_{c1} < 48.5\%$ reported by Yamada and Osaka (1992) based on the low speed flow visualization. The cause is attributable to the different rib arrangements and flow types between the two cases. The flow fields studied in the present work are spatially periodic duct flow with a rib array mounted on one duct wall whereas those investigated by Yamada and Osaka are boundary layer flows with a single rib mounted on a flat plate.

For a still lower value of $\beta = 22\%$, the multi-jets become weaker and the size of reattachment induced recirculating flow region augments toward $X/H = 0$, as shown in Fig. 6. As β is continuously lowered to 10 percent, Fig. 7 indicates that the multi-jets behind the perforated ribs eventually vanish and the

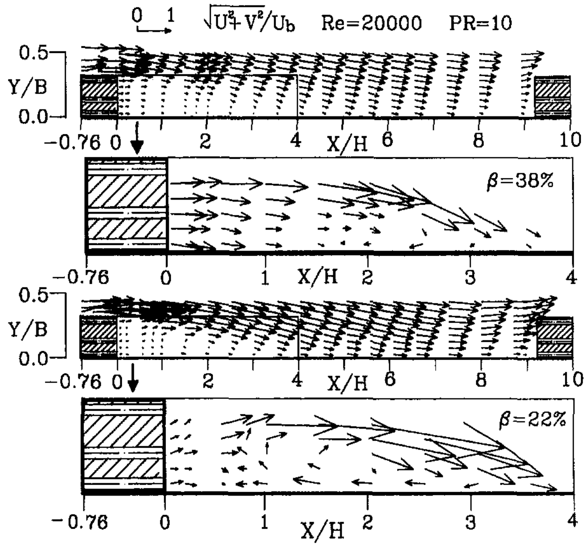

Fig. 6 Longitudinal mean flow patterns in terms of velocity vectors for $\beta = 38$ percent and $\beta = 22$ percent (see Fig. 5 caption)

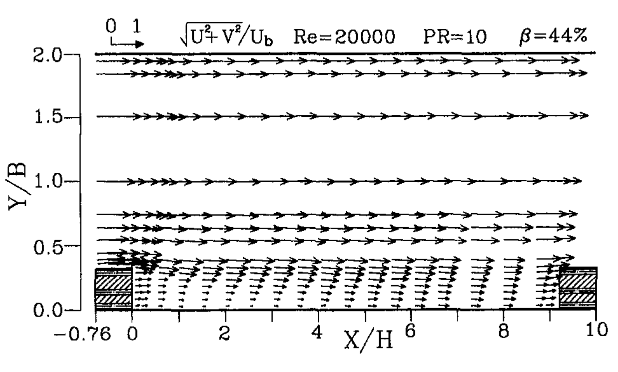

Fig. 5 Longitudinal mean flow pattern in terms of velocity vectors for $\beta = 44$ percent (Uncertainty in U/U_b and V/U_b: less than ±3.2 percent)

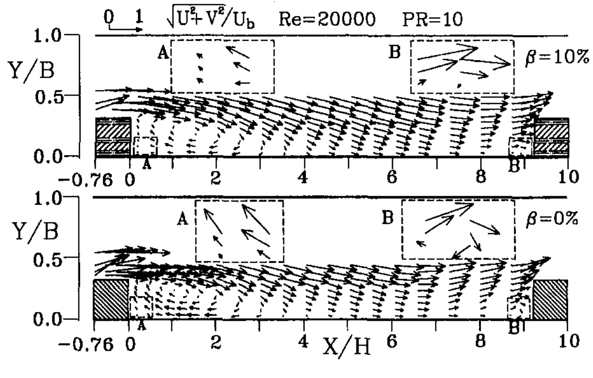

Fig. 7 Longitudinal mean flow patterns in terms of velocity vectors for $\beta = 10$ and 0 percent (see Fig. 5 caption)

flow pattern is effectively similar to that of impermeable ribs (Fig. 7, $\beta = 0\%$). In other words, there exists also a critical range of rib open area ratio ($10\% < \beta_{c2} < 22\%$) below which the perforated ribs are effectively impermeable and the flow pattern is typified by the well organized wake recirculating bubble and corner vortex at the rib bottom front corner. Previous laser holographic interferometry study by the present leading author (Hwang and Liou, 1994) reported the permeability limit of the perforated ribs as a function of β and Reynolds number based on flow visualization of interferograms. According to their critical curve, β_{c2} is 20% at $\mathrm{Re} = 2 \times 10^4$ which is consistent with the present LDV results $10\% < \beta_{c2} < 22\%$.

It is noted that the steadiness of the mean flow fields illustrated in Figs. 5 to 7 should be examined since the LDV method used is a point measurement scheme. One way is to compare the mean velocity resultant vector field of two-component LDV measurements with that of one-component LDV measurements. The differences are found to be within 3.5%.

Figure 8 presents a summary of the related parameters characterizing the above discussed flow fields. The reattachment length X_R is a well-known parameter often used for computational comparison since heat transfer rate around the reattachment point is maximum. It is the streamwise distance ΔX from the flow separation point to the reattachment point, as depicted on the top portion of Fig. 8. Historically, X_R behind a backward-facing step is a weak function of Re for turbulent flows. X_R in the present work is found to be weakly dependent on the value of β although it reveals a two-stage feature with about $X_R/H = 3.8$ for $\beta = 0\%$ and 10% and $X_R/H = 3.4$ for $\beta = 22\%$ and 38%. The stage difference in the reattachment length is due to the presence of above-mentioned critical range $10\% < \beta_{c2} < 22\%$ above which the multi-jets are present whereas below which absent. Without multi-jets, $\beta < \beta_{c2} < 22\%$, the fluids in front of the rib have to flow over the rib top with a larger acceleration, a contraction throat occurring slightly downstream of the rib and, in turn, a slightly longer reattachment length, as shown in Fig. 7. Also, comparing Fig. 7 with Fig. 6, one finds that the height of the primary recirculation zone is larger than the rib height for $\beta = 0\%$ and 10% whereas it is lower for $\beta = 22\%$ and 38%. Note that both $\beta = 0$ and $\beta = 10\%$ cases have the same $X_R = 3.8H$ since they are impermeable and operated at the same Re. For the cases of $\beta = 22$ and $\beta = 38\%$, the ribs are permeable and the same $X_R = 3.4H$ is still found although the flow rates over the rib top are different between the two cases. The reason is the weak dependence of X_R upon Re for ribbed turbulent duct flows, as reported by Liou and Kao (1988). Once the multi-jets emerge from the rib rear edge, $\beta > \beta_{c2} > 10\%$, the primary recirculation zone is pushed downstream by the multi-jets. The larger the value of β, the stronger the multi-jets are and the further the primary recirculation zone or its front stagnation point S_p (Fig. 8) is pushed. Also recall that the reattachment length is a weak function of β. As a result, the length of the primary recirculation zone, L_R, decreases with increasing β and eventually vanishes at $\beta = 44\%$, as shown in Fig. 8. Similarly, the absolute value of the nondimensionalized maximum negative streamwise mean velocity in the primary recirculation zone, U_{mn}/U_b in Fig. 8, decreases from 0.34 at $\beta = 0\%$ to only 0.06 at $\beta = 38\%$, and finally 0 at $\beta = 44\%$. The value 0.34 at $\beta = 0\%$ in the present study is close to 0.3 reported by Liou et al. (1993a) for the fully developed turbulent flow in a channel with two opposite square rib-disturbed walls.

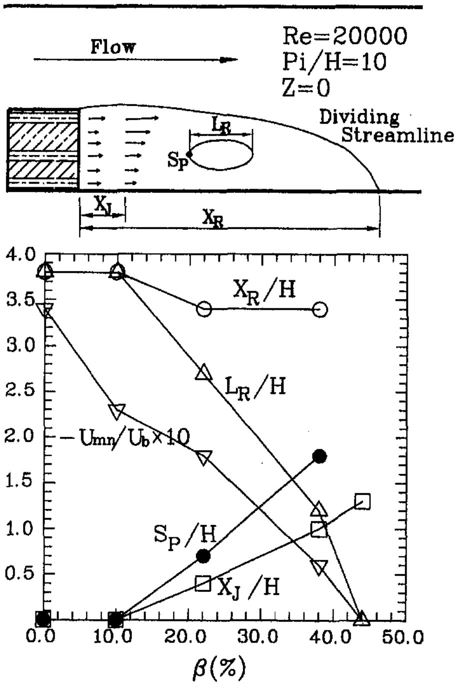

Fig. 8 Variation of reattachment length (X_R), recirculation zone length (L_R), stagnation point (S_P), jet effective length (X_J), and maximum negative axial mean velocity (U_{mn}) with rib open area ratio (β) (Uncertainty in X_R and L_R: less than ±0.2 mm; in S_P and X_J: less than ±0.1 mm)

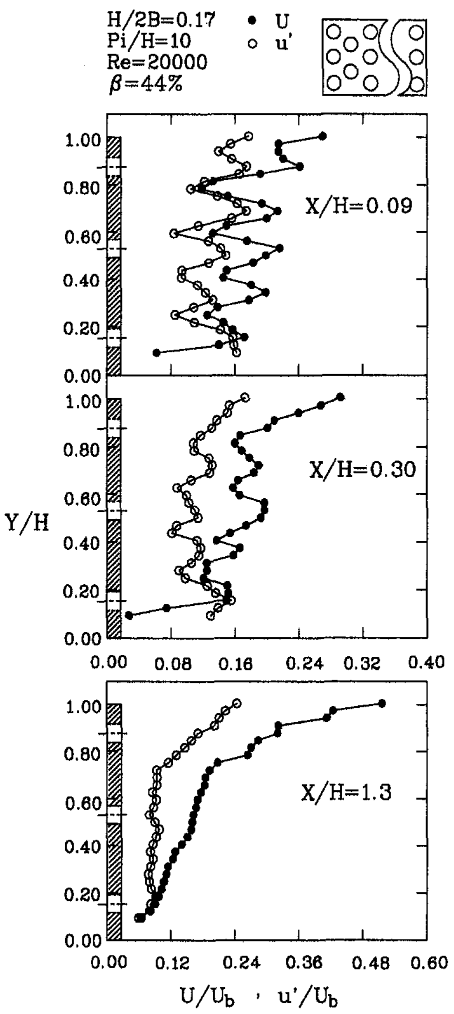

Fig. 9 Streamwise evoluation of axial mean velocity and turbulence intensity profiles of multi-jets (Uncertainty in U/U_b: less than ±3.2 percent; in u'/U_b: less than ±4.4 percent)

The detailed axial mean velocity and turbulence intensity profiles of the aforementioned multi-jets, featured by zigzags, and their streamwise evolution are depicted in Fig. 9 for the case of $\beta = 44$ percent. The multi-jets interact each other due to the Coanda effect such that zigzags gradually become smooth as X/H is increasing up to $X/H = 1.3$. In the present study $X/H = 1.3$ is defined as the effective jet length, designated as X_j, for $\beta = 44$ percent. As expected, Fig. 8 shows that X_j increases with increasing β for $\beta > \beta_{c2} > 10$ percent. It is worth mentioning here that X_j does not increase with decreasing β since the perforated rib gradually becomes impermeable and, hence, the jet velocity becomes smaller when β is decreased, as evidenced by Fig. 6. Note that in the critical range $38\% < \beta_{c1} <$ 44 percent, above which (i.e., $\beta > \beta_{c1} > 38\%$) the primary recirculation zone is absent, X_j only needs to be about one third of the reattachment length X_R. It is also worth mentioning here that the multi-jets induced high turbulence intensities (Fig. 9) are closely related to the enhancement of heat transfer in the channel roughened by perforated ribs, as will be addressed shortly. Quantitatively, the multi-jets induced axial turbulence intensities u'/U_b range from 8 to 18 percent which is about 7 to 15 times those in the bulk flow. For reference purpose, at $X_r = 0$ reference station (Fig. 1) the u'/U_b in the core flow region (90% of cross-sectional area) and boundary layer (5% of channel height) are within 1.2% and 9%, respectively.

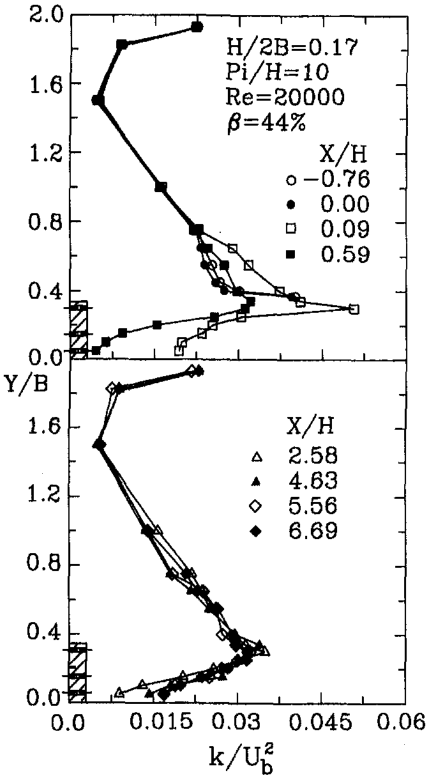

Fig. 11 Turbulent kinetic energy profiles at various lateral cross-sections for β = 44 percent (see Fig. 10 caption)

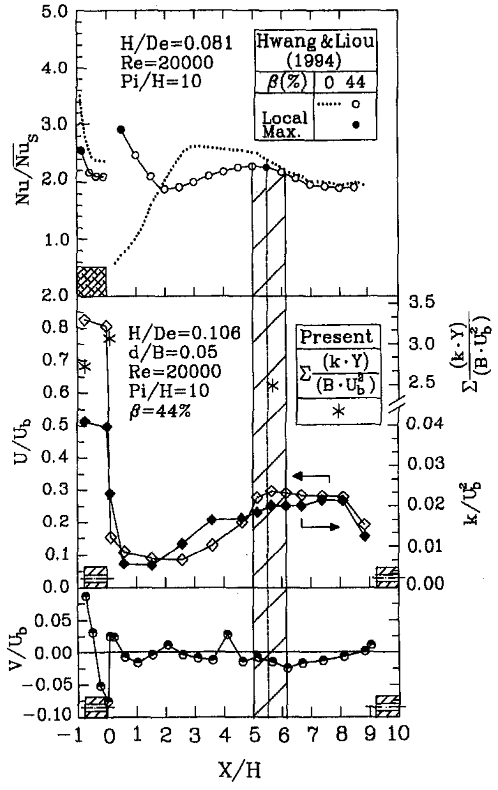

Fig. 10 Distributions of local Nusselt number, near wall mean velocity components and turbulent kinetic energy (Uncertainty in k/U_b^2: less than ±7.4 percent)

Turbulent Fluid Flow and Heat Transfer. One of the purposes of the present turbulent fluid flow study is to provide rationale for the corresponding local heat transfer coefficient distribution shown in Fig. 10. As can be seen, the local heat transfer deterioration around the rib bottom rear corner of the solid-type ribs ($\beta = 0$ percent, dashed line) has been improved significantly by using the perforated ribs ($\beta = 44\%$, open circle). For $\beta = 44$ percent the peak Nu/Nu_s (solid circle) located around $X/H = 5 \sim 6$ is due to the expanding flow's approaching the bottom duct wall, as shown by the near wall ($d/B = 0.05$ or 1 mm from the wall) negative transverse mean velocity (V/U_b) distribution between $X/H = 5$ and $X/H = 8$ in Fig. 10 and vector field in Fig. 5. The approaching flow reduces the boundary layer thickness around $X/H = 5 \sim 6$ and has a higher near wall convection mean velocity U/U_b and turbulent kinetic energy k/U_b^2. The second peak Nu/Nu_s appears near the rib top front corner results from the near-rib large convective mean velocity U/U_b and turbulent kinetic energy k/U_b^2 (Fig. 10) associated with the steep flow turning as indicated by the large V/U_b at corresponding position (Fig. 10). The highest peak Nu/Nu_s occurs immediately downstream of the perforated ribs, whose appearance cannot be illustrated by the near wall U/U_b, V/U_b, and k/U_b^2 distributions depicted in Fig. 10 and needs to be further elaborated on. First, the perforations augment the rib heat transfer area. The conduction removes the heat from the heated wall near the rib bottom rear corner and the conducted heat is subsequently convected away by the flow over the rib and through the perforations. Second, the multi-jets emerging from the perforated rib's rear edge tend to interact and merge each other within $X/H < 1.3$, as addressed previously. The emergence and merger of multi-jets lead to relatively high turbulent kinetic energy distribution immediately downstream of perforated ribs, as shown by Fig. 9 and Fig. 11, especially at $X/H = 0.09$. Third, the * symbol in Fig. 10 represents the duct height averaged turbulent kinetic energy. The results are consistent with the solid circle on the Nu/Nu_s curve. The above three points illustrate the appearance of the highest peak Nu/Nu_s immediately behind the perforated ribs although the heat transfer results were made with perforated square ribs whereas the fluid flow data were taken with perforated rectangular ribs ($W_r/H = 0.76$). There is one more point worthy of addressing. In Fig. 10, it seems that the Nusselt number with perforated ribs is lower than with solid ones in some places. However, the overall heat transfer coefficients around the perforated and solid ribs had been compared by integration to show the heat transfer improvements attained by the perforated ribs in the work of Hwang and Liou (1994) using laser holographic interferometry.

As mentioned in the Introduction, the heat transfer investigation of β effects in the work of Hwang and Liou (1994) con-

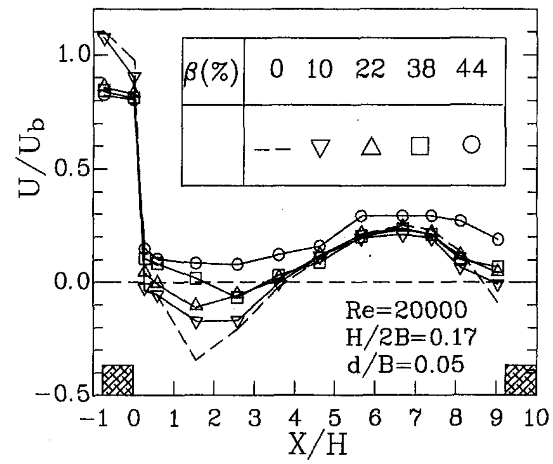

Fig. 12 Near wall axial mean velocity distributions (d = normal distance from wall) (see Fig. 5 caption)

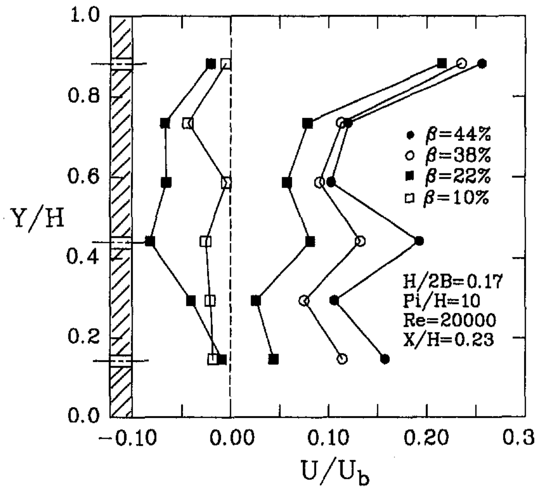

Fig. 14 Streamwise mean velocity profiles at a short distance behind the perforated rib for various rib open area ratios

cluded that $\beta = 44\%$ provided the best thermal performance under the same pumping power condition, i.e., both heat transfer rate and friction loss are considered. Among $\beta = 0\%$, 10%, 22%, 38%, and 44% examined in the present study, $\beta = 44\%$ provides the largest augmentation of heat transfer area due to perforations and the highest turbulent kinetic energy immediately behind the rib due to the strongest multi-jets emerging from the rib rear edge. In addition, Fig. 12 depicts that $\beta = 44\%$ gives the highest positive convective mean velocity near the wall for the region in between ribs. Moreover, the friction factor results of Fig. 4 indicate that a minimum friction loss is associated with $\beta = 44\%$. Consequently, our fluid dynamic study supports the previous heat transfer conclusion of the best rib open area ratio of $\beta = 44$ percent for heat transfer augmentation under the same pumping power condition.

Reynolds Shear Stress and Isotropy. It is well known that heat transfer is affected by momentum transfer and turbulent momentum transfer is related to Reynolds stresses. In addition, shear in the mean flow is a common source of energy for turbulent velocity fluctuations. Turbulence modelling of the relevant fluid flow and heat transfer needs a better understanding of the shear stress distribution. The contour maps of the dimensionless Reynolds shear stress for $\beta = 10\%$ and 38% are thus depicted in Fig. 13. Large values of $-\overline{uv}/U_b^2$ are distributed along the shear layers where steep mean-velocity gradients prevail (Figs. 6 and 7). As previously discussed, in the case of $\beta = 10\% < \beta_{c2}$ the perforated ribs are effectively impermeable and the main shear layer is the separation-bubble shear layer originating from the rib top. The peak value of $0.08U_b^2$ is found to occur early in the separation shear layer, along a narrow and short horizontal segment of about $1H$ in length and $1H$ above the bottom wall. In contrast, in the case of $\beta = 38\% > \beta_{c2}$ the perforated ribs are permeable and the multi-jets emerging from the rear edge interact each other and with the main separation-bubble shear layer. As a result, the peak value of $0.09U_b^2$ extends the entire region in-between ribs along a band of $0.7H \pm 0.2H$. In general, the $-\overline{uv}/U_b^2$ level of $\beta = 38\%$ is higher than that of $\beta = 10\%$. In particular, immediately behind the rib, $0 < X/H < 2$, the $-\overline{uv}/U_b^2$ level of $\beta = 38\%$ is nearly two times that of $\beta = 10\%$ due to the higher mean velocity gradients associated with the emerging jets for the former, as shown in Fig. 14. This latter observation is consistent with the heat transfer improvement of permeable perforated ribs ($\beta > \beta_{c2}$ or β = 22, 38, and 44 percent) over impermeable ribs ($\beta < \beta_{c2}$ or β = 0 and 10 percent) for the region $0 < X/H < 2$ addressed earlier in Fig. 10.

From the turbulence modelling point of view, it is important to know the relative magnitudes of three velocity fluctuating components. Figure 15 shows that the three turbulence intensity components are as high as 19 to 24 percent of U_b in the rib top ($Y/B = 0.34$) separated shear layer and, in general, the turbulence is not isotropic with $u' > w' > v'$. The latter trend is similar to that reported in the fully developed smooth duct flow.

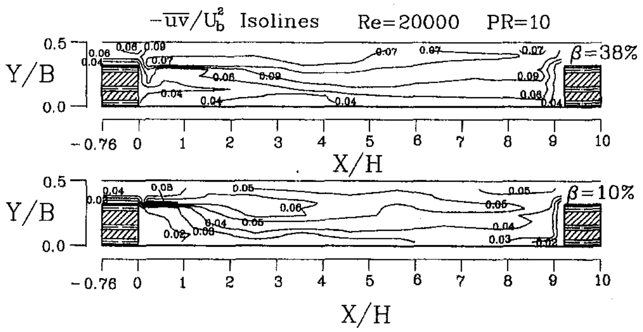

Fig. 13 Contours of Reynolds shear stress for β = 10 and 38 percent (Uncertainty in $|-\overline{uv}|/U_b^2$: less than ±4.8 percent)

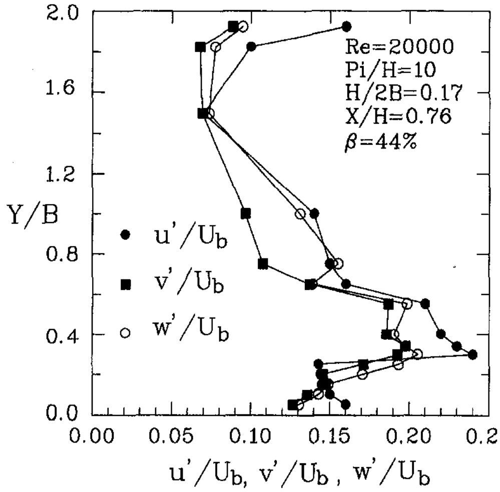

Fig. 15 Profiles of three turbulence intensity components at $X/H = 0.76$ and $Z = 0$ for $\beta = 44\%$ (Uncertainty in u'/U_b, v'/U_b, and w'/U_b: less than ±4.4 percent)

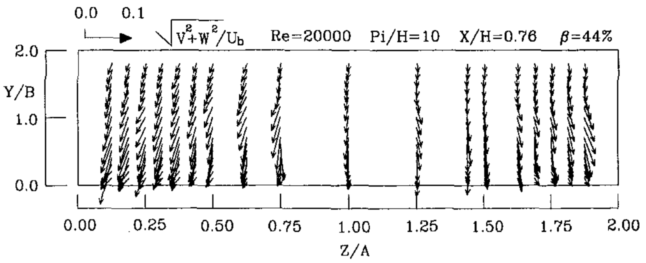

Fig. 16 Secondary flow vectors in $X/H = 0.76$ plane for $\beta = 44$ percent (Uncertainty in $(V^2 + W^2)/U_b^2$: less than ±3.2 percent)

Flow Characteristics in Lateral Cross-Section. The secondary flow pattern generally varies with the lateral cross-sectional shape (Brundrett and Baines, 1964). The classical secondary flow pattern in a smooth channel under the fully developed condition is characterized by eight triangular vortex cells. It is interesting to see how the secondary flow pattern changes as a perforated rib array is mounted on one of the duct walls. Figure 16 is a vector plot of the measured results of the transverse and spanwise mean velocity components in $X/H = 0.76$ cross-section for the best thermal performance case ($\beta = 44$ percent). It is observed that the mean secondary flow pattern lacks of well-organized recirculation cells due to the presence of multi-jets emerging from the rib rear edge. The mean secondary flow reveals a downward and slightly spanwise motion. This downward motion is consistent with the mean flow field in the longitudinal cross-sectional plane shown in Fig. 5. Similar mean secondary flow pattern is found for other lateral cross-sectional planes. It is well worth mentioning here that the above presented secondary flow patterns for duct flows with $\beta = 44$ percent is different from that for duct flows with $\beta = 0$ percent. Previous hot wire measurements of secondary flow in a rectangular duct with an array of solid square ribs ($\beta = 0\%$) (Fujita et al., 1989) indicated the presence of two large counterrotating longitudinal vortices near side walls. The LDV measurements of ribbed channel flows with solid rib arrays ($\beta = 0$ percent) mounted on two opposite walls (Liou et al., 1993a) showed the presence of four longitudinal vortices. Quantitatively, the magnitudes of V and W in lateral cross-sections are only 0.02 to 0.1 U_b in the present case of $\beta = 44$ percent and approximately four times those in the smooth channel (Speziale, 1986) and 0.4 times those in the duct with a solid rib array (Fujita et al., 1989).

Conclusions

The following new and significant fluid dynamic information is drawn from the data presented:

1. There exists a critical range of rib open area ratio, 38 percent < β_{c1} < 44%, above which there are no primary and corner recirculation zones behind and ahead of perforated ribs, respectively.
2. There exists a second critical range of rib open area ratio, 10 percent < β_{c2} < 22 percent, above which the perforated ribs are permeable and below which impermeable.
3. There exists a critical range of rib open area ratio, 38 percent < β_{c1} < 44 percent, below which and above a second critical range of rib open area ratio, 10 percent < β_{c2} < 22 percent, the corner vortex ahead of the rib is still absent but a primary recirculation zones appears in the region in-between ribs. The center of the primary recirculation zone moves upstream from near the reattachment point and its size extends toward the preceding rib as the rib open area ratio is decreased toward β_{c2}.
4. Below β_{c2}, both the primary recirculation zone behind the rib and the corner vortex ahead of the rib are present. Moreover, the primary recirculation zone is now equivalent to the separation bubble originating from the rib top shear layer with its length equaling the reattachment length.
5. The three local peaks in the heat transfer coefficient distribution reported previously are appropriately explained in the present study in terms of the expanding flow's approaching the duct wall in-between ribs, the large convective velocity and turbulent kinetic energy associated with steep flow turning around the rib top front corner, and in particular the augmented turbulent kinetic energy due to the interaction of multi-jets issuing from the rear edge of the perforated ribs. The above fluid dynamics factors together with the maximum augmented heat transfer area and minimum friction loss due to perforations provide the rationale for the previous heat transfer conclusion of the best rib open area ratio of $\beta = 44$ percent for heat transfer augmentation under the same pumping power condition.
6. For $\beta = 44$ percent, measurements in the cross-sectional plane indicate that transverse and spanwise mean velocity components are only 0.02 to 0.1 times bulk mean velocity and about 0.4 times those in the duct with a solid rib array.

Acknowledgments

Support for this work was provided by the National Science Council of the Republic of China under contracts NSC83-0401-E007-014 and NSC84-2212-E007-049.

References

Brundrett, E., and Baines, W. D., 1964, "The Production and Diffusion of Vorticity in Duct Flow," *Journal of Fluid Mechanics*, Vol. 19, pp. 375–394.

Castro, I. P., 1971, "Wake Characteristics of Two-Dimensional Perforated Plates Normal to an Air-Stream," *Journal of Fluid Mechanics*, Vol. 46, part 3, pp. 599–609.

Chang, B. H., and Mills, A. F., 1993, "Turbulent Flow in a Channel with Transverse Rib Heat Transfer Augmentation," *International Journal of Heat and Mass Transfer*, Vol. 36, No. 6, pp. 1159–1169.

Durst, F., Melling, A., and Whitelaw, J. H., 1976, *Principles and Practice of Laser-Doppler Anemometry*, Academic Press, New York, Chapter 9.

Fujita, H., Yokosawa, H., and Hirota, M., 1989, "Secondary Flow of the Second Kind in Rectangular Ducts with One Rough Wall," *Experimental Thermal and Fluid Science*, Vol. 2, pp. 72–80.

Hwang, J. J., and Liou, T. M., 1994, "Augmented Heat Transfer in a Rectangular Channel with Permeable Ribs Mounted on the Wall," ASME *Journal of Heat Transfer*, Vol. 116, pp. 912–920.

Ichimiya, K., and Mitsushiro, K., 1988, "Enhancement of the Heat Transfer of Wide Temperature Range in a Narrow Passage," *Proceedings of Experimental Heat Transfer, Fluid Mechanic, and Thermodynamics*, Shah, R. K., Ganic, E. N., and Yang, K. T., eds., Dubrovnik, Yugoslavia, pp. 659–664.

Ichimiya, K., Katayama, M., Miyazawa, T., and Kondoh, H., 1991, "Experimental Study on Effects of a Single Porous-Type Roughness Element in a Parallel-Plate Duct," *Experimental Heat Transfer*, Vol. 4, pp. 319–330.

Liou, T. M., and Kao, C. F., 1988, "Symmetric and Asymmetric Turbulent Flows in a Rectangular Duct with a Pair of Ribs," ASME JOURNAL OF FLUIDS ENGINEERING, Vol. 110, pp. 373–379.

Liou, T. M., and Lin, J., 1988, "Measurements of Turbulent Flow in a Duct with Repeated Ribs Applied to Two Opposite Walls," *Journal of the Chinese Institute of Engineers*, Vol. 11, No. 4, pp. 319–326.

Liou, T. M., Chang, Y., and Hwang, D. W., 1990, "Experimental and Computational Study of Turbulent Flows in a Channel with Two Pairs of Turbulence Promoters in Tandem," ASME JOURNAL OF FLUIDS ENGINEERING, Vol. 112, pp. 302–310.

Liou, T. M., and Hwang, J. J., 1992, "Turbulent Heat Transfer Augmentation and Friction in Periodic Fully Developed Channel Flows," ASME *Journal of Heat Transfer*, Vol. 114, pp. 56–64.

Liou, T. M., Hwang, J. J., and Chen, S. H., 1992, "Turbulent Transport Phenomena in a Channel with Periodic Rib Turbulators," *AIAA Journal of Thermophysics and Heat Transfer*, Vol. 6, No. 3, pp. 513–521.

Liou, T. M., Wu, Y. Y., and Chang, Y., 1993a, "LDV Measurements of Periodic Fully Developed Main and Secondary Flows in a Channel with Rib-Disturbed Walls," ASME JOURNAL OF FLUIDS ENGINEERING, Vol. 115, pp. 109–114.

Liou, T. M., Hwang, J. J., and Chen, S. H., 1993b, "Simulation and Measurement of Enhanced Turbulent Heat Transfer in a Channel with Periodic Ribs on

One Principal Walls," *International Journal of Heat and Mass Transfer,* Vol. 36, No. 2, pp. 507–517.

Speziale, C. G., 1986, "The Dissipation Ratio Correlation and Turbulent Secondary Flows in Noncircular Ducts," ASME JOURNAL OF FLUIDS ENGINEERING, Vol. 108, pp. 118–120.

Tanasawa, T., Nishio, S., and Takano, K., 1984, "High-Performance Surface for Forced-Convection Heat Transfer Using Novel Turbulence Promoters," ASME Paper 84-HT-69.

Tanasawa, T., Nishio, S., Takano, K., and Tado, M., 1983, "Enhancement of Forced convection Heat Transfer in a Rectangular Channel Using Turbulence Promoters," *Proceedings ASME-JSME Thermal Engineering Joint Conference,* pp. 395–402.

Yamada, H., and Osaka, H., 1992, "Flow Around a Permeable Rectangular Plate Standing Vertically on the Flat Wall, 2nd report, Effects of the Aspect and the Open Area Ratios," *Trans. JSME,* Vol. 56, No. 546, pp. 120–128 (in Japanese).

K. Balatka
Lecturer.

S. Mochizuki
Professor.

Department of Mechanical Systems Engineering,
Tokyo University of A. & T.,
Koganei-shi, Naka-cho,
184-8588 Tokyo, Japan

Numerical Analysis of the Flow in an Annular-Conical Passage

The purpose of this paper is to bring new insights into the flow phenomena in an annular-conical passage, which—as previously disclosed experimentally—forms a toroidal-vortex street. The two-dimensional, time dependent Navier-Stokes equations are solved with an explicit finite-difference scheme based on the Marker and Cell method. Solutions are obtained for four different cone apex angles (β = 60, 90, 120, and 180 deg). For each apex angle three cases of different passage spacing are computed. The Reynolds number ranges from Re = 100 ~ 5000. The stress is put on the initiation and subsequent development of the toroidal-vortex street. Critical Reynolds number for several parameter settings is determined and compared with experimental results.

1 Introduction

The motivation for the present research comes from the previously, broadly studied problem of the flow behavior in a passage between two parallel disks. An interested reader is encouraged to consult the works of Jackson and Symmons (1965), Ishizawa (1965, 1966), Raal (1978), Mochizuki (1993), and others.

The characteristic feature of a channel between two parallel disks is that the cross-sectional area increases in the flow direction. This may expose the flow to an adverse pressure gradient which, in the presence of wall friction, is sufficient to form separation and reverse flow with reattachment farther downstream (assuming the Reynolds number is larger than a certain critical value). Although some speculations over a possible instability in the flow have been made by Raal (1978), the separation was generally considered to form steady annular bubbles close to the passage inlet, as reported in Ishizawa (1965, 1966) and Raal (1978). In fact, this could not have been otherwise, since the authors worked with steady equations. The instability predictions were confirmed by Mochizuki and Yang (1985) who carried out an extensive experimental and numerical investigation on the flow between two parallel disks. Carrying out flow visualization experiments they disclosed that when the Reynolds number is gradually increased the flow forms three distinctive patterns:

1. Steady flow without any separation of the shear layer when $Re < Re_c$.
2. Self-sustained oscillating flow that decays downstream, $Re_c < Re < Re_t$.
3. Self-controlled flow fluctuations followed by a laminar-to-turbulent transition and subsequent reverse transition for $Re > Re_t$.

Re_c and Re_t denote the critical and transition Reynolds numbers, respectively. The flow unsteadiness is in the second and third case caused by a vortex street consisting of vortices that periodically separate from alternate side walls. The visual observations are supported by hot-wire measurements that confirm periodic variations in radial velocities. Solutions of the unsteady vorticity-transport equation exhibiting periodic separation-bubble generation are also presented. The computational results were in partial agreement with the experimental observations. The flow channel between two parallel disks is one of the two extreme cases of a more general flow passage shape, that is a channel between two coaxial cones with parallel walls. Assuming the cone apex angle β is chosen to be 180 deg, one obtains the channel between two parallel disks. On the other hand, if the apex angle is set to 0 deg a channel between two concentric cylinders is formed. The flow passage with β = 0 deg, as can be expected, does not produce any instability such as vortex shedding. Since the problem of what happens when the cone apex angle β is set to be between the two extreme cases 0 deg and 180 deg has not, until recently, been addressed, Balatka et al. (1995, 1996) started systematic experimental investigation of the flow in an annular-conical passage with straight and parallel walls. The annular-conical passage is widely used in various technical applications such as a valve of an automobile engine or a poppet nozzle used for direct fuel injection into the cylinder of a gasoline engine, etc. (One of the crucial factors for improving fuel combustion is to advance the atomization process, which might also be affected by the behavior of flow passing through an annular-conical passage in a valve. The great efforts that are being made by the automobile industry to produce a clean and efficient engine even further underline the importance of studying the flow behavior inside the annular-conical passage.)

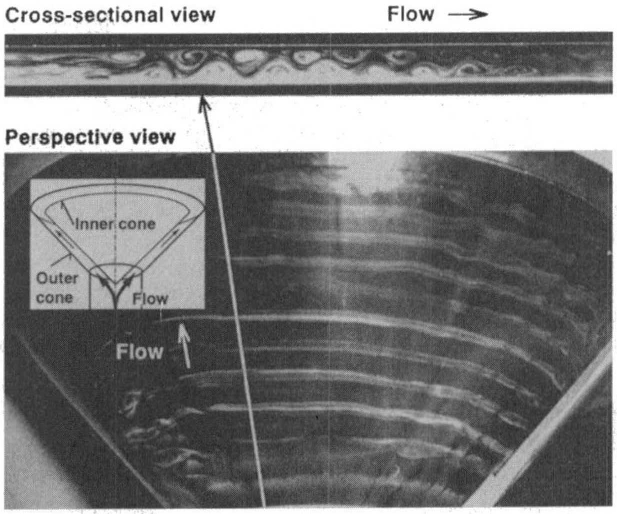

Fig. 1 Perspective and cross-sectional view of the toroidal-vortex street, Re = 1200, cone apex angle β = 90 deg, nondimensional passage spacing ψ = 0.3. The flow is supplied from a straight inlet pipe into the passage formed between the inner and outer cone.

Contributed by the Fluids Engineering Division for publication in the JOURNAL OF FLUIDS ENGINEERING. Manuscript received by the Fluids Engineering Division July 23, 1996; revised manuscript received February 25, 1998. Associate Technical Editor: M. M. Sindir.

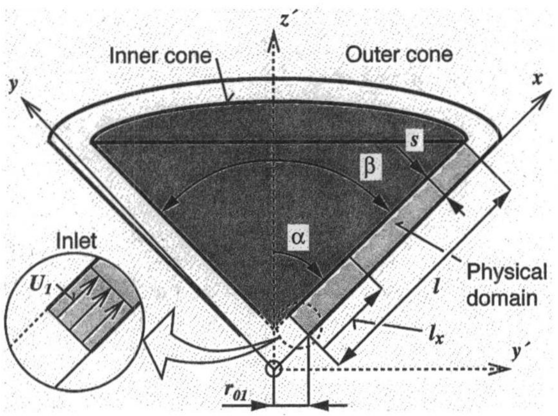

Fig. 2 Sectional view of the annular-conical passage and location of the two-dimensional physical domain on which the numerical modeling is performed. The flow entering the flow passage is assumed to have a uniform velocity profile with the velocity U_1.

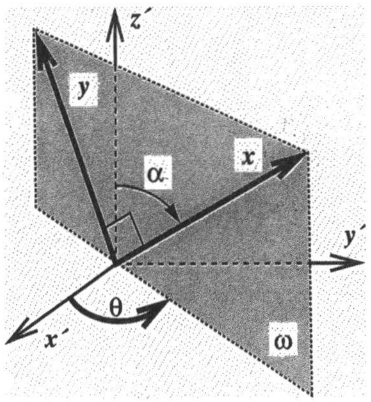

Fig. 3 Conical coordinate system. The Cartesian system is represented by (x', y', z') while the conical coordinates are denoted as (x, y, θ). Note that the x and y coordinates are always perpendicular and rotate around the cartesian within the plane ω. The x axis is set at an angle α from the Cartesian z' axis. (Compare also with Fig. 2.)

The presented studies by Balatka et al. (1995, 1996) showed that the flow behavior in the annular-conical passage is rather complicated due to a flow separation caused by an adverse pressure gradient, which is basically induced by the geometry of the flow passage. The flow visualization experiments revealed that the flow separation forms a vortex street with axially symmetric toroidal vortices periodically generated on alternate sidewalls of the flow passage, as shown in Fig. 1. This phenomenon is similar to that formerly observed by Mochizuki and Yang (1985). The flow phenomenon (termed here as toroidal-vortex street or self-sustained oscillating flow) occurs in a certain range of the Reynolds numbers during the transition of flow from the steady laminar regime to turbulence. Thus the flow can be approximately divided into three regimes:

1. Steady laminar flow
2. Self-sustained oscillating flow
3. Turbulent flow.

In spite of efforts taken, it was impossible to determine by the experiments whether the instability in the form of toroidal-vortex street is fundamentally formed by the annular-conical passage or occurs as a result of certain upstream history effects. It is one of the objectives of this paper to carry out a "pure" numerical experiment which could help answer this question. Due to many geometrical parameters that might influence the flow characteristics, extensive experimental study would be required to provide a general description of the flow in the annular-conical passage. Numerical analysis makes this more feasible and another objective of the present study is to develop a computational scheme which can easily treat arbitrary shapes of the annular-conical passage and thus provide a wide range of information on the flow behavior. The present work covers four different apex angles (β = 60, 90, 120, and 180 deg) and three different passage spacings (ψ = 0.2, 0.3, and 0.4). The stress is put on the first two flow regimes where the critical Reynolds number, which indicates the boundary between laminar flow and the onset of the self-sustained oscillating flow, is investigated in relation to the apex angle and a dimensionless passage spacing. The Reynolds number ranges from Re = 100 to Re = 5000. The numerical results are then compared with experimental results. Since the flow visualization experiment revealed strong two-dimensional character of the flow phenomenon, the computational scheme is derived and used in two dimensions as well.

2 Numerical Modeling

2.1 Dimensionless Parameters and Conical Coordinates.

Figure 2 shows the sectional view of the annular-conical flow passage and the geometry of a physical domain on which the equations are solved. The annular-conical passage is fitted into a conical coordinate system presented in Fig. 3. This figure also shows notation used to describe the geometry of the annular-conical passage. Full geometry specification of such a passage requires a set of three independent nondimensional geometric parameters. A convenient set used in the present work consists of the apex angle β, the nondimensional spacing ψ, and the nondimensional length φ as defined in the following equations:

$$\psi = \frac{s}{r_{01}} \quad \varphi = \frac{l}{r_{01}} \tag{1}$$

The Reynolds number used in the present study is defined as:

$$\mathrm{Re} = \frac{U_1 \cdot 2s}{\nu^*} \tag{2}$$

where U_1 denotes the average inlet-flow velocity, $2s$ the hydraulic diameter with s representing the cone spacing, and ν^* is the kinematic viscosity of air.

Nomenclature

C = geometric parameter (1)
f = separation frequency
l = flow passage length (m)
l_x = distance from inlet (m)
p = pressure (1)
r_{01} = inlet radius (m)
Re = Reynolds number (1)
s = cone spacing (m)
Sl = Strouhal number
U = mean local flow velocity (m/s)
U_1 = inlet flow velocity (m/s)
u = x-dir. velocity component (1)
v = y-dir. velocity component (1)
x', y', z' = cartesian coordinates
x, y, θ = conical coordinates
$\alpha = \beta/2$ (1)
β = cone apex angle (1)
ϵ = SOR tolerance (1)
ω = plane of the x and y coordinates
φ = nondimensional length (1)
φ_x = nondim. distance from inlet (1)
ν^* = kinematic viscosity ($\mathrm{m^2/s}$)
θ = azimuth angle (1)
ψ = nondimensional spacing (1)

The conical coordinate system, Fig. 3, which was developed by the authors, is described as follows: Coordinates x and y are perpendicular to each other and lie in the plane ω which also includes the abscissa z' of the cartesian coordinates (x', y', z'). Remaining perpendicular, the x and y coordinates can rotate around the coordinate origin. The x axis is chosen to be at an angle α from the Cartesian z' axis. The plane ω can rotate around z' with its position determined by the angle θ. The transformation equations between the Cartesian (x', y', z') and conical (x, y, θ) coordinates are:

$$x' = (x\cdot\sin\alpha - y\cdot\cos\alpha)\cdot\cos\theta$$

$$y' = (x\cdot\sin\alpha - y\cdot\cos\alpha)\cdot\sin\theta$$

$$z' = x\cdot\sin\alpha + y\cdot\cos\alpha \qquad (3)$$

Two-dimensional, incompressible Navier-Stokes equations in conservation form, transformed into conical coordinates are as follows:

$$\frac{\partial u}{\partial t} + \frac{1}{C}\cdot\frac{\partial(C\cdot u^2)}{\partial x} + \frac{1}{C}\cdot\frac{\partial(C\cdot u\cdot v)}{\partial y} + \frac{\partial p}{\partial x} = \mathrm{RHS}_x, \qquad (4)$$

$$\frac{\partial v}{\partial t} + \frac{1}{C}\cdot\frac{\partial(C\cdot u\cdot v)}{\partial x} + \frac{1}{C}\cdot\frac{\partial(C\cdot v^2)}{\partial y} + \frac{\partial p}{\partial y} = \mathrm{RHS}_y, \qquad (5)$$

$$\mathrm{RHS}_x = \frac{1}{\mathrm{Re}}\left(\frac{\partial^2 u}{\partial x^2} + \frac{\partial^2 u}{\partial y^2} + \frac{\sin\alpha}{C}\cdot\frac{\partial u}{\partial x} - \frac{\cos\alpha}{C}\cdot\frac{\partial u}{\partial y} - \frac{\sin^2\alpha}{C^2}\cdot u + \frac{\sin\alpha\cdot\cos\alpha}{C^2}\cdot v\right), \qquad (6)$$

$$\mathrm{RHS}_y = \frac{1}{\mathrm{Re}}\left(\frac{\partial^2 v}{\partial x^2} + \frac{\partial^2 v}{\partial y^2} + \frac{\sin\alpha}{C}\cdot\frac{\partial v}{\partial x} - \frac{\cos\alpha}{C}\cdot\frac{\partial v}{\partial y} + \frac{\sin\alpha\cdot\cos\alpha}{C^2}\cdot u - \frac{\cos^2\alpha}{C^2}\cdot v\right), \qquad (7)$$

where

$$C = x\cdot\sin\alpha - y\cdot\cos\alpha, \quad \alpha = \frac{\beta}{2}. \qquad (8)$$

The continuity equation is given by:

$$\frac{1}{C}\cdot\frac{\partial(C\cdot u)}{\partial x} + \frac{1}{C}\cdot\frac{\partial(C\cdot v)}{\partial y} + \frac{\partial p}{\partial x} = 0 \qquad (9)$$

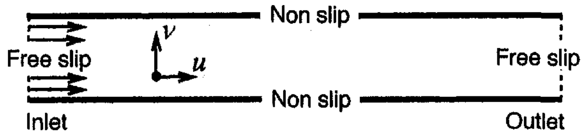

Fig. 4 Boundary conditions used for solving the Navier-Stokes equations on the annular-conical passage

2.2 Boundary Conditions and Mapping. Boundary conditions employed in this analysis are sketched in Fig. 4. Due to the structure of the experimental apparatus it was impossible to measure the inlet velocity profile and apply a similar profile as the inlet boundary condition. The flow changes its direction while passing through a brief contraction in the inlet part of the test section to enter the passage between the two coaxial cones, see Fig. 1. The inlet velocity profile will be neither parabolic nor uniform, however, since it is desired to show that the phenomenon is an inherent feature of the annular-conical flow passage with ideal boundary conditions (without a predeveloped boundary layer), a uniform inlet velocity profile boundary condition is used. Nonslip boundary condition, that is both velocity vector components equal to zero, is assumed at the walls. Since a highly convective flow in a diffuser will be solved, an outlet boundary condition needs to be carefully prescribed. Standard outlet boundary conditions, such as:

$$\frac{\partial u}{\partial x} = 0, \quad \frac{\partial v}{\partial x} = 0 \qquad (10)$$

or the prescription of a fully developed velocity profile (Poiseuille velocity profile), do not apply for solving this problem. The boundary conditions in (10) are unacceptable simply because the velocity in a diffuser flow continuously decreases and up to a certain distance in the downstream direction may still be affected by the upstream fluctuations. Assuming that the self-sustained oscillations are gradually damped as the flow proceeds downstream and the flow finally reaches a steady state with the velocity distribution of a fully developed diffusing flow, the problem of the outlet boundary condition was eventually solved by "sending the mesh exit location to infinity." This was done by applying an infinite to finite mapping to the physical domain. The physical domain was thus divided into two parts. The first part was mapped linearly while the second one used a transformation to set the outlet at infinity. The infinite to finite mapping is accomplished through the following transformation equation:

$$x = \frac{(\xi_0 - \xi_t)^2}{\xi_0 - \xi} + 2\cdot\xi_t - \xi_0 \qquad (11)$$

where ξ is the coordinate which replaces x in the computational domain, ξ_0 is the value of ξ at the mesh exit, and ξ_t denotes the location from where the transformed region begins. The ξ_t parameter is chosen at some reasonable distance downstream of the flow passage inlet. Since at infinity the diffuser has an infinitely large cross-sectional area, the following boundary conditions can be prescribed at the outlet:

$$u = 0, \quad \frac{\partial v}{\partial x} = 0 \qquad (12)$$

The dummy values that are necessary for obtaining the flow field variables near inlet and nonslip wall boundaries are calculated by parabolic extrapolation. A linear extrapolation is sufficient to obtain the outlet dummy values.

2.3 Numerical Procedure. The applied computational scheme is based on the HSMAC method of Hirt and Cook (1972). The scheme utilizes an explicit, second-order accurate Adams-Bashforth type of temporal differencing, third-order accurate upwind differencing for convection, and fourth-order accurate central differencing for diffusion terms.

Before the results shown in this study were computed, an extensive numerical testing was carried out to validate the computational scheme and obtain optimum parameter settings. The computational scheme was first tested on the flow between two parallel plates. Computed profiles for the fully developed laminar flow were compared with an analytical solution and found to differ by less than 1 percent. The equations were then rewritten in the conical coordinates and tested on various grid sizes including 335 × 49, 285 × 39 and 185 × 29 grid for an apex angle $\beta = 90$ deg, passage spacing $\psi = 0.4$ and Re = 5000. The results were compared with the experimental investigation available in Balatka et al. (1995) and Balatka et al. (1996). It was found that the 185 × 29 grid is insufficient to model the experimentally observed phenomenon of the toroidal-vortex

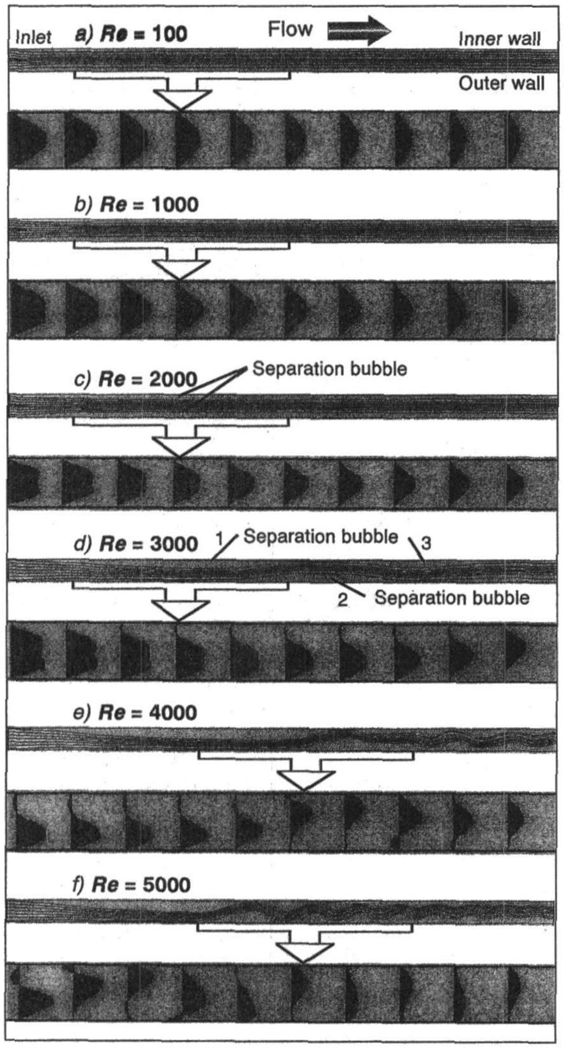

Fig. 5 Streamline patterns and velocity profiles obtained by numerical simulation when the Reynolds number was gradually increased. The results were computed for an apex angle β = 90°, spacing ψ = 0.4 and length $\varphi = \infty$.

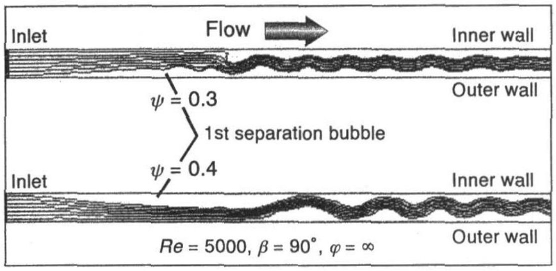

Fig. 6 Comparison of the streamline patterns for two different values of the cone spacing ψ. The flow pattern is seen to be inverted with respect to the inner and outer wall.

street. The grid sizes 335 × 49 and 285 × 39 (and those in between) produced the same qualitative results, as the experimental observations. The vortex shedding frequency varied within two percent while the separation point of the first inner wall separation bubble was found not to change its location when the grid was refined. Since the computational time greatly increases as the grid is refined, grid size 285 × 39 was selected for the numerical investigation. The tolerance for convergence of SOR used to satisfy the continuity equation is $\epsilon = 0.002$, values 5 times greater and 4 times smaller produce negligible changes in the results. Further decrease in ϵ results in immense computational times. The time step is typically set between 0.005 (when vortex shedding takes place) and 0.01 (no vortex shedding) to keep the Courant numbers less than unity. In terms of real time values, such time steps correspond approximately 0.00007 s and 0.0011 s, respectively. The former value was used to compute flows where the vortex shedding with the typical frequency of 6 Hz occurs. To examine solution independence of the initial conditions, the solution for Re = 5000 is obtained in three different ways. First, a final solution was developed from the uniform flow initial condition by gradually increasing the Reynolds number and letting the flow develop for each of the set Reynolds number. Second, a final solution was obtained directly from the uniform flow initial condition and third, a final solution was obtained when assuming a Poiseuille flow throughout the flow passage as an initial condition. These final solutions were the same for all three cases, so we can assume that the results are independent of the initial conditions.

3 Results and Discussion

3.1 Changes in Flow Pattern When Increasing the Reynolds Number. Let us first examine how the flow changes when increasing the Reynolds number. The experimental study Balatka et al. (1996) showed that a steady laminar flow exists in the flow passage for low Reynolds numbers. As the Reynolds number is increased, the flow gradually undergoes transition and, at a Reynolds number of about Re = 400 (β = 90 deg), starts to form a toroidal vortex street.

Computations were performed for each geometry case (ψ = 0.2, 0.3, 0.4 and β = 60, 90, 120 deg) for the following Reynolds numbers: Re = 100, 1000, 2000, 3000, 4000, and 5000. The streamline patterns and selected velocity profiles are shown in Fig. 5. The flow is laminar and steady for Re = 100. When the Reynolds number is increased to Re = 1000, Fig. 5(*b*) the flow forms velocity profiles with inflection points which indicates that the flow has become potentially unstable and that separation can be expected when the Reynolds number is further increased. Indeed, a backflow is detected for the next computed Reynolds number Re = 2000. Two almost symmetric (with respect to the axis in the passage center parallel with the side walls) separation bubbles are formed along both walls near the entrance. They are, however, small and invisible in Fig. 5(*c*). The separation bubbles increase in their size and relocate to form an asymmetric pattern for Re = 3000 as can be seen in Fig. 5(*d*). The flow is at this stage steady, creating three separation bubbles near the flow passage inlet. As the flow proceeds downstream, it reattaches and continues toward the outlet as a steady, laminar flow. Behavior of the flow substantially changes when the Reynolds number is set to Re = 4000, Fig. 5(*e*). The third steady separation bubble breaks down and only the first and second one remain shedding vortices to the downstream region thus producing the vortex street. The toroidal vortex street is well established at Re = 5000 with a regular vortex shedding.

As can be seen in Fig. 5, the first separation bubble is formed at the inner wall. A similar kind of steady separation was, in the case of ψ = 0.4, observed in the experiment as well; however, the first separation bubble was always formed at the outer wall. This is suspected to be caused by the influence of a rounded corner at the transition from the inlet pipe into the test section, see Fig. 1. It is so far unsolved as to why in the numerical simulation for this particular parameter setting, the first separation bubble formed at the inner wall. The authors believe that if an appropriate disturbance is introduced at the opposite wall, the flow pattern will be reversed with the first separation bubble generated at the outer wall.

When the spacing is set to ψ = 0.3, for example, keeping the other parameters the same the separation bubble occurs first at the outer wall see Fig. 6. A similar change in the separation

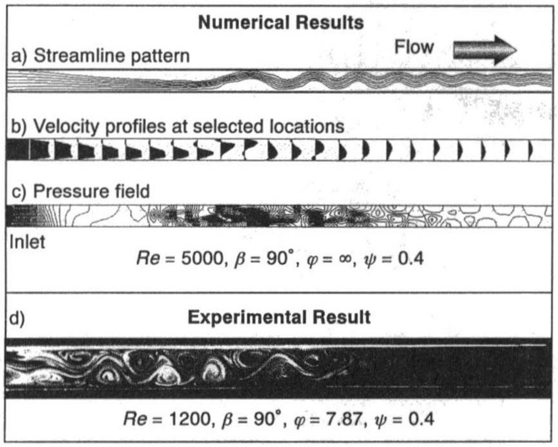

Fig. 7 Toroidal vortex street-comparison with the experiment. (*a*) Shows the streamline pattern, (*b*) depicts the velocity vectors at different locations and (*c*) shows the pressure field. Photograph of the flow phenomenon, obtained during the experimental investigation is shown in (*d*).

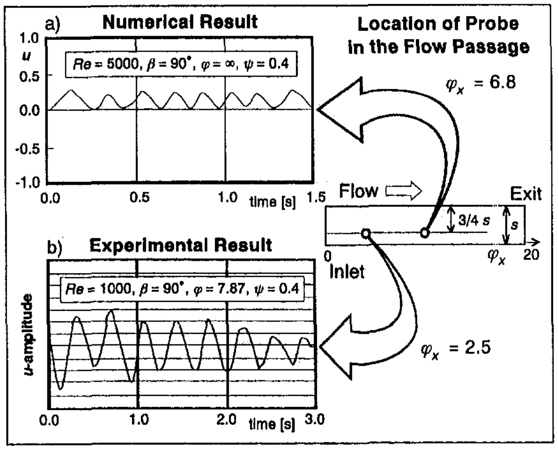

Fig. 8 Time variation of *u*-velocity. Graph (*a*) shows the variation of *u*-velocity obtained by marching solution in time. Graph (*b*) displays the result of hot-wire measurements.

bubble arrangement is also observed when the apex angle β is changed, for instance at 60 deg. This problem of determining whether the first separation bubble is generated on the inner and outer wall depending on where a certain disturbance occurs, or if it depends on the geometrical parameters, may be a good one to investigate further.

3.2 Modeling of the Toroidal-Vortex Street and Comparison With Experiment. One of the major achievements of this work is the gaining of the knowledge that the toroidal-vortex street is formed by the annular-conical flow passage itself and is not the result of an upstream history effect. The toroidal-vortex street exists as one of the solutions of the Navier-Stokes equations even in the case when the ideal boundary conditions (see Fig. 4) are prescribed. This could have never been clarified by the experiment which always suffers from an undefined inlet velocity profile or a random upstream disturbance, for example. The qualitative evidence is given in Fig. 7(*a*), which shows the streamline pattern of the toroidal-vortex street in an annular-conical passage with an apex angle, $\beta = 90$ deg, spacing $\psi = 0.4$ and a Reynolds number, $\mathrm{Re} = 5000$. Figure 7(*b*) displays the computed velocity vectors at several selected locations in the flow and the pressure contours are shown in Fig. 7(*c*). For a comparison, the photograph of the toroidal-vortex street, obtained during the experimental investigation is presented in Fig. 7(*d*). As can be seen, there is a good qualitative similarity between the numerical result and the experimental observation. It is noted, however, that the Reynolds numbers are somewhat different. The toroidal-vortex street in the experiment was observed in the range of $\mathrm{Re} = 400 \sim 2000$ with Reynolds numbers $\mathrm{Re} = 2000$ already displaying the traces of turbulent-like behavior. The numerical simulation predicts the onset of the toroidal-vortex street between $\mathrm{Re} = 3000 \sim 4000$. This difference is believed to be caused by two reasons in particular. First, the numerical simulation is performed under ideal boundary conditions (numerically prescribed) with a uniform profile at the flow passage inlet. This, in comparison with the experiment, makes for better flow stability. Considering the fact that diffusing flows are very sensitive to the upstream conditions of the flow, the increase in the vortex-street-onset Reynolds number seems to be reasonable. In fact, some computations were performed assuming a parabolic velocity profile at the inlet. This yields the vortex-street-onset Reynolds numbers between 300 to 500. Second, certain effects may be expected to arise from treating the flow as axisymmetric, which—strictly speaking—is not true in reality.

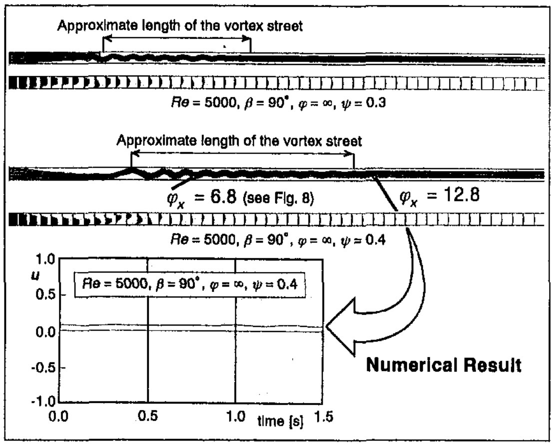

Fig. 9 Toroidal vortex street—overall view of the linearly mapped flow passage. The streamline patterns and velocity vectors at various locations in the test section are displayed. The graph shows time variation of *u*-velocity at a downstream location $\varphi_x = 12.8$.

Figure 8 shows the comparison between the numerical and experimental oscillations of u-velocity. An experimental probe, a hot wire, was set at the place where the most regular signal associated with the well developed vortex street was detected. That is at a distance $s/4$ from a passage wall in the transverse direction and at a distance $\varphi_x = l_x/r_{01} = 2.5$ from the passage inlet in the streamwise direction. The numerical probe was set at the same transverse location but it had to be moved downstream to $\varphi_x = 6.8$ in order to detect the variations in u-velocity caused by the developed vortex street. This is because the flow needs a longer distance to develop and form the vortex street due to the uniform velocity profile prescribed at the passage inlet. It can be seen from the comparison of these results that the nature of oscillations in the numerical flow field is similar to that obtained experimentally. Processing the signal from the hot-wire anemometer by an FFT frequency analyzer yields the separation frequency of approximately 2.6 Hz. Numerically obtained separation frequency is, for the above conditions, approximately 6 Hz. Defining the Strouhal number as

$$Sl = \frac{2s \cdot f}{U}, \qquad (13)$$

where U is the mean local velocity at the place where the frequency was measured, the experiment and numerical simula-

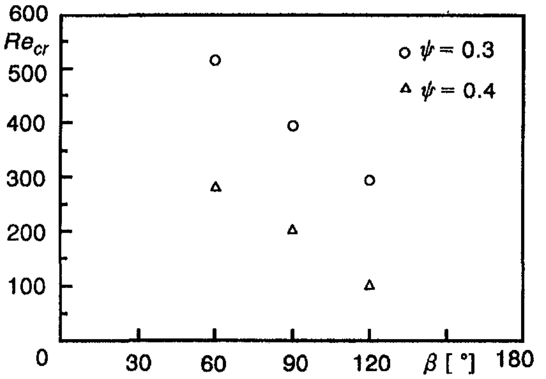

Fig. 10 Experimentally obtained critical Reynolds numbers plotted as a function of the apex angle β and nondimensional passage spacing ψ

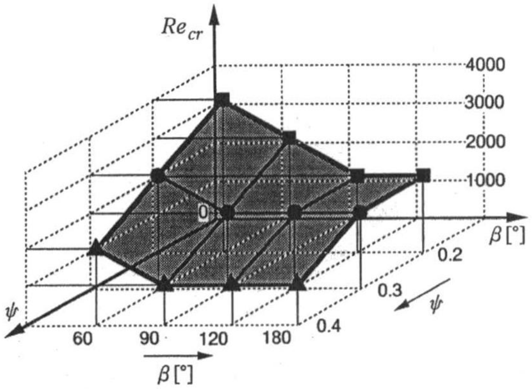

Fig. 11 Numerically obtained critical Reynolds numbers plotted as a function of the apex angle β and nondimensional passage spacing ψ

tion give almost the same *Sl* value that is 0.81 and 0.8, respectively.

Figure 9 shows the overall view of the linearly mapped physical domain, which is about 1 m long. Experiments were performed on a flow passage with about 400 mm in length. The overall view is included here to demonstrate the fact that the upstream generated toroidal-vortex street gradually diminishes as the flow proceeds downstream and finally reaches a steady state with the fully developed diffusing flow. To support this statement a graph which shows the variation of u-velocity at a downstream location ($\varphi_x = 12.8$) is included in Fig. 9. Comparing the u-velocity variation at $\varphi_x = 6.8$ (see Fig. 8) and $\varphi_x = 12.8$ (see Fig. 9) it is clear that the oscillations are damped in the downstream region as shown by the nonvarying u-velocity in the graph for $\varphi_x = 12.8$. Physically, this process takes place as a result of prevailing viscous forces in the downstream region, emphasized by the deceleration caused by the diffuser effect, which can be noticed in the velocity profiles displayed beneath the streamline pattern in Fig. 9. A certain contribution may also be expected from the azimuthal straining which elongates the vortex lines.

The flow patterns presented in Fig. 9 for $\psi = 0.3$ and 0.4, also reveal that the phenomenon significantly changes when the cone spacing ψ is changed. As the gap decreases, the place where the vortices are generated moves upstream and the downstream distance up to which the vortices propagate is decreased. Clearly, further research is necessary to explore various important scalings, such as the vortex frequencies or spacings, or the length of the zone containing the vortices (before they are damped).

3.3 Numerical Investigation of the Critical Reynolds Number and Comparison With Experiment. The critical Reynolds number, that is the lower bound Reynolds number below which the flow remains laminar, steady and without separation was experimentally investigated in Balatka et al. (1996). The critical Reynolds number was studied there on the basis of flow visualization and it was found that the critical Reynolds number varies with a change in the geometric parameters ψ and β. The results are reproduced in Fig. 10. As the graph indicates, the critical Reynolds number decreases with an increase in the apex angle β as a result of an increasing adverse pressure gradient. Similarly, an increase in the passage spacing ψ produces a stronger adverse pressure gradient, which reduces the critical Reynolds number (viscous effects may play their role as well).

Results of the numerical investigation of the critical Reynolds number, that is the Reynolds number below which the flow is laminar, steady and without any separation, are presented in Fig. 11. Notice that several more parameter settings including the extreme case of $\beta = 180$ deg are numerically investigated. The graph shows that the critical Reynolds number increases as the passage spacing ψ is decreased from 0.4 to 0.2. A similar trend can be observed in the experimental result, Fig. 10. On the other hand, the critical Reynolds number is decreased with an increase in the apex angle β. This trend can also be observed in the experimental results, Fig. 10. The shaded region in Fig. 11 indicates the boundary between the flow with and without separation, the critical Reynolds number, for given parameters ψ and β. If the flow is simulated for such a parameter setting that yields a Reynolds number on or above the shaded surface in Fig. 11, it will separate. The flow will, however; remain without separation if the Reynolds number falls under the shaded surface. Further numerical experiments are, however; necessary to map the flow behavior more accurately.

4 Summary

The flow in an annular-conical passage is studied on the basis of numerical analysis. For this purpose a new coordinate system which fits the flow passage was derived and the Navier-Stokes equations were transformed into it. Subsequently computer code, which handles an annular-conical passage with arbitrary apex angle β and passage spacing ψ and is capable of solving highly convective flow, was developed.

Solutions were obtained for four different apex angles (β = 60, 90, 120, 180 deg) and three passage spacings (ψ = 0.2, 0.3, 0.4). The Reynolds number ranged from Re = 100 to 5000. Changes in the computed flow pattern for increasing Re were found to be similar to those observed experimentally. The numerical results revealed that the instability, toroidal-vortex street, exists in an annular-conical passage under pure boundary conditions and is an inherent feature of the flow flowing through such a passage. The experimentally and numerically obtained Strouhal number was found to coincide. It was shown that the flow pattern varies with a change in the passage spacing and that vortices are damped downstream. The computed trends for the critical Reynolds number were similar to those previously obtained by the experimental investigation.

Acknowledgment

The authors would like to express their gratitude to Dr. A. Murata who always found time for stimulating discussions, particularly about the magic world of CFD.

References

Balatka, K., et al., 1996, "Flow in an Annular-Conical Passage," *JSME International Journal,* Vol. 39, No. 1, pp. 66–71.

Balatka, K., et al., 1995, "Experimental Investigation of Flow in an Annular-Conical Passage," *Journal of Flow Visualization and Image Processing,* Vol. 2, No. 2, pp. 113–123.

Hirt, C. W., and Cook, J. L., 1972, "Calculating Three-Dimensional Flows around Structures and over Rough Terrain," *Journal of Computational Physics,* Vol. 10, pp. 324–340.

Ishizawa, S., 1966, ''The Axi-Symmetric Laminar Flow in an Arbitrary Shaped Gap (2nd Report),'' *Bulletin of JSME,* Vol. 8, No. 31, pp. 353–367.

Ishizawa, S., 1965, ''The Axi-Symmetric Laminar Flow in an Arbitrary Shaped Gap (1st Report),'' *Bulletin of JSME,* Vol. 9, No. 33, pp. 86–103.

Jackson, J. D., and Symmons, G. R., 1965, ''An Investigation of Laminar Radial Flow Between Two Parallel Disks,'' *Applied Scientific Research,* Vol. 15, pp. 59–75.

Mochizuki, S., 1993, ''Unsteady Flow Phenomena and Heat Transfer in Rotating-Disk Systems,'' *Proceedings of the 6th International Symposium on Transport Phenomena,* Seoul, Vol. 3, pp. 279–289.

Mochizuki, S., and Yang, W. J., 1985, ''Self-Sustained Radial Oscillating Flows Between Parallel Disks,'' *Journal of Fluid Mechanics,* Vol. 154, pp. 377–397.

Raal, J. D., 1978, ''Radial Source Flow Between Parallel Disks,'' *Journal of Fluid Mechanics,* Vol. 85, pp. 401–416.

Turbulent Flow Past an Array of Bluff Bodies Aligned Along the Channel Axis

Tong-Miin Liou
Professor. Fellow ASME

Shih-Hui Chen
Graduate Student.

Department of Power Mechanical Engineering,
National Tsing Hua University,
Hsinchu, Taiwan 30043

Computations and measurements of time mean velocities, total fluctuation intensities, and Reynolds stresses are presented for spatially periodic flows past an array of bluff bodies aligned along the channel axis. The Reynolds number based on the channel hydraulic diameter and cross-sectional bulk mean velocity, the pitch to rib-height ratio, and the rib-height to channel-height ratio were 2×10^4, 10, and 0.13, respectively. The unsteady phase-averaged Navier-Stokes equations were solved using a Reynolds stress model with wall function and wall-related pressure strain treatment to reveal the feature of examined unsteady vortex shedding flow. Laser Doppler velocimetry measurements were performed to measure the velocity field. Code verifications were performed through comparisons with others' measured developing single-rib flow and our measured fully developed rib-array flow. The possible causes for the differences between the experiments and computations are discussed. The calculated phase-averaged flow field clearly displays the vortex shedding behind the rib and is characterized in terms of shedding Strouhal number, vortex trajectory, vortex celerity, and vortex travelling distance in a phase cycle. Furthermore, the difference between the computed developing single-rib flow and fully developed rib-array flow is addressed.

Introduction

The arrangement of bluff bodies along the length of a passage to periodically disrupt the flow, as depicted in Figs. 1 and 2, is a widely adopted technique for heat exchange systems. Transverse and/or longitudinal vortices existing in this type of configuration are found to influence the pressure loss and mixing between the cold flow and hot walls (Fiebig, 1995; Suzuki, 1996). The design of a heat exchanger requires a thorough understanding of the vortex structure and its role in affecting heat transfer. Most previous studies were related to a single cylinder of circular or rectangular cross-section immersed in freestreams, while less studies pertinent to flow passing through cylinders in confined ducts. Some works relevant to this paper are cited below.

In studying laminar flows around and behind square and circular cylinders, Davis et al. (1984), Franke et al. (1990), Suzuki et al. (1993, 1994a), and Li and Humphrey (1995) numerically solved the unsteady Navier-Stokes equations. Among them, Davis et al. (1984) experimentally performed smoke-wire visualization and numerically solved two-dimensional unsteady Navier-Stokes equations to study laminar flows past a single rectangular cylinder in a confined channel. The effects of Reynolds number, blockage ratio, inlet velocity profile, and cylinder aspect-ratio were investigated. They found that the vortex shedding and drag force were more influenced by the effects of blockage ratio and inlet velocity profile. Suzuki et al. (1993) performed a two-dimensional numerical calculation for unsteady laminar flows in a channel obstructed with a square rod. The effects of rod sizes, Reynolds number, and inlet flow velocity profiles on the instantaneous flow structure were investigated. The blockage ratio was found to be a major factor governing the appearance of the crisscross motion of the vortex. From the calculated instantaneous velocity fields Suzuki et al. (1994a) addressed the mechanism of criss-cross motion and the role of nonzero value of cross-correlation between the streamwise and lateral velocity fluctuating components.

For confined turbulent flows past bluff bodies, which usually occur in practice, stochastic three-dimensional turbulent fluctuations are superimposed on the periodic vortex-shedding motion in the wake region. The simulation of large coherent structures in the turbulent wake flow is difficult because of the widespread spectrum of scales. Large eddy simulation is a promising one to solve this problem and attracts much attention (Tamura et al., 1990; Werner and Wengle, 1991; Murakami et al., 1993; Yang and Ferziger, 1993), but its computer resource requirement still limits its wide engineering application. Phenomenological turbulence modeling is a practical alternative choice but needs further improvements. Rodi (1993) reviewed the simulations of turbulent flows past a bluff body and concluded the general superiority of Reynolds stress model over $k - \epsilon$ model and the promising application of large eddy simulation. Franke and Rodi (1993) calculated the turbulent flow past a rectangular cylinder behind which a von Karman vortex street existed according to the experiments. They compared four different turbulence models: $k - \epsilon$ model and Reynolds stress model (RSM) (Launder et al., 1975), each with wall function and one-equation near wall treatment (also referred to as two-layer model). In using the RSM model the wall-related pressure-strain model of Gibson and Launder (1978) was adopted. They found that the $k - \epsilon$ model with wall function did not produce any vortex shedding at all whereas the other three models predicted vortex shedding. Among them, the RSM variants produced results in fairly good agreement with experiments. Johansson et al. (1993) used a finite volume code with a $k - \epsilon$ model and wall function to calculate the unsteady turbulent flow around and behind a triangular-shaped flameholder. The periodic motions in the vortex street were shown to be far more important than the turbulent stochastic motions in exchanging momentum in the transversal direction. Durao (1988) measured the turbulent wake flow field of a square cylinder using laser-Doppler velocimetry (LDV). The experiments were performed in a water channel with a blockage ratio of 0.14 and Reynolds number based on the cylinder height of 14000. They showed that in the zone of highest

---

Contributed by the Fluids Engineering Division for publication in the JOURNAL OF FLUIDS ENGINEERING. Manuscript received by the Fluids Engineering Division July 31, 1997; revised manuscript received May 18, 1998. Associate Technical Editor: P. R. Bandyopadhyay.

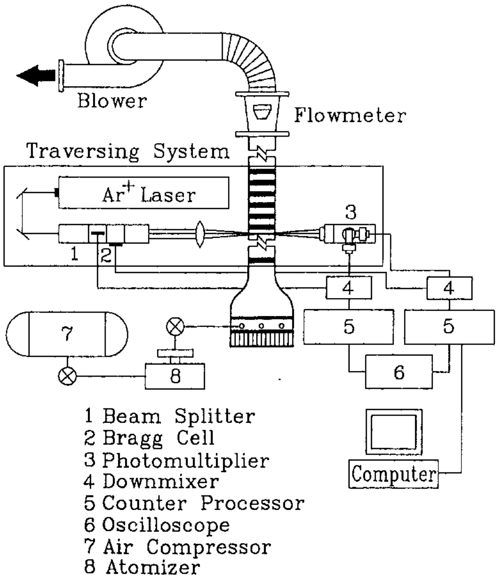

Fig. 1 Sketch of configuration, coordinate system and dimensions of the test section (Uncertainty in *H*: ±0.1 mm, in *W*$_r$: ±0.1 mm, in *A* and *B*: ±0.3 mm, in axial position: ±0.1 mm, in transverse position: ±0.1 mm, in spanwise position: ±0.1 mm)

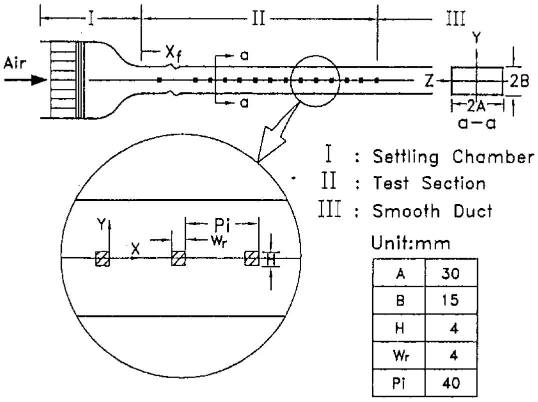

Fig. 2 Schematic drawing of overall experimental system

velocity oscillations the energy associated with the turbulent fluctuations is about 40 percent of the total energy, including periodic and turbulent fluctuations. Lyn and Rodi (1994), and Lyn et al. (1995) measured the turbulent wake flow of a square cylinder using LDV. The experiments were performed in a water channel with a blockage ratio of 0.07 and Reynolds number based on the cylinder height of 21,400. Lyn and Rodi (1994) focused on the turbulent shear layer and associated recirculation region on the top and bottom walls due to flow separation from the forward corner of the cylinder. Lyn et al. (1995) focused on the turbulent near-wake flow around the cylinder.

Studies involving more than one detached cylinder arranged in a channel are seldom found in the available literature. For two cylinders in tandem, Tatsutani et al. (1993) performed dye visualization and direct numerical simulation using a two-dimensional unsteady Navier-Stokes code with QUICK scheme (Leonard, 1979) to investigate the effect of the cylinder separation distance on the flow behavior and heat transfer of the downstream cylinder. The investigated Reynolds number based on cylinder diameter ranged between 200 and 1600, the blockage ratio was 0.2, and the cylinder separation distance-height ratio was between 0.25 and 4. At a critical separation distance, the flow was found to be bistable and alternate between two patterns, i.e., a closed intercylinder gap recirculation and an oscillating wake forming behind the upstream cylinder. A correlation between the critical spacing and Reynolds number was obtained numerically. Valencia (1996) also numerically studied the effect of the cylinder separation distance on the flow and heat transfer for three cylinder separation distance to cylinder height ratios (Pi/H) of 1, 2, and 4. The investigated Reynolds number based on cylinder height ranged between 100 and 500. He found that a value of $Pi/H = 4$ resulted in the largest heat transfer enhancement among Pi/H values examined because of the oscillating flow appearing in the intercylinder gap.

For an array of bluff bodies built-in a channel and detached from the wall, Karniadakis et al. (1988), Amon and Mikic (1991), Suzuki et al. (1994b), and Liou et al. (1995, 1997) investigated the in-line array of cylinders whereas Oyakawa and Mabuchi (1983), Oyakawa et al. (1986), Yao et al. (1987, 1989), and Treidler and Carey (1990) all experimentally studied the staggered array of cylinders. For an in-line array of obstacles, Karniadakis et al. (1988) computationally showed that cylinder-induced laminar flow instabilities produced comparable heat transfer with that of turbulent flows in unobstructed channels while incurring significantly less dissipation. Amon and Mikic (1991) and Suzuki et al. (1994b) both numerically

Nomenclature

A = half width of duct (30 mm)
B = half height of duct (15 mm)
C_p = pressure coefficient
D_e = duct hydraulic diameter (40 mm)
f = vortex shedding frequency
H = rib height (4 mm)
k = turbulent kinetic energy
Pi = pitch length (40 mm)
Re = Reynolds number based on channel hydraulic diameter ($\equiv \rho U_{\text{ref}} D_e/\mu_l$)
Re$_H$ = Reynolds number based on rib height ($\equiv \rho U_{\text{ref}} H/\mu_l$)
St = Strouhal number ($\equiv fH/U_{\text{ref}}$)
T = period of a vortex shedding cycle
$\bar{u}$ = long-time mean streamwise velocity
$\langle u\rangle$ = phase-averaged streamwise velocity
u'' = streamwise total fluctuation intensity = $(\overline{\langle u'u'\rangle + \tilde{u}\tilde{u}})^{1/2}$
U_{ref} = duct bulk mean velocity as a reference velocity, $U_{\text{ref}} = 7.78$ (m/s)
U_c = vortex celerity
$-\overline{u'v''}$ = total time-mean shear stress = $-\overline{\tilde{u}\tilde{v}} - \overline{\langle u'v'\rangle}$
$\langle u'v'\rangle$ = phase-averaged turbulent shear stress
$\bar{v}$ = long-time mean transverse velocity
$\langle v\rangle$ = phase-averaged transverse velocity
v'' = transverse total fluctuation intensity = $(\overline{\langle v'v'\rangle + \tilde{v}\tilde{v}})^{1/2}$
W_r = rib width (4 mm)
X = streamwise coordinate
X_R = reattachment length
Y = transverse coordinate
Y_p^+ = the distance of first grid points from the wall in wall coordinate
ϵ = dissipation rate of turbulent kinetic energy
ρ = air density
μ_l = laminar viscosity
$\langle \varphi\rangle$ = phased-average value of instantaneous variable φ
φ' = turbulent fluctuation of instantaneous variable φ
$\bar{\varphi}$ = long-time mean value of instantaneous variable φ
$\tilde{\varphi}$ = periodic fluctuation of instantaneous variable φ
φ'' = total fluctuation of instantaneous variable φ

investigated self-sustained oscillating laminar flows. Only Liou et al. (1995) and Liou et al. (1997) performed spatially periodic turbulent heat transfer and fluid flow measurements, respectively. Their laser holographic interferometry (LHI) data (Liou et al., 1995) indicated the presence of vortex shedding behind the ribs when the distance between the rib array and the wall was arranged above an appropriate distance. The complementary laser-Doppler velocimetry data (Liou et al., 1997) provided the fluid dynamic explanation to the LHI results and revealed the importance of the vortex shedding on the heat transfer augmentation.

The above relevant studies have provided valuable information related to flows past one or two cylinders in a channel. Until the present work, there are very few experimental studies and, in particular, no computational studies on turbulent fluid flows in a channel with an array of bluff bodies detached from the wall. The main purpose of this article is therefore to investigate the turbulent flow in a channel with a detached rib array by both LDV measurements and numerical simulations. The LDV measurements provide mean velocity and turbulent intensity profiles for assessing the computational results. The numerical simulations additionally reveal the instantaneous flowfield information since the unsteady phase-averaged Navier-Stokes equations incorporated with the second moment closure turbulence model are solved. As addressed in the above survey of published works, in simulating turbulent flows past a rectangular bluff body Rodi (1993) concluded the general superiority of Reynolds stress model over $k - \epsilon$ model and Franke and Rodi (1993) reported the failure of $k - \epsilon$ model with wall function in producing any vortex shedding. Similarly, our preliminary computations using $k - \epsilon$ model with wall function also indicated the lack of vortex shedding and poor prediction of streamwise time mean velocity variation (shown shortly in Fig. 4). Thus a Reynolds stress model with wall function and the wall-related pressure-strain model of Craft and Launder (1992), which avoids the inappropriate near-wall enhancement of isotropisation at impingement/reattachment region, is adopted in this study. Computational results based on the aforementioned two different wall-related pressure-strain models adopted in the present study and the work of Franke and Rodi (1993) are subsequently compared. In addition, a comparison of flow features between the developing flow around a single rib and spatially periodic fully developed flow around the rib of a rib array is made.

Mathematical Formulation

Governing Equations. Figure 1 depicts the coordinate system to be used for formulating the governing equations and describing the results. Following the concept of Reynolds decomposition an instantaneous quantity φ is split into

$$\varphi = \langle \varphi \rangle + \varphi' \tag{1}$$

where $\langle \varphi \rangle$ is the mean value and φ' the stochastic turbulent fluctuation. It is expected from the preceding literature survey that the large-scale coherent vortex shedding may appear behind the rib bluff-bodies. The mean value $\langle \varphi \rangle$ may therefore vary slowly with time and must be the so called ensemble (or phase) averaged value. Applying Eq. (1) to the incompressible continuity and Navier-Stokes equations, one obtains the following ensemble (or phase) averaged governing equations:

$$\frac{\partial \langle u_i \rangle}{\partial x_i} = 0 \tag{2}$$

$$\frac{\partial \langle u_i \rangle}{\partial t} + \frac{\partial}{\partial x_j} (\langle u_j \rangle \langle u_i \rangle) = -\frac{1}{\rho} \frac{\partial \langle p \rangle}{\partial x_i} + \frac{\partial}{\partial x_j} \left(\nu \frac{\partial \langle u_i \rangle}{\partial x_j} - \langle u_i' u_j' \rangle \right) \tag{3}$$

Due to the periodic vortex shedding behind the rib bluff bodies, the ensemble averaged value $\langle \varphi \rangle$, as suggested by Hussain and Reynolds (1970), can be further decomposed into

$$\langle \varphi \rangle = \bar{\varphi} + \tilde{\varphi} \tag{4}$$

where $\bar{\varphi}$ is the long-time-averaged value and $\tilde{\varphi}$ the periodic fluctuation. In summary, an instantaneous quantity can be expressed as

$$\varphi(t) = \bar{\varphi} + \tilde{\varphi}(t) + \varphi'(t) = \bar{\varphi} + \varphi''(t) \tag{5}$$

where $\varphi''(t)$ stands for the total fluctuation.

Turbulence Models. The Reynolds stresses $\langle u_i' u_j' \rangle$ in Eq. (3) must be modeled to close the governing equations. The transport equations for the Reynolds stresses can be written in the following Cartesian tensor form:

$$\frac{\partial}{\partial x_k} (\langle u_k \rangle \langle u_i' u_j' \rangle) = D_{ij} + P_{ij} + \phi_{ij} - \frac{2}{3} \delta_{ij} \epsilon \tag{6}$$

in which

$$D_{ij} = \frac{\partial}{\partial x_k} \left(c_\mu \frac{\langle k \rangle^2}{\langle \epsilon \rangle} \frac{\partial \langle u_i' u_j' \rangle}{\partial x_k} \right) \tag{7}$$

$$P_{ij} = -\left(\langle u_i' u_k' \rangle \frac{\partial \langle u_j \rangle}{\partial x_k} + \langle u_j' u_k' \rangle \frac{\partial \langle u_i \rangle}{\partial x_k} \right) \tag{8}$$

$$\phi_{ij} = -c_1 \frac{\langle \epsilon \rangle}{\langle k \rangle} \left(\langle u_i' u_j' \rangle - \frac{2}{3} \delta_{ij} \langle k \rangle \right) - c_2 \left(P_{ij} - \frac{1}{3} \delta_{ij} P_k \right) + \phi_{ij}^{\text{wall}} \tag{9}$$

are, respectively, the diffusion, production, and pressure strain terms. The wall-related pressure-strain model of Craft and Launder (1992), which avoids the inappropriate near-wall enhancement of isotropisation at impingement/reattachment region associated with the standard $k - \epsilon$ model, is adopted in this study

$$\begin{aligned} \phi_{ij}^{\text{wall}} = {} & c_1' \frac{\langle \epsilon \rangle}{\langle k \rangle} \langle u_i' u_j' \rangle n_k n_m \delta_{ij} \\ & - \frac{3}{2} \langle u_i' u_k' \rangle n_j n_k - \frac{3}{2} \langle u_j' u_k' \rangle n_i n_k) f - (c_2' \langle u_k' u_m' \rangle \\ & + c_3' k n_k n_m) \frac{\partial \langle u_k \rangle}{\partial x_m} (n_q n_q \delta_{ij} - 3 n_k n_m) f \\ & - c_4' \left(\tilde{\phi}_{km} n_k n_m \delta_{ij} - \frac{3}{2} \tilde{\phi}_{ij} n_j n_m - \frac{3}{2} \tilde{\phi}_{ik} n_j n_m \right) \end{aligned} \tag{10}$$

where n_i is the unit vector component in the x_i direction and the wall-proximity function $f = (c_\mu^{0.75} \langle k \rangle^{1.5} / \epsilon \kappa \Delta n)$ with Δn being the normal distance from the wall. In the Eq. (10), $\tilde{\phi}_{ij}$ takes the following forms:

$$\tilde{\phi}_{ij} = \left(\langle u_i' u_k' \rangle - \frac{2}{3} \delta_{ik} \langle k \rangle \right) \frac{\partial \langle u_j \rangle}{\partial x_k} \tag{11}$$

$c_1' = 0.5$, $c_2' = 0.08$, $c_3' = 0.13$, $c_4' = 0.10$ (Craft and Launder, 1992). The $k - \epsilon$ model is used in connection with wall functions to determine the Reynolds stresses $\langle u_i' u_j' \rangle$. The eddy viscosity concept is adopted to relate the eddy viscosity $\langle \nu_t \rangle$ to the turbulent kinetic energy $\langle k \rangle$ and its rate of dissipation $\langle \epsilon \rangle$, i.e., $\langle \nu_t \rangle = c_\mu \langle k \rangle^2 / \langle \epsilon \rangle$.
The equations for $\langle k \rangle$ and $\langle \epsilon \rangle$ are given as

$$\frac{\partial\langle k\rangle}{\partial t}+\frac{\partial}{\partial x_j}(\langle u_j\rangle\langle k\rangle)=D_k+P_k-\langle\epsilon\rangle$$
$$=\frac{\partial}{\partial x_j}\left[\left(\nu+\frac{\nu_t}{\sigma_k}\right)\left(\frac{\partial\langle k\rangle}{\partial x_j}\right)\right]+P_k-\langle\epsilon\rangle \quad (12)$$

$$\frac{\partial\langle\epsilon\rangle}{\partial t}+\frac{\partial}{\partial x_j}(\langle u_j\rangle\langle\epsilon\rangle)=D_\epsilon+\frac{\langle\epsilon\rangle}{\langle k\rangle}(C_{\epsilon1}P_k-C_{\epsilon2}\langle\epsilon\rangle)$$
$$=\frac{\partial}{\partial x_j}\left[\left(\nu+\frac{\nu_t}{\sigma_\epsilon}\right)\left(\frac{\partial\langle\epsilon\rangle}{\partial \underline{\underline{X}}_j}\right)\right]+\frac{\langle\epsilon\rangle}{\langle k\rangle}(C_{\epsilon1}P_k-C_{\epsilon2}\langle\epsilon\rangle) \quad (13)$$

where $P_k = -\langle u_i' u_j'\rangle(\partial\langle u_i\rangle/\partial x_j)$ is the generation rate of turbulent kinetic energy. The symbols D_k and D_ϵ are the diffusion terms of the $\langle k\rangle$ and $\langle\epsilon\rangle$ equations, respectively. The empirical constants such as C_1, C_2, $C_{\epsilon1}$, $C_{\epsilon2}$, C_μ, σ_k and σ_ϵ are 1.8, 0.6, 1.44, 1.92, 0.09, 1.0, and 1.3, respectively (Rodi, 1984).

Numerical Method of Solution

By using the control-volume based finite differce method of Patankar (1980), governing equations were integrated over a finite number of control volumes covering the entire solution domain, with each control volume containing a grid point. The convection terms of all equations, including the equations of scalar variables, were discretized by a third-order upwind scheme QUICK (Leonard, 1979) and the diffusion and source terms were discretized by the second order central difference. The time derivative was discretized by a first-order accurate fully implicit method with a relatively small nondimensionalized time step $\Delta t^* = \Delta t U_{\text{ref}}/H = 0.05$. More than 100 time steps per shedding cycle were used to achieve time resolution and accuracy.

As for handling the pressure-velocity coupling arising in incompressible flow equations, the PISO (Pressure Implicit with Splitting of Operators) (Issa, 1985) method is utilized in this study for a stable and faster convergence at each time step. The grid system is non-staggered and the momentum interpolation method of Rhie and Chow (1983) is adopted. The resulting set of algebraic equations was solved with the line-by-line TDMA (Tridiagonal-Matrix Algorithm). The calculated results at each time step were declared convergent when the maximum of individual sum of absolute cell residues in the entire domain for each dependent variable normalized by the respective inlet flux was less than a prescribed convergence criterion, typically a value of 0.05 percent.

Boundary Conditions and Grid Layout. The inlet axial velocity, Reynolds stresses, and turbulent kinetic energy profiles are prescribed according to the measured data. The dissipation rate of turbulent kinetic energy is calculated from the prescribed inlet turbulent kinetic energy and a length scale (~0.01 times channel height). At the outlet, a convective boundary condition is prescribed. As the wall functions are employed to bridge the viscous sublayer, the momentum and turbulent kinetic energy at all solid boundaries are evaluated from the logarithmic law of wall, while the energy dissipation rate is determined from the local equilibrium. The nearest nodes from the walls are located within the interval $y^+ \fallingdotseq 18 \sim 45$. The nearest wall Reynolds stresses obtained with Craft and Launder's wall-reflection terms (1992) are

$$\frac{\langle u'u'\rangle}{k}=1.071;\quad \frac{\langle v'v'\rangle}{k}=0.299;\quad \frac{-\langle u'v'\rangle}{k}=0.248 \quad (14)$$

The computations to be reported in the following sections were performed on a 282 × 42 grid. Additional runs for the coarser (162 × 32) and finer (322 × 62) meshes were undertaken for a check of grid independence. The distance from the near-wall node to the nearest wall was kept constant for the three runs. A comparison of the results showed that the maximum changes of 0.8 percent in the axial velocity profiles between 282 × 42 and 322 × 62 grid sizes were smaller than 3.2 percent found between 282 × 42 and 162 × 32 mesh sizes. Consequently, the accuracy of the solutions on a 282 × 42 grid size is deemed satisfactory.

Experimental Setup and Conditions

Test Section. The test section (Fig. 2) made of 5-mm Plexiglas was 900 mm in length and 60 mm × 30 mm ($2B \times 2A$) in cross-sectional area. Plexiglas square ribs of size 4 mm × 4 mm ($W/H = 1$ and $H/2B = 0.13$ or $H/D_e = 0.1$) were detached from the bottom wall ($Y = 0$) and aligned with the duct centerline. The leading edge of the first rib was placed 100 mm downstream of the bell-shaped 10:1 contraction. There were 19 ribs in the rib array. Double-sided adhesive tape of 0.10 mm thickness were used to fix the ribs to the plexiglas side walls and to ensure no end-wall effects.

Apparatus and Test Conditions. The LDV experimental setup and flow system in the present work, as shown in Fig. 1, is basically the same as that described in the work of Liou et al. (1997). Refer to this earlier paper for more detail. Air was drawn through the test section by a blower (3500 rpm, three-phase, 1 hp) at the downstream end.

The rib pitch-to-height ratio Pi/H and Reynolds number based on the duct hydraulic diameter (40 mm) and bulk mean velocity $U_{\text{ref}} = 7.78$ m/s were fixed at 10 and 2×10^4, respectively. $Pi/H = 10$ was chosen since it provided the best thermal performance for the attached rib case (Liou et al., 1995). The mean flow at the location where the first rib was installed had a boundary layer thickness of 1.4 mm (or $\delta/H = 0.35$). The uniformity of mean velocity profile over the center 80 percent of duct height is within ±2 percent of U_{ref} and the corresponding turbulence intensity is 0.9 percent of U_{ref}. At a sufficient distance downstream of the first rib, it is expected that the flow pattern will repeat itself from pitch to pitch, i.e., becomes spatially periodic (Liou et al., 1997). Along the central plane $Z/A = 0$, LDV measurements of periodically fully developed flow were obtained between the 10th and 11th ribs. The bulk mean velocity was used to non-dimensionalize the experimental results.

There were typically 4096 realizations averaged at each measuring location. The statistical errors in the mean velocity and turbulence intensity were less than 1.6 and 2.2 percent, respectively, for a 95 percent confidence level. Representative values of other uncertainty estimates are noted in figure captions. More detailed uncertainty estimates and velocity bias correlations are included in Liou et al. (1990 and 1993). For the range of atomizer pressure setting used, the saline solution was mixed to produce particles from 0.5 to 1.2 μm. This particle diameter range is able to follow turbulence frequencies exceeding 1 KHz (Durst et al., 1976).

Results and Discussion

Spatially Developing Time Mean Flow. Owing to limited experimental data available, code validation in the present study is performed in two stages. Computations were firstly made for a developing flow past a single rib located along the axis of the channel and subsequently for a spatially periodic fully developed flow around the rib of a rib array. The results of the former is presented in Figs. 3 and 4 and those of the latter will be given in the next section. Our computed mean velocity vector field depicted in Fig. 3 and the experiment of Lyn and Rodi (1994) both show that the shear layers separate at rib's front edge to form a symmetric wake behind the rib. The wake length is an important characteristic length often used for validating computation and is defined as the axial position where the wake

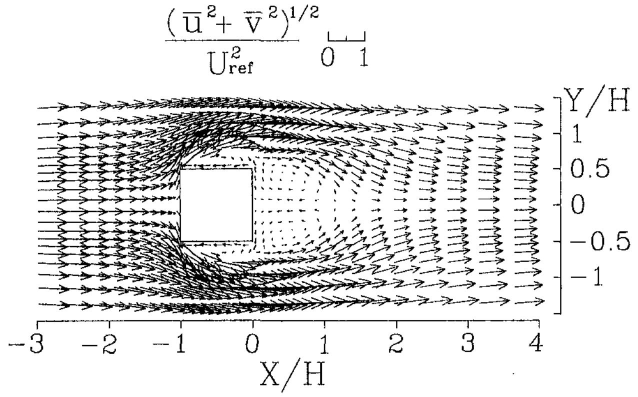

Fig. 3 Computed resultant time mean velocity vector field in *X*-*Y* plane for a developing flow past a single rib in a rectangular duct

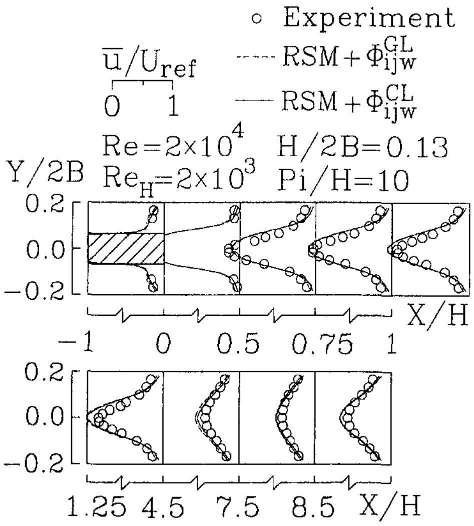

Fig. 5 Measured and computed streamwise evolution of $\overline{u}/U_{ref}$ profiles in one pitch module (Uncertainty in $\overline{u}/U_{ref}$: less than ±3.2 percent)

saddle point occurs, i.e. zero streamwise mean velocity along the channel axis. Figure 4 shows the streamwise mean velocity variation with X/H behind the rib and along the channel centerline. The experimental data from Durao et al. (1988) and Lyn et al. (1995) and computed result from Franke and Rodi (1993) are included in Fig. 4 for comparison. The negative $\overline{u}/U_{\rm ref}$ indicates the wake recirculation and $\overline{u}/U_{\rm ref} = 0$ the wake saddle point. It is found that the centerline axial mean velocity recovers fast as X/H increases from 1 to 2 and gradually levels off beyond $X/H = 3$. In general, the RSM with wall function and ϕ^{CL}_{ijw} (Craft and Launder, 1992) adopted in the present study (solid line) provides a better agreement with the measured results than the model used ϕ^{GL}_{ijw} (Gibson and Launder, 1978), especially for $0 < X/H < 3$. The dimensionless wake lengthes (X_R/H) of the present computation by using the wall-related pressure strain models ϕ^{GL}_{ijw} and ϕ^{CL}_{ijw} are 0.5 and 1.1, respectively. The X_R/H obtained by the computation of Franke and Rodi (1993) and measured by Durao et al. (1988) and Lyn et al. (1995) are 0.5, 0.83 and 0.9, respectively. As has been mentioned in the last paragraph of Introduction, Fig. 4 depicts that the $k - \epsilon$ model with wall function gives a poor prediction.

One possible explanation for the better agreement between the present calculations with other calculations in Fig. 4 than with the experimental data could be subtle differences in the experiment, such as inlet flow conditions, three-dimensional effects, etc., which are not exactly incorporated in the simulations due to the following reasons. In general, the inlet flow conditions including inlet $\langle u\rangle$, $\langle v\rangle$, $\langle k\rangle$, $\langle\epsilon\rangle$, $\langle u_i'u_j'\rangle$ and $\langle\nu_t\rangle$ are often not all measured in the experiment, resulting in incomplete inlet flow conditions to be used for numerical simulations. In the present study, the inlet flow conditions are prescribed according to those described in the works of Franke and Rodi (1993) and Bosch and Rodi (1996) as follows. At the inlet reference plane, $x = 4.5$ H upstream of the rib, the flow enters with only a streamwise component $U_{\rm ref}$, an experimental turbulence level of $u''/U_{\rm ref} = 0.02$, instead of specifying the inlet mean velocity and turbulent kinetic energy profiles which are not available. A ratio of $\nu_t/\nu = 100$ is assumed to compute the inflow value of ϵ. Computations using the partly simplified and partly assumed inlet flow conditions are therefore expected to capture the measured flowfield behind the rib to some extent only, as shown in Fig. 4. However, this ia a unique set of inlet flow conditions which one could get so far, since it was adopted computationally (Franke and Rodi, 1993; Bosch and Rodi, 1996) and measured experimentally (Lyn et al., 1995) by the same research group of Rodi. In addition, the preceding survey indicates that the inflow velocity profile is one of the major factors affecting the flow characteristics downstream of the rib (Davis et al., 1984). The above factors may provide the rationale for the better agreement between the present calculations with the calculations of Franke and Rodi (1993) due to the same set of inlet conditions used by the two works. To improve

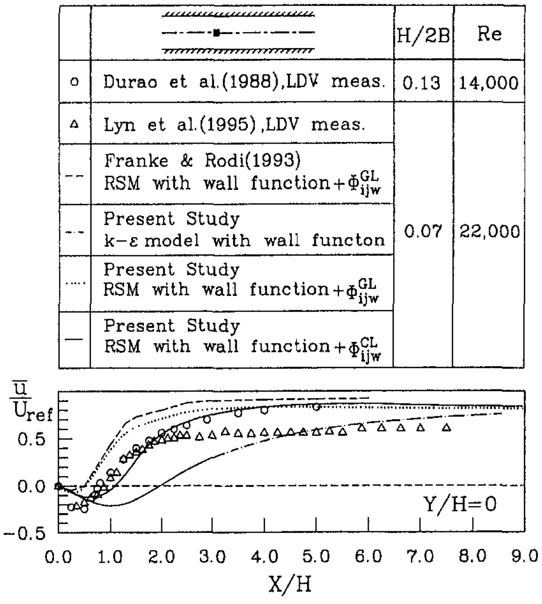

		H/2B	Re
o	Durao et al.(1988),LDV meas.	0.13	14,000
△	Lyn et al.(1995),LDV meas.	0.07	22,000
--	Franke & Rodi(1993) RSM with wall function+Φ^{GL}_{ijw}		
-·-	Present Study k−ε model with wall functon		
·····	Present Study RSM with wall function+Φ^{GL}_{ijw}		
—	Present Study RSM with wall function+Φ^{CL}_{ijw}		

Fig. 4 Streamwise time mean velocity variation along the duct centerline behind the rib

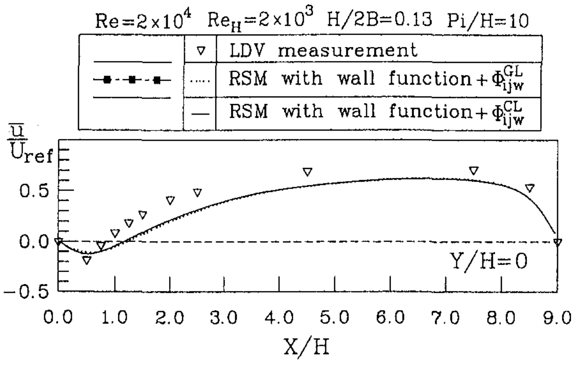

Fig. 6 Measured and computed centerline streamwise time mean velocity as a function of *X*/*H*

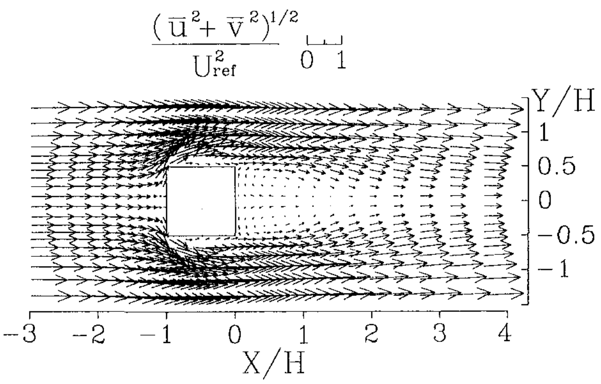

Fig. 7 Computed resultant time mean velocity vector field in *X*-*Y* plane for a spatially periodic fully developed flow past a rib array in a rectangular duct

the agreement between the computations and measurements, a large eddy simulation is being undertaken and the results will be published in the near future.

Our previous LDV measurements of duct flows with detached ribs (Liou et al., 1997) showed that the secondary mean velocities were in the range of 1 to 10 percent of U_{ref}, approximately four times those in the smooth channel (Speziale, 1986). It is therefore believed that three-dimensional effect has also some contribution to the disagreement between the calculations and measurements shown in Fig. 4. Another point worthy of addressing is the behavior in the wake. The present 2-D calculations based on the wall-related pressure strain models ϕ_{ijw}^{GL} and ϕ_{ijw}^{CL} predict wake lengthes of 0.5 and 1.1, respectively, which are respectively shorter and longer thant 0.9 of 3-D measurements by Lyn et al. (1995), and similar and opposite to what is observed in 2-D versus 3-D computations of circular cylinders. This observation suggests the importance of the wall-related pressure strain model adopted on the calculated length of backflow region.

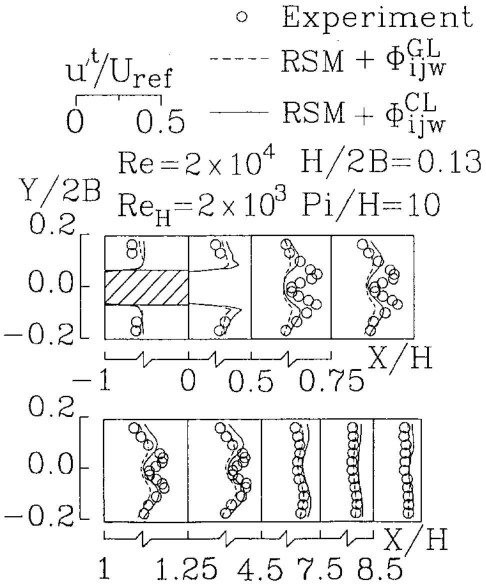

Fig. 9 Measured and computed periodic fully developed streamwise total fluctuation intensity and Reynolds stress profiles in one pitch module (Uncertainty in u'^t/U_{ref}: less than ±4.4 percent)

One may question that the flow near the corners of the rib is not well resolved. The advantage of using wall functions to bridge the viscous sublayer is to save the number of grid cells closely adjacent to the wall. The employment of wall functions requires that the first grid points from the walls be located in the logarithmic region of the law of the wall. In the present calculations the first grid points from the rib's four walls are located in the region of $18 \le Y_p^+ \le 45$ which is within the logarithmic part of the law of the wall and close to $16 \le Y_p^+ \le 50$ reported by Bosch and Rodi (1996). Some calculations of the flow around a free-standing rib were performed with a finer mesh by Bosch and Rodi (1996), but only small differences resulted. For more resolution in the regions around the rib's corners, a low-Re version of turbulence model is suggested for future study.

Spatially Fully Developed Time Mean Flow

Fully Developed Time Mean Velocity Field. As mentioned in the Introduction, the results presented in this section are not

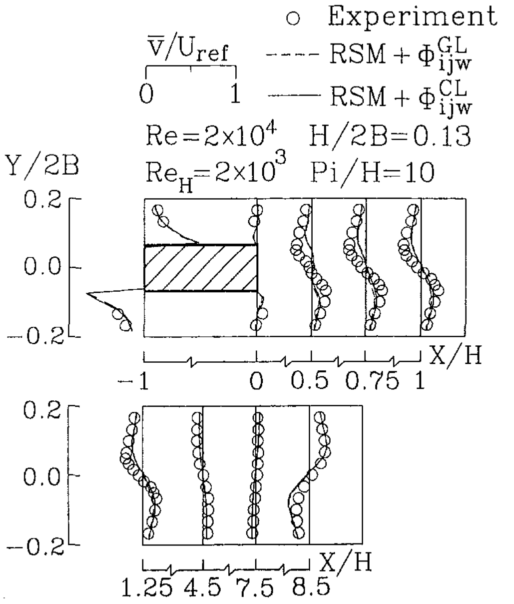

Fig. 8 Streamwise evolution of the measured and computed periodic fully developed transverse time mean velocity profile in one pitch module (Uncertainty in $\overline{V}/U_{ref}$: less than ±3.2 percent)

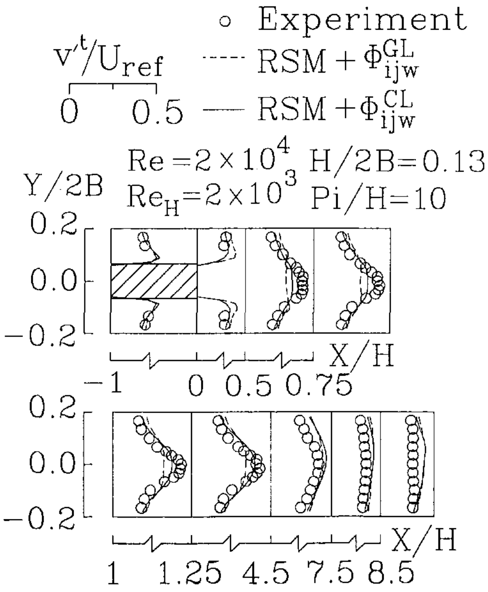

Fig. 10 Measured and computed periodic fully developed transverse total fluctuation intensity and Reynolds stress profiles in one pitch module (Uncertainty in v'^t/U_{ref}: less than ±4.4 percent)

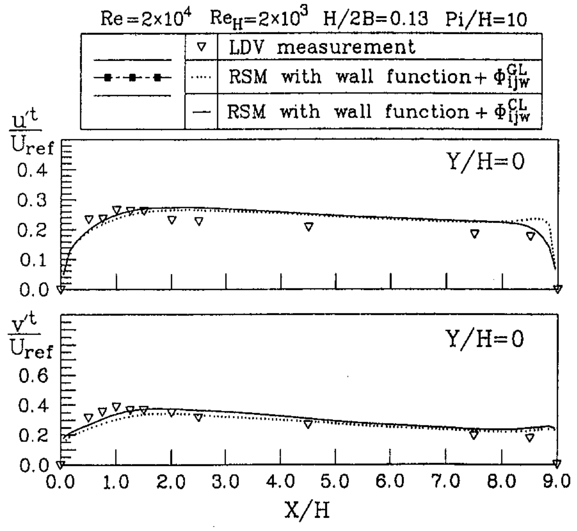

Fig. 11 Measured and computed streamwise and transverse total fluctuation intensity along the channel centerline downstream of the rib

readily available in the existing literature. Figure 5 shows the spatially periodic fully developed streamwise mean velocity profiles in one pitch module for Re = 2×10^4 and $Pi/H = 10$. The profiles obtained by experiments and computations are quite symmetric and Gaussian in shape throughout the pitch module. The velocity defect is the largest behind the rib, reaches a minimum at $X/H = 7.5$, and then increases again at $X/H = 8.5$ which is 0.5 rib heights before the next rib. The later increase in the velocity defect, lacking in the single rib case depicted in Fig. 4, is due to the core-flow retardation by the successive rib and flow acceleration in the gap region between the rib and duct wall. At almost every streamwise station X/H, the velocity profile has two inflection points in the shear layer along the rib top and bottom. The agreement between the computed and measured axial mean velocity profiles is satisfactory, typically within 5 percent of U_{ref}, except in the near wake center region where the disagreement ranges from 5 to 30 percent of U_{ref}. Figure 6 shows the variation of the measured and computed spatially periodic fully developed streamwise mean velocity with X/H behind the rib and along the channel centerline. The experimental trend is computationally captured. There is no noticeable difference between the predicted results of the models ϕ_{ijw}^{CL} and ϕ_{ijw}^{GL} in Figs. 5 and 6. This is in part because for the periodic fully developed case the centerline mean velocity upstream of the rib decreases from a maximum of 0.7 U_{ref} to zero at the rib's front edge, whereas for the developing flow case the centerline mean velocity decreases from U_{ref} to zero.

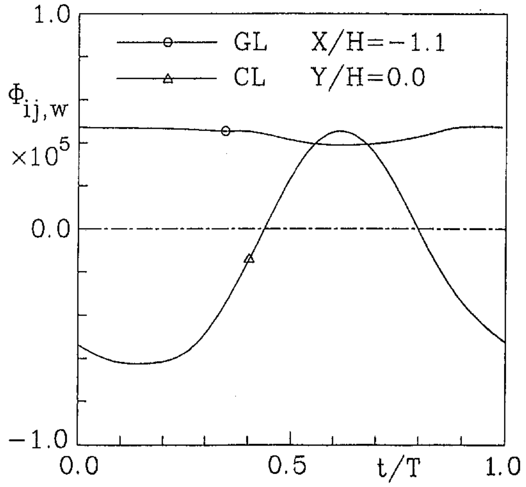

Fig. 12 Time evolution of ϕ_{ijw} at $X/H = -1.1$, $Y/H = 0.0$ for two near-wall pressure strain treatment (ϕ_{ijw}^{GL} and ϕ_{ijw}^{CL}) in one shedding cycle

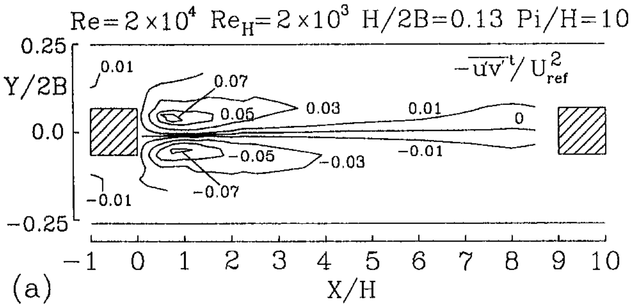

Fig. 13(a)

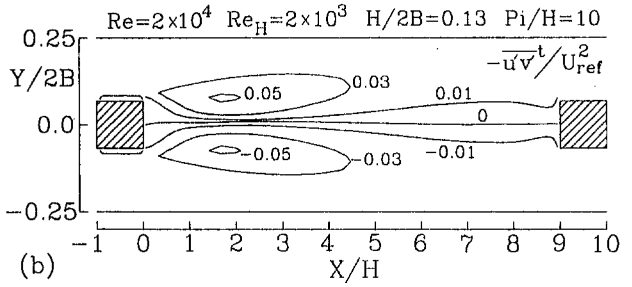

Fig. 13(b)

Fig. 13 Total time-mean shear stress contours in one pitch module: (*a*) experiment and (*b*) computation ($-u'v'^t/U_{\text{ref}}^2$: less than ±4.8 percent)

The computed vector plots of the periodic fully developed mean velocity field around the rib is depicted in Fig. 7. For the case of a rib array, the shear layers along the rib top and bottom both separate at rib's rear edge to form a wake shorter than that for the single rib case, as can be seen from Fig. 7 and the experimental data in Fig. 6. A similar difference in the separation point can also be found for the cases of flow through the single and multiple attached rib pairs (Liou et al., 1990; Liou et al., 1993). Physically, for the periodic fully developed case the fluid flow has adjusted itself many times from pitch to pitch such that the turning angle around the rib top front corner is smaller than that of the developing case (Fig. 3). The larger turning angle for the latter leads to an earlier separation at the rib top front corner. The dimensionless wake lengthes X_R/H obtained by the present measurements and computations are 0.92 and 1.3, respectively, for the periodic fully developed flow. It should be pointed out that although the X_R/H for the periodic fully developed flow and for the single rib flow by Durao et al. and Lyn et al. are almost the same, the length of the separated flow region in the works of Durao and Lyn et al. are about one rib height longer than that of the present study due to the occurrence of separation at rib front corners for the former.

The velocity defect in the wake exists through the entire pitch module in the present case, whereas the velocity defect recovers to about 90 percent of the bulk mean velocity at about $X/H = 5.0$ in the single cylinder case of Durao et al. (Fig. 4). The above comparison indicates that the interference between multiple ribs for the rib pitch-to-height ratio $PR = 10$ examined is less significant in the near wake region, but more influential on the far wake field and rib top and bottom flow separation points, as compared with the single rib case.

Figure 8 depicts the periodic fully developed transverse mean velocity profiles in one pitch module for $Pi/H = 10$ and Re = 2×10^4. Reasonable agreement between the computed and measured results has been demonstrated. Typical discrepancies are 1 to 17 percent of U_{ref} in the near wake region and 7 percent

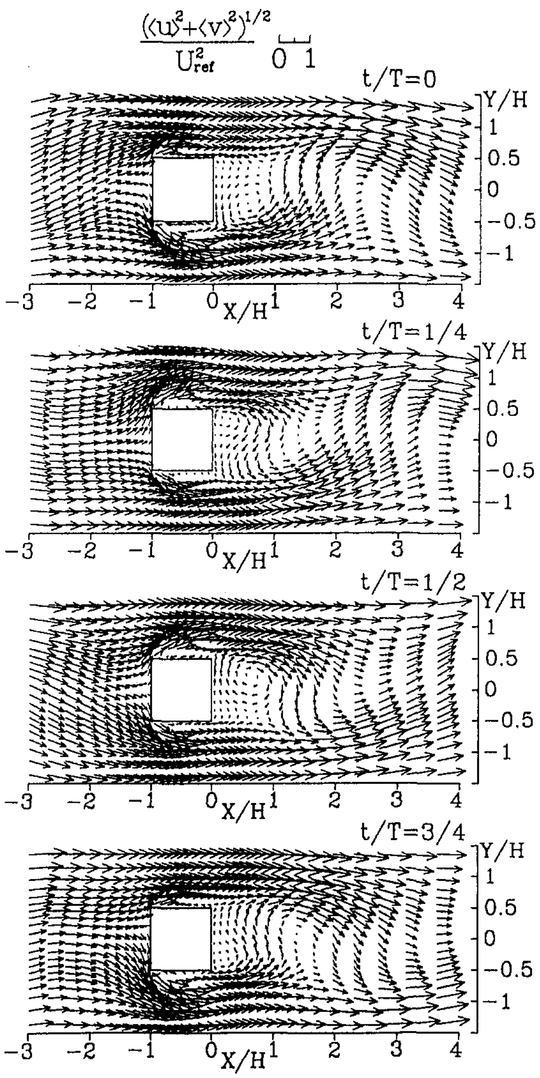

Fig. 14(*a*) Present computed phase-averaged velocity vector plots at four phases for periodic fully developed flow past a rib array

of U_{ref} in other regions. Comparing those around the rib's rear edge and in the wake region, the level of $\overline{v}/U_{\mathrm{ref}}$ is larger around the rib's leading edge $X/H = -1$ where the core flow turns into the gap region between the rib and the duct wall because of the blocking effect of the rib. The antisymmetric $\overline{v}/U_{\mathrm{ref}}$ profiles at $X/H = 8.5$ and $X/H = 0.5$ are opposite and indicate flow contraction and expansion immediately upstream and downstream of the rib bluff body, respectively.

Periodic Fully Developed Total Fluctuation Intensity and Reynolds Stress. Figures 9 and 10, respectively, depict the measured and computed periodic fully developed total streamwise and transverse fluctuation intensity profiles in one pitch module for $Pi/H = 10$ and $\mathrm{Re} = 2 \times 10^4$. The streamwise fluctuation intensity profiles of the near wake stations have two evident maxima in the upper and lower shear layer regions, while the transverse fluctuation intensity has one peak in the wake center region. The discrepancy between the measured and computed u''/U_{ref} is larger in the wake region, up to about 22 and 18 percent of U_{ref} for ϕ_{ijw}^{GL} and ϕ_{ijw}^{CL}, respectively. As a reference, the largest discrepancy between the computation by Franke and Rodi (1993) and the experiments of Lyn et al. (1994) and Durao (1988) for a developing flow past a single rib is about 14 and 30 percent of U_{ref}, respectively. The larger discrepancy in the wake region suggests the necessity of a further improvement in the turbulence model for wake region. To more clearly demonstrate the difference between the computed results using ϕ_{ijw}^{GL} and ϕ_{ijw}^{CL}, the total streamwise and transverse fluctuation intensity distribution along the channel centerline downstream of the rib is depicted in Fig. 11. The computation with ϕ_{ijw}^{GL} shows a peculiar peak in the total streamwise fluctua-

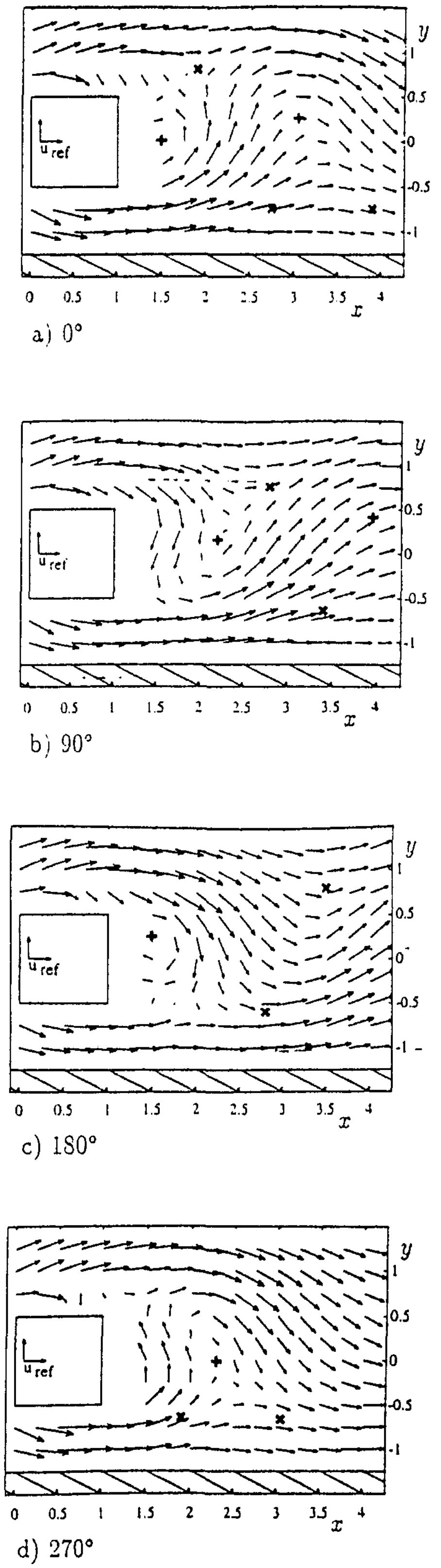

a) 0°

b) 90°

c) 180°

d) 270°

Fig. 14(*b*) Measured phase-averaged velocity vector plots at four phases for a developing flow past a single rib (Bosch et al., 1996)

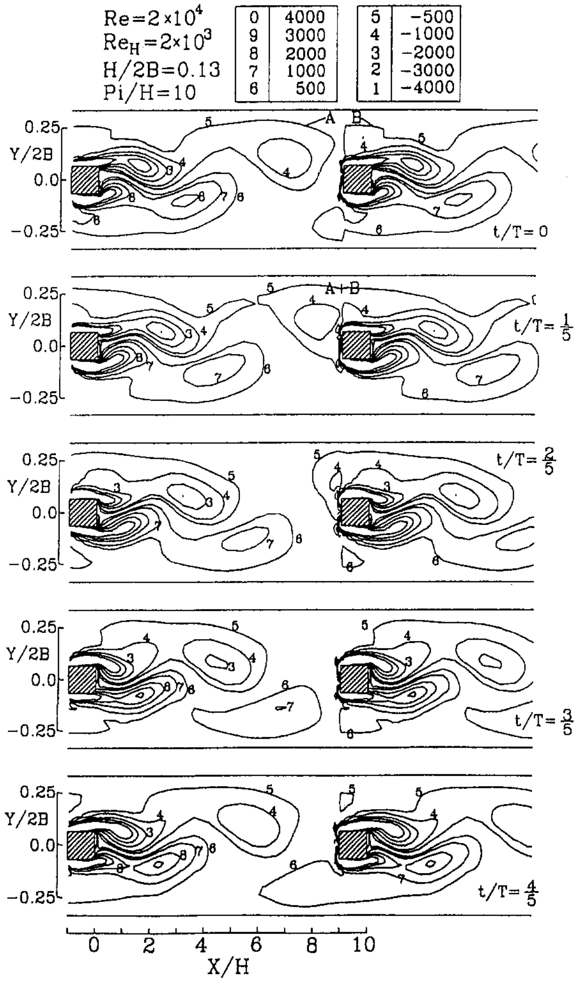

Fig. 15 Computed phase-averaged vorticity contours for spatially fully developed detached ribbed channel flow

tion intensity at $X/H = 8.8$, as compared with the computation with ϕ_{ijw}^{CL}. The peculiar peak is due to the inappropriate near-wall enhancement of isotropisation at impingement/reattachment region associated with ϕ_{ijw}^{GL}, as evidenced by Fig. 12. Because of this relative advantage of ϕ_{ijw}^{CL} over ϕ_{ijw}^{GL}, only the computed results associated with ϕ_{ijw}^{CL} will be shown in the following section.

The presence of the shear in the mean flow is an important source for the turbulence generation. Figures 13(*a*) and 13(*b*), respectively, show the measured and computed contours of the total shear stress in one pitch module for $Pi/H = 10$ and $\mathrm{Re} = 2 \times 10^4$. Both measurements and computations depict the large shear stress along the upper and lower wake shear layers. The measured maximum shear stress $-u'v''/U_{\mathrm{ref}}^2 = 0.07$ is located around $X/H = 1.0$, while the calculated maximum $-u'v''/U_{\mathrm{ref}}^2 = 0.05$ is around $X/H = 1.6$. The present measured and computed maximum shear stresses are smaller than $-u'v''/U_{\mathrm{ref}}^2 = 0.2$ measured by Durao et al. (1988) for the single rib case. The reason is again attributable to the quicker velocity defect recovery of their single rib case due to a lack of flow retardation by the presence of the successive rib.

Unsteady Flow

Periodic Fully Developed Phase-Averaged Velocity Field. The vortex shedding phenomenon cannot be revealed by the above long-time-averaged flow field; however, it can be demonstrated by the phase-averaged flow field. Figures 14(*a*) and 14(*b*), respectively, show the present computed phase-averaged velocity vector plots for the periodic fully developed flow and the corresponding plots for a developing flow past a single rib measured by Bosch et al. (1996) at four phases. The vortex shedding is clearly demonstrated in these plots. Comparing the velocity vectors in Figs. 14(*a*) and 14(*b*), generally good agreement in trend can be seen concerning the vortex formation and shedding; however, the downstream velocity profiles and transport of the vortices are different due to the interference of the downstream rib for the spatially fully developed flow case. Figure 15 shows the phase-averaged vorticity contours at 5 phases for the periodic fully developed flow. The vortex shedding revealed from Fig. 15 has a single frequency of $\mathrm{St} = 0.142$. For the case of flow passing through a single rib, the Strouhal numbers reported by Durao et al. (1988) and Lyn et al. (1995) were 0.139 and 0.135, respectively. The Strouhal numbers of the spatially periodic fully developed flow and single-rib developing flow are close. This together with the similar phase-averaged flow patterns in the rib near wake between the two cases (Fig. 14) suggest that the interference of multiple ribs does not effectively affect the vortex shedding. Figure 15 also shows that the shedding vortices of the previous rib just bump into the next rib and merge into the new born vortex (e.g., $t = 2T/5$).

Figure 16(*a*) depicts the vortex peak trajectory in one cycle of vortex shedding. The location of the vorticity peak (X_p and Y_p) can be identified as the vortex center. It is seen that the vortex (solid circle in Fig. 16(*a*)) goes straight in the lower half of the channel for $X_p/H \leqq 5.3$. Beyond $X_p/H = 5.3$, it gradually moves toward the lower side of the downstream rib ($t = \frac{4}{5}T$, Fig. 15) as a result of the blockage effect of the downstream rib. Figure 16(*a*) further indicates the decaying of vorticity peak value with increasing streamwise coordinate (open circle in Fig. 16(*a*)). The vorticity peak decays rapidly for $X_p/H \leqq 5.3$ and at a slower rate downstream of $X_p/H = 5.3$ due to the presence of the successive rib. Figure 16(*b*) depicts the variation of the streamwise location of the vortex peak with time. The slope of the curve gives the vortex celerity U_c. Within the range of $4.0 < X_p/H < 9.0$, the vortex celerity is almost a constant of $U_c = 0.84\ U_{\mathrm{ref}}$, which is slightly higher than $0.78\ U_{\mathrm{ref}}$ of Lyn and Rodi (1995) obtained for a developing flow past a single rib. The uncertainties in the reported vortex celerities of Lyn and Rodi (1995) and present study are 6 and 3 percent, respectively. The streamwise separation of successive vorticity peaks in the wake region can be considered as a distance travelled by a vortex in one cycle, i.e., $1 = U_c/f$. In the present

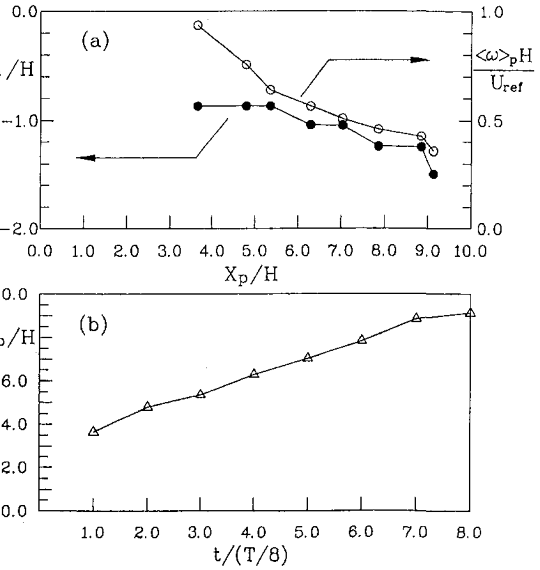

Fig. 16(*a*) Trajectory of vortex peak and variation of vortex peak value with *X/H*; (*b*) time history of streamwise vortex peak location

periodic fully developed case, the vortex travelling distance per cycle is about 5.9 H, which is smaller than the pitch (10 H) and again quite close to the value of 5.8 H obtained by Lyn and Rodi (1995) for the developing single rib flow.

At this point, it may be interesting to mention that the crisscross motion, reported by Suzuki et al. (1993, 1994a) for laminar flows over a single rib with a blockage ratio ranged over 0.1–0.5, is not present in the present work with a blockage ratio of 0.13. This difference may be due to the different flow regimes of two cases.

Conclusions

The following conclusions are drawn from the data presented:

(1) The numerical computations and LDV measurements of long-time-averaged mean velocities, total fluctuation intensities, and Reynolds shear stress for the spatially periodic turbulent flow past an array of bluff bodies aligned along the channel axis are reported for the first time. In general, the experimental trend is computationally captured. For most regions, the disagreements between measured and simulated mean velocity and total fluctuation intensity profiles are typically within 7 and 10 percent of U_{ref}, respectively, whereas the disagreements in the near wake center region range from 1 to 30, and 4 to 18 percent of U_{ref}, respectively.

(2) Code validations based on the developing single-rib flow as well as spatially fully developed rib-array flow suggest that in general, a better prediction is attained by the Reynolds stress model with wall function and wall-related pressure strain treatment of Craft and Launder (1992).

(3) Fluid flow separates at the rib top and bottom rear corners for the case of spatially fully developed rib-array flow whereas it separates at the rib top and bottom front corners for the case of developing single-rib flow. The reason is that the flow turning angle around the rib top front corner is smaller for the former than the latter.

(4) For the rib pitch to height ratio examined, both the phase-averaged flow field (featured by the vortex shedding strouhal number, vortex celerity, vortex travelling distance in a phase cycle) and long-time-averaged flow field (featured by the mean wake length behind the rib near edge) indicate the interference between ribs is less significant in the rib near wake region and more influential on the rib far wake region and rib top and bottom flow separation points.

Acknowledgments

This research was supported by the National Science Council of the Republic of China under Contracts NSC83-0401-E007-014 and NSC84-2212-E007-049.

References

Amon, C., and Mikic, B. B., 1991, "Spectral Element Simulations of Unsteady Forced Convective Heat Transfer: Application to Compact Heat Exchanger Geometries," *Numerical Heat Transfer*, Part A, Vol. 19, pp. 1–19.

Bosch, G., Kappler, M., and Rodi, W., 1996, "Experiments on the Flow Past a Square Cylinder Placed near a Wall," *Experimental Thermal and Fluid Science*, Vol. 13, pp. 292–305.

Bosch, G., and Rodi, W., 1996, "Simulation of Vortex Shedding Past a Square Cylinder near a Wall," *International Journal of Heat and Fluid Flow*, Vol. 17, No. 3, pp. 267–275.

Craft, T. J., and Launder, B. E., 1992, "New Wall-Reflection Model Applied to the Turbulent Impinging Jet," *AIAA Journal*, Vol. 30, pp. 2970–2975.

Davis, R. W., Moore, E. F., and Purtell, P., 1984, "A Numerical-Experimental Study of Confined Flow Around Rectangular Cylinders," *Physics of Fluids*, Vol. 27, No. 1, pp. 46–59.

Durao, D. F. G., Heitor, M. V., and Pereira, J. C. F., 1988, "Measurements of Turbulent and Periodic Flows around a Square Cross-Section Cylinder," *Experiments in Fluid*, Vol. 6, pp. 298–304.

Durst, F., Melling, A., and Whitelaw, J. H., 1976, *Principles and Practice of Laser-Doppler Anemometry, Academic Press*, New York, Chapter 9.

Fiebig, M., 1996, "Embedded Vortices in Internal Flow: Heat Transfer and Pressure Loss Enhancement," *International Journal of Heat and Fluid Flow*, Vol. 16, pp. 376–388.

Franke, R., Rodi, W., and Schonung, B., 1990, "Numerical Simulation of Laminar Vortex Shedding Flow Past Cylinders," *Journal of Wind Engineering and Industrial Aerodynamics*, Vol. 35, pp. 237–257.

Franke, R., and Rodi, W., 1993, "Calculation of Vortex Shedding past a Square Cylinder with Various Turbulence Models," *Turbulent Shear Flow 8*, Durst, F. et al., eds, Springer, New York, pp. 189–204.

Gibson, M. M., and Launder, B. E., 1978, "Ground Effects on Pressure Fluctuations in the Atmospheric Boundary Layer," *Journal of Fluid Mechanics*, Vol. 86, pp. 491–511.

Hussain, A. K. M. F., and Reynolds, W., 1970, "The Mechanics of an Organized Wave in Turbulent Shear Flow," *Journal of Fluid Mechanics*, Vol. 41, pp. 241–258.

Issa, R. I., 1985, "Solutions of the Implicitly Discretized Fluid Flow Equations by Operator Splitting," *Journal of Computational Physics*, Vol. 62, pp. 40–65.

Karniadakis, G. E., Mikic, B. B., and Patera, A. T., 1988, "Minimum Dissipation Transport Enhancement by Flow Destabilization: Reynolds Analogy Revisited," *Journal of Fluid Mechanics*, Vol. 192, pp. 365–391.

Kawaguchi, Y., Suzuki, K., and Sato, T., 1985, "Heat Transfer Promotion with a Cylinder Array Located Near the Wall," *International Journal of Heat and Fluid Flow*, Vol. 6, No. 4, pp. 249–255.

Launder, B. E., Reece, G. J., and Rodi, W., 1975, "Progress in the Development of a Reynolds-Stress Turbulence Closure," *Journal of Fluid Mechanics*, Vol. 68, pp. 537–566.

Leonard, B. P., 1979, "A Stable and Accurate Convective Modelling Procedure Based on Quadratic Upstream Interpolation," *Computer Methods in Applied Mechanics and Engineering*, Vol. 19, pp. 59–99.

Li, G., and Humphrey, J. A. C., "Numerical Modelling of Confined Flow past a Cylinder of Square Cross-Section at Various Orientations," *International Journal for Numerical Methods in Fluids*, Vol. 20, pp. 1215–1236.

Liou, T. M., Chang, Y., and Hwang, D. W., 1990, "Experimental and Computational Study of Turbulent Flows in a Channel with Two Pairs of Turbulence Promoters in Tandem," ASME JOURNAL OF FLUIDS ENGINEERING, Vol. 112, pp. 302–310.

Liou, T. M., Wu, Y. Y., and Chang, Y., 1993, "LDV Measurements of Periodic Fully Developed Main and Secondary Flows in a Channel with Rib-Disturbed Walls," ASME JOURNAL OF FLUIDS ENGINEERING, Vol. 115, pp. 109–114.

Liou, T. M., Wang, W. B., and Chang, Y. J., 1995, "Holographic Interferometry Study of Spatially Periodic Heat Transfer in a Channel with Ribs Detached from One Wall," ASME *Journal of Heat Transfer*, Vol. 117, pp. 32–39.

Liou, T. M., Yang, C. P., and Lee, H. L., 1997, "LDV Measurements of Spatially Periodic Flows over a Detached Solid-Rib Array," ASME JOURNAL OF FLUIDS ENGINEERING, Vol. 119, No. 2, pp. 383–389.

Lyn, D. A. and Rodi, W., 1994, "The Flapping Shear Layer Formed by Flow Separation from the Forward Corner of a Square Cylinder," *Journal of Fluid Mechanics*, Vol. 267, pp. 353–376.

Lyn, D. A., Einav, S., Rodi, W., and Park, J. H., 1995, "A Laser-Doppler Velocimetry Study of Ensemble-Averaged Characteristics of the Turbulent Near Wake of a Square Cylinder," *Journal of Fluid Mechanics*, Vol. 304, pp. 285–319.

Marumo, E., Suzuki, K., and Sato, T., 1985, "Turbulent Heat Transfer in a Flat Plate Boundary Layer Disturbed by a Cylinder," *International Journal of Heat and Fluid Flow*, Vol. 6, No. 4, pp. 241–248.

Murakami, S., Mochida, A., Rodi, W., and Franke, R., 1993, "Large Eddy Simulation of Turbulent Vortex Shedding Flow Past 2D Square Cylinders," *Engineering Applications of Large Eddy Simulation*, FED-Vol. 162, ASME, pp. 113–120.

Oyakawa, K., and Mabuchi, I., 1983, "Fluid Flow and Heat Transfer in a Parallel Plate Duct Containing a Cylinder," *Bulletin of JSME*, Vol. 48, No. 432, pp. 1509–1519.

Oyakawa, K., Shinzato, T., and Mabuchi, I., 1986, "Effect on Heat Transfer Augmentation of Some Geometric Shapes of a Turbulence Promoter in a Rectangular Duct," *Bulletin of JSME*, Vol. 29, No. 256, pp. 3415–3420.

Patankar, S. V., 1980, *Numerical Heat Transfer and Fluid Flows*, McGraw-Hill, New York.

Rhie, C. M. and Chow, W. L., 1983, "Numerical Study of the Turbulent Flow past an Airfoil with Trailing Edge Separation," *AIAA Journal*, Vol. 21, pp. 1525–1532.

Rodi, W., 1984, *Turbulence Models and Their Applications in Hydraulics*, McGraw-Hill, New York.

Rodi, W., 1993, "On the Simulation of Turbulent Flow Past Bluff Bodies," *Journal of Wind Engineering and Industrial Aerodynamics*, Vol. 46 & 47, pp. 3–19.

Speziale, C. G., 1986, "The Dissipation Ratio Correlation and Turbulent Secondary Flows in Noncircular Ducts," ASME JOURNAL OF FLUIDS ENGINEERING, Vol. 108, No. 1, pp. 118–120.

Suzuki, K., 1996, "Flow Modification and Heat Transfer Enhancement with Vortices," *The Ninth International Symposium on Transport Phenomena in Thermal-Fluids Engineering*, Singapore, June 25–28, pp. 72–83.

Suzuki, H., Inoue, Y., Nishimura, T., Fukutani, K., and Suzuki, K., 1993, "Unsteady Flow in a Channel Obstructed by a Square Rod (Crisscross Motion of Vortex)," *International Journal of Heat and Fluid Flow*, Vol. 14, No. 1, pp. 2–9.

Suzuki, K. and Suzuki, H., 1994a, "Instantaneous Structure and Statistical Feature of Unsteady Flow in a Channel Obstructed by a Square Rod," *International Journal of Heat and Fluid Flow,* Vol. 15, No. 6, pp. 426–437.

Suzuki, K., Xi, G. N., Inaoka, K., and Hagiwara, Y., 1994b, "Mechanism of heat Transfer Enhancement Due to Self-Sustained Oscillation for an In-Line Array," *International Journal of Heat and Mass Transfer,* Vol. 37, Suppl. 1, pp. 83–96.

Tamura, T., Ohta, I. and Kuwahara, K., 1990, "On the reliability of Two-Dimensional Simulation for Unsteady Flows Around a Cylinder-type Structure," *Journal of Wind Engineering and Industrial Aerodynamics,* Vol. 35, pp. 275–298.

Tatsutani, K., Devarakonda, R. and Humphrey, J. A. C., 1993, "Unsteady Flow and Heat Transfer for Cylinder Pairs in a Channel," *International Journal of Heat and Mass Transfer,* Vol. 36, No. 13, pp. 3311–3328.

Treidler, B., and Carey, V. P., 1990, "On the Flows Past an Array of Staggered Ribs in a Channel," *Proceedings of Int'l Symposium on Applications of Laser-Doppler Anemometry to Fluid Mechanics,* Lisbon, Portugal, pp. 4.3.1–4.3.6.

Werner, H. and Wengle, H., 1991, "Large-Eddy Simulation of Turbulent Flow over and around a Cube in Plate Channel," *Proc. 8th Symp. on Turbulent Shear Flows,* 19–4, Munich.

Valencia, A., 1996, "Unsteady Flow and Heat Transfer in a Channel with a Built-In Tandem of Rectangular Cylinders," *Numerical Heat Transfer,* Part A, Vol. 29, pp. 613–623.

Yang, K. S., and Ferziger, J. H., 1993, "Large-Eddy Simulation of Turbulent Obstacle Flow Using a Dynamic Subgrid-Scale Model," *AIAA Journal,* Vol. 31, No. 8, pp. 1406–1413.

Yao, M., Nakatani, M., and Suzuki, K., 1987, "An Experimental Study on Pressure Drop and Heat Transfer in a Duct with a Staggered Array of Cylinders," ASME-JSME *Thermal Engineering Joint Conference,* Marto, P. J., and Tanasawa, I., eds., Vol. 5, pp. 189–196.

Yao, M., Nakatani, M., and Suzuki, K., 1989, "Flow Visualization and Heat Transfer Experiments in a Duct with a Staggered Array of Cylinders," *Experimental Thermal and Fluid Science,* Vol. 2, pp. 193–200.

Yoshiki Yoshida
Associate Professor.

Yoshinobu Tsujimoto
Professor.

Osaka University,
Engineering Science,
1-3 Machikaneyama, Toyonaka,
Osaka 560-8531, Japan

Takashi Kawakami
Manager,
Mitsubishi Heavy Industries, LTD.,
Takasago Machinery Works,
2-1-1 Shinhama, Takasago,
Hyogo 676-8686, Japan

Toru Sakatani
Researcher,
Kobe Steel, LTD.,
Technology Department,
1-5-5 Nishiku, Kobe,
Hyogo 651-2271, Japan

Unbalanced Hydraulic Forces Caused by Geometrical Manufacturing Deviations of Centrifugal Impellers

When an impeller has geometrical manufacturing deviations, synchronous vibration occurs from an unbalanced hydraulic force rotating with the impeller. This phenomenon is termed ''Hydraulic unbalance.'' In this study, experiments and analyses were carried out to study the hydraulic unbalance. We made several model impellers with intentional ''manufacturing deviations'': in vane angle, vane pitch, and with eccentricity. Hydraulic forces were estimated from the rotor vibrations. The results of the experiments showed that the magnitude of the hydraulic force increased as the increase of the extent of manufacturing deviations. It was also shown that the amplitude and the phase of the vibration due to the unbalanced hydraulic force depend on the flow rate. This character of the unbalanced hydraulic force is quite different from that of the mass unbalance force, which is independent of the flow rate. A two-dimensional inviscid flow analysis was carried out to clarify the characteristic of the unbalanced hydraulic force. It was found that the hydraulic force can be divided into three components which are constant, linear and parabolic function of the flow rate. Applications of the present results show that the ''hydraulic unbalance'' of a high-speed pump impeller manufactured within a geometrical tolerance recommended by a typical standard can be larger than the ordinary ''mechanical unbalance.'' It was thus shown that the hydraulic unbalance is one of the important factors in the balancing of high-speed pump rotors.

Introduction

A pump impeller with manufacturing deviations exhibits synchronous vibrations caused by rotating radial thrusts. These rotating loads can be separated into the ''hydraulic unbalance,'' and the ''mechanical unbalance.'' The former is caused by the asymmetric pressure and momentum flux distribution around the impeller, which rotate with the impeller. The hydraulic unbalance is a synchronous excitation whose magnitude is proportional to the 2nd power of the impeller rotational speed.

France (1993) described in his paper, ''Generally speaking the magnitude of hydraulic unbalance generated by an impeller is greater than the residual mass unbalance component.'' Further, Verhoeven (1988a, 1988b) and Bolleter et al. (1989) also stated the same views. Yamaguchi et al. (1981) tested a pump-turbine runner in which one outlet flow path area was made five percent smaller than the others, and found that this geometrical deviation virtually had no influence on the radial thrust. Guelich et al. (1987) tested a semi-axial pump impeller with the outlet angle of one vane increased from 36 deg to 51 deg, and found that the rotating radial thrust increased to about twice of the original values over the entire flow range. However, this variation of +15 deg is much larger than any manufacturing tolerance. The importance of the hydraulic unbalance caused by the geometrical manufacturing deviation can be recognized from these studies. However, the relations between the unbalanced hydraulic force and the variation of the geometrical deviation are not fully understood yet, both quantitatively and qualitatively.

The purpose of this study is to obtain a quantitative understanding of the hydraulic unbalanced force due to geometrical manufacturing deviations of centrifugal impellers. First, we report about the measured unbalanced hydraulic forces of model impellers with intentional manufacturing deviations, in order to elucidate the characters of the hydraulic unbalanced force. Second, two-dimensional inviscid flow analysis is carried out to understand those characters. Finally, the hydraulic unbalance of a prototype high-speed pump impeller manufactured within the geometrical tolerance is discussed based on the obtained results.

Experimental Apparatus

The unbalanced hydraulic forces of model impellers were determined from the rotor vibrations at supercritical speed. In order to make the natural frequency as small as possible, we used a vertical suspended shaft system, as shown in Fig. 1.

The bearing cartridge supports the main shaft through two bearings, and the cartridge, hung by the gimbals, can execute a free pendulum motion. D.C. motor drives the main shaft through the drive pulley and the flexible coupling. Four identical conical springs support the lower end of the bearing cartridge, and adjust the natural frequency of the pendulum motion. Two gap sensors are installed perpendicularly facing to the bearing cartridge with each other to measure the shaft vibrations. The output of the sensor was calibrated to obtain the displacement at the position of the impeller.

Figure 2 shows the details around the impeller. Test impeller is a simplified model of a shrouded centrifugal impeller for a boiler feed pump. The flow is supplied to the impeller after passing through a booster pump, an area-type flow meter, and a control valve. The impeller discharges the flow directly into the reservoir without a vaned diffuser or a volute casing. The reservoir has a circumferential symmetry to prevent the streamlines leaving the impeller to be disturbed by the wall of the reservoir. Then, the fluid interaction between impeller and cas-

---

Contributed by the Fluids Engineering Division for publication in the JOURNAL OF FLUIDS ENGINEERING. Manuscript received by the Fluids Engineering Division April 2, 1997; revised manuscript received February 26, 1998. Associate Technical Editor: B. Schiavello.

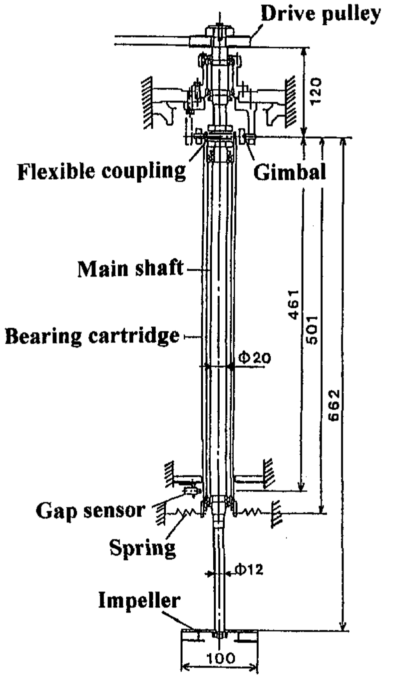

All units in mm

Fig. 1 Experimental apparatus (shaft system)

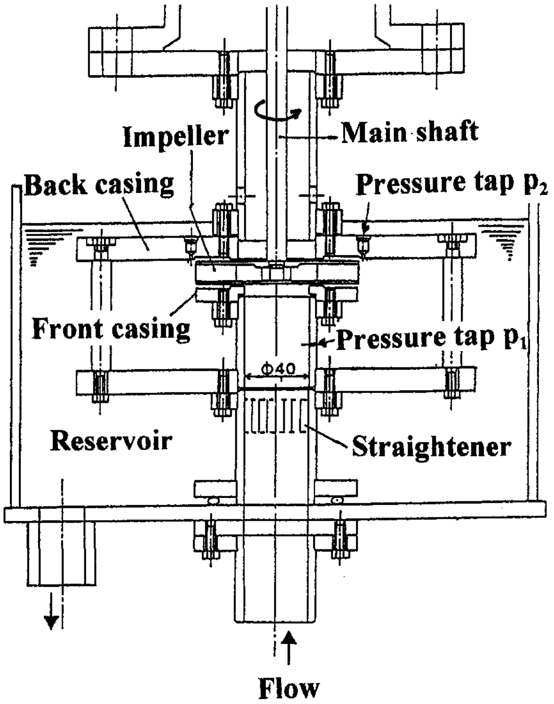

Fig. 2 Experimental apparatus (details around impeller)

ing is nearly absent in the present study. This interaction will be studied in the future in order to simulate more realistic pump conditions. During the experiments, the axial clearance between the impeller and front/back casing is kept to be 0.3/0.35 mm, respectively, because of the leakage prevention. The pressure tap is placed at the impeller outlet ($r/r_2 = 1.06$) on the back casing, and the static pressure (p_{2s}) is measured with a manometer.

Table 1 shows the principal dimensions of the test impellers. The impellers are strictly two-dimensional with 5 vanes having constant width ($b_1 = b_2 = b$) and axial leading edge (r_1 = constant hub-to-tip) and constant vane angle ($\beta_1 = \beta_2 = \beta$), i.e., logarithmic vanes with baseline vane angle $\beta = 20$ deg. Thus in the present study two dimensional purely radial flow impellers are investigated, experimentally and theoretically. Seven impellers without and with intentional geometrical deviations, as shown in Fig. 3 and Table 2, were tested. No. 1 impeller (baseline) has no geometrical deviation. One vane of Nos. 2, 3, 4, and 5 impellers has larger vane angle β^* ($=\beta_1^* = \beta_2^*$) = 22.5, 25, 27.5 and 25 deg, respectively. Nos. 2, 3, and 4 impellers are with uneven inlet pitch and with even outlet pitch. No. 5 impeller is with uneven outlet pitch and with even inlet pitch. The vanes of Nos. 6 and 7 impellers are located around an eccentric center with an eccentricity "**e**" from the center of rotation. This type of manufacturing deviation is frequently found in sand-cast impellers. These test impellers were manu-

Nomenclature

b = impeller width ($b_1 = b_2 = b$)
C_p = pressure coefficient ($=(p - p_{1t})/\rho u_2^2$)
c = vane chord length
e = eccentricity
F = unbalanced hydraulic force
$\mathbf{F}$ = vector of unbalanced hydraulic force
F^* = nondimensional value of F (normalized by $\rho u_2^2 r_2 b_2$)
$\mathbf{F}^*$ = nondimensional value of $\mathbf{F}$ (normalized by $\rho u_2^2 r_2 b_2$)
F_i = divided component of F
G = residual mass unbalance (mm/s)
i = imaginary index
M = mass of attached weight
N = number of vanes
n = rotational speed (rpm)
p = pressure
Q = flow rate
r = radius
t = vane thickness
s = length along vane
u = peripheral velocity of impeller
v = absolute velocity
w = complex conjugate velocity ($=v_x - iv_y$)
z = complex coordinate ($=x + iy$)
α = angle made by tangent of vane and x-axis (See Fig. 7)
β = vane angle (baseline)
β^* = vane angle with manufacturing deviation
γ = vortex distribution
ϵ = amplitude of shaft vibration at impeller position (zero-to-peak)
ρ = fluid density
ϕ = impeller outlet flow coefficient ($=Q/2\pi r_2 b_2 u_2$)
$\phi_{\text{shockless}}$ = shockless outlet flow coefficient ($=(r_1/r_2)^2 \times \tan\beta_1 = 0.09$, $\beta_1 = 20$ deg.)
Ψ = pressure coefficient ($=(p_{2t} - p_{1t})/\rho u_2^2$)
Ψ_s = static pressure coefficient ($=(p_{2s} - p_{1t})/\rho u_2^2$)
$\Psi_{\text{shut off}}$ = pressure coefficient at shut off
Ω = angular velocity of impeller

Superscript

$\bar{}$ = conjugate complex

Subscripts

b = vane
s = static pressure
t = total pressure
x = component of x-direction
y = component of y-direction
1 = impeller inlet
2 = impeller outlet
o = component independent of flow rate
ϕ = component dependent on flow rate

Table 1 Principal dimensions of test impeller

inlet radius	r_1	25 mm
outlet radius	r_2	50 mm
impeller width	$b_1=b_2$	10 mm
vane angle (baseline)	$\beta\ (=\beta_1=\beta_2)$	20 deg.
number of vanes	N	5
vane thickness	t	1 mm
vane chord length	c	73.1 mm

factured by using N.C. mill to keep the accuracy of the intentional "manufacturing deviations." The mechanical unbalance was kept minimum by using a precision dynamic balancing machine. The residual mass unbalance of the test impellers was $G = 0.1-0.15$ mm/s at the test running speed $n = 500$ rpm. This speed is very low in relation to the actual pumps, however, it is approximately three times of the critical speed of the test rotor (163 rpm), as mentioned later.

Experimental Procedure

To examine the vibrational characteristics of the rotor system, an experiment was carried out by using No. 1 impeller with a weight of mass $M = 0.5$ gr. or 1.0 gr. attached on the back-shroud at the impeller outer radius. This experiment was carried out with the impeller in air, so that the hydraulic force on the impeller can be neglected. Figure 4 shows the amplitude (zero-to-peak) of the impeller lateral vibration: ϵ against the running speed: n. This figure includes the results of the calculation by using the equivalent mass and stiffness of the rotor system which were determined from the free vibrations in air. The resonance appears at the natural frequency 167 rpm (2.75 Hz), and the experimental amplitudes agree well with the calculated values. At supercritical speed, it is well known that the impeller should be displaced in the direction opposite to the attached weight. In the present measurement, this occurred at the speeds larger than twice the critical speed.

Figure 5 shows the amplitude of the shaft vibration (zero-to-peak): ϵ plotted against mass of the weight: M attached on the back-shroud at the outer radius, for the running speed 400, 500, and 600 rpm in air. For the constant running speed, the relation between the amplitude and mass is linear, while some scatters were observed over 1.5 gr. The amplitude depends on the running speed; i.e., the amplitudes decrease as the increase of the running speed further from the critical speed, as shown in Fig. 4. From these results and the limitation of the flow rate, we selected 500 rpm for the test running speed which is three times as large as the critical speed. The maximum amplitude of the shaft vibration in present entire experiments is about 80 μm. This value is much smaller than the intentional manufacturing deviations of the test impellers. The theoretical calculation (Tsujimoto et al., 1988) shows that the fluid-induced forces caused by the shaft vibrations are negligible compared with the unbalanced hydraulic forces caused by the geometrical deviations of the present test impellers.

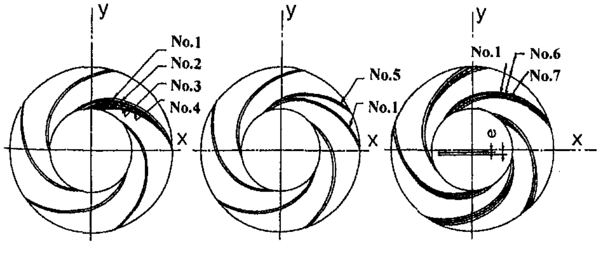

Fig. 3 Test impellers with intentional geometrical deviations (center of rotation is (x, y) = (0, 0), geometrical center of vane is (x, y) = (0, $-e$) in case of No. 6 and No. 7 impeller)

Table 2 Geometrical deviations of test impellers. (No. 1 impeller is baseline without geometrical deviation. Nos. 2–7 impellers have the intentional geometrical deviations in vane angle, vane pitch, and center of vane.)

No. of test impeller	Geometrical deviation
No. 1 (baseline)	without geometrical deviation 5 vanes with $\beta_1=\beta_2=20$ deg. have equal pitch
No. 2	5 vanes have equal outlet pitch, one vane with $\beta_1^*=\beta_2^*=22.5$ deg., i.e. shorter length
No. 3	5 vanes have equal outlet pitch, one vane with $\beta_1^*=\beta_2^*=25$ deg., i.e. shorter length
No. 4	5 vanes have equal outlet pitch, one vane with $\beta_1^*=\beta_2^*=27.5$ deg., i.e. shorter length
No. 5	5 vanes have equal inlet pitch, one vane with $\beta_1^*=\beta_2^*=25$ deg., i.e. shorter length
No. 6	with eccentric geometrical center eccentricity: $e/r_2=0.02$
No. 7	with eccentric geometrical center eccentricity: $e/r_2=0.04$

Note: All vanes have a logarithmic configuration, $\beta=\beta_1=\beta_2$, $\beta^*=\beta_1^*=\beta_2^*$ along with constant width ($b_1=b_2=b$). The vane thickness is constant t=1 mm, with t/c(= thickness/chord length)=0.014

The unbalanced hydraulic forces were estimated as follows. We assume that the shaft vibrations caused by the unbalanced hydraulic force are the same as those caused by the centrifugal force due to a mechanical unbalance. Therefore, we determined the magnitude of the unbalanced hydraulic force by using the relation of Fig. 5 as the calibration curve, and the directions of the hydraulic unbalanced force were determined from the phase of the shaft vibration. Figure 6(a) shows the result of FFT analysis, and Fig. 6(b) the orbit of the shaft vibration for the case of No. 5 impeller in water. One vane of No. 5 impeller has larger vane angle ($\beta^* = 25$ deg) than other vanes ($\beta = 20$ deg, baseline). The synchronous and natural frequency components can be found in the spectrum. In the present study, we focus on the unbalanced hydraulic forces rotating with the impeller, and hence we examine the synchronous component hereafter.

In the $x - y$ frame rotating with the impeller as shown in Fig. 3, the vector of unbalanced hydraulic force $\mathbf{F}$ is represented by $\mathbf{F}_x$ (x-direction) and $\mathbf{F}_y$ (y-direction) components, and normalized by $\rho u_2^2 r_2 b_2$. Thus, the normalized force $\mathbf{F}^*$ is defined as follows.

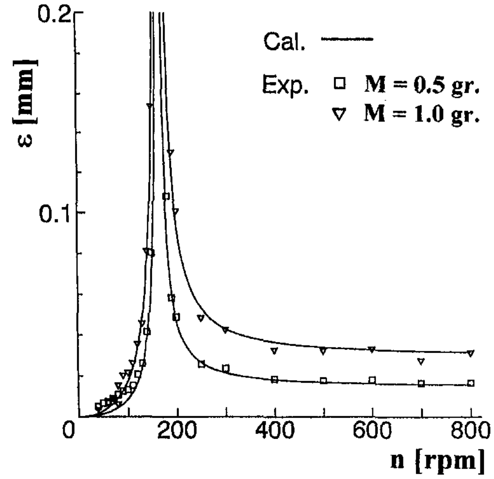

Fig. 4 Amplitude of the shaft vibration ϵ versus rotational speed n (for No. 1 impeller in air, uncertainty in $\epsilon \pm 2$ μm, $M \pm 0.05$ gr, in $n \pm 2$ rpm)

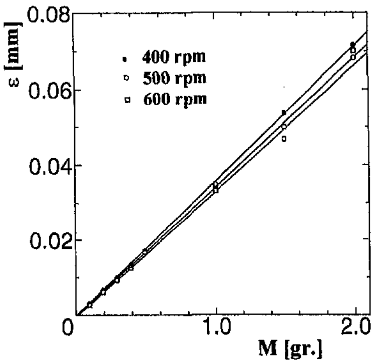

Fig. 5 Amplitude of the shaft vibration ϵ versus mass of the weight M (for No. 1 impeller in air, uncertainty in ϵ ± 2 μm, in M ± 0.05 gr., in n ± 2 rpm)

$$\mathbf{F}^* = \mathbf{F}_x^* + \mathbf{F}_y^* = \frac{\mathbf{F}_x + \mathbf{F}_y}{\rho u_2^2 r_2 b_2}$$

where $u_2 = r_2\Omega$, r_2 = radius of the impeller outlet, b_2 = impeller width.

The effect of small mechanical unbalance of the test impeller was estimated from the test in air, and a correction was made on the measured unbalance force in water. Uncertainty in the amplitude and the phase of the shaft vibration are ±2 percent and ±3 deg. It is estimated that total uncertainty in the measured unbalanced hydraulic force $|\mathbf{F}^*|$ is less than 0.005.

Analysis

Here, we attempt to estimate the unbalanced hydraulic force from two-dimensional potential flow calculation. It is assumed that the flow is two-dimensional, inviscid, and incompressible, and the vanes are sufficiently thin. We apply singularity method directly in the physical plane as shown in Fig. 7. We consider the case without a vaned diffuser and volute casing, and without inlet prerotation. Therefore, the flow is steady in the frame rotating with the impeller.

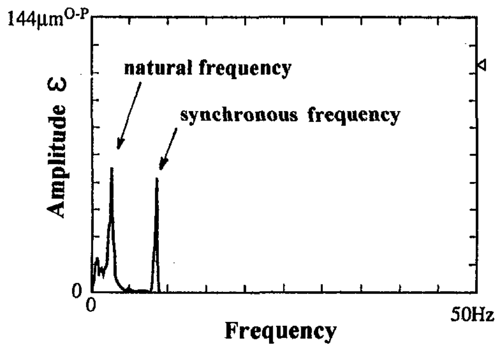

Fig. 6(a) Spectrum analysis

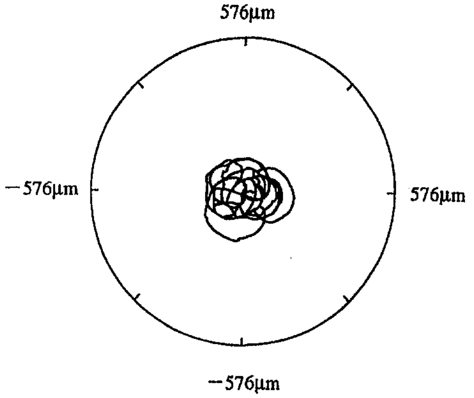

Fig. 6(b) Orbit

Fig. 6 Shaft vibration (for No. 5 impeller in water, ϕ = 0.12 ± 0.002, uncertainty in ϵ ± 2 μm, in frequency ± 0.2 Hz)

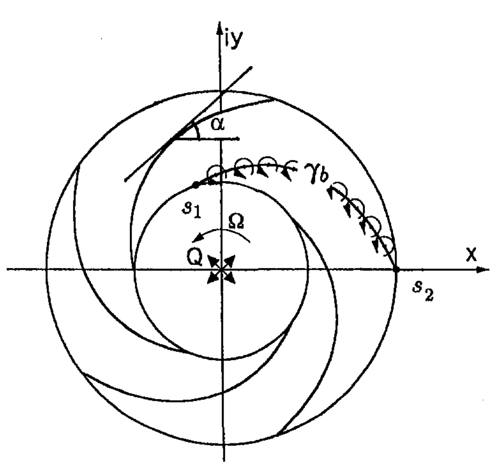

Fig. 7 Impeller in Z-plane for analysis

Basic Equation. We consider a stationary frame $z = x + iy$, as shown in Fig. 7. The impeller rotates with the angular velocity Ω. We put a source Q at the center of the impeller, and represent the vanes by the vortex distribution $\gamma_b(s)$. Then, the complex conjugate absolute velocity $w = v_x - iv_y$ at position z can be written as follows.

$$w = v_x - iv_y = \frac{Q}{2\pi z} + \frac{1}{2\pi i}\sum^{N}\int_{s_1}^{s_2}\frac{\gamma_b(s)}{z - z_b(s)}\,ds \qquad (1)$$

where Σ signifies the sum over all the vanes.

Boundary Condition. The condition that the relative velocity normal to the blade surface is vanishing can be written as follows:

$$\text{Imag}\{e^{i\alpha}(v_x - iv_y + i\Omega\bar{z})\} = 0 \quad \text{at} \quad z = z_b \qquad (2)$$

where α is the angle made by the tangent of the vane and the

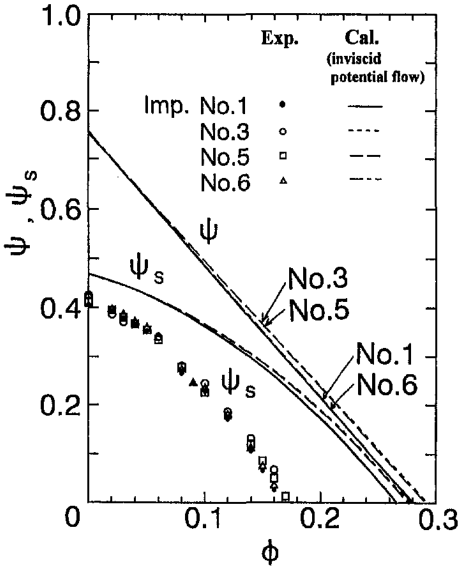

Fig. 8 Pressure performances of test impeller, pressure coefficient Ψ/Ψ_S versus flow coefficient ϕ with calculated results (for Nos. 1, 3, 5, and 6 impellers, experimental uncertainty in ϕ ± 0.002, in Ψ_s ± 0.005)

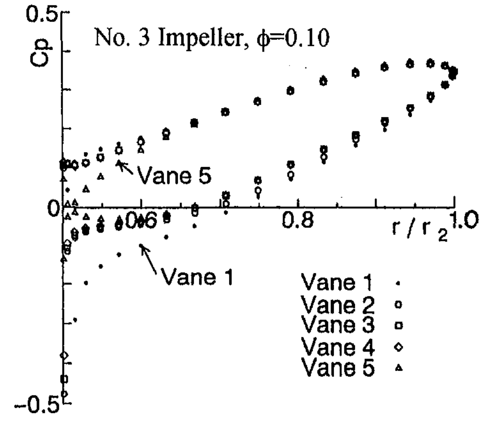

Fig. 9(a) Pressure distribution on vane

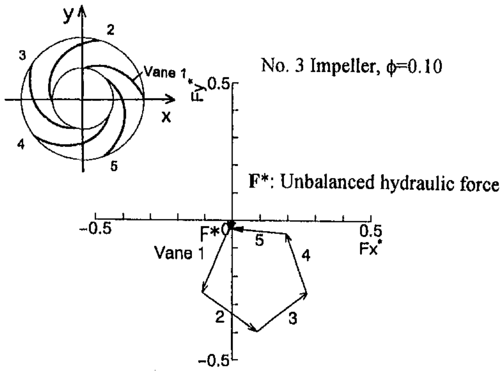

Fig. 9(b) Hydraulic force on vane

Fig. 9 Pressure distribution and hydraulic force on vane (for No. 3 impeller, Vane 1 has deviation, $\phi = 0.10$)

x-axis in Fig. 7. The Kutta's condition at the trailing-edge of each vane can be written as;

$$\gamma_b(s_2) = 0 \tag{3}$$

Then the problem can be reduced to solving the integral Eq. (1) with boundary conditions Eqs. (2) and (3) for the vortex distribution on the vanes. This integral equation can be reduced to a set of linear equations in terms of the value of γ_b at discrete positions on the vane, from which the vortex distribution γ_b is determined.

Hydraulic Force. By applying the conservation law of momentum to the region between a circle of radius r_2 and an infinitely small circle around the center of the impeller, we can express the unbalanced hydraulic force as follows. (Imaichi et al., 1980)

$$F_x - iF_y = i\rho \sum^{N} \left\{ \int_{s_1}^{s_2} \gamma_b(s) \left[\frac{Q}{2\pi z_b(s)} + i\Omega \bar{z}_b(s) \right] ds \right\} \tag{4}$$

The first term represents the force on the vane vortices due to the velocity induced by the source Q, the second term due to the rotation Ω of the impeller.

Flow Rate Dependence of Force Components. In order to elucidate the dependence of the hydraulic force from the flow rate, we separate the vane vortex distribution $\gamma_b(s)$ into the following two components:

$$\gamma_b(s) = \gamma_0(s) + \gamma_\phi(s)$$

(i) $\gamma_o(s)$: vortex distribution proportional to Ω, and independent of Q. This component represents the vortex distribution at the shut off condition, and the pressure coefficient at shut off can be written as follows.

$$\psi_{\text{shut off}} = \frac{1}{2\pi r_2 u_2} \sum^{N} \int_{s_1}^{s_2} \gamma_0(s) ds$$

(ii) $\gamma_\phi(s)$: vortex distribution proportional to Q, and independent of Ω. By using this vortex, Euler's law which gives the pressure coefficient Ψ at flow rate Q can be written as follows.

$$\begin{aligned} \psi &= \psi_{\text{shut off}} + \frac{1}{2\pi r_2 u_2} \sum^{N} \int_{s_1}^{s_2} \gamma_\phi(s) ds \\ &= \psi_{\text{shut off}} - \text{constant} \times \frac{Q}{2\pi r_2 u_2} \end{aligned}$$

After the separation of vortex distribution into the two components, we can divide the unbalanced hydraulic force into the following three components.

$$F = F_1 + F_2 + F_3$$

(i) $$F_1 = i\rho \sum^{N} \int_{s_1}^{s_2} \gamma_0(s)[i\Omega \bar{z}_b(s)] ds$$

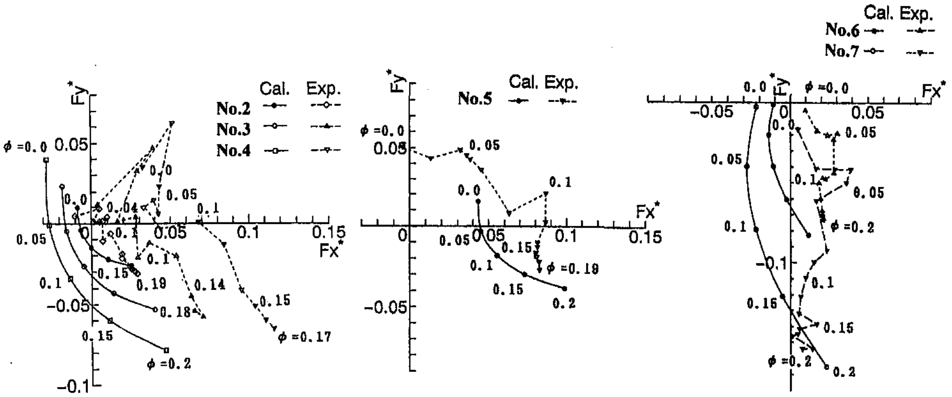

Fig. 10 Unbalanced hydraulic forces (experiments and calculations, experimental uncertainty in $|F^*| \pm 0.005$, in $\phi \pm 0.002$). (a) No. 2, 3 and No. 4 impeller; (b) No. 5 impeller; (c) No. 6 and No. 7 impeller.

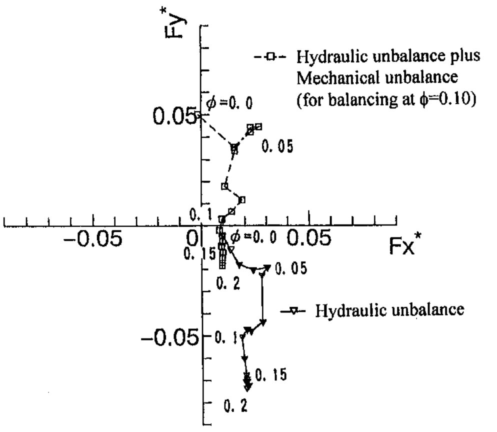

Fig. 11 Unbalanced hydraulic forces after the balancing with mechanical unbalance (for No. 6 impeller, uncertainty in $|F^*|$ ± 0.005, in ϕ ± 0.002)

(ii)

$$F_2 = i\rho \sum^{N} \int_{s_1}^{s_2} \left\{ \gamma_0(s) \left[\frac{Q}{2\pi z_b(s)} \right] + \gamma_\phi(s)[i\Omega \bar{z}_b(s)] \right\} ds$$

(iii)

$$F_3 = i\rho \sum^{N} \int_{s_1}^{s_2} \gamma_\phi(s) \left[\frac{Q}{2\pi z_b(s)} \right] ds$$

Component F_1, F_2, and F_3 are constant, proportional, and parabolic functions of flow rate Q, respectively. The force directions of the three components are different with each other. This clearly shows that the magnitude and the direction of the unbalanced hydraulic force change continuously with flow rate.

Experimental and Analytical Results

Figure 8 shows the static pressure performance of the test impellers. The shockless flow rate is $\phi = \phi_{\text{shockless}} = 0.09$ for the $\beta_1 = 20$ deg. The figure includes the calculated static/total pressure performance curves (shown by Ψ_s/Ψ, respectively). The differences among the pressure performances of test impellers are small except at large flow rate. The calculated results show the same tendency. A comparison between measurements and calculations for the performance is not here applicable, because the theory is based on fully inviscid flow and so is not adequate for performance prediction.

Figure 9 shows the calculated results of the pressure distributions and the hydraulic forces on the vanes. Figure 9(*a*) shows the comparison of the pressure distributions on each vane of No. 3 impeller. In this impeller, No. 1 vane has a larger vane angle ($\beta^* = 25$ deg) than other vanes ($\beta = 20$ deg, baseline).

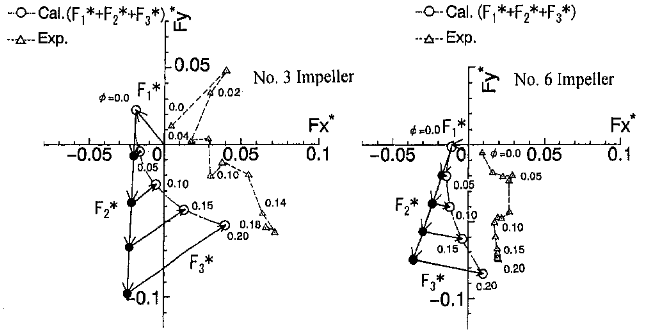

Fig. 12 Divided unbalanced hydraulic force into three components: F_1, F_2, F_3 (for Nos. 3 and 6 impeller, experimental uncertainty in $|F^*|$ ± 0.005, in ϕ ± 0.002)). (*a*) No. 3 impeller; (*b*) No. 6 impeller.

Table 3 Principal dimensions of high-speed pump impeller (for estimation of the hydraulic unbalance on actual pump impeller)

speed	n	3600 rpm
radius	r_2	165 mm
width	b_2	28 mm
weight	M	20 kg
density of fluid	ρ	1000 kg/m³

Therefore, the pressure difference between the pressure and suction side of No. 1 vane is larger than that of the others. However, it is noteworthy that the pressure difference of No. 5 vane (without geometrical deviation ($\beta = 20$ deg)) located at the suction side of No. 1 vane is smaller than that of the other vanes.

The hydraulic forces on each vane are estimated by integrating the pressure distribution around the vane with considering the "leading edge suction force" (as defined in the thin airfoil theory). Figure 9(*b*) shows the vector of the hydraulic forces on each vanes in the $x - y$ frame rotating with the impeller as shown in the figure. The hydraulic force on No. 1 vane is larger, and that on No. 5 vane is smaller. As a result, the unbalanced hydraulic force $\mathbf{F}^*$ occurs in $-y$ (negative) direction for this example. The unbalanced hydraulic force is much smaller than the hydraulic forces on each vane.

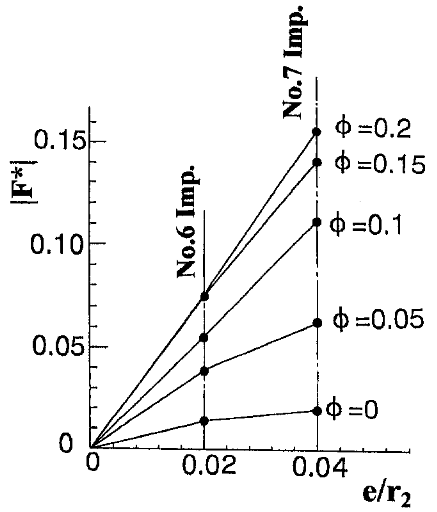

Fig. 13(*a*) $|F^*|$ versus eccentricity e/r_2

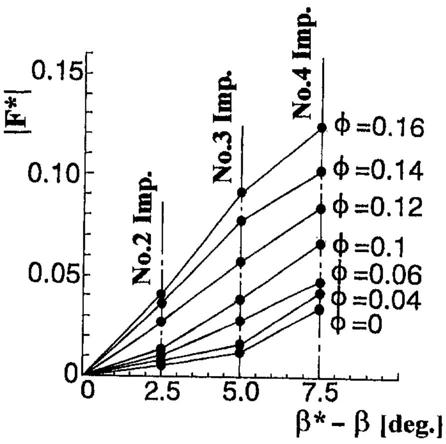

Fig. 13(*b*) $|F^*|$ versus deviation of vane angle $\beta^* - \beta$

Fig. 13 Unbalanced hydraulic force $|F^*|$ versus eccentricity e/r_2 and deviation of vane angle $\beta^* - \beta$ (for Nos. 6, 7 impellers and Nos. 2, 3, 4 impellers, experimental uncertainty in $|F^*|$ ± 0.005)

Figure 10 shows the hydraulic unbalanced forces of all test impellers determined from the experiments and from the calculations. Small font numbers in the figure indicate the impeller outlet flow coefficient: $\phi \equiv Q/2\pi r_2 b_2 u_2$. The shockless flow coefficient related to the impeller outlet is $\phi_{\text{shockless}} = 0.09$ for the baseline vane angle $\beta_1(=\beta) = 20$ deg. From these figures, it is found that:

- The magnitude of the unbalanced hydraulic force increases as the increase of the manufacturing deviation (No. 2–No. 4, No. 6–No. 7 impeller).
- The magnitude and the direction of the unbalanced hydraulic forces depend on the flow rate. This character (dependence on the flow rate) of the unbalanced hydraulic force is quite different from that of the centrifugal force caused by mechanical unbalance, which is independent of the flow rate.

The calculated results agree with the experiment values qualitatively, as to the dependence on the flow rate. Therefore, we can say that two-dimensional inviscid flow analysis is useful to obtain the basic characteristics of the unbalanced hydraulic forces. However, we can not use these analytical results to balance an actual pump impeller, because of the lack of the quantitative agreement with the experiment results.

Discussion

In the above observation, there is one important point. The synchronous vibration caused by the hydraulic unbalance is quite different from that caused by the mechanical unbalance concerning the dependence on the flow rate. An experiment was carried out to elucidate this difference. No. 6 impeller has the geometrical deviation: i.e., eccentric geometrical center, and hence the unbalanced hydraulic force occurs as shown by the full line in Fig. 11. We added a counterweight on the impeller back-shroud to balance the hydraulic unbalance at the flow rate $\phi = 0.10$. The broken line in Fig. 11 shows the results after the addition of the counterweight. The total unbalanced force at the flow rate $\phi = 0.10$ is decreased as expected. However, the unbalanced force is increased at low flow rate. From this experiment, we can conclude that the hydraulic unbalance can be balanced at only one flow rate by adding a counterweight, or mechanical unbalance, since the hydraulic unbalance dependence on the flow rate.

In the previous section, we showed analytically that the unbalanced hydraulic force can be divided into three components: the constant component F_1, the component F_2 which changes linearly with flow rate, and the component F_3 which changes parabolically with flow rate. Figure 12 shows these three components for No. 3 and No. 6 impeller. As we increase the flow rate, the contributions of the components F_2 and F_3 become larger. These figures show how each component contributes to the change in the total force as the change of the flow rate.

To find out the practical meaning of the present result, we estimate the hydraulic unbalance which might occur in an actual high-speed pump impeller manufactured within the geometrical tolerance recommended by a typical standard. The dimensions of the examined impeller are given in Table 3. The JIS (Japanese Industrial Standard) B8327 (1989) test code regulates the deviation of the vane pitch to be less than two percent of the averaged pitch. This value corresponds to the eccentricity $e/r_2 = 0.0044$ for the present case. Figure 13(a) shows the relation between the eccentricity: ϵ versus the normalized value of unbalanced hydraulic force: $|\mathbf{F}^*|$ obtained from Fig. 10. This figure shows that the hydraulic unbalance force corresponding to $e/r_2 = 0.0044$ at the flow rate $\phi = 0.10$ is $|\mathbf{F}^*| = 0.013$. The residual mass unbalance corresponding to the unbalanced hydraulic force $|\mathbf{F}^*| = 0.013$ is $G = 30.8$ mm/s in case of the examined impeller, which is about five times as large as ISO 1940-1 (1986) recommendation $G = 6.5$ mm/s for mechanical unbalance. This estimation shows that the hydraulic unbalance of a high-speed pump impeller manufactured within the geometrical tolerance can be much larger than the ordinary mechanical unbalance. Moreover, from Fig. 13(a) and (b), it is shown that the unbalanced hydraulic forces $|\mathbf{F}^*|$ increase as the flow coefficient increases, since the component F_2 and F_3 contribute mainly to the total force at the larger flow rate. It should be noted that the above estimation becomes severer at larger flow rate.

Conclusion

The unbalanced hydraulic forces on centrifugal impellers due to the manufacturing deviations were studied from the experiments and the analyses. It was found that the magnitude of the unbalanced hydraulic force increases as the increase of the manufacturing deviation, and also that the magnitude and the direction of the unbalanced hydraulic force depend on the flow rate. Two-dimensional inviscid flow analysis can explain the character concerning the flow rate dependence. The flow analysis shows that the unbalanced hydraulic force can be divided into the three components which are constant, linear, and parabolic functions of the flow rate. Therefore, the hydraulic unbalance can be balanced at only one flow rate by adding mechanical unbalance. From the application of the present results to a high-speed pump impeller manufactured within the geometrical tolerance, it was shown that the hydraulic unbalance can be larger than the ordinary mechanical unbalance. Hence, we can conclude that the hydraulic unbalance is one of the important factors in high-speed pump rotordynamics.

Acknowledgment

The authors would like to acknowledge the effort of Mr. Morishige in support of this program as an undergraduate project at Osaka University. They should be also deeply grateful to Dr. Bruno Schiavello of Ingersoll-Dresser Pump Company for his extremely helpful and useful comments.

References

Bolleter, U., Leibungut, E., Sturchler, R., and McCloskey, T., 1989, "Hydraulic Interaction and Excitation Forces on High Head Pump Impellers," *Proceedings of the 3rd Joint ASCE/ASME Mechanics Conference*, pp. 187–194.

Imaichi, K., Tsujimoto, Y., and Yoshida, Y., 1980, "An Analysis of Interaction Effects of Radial Impeller in Volute Casing," *Proceedings of the 10th IAHR Symposium*, Tokyo, pp. 635–647.

France, D., 1993, "A Review of Vibration Problems in Power Station Boiler Feed Pumps," NASA C.P. No. 3239, pp. 249–276.

Guelich, J., Jud, W., and Hughes, S. F., 1987, "Review of Parameters Influencing Hydraulic Forces on Centrifugal Impellers," *Proc. Inst. Mech. Engrs.*, Vol. 201, No. A3, pp. 164–174.

Tsujimoto, Y., Acosta, A. J., and Brennen, C. E., 1988, "Theoretical Study of Fluid Forces on a Centrifugal Impeller Rotating and Whirling in a Volute," ASME *Journal of Vibration, Acoustics, Stress, and Reliability in Design*, Vol. 110, No. 3, pp. 263–269.

Verhoeven, J., 1988a, "Rotordynamic Considerations in the Design of High Speed, Multistage Centrifugal Pumps," *Proceedings of the 5th International Pump Users Symposium*, pp. 81–92.

Verhoeven, J., 1988b, "Unsteady Hydraulic Forces in Centrifugal Pumps," *Part-load Pumping Operation, Control and Behavior, Inst. Mech. Engrs.*, C348/88, pp. 153–165.

Yamaguchi, Y., and Miura, S., 1981, "Characteristics of Radial Force Fluctuations on Runners of Francis-type Pump-Turbines," *Bull. JSME*, Vol. 24, No. 195, pp. 1586–1593.

Y. Dong
Graduate Student.

B. Lakshminarayana
Evan Pugh Professor.

The Pennsylvania State University,
Department of Aerospace Engineering,
University Park, PA 16802

D. Maddock
Staff Development Engineer,
GM Powertrain Group,
General Motors Corporation,
Ypsilanti, MI 48198

Steady and Unsteady Flow Field at Pump and Turbine Exits of a Torque Converter

The steady and unsteady flow field at the pump and the turbine exit of a 245 mm diameter automotive torque converter was measured by a miniature high-frequency-response five-hole probe and a high-frequency-response total pressure Pitot probe in the stationary reference frame. The data were decomposed into blade periodic, blade aperiodic, and unresolved unsteady components. The periodic flow data shows that the pump exit flow has four major zones; the free-stream flow, the blade wake flow, the core-suction corner separation flow, and the mixing zone. The unsteady flow data shows that the unsteadiness in the free-stream is uniform, and the unsteadiness in the wake mixing flow zone is very high. The turbine exit flow is almost fully developed at the measurement plane, the flow field is uniform in the tangential direction, and only radial gradients in flow properties exist. A region of separated flow with high unsteadiness and high axial component of vorticity was observed at the measurement plane near the core.

Introduction

The torque converter is a hydrodynamic, closed-loop, multicomponent turbomachine, used in the automatic transmission of the vehicle, as a means of transmitting the power and torque from the engine to the transmission and to provide torque amplification during vehicle launch conditions. A typical torque converter consists of a pump, turbine, and stator, employing oil as the working fluid. The performance of the torque converter is of great significance to the vehicle. Increased converter torque multiplication enhances vehicle acceleration, while improvement of converter efficiency results in increased vehicle fuel economy. Since several million torque converters are built every year, even a small torque converter efficiency improvement will result in major fuel savings. The objective of the Penn State research program is to improve the performance of the torque converter through a better understanding of the flow field. The objective of the experimental program, which is focused on the flow field measurement downstream of each element and inside blade passages, is to obtain accurate data needed for the flow analysis, correlation, computer code validation, and design of next generation torque converters.

The earlier flow measurements were carried out by two groups: the University of Virginia using a laser Doppler velocimeter and The Pennsylvania State University using a miniature five-hole probe. Both of them employed a 230 mm diameter torque converter. Brun et al. (1996 and 1997) measured three components of velocity inside the pump and turbine passage (inlet, quarter, mid-chord, and exit plane). Marathe et al. (1997) measured the turbine exit flow using a high-frequency-response five-hole probe. Both of these measurements indicate that the flow field is highly three dimensional and unsteady, with large regions of separated flow. A review of these investigations and an assessment of the fluid dynamics of an automotive torque converter are given by Von Backstrom and Lakshminarayana (1996).

A new 245 mm diameter torque converter, simulating a more recent production design, was investigated at Penn State. The objective of this research is to provide detailed and accurate knowledge of the pump and turbine exit flow. An improved miniature five-hole probe, which has a higher frequency response and higher natural frequency than the earlier probe, was used to measure the pump and turbine exit flow field. In addition, a high-frequency-response miniature total pressure Pitot probe was developed and used to check the accuracy of the five-hole probe data. The steady and unsteady flow field data are presented and interpreted in this paper.

Experimental Facility and Measurement Technique

Figure 1 shows the test section of the 245 mm diameter torque converter. The pump has 32 blades with 1 mm constant blade thickness. The pump inlet blade angle is −30.0 deg and the outlet blade angle is 10.0 deg. The turbine has 36 blades with 1 mm constant blade thickness. The inlet blade angle is 61.4 deg and outlet blade angle is −62.6 deg. The pump exit measurement plane is 5.57 mm downstream of the pump blade trailing edge in the axial direction. The turbine exit measurement plane is 4.52 mm downstream of the turbine blade trailing edge at the core. The flow field was measured at five different operating conditions, speed ratios (defined as n_t/n_p) 0.8, 0.6 (design point), 0.4, 0.2, and 0.065. Only the data at the design speed ratio of 0.6 are presented and interpreted in this paper. The test speed of the pump is 1160 rpm, and the turbine speed is 696 rpm at a speed ratio 0.6. At this condition, the torque converter has a 75.54 percent overall efficiency and a 1.259 torque ratio at the Penn State Facility. A detailed description of the experimental facility and the data acquisition system is given by Marathe et al. (1997).

The high-frequency-response five-hole probe used in this study is an improvement over the previous design (Marathe et al., 1997). Five Kulite XCQ-080-100A pressure transducers are mounted in the probe and function as the sensing elements. The probe tip diameter is increased from 1.67 mm to 2.13 mm, and the frequency response is increased to 9 kHz. Most importantly, the probe's natural tubing-diaphragm oscillation frequency is increased to 6 kHz. This allows a low pass digital filter to be used during the data processing to filter out the fluctuation of the tubing-diaphragm oscillation without losing the flow field information. The spectrums of the pump and turbine exit total pressures at one typical radial location are shown in Fig. 2. These are the spectrums derived using a low pass digital filter. It is clear that the probe natural oscillation has been filtered

---

Contributed by the Fluids Engineering Division for publication in the JOURNAL OF FLUIDS ENGINEERING. Manuscript received by the Fluids Engineering Division May 28, 1997; revised manuscript received January 13, 1998. Associate Technical Editor: P. M. Sockol.

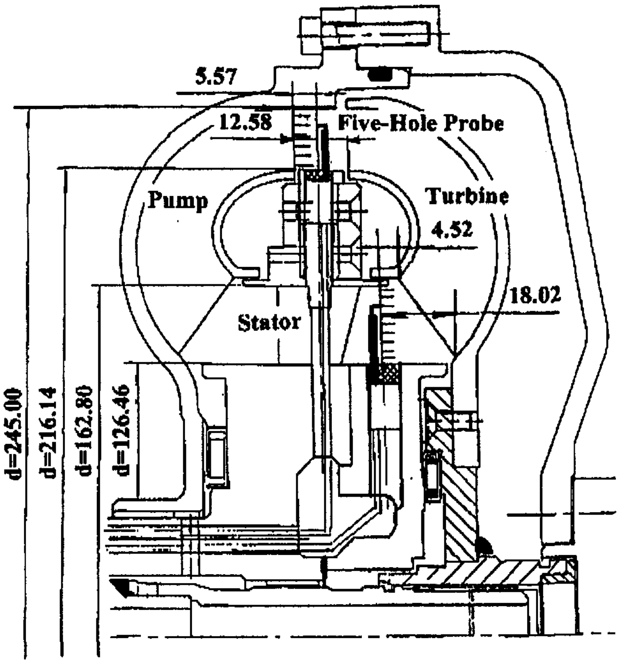

Fig. 1 245 torque converter test section (unit: mm)

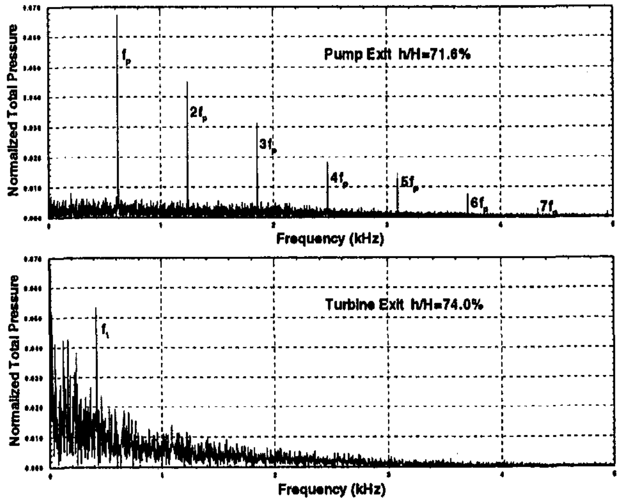

Fig. 2 Pump and turbine total pressure spectrums (SR = 0.6)

Table 1 Relative magnitude of various components of unsteadiness (all values shown here are total RMS value of fluctuating quantities and not the absolute levels)

Flow parameter	P_o (psi)		V_a (m/s)	
Time mean value	36.076	100%	14.099	100%
Blade periodic RMS	0.6140	1.70%	0.5393	3.83%
Blade aperiodic RMS	0.0585	0.16%	0.0376	0.27%
Blade unresolved RMS	0.1007	0.28%	0.0410	0.29%
Revolution periodic RMS	0.0462	0.12%	0.0124	0.09%
Revolution aperiodic RMS	0.0565	0.16%	0.0245	0.17%
Revolution unresolved RMS	0.2789	0.77%	0.1498	1.06%
Unresolved unsteady RMS	0.7869	2.18%	0.4040	2.87%

out. The flow field signal in the spectrum will be discussed later. A 0.7 mm tip diameter high-frequency-response total pressure Pitot probe was developed to assess the accuracy of the five-hole probe. The frequency response of this total pressure Pitot probe is very high, over 15 kHz, due to the very short tubing length of the probe. The natural frequency of this probe is 11 kHz.

The five-hole probe was calibrated in a water tunnel with an angle measurement accuracy of ±1 deg, and the velocity measurement accuracy of ±0.15 m/s. The accuracy of pressure measurement depends on the transducer zero point drift, which is calibrated at the beginning and end of each measurement. The maximum error is about ±0.05 psi. The position and angle of the probe setting are measured to an accuracy of ±0.1 mm and ±0.1 deg. The maximum cumulative error in the velocity and the pressure is estimated to be 3 and 0.8 percent. Detailed uncertainty analysis is given in Dong (1998).

The experimental data was acquired at 6 radial locations at the pump exit (from $h/H = 18.2$ to 86.1 percent), and at 7 radial locations at the turbine exit (from $h/H = 10.7$ to 88.1 percent). The data acquisition system is clocked by the shaft encoder with 50 points across the passage. The data processing procedure used in this research, which has been discussed by Marathe et al. (1997), is as follows: (1) Calculate the instantaneous pressures (p_1, p_2, p_3, p_4, p_5) from instantaneous voltages using the pressure transducer calibration curve; (2) Use a digital low pass filter to filter the fluctuation due to the probe natural oscillation; (3) Calculate the instantaneous flow parameters (P_o, P, V_z, V_θ, V_r) from instantaneous pressures using the five-hole probe calibration, including the corrections due to the probe spatial error and the unsteady effects; (4) The instantaneous flow parameters are decomposed into time mean value and unsteady components, which are listed in Table 1.

After the time averaging, each flow parameter is decomposed into 8 components: mean, blade periodic, blade aperiodic, blade unresolved, revolution periodic, revolution aperiodic, revolution unresolved, and total unresolved unsteadiness. The mean value

Nomenclature

D, d = diameter
f = frequency
h = spanwise distance
H = blade height
h/H = relative radial position
n = pump or turbine rotating speed
p = pressure of the five-hole probe
P = pressure (Eq. (3))
P.S. = pressure side of the blade
S.S. = suction side of the blade
s = tangential position
S = blade spacing
s/S = relative tangential position
SR = speed ratio, turbine speed/pump speed
V = absolute velocity, stationary frame (Eq. (2))
W = relative velocity, pump, or turbine rotating frame
α = pitch angle, measured from the radial direction
β = yaw angle, measured from the tangential direction
ρ = density
ω = rotating speed of pump or turbine
Ω_z = axial vorticity, normalized by 2ω (Eq. (4))

Subscript

p = pump or pump rotating frame
r = rotating frame
t = turbine or turbine rotating frame
r, θ, z = radial, tangential and axial component
o = total or stagnation properties
s = stator or static pressure
hub = reference pressure at stator hub
ref = reference velocity or pressure (Eqs. (2) and (3))
uns = unresolved unsteadiness RMS value (Eq. (1))

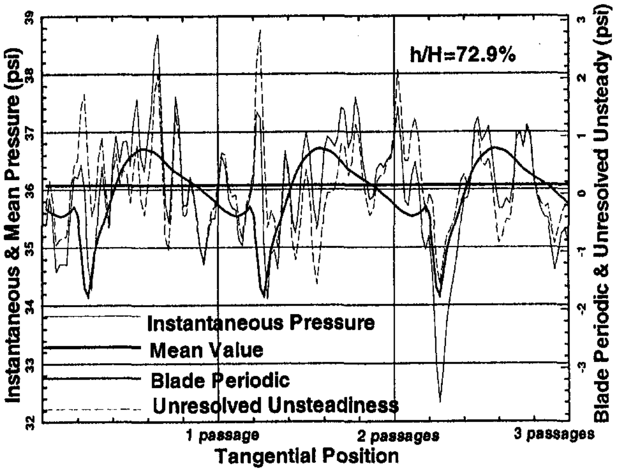

Fig. 3 Decomposition of unsteady total pressure data (SR = 0.6)

is the time average of the complete data set. The blade periodic value is the averaged blade-to-blade profile of the flow field. The blade aperiodic value is the difference in the flow field between each blade passage and the blade periodic value. The revolution periodic quantity is the averaged value from revolution-to-revolution in each cycle. The revolution aperiodic value is the variation in flow properties from revolution to revolution. The total unresolved unsteadiness is associated with the fluctuation not clocked with the blade, the shaft, and the cycle frequencies. It includes the electronic noise, the random error in data acquisition and processing, the pressure fluctuation in the oil charging system, and the fluctuation due to the turbulent flow. The largest contribution to the total unresolved unsteadiness is from the flow field; more specifically from the random turbulence.

Figure 3 shows the decomposition of the total pressure data from the high frequency Pitot probe at a radial location of 73 percent from the core and at a speed ratio 0.6. The data for three blade passages are shown. The time mean value, blade periodic, and the total unresolved unsteadiness are the dominant components. The other values are found to be small, within the range of ±0.2 psi, and are not shown here. The RMS values of various unsteady quantities for the total pressure and the total velocity at $h/H = 72$ percent and SR = 0.6 are listed in Table 1. It is clear that the mean, the blade periodic, and the unresolved unsteadiness are the three dominant terms. The steady flow field presented in this paper is the sum of the time mean and the blade periodic value at each measurement grid point. Only the total unresolved unsteadiness blade periodic RMS values at each grid point are presented to characterize the unsteady flow field. The unresolved unsteadiness (blade periodic RMS value), denoted by the subscript uns, is defined by the following equation:

$$(A_{uns})_i = \frac{1}{N_c}\frac{1}{N_r}\frac{1}{N_b}\sqrt{\sum_{l=1}^{N_c}\sum_{k=1}^{N_r}\sum_{j=1}^{N_b}(A'_{i,j,k,l})^2} \tag{1}$$

where A is the flow parameter, $A'_{i,j,k,l}$ is the instantaneous unresolved unsteadiness, N_c is the number of cycle in each data set, N_r is the number of revolution in each cycle, and N_b is number of blade passage in each revolution.

The velocity and pressure in this paper are normalized as follows:

$$V_{\text{normalized}} = \frac{V}{V_{\text{ref}}}, \quad V_{\text{ref}} = \frac{n_p}{60}\pi D_p\sqrt{1 - \frac{n_t}{n_p}} \tag{2}$$

$$P_{\text{normalized}} = \frac{P - P_{\text{hub}}}{P_{\text{ref}}} \quad P_{\text{ref}} = \frac{1}{2}\rho V_{\text{ref}}^2 \tag{3}$$

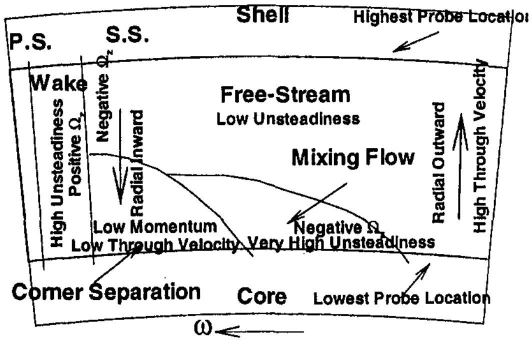

Fig. 4 Schematic of pump exit flow pattern (SR = 0.6)

where P_{hub} is the static pressure on the stator hub, whose values vary from 16 to 18 psi. For the speed ratio 0.6, the reference velocity is $V_{\text{ref}} = 9.411$ m/s, and the reference pressure is $P_{\text{ref}} = 5.504$ psi. The unresolved unsteadiness in total pressure and static pressure is normalized by the P_{ref}. The unresolved unsteadiness in total velocity is normalized by the local steady total velocity. All unresolved unsteadiness presented in this paper are RMS values.

Pump Exit Flow Field

It is clear from Fig. 2 that the pump blade passing frequency is the dominant periodic signal at the pump exit. Eight harmonics are present in the total pressure spectrum. The amplitude of the first three harmonics is over 0.17 psi. The spectrum of the pump exit flow parameters show no other periodic signals, such as those associated with the pump and turbine shaft frequency, turbine blade passing frequency, and pump and turbine blade passing frequency combinations (such as $f_p - f_t$, or $2f_t - f_p$). Hence the pump exit flow at the measurement plane is dominated by the pump passage flow, all other effects are too small to be observed. The turbine inlet flow is at a low incidence at a speed ratio of 0.6, causing the turbine blade upstream effects to be small.

Flow Structure at Pump Exit. The torque converter pump exit flow has a "jet-wake" pattern similar to those observed in other radial turbomachinery. Based on the flow field data and the later discussion, the nature of the pump exit flow at the speed ratio 0.6 is summarized in Fig. 4. The pump exit flow structure can be seen clearly from the contour plots of absolute total pressure and its unresolved unsteadiness (Fig. 5(*a*) and (*b*), the relative total velocity vector plot and its unresolved unsteadiness (Fig. 6(*a*) and (*b*)), and the contour plot of the static pressure and its unresolved unsteadiness (Fig. 7(*a*) and (*b*)).

The pump exit flow field has four regions; free-stream region, blade wake region, corner flow separation wake region, and the high mixing flow region. The flow field is dominated by the "jet flow"; that is the free-stream. The free-stream flow occupies more than 60 percent of the passage area. In the free-stream, the tangential gradient of absolute total pressure is small (Fig. 5(*a*)), and its unresolved unsteadiness are minimal and close to uniform (Fig. 5(*b*)). The relative total velocity is high on the pressure side and low on the suction side (Fig. 6(*a*)). The "wake flow" is the combination of the blade wake and the corner flow region. The wake is nearly radial, and covers about 10 percent of the passage area. The wake shape can be seen clearly from the unresolved unsteadiness total pressure contour plot (Fig. 5(*b*)). As in the normal turbomachine blade wake, the total pressure is low (Fig. 5(*a*)), the static pressure is high (Fig. 7(*a*)), the flow is underturned on the pressure side and overturned on the suction side (Fig. 8(*a*)), and the unsteadiness are high. The corner flow separation region is in

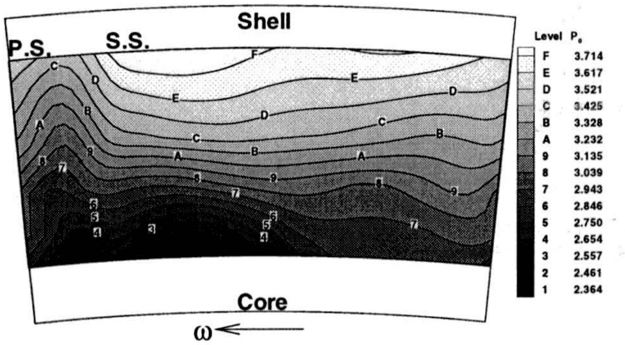

Fig. 5(*a*) Normalized blade periodic total pressure (P_o)

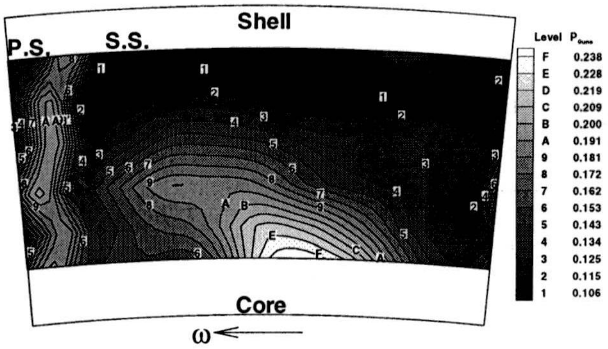

Fig. 5(*b*) Normalized unresolved unsteadiness in total pressure ($P_{o,\text{uns}}$)

Fig. 5 Absolute total pressure at pump exit (SR = 0.6)

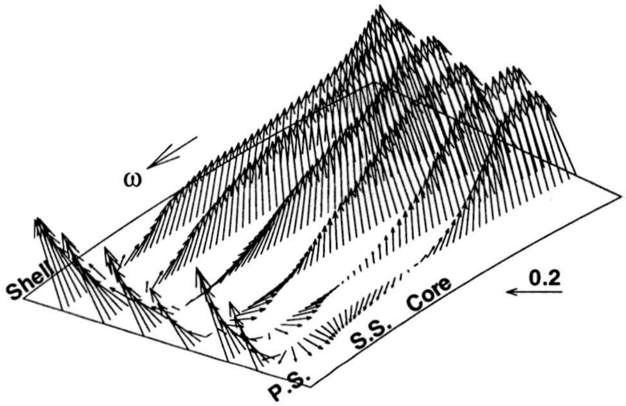

Fig. 6(*a*) Normalized relative total velocity vectors (W_{po})

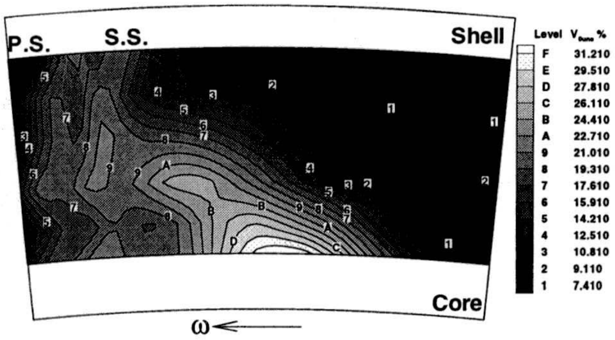

Fig. 6(*b*) Unresolved unsteadiness in relative total velocity ($W_{op,\text{uns}}$ %)

Fig. 6 Relative total velocity at pump exit (SR = 0.6)

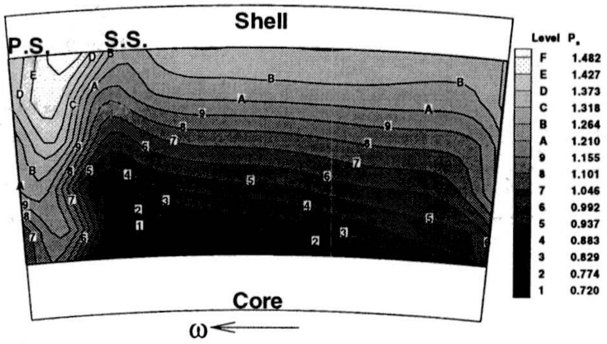

Fig. 7(*a*) Normalized blade periodic static pressure (P_s)

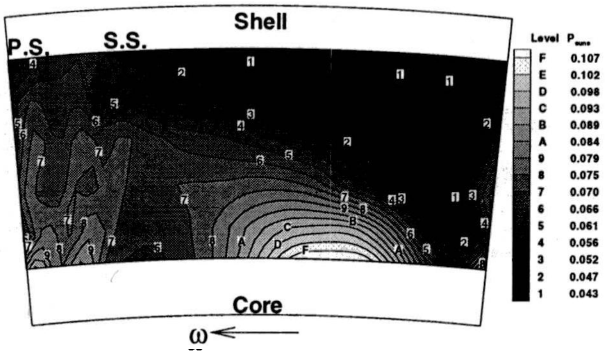

Fig. 7(*b*) Unresolved unsteadiness in static pressure (P_{suns})

Fig. 7 Static pressure at pump exit (SR = 0.6)

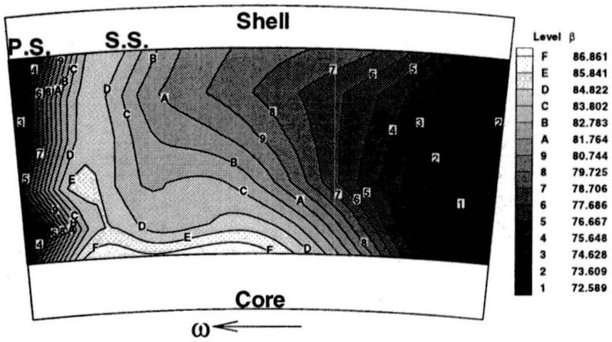

Fig. 8(*a*) Blade periodic absolute flow yaw angle (β in degree)

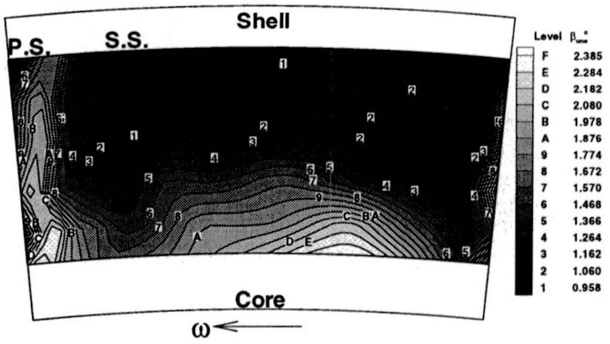

Fig. 8(*b*) Unresolved unsteadiness in yaw angle (β_{uns} in degree)

Fig. 8 Absolute flow yaw angle at pump exit (SR = 0.6)

the corner of the core and the suction side. It covers about 10 percent of the passage area. In this region, the total pressure and total velocity are very low, the unresolved unsteadiness of the flow parameters are relative high, and no backflow is observed. The high mixing flow region is located beside the corner separation wake, near the core and the mid-pitch region. It covers about 10 percent of the passage area.

Free-Stream Flow. As the dominant part of the "jet flow," the free-stream covers a substantial part of the passage area. In this region, the absolute total pressure is high near the shell and low near the core (Fig. 5(*a*)). This could be attributed to two reasons. The first reason is the effect of rotation. The shell has a larger radius and the absolute total velocity is higher in this region. The second reason is the static pressure distribution (Fig. 7(*a*)), which is high near the shell and low near the core due to the centrifugal force effect. It is noted that in the free-stream region, both the absolute total pressure and the static pressure have very small tangential gradients, and the radial gradients dominate. In the free-stream flow, the relative total velocity is high on the pressure side, low on the suction side. This is the dominant feature of the pump exit flow, and this will be discussed later. The reasons for such a free-stream velocity profile has been explained by Backstrom and Lakshminarayana (1996). Another reason is that the blockage caused by very low velocities on the suction side pushes the flow to the pressure side.

The main feature of the unsteady flow in the free-stream is that the random fluctuation level is relatively low and uniform. In the free-stream, the unresolved unsteadiness in relative total velocity is about 7 to 13 percent of the local velocity (Fig. 6(*b*)). The unresolved unsteadiness in absolute total pressure is similar in magnitude to those of velocity. The unresolved unsteadiness in absolute yaw angle is only about 1.2 deg (Fig. 8(*b*)). These unsteady levels are much lower than that observed in the wake, corner separation, or mixing flow area.

Blade Wake Flow Region. The shape of the blade wake can be clearly ascertained from the unresolved unsteadiness in total pressure contours (Fig. 5(*b*)). The blade wake is nearly radial and covers about 10 percent of the passage area. As in other turbomachinery blade wake flow, the total pressure is lower (Fig. 5(*a*)) and the static pressure is higher than the free-stream region (Fig. 7(*a*)). The velocity deficit in the wake can be clearly seen in Fig. 6(*a*). The blade wake region has a large inward velocity (toward the core) caused by the secondary flow. The secondary flow tends to accumulate and separate near the core region as explained later. The flow is underturned on the pressure side and overturned on the suction side. At the measurement plane, the unresolved unsteadiness in total pressure is about 50 to 70 percent higher than that in the free-stream. The unresolved unsteadiness in relative total velocity in the wake is about 14 to 18 percent of the local velocity. This is substantially higher than those encountered in other turbomachinery, and this should result in severe unsteady flow in the turbine passage downstream.

Corner Separation Wake Flow. This region is located on the corner of the core and the suction side. The size of this region is about 10 percent of the passage area. The main feature of this region is that the relative through flow velocity is very low (Fig. 6(*a*)), close to zero; and the radial inward velocity is the dominant component. The flow is separated in the suction-core surface corner. This can be seen in Figs. 4 to 8. Three factors can be attributed to this flow separation. First, there is a large radial inward flow along the blade suction side, so that the low momentum fluid is transported to the core-suction corner. The accumulation of the low momentum fluid causes flow separation. Second, the torque converter pump is a radial-axial mixed-flow pump. The centrifugal force is the major factor in the tangential momentum increase with the blade flow turning playing a secondary role (Lakshminarayana, 1996). So the torque converter pump flow should be more like the centrifugal pump impeller flow, where flow separation exists on the blade suction side. Third, the core of the pump blade passage has a convex curvature, and there is a tendency for the flow to separate on the convex surface.

In the suction-core corner, the absolute total pressure is very low (Fig. 5(*a*)). This could be attributed to three causes. First, the static pressure is very low in this region. The radial pressure gradient is from the shell to the core, hence the static pressure on the core-suction corner has a minimum value. Second, the corner separation is the result of accumulation of the low momentum fluid. The low stagnation pressure fluid is transported by the radial inward flow along the suction side to the corner. Third, the flow separation region has a high dissipation rate due to high flow fluctuation. The total pressure loss should be very high in this corner. The unresolved unsteadiness levels are relatively high in this corner. The unresolved unsteadiness in relative total velocity is about same level as that in the blade wake; about 19 percent of the local velocity.

High Mixing Flow Region. This flow region is in the shape of a triangle. It is located beside the corner flow separation region on the core near the mid-pitch region. The size is about 10 percent of the passage area. The steady relative total velocity and absolute flow yaw angle have very large tangential gradients in this region (Fig. 6(*a*) and Fig. 8(*a*)). It is believed that this gradient and the secondary flow are the direct reasons of the flow mixing.

The most significant feature in this region is that the flow unsteadiness is very high, even higher than that in the blade wake. The unresolved unsteadiness in absolute total pressure in this region is about 1.0 to 1.3 psi (Fig. 5(*b*)), which is about 15 to 30 percent higher than that in the blade wake (0.8 to 1.0 psi in the wake). The unresolved unsteadiness in relative total velocity is about 23 to 31 percent (Fig. 6(*b*)), which is about 6 to 15 percent higher than that in the wake. This indicates the presence of strong random flow fluctuations and intense flow mixing. In the core-suction corner, the through flow velocity is very low due to the flow separation. On the pressure side, the volume flow rate of the free-stream increases due to the blockage effect caused by the corner separation. In the middle area of these two regions, the velocity gradient is very high. So, it is believed that the corner flow separation and its blockage effect result in large tangential gradients in velocity. It is anticipated that the total pressure fluctuation will dissipate quickly as the flow progresses downstream due to the high viscosity of the oil.

Secondary Flow and Axial Vorticity. A strong secondary flow, which is counter-clockwise viewed from the downstream of the pump rotor, is found at the pump exit flow field (Fig. 9(*a*)). The secondary flow velocity in this paper is defined as the measured velocity vector minus the ideal flow velocity vector. The ideal flow velocity is calculated by the local axial velocity and mass-averaged flow angles. The flow is radial outward (from core-to-shell) on the pressure side, with large inward velocity on the suction side. At the core-suction corner, the magnitude of the radial inward velocity is about 60 to 70 percent of the mass averaged through flow velocity. Major causes of secondary flow in radial machinery is analyzed by Lakshminarayana (1996). The secondary flow in these passages is caused by the presence of vorticity in viscous shear layers combined with the flow turning, the passage meridional curvature, the rotation effect through the Coriolis force, and the centrifuging of the blade boundary layers. These sources and their effect will introduce complex flow features making it difficult to identify the dominant sources. This can only be done by isolating various sources through the basic experiment or the numerical simulation. For example, the blade turning would introduce secondary flow from pressure to suction surface near the shell and the core. This feature exists only near the shell (Fig. 9(*a*)), but the core secondary flow is from the suction to the pressure surface. The rotation effect on blade boundary layer should develop radial outward flow on both the pressure and

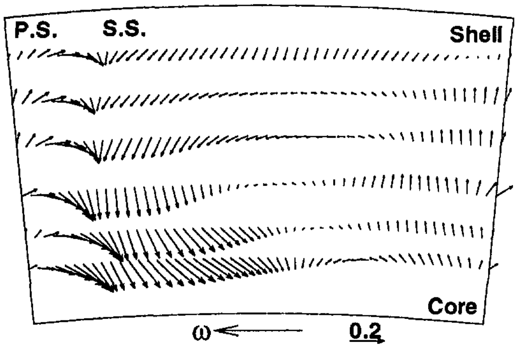

Fig. 9(*a*) Normalized secondary flow vectors

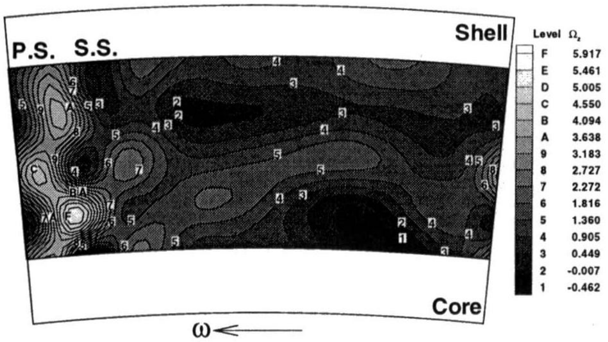

Fig. 9(*b*) Normalized relative axial vorticity (Ω_z)

Fig. 9 Secondary flow and vorticity at pump exit (SR = 0.6)

suction surface boundary layers. In the data shown, this effect is observed only on the pressure side. The meridional curvature should introduce radially outward flow, this exists on the pressure side only. Hence the shell flow and the pressure side flow are dominated by these sources.

Since the data available are only at one axial location, only the axial component of the vorticity can be calculated using the equation:

$$\Omega_Z = \left(\frac{\partial(rV_\theta)}{\partial r} - \frac{\partial V_r}{r\partial\theta}\right)\frac{1}{2\omega} \qquad (4)$$

The axial vorticity derived from these data is shown in Fig. 9(*b*). The shape of the blade wake can be seen clearly in these contours. A large positive (clockwise) axial vorticity is found in the blade wake (Fig. 9(*a*) and (*b*)). The positive axial vorticity is due to the radial velocity along the blade, inward on the suction side and outward on the pressure side. Along the suction side, a negative (counter clockwise) axial vorticity is observed. In addition, a large counter clockwise vortex is found near the core. The center of the vortex is near the center of the high mixing flow region. Compared with the secondary flow vector (Fig. 9(*a*)), it is clear that this is the secondary flow vortex. As it has been discussed earlier, this vortex is mainly caused by the pump rotation (the Coriolis force).

Passage Averaged and the Integrated Flow Field. The radial distribution of the blade-to-blade mass averaged values of the flow properties at the pump inlet and the exit are shown in Fig. 10(*a*) and 10(*b*), respectively. The stator exit (pump inlet) data was measured by a conventional five-hole probe on a 6 × 25 stator exit grid. It is clear that the flow at the pump inlet near the core has a large axial velocity defect (Fig. 10(*a*)) approaching separation. But, at the pump exit, the axial velocity is almost uniform in the radial direction. The volume flow is redistributed along the blade height. This indicates the presence of very strong flow mixing and migration inside the pump passage. It is believed that the secondary flow is the major cause for this spanwise mixing (Backstrom and Lakshminarayana, 1996).

As the pump inlet total pressure is very small and almost radially uniform (Fig. 10(*a*)), the pump total pressure rise distribution is nearly the same as the pump exit total pressure distribution (Fig. 10(*b*)). It is high near the shell and low near the core. The reason for this kind of distribution was discussed earlier. Since the blade speed is very high, the absolute velocity is much larger than the relative velocity. A small error in the absolute velocity measurement could cause large error in the relative flow angle. The derived relative flow yaw angle is not accurate at the pump exit measurement, hence the pump exit flow deviation angle cannot be determined accurately. Both the absolute and the relative flow angle are uniform across the span (Fig. 10(*b*)) as well as all the radial velocity components.

In general, the main feature of the pump exit flow field is the flow concentration on the pressure side and the shell. The relative velocity defect along the suction side causes the radial inward secondary flow driven by the Coriolis force and the passage meridional curvature effect. The accumulation of the low momentum fluid causes the flow separation on the core-suction corner. And the high mixing flow region is the result of the corner separation and its blockage effect. The highest total pressure loss is near the core-suction corner area.

Turbine Exit Flow Field

The spectrum of the absolute total pressure at the turbine exit at one typical radial location is shown in Fig. 2. It should be noted that the periodic signal is much weaker than those observed at the pump exit flow. Only the first harmonic of the turbine blade passing frequency is observed. The blade wake is almost completely decayed at the measurement plane. The maximum variation in the blade periodic total pressure in the tangential direction is about 0.15 psi, which is much less than the blade periodic total pressure variation of 2.1 psi at the pump exit. At the radial location 88.3 percent, which is the closest location to the core (Dong, 1998), three periodic signals f_t, $2f_t$, and $f_p - f_t$ are observed. At this position, the probe is closer to the turbine blade trailing edge than at any other measurement positions. The turbine blade wake decay at this location is less compared to that at the shell location. It should also be noted that the $f_p - f_t$ signal is the dominant periodic signal in the total pressure at this radius. The upstream pump exit blade periodic flow influences the turbine exit periodic flow near the core.

The magnitude of the broad-band fluctuation of the total pressure at low frequency (0 to 0.5 kHz) is about the same level as the pump exit broad-band fluctuation. However, the broad-band fluctuation of the total pressure at high frequency (higher than 0.5 kHz) is only about half of the corresponding pump exit fluctuation. The spectrum of flow parameters at the turbine exit does not reveal the presence of pump blade passing frequency, except at the radial location near the core. This indicates that the pump induced periodic fluctuations are completely decayed as the flow passes through the turbine passage, since the oil is highly viscous, and the dissipation rate is high. The turbine exit flow field at the speed ratio 0.8 was also measured using a miniature conventional five-hole probe to determine the upstream potential effect of the stator blade. This probe can only measure time average flow properties of the turbine exit flow field. However, the data can be used to assess the upstream potential effect of the stator blade. The probe was traversed at 7 radial and 7 tangential locations to cover one stator blade spacing. The flow field data show that upstream potential effect of the stator blade has no significant influence on the total pressure and total velocity at the turbine exit measurement plane. The major effects are on the axial velocity and yaw angle near the core, amounting to about 20 percent and 4 deg variations, respectively. This effect is much smaller at other

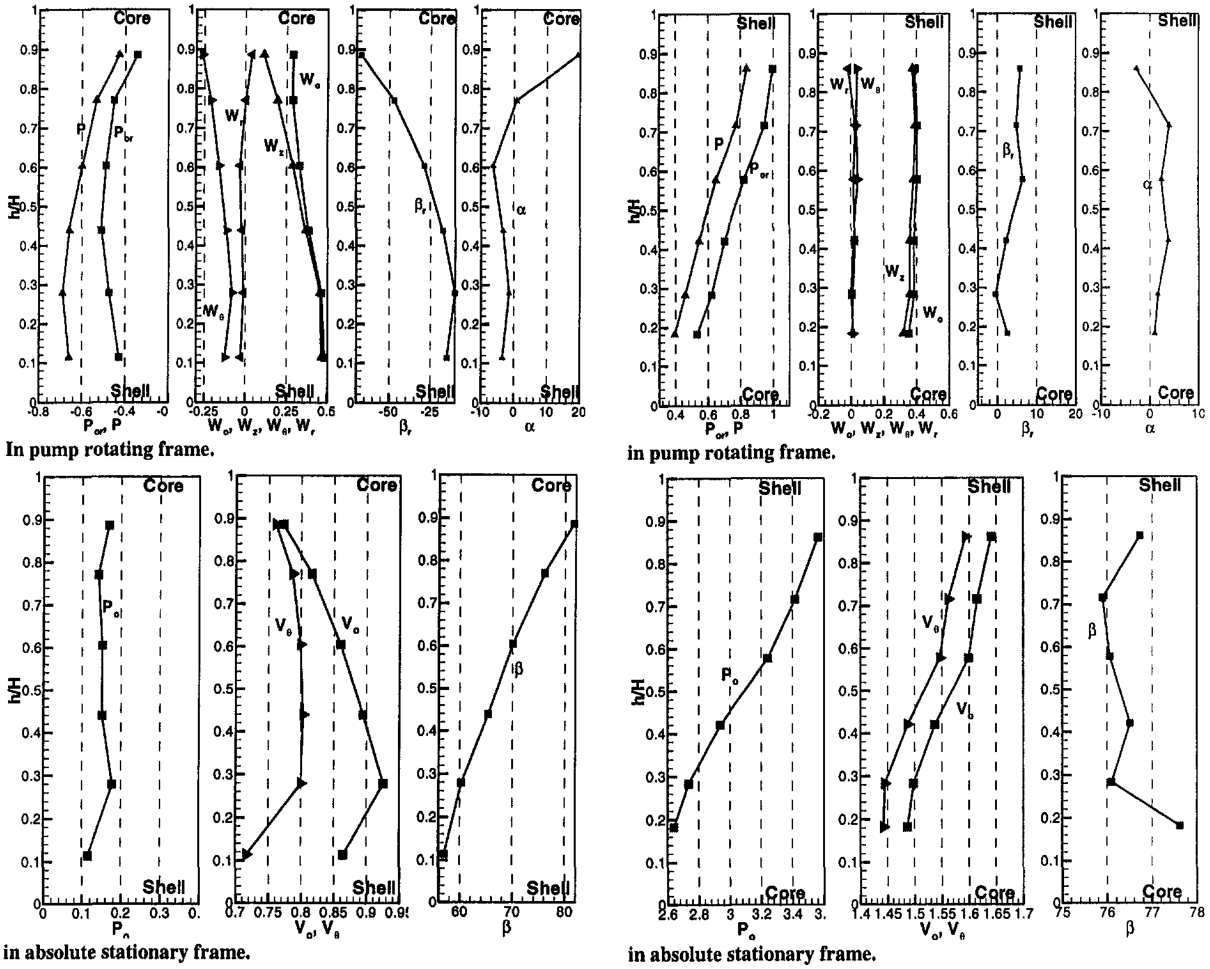

Fig. 10(*a*) Pump inlet flow

Fig. 10(*b*) Pump exit flow

Fig. 10 Normalized radial distribution of mass averaged flow properties (SR = 0.6)

radial locations due to the longer streamwise distance between the stator blade leading edge and the turbine exit measurement plane.

Absolute Total Pressure. The absolute total pressure at the turbine exit for the speed ratio of 0.6 is shown in Fig. 11(*a*). The most remarkable feature is that flow is uniform in the tangential direction and only radial gradients dominate the total pressure variation. This is consistent with the spectrum (Fig. 2). The total pressure is high near the core and the shell (indicating lower pressure drop or output), and low near 60 percent span. Such a total pressure distribution could be attributed to three causes. First, the flow near the core is not well behaved inside the turbine passage, with possible flow separation on the core. Such flow separation was found in the turbine passage of the 230 mm torque converter (Brun et al., 1997), and is probably due to convex curvature effect. Hence, the total pressure drop in the turbine near the core is small, and the absolute turbine exit total pressure is high near the core. Second, the total pressure at the turbine inlet is very high near the shell, hence the turbine exit total pressure near the shell should also be high. The third cause is the presence of meridional curvature effect, which results in higher relative pressure near the shell.

The unresolved unsteadiness in total pressure at turbine exit is shown in Fig. 11(*b*). It is high near the core because of the three following reasons. First, the measurement plane near the core is closer to the turbine trailing edge than that near the shell. The blade wake near the core has decayed less than that at other radial locations. Hence, the unsteady flow fluctuation should be higher near the core. Second, the flow is probably separated near the core inside the passage due to the presence of convex curvature. The separated flow probably reattaches before reaching the measurement plane, since no negative axial velocity is found at the turbine exit.

The reason of the flow separation is given by Backstrom and Lakshminarayana (1996). It is caused by convex curvature of the torus. This is confirmed by the radial distribution of axial velocity (explained later), which is low near the core and high near the shell. Third, the pressure decreases from the shell to the core, caused by the meridional curvature of the flow path. The low momentum fluid is forced to move from the shell to the core along the blade surface by the pressure gradient. So, the high unsteadiness near the core is the result of the core flow separation and the accumulation of low momentum fluid. The unresolved unsteadiness in total pressure is low and uniform at most locations (Fig. 11(*b*)). The magnitude of this unsteadiness is only about 30 percent of that observed in the freestream of the pump exit flow. The turbine wake position can be determined from these unsteadiness contours (Fig. 11(*b*)). The unsteady level is about 8 to 15 percent higher than that in the passage flow.

Relative Total Velocity and Yaw Angle. The relative total velocity vectors at the turbine exit are shown in Fig. 12(*a*). Except for one location near the core, the relative total velocity is uniform in both the magnitude and the direction across the entire passage. The relative total velocity at the shell is about 40 percent higher than that at the core. It is believed that this

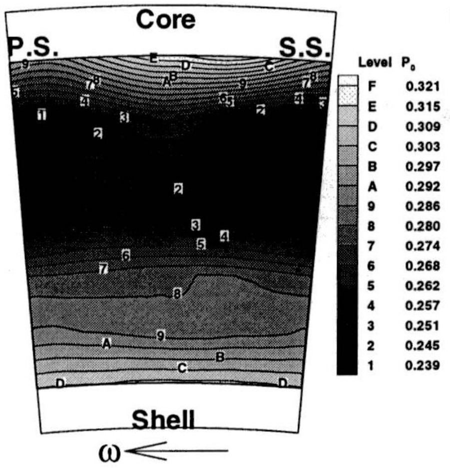

Fig. 11(*a*) Normalized blade periodic total pressure (P_o)

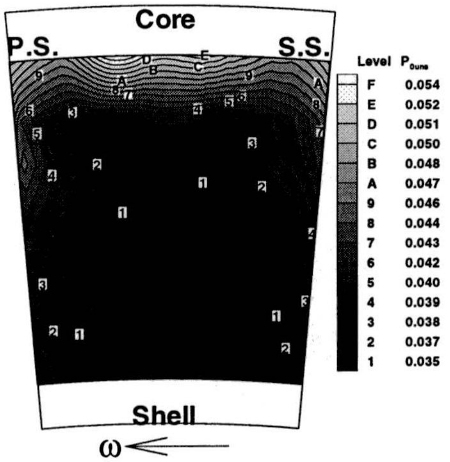

Fig. 11(*b*) Unresolved unsteadiness in total pressure ($P_{o,\mathrm{uns}}$)

Fig. 11 Normalized absolute total pressure at turbine exit (SR = 0.6)

is due to the blockage effect caused by the flow separation inside the turbine passage near the core. It is clear from the radial distribution of axial velocity (presented later) that the through flow velocity increases near the shell due to the blockage caused by flow separation near the core. The unresolved unsteadiness in relative total velocity is shown in Fig. 12(*b*). It is high near the core due to reasons mentioned earlier. In most of the passage area, from $h/H = 11$ to 75 percent, the unresolved unsteadiness in relative total velocity is uniform, with values ranging from 7.9 to 9.3 percent of the local velocity. This is consistent with the unresolved unsteadiness in total pressure.

The turbine exit relative flow yaw angle is shown in Fig. 13(*a*). The turbine exit blade angle is −62.5 deg. In most of the passage area, from $h/H = 15$ to 75 percent, the flow is well aligned with the turbine blade and the deviation angle is less than 5 deg. The largest yaw angle variation in the tangential direction is only about 1 deg across the passage. The maximum radial variation of the yaw angle is about 5 deg. The flow near the core is underturned by about 10 deg, because of the existence of core flow separation. The unresolved unsteadiness in yaw angle is shown in Fig. 13(*b*). The random fluctuation in yaw angle in most of the passage area (shell to 70 percent span) is about 5 to 8 deg. At the core region, the unresolved unsteadiness in yaw angle is high (about 11 to 14 deg) because of the core flow separation.

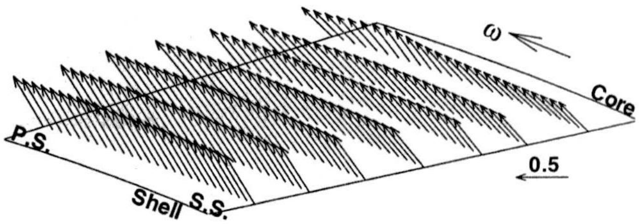

Fig. 12(*a*) Relative total velocity vectors (W_{to})

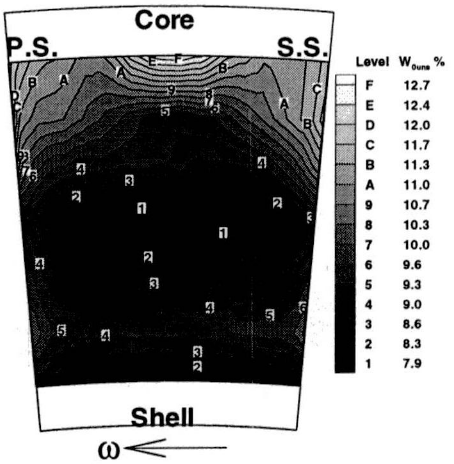

Fig. 12(*b*) Unresolved unsteadiness in relative total velocity ($W_{ot,\mathrm{uns}}$)

Fig. 12 Normalized relative total velocity at turbine exit (SR = 0.6)

Secondary Flow and Axial Vorticity. The secondary flow vectors at the turbine exit are shown in Fig. 14(*a*). Compared with the secondary flow at the pump exit, the turbine exit secondary flow is much weaker. It was explained earlier that the Coriolis force has a dominant effect on the pump exit secondary flow. At the turbine exit, the rotational speed is low, 60 percent of the pump speed. The Coriolis force is smaller than that at the pump exit. The two other factors, the blade turning and passage meridional curvature, should be the dominant sources of the turbine exit secondary flow. The turbine blade has a total 124 deg blade turning angle. The turbine exit secondary flow structure is not easy to assess from the secondary flow vector plot (Fig. 14(*a*)). The presence of radial velocity is not only due to the secondary flow, but also due to torus curvature. At the turbine exit measurement plane, the streamline is not in the axial direction, especially near the core. However, if the radial component was removed from the secondary flow vector, two circulation patterns could be observed in the turbine exit flow. One is the counter clockwise circulation on the outer passage, and the other is the clockwise circulation on the inner passage. Hence, it is believed that the blade turning is the major reason for the observed structure of secondary flow.

The turbine exit axial vorticity is shown in Fig. 14(*b*). The axial vorticity is small and less than the relative eddy (-2ω) everywhere, except in the core region. Near the core region, appreciable vorticity exists due to upstream core flow separation and due to the vicinity of the blade trailing edge. As explained earlier, the measurement station is closest to the blade trailing at this location; and the secondary flow has not yet decayed at this location.

Mass Averaged Flow Radial Distribution. The radial distribution of the mass averaged flow parameters at the turbine exit is shown in Fig. 15. The radial gradient of absolute stagnation and static pressures are very small. The axial velocity is low near the core and high near the shell. This is due to the

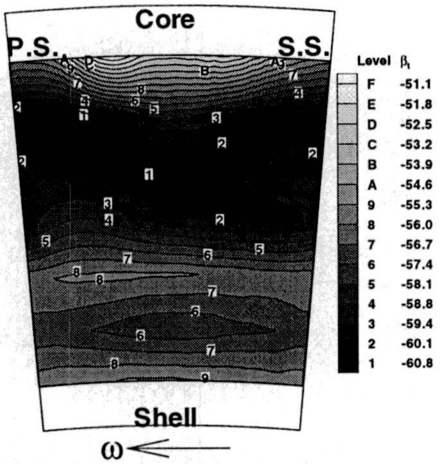

Fig. 13(*a*) Blade periodic relative flow yaw angle (β_t in degree)

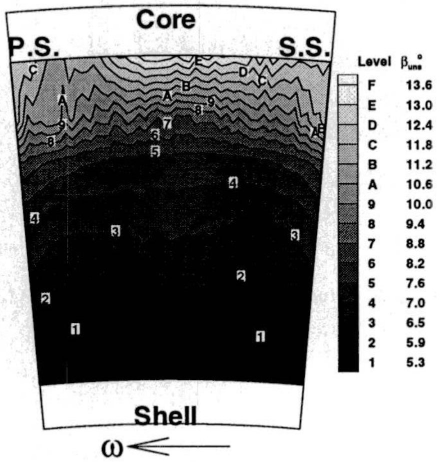

Fig. 13(*b*) Unresolved unsteadiness in relative yaw angle (β_{tuns} in degree)

Fig. 13 Relative flow yaw angle at turbine exit (SR = 0.6)

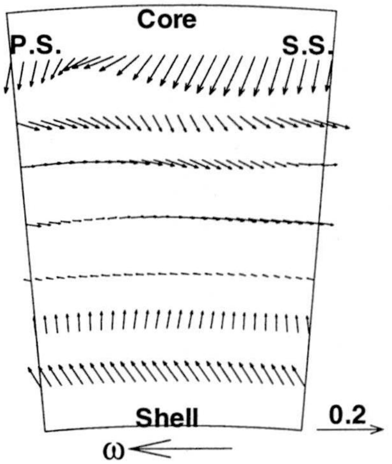

Fig. 14(*a*) Secondary flow vectors

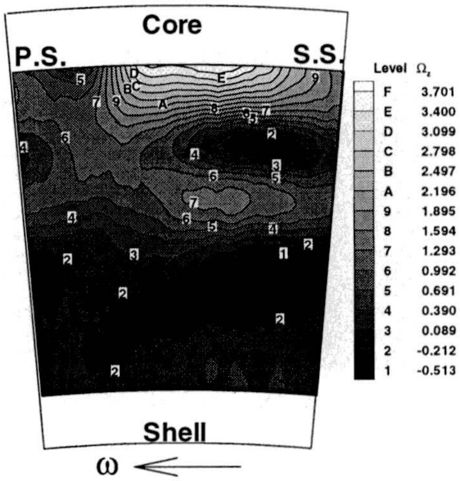

Fig. 14(*b*) Normalized axial vorticity (Ω_z)

Fig. 14 Secondary flow and vorticity at turbine exit (SR = 0.6)

blockage effect caused by core flow separation in the turbine passage. The relative flow angle (β_t) is very close to the turbine exit blade angle from the shell to 80 percent span. Hence, the turbine exit flow deviation is very small and is less than 5 deg. The largest deviation occurs near the core because of the flow separation on the core. The absolute flow yaw angle (β) has over 50 deg variation from the shell to the core at the turbine exit. This means that the stator will have a large incidence variation from hub-to-tip resulting in severe off design conditions. This will increase the total pressure loss inside the stator passage. Negative radial flow is found in the whole passage and is large near the core, caused by meridional flow curvature. An additional effect is the streamline curvature in the blade-to-blade plane.

Overall Performance of the Torque Converter

The overall performance of the torque converter can be ascertained by examining the data at stator exit (or pump inlet Fig. 10(*a*)), pump exit (or turbine inlet Fig. 10(*b*)), and turbine exit (or stator inlet Fig. 15). The pressure rise (P_o, Fig. 10(*a*) and (*b*)) across the pump is higher at the shell and much lower at the core. This is mainly caused by the flow separation and ''jet-wake'' structure that exists within the pump in this region. The axial velocity is highly nonuniform at the pump inlet, with evidence of flow separation near the core as it approaches the pump leading edge, but the axial velocity is uniform from core to shell at the pump exit (Fig. 10(*b*)). This indicates that major mixing occurs inside the pump passage, caused by the secondary flow and the ''jet-wake'' structure. The absolute tangential velocity and the absolute flow angle are fairly uniform at both the pump inlet and the exit. The absolute turning angle near the shell is about 25 deg and almost zero near the core. This, combined with low axial velocity near the core, indicates that the core region is the most inefficient region and most of the pressure rise in this region occurs due to the shear pumping effect (Lakshminarayana, 1978).

The turbine performance can be discerned by examining Fig. 10(*b*) and Fig. 15. The turbine inlet flow encounters large radial gradient in absolute stagnation pressure, with the lowest values occurring near the core. The core flow in this region further deteriorates as it is transported through the turbine. The stagnation pressure drop near the core is much lower than that near the shell. This clearly reveals that major improvements in torque converter performance can be achieved through flow improvement in the core regions of the pump and the turbine to avoid flow separation. The passage averaged axial velocity is fairly uniform at the turbine inlet (Fig. 10(*b*)) and deteriorates near the core as it progresses through the turbine. The absolute flow turning angle near the shell and core are 80 and 30 deg, respectively, further confirming the inefficiency of the core region.

The stator performance can be ascertained by examining the data in Fig. 15 (stator inlet) and Fig. 10(*a*) (stator exit). The

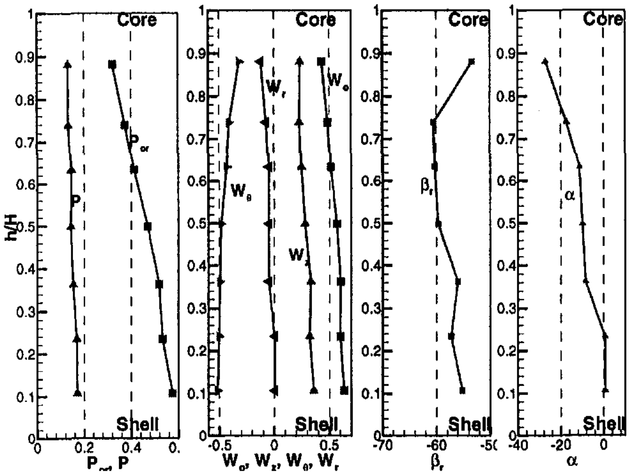

in turbine rotating frame.

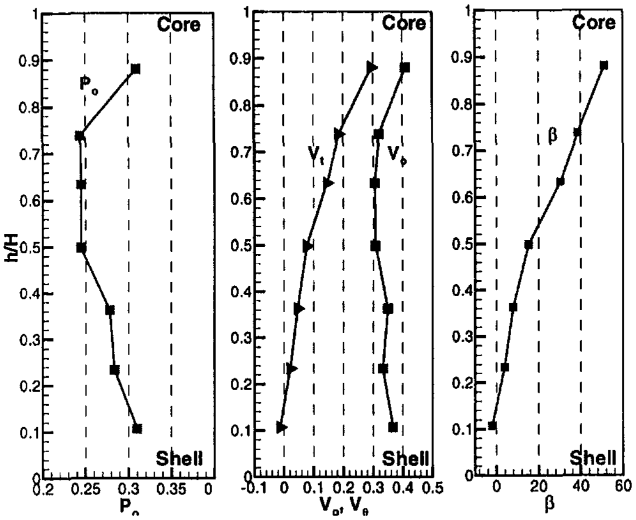

in absolute stationary frame

Fig. 15 Normalized radial distribution of mass averaged flow properties at turbine exit (SR = 0.6)

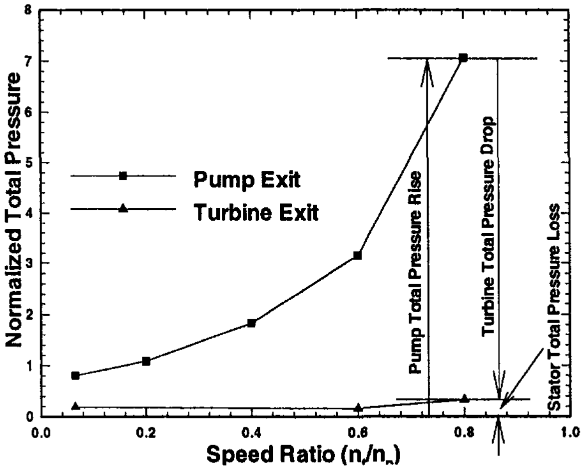

Fig. 16 Absolute total pressure change across elements versus speed ratio

maximum stagnation pressure loss occurs near the shell. The axial velocity profile deteriorates as the flow progresses through the stator, with core flow encountering a large velocity reduction. The flow turning is maximum near the shell region (about 60 deg) and minimum near the core region (about 25 deg). This is mainly caused by redistribution of axial velocity, secondary flows and flow separation near the shell endwall.

The mass averaged absolute total pressure rise in the pump and the total pressure drop in the turbine at various speed ratios are shown in Fig. 16. The total pressure loss in the stator is equal to the pump pressure rise minus the turbine pressure drop. At the high speed ratio, the total pressure loss in the stator is only a small fraction of the pump total pressure rise. For speed ratios 0.6 and 0.8, the total pressure losses in the stator are about 4.96 and 4.67 percent of the pump total pressure rise, respectively. Most of the pump energy is absorbed by the turbine at these speed ratios and the torque converter efficiency is high. At low speed ratio (0.065), the total pressure loss in the stator is a larger fraction of the pump pressure rise, caused mainly by the large incidence to the stator.

The torque for each element is also calculated using the measured flow field data. They are 23.10, 31.80, and 8.70 Nm for pump, turbine, and stator, respectively, at a speed ratio of 0.6. These values are approximate values, because only about 75 percent flow area is measured at the exit of each element. The pump and turbine torque measured by the load cells are 24.98 and 31.45 Nm. So, the tare torque of the test facility on the pump side is 1.88 Nm, and the tare torque on the turbine side is 0.35 Nm. The hydraulic or Euler efficiency was calculated based on the measured stagnation pressure and velocity (Lakshminarayana, 1996). Its value is found to be 82.6 percent at speed ratio 0.6. It should be remarked here that the hydraulic efficiency is based on the five-hole probe data, which does not include the flow field near the core and shell. Hence this efficiency is higher than the measured overall torque converter efficiency mentioned earlier (75.54 percent), which also include the mechanical loss.

Conclusion

The following conclusions are drawn from this investigation:

(1) The pump and turbine blade passing frequencies are the dominant periodic components at the pump and the turbine exit, respectively.

(2) The pump exit flow field has four major regions; the free-stream, the pump blade wake, the core-suction corner separation, and the intense mixing region. The flow is well behaved on the outer half of the passage near the shell. On the bottom half passage near the core, the flow is complex due to the core-suction corner flow separation, very high radial inward flow in the separation zone, and very strong unsteadiness in the mixing flow zone.

(3) The main feature of the pump exit flow field is the flow concentration near the pressure side and the shell. The relative velocity defect along the suction side causes a strong radially inward secondary flow. The rotation has a dominant influence on the pump exit secondary flow, especially near the core-suction side corner.

(4) A flow separation zone is observed at the turbine exit flow near the core, where high unsteadiness and clockwise vorticity exist. The turbine flow turning is the major cause of the turbine exit secondary flow, which is much weaker than the pump exit secondary flow. The turbine blade passage meridional curvature and the flow blockage effects, and the turbine flow separation on the core dominate the radial distribution of the turbine exit flow properties.

(5) The core region is the most inefficient region in the pump passage, and most of the pump pressure rise in this region is due to shear pumping effect. The total pressure drop across the turbine near the core is much lower than that near the shell. The core regions of both the pump and turbine are inefficient. The torque converter performance can be improved through flow redesign of core region to avoid flow separation.

Acknowledgment

This project was sponsored by GM Powertrain, a Division of the General Motors Corporation. Assistance by J. Burningham and B. Marathe is gratefully acknowledged.

References

Brun, K., Flack, R. D., and Gruver, J. K., 1996, ''Laser Velocimeter Measurement in the Pump of a Torque Converter,'' ASME *Journal of Turbomachinery,* Vol. 118, No. 3, pp. 562–577.

Brun, K. and Flack, R. D., 1997, ''Laser Velocimeter Measurements in the Turbine of an Automotive Torque Converter,'' ASME *Journal of Turbomachinery,* Vol. 119, No. 3, pp. 646–662.

Dong, Y., 1998, ''An Experimental Investigation of Fluid Dynamics of An Automotive Torque Converter,'' Ph.D thesis The Pennsylvania State University.

Marathe, B. V. Lakshminarayana, B., and Maddock, D. G., 1997, ''Experimental Investigation of Steady and Unsteady Flow Field Downstream of Automotive Torque Converter Turbine and Inside the Stator,'' ASME *Journal of Turbomachinery,* Vol. 119, No. 3, pp. 624–645.

Lakshminarayana, B., 1996, *Fluid Dynamics and Heat Transfer of Turbomachinery,* Wiley-Interscience Publication.

Lakshminarayana, B., 1978, ''On the Shear Pumping Effect in Rocket Pump Inducers,'' Book chapter in *Pumps-Analysis, Design and Application,* Vol. 1, Worthington Pump Inc., pp. 49–68.

Von Backstrom, T. W., and Lakshminarayana, B., 1996, ''Fluid Dynamics and Performance of Automotive Torque Converters: an Assessment,'' ASME JOURNAL OF FLUIDS ENGINEERING, Vol. 118, No. 4, pp. 665–676.

C. Offtinger Brissaud
Research Engineer.

C. Henry
Associate Professor.

R. Morel
Professor.

F. Spettel
Associate Professor.

Equipe Hydraulique I.N.S.A. Lyon,
Laboratoire de Mécanique des
Fluides et d'Acoustique,
U.M.R. CNRS 5509 E.C.L., U.C.B. Lyon I,
20, ave A. Einstein,
69621 Villeurbanne, Cedex
France

Investigation and Control of Backflow Ahead of a Shrouded Inducer

Incorporating a backflow recirculator is a way to reduce part load instabilities of inducers. Experimental results demonstrate that two devices with simple geometry considerably soften pressure pulsations in suction and discharge pipes associated with part load instabilities, even at low NPSH conditions and low flowrates. This is accomplished with negligible adverse effects on pump performance.

Introduction

The major drawback of using inducers is their part load instabilities due to swirling backflow (Sloteman et al., 1984). If the interaction between this backflow and the main stream can be eliminated, it would be possible to eliminate or at least to damper instabilities.

Wong et al. (1965), have taken high energy fluid from the discharge of a turbopump and injected it upstream of its inducer to improve flow distribution and eliminate cavitation and instabilities.

Abramian et al. (1988) have placed a series of perforated disks in an attempt to reduce reversal flow. The efficiency of this device in attenuating pressure pulsations under cavitating conditions remains to be proved.

Sloteman et al. (1984) have studied backflow recirculator placed upstream of an inducer, displacing the backflow out of the passage. Kasztejna et al. (1985) have tested a similar device with a centrifugal pump. These devices achieved stable operation at all NPSH conditions and at low flow rates, without adverse effects on pump performance.

Thus, local modifications of the casing wall in front of an inducer seem to be a good way of reducing part load instabilities and cavitation surge, in particular, without penalizing operation at the best efficiency flow rate.

Two devices of simple geometry, displacing the swirling backflow out of the passage, have been tested at the INSA Fluid Mechanics Laboratory, Lyon.

Test Apparatus

The investigations were always conducted in test facility arranged in a closed-loop circuit, as shown in Fig. 1. The water was always deaerated until there was no visible bubble in the transparent suction line. The shrouded inducer is placed in front of a centrifugal pump on the same shaft. A detailed presentation of the test loop is presented along with key design data and performance of the inducer in the reference (Offtinger et al., 1997). The main design parameters of the inducer are given in Table 1.

The first device (Fig. 2) consists in a cavity cut out of the casing just upstream of the inducer. The length of this cavity corresponds to the maximum axial extension upstream of the backflow cavitation at the pump best efficiency flowrate. The second device (Fig. 3) is a pierced ring placed in the cavity. These backflow recirculators, which are completely outside the mainstream, extract the backflow fluid because the high swirl velocity component causes a radial pressure gradient which forces the fluid to move radially into the annular slot. In the arrangement of Fig. 3, the fluid moves axially through the holes and then back into the mainstream.

Flow fields at the inlet and the outlet of the inducer were investigated under noncavitating conditions with and without the cavity, using a five hole probe. No measurements were made with the pierced ring because the passage of the probe through the ring, obstructing a hole, would have modified the effect of the device in the explored area. Experiments were carried out for two flow coefficients: the first one $\delta_1 = 0.384$ corresponding to the unshrouded inducer shockless flow coefficient at the tip, and the second one $\delta_2 = 0.249$ corresponding to $0.645\delta_1$. The measurement procedure is described in the references (Offtinger-Brissaud, 1997 and Offtinger et al., 1997). Some measurements were made inside the cavity in order to determine the direction of the flow in this area.

The visualization of the flow upstream and downstream (between inducer and centrifugal impeller) of the inducer through a 500 mm long clear suction pipe allowed us to map the inception and the evolution of the different forms of cavitation appearing upstream of the inducer. Similar studies have been made by Acosta (1992) and Tsujimoto (1995). The plane σ/δ is explored using two different methods, first, the flowrate is reduced at constant σ and then σ is lowered at constant flowrate coefficient.

Pressure fluctuations in suction and discharge pipes associated with cavitation figures upstream of the inducer were studied. The suction pressure transducer is located 2 m upstream of the inducer. The discharge pressure transducer is located 1 m downstream of the centrifugal impeller. The plane σ/δ was investigated at 120 regularly distributed operating points ($0.02 \le \sigma \le 0.12$ and $0.090 \le \delta \le 0.340$). More details about the measurement procedure are presented in the reference (Offtinger et al., 1997).

Contributed by the Fluids Engineering Division for publication in the JOURNAL OF FLUIDS ENGINEERING. Manuscript received by the Fluids Engineering Division October 8, 1997; revised manuscript received February 23, 1998. Associate Technical Editor: B. Schiavello.

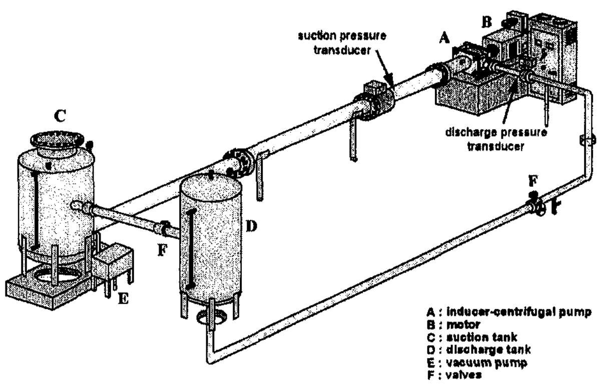

Fig. 1 Test loop

Table 1 Inducer characteristics

Rotation speed	2960 rpm
Number of blades	3
Schockless flow coefficient at tip	0.384
Suction specific speed	456.45
Hub to tip ratio at inlet	$r_h/r_t = 0.354$
Hub to tip ratio at outlet	$r_h/r_t = 0.393$
Best efficiency flow coefficient	0.31
Radial clearance	$0.0011r_t - 0.0044r_t$
Sweep angle	7.92°

		Tip	Hub
Blade thickness/chord		0.0118	0.0412
Solidity		1.6	1.77
Stagger angle	relative	80.35°	61.51°
Inlet blade angle	to axial	81.88°	71.71°
Outlet blade angle	direction	76.71°	50.71°

Variations of available NPSH are carried out by adjusting the pressure above the free surface of the water in the suction tank (C). The minimum available NPSH coefficient that can be reached is about 0.019. Compressed air is injected into the suction tank, in order to increase the pressure for non cavitating performance measurements.

The temperature of the water is measured with a mercury thermometer in the suction tank.

Steady state pressures are measured using Rosemount 1151DP differential pressure transducers whose maximum ranges are 20.10^5 Pa (head), 7.10^5 Pa and 37.10^3 Pa (five holes probe measurements). The pressure at the inlet of the inducer (for the calculation of NPSH) is measured using a Rosemount 1151AP absolute pressure transducer whose maximum range is 187.10^3 Pa. These Rosemount transducers keep their own calibration in memory and the accuracy is from 0.1 to 0.2 percent of the measurement range, this being superior or equal to $\frac{1}{6}$ of the maximum range calibrated.

Measurements of pressure fluctuations in the suction and discharge pipes are carried out with ENTRAN EPX piezoresistive transducers whose pass band is 13 kHz. These unsteady pressure transducers are placed in inserts (Fig. 4) to avoid positioning problems and to protect them from cavitation bubbles. The measurement range of the suction and discharge transducers are 1 bar and 7 bars, respectively, with measurement uncertainties of ±1 percent and ±0.7 percent of these ranges. The cut-off frequency due to the cavity of the inserts is 1100 Hz, which is much higher than the frequencies of cavitation aspects associated with massive flow instabilities in the suction/discharge piping. The maximum amplification factor corresponding to the maximum frequency 160 Hz is 1.0004. To avoid zero drift with temperature, a static calibration of the transducers is carried out every three measurements.

Estimation of experimental uncertainties are: head coefficient $\psi \pm 0.0003$, efficiency $\eta \pm 0.01$, flow coefficient $\delta \pm 0.004$, undimensional NPSH $\sigma \pm 0.0001$, undimensional peak to peak amplitude of suction pressure $p_s \pm 0.0013$, undimensional peak to peak amplitude of discharge pressure $p_d \pm 0.0065$.

Experimental Results

Performance Curves. The noncavitating performance curves of the combination inducer-centrifugal pump are given in Fig. 5. The total head curves are the same with and without backflow control over a wide range of flow rates. At flow rates below 40 percent of design flow, the head is increased by the devices and consequently the inflection in the curve is strongly attenuated. This increase is higher with the pierced ring. The devices induce a rise in shaft power and therefore a decrease in efficiency which reaches at most 2 percent with the cavity and 3 percent with the pierced ring, near and above the best efficiency flow rate. At low flow rates, the efficiency remains unchanged because of the simultaneous increase of total head and shaft power.

The curves of NPSH required at 3 percent head loss (full pump) are presented in Fig. 6. The presence of the cavity leads to improved operation of the combination inducer-centrifugal pump under cavitating conditions. For flow rate coefficients from 0.09 to 0.23, air leak into the tank makes impossible to sufficiently reduce the pressure in the suction tank down to the level needed for producing a pump head drop of 3 percent or more. With the pierced ring the vacuum pressure can not be lowered as much needed to reach a 3 percent head drop for all flow rate coefficients lower than $\delta = 0.27$.

Flow Fields at the Inlet and the Outlet of the Inducer. Figure 7 presents a comparison for two flowrate coefficients of the meridional and the tangential velocities measured at the inlet and the outlet of the inducer without a device and with the cavity.

At the design flow coefficient (shockless at the tip), the cavity induces at the inlet a slight deficit of flow at the tip which is correlated with an increase of the tangential velocity component rotating in the same direction as the inducer rotation (positive prerotation). At the outlet, the velocity field is not modified.

At partial flow coefficient δ_2, some reverse flow localized at the tip appears at the inlet without a device. In connection

Nomenclature

C = fluid absolute velocity
U = blade peripheral speed
P = peak to peak amplitude of pressure pulsation
p = nondimensional peak to peak amplitude of pressure pulsation = $P/(U_t^2/g)$
r = radius

S = suction specific speed = $N(\text{rpm})\sqrt{Q(m^3/s)}/\text{NPSH}(m)^{3/4}$
δ = flow coefficient = $Q/(U_t r_t^2)$
μ = head coefficient = $H/(U_t^2/g)$
η = efficiency
σ = nondimensional NPSH = $\text{NPSH}/(U_t^2/g)$

Subscripts

d = discharge
m = meridional
s = suction
t = tip
u = tangential

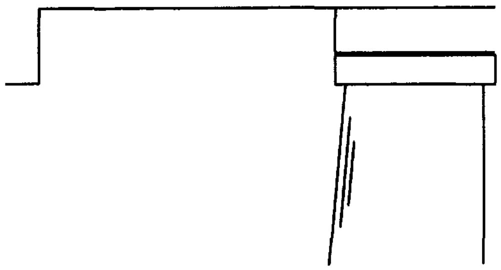

Fig. 2 Cavity

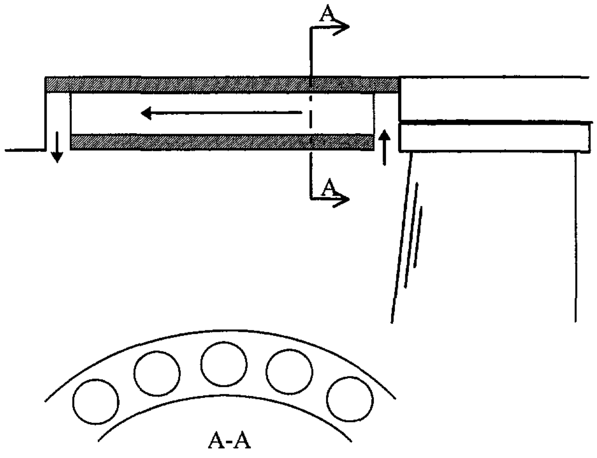

Fig. 3 Pierced ring

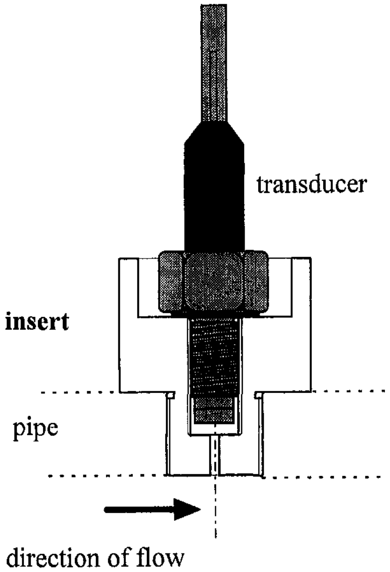

Fig. 4 Insert and pressure transducer

with the inlet recirculation, the tangential velocity component increases strongly near the tip. With the cavity, as expected, the recirculation is moved out of the passage but the prerotation region extends across a wider part of the passage. At the outlet, recirculation also exists at the tip in both configurations, but with the cavity the reverse flow is localized in a very restricted part of the passage near the tip. On the outer half of the blade height, the tangential velocity component at outlet is reduced with the cavity.

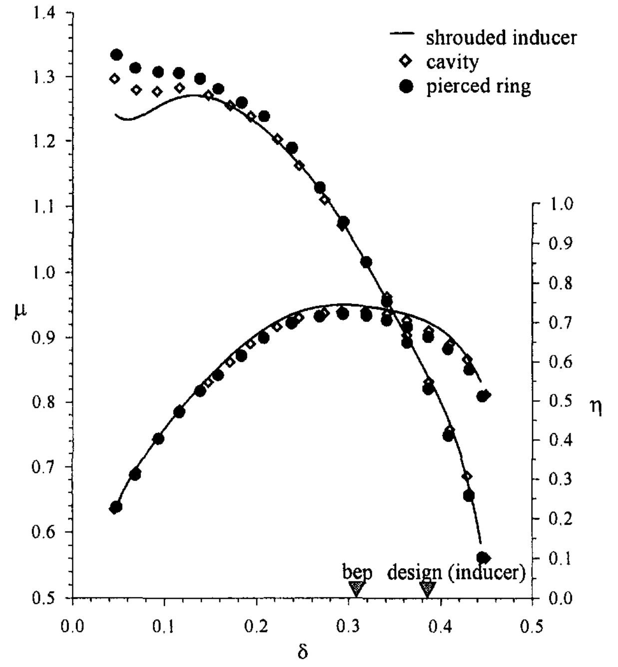

Fig. 5 Noncavitating overall performance curves of the combination inducer-centrifugal pump (experimental uncertainties are $\mu \pm 0.0003$, $\delta \pm 0.004$, $\eta \pm 0.01$)

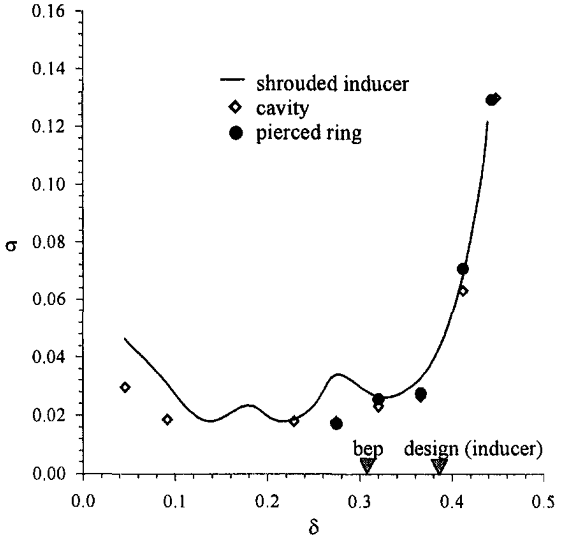

Fig. 6 Cavitating performance curves of the combination inducer-centrifugal pump (experimental uncertainties are $\sigma \pm 0.0001$)

Map of Cavitation. A visualization study of cavitation has been made in both configurations presented in this paper. The maps of cavitation obtained without a device and with the cavity are presented in Figs. 8 and 9, respectively. The curves of NPSH required at 3 percent head loss have been plotted under these maps for comparison. There is no fundamental difference of the cavitation maps between these two configurations but the volume of vapor visible in the clear pipe is lower with the cavity.

When the flowrate is reduced for a fixed NPSH, it is possible to observe successively, blade cavitation then backflow cavitation. The shroud is not transparent, thus the blade cavitation is only visible at the leading edge of the blades on the suction side. The backflow cavitation appears near the outer radius of the inducer inlet, then develops going upstream in the form of

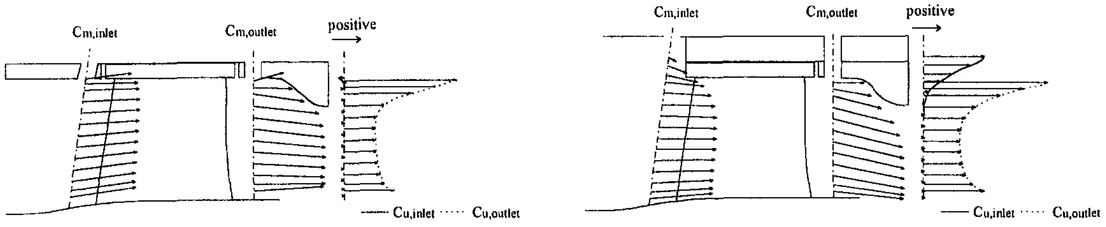

(a) Design flow rate δ_1 without device

(b) Design flow rate δ_1 with cavity

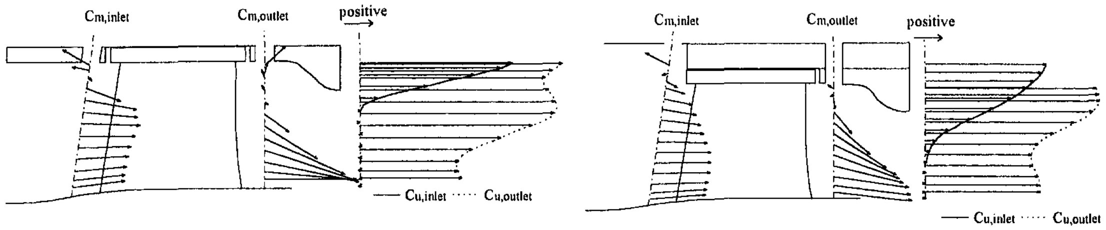

(c) Partial flow rate $\delta_2 = 0.645\ \delta_1$ without device

(d) Partial flow rate $\delta_2 = 0.645\ \delta_1$ with cavity

Fig. 7 Meridional velocity C_m and tangential velocity C_u at inducer inlet/outlet

backflowing cones (Fig. 10) (one cone for each vane) and pulsation of cavitation length takes place. At lower flowrates the vapor contracts towards the inner radii and forms a fluctuating vapor core at the center of the pipe (Fig. 11). With the cavity this vapor core becomes steady at very low flow coefficients.

The inception of cavitation surge (massive low frequency flow oscillations) can be observed very clearly when the NPSH is reduced at constant flowrate. This inception line is marked out by solid circles in Figs. 8 and 9. For flow coefficients upper than $\delta = 0.25$, a stable super cavitating flow takes place at very low NPSH.

Visualizations allowed us to differentiate in the plane σ/δ certain domains characterized by different forms of cavitation. First, a zone A of steady flow where only blade cavitation can be seen, then domains B and C where backflow cavitation develops and begins to pulsate, then a region D where a pulsating vapor core is present at the center of the suction pipe, and lastly, domains E and F of backflow cavitation surge and blade cavitation surge.

With the pierced ring no quantitative map can be drawn because the backflow cavitation is trapped in the area of the suction pipe covered by the device for all flow coefficients greater than $\delta = 0.12$. At very low flowrates backflow cavitation exits from the pierced ring going upstream but no vapor core forms at the center of the pipe. The very significant attenuation of the cavitation due to the pierced ring can be seen in Figs. 12 and 13, which show the flow upstream of the inducer for

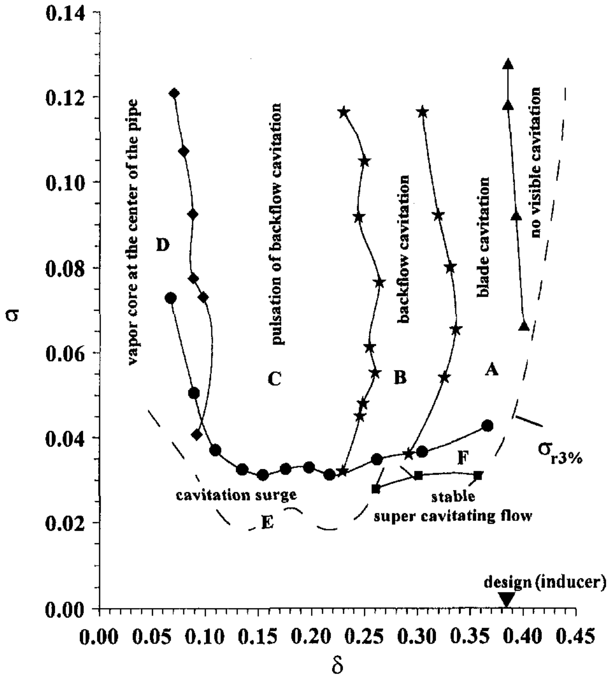

Fig. 8 Map of cavitation without device

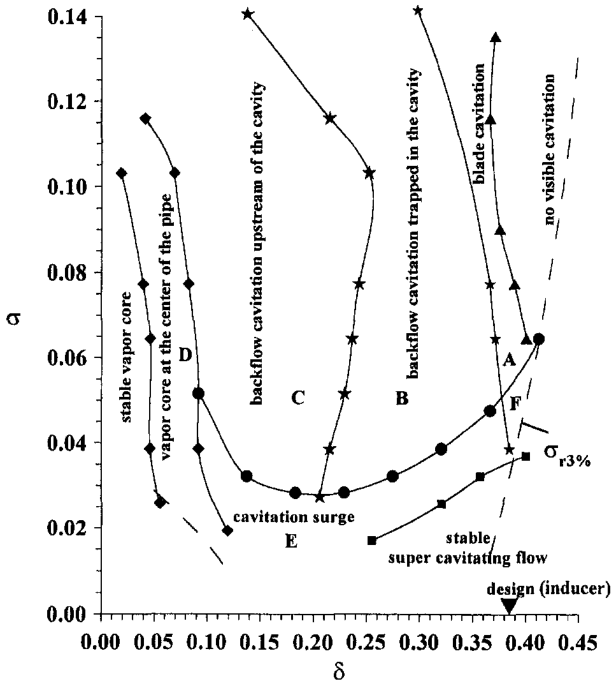

Fig. 9 Map of cavitation with the cavity

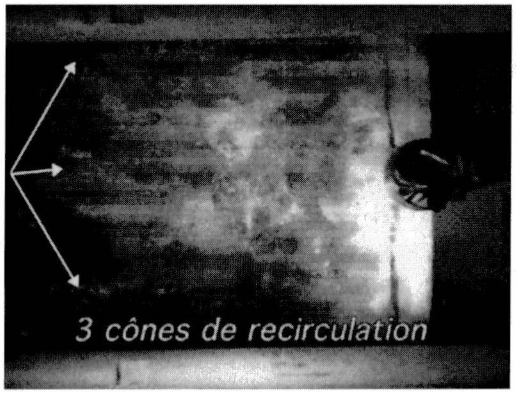

Fig. 10 Backflowing cones without device

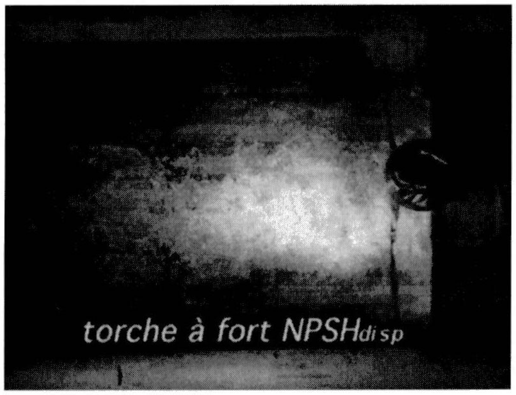

Fig. 11 Vapor core at the center of the pipe without device

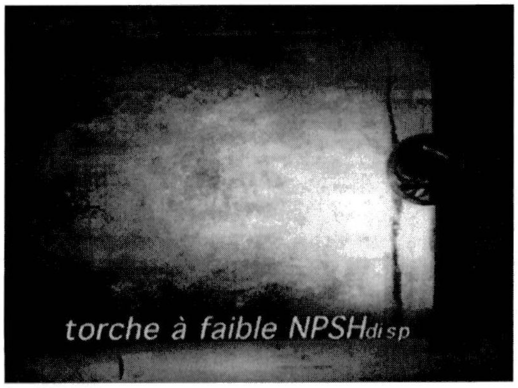

Fig. 12 $\delta = 0.09$ $\sigma = 0.0258$ without device

the same critical operating conditions (very low flow coefficient and very low NPSH) without a device and with the pierced ring, respectively.

Pressure Pulsations in Pipes. Pressure pulsations in suction and discharge pipes have been measured in order to quantify part load instabilities associated with cavitation forms in each configuration. The nondimensional peak to peak amplitude of each signal has been plotted, resulting in contour plots of amplitude levels for the suction (Fig. 14.I) and discharge (Fig. 14.II) signals in each configuration. The domains of cavitation identified with the visualizations have been drawn over the maps in the configurations without a device and with the cavity.

Figure 14.I(a) shows that for the shrouded inducer, peak to peak amplitudes of suction pressure pulsations p_s are moderate

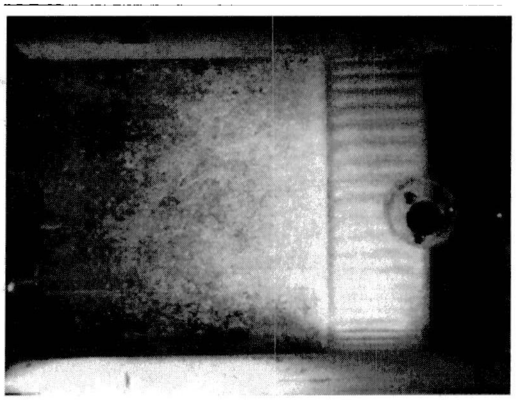

Fig. 13 $\delta = 0.09$ $\sigma = 0.0258$ with the pierced ring

in domains B and C and very high in the region E of the backflow cavitation surge.

The cavity induces (Fig. 14.I(b)) a softening of p_s in all the tested operating conditions and particularly the elimination in domain E of the highest peak to peak amplitude without device (red spot). Moderate pulsations remain in region C at low flow coefficients. With the pierced ring (Fig. 14.I(c)) p_s is weak all across the plane σ/δ.

An important reduction of pressure pulsations in the suction pipe is obtained with the two devices and particularly with the pierced ring.

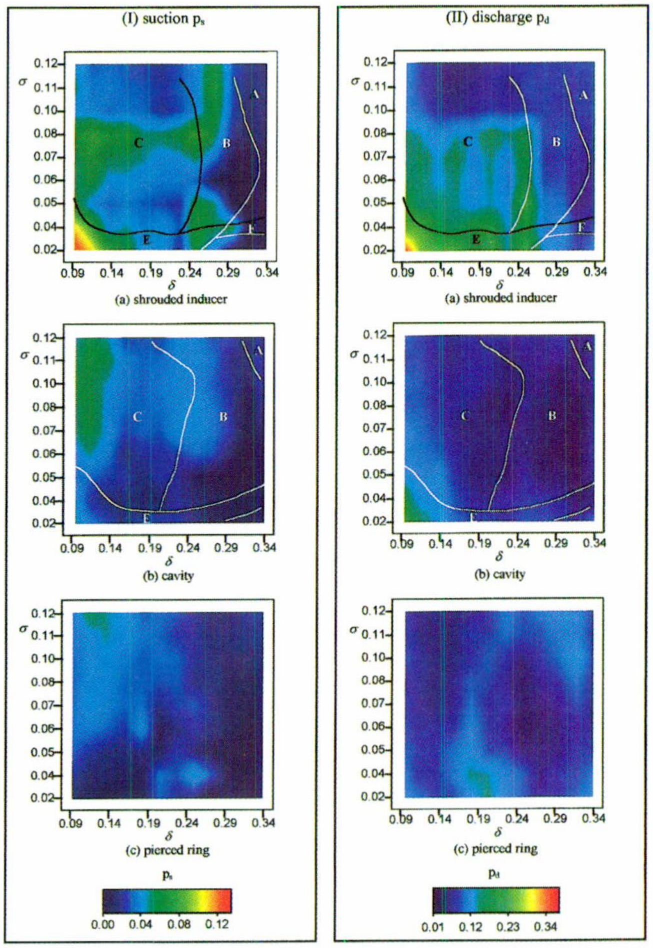

Fig. 14 Peak to peak amplitudes of pressure pulsations (experimental uncertainties are $p_s \pm 0.0013$ $p_d \pm 0.0065$)

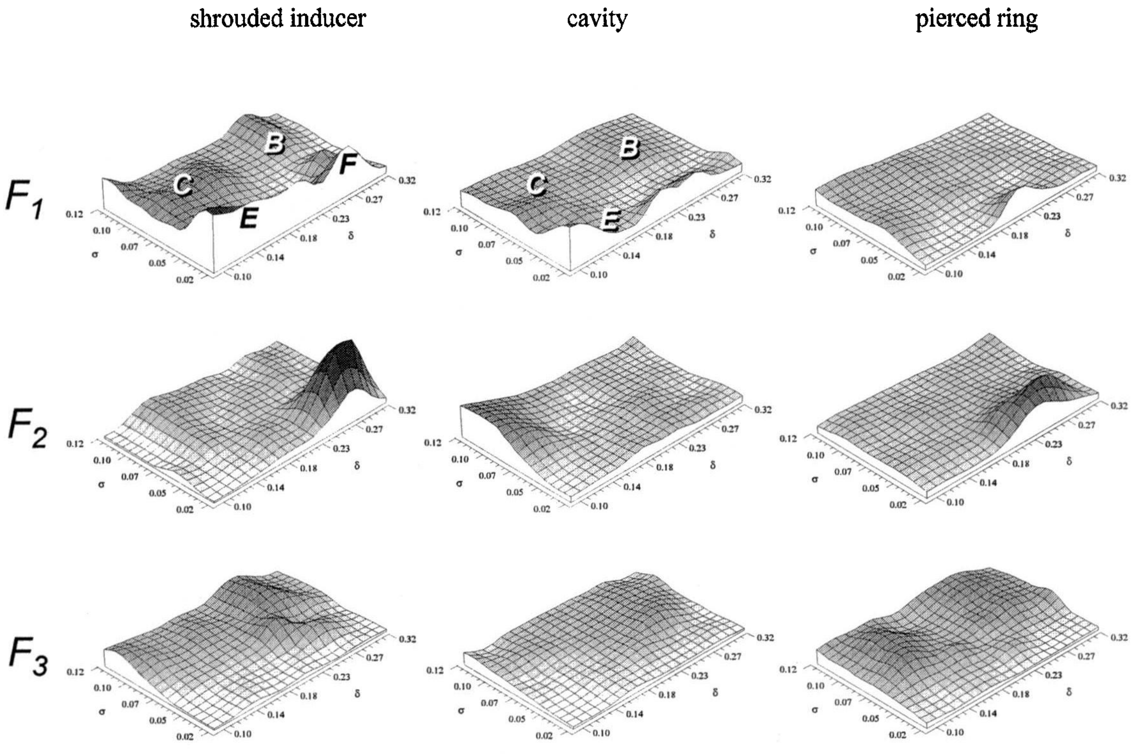

Fig. 15 Suction pressure amplitudes in three different frequency ranges (vertical scale 1 cm ——→ 0.0356)

For the shrouded inducer, peak to peak amplitudes of discharge pressure pulsations p_d (Fig. 14.II(a)) are weak except in the region of low σ and low flowrate coefficients. In the domain E, backflow cavitation surge induces pressure pulsations at the suction as well as at the discharge of the pump and therefore the values of p_d are high.

The cavity (Fig. 14.II(b)) and the pierced ring (Fig. 14.II(c)) strongly attenuate the discharge pressure pulsations for almost all operating conditions.

As a general rule, the frequency spectra of suction pressure signals show three peaks in three different frequency ranges: low frequencies F_1 included within 0 and 20 Hz, medium frequencies F_2 = 20 to 70 Hz and high frequencies F_3 = 70 to 160 Hz (rotational speed = 2960 rpm, 3 vanes).

Figure 15 shows amplitude level maps of the three peaks in the three configurations, pointing out the areas of the plane σ/δ where each frequency range is present.

Thus, for the shrouded inducer, in domain B of the inception of backflow recirculation, moderate pressure pulsations take place at low and high frequencies simultaneously. In domain C, pulsations of backflow recirculation also generate moderate pressure pulsations at low and high frequencies. The backflow cavitation surge leads to very high amplitudes of pressure pulsations only at low frequency. High and moderate frequency components are present simultaneously in the frequency spectra of domain F.

With the cavity, the softening of pressure pulsations applies for all frequency ranges. A peak of low frequency still emerges in the frequency spectra at low NPSH. The hump in the map of F_2 amplitude obtained without a device at low NPSH and high flow coefficients does not exist any longer, while this frequency range predominates for the low flow coefficients and high NPSH.

With the pierced ring, only a small region of pressure pulsation with moderate amplitude persists. In this area two frequency ranges are found, as in the case of domain F without a device. At high σ, pulsations show high frequencies and weak amplitudes.

Conclusion

The use of a backflow recirculator is a solution for controlling backflow at the inlet of an inducer which is responsible for cavitation surge. Two devices of simple geometry placed in front of a three bladed shrouded inducer have been tested. The result of these tests indicate that stable operation is achieved at nearly all NPSH and flow conditions. This is accomplished with marginal adverse effect in pump performance in terms of head and efficiency.

The cavity removes the backflow out of the passage at least for flow coefficients greater than 0.249 (corresponding to 0.645 times design flow coefficient). This device attenuates pressure pulsations especially in the case of cavitation surge, but cavitation figures observed without a device still exist.

With the pierced ring, backflow cavitation is trapped in the device for almost all operating conditions, resulting in very small pressure pulsations amplitudes. The backflow does only develop at very low flow coefficients and extends upstream, but both the volume of vapor and also the pressure pulsations amplitudes are low.

Acknowledgments

This work was carried out with the support of EDF-DER (Electricité De France—Direction des Etudes et Recherches) and GEC ALSTHOM—Bergeron.

References

Wong, G. S., MacGregor, C. A., and Hoshide, R. K., 1965, "Suppression of Cavitation and Unstable Flow in Throttled Turbopumps," *Journal of Spacecraft and Rocket*, Vol. 2, No. 1, Jan.-Feb., pp. 73–80.

Sloteman, D. P., Cooper, P., and Dussourd, J. L., 1984, "Control of Backflow at the Inlets of Centrifugal Pumps and Inducers," *Proceedings of the First International Pump Symposium*, Texas A&M University, College Station, TX, pp. 9–22.

Kasztejna, P. J., Heald, C., and Cooper, P., 1985, ''Experimental Study of the Influence of Backflow Control on Pump Hydraulic-Mechanical Interaction,'' *Proceedings of the Second International Pump Symposium,* Texas A&M University, College Station, TX, pp. 33–40.

Abramian, M., Howard, J. H. G., and Hermann, P., 1988, ''An Investigation of Axial Pump Backflow and a Method for its Control,'' ASME Paper 88-GT-31, June, 8 pp.

Acosta, A. J., 1992, ''Flow in Inducer Pumps, an Aperçu,'' *4th Symposium of Transport Phenomena and Dynamics of Rotating Machinery,* Honolulu, Hawaï, Apr., 13 pp.

Tsujimoto, Y., Yoshida, Y., Maekawa, Y., Watanabe, S., and Hashimoto, T., 1995, ''Observations of Oscillating Cavitations of an Inducer,'' FED-Vol 226, *Cavitation and Gas-Liquid Flow in Machinery Devices,* ASME, pp. 127–134.

Pagnier, P., 1994, ''Etude des Instabilités de Fonctionnement à Débit Partiel, de Roue de Gavage (Inducteurs) en Alimentation de Pompes Centrifuges,'' Thesis, INSA de Lyon, France, 203 pp.

Offtinger-Brissaud, C., 1997 ''Analyse et réduction des instabilités de fonctionnement à débit partiel d'un inducteur fretté placé en alimentation d'une pompe centrifuge,'' thesis, INSA de Lyon, France, 209 pp.

Offtinger, C., Henry, C., and Morel, R., 1997, ''Instabilités de Fonctionnement à Débit Partiel d'un Inducteur Fretté, Comparison avec le Cas non Fretté,'' *La Houille Blanche,* No. 4/5, May, pp. 34–38.

Offtinger, C., Henry, C., Morel, R., and Spettel, F., 1997, ''Experimental Comparison of Flow Fields at the Inlet and the Outlet of an Inducer with Shrouded and Unshrouded Configuration,'' ASME JOURNAL OF FLUIDS ENGINEERING, Vol. 119, Dec. pp. 954–959.

A Design Method for High-Speed Propulsor Blades

Paul E. Griffin
Graduate Student.

Spyros A. Kinnas
Assistant Professor.

Ocean Engineering Group,
Department of Civil Engineering,
The University of Texas at Austin,
Austin, TX 78712

This study uses a nonlinear optimization method coupled with a vortex lattice cavitating propeller analysis method to design efficient propeller blades. Different constraints are imposed to improve propeller design. Several advancements in the method are shown, including the option for quadratic skew, user specified skew distribution, and a constraint limiting the minimum pressure in wetted regions of the blade. Results for a series of fully wetted runs demonstrate the effectiveness of the constraint on minimum pressure in preventing the onset of bubble or mid-chord cavitation. A comparison of a design in uniform inflow with a design in non-axisymmetric inflow indicates that a propeller designed by the present method in non-axisymmetric inflow has more favorable cavitating flow characteristics than a propeller design assuming uniform inflow. Results are also shown for a series of runs utilizing the cavity constraints. These results indicate that the present method can be used to improve on propeller designs by imposing constraints on the cavity area and cavity volume velocity harmonics, as well as by using a quadratic skew distribution.

Introduction

High-speed propulsor blades[1] for ocean vehicle applications must deal with the trade-off of high efficiencies of propulsion with controlled amounts of cavitation. The least desirable types of cavitation are bubble and cloud cavitation. These types of cavitation are undesirable because they involve a rapid formation and collapse of cavities that can lead to erosion of the propeller blade. Traditional design methods first determine the optimum circulation distribution in the circumferentially averaged inflow (Coney, 1989) and then use an inverse method to design the blade that produces that circulation distribution (Kerwin, 1973 and Kerwin, 1994). These designs are then analyzed in the actual nonaxisymmetric inflow and adjusted in a trial-and-error manner until the design criteria and the constraints on cavity size and induced hull pressures are satisfied.

A nonlinear optimization method was recently developed by Mishima (1996) and Mishima and Kinnas (1997) for the design of cavitating propeller blades subject to non-axisymmetric inflows. References on the subject of optimization as applied to propeller design may be found in Mishima and Kinnas (1997), while a complete review of current methods for the optimization of lifting surfaces is given by Sparenberg (1995). This method is implemented in a computer code known as CAVOPT-3D, which stands for CAVitating blade OPTimization-3D. The method determines the geometry of the blade by minimizing the required horsepower for given required thrust and certain design constraints. These constraints include upper bounds on the extent of the cavity, the amount of face cavitation, the linear skew, and the cavity velocity harmonics (which are directly related to the propeller induced pressure fluctuations on the ship's hull). The result of the method is an optimum cavitating propeller design.

The following study uses CAVOPT-3D along with current advancements to design cavitating propeller blades with different design conditions and constraints. The resulting propeller designs are compared to each other.

There are several current advancements to the method. First, the method allows the propeller blade to have a quadratic skew distribution. Previously, the only options were for no skew or a linear skew distribution. Second, the initial guess for the optimization has been improved by allowing the user to choose the skew distribution for the initial geometry. There are two options for assigning the initial skew. The user can give as input the initial skew distribution or have a zero initial skew assigned by the method. Also new to the method is the option for prescribed skew during the optimization process. Finally, a constraint limiting the minimum pressure in noncavitating areas of the blade is implemented. This constraint is intended to avoid regions on the blade which could be susceptible to mid-chord or bubble cavitation.

The Optimization Method

CAVOPT-3D is a design method that produces the most efficient cavitating propeller design for a given set of design conditions and constraints. The method couples a cavitating propeller analysis method in non-axisymmetric inflow (HPUF-3AL) (Lee, 1979; Kerwin, 1986; Kinnas and Pyo, 1997) with a nonlinear optimization scheme (Mishima, 1996 and Mishima and Kinnas, 1997). The propeller analysis method models the three-dimensional unsteady cavitating flow around a propeller by representing the blade as a discrete vortex and source lattice which is located on the blade mean camber surface. The method employs a non-linear leading edge correction and trailing wake alignment. The time dependent cavity extent is determined by requiring the pressure everywhere on the cavity to be equal to vapor pressure and the cavity height (thus volume) is determined by integrating the cavity source distribution over the cavity surface. The analysis method and the optimization method have been thoroughly numerically validated by Mishima and Kinnas (1997). Several comparisons with experiments have been used for the validation of the analysis method, including comparisons of thrust and torque coefficients (Kinnas and Pyo, 1997) and comparisons of cavity patterns (Choi and Kinnas, 1997).

The method describes the propeller geometry with a cubic B-spline polygon net. A design variable vector containing the coordinates of the B-spline vertices defines the polygon net. Traditional geometry definitions require the radial distributions of pitch, rake, skew, chord, maximum thickness, maximum camber, and chord-wise distributions of camber and thickness. For the numerical optimization scheme, the B-spline representation has advantages over the traditional propeller geometry format. The B-spline representation is helpful because it reduces

---

[1] Conventional, super-cavitating, or surface-piercing.

Contributed by the Fluids Engineering Division for publication in the JOURNAL OF FLUIDS ENGINEERING. Manuscript received by the Fluids Engineering Division October 14, 1997; revised manuscript received April 27, 1998. Associate Technical Editor: J. Katz.

the computation time by allowing the propeller geometry to be defined with fewer parameters than the traditional method.

CAVOPT-3D users must specify the design conditions for their target propeller. These conditions include:

- advance coefficient (J_s)
- cavitation number (σ_n)
- Froude number (F_n)
- number of blades (Z)
- hub radius (r_H)
- required thrust coefficient (K_{T_o})

The optimization method minimizes the torque for a given value of thrust. This problem is defined as follows:

$$\text{minimize} \quad f(\mathbf{x}) = K_Q(\mathbf{x})$$

$$\text{with} \quad h(\mathbf{x}) = \frac{K_T(\mathbf{x}) - K_{T_o}}{K_{T_o}} = 0 \qquad (1)$$

where $K_Q(\mathbf{x})$ is the torque coefficient, $K_T(\mathbf{x})$ is the thrust coefficient, K_{T_o} is the required thrust coefficient, and $\mathbf{x}$ is the design variable vector defining the blade geometry. Thus, the objective function, $f(\mathbf{x})$, represents the torque, and the equality constraint, $h(\mathbf{x}) = 0$, is given in terms of thrust. The objective function is to be minimized in the presence of the equality constraint and the inequality constraints $g_i(\mathbf{x}) \leq 0$. The program user has the choice of imposing several inequality constraints in CAVOPT-3D. The available inequality constraints are defined as follows:

$$\begin{aligned} \text{CA} &\leq \text{CAMAX} \\ \text{FA} &\leq \text{FAMAX} \\ \text{SK} &\leq \text{SKMAX} \\ \text{VV} &\leq \text{VVMAX} \qquad (2) \end{aligned}$$

The values on the left-hand side of Eqs. (2) are the instantaneous values for a particular iteration. The right-hand side of the constraint represents the limit to the value on the left-hand side. The limits are specified by the program user. The cavity area constraints CAMAX and FAMAX, respectively, represent the maximum allowable back and face cavity area to blade area ratios. VVMAX is the maximum allowable blade rate cavity volume velocity harmonics, nondimensionalized on nR^3. SKMAX is the maximum allowable skew at the tip.

Recent Improvements

One-Variable Quadratic Skew in CAVOPT-3D. A new option is introduced in CAVOPT-3D which uses a quadratic skew distribution during optimization. A blade with this type of skew distribution has forward skew at the inner radii and backward skew at the outer radii. These types of skew are very common in recent propeller designs. For the quadratic skew option, the user inputs the skew at the tip as well as a parameter RFOR, which is the radius at which the skew reaches a maximum forward value. RFOR is not only used to control the location of forward skew, but it can be adjusted so that a desired forward skew angle is attained. Using skew as a function of radius and radius squared, and setting the derivative of skew with respect to radius equal to zero at RFOR, the quadratic skew distribution is given by:

$$\theta(r) = \left[\frac{\text{SK}(r - r_H)^2}{(1 - r_H)^2 - 2(\text{RFOR} - r_H)(1 - r_H)}\right] - 2\left[\frac{\text{SK}[\text{RFOR} - r_H](r - r_H)}{(1 - r_H)^2 - 2(\text{RFOR} - r_H)(1 - r_H)}\right] \qquad (3)$$

Where SK is the skew at the tip, r_H is the hub radius over blade radius, r is radial distance over blade radius, and $\theta(r)$ is the skew. The parameters used for the determination of the quadratic skew are shown in Fig. 1.

Improving Initial Geometry. CAVOPT-3D is an optimization routine that begins with a certain propeller geometry, and then optimizes this initial geometry based on the user imposed constraints. In the original version of CAVOPT-3D, the initial geometry is arbitrarily chosen to be a blade with no skew, no rake, a constant pitch, and a standard camber distribution. In the present version, the user has the option of specifying the skew distribution for the initial geometry. The user also has the option of using that specified skew distribution at each iteration of the optimization process, rather than allowing the code to optimize the skew. This is useful in cases where the propeller designers know what kind of skew distribution they would like

Nomenclature

C_p = pressure coefficient, $C_p = (p - p_{shaft})/\rho n^2 D^2$
D = propeller diameter
F_n = Froude number, $F_n = (n^2 D/g)$
f_o = maximum camber in a chord-wise strip
$f(x)$ = objective function for the minimization problem
$g_i(x)$ = ith inequality constraint for the minimization problem
$h(x)$ = equality constraint for the minimization problem
g = acceleration of gravity
J_s = advance coefficient based on ship speed, $J = (V_s/nD)$
K_T = thrust coefficient, $K_T = (T/\rho n^2 D^4)$
K_Q = torque coefficient, $K_Q = (Q/\rho n^2 D^5)$
n = number of propeller revolutions per second
p_{shaft} = pressure at propeller shaft
p_v = vapor pressure
r = radius of point on propeller/R
r_H = propeller hub radius/R
R = propeller radius
RFOR = radius of forward skew/R
t_o = maximum blade thickness in a chord-wise strip
T = propeller thrust
V_s = ship speed
Z = number of blades
Γ = circulation
ρ = fluid density
η = propeller efficiency, $\eta = (J_s/2\pi)(K_T/K_Q)$
ρ = density of water
σ_n = cavitation number based on RPS n, $\sigma_n = (p_{shaft} - p_v/0.5\rho n^2 D^2)$
θ = blade angle
$\theta(r)$ = skew at radius r
CA = maximum back cavity area/Blade area
FA = maximum face cavity area/Blade area
SK = skew at tip
VV = blade rate cavity volume velocity harmonics/nR^3
DPV = $\sigma_n/2. -$ CPMIN
CPMIN = maximum $- C_p$ value over wetted portion of blade
CAMAX = allowable maximum back cavity area/Blade area
FAMAX = allowable maximum face cavity area/Blade area
SKMAX = allowable maximum skew at the tip
VVMAX = allowable maximum blade rate cavity volume velocity harmonics/nR^3
PTOL = allowable tolerance between DPV and zero

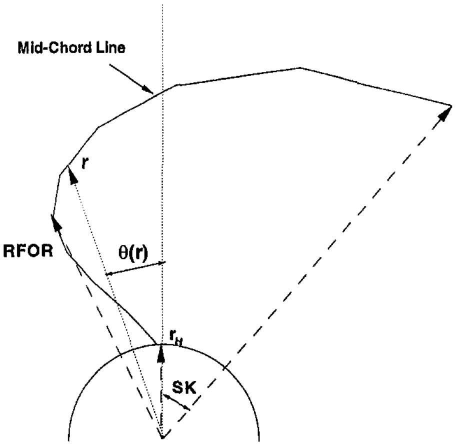

Fig. 1 Quadratic skew parameters

the propeller to have. In this case, the method will optimize the blade geometry at the specified skew.

Minimum Pressure Constraint. In CAVOPT-3D the cavitation number and pressure coefficient are defined by Eq. (4) and Eq. (5), respectively.

$$\sigma_n = \frac{p_{shaft} - p_v}{0.5\rho n^2 D^2} \tag{4}$$

$$C_p = \frac{p - p_{shaft}}{\rho n^2 D^2} \tag{5}$$

Rearranging and combining these equations with $p = p_v$ leads to:

$$-C_p = \frac{\sigma_n}{2} \tag{6}$$

Equation (6) describes the point of cavitation inception. In other words, cavitation occurs when $-C_p \geq \sigma_n/2$. When this is true, the pressure drops below vapor pressure and cavitation will occur.

Using this relation, the pressure on the propeller blade can be examined to determine exactly where cavitation occurs. Currently, HPUF-3AL only detects cavities that begin at the leading edge of the propeller. Sometimes, however, the pressure on the blade may drop below vapor pressure somewhere towards the middle of the blade chord. This type of cavitation, which can be interpreted as bubble or mid-chord cavitation, is not detected by HPUF-3AL.

A constraint has been implemented to limit the pressure on certain parts of the blade so that it will not drop below vapor pressure plus a tolerance. This tolerance allows for uncertainties in the pressure evaluation and/or cavitation inception. The areas of the blade on which this constraint is applied include all points downstream of leading edge cavitation on the suction side. More specifically, for a fully wetted propeller, the whole blade is searched for the minimum pressure point. On the other hand, for a blade with regions of partial cavitation, only the areas not covered by the cavity are searched. The constraint is defined as follows:

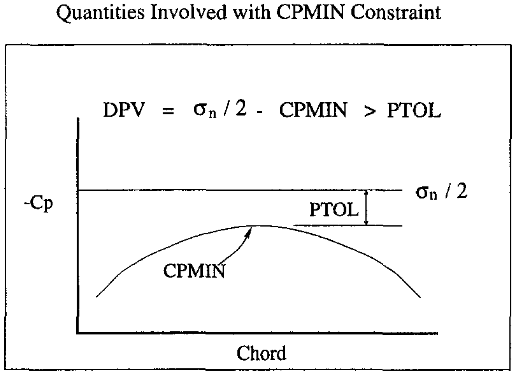

Fig. 2 Minimum pressure constraint

Table 1 Span-wise distribution of t_o/D

r/R	0.20	0.30	0.40	0.50	0.60
t_o/D	0.0450	0.0370	0.0297	0.0232	0.0176
r/R	0.70	0.80	0.90	0.95	1.00
t_o/D	.0128	.0087	.0054	.0041	.0030

$$\text{PTOL} < \text{DPV} \tag{7}$$

where DPV = $\sigma_n/2$ − CPMIN and CPMIN is the maximum value of $-C_p$ over the considered portion of the blade. The constraint is illustrated in Fig. 2.

The current model only handles the dynamics of sheet cavitation. However, bubble cavitation (which often occurs when the pressure drops below vapor pressure at mid-blade (Briancon-Marjollet et al., 1990) can be avoided by simply applying the minimum pressure constraint.

Results

This section presents results for several CAVOPT-3D runs. First, results are given for design in uniform inflow, and then results for design in non-axisymmetric inflow are shown. Each CAVOPT-3D run took approximately seven hours of CPU time on an Alpha 600(5/266). For all runs, the thickness distribution of the blade is given by structural constraints. A NACA 66 thickness distribution is used in the chord-wise direction and the span-wise distribution of maximum thickness to diameter ratio is given in Table 1. This thickness distribution is the same as the one used in Mishima (1996). The values are held constant throughout the optimization process.

Design in Uniform Inflow. This section compares the results for propeller designs in uniform inflow. Several runs were performed for the same set of design conditions, with different tolerances for the minimum pressure constraint. The design conditions for these runs are as follows:

$$J_s = 1.0, \quad \sigma_n = 2.5, \quad F_n = 5.0, \quad Z = 3, \quad r_H = 0.2,$$
$$\text{and} \quad K_T = 0.15.$$

The only constraint imposed on these three runs is the constraint on minimum pressure. For each run, this constraint is applied differently. Run UN1 is an unconstrained case with a constant given chord distribution. It is the same as the fully wetted propeller design presented in Mishima (1996). Mishima and Kinnas (1997) showed that the results of this CAVOPT-3D design agree well with those obtained from the PBD-10 design method (Greeley and Kerwin, 1982). Runs UN2 and UN3 have PTOL values of 0.020 and 0.200 respectively. The constraint and resulting values of K_T, K_Q, and η are given in Table 2. At this point it should be noted that the method of

Table 2 *PTOL* values and resulting K_T, K_Q, and η for three CAVOPT-3D runs in uniform inflow

CAVOPT-3D Propellers in Uniform Inflow				
Run	*PTOL*	K_T	K_Q	η
UN1	Not Imposed	0.1499	0.0298	0.7993
UN2	0.020	0.1500	0.0299	0.7989
UN3	0.200	0.1500	0.0300	0.7947

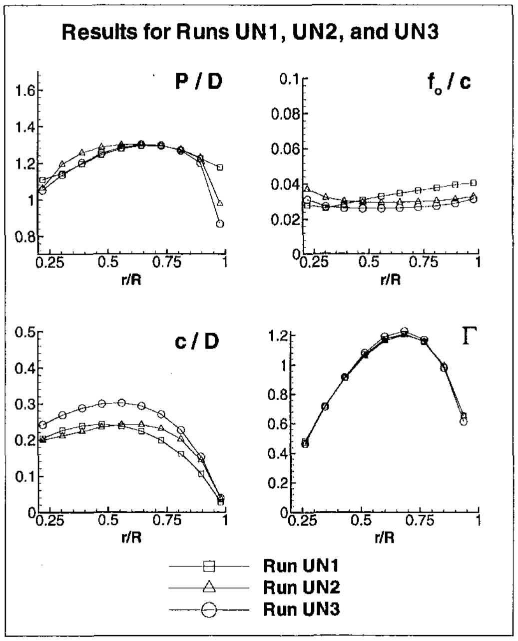

Fig. 3 $P/D, f_o/c, c/D$, and circulation distribution for the three CAVOPT-3D runs in uniform inflow

Greeley and Kerwin (1982) indirectly applies a similar criterion on the pressure distribution on each section of the blade by employing the "cavitation bucket diagrams" (Brockett, 1966). The main difference between the present method with previous methods consists of the fact that the present method applies a minimum pressure constraint based on the 3-D unsteady pressure distribution as opposed to the pressure distributions inferred from 2-D charts in a stripwise fashion.

The resulting performance characteristics for these three runs are all very similar. The efficiency of Run UN1 and UN2 are practically identical, and that of Run UN3 only differs by half of a percent. The near identical performance of the three propellers indicates they should also have a very similar circulation distribution, as shown in Fig. 3. Also shown in this figure are the pitch, camber, and chord distributions for the three designs. The pitch distribution for the three cases is similar up to r/R of 0.85. Beyond this point towards the tip, the three cases have differing values of P/D. This difference may come from the fact that the outer span-wise strip is not considered in the minimum pressure constraint. The camber shows a decreasing trend in the outer half of the blade as the constraint becomes stricter. The general trend of c/D in the outer half of the blade is an increasing c/D as stricter limits on minimum pressures are imposed. This is also reflected by the slight decrease in the efficiency due to the increase of frictional losses. A frictional coefficient $C_f = 0.004$ has been applied (only on the wetted surface of the blade) in all of the runs presented in this paper.

For Runs UN2 and UN3 the minimum pressure constraint is applied. It is expected that the pressure distributions for these designs will fall below the margin that defines the occurrence of cavitation (see Fig. 2). As discussed previously, cavitation will occur when the value of $-C_p$ rises above $\sigma_n/2$. Figure 4 shows the chord-wise distribution of the pressure coefficient for several different span-wise strips. For clarity, only the four strips closest to the tip are shown. The rest of the strips exhibit pressure distributions which are lower than those at the outer strips. These are the strips located at r/R values of 0.94, 0.85, 0.77, and 0.68.

Cavitation is expected when the value of $-C_p$ rises above the horizontal line representing $\sigma_n/2$. The value of PTOL in the minimum pressure constraint is the tolerance within which $-C_p$ can approach the horizontal line from below. Notice that the outermost strip is always in violation of the constraint. In this study, the outermost strip is excluded from consideration in determining the point of minimum pressure. The outermost strip is excluded in the constraint to avoid an over-restrictive constraint in the vicinity of the tip, where tip vortex cavitation often occurs.

With no constraint imposed, Run UN1 has several strips with pressures that indicate mid-chord cavitation. No cavitation is detected in this case because the pressure at the leading edge is below vapor pressure, and HPUF-3AL only detects leading edge cavitation. It is clear from the pressure distribution for this propeller (Fig. 4) that the blade should be cavitating.

Runs UN2 and UN3 both have pressure coefficient distributions that lie completely below the $\sigma_n/2$ horizontal line for the considered span-wise strips. In fact, they both come within their respective values of PTOL to the cavitation line. This provides a verification of the accurate implementation of the imposed minimum pressure constraint.

Runs UN2 and UN3 show the effectiveness of the constraint on minimum pressure. The pressure distributions for these two runs show that the blades are free of mid-chord cavitation for r/R values less than 0.94.

Design in Non-Axisymmetric Inflow. The following study compares the results from several CAVOPT-3D runs. The runs were all performed for the same set of design conditions. The design conditions chosen are the same as those used in Mishima (1996). These conditions are as follows:

$$J_s = 1.2,\quad \sigma_n = 2.5,\quad F_n = 5.0,\quad Z = 3,\quad r_H = 0.2,$$
$$\text{and}\quad K_T = 0.2.$$

The non-axisymmetric inflow wake used with CAVOPT-3D has only an axial component of velocity. This is the same inflow wake used in Mishima (1996). The axial velocity distribution for this inflow is shown in Fig. 5. It should be noted that the circumferentially averaged inflow of that shown in Fig. 5 happens to be uniform in this case. However, the conclusions to be drawn in the rest of this paper are also applicable in the case the averaged inflow varies in the radial direction.

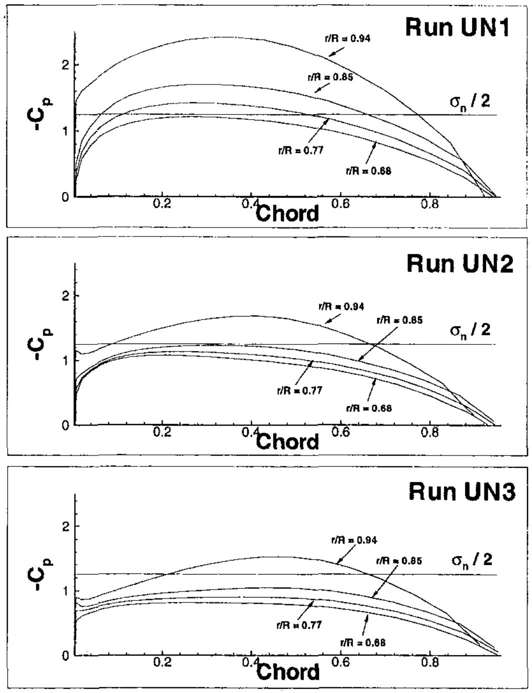

Fig. 4 Pressures for the three CAVOPT-3D runs with uniform inflow (suction side only)

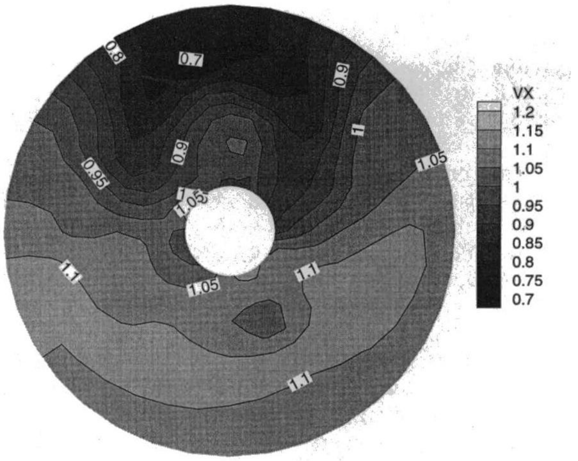

Fig. 5 Non-axisymmetric inflow velocity field used in CAVOPT-3D runs

Design in Uniform Inflow Versus Design in Non-Axisymmetric Inflow. This section compares results for two CAVOPT-3D runs. One is a design in uniform inflow that is subsequently analyzed by HPUF-3AL in a non-axisymmetric flow field. The geometry and performance of this propeller are compared with the geometry and performance of a propeller designed by CAVOPT-3D in nonaxisymmetric flow. The purpose of this comparison is to show differences between CAVOPT-3D design in non-axisymmetric inflow and a design method that only considers the propeller in uniform inflow. These comparisons are shown in Figs. 6 and 7.

The left side of Fig. 7 represents the nonaxisymmetric inflow performance of a propeller designed only for uniform inflow. The right portion of the figure shows the performance of a propeller optimized for non-axisymmetric inflow. The two propeller designs have nearly identical values of efficiency. The propellers also have comparable geometries. More specifically, the P/D, f_o/c, and c/D distributions shown in Fig. 6 have similar trends, but they also have subtle differences. These geometric variations lead to differences in cavity volume and cavity volume velocity. CAVOPT-3D in non-axisymmetric inflow was able to reduce the cavity volume and cavity volume velocity by significant amounts.

Note that the value of K_T of the design in uniform inflow (when analyzed in non-axisymmetric inflow) is smaller than the required value, due to the presence of of supercavitation, as opposed to the design in non-axisymmetric inflow which satisfies the thrust requirement automatically. In the case of the design in uniform inflow the initial requirements must be adjusted to guarantee the required thrust in non-axisymmetric inflow.

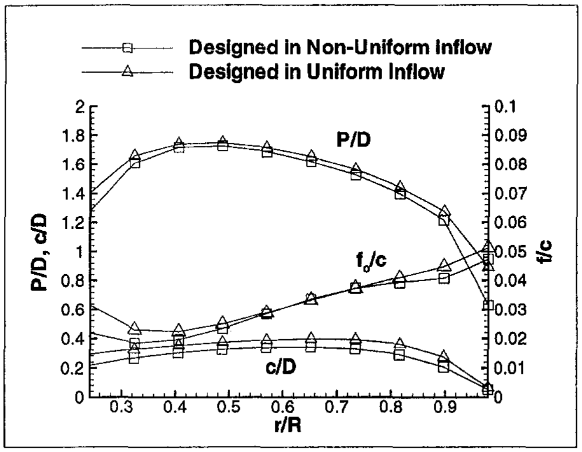

Fig. 6 Blade geometry comparison for propellers designed in uniform and non-axisymmetric inflow

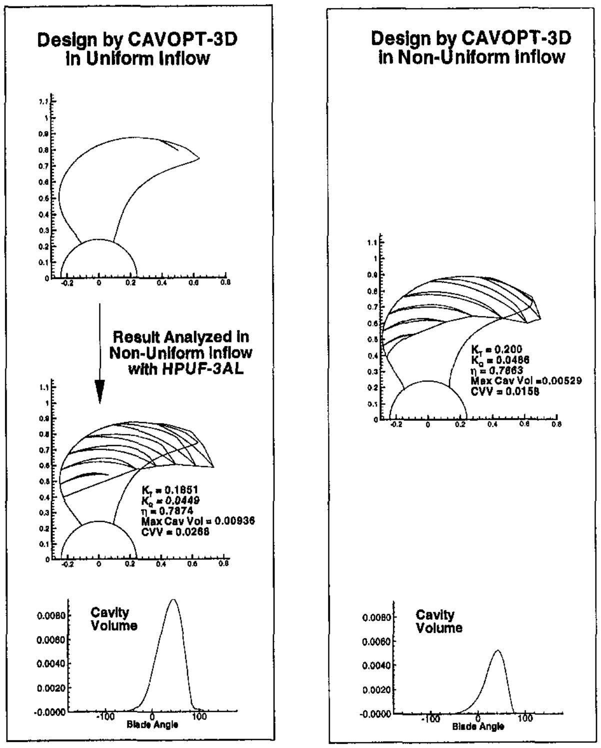

Fig. 7 Cavity characteristic comparison for propellers designed in uniform and non-axisymmetric inflow

Design With Cavity and Skew Constraints. The purpose of this study is to demonstrate how the different design constraints in CAVOPT-3D can be used to design propellers with favorable characteristics. The constraints CAMAX, SKMAX, VVMAX, and FAMAX are used in this study. The back cavity area and volume velocity constraints are both used to limit the effects of cavity volume velocity induced hull pressures. Restrictions on the cavity area limit VV indirectly by decreasing the cavity volume. The skew constraint and the option for fixed skew allow for a favorable skew distribution to be reached. Quadratic skew distributions are favorable because they decrease the effects of unsteady forces while allowing for more of a balance between backward and forward skew which leads to blades with better structural behavior (Parsons and Greenblatt, 1978). The face cavitation constraint is used to limit or completely avoid face cavitation.

Table 3 lists the constraints imposed as well as the resulting propeller characteristics for the CAVOPT-3D runs considered in this section.

Run 0 is identical to a run performed in Mishima (1996). This is an unconstrained run, which means there are no constraints on the area of cavitation or the cavity volume velocity harmonics. This run also has no skew optimization with a value of zero assigned to the skew. Run 0 can be considered a good starting point for this study. CAVOPT-3D is used in an attempt to get propeller designs that perform better than Run 0. This improved performance is achieved in the characteristics of cavity area, cavity volume velocity harmonics, and skew distribution.

Runs 1–5 are similar in that they all use a quadratic skew distribution. Runs 2, 4, and 5 have optimized quadratic skew with a radius of forward skew RFOR = 0.4. This means that the location of forward skew is fixed during the optimization,

Table 3 Results from a series of CAVOPT-3D runs (MCV is maximum cavity volume, MCA is maximum cavity area, and Angle is the blade rotation angle (from the vertical) at maximum cavity volume)

CAVOPT-3D Constraints

Run	CAMAX	Skew	VVMAX	FAMAX
0	—	—	—	—
1	—	Fixed	—	—
2	0.3	SKMAX = 45	—	—
3	0.3	Fixed	0.0106	—
4	0.3	SKMAX = 45	0.0106	—
5	0.3	SKMAX = 45	0.0090	—
6	—	Fixed	—	0

CAVOPT-3D Results

Run	K_T	K_Q	η	VV	MCV	MCA	Angle
0	0.2000	0.0492	0.7771	0.0160	0.00527	0.5600	24
1	0.2000	0.0486	0.7863	0.0158	0.00529	0.5745	42
2	0.1999	0.0486	0.7863	0.0132	0.00450	0.3002	42
3	0.2000	0.0488	0.7827	0.0105	0.00368	0.2987	36
4	0.1999	0.0486	0.7859	0.0109	0.00363	0.3000	42
5	0.2000	0.0487	0.7846	0.0094	0.00301	0.2999	42
6	0.1999	0.0486	0.7861	0.0179	0.00604	0.5450	42

but the skew pattern is allowed to be optimized. Runs 1 and 3 use the fixed skew option[2] with a quadratic skew distribution. This skew distribution, shown in Table 4, is taken from the final propeller design of Run 4. Runs 2 and 5 resulted in skew distributions similar to that of Run 4, with maximum skews of 37.5 and 37.65 deg, respectively. Runs 1–5 are arranged in order of decreasing maximum cavity volume (MCV).

Figure 8 shows CAVOPT-3D results for Runs 2, 4, and 5. The propeller geometry is given as well as the circulation distribution, cavity volume, and cavity plan-forms. The information is given for the final geometry from the optimization process for each run.

Runs 2, 4, and 5 are all being constrained by CAMAX = 0.3. This results in all of them having a cavity area of 30 percent of the blade area. Run 2 has no restriction on the cavity volume velocity harmonics, while Run 4 has VVMAX = 0.0106 and Run 5 has VVMAX = 0.0090. The result of the volume velocity restriction in the case of Run 4 is a decreased cavity volume and thus, a decreased value for the cavity volume velocity harmonics compared with Run 2. With an even tighter restriction on the volume velocity harmonics, Run 5 results in an even smaller cavity volume and volume velocity.

The center plot of Fig. 8 shows cavity volume with blade rotation angle. It is clear that Run 2 has the largest cavity volume, while Run 5 has the smallest cavity volume of the three. Also note that the maximum volume for each case occurs at the same blade rotation angle of 42 deg. The decreasing cavity volume from Run 2 to 5 is also visible in the cavity plan-forms. Recalling that all of the cases have the same cavity area, the decrease in cavity volume is evident in the decrease in cavity thickness at the tip of the blades. As expected, the circulation distributions (in steady non-cavitating flow) for Runs 2, 4, and 5 are nearly identical.

Table 4 Span-wise distribution of skew (in degrees) used in the fixed skew cases (also the final skew distribution of Run 4)

r/R	0.22	0.31	0.39	0.47	0.56
$\theta(r)$	−0.96	−3.90	−5.11	−4.53	−2.16
r/R	0.64	0.73	0.81	0.89	0.98
$\theta(r)$	2.00	7.95	15.72	25.51	37.56

The fixed skew option can be helpful in cases where CAVOPT-3D does not converge to an optimum geometry. Runs 1 and 3 both use the fixed skew option. These two runs were first attempted without the fixed skew option. Run 4 is the successful Run 3 attempt with optimized skew. Run 1, however, was not successful when attempted with optimized skew. Figure 9 shows the convergence history with number of analysis runs, cavity plan-forms, and blade geometry results for Runs 1 and 3.

Face Cavitation

Face cavitation is always a concern in cavitating propeller design. Large amounts of face cavitation can limit the performance of a propeller. All designs in this paper were analyzed with HPUF-3AL. The three designs in uniform inflow showed no face cavitation. Negligible amounts of face cavitation were

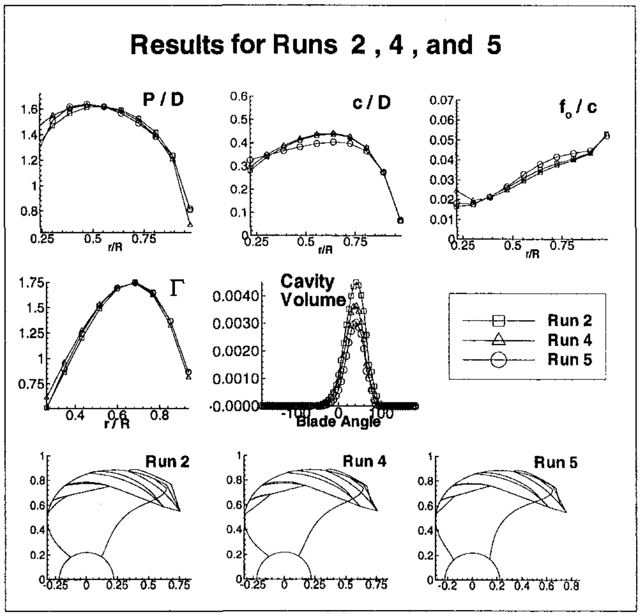

Fig. 8 Propeller geometry, circulation distribution (in steady noncavitating flow), cavity volumes, and cavity plan-forms with maximum cavity volume for Runs 2, 4, and 5

---

[2] Constant skew throughout the optimization process.

detected for the propellers designed by Runs 0–5 in the design in non-axisymmetric inflow section. The area of face cavitation was less than one percent of the blade area for these runs. This cavitation was so small that it did not have any effect on the propeller performance. CAVOPT-3D can be used to eliminate face cavitation by setting the constraint FAMAX equal to zero. Run 6 uses the same conditions and constraints as Run 1 with the addition of a zero face cavitation constraint. The resulting propeller from Run 6 has K_T, K_Q, and η values that are practically identical to those from Run 1. The two propellers also have practically identical geometries, as shown in Fig. 10. Run 6 resulted in slightly higher values of maximum cavity volume and cavity volume velocity. Maximum cavity volume and cavity volume velocity can be reduced by combining the face cavity area constraint with the cavity volume velocity constraint.

Conclusions and Future Work

The results of this study indicate that the present method is a useful tool for the design of cavitating propellers. It is shown that the method has an advantage over design methods which only consider the circumferentially averaged inflow. By designing propellers in non-axisymmetric inflows, the method produces propellers with more favorable cavitation characteristics, such as smaller cavity volume and volume velocity. By imposing constraints on cavity area and cavity volume velocity harmonics, the user can systematically improve the performance of designed propellers. This improved performance is in the cavity characteristics such as cavity volume velocity and cavity extent. For example, the cavity volume velocity constraint can be used to improve on a propeller design by producing a propeller with a similar efficiency, but lower cavity volume velocity, i.e., smaller pressure fluctuations on the ship hull. It is also demonstrated that the designer can use the quadratic skew and user specified skew option to design propellers with more favorable characteristics. The constraint on minimum pressure is verified and it is established as an effective tool in preventing the onset of mid-chord or bubble cavitation.

Future work should focus on improvements on the initial geometry in the optimization process. This would include the option for the user to specify all aspects of the initial geometry. This feature is expected to drastically reduce the number of required iterations, and therefore CPU time.

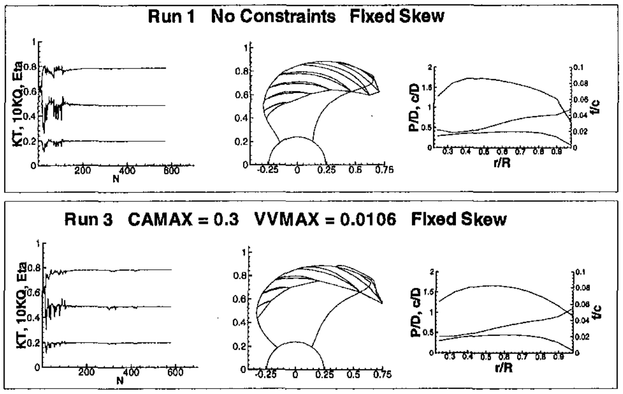

Fig. 9 CAVOPT-3D results for the fixed skew runs

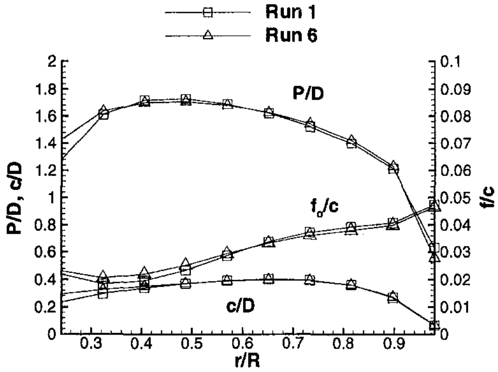

Fig. 10 Blade geometry comparison for propeller designs produced by Run 1 and Run 6

Acknowledgment

Support for this research was provided by Phase II of the "Consortium on Cavitation Performance of High Speed Propulsors" with the following members: David Taylor Model Basin, Daewoo Shipbuilding and Heavy Machinery, El Pardo Model Basin, Hamburg Ship Model Basin, Hyundai Maritime Research Institute, KaMeWa AB, Michigan Wheel, Rolla SP Propellers SA, Sulzer-Hydro GMBH, Ulstein Propellers, Volvo-Penta of the Americas, and Wärtsilä Propulsion.

References

Briancon-Marjollet, L., Franc, J., and Michel, J., 1990, "Transient Bubbles Interacting with an Attached Cavity and the Boundary Layer," *Journal of Fluid Mechanics*, Vol. 218, pp. 355–376.

Brockett, T., 1966, "Minimum Pressure Envelopes for Modified NACA-66 Sections with NACA a = 0.8 Camber and Buships Type I and Type II Sections," DTNSRDC, Teddington, England.

Choi, J.-K., and Kinnas, S., 1997, "Cavitating Propeller Analysis inside of a Tunnel," *Proc. Cavitation and Multiphase Flow Forum*, Vancouver, Canada. Fluids Engineering Division, ASME.

Coney, W. B., 1989, "A Method for the Design of a Class of Optimum Marine Propulsors," Ph.D. thesis, MIT, Department of Ocean Engineering.

Greeley, D., and Kerwin, J., 1982, "Numerical Methods for Propeller Design and Analysis in Steady Flow," *Trans. SNAME*, Vol. 90.

Kerwin, J., 1973, "Computer Techniques for Propeller Blade Design," *International Shipbuilding Progress*, Vol. 20, No. 227.

Kerwin, J., Keenan, D., Black, S., and Diggs, J., 1994, "A Coupled Viscous/Potential Flow Design Method for Wake Adapted Multi-Stage, Ducted Propulsors Using Generalized Geometry," *Trans. SNAME*, Vol. 102.

Kerwin, J., Kinnas, S., Wilson, M., and McHugh, J., 1986, "Experimental and Analytical Techniques for the Study of Unsteady Propeller Sheet Cavitation," *Proc. Sixteenth Symposium on Naval Hydrodynamics*, Berkeley, CA.

Kinnas, S., and Pyo, S., 1997, "Propeller Wake Alignment Models in Uniform and Inclined Inflow," *Proc. Propellers/Shafting '97 Symposium*, Virginia Beach, VA., Soc. Naval Arch. & Marine Engnrs.

Lee, C., 1979, "Prediction of Steady and Unsteady Performance of Marine Propellers with or without Cavitation by Numerical Lifting Surface Theory," Ph.D. thesis, M.I.T., Department of Ocean Engineering.

Mishima, S., 1996, "Design of Cavitating Propeller Blades in Non-Uniform Flow by Numerical Optimization," Ph.D. thesis, Department of Ocean Engineering, MIT.

Mishima, S., and Kinnas, S., 1997, "Application of a Numerical Optimization Technique to the Design of Cavitating Propellers in Non-Uniform Flow," *Journal of Ship Research*, Vol. 41, pp. 93–107.

Parsons, M. G., and Greenblatt, J. E., 1978, "Optimization of Propeller Skew Distribution to Minimize the Vibratory Forces and Moments Acting on the Propeller Hub," The University of Michigan, Department of Naval Architecture and Marine Engineering.

Sparenberg, J., 1995, *Hydrodynamic Propulsion and Its Optimization-Analytic Theory*, Kluwer Academic Publishers, Dordrecht, The Netherlands.

F. Nasuti
Ph.D. Research Assistant.

R. Niccoli
Graduate Student.

M. Onofri
Professor of Aerospace Propulsion.

Dipartimento di Meccanica e Aeronautica,
Università di Roma "La Sapienza,"
Via Eudossiana 18, Roma 00184, Italy

A Numerical Methodology to Predict Exhaust Plumes of Propulsion Nozzles

A simple methodology to simulate the mixing layers that occur between nozzle exhaust jet and the external air is proposed. The method is based on a simplified model of the plume, that replaces the mixing layer with a contact discontinuity surface, thus avoiding the cumbersome calculation of the turbulent mixing of two flows with different chemical composition. The contact discontinuity is numerically treated by an advanced fitting technique, capable of tracking the discontinuity by points floating over the computational grid. The numerical method is discussed and its capability is demonstrated with validation tests, as well as with a discussion of some practical applications for underexpanded nozzle flows.

Introduction

The design of engines for future launchers and satellites relies on the analysis of any factor affecting their performances. One of these factors is the development of advanced technologies for nozzles, that also requires the capability to perform numerical analyses of the relevant flowfields. In particular, the prediction of nozzle exhaust plumes has been the goal of a large number of studies during the last thirty years, because of its practical implications (Sutton, 1992).

The parameters of interest in the plume behavior, as well as the approach of the study, depend on the class of engine considered, and on its working environment. For instance, nozzle exhaust plumes of engines working in rarefied atmosphere have been widely analyzed in recent studies, mainly because of the implications on spatial rendezvous and to evaluate the effects of possible impingements of the plume on the satellite surface. In these cases numerical methods typical for rarefied gas solutions have been exploited (Rochelle et al., 1995, Lumpkin et al., 1995).

In the present study, engines working in a continuous medium are considered. Many studies have been performed to simulate the exhaust plumes of these nozzles. They span from the pioneer one-dimensional methods (Latvala and Anderson, 1958), to the more recent three-dimensional advanced solutions, based on multi-zonal approach and adaptive grids (Wang, 1993, Williams et al., 1993, Cumber et al., 1995). Nevertheless, despite the progress achieved in the computer power, the design methods are often burdened by the time-consuming numerical solutions, performed to have a knowledge of the flow behavior. Therefore, studies are still necessary to introduce more effective approaches, able to circumvent the tremendous request of computational time that the common methodologies require.

In particular, strong gradients take place at the interface between plume and external free-stream, due to the large differences of entropy and velocity of the two flows. They lead to the formation of vortical structures with different flow scales, and eventually to the occurrence of a turbulent mixing layer. Moreover, the two streams feature different thermodynamic characteristics and flow properties that make nonequilibrium models necessary to describe adequately the mixing process. Therefore, the numerical solution of the region of the jet interfaces requires a clustering of computational points, able to appreciate the smallest scales of the local vortices, and the use of adaptive grids, changing in time to follow the time evolution of the mixing region.

In cases where the study of the plume behavior is devoted to the prediction of their noise or pollution, the analysis is focused on the behavior of the mixing layer more than on the main flow. Numerical methods that solve accurately this layer are necessary, and no simplification in the description of the region can be acceptably introduced.

On the contrary, if the interest is on other aspects, like the interaction with other components of the vehicle or the prediction of the performances of advanced engines, the analysis is focused on the main exhaust jet more than on the thickness and stability of its boundary. In these cases, the detailed solution of the mixing layer is not mandatory and simplifications in the treatment of the region can be introduced. For instance, in many practical applications the use of pioneer methods based on one-dimensional approaches is often still indicated as one of the most convenient solutions (Bigert, 1993, Nash et al., 1994).

The aim of this paper is to present a simple methodology to simulate nozzle exhaust plumes of engines working in a continuous medium, and to compute efficiently the corresponding steady-state solution of the flowfield. The methodology is based on the replacement of the mixing layer of the plume boundary by a contact discontinuity, and on the solution of the flowfield by a technique capable to fit and track such flow discontinuity. Of course, such a simulation of the plume boundary will not allow the growth of the mixing layer, which will always maintain its zero-thickness, and will be described by its average values. In the following, the simplified model of the plume and the numerical methodology are illustrated, and then the validation tests performed to demonstrate its capability are reported.

The Simplified Model of the Plume Boundary

A typical configuration of exhaust plume and external flow for an underexpanded nozzle is shown in Fig. 1(*a*). It is worth noticing that in the region of mixing layer a dramatic change of entropy and velocity occurs, and the numerical solution requires the use of grid meshes of the order of magnitude of the smallest vortices that take place there. Coarser grids would provide inaccurate results that could affect the quality of the solution also in the surrounding regions. Moreover, since the location of the region of the mixing layer is not known a priori, cumbersome procedures should be used, based on adaptive grids changing during the integration.

Contributed by the Fluids Engineering Division for publication in the JOURNAL OF FLUIDS ENGINEERING. Manuscript received by the Fluids Engineering Division January 19, 1997; revised manuscript received March 13, 1998. Associate Technical Editor: M. N. Dhaubhadel.

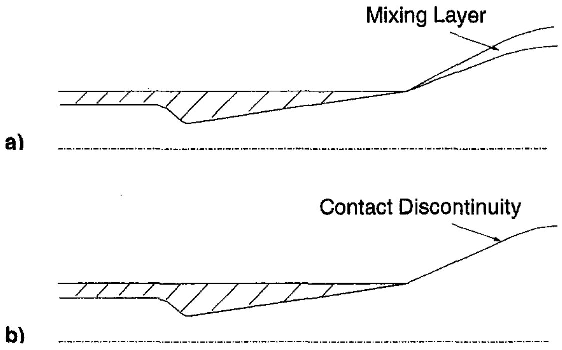

Fig. 1 Sketch of physical problem (*a*) and simplified model (*b*)

For this reason, solutions based on a simplified flow model that does not consider the viscous effects in the mixing layer are often used for the analysis. Most of the inviscid simulations reported in the literature are based on the integration of the Euler equations written in conservative form, which, due to the large gradients of the thermodynamic variables, may lead to well-known numerical problems (Nasuti, 1996, Broglia et al., 1997), that are summarized here in three main items: (*i*) The numerical viscosity may open the wake with unphysical behaviors if the local grid mesh is too large; (*ii*) The spurious production of entropy can change the behavior of the predicted plume shape; (*iii*) Possible instabilities of the calculation can be avoided by introducing locally a suitable amount of artificial viscosity, that can lead to a lowering of the order of accuracy of the solution, and eventually to the enhancement of the problems indicated in the first two items.

The tendency to obtain unphysical predictions of the field around the mixing layer region is enhanced by the fact that the order of magnitude of a typical mesh for Euler calculations is the same as the mixing layer thickness for practical nozzle applications.

Therefore, to avoid the above-mentioned effects, a clustering of computational points in the region is necessary. Due to the consequent burden of computational time, different approaches are still used like the method of characteristics for the inviscid case (Fox, 1983) or simplifications of the equations in that region for the viscous case (Vatsa et al., 1982).

An alternative method was suggested by Zannetti and Onofri (1983 and 1984). It replaces the mixing layer by a contact discontinuity that split the two fields with different values of entropy (Fig. 1(*b*)), following a similar idea proposed by Salas (1974) with a space-marching approach. This simplified plume boundary changes its slope in order to find a matching between the local conditions of the two flows. In particular, the pressure and the normal component of velocity are continuous across the discontinuity, while the tangential component is discontinuous, allowing the formation of a slip flow along a separation surface between external and internal flows.

Following this approach, the main features of the phenomenon, i.e., the pressure continuity and the entropy and velocity discontinuity across the mixing layer, can be easily represented without any need to compute the turbulent mixing process of flows with different compositions, and thus avoiding the burden due to the clustering of grid points in that region.

A validation of the method for two-dimensional problems was performed by Oggiano et al. (1984) and Zannetti et al. (1986). Those results showed an excellent agreement with the experimental data measured in the base flow region.

From a numerical point of view, the difficulty to fit and track a contact discontinuity located within the computational field, led at that time to a formulation based on the splitting of the flowfield in two sub-regions divided by the contact discontinuity: the external flow and the plume region. Since the shape of the discontinuity changes during the transient evolution of the solution, the grids of the two sub-regions must be redefined at each iteration step. This is accomplished in the easiest way by using nonorthogonal grids, where the radial sizes of the meshes are computed by normalization with the distance between the external boundary of the flowfield and the discontinuity line. As a consequence, possible drawbacks of such technique were represented by the need of continually redefining the computational grid, and by the use of nonorthogonal grids, that can be less accurate and usually more cumbersome than the orthogonal ones, particularly near the wall.

In the present paper, this simplified model of the plume is reproposed for two-dimensional and axisymmetric flows, with a different numerical technique that allows circumventing the difficulties mentioned above. In fact, the evolutions of the fitting technique recently performed by Nasuti and Onofri (1995 and 1996) allow the fitting and tracking of discontinuities floating in the meshes of the computational field. Thus, in this case there is no reason to redefine the grid during the integration and every kind of grid can be used.

A tentative profile of the contact discontinuity line is provided at the beginning of the integration. Since, in general, it is not congruent with the initial flowfield and with its boundary conditions, a transient flow takes place, during which the discontinuity changes its shape, and thus the fitted points move floating in the meshes of the computational grid. At the end of this time marching evolution a final configuration is asymptotically achieved.

Details on the main features of this version of the fitting technique are reported in Nasuti and Onofri (1996), while the fitting and tracking of the jet boundary as a discontinuity line are described in the following section.

The Numerical Method

The numerical method of solution is based on a fitting technique of the contact discontinuity simulating the plume boundary. This procedure is independent of the scheme implemented for the solution of the other regions of the flowfield and therefore can be coupled with any scheme, like the common methods of solution of the Euler or Navier-Stokes equations written in conservative form. In the present work, the fitting technique has been implemented as coupled with a nonconservative formulation of the governing equations. It represents the most natural coupling because of its structure based on the propagation of signals along the time-dependent characteristic surfaces of the Euler equations, as will be clearer in the following.

The Euler equations are thus solved according to the time dependent λ scheme (Moretti, 1987). In this case, the nonconservative form of the equations is expressed in terms of the unknowns speed of sound (a), velocity ($\mathbf{v}$), and entropy (s). The discretization of derivatives is performed by upwind differences, to emphasize the effect of the propagation of signals, simulated by signals running along four bicharacteristic lines and the streamline direction. The time integration follows a two-level explicit scheme, having second-order accuracy, also described in detail in Moretti (1987). The coupling between λ scheme and fitting procedure yields a good solution of both continuous and discontinuous regions of the flowfield, provided that all the flow discontinuities are explicitly computed. The fitting of the shocks is performed following Nasuti and Onofri (1996), whereas the fitting of the jet boundary is described in the following.

The boundary of the plume is modeled as a contact discontinuity (CD). The fitting of the CD is performed in a way similar to the floating shock-fitting, but with the proper differences. In particular, the CD-points are defined as the intersections between the actual position of the discontinuity and the computational grid (Fig. 2); all of the information about these points is stored at random in specific arrays.

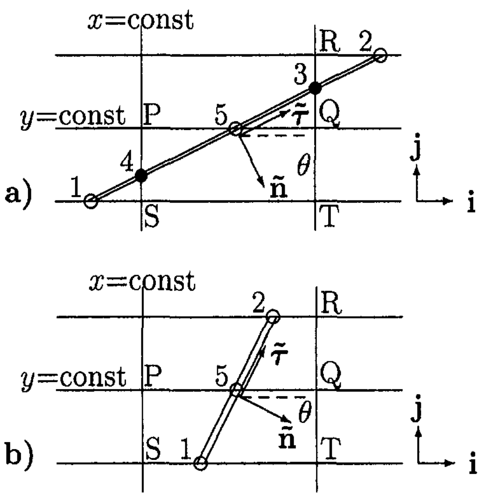

Fig. 2 Contact discontinuity points: ○ = x − CD, ● = y − CD. (*a*) CD crossing both families of grid lines; (*b*) grid-aligned CD.

Each mesh node is marked to identify easily if a CD-point is located in its neighborhood. This control is needed to avoid differentiation across the CD in the solution of the continuous region of the flowfield. Then, after the flow variables in the continuous region have been computed, the CD is updated as follows:

1. For each CD-point the local slope of the CD is computed by connecting the CD-point with its upstream neighbour CD-point. For example, if the flow in Fig. 2 comes from the left, the local slope in the CD-point 5 is obtained as the slope of the line 4–5 for the configuration shown in Fig. 2(*a*), and of the line 1–5 for cases similar to Fig. 2(*b*).
2. The jump relations are enforced between the two sides of each CD-point. In particular, for each side it is possible to find suitable variables, whose values can be assumed as known. These variables are related to the signals propagating along and toward the discontinuity and are: the velocity components parallel to the CD, the entropy values on both sides of the CD, and one Riemann variable for each side of the CD. To write the jump relations, the following symbols are introduced: $\tilde{u}$ and $\tilde{v}$ for the components of the velocity vector $\mathbf{v}$ along the directions $\mathbf{n}$ and $\boldsymbol{\tau}$ of Fig. 2; a for the speed of sound; s for the entropy; p for the pressure; W for the local velocity of the CD in the direction $\mathbf{n}$; R_1^x for the Riemann variable propagating with velocity $\tilde{u} + a$; R_2^x for the Riemann variable propagating with velocity $\tilde{u} - a$; γ for the gas ratio of specific heats; the subscripts $(\ )_A$ and $(\ )_B$ denote the two sides of the CD. The jump relations are then written as a system of five equations in the unknowns a_A, a_B, $\tilde{u}_A$, $\tilde{u}_B$, and W:

   $$p_A(a_A, s_A) = p_B(a_B, s_B) \tag{1}$$

   (pressure continuity across the CD)

   $$\tilde{u}_A = W \tag{2}$$

   $$\tilde{u}_B = W \tag{3}$$

   (no mass flow across the CD)

   $$\frac{2}{\gamma - 1} a_A + \tilde{u}_A = (R_1^x)_A \tag{4}$$

   $$\frac{2}{\gamma - 1} a_B + \tilde{u}_B = (R_2^x)_B \tag{5}$$

   (Riemann variable definition)

   The solution of these equations is then used to update the values of the flow variables in the mesh nodes bracketing the CD-point, like nodes P and Q for the CD-point 5 in Fig. 2(*b*). A more complex procedure is used to update nodes close to both an x-CD and a y-CD, like the node Q in Fig. 2(*a*): the values coming from the two CD-points (5 and 3 in the example) are weighted in a new one with a criterion based on the angle between the CD and the coordinate line. In order to give more relevance to points lying on the coordinate closer to the direction $\mathbf{n}$, this weight is defined as

   $$\mathscr{W} = |\mathbf{n}\cdot\mathbf{i}|, \quad \text{for an } x\text{-CD},$$

   $$\mathscr{W} = |\mathbf{n}\cdot\mathbf{j}|, \quad \text{for a } y\text{-CD}$$

   where $\mathbf{i}$ and $\mathbf{j}$ are the unit vectors of the x and y axis directions, respectively, defined in Fig. 2.
3. The CD-point is displaced according to its velocity W. In particular, following the definitions of Fig. 2, and indicating with Δt the time step, an x-CD moves a length Δx

   $$\Delta x = \frac{W \Delta t}{\cos \theta} \tag{6}$$

   The displacement of a y-CD is analogous. Care is needed when a CD-point in its movement passes over a mesh node. In this case, the value of the variables at that node is replaced by the values on the side of the CD that lies between the new position of the CD-point and the node. A different procedure is needed when two CD-points, an x-CD and a y-CD, pass over the same mesh node. For example 5 and 3 pass over Q in Fig. 2(*a*). The values in the mesh node Q traversed by the pair of CD-points are updated with the CD values, which are taken as the mean values of the two CD-points, weighted by the above defined $\mathscr{W}$. Nevertheless, since the displacement Δx is obtained from (6) dividing by $\cos \theta$, numerical inaccuracies may occur when the CD is almost parallel to one coordinate line. Because of such inaccuracies, it may happen that only one of the two shock-points passes over Q. In this case, the movement of the CD-point having greater $\mathscr{W}$ is assumed as correct, while the other CD-point is removed.
4. A new CD-point is introduced to connect two CD-points, whenever they have their intermediate point missing, because of the extension of the CD or for some numerical inaccuracy like the one mentioned in the above item. Such a situation is easily detected by considering that each CD-point (C) must have two neighboring points, except at the boundaries of the flowfield. If one of these is missing, a new CD-point is introduced by looking for a CD-point in a larger neighborhood and then fitting the intersection with each coordinate line of the straight line connecting C with the neighboring CD-point found.

In the above procedure to fit the CD that simulates the jet boundary the following assumptions have been made:

- The CD-points are assigned as initial condition of the plume boundary in the flowfield, located in arbitrary position.
- The CD line is fastened at the nozzle lip, where the solution is computed locally by solving the theoretical two-dimensional analogy of the Riemann problem between two parallel different streams.
- No detection is performed during the integration to fit new CD-points, except for the new connecting points added as described in item 4; that allows the extension of the discontinuity line from its initial length.

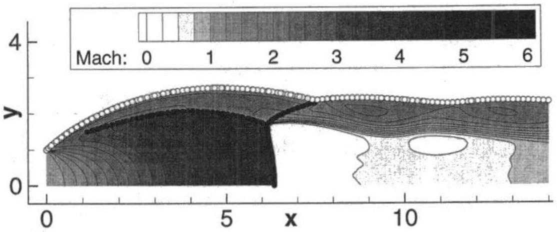

Fig. 3 Mach number contour lines, shock-points (●) and CD-points (○) for a sonic jet expanding in still air with the ratio $p_j/p_a = 12$

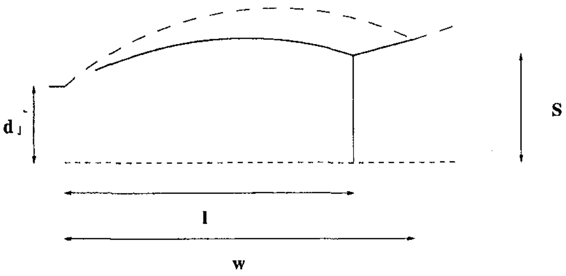

Fig. 5 Characteristic lengths for a jet exhausting from a sonic orifice

- The initial CD line can extend, as above stated, but cannot fork, neither break up in separated pieces.
- Limiters for the slope of the CD line are enforced, in order to avoid the formation of curls with small radius of curvature, too complicated to be handled by this approach. This artifice has been introduced to overcome possible instabilities occurring during the numerical transient. In practice, the position of a CD-point cannot be farther than a threshold value from the line connecting its neighboring CD-points.
- The CD-points moving in locations outside the computational field are removed.

Summarizing, each time iteration of the computation is carried out according to the following steps:

1) *Integration of the equations* all over the mesh nodes (here performed by the λ-scheme).

2) *Fitting and tracking of the shocks.*
   2(*a*) Detection of the formation of new shocks.
   2(*b*) Calculation of the local slope of the shocks, by connecting the neighboring points detected.
   2(*c*) Enforcement of the Rankine-Hugoniot relations between the two sides of each shock-point, to update the variables in the high-pressure side and the velocity of propagation of the shock-front.
   2(*d*) Displacement of the shock-points, according to the velocity of propagation of the shock-front.
   2(*e*) Introduction of connecting shock-points whenever, for some reason, two neighboring points have their intermediate point missing.
3) *Fitting and tracking of the CD.*
   3(*a*) Calculation of the local slope of the CD, by connecting the neighboring points detected.
   3(*b*) Enforcement of the jump relations between the two sides of each CD-point, to update the variables on both sides of the CD and the velocity of propagation of the CD front.
   3(*c*) Displacement of the CD-points, according to the velocity of propagation of the CD front.
   3(*d*) Introduction of connecting CD-points whenever, for the extension of the CD or for some numerical inaccuracy, two neighboring points have their intermediate point missing.

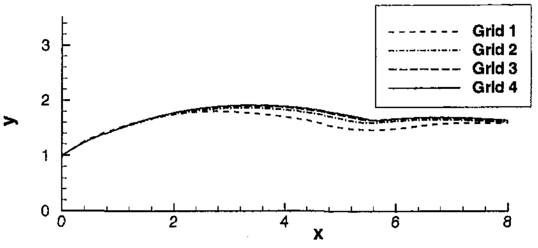

Fig. 4 Position of the jet boundary computed over different grids for a sonic jet expanding in still air with the ratio $p_j/p_a = 6$

It is worth stressing that here emphasis is given also to step 2), which is not mandatory, but it has been used for the present computations. In fact, the model of the jet boundary could be used also coupled with other approaches for the integration of the equations not based on shock-fitting but on widespread shock-capturing procedures. In this case, only steps 1) and 3) will be carried out and step 3) will avoid the clustering of grid points otherwise needed in the region of the jet boundary.

The computation starts with an initial tentative shape of the plume boundary, which is given by the solution of the two-dimensional analogy of the Riemann problem: depending on the pressure ratio between jet and ambient, and on the features of the external flow, different situations can occur, that will be described in the next section.

Results

The model has been validated by comparisons with semi-analytical and experimental data concerning axisymmetric free jets exhausting from sonic or supersonic nozzles into still air or supersonic air streams. Ambient pressure and external stream Mach number are indicated with p_a and M_a respectively, whereas p_j and M_j indicate pressure and Mach number at the exit of the nozzle. The exhaust gas is air, with $\gamma = 1.4$.

The first test case is a sonic nozzle with exhaust jet in still air ($M_a = 0$), considered for different pressure ratios p_j/p_a. The typical structure of the flowfield of an underexpanded nozzle exhaust jet, is shown by the Mach number isocontours for the expansion ratio $p_j/p_a = 12$ (Fig. 3), computed over a grid of 6000 cells in about 30 minutes on a IBM/Risc 6000 machine. In Fig. 3 the fitted discontinuity points are superimposed to the flowfield contour lines as 115 shock-points (●) and 148 CD-points (○). At the nozzle lip the flow expands up to the external pressure, by a centered expansion fan. Downstream, there is a further expansion due to both the axisymmetric effect of a diverging flow and to the reflection on the symmetry axis of the expansion waves coming from the nozzle lip. To match the

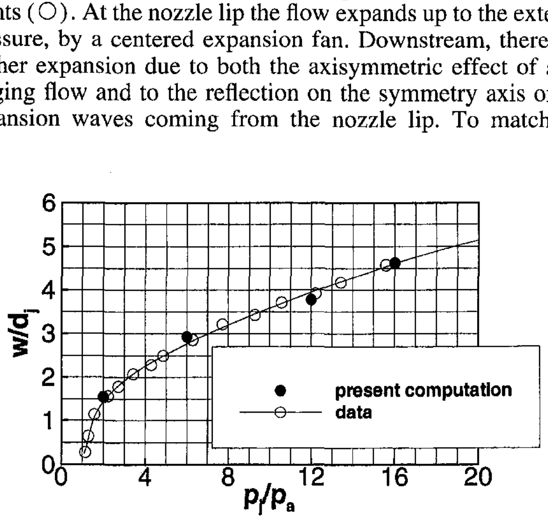

Fig. 6 Prediction of the nondimensionalized primary wavelength as function of the jet pressure ratio

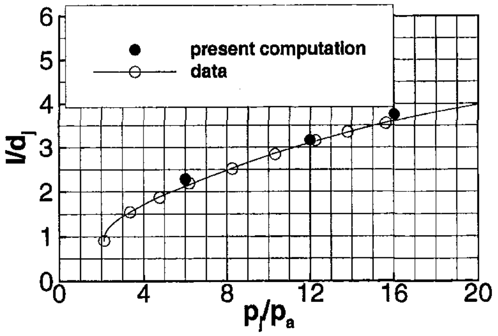

Fig. 7 Prediction of the nondimensionalized location of the Mach disk as function of the jet pressure ratio

constant ambient pressure, the boundary of the jet bends and forms a bow, generating the compression waves necessary to compensate the expansion effect. These compression waves eventually coalesce to form an oblique shock. Its Mach reflection on the axis generates a Mach disk and, finally, the reflected shock-branch impinges again on the boundary, which suddenly bends upwards yielding a centered expansion fan. The same process occurs in the subsequent "periods" of the boundary, having the well-known chain-like structure of a gaseous jet exhausting supersonically into still air.

The analysis of the accuracy of the technique has been performed by comparing the solutions computed over the following four grids:

Grid 1	Grid 2	Grid 3	Grid 4
30 × 12	60 × 24	90 × 36	120 × 48

The results show that a good prediction of the jet boundary is obtained with a small number of grid points. Figure 4 shows the behavior of the jet boundary.

In order to compare different jets and experimental data, some typical characteristic lengths are displayed in the sketch of Fig. 5. They are: (*i*) the primary wavelength *w*, that is the length of the first periodic segment of the free jet; (*ii*) the distance *d* from the plane of the jet exit, measured along the jet axis, to the Mach disk; and (*iii*) the diameter *S* of the Mach disk.

Based on the experimental study reported in Love et al. (1959), the numerical results obtained for the characteristic lengths of the jet of air exhausting from a sonic orifice into still air are compared with data. Four jets have been computed, having the following pressure ratios p_j/p_a: 2, 6, 12, 16. Figure 6 shows the behavior of the primary wavelength *w*, nondimensionalized with the nozzle exit diameter d_j. The agreement between data and the present results is good. Also the behavior of the distance *l* of the Mach disk from the nozzle exit, nondimensionalized with the nozzle exit diameter d_j, shows good agreement between numerics and experiments (Fig. 7). It is worth noticing the absence of the point relevant to the numerical simulation at $p_j/p_a = 2$. Indeed, since in this case the shock waves are quite weak, they are correctly computed as compression waves, spreading in a space interval rather than in a well-determined location. Finally, Fig. 8 displays the behavior of the diameter of the Mach disk *S*, nondimensionalized with the nozzle exit diameter d_j. It shows that *S* is a more difficult parameter to predict, especially for lower values of p_j/p_a characterized by corresponding smaller Mach disk diameter and lower shock intensity.

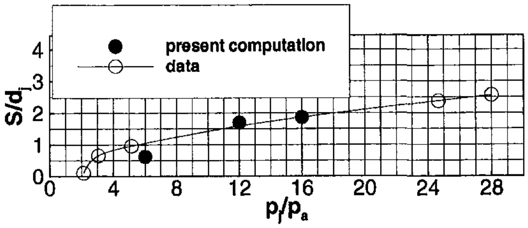

Fig. 8 Prediction of the nondimensionalized diameter of the Mach disk as function of the jet pressure ratio

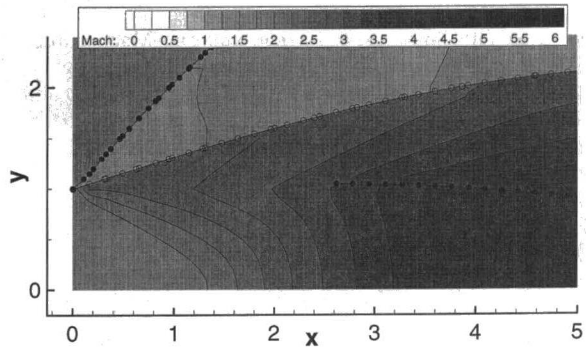

Fig. 9 Mach number contour lines, shock-points (●) and CD-points (○) for a $M_j = 1.8$ jet expanding in a supersonic stream ($M_a = 2$) with the ratio $p_j/p_a = 8$

As an example of a case with external supersonic stream instead of quiescent air, the following test has been computed. A different two-dimensional analogy of the Riemann problem occurs at the nozzle lip, with two discontinuities, a shock and a CD, and an expansion fan. The flow structure obtained for the case of an underexpanded jet ($p_j/p_a = 8$) exhausting at Mach $M_j = 1.8$ from a duct in a supersonic stream characterized by $M_a = 2$, is displayed in Fig. 9 by Mach number isocontours and flow discontinuities. From the enlargement of the picture of the nozzle lip region, the capability of the method to handle general cases of external supersonic stream with both underexpanded and overexpanded jets can be appreciated. In fact, the above case describes equivalently under- and over-expanded jets. In particular, before axisymmetric effects become important, the nozzle lip region shown in Fig. 9 also represents the overexpanded case ($p_j/p_a = 0.125$), with the exhaust jet in the upper region ($M_j = 2$) and the external flow in the lower region ($M_a = 1.8$).

Another series of tests concerns the implementation of the present method to solve jets exhausting from actual nozzles. These tests are interesting also because of the availability of results obtained by the method of characteristics. In fact, the comparison provides an assessment of the quality and precision of the numerical solution.

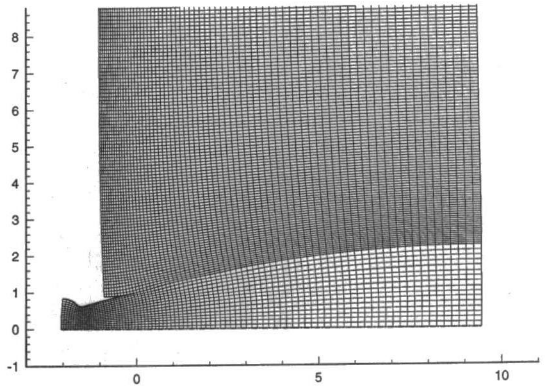

Fig. 10 Computational grid for a conical nozzle exhausting in still air

A conically divergent nozzle has been considered, having semi-divergence angle $\theta_j = 15$ deg, and exit Mach number $M_j = 2.5$, and exhausting in still air with a jet pressure ratio $p_j/p_a = 17$. The exhaust gas is again air and the chamber to ambient pressure ratio is $p_c/p_a = 1401$. The calculation has been performed on the orthogonal grid, based on two sub-grids, shown in Fig. 10. The upper sub-grid has 70 × 120 cells, while the lower has 90 × 16.

Figure 11 shows the numerical solution obtained in terms of Mach number contour lines. The flowfield is characterized by an expanding plume and by an oblique jet shock that appears near the plume boundary, almost parallel to it. The contact discontinuity points that simulate the plume boundary, and the fitted shock-points, are denoted by squares and circles, respectively. Superimposed are also shown, with dark squares and circles, the results by Love and Lee (1958), who used the classical method of characteristics and computed also the jet shock. The comparison shows a good agreement.

As a final test to show the capability of the method to solve complicated flowfields, a strong interaction between shock and jet boundary has been considered (Fig. 12). A primary nozzle exhausts its jet over an axisymmetric plug, whose shape produces compression waves rapidly coalescing in a shock which interacts with the jet boundary. Due to this interaction the CD bends abruptly outwards. The operation of such a nozzle is of course clearly undesirable, due to the recompression occurring over the plug surface; nevertheless it has been reported here as an example showing the ability of the method in dealing with abrupt changes in the jet boundary profile.

Conclusions

A simplified model that replaces the mixing layer at the boundary of nozzle exhaust plumes as a flow discontinuity has been reproposed and implemented in a numerical method based on the fitting of discontinuities. Following this approach, it is possible to avoid the complex calculation of the turbulent mixing of flows with different thermodynamic characteristics, while the main features of the flow behavior across the mixing layer can be correctly accounted for. The analysis of the flowfields computed for different nozzles and pressure ratios, demonstrates the capability of the method. Indeed, the results yield a good reproduction of theoretical and experimental data.

The possibility to implement the proposed method coupled with different schemes for the computation of the flowfield, indicates that it can be a useful tool to save computational time when the details of the mixing process at the boundary of the jet are not of interest.

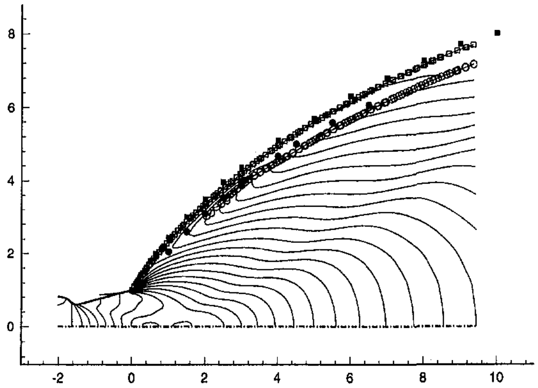

Fig. 11 Conical nozzle exhausting in still air: numerical solution for Mach number contour lines, shock-points (○) and CD-points (□), compared with the prediction of shock-points (●) and jet boundary (■) of Love and Lee (1958)

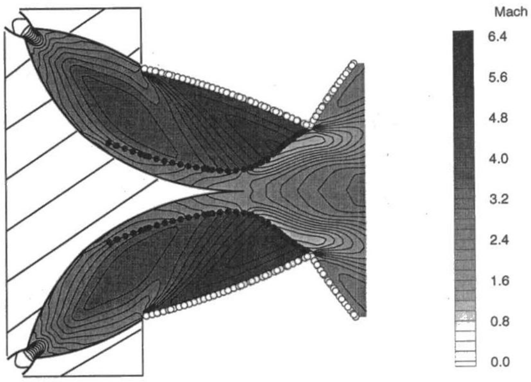

Fig. 12 Example of plug nozzle with a strong shock-jet boundary interaction. Mach number contour lines, shock-points (●) and CD-points (○).

The method is currently being exploited for the analysis of plug nozzle flowfields in the framework of the Future European Space Transportation Investigations Programme (FESTIP) of the European Space Agency.

Acknowledgments

The study has been carried out by partial funding of ASI (Italian Space Agency), ESA (European Space Agency), and MURST (Italian Secretary of University and Scientific-Technical Research).

References

Bigert, M., 1993, "Comparison of a Classical de Laval Nozzle and a Self-Adaptable Nozzle," Volvo Flygmotor Advanced Rocket Propulsion Technologies, Technical Note n. 3, ESA/ESTEC Contract No. 10241.

Cumber, P. S., Fairweather, M., Falle, S. A. E. G., and Giddings, J. R., 1995, "Predictions of the Structure of Turbulent, Highly Underexpanded Jets," ASME JOURNAL OF FLUIDS ENGINEERING, Vol. 117, pp. 599–604.

Broglia, R., Di Mascio, A., Favini, B., Nasuti, F., Onofri, M., and Paciorri, R., 1997, "CFD Analysis of Axisymmetric Plug Nozzle Flowfields," Technology and Research Projects, ESTEC/Contract No. 12019/96/NL/FG, ESA/ESTEC, Noordwijk, The Netherlands.

Fox, S. M., 1983, "Effects of Plume Impingement on a Momentum Bias Communications Satellite," *Journal of Spacecraft and Rockets*, Vol. 20, pp. 55–60.

Latvala, E. K., and Anderson, T. P., 1958, "Experimental Determination of Jet Spreading from Supersonic Nozzles at High Altitudes," Arnold Engineering Development Center AEDC-TN-58-98, Tullahoma, TN.

Love, E. S., and Lee, L. P., 1958, "Shape of Initial Portion of Supersonic Axisymmetric Free Jets at Large Pressure Ratios," NACA TN-4195.

Love, E. S., Grigsby, C. E., Lee, L. P., and Woodling, M. J., 1959, "Experimental and Theoretical Studies of Axisymmetric Free Jets," NACA TR R-6.

Lumpkin, F. E., Le Beau, G. J., and Stuart, P. C., 1995, "A CFD/DSMC Analysis of Plumes and Plume Impingement during Shuttle/Mir Docking," AIAA Paper 95-2034.

Moretti, G., 1987, "A Technique for Integrating Two-Dimensional Euler Equations," *Computer and Fluids*, Vol. 15, pp. 59–75.

Nash, K. L., Whitaker, K. W., and Freeman, L. M., 1994, "Predicting Exhaust Plume Boundaries with Supersonic External Flows," *Journal of Spacecraft and Rockets*, Vol. 31, pp. 773–777.

Nasuti, F., 1996, "Computational Fluid Dynamic Analysis of Plug Nozzle Flows," EWP-1910, ESA/ESTEC, Noordwijk, The Netherlands.

Nasuti, F., and Onofri, M., 1995, "Numerical Prediction of Nozzle Exhaust Plumes," *XII International Symposium on Air Breathing Engines*, ISABE 95-7042, Melbourne, Australia.

Nasuti, F., and Onofri, M., 1996, "Analysis of Unsteady Supersonic Viscous Flows by a Shock Fitting Technique," *AIAA Journal*, Vol. 34, pp. 1428–1434. See also AIAA Paper 95-2159, July, 1995.

Oggiano, M. S., Onofri, M., Onorato, M., and Zannetti, L., 1984, "Multicomponent Calculations of the Aerodynamic Characteristics of Aircraft After-Bodies," 14th Congress of the International Council of the Aeronautical Sciences, ICAS-84-1.10.3, Toulouse, France.

Rochelle, W. C., Huges, J. R., Leahy, K. S., and Fitzgerald, S. M., 1995, "Plume Impingement Heating to International Space Station (ISS)," AIAA Paper 95-2132.

Salas, M. D., 1974, ''The Numerical Calculation of Inviscid Plume Flow Fields,'' AIAA Paper 74-523.

Sutton, G. P., 1992, *Rocket Propulsion Elements,* Wiley, New York, Sixth Edition.

Vatsa, V. N., Werle, M. J., Anderson, O. L., and Hankins, G. B., 1982, ''Solution for Three Dimensional Over- or Underexpanded Exhaust Plumes,'' *AIAA Journal,* Vol. 20, pp. 1188–1194.

Wang, T. S., 1993, ''Numerical Analysis of Base Flowfield at High Altitude for a Four-Engine Clustered Nozzle Configuration,'' AIAA Paper 93-1923.

Williams, M., Lim, D., and Ungewitter, R., 1993, ''An Adaptive Grid/Navier-Stokes Methodology for the Calculation of Nozzle Afterbody Base Flows with a Supersonic Freestream,'' AIAA Paper 93-0192.

Zannetti, L., and Onofri, M., 1983, ''Interazione del flusso interno ad un ugello e del getto con l'aerodinamica esterna in regime transonico,'' *Atti VII Congresso Nazionale* AIDAA, Napoli, Italy.

Zannetti, L., and Onofri, M., 1984, ''Aerodynamics of Aircraft After Body: Numerical Simulation,'' AIAA Paper 84-0284.

Zannetti, L., Onofri, M., et al., 1986, ''Report of the Working Group on Aerodynamics of Aircraft Afterbody,'' AGARD-AR-226.

Three-Dimensional Blade Boundary Layer and Endwall Flow Development in the Nozzle Passage of a Single Stage Turbine

D. Ristic
Graduate Student.

B. Lakshminarayana
Evan Pugh Professor of Aerospace Engineering and Director, Center for Gas Turbines & Power.

Center for Gas Turbines & Power,
Pennsylvania State University,
University Park, PA 16802

The three-dimensional viscous flow field development in the nozzle passage of an axial flow turbine stage was measured using a ''x'' hot-wire probe. The measurements were carried out at two axial stations on the endwall and vane surfaces and at several spanwise and pitchwise locations. Static pressure measurements and flow visualization, using a fluorescent oil technique, were also performed to obtain the location of transition and the endwall limiting streamlines. The boundary layers on the vane surface were found to be very thin and mostly laminar, except on the suction surface downstream of 70 percent axial chord. Strong radial pressure gradient, especially close to the suction surface, induces strong radial flow velocities in the trailing edge regions of the blade. On the endwalls, the boundary layers were much thicker, especially near the suction corner of the casing surface, caused by the secondary flow. The secondary flow region near the suction surface-casing corner indicated the presence of the passage vortex detached from the vane surface. The boundary layer code accurately predicts the three-dimensional boundary layers on both vane surfaces and endwall in the regions where the influence of the secondary flow is small.

Introduction

The dominant viscous effects in the nozzle passage are due to horseshoe vortex near the leading edge of end walls; secondary flow and passage vortex near endwalls; and three-dimensional blade and wall boundary layers due to transverse pressure gradient and three-dimensional blade geometry. These viscous effects and trailing edge base pressure loss account for all the losses and inefficiency in subsonic nozzles. A detailed understanding of the viscous effects is a prelude to design of more efficient turbine stages and improved cooling techniques.

The development of secondary flow and passage vortex is not very well understood in realistic blade configurations, since the majority of the data have been acquired in rectilinear cascades (e.g., Sieverding, 1985; Gregory-Smith, 1988). Joslyn and Dring (1990), Zeschky and Gallus (1993), and Zaccaria and Lakshminarayana (1995) have obtained detailed measurements at the exit of the nozzle/stator, but no measurements were obtained inside the passage or in the viscous regions. The presence of radial pressure gradient in an annular nozzle influences the roll up and transport of secondary flow and passage vortex. The three-dimensional boundary layers present on both walls and vanes are also caused by the transverse pressure gradient. The three-dimensional boundary layers also arise due to the three-dimensional shape of the surface, or due to the interaction of wall and vane boundary layers. These three-dimensional viscous layers cause transport of momentum and energy in transverse directions producing appreciable spanwise and pitchwise mixing, resulting in three-dimensional flow and losses in these passages.

The data on turbine vane and blade cascade boundary layers are scarce. Bammert and Sandstede (1980) measured boundary layer profiles on smooth and rough surfaces of a turbine blade cascade. The boundary layer thickness increased uniformly along the suction surface, but on the pressure surface the boundary layer thickness started to decrease at 50 percent chord due to the presence of favorable pressure gradient. Hodson (1983) observed that the periodic unsteadiness due to upstream nozzle on the rotor blade boundary layers influence the transition and boundary layer development. This unsteadiness also contributed to an increase in the profile losses. The flow was found to be fully laminar along the pressure surface and the transition from laminar to turbulent flow occurred at 78 percent of the chord. Mee et al. (1992) performed detailed measurements on a transonic turbine cascade with a turning angle of 111 degrees and the inlet Mach number was 0.31. The measured velocity profiles indicate a thin unsteady separation bubble occurring on the suction surface close to the location where the favorable pressure gradient ends.

The major objective of this research is to understand the characteristics of three-dimensional viscous layers on nozzle vane, casing, and hub endwall surfaces of the nozzle passage in a single-stage axial flow turbine. These investigations should lead to improvements in vane design, efficiency, and cooling methods. The objectives include the following: (*a*) Investigate the nature of nozzle vane passage boundary layer and endwall secondary flow development, including transition, laminar and turbulent flow regions, and variation of the boundary layer integral properties along the blade and endwall surfaces; (*b*) investigate the interaction between the secondary flow regions and the three-dimensional boundary layers on vanes; (*c*) predict the boundary layer characteristics using three-dimensional boundary layer procedure and assess the ability of these procedures to predict the viscous flow field accurately.

Contributed by the Fluids Engineering Division for publication in the JOURNAL OF FLUIDS ENGINEERING. Manuscript received by the Fluids Engineering Division February 15, 1996; revised manuscript received February 24, 1998. Associate Technical Editor: Wing Ng.

Table 1 Vane, blade, and performance parameters

Hub to tip ratio:	0.7269	Vane (inlet velocity) Re:	$(3 \sim 4) \times 10^5$
Tip radius:	0.4582 m	Blade (inlet velocity) Re:	$(3 \sim 5) \times 10^5$
Blade height:	0.1229 m	Ave. tip clearance:	0.97 mm
Nozzle—Number of blades:	23	Rotor—number of blades:	29
—Chord: (tip)	0.1768 m	—Chord: (tip)	0.1287 m
—Spacing (tip)	0.1308 m	—Spacing: (tip)	0.1028 m
—Max. thickness: (tip)	38.81 mm	—Max. thickness: (tip)	22.0 mm
—Turning angle:	70°	—Turning angle:	95°tip, 126°hub
Rotor efficiency design: η_{rot}	0.8815	—Hub loading coefficient: Ψ	2.63
Total-to-total isentropic η_T efficiency	0.8930	—Pitchline loading coefficient: Ψ	1.88

The investigation reported in this paper is carried out in a low speed single stage turbine, with state-of-the art blading. A two-sensor, crossed, hot-wire probe is used to obtain detailed boundary layer measurements on the vane and in the endwall regions. Flow visualization of the transition and limiting streamlines is performed using the fluorescent oil technique. The boundary layer development and characteristics were also investigated by performing a computational simulation using a three-dimensional boundary layer code. The predicted boundary layer and secondary velocity profiles and other properties are compared with the experimental data.

Experimental Facility and Measurement Technique

The axial flow turbine used in this investigation is an open circuit facility. Two downstream axial flow fans provide the required pressure rise. Details of the stage, blading, and performance parameters of the AFTRF are given in Table 1. Details of the vane and blading design, the facility, and the inlet flow properties can be found in Lakshminarayana et al. (1992). The blading was designed by the General Electric Company and is representative of modern axial flow turbine (HP). The diameter of the facility is 91.4 cm, the hub to tip ratio is 0.73. The stator has 23 nozzle guidevanes followed by 29 rotor blades, with outlet guidevanes located 3 rotor chords downstream of the turbine stage. The nozzle geometry is shown in Fig. 1. One of the unique capabilities of the facility is the provision for the variation of the nozzle-rotor spacing from 20 to 50 percent nozzle vane chord. In the present research program, the blade row spacing is 20 percent of the nozzle vane chord at mid radius. All measurements in the current investigation were performed at a corrected speed of 1300 rpm, constant mass flow rate of 10.53 kg/s, and pressure ratio (P_{01}/P_{02}) of 1.078. The throttle setting is kept at a fixed position throughout the experiments. The inlet boundary layer thickness was 10 percent of span at the casing and 6% of span at the hub. The free-stream turbulence at inlet was 1–1.5 percent.

A two-sensor hot-wire probe was used to determine the instantaneous velocity components in two directions simultaneously. The plane containing ''x'' wire was parallel to the vane or the wall surface as shown in Fig. 1. On the vane surface, the probe is aligned so as to measure V_r and V_s as shown in Fig. 1. On the endwall surfaces, it is aligned to measure V_s and V_c. The probe was calibrated for flow velocity, angularity, temperature, and wall vicinity effects.

The calibration is performed in a jet at various temperatures. The angular calibration of the crosswire sensor is performed using the method developed by Blanco et al. (1993). The calibration procedure developed here involves measurement of the output voltage of individual sensors for a fixed jet velocity over a range of temperatures and applying the derived correction to the data (Radeztsky et al., 1993). Additional complexities of hot-wire measurements in close proximity to a wall is the increase in heat transfer from the sensor to the surface. The probe was calibrated for the near-wall effects, and this calibration is included in the data processing technique. The data are thus corrected for near-wall effect as well as temperature drifts. A detailed uncertainty analysis is given in Ristic (1995). The sources of error are calibration, spatial error of the sensor, positioning accuracy, wire aging, and temperature effects. A detailed analysis of these errors indicates that the uncertainty in velocity measurement is ±0.9 percent within the boundary layer. The maximum error in flow angle measurement is 1.2 deg.

Nomenclature

c_p = blade static pressure coefficient
c = axial chord
c_t = axial chord at blade tip
c_m = axial chord at midspan
H_{ss} = shape factor. (δ_s^*/Θ_s)
P, p = pressure
P_o = total pressure
r = radius measured from facility centerline
Re = Reynolds number
s, c, n = coordinates in the streamwise, crosswise, and normal direction (Fig. 1)
s, r, n = coordinates in streamwise, radial, and normal directions (Fig. 1)
S = pitchwise distance normalized by blade spacing ($S = 0.0$ suction, $S = 1.0$ pressure surface)
Tu = turbulence intensity (Eq. (1))
U_m = rotor blade speed at midspan
u^+ = friction velocity $\sqrt{(\tau_w/\rho)}$
V = total or mean velocity ($\sqrt{V_r^2 + V_x^2 + V_\theta^2}$ or $\sqrt{V_s^2 + V_n^2 + V_c^2}$)
V_{x1} = axial velocity at inlet
v' = velocity fluctuation
v_s', v_c' = instantaneous velocity fluctuation in the streamwise and cross-wise flow directions
x = axial distance measured from the leading edge
$y^+ = nu^+/\mu$
α = flow angle measured from axial direction
δ = boundary layer thickness
δ_s^* = displacement thickness in the streamwise direction
Θ_s = momentum thickness in the streamwise direction
μ = molecular viscosity
ρ = density
ϕ = radial flow angle measured from the cylindrical plane
Ψ = loading coefficient ($\Delta ho/U_m^2$)

Subscript

edge = conditions at boundary layer edge
h, t = hub and tip
s = streamwise direction
s, n, c = streamwise, normal, and crossflow components (Fig. 1)
s, r, n = streamwise, normal and radial components (Fig. 1)
x, r, θ = axial, radial and tangential components

Superscripts

$'$ = fluctuations from the mean

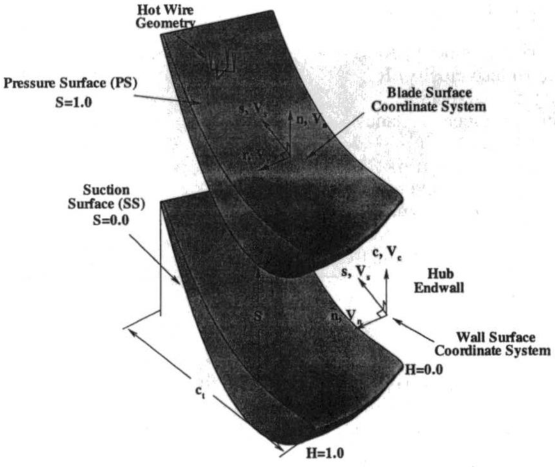

Fig. 1 Coordinate system and notation used in the investigation. The orientation of the hot wire probe for a typical pressure surface measurement is also shown.

All measurements were taken with the plane of the sensors oriented parallel to the surface (Fig. 1). The data acquired were sampled at a 10 kHz sampling frequency with a low pass filter set at 9.7 kHz to avoid aliasing from the higher frequencies. The data were averaged over a 25.6 s interval to allow accurate averaging of the flow properties. The suction surface and casing surface boundary layers were measured at $x/c_m = 0.85$ at 12 radial and 9 tangential locations, respectively. The pressure surface and hub surface boundary layers were measured at $x/c_m = 0.94$ at 7 radial and 7 tangential locations, respectively. Only representative and typical data are presented and interpreted in this paper. For comprehensive data and interpretation, see Ristic (1995).

To determine the limiting streamlines angles and regions of laminar, transitional, and turbulent flow on the nozzle vane and endwall surfaces, a fluorescent oil technique was used. A thin layer of oil remains for a longer period of time on the surface in regions of low shear stress (i.e., laminar and transition). With the addition of fluorescent compounds, the aviation oil would emit light after exposure to ultraviolet (black light fluorescent tubes) radiation. A thin layer of oil was deposited on the surface, before the experiment, using an atomizer to prevent formation of streaks and droplets. After a short run (5–10 min), the oil patterns were photographed using standard color film, full aperture opening, and an exposure of 30 s. The transition on the suction surface occurs in the region $x/c_m = 0.7$ to 0.8, while the pressure surface boundary layer is found to be laminar throughout. Hence, the suction surface boundary layer is turbulent and the pressure surface boundary layer is laminar in the region of measurement. The casing and hub wall boundary layers are turbulent.

Boundary Layer Code

In many situations where the viscous layers are thin, the flow field can be accurately resolved using a boundary layer code, which is one to two orders magnitude more efficient (computationally) than the Navier-Stokes code. Furthermore, large numbers of grid points can be used to resolve the viscous layers, including the near wall region and the skin friction stress. On the other hand, the Navier-Stokes procedure is limited by the number of grid points that can be used in the viscous layers. For example, if the viscous layers (away from the endwall regions) are 1 to 5 percent of spacing (as is the case under investigation), the number of grid points usually employed in this region is limited to very few, which cannot adequately resolve the viscous layers and losses. In regions where elliptic effects (such as secondary flow and viscous layers in the wall regions) are present, the boundary layer approximation is not valid; hence, it is better to use a Navier-Stokes code. In the present program, a boundary layer program is used for the vane boundary layers away from the endwalls.

A boundary layer code is used to predict the viscous layers on the vane surfaces and on the end wall surfaces away from the secondary flow region. The boundary layer code developed by Anderson (1985) is used for the prediction of boundary layer properties. This technique includes three separate steps: coordinate transformation of the general nonorthogonal surface of the nozzle vane; calculate of the boundary layer edge conditions from the known static pressure distribution (Zaccaria et al., 1996); and a three-dimensional boundary layer analysis to predict the boundary layer growth. Approximately 100 grid points are used within the boundary layer. The algebraic eddy viscosity model due to Cebeci and Smith (1974) is used for the turbulence closure, and the transition location is specified based on the flow visualization experiment. The computational domain included the region from hub-to-tip and zero radial velocity is prescribed as edge (hub and annulus wall) conditions. The numerical integration of the three-dimensional boundary layer equations is based on the first-order forward differencing for streamwise spatial derivatives, an upwind scheme in the radial direction (to capture flow reversal in radial direction) and central differencing in the normal direction. The resulting linear algebraic equations are solved by a block tridiagonal solver.

Experimental Results and Discussion

Blade Suction Surface Boundary Layer ($x/c_m = 0.85$). The data were taken at 12 radial stations along the suction surface from $H = 0.05$ to 0.95 (Fig. 1). A tangential survey was accomplished by traversing the probe toward the surface. At the moment of contact, an electrical connection was established and the surface location was recorded. All velocities are normalized by the upstream axial velocity V_{x1}, S is the normalized vane-to-vane distance with $S = 0.0$ corresponding to the vane suction surface and $S = 1.0$ corresponding to the vane pressure surface. The notations used for velocity components are shown in Fig. 1. The velocities are decomposed into streamwise (V_s), normal (V_n), and radial (V_r) components. Near the wall V_n is nearly zero; hence, V_s and V_r are measured directly by the "x" wire. The total velocity is given by $\sqrt{V_s^2 + V_r^2}$. The total velocity profiles are plotted in Fig. 2, the radial velocity profiles (V_r) are shown in Fig. 3. The velocity profile in boundary layer coordinate is shown in Fig. 4 for $H = 0.2–0.7$, the region least influenced by the secondary flow.

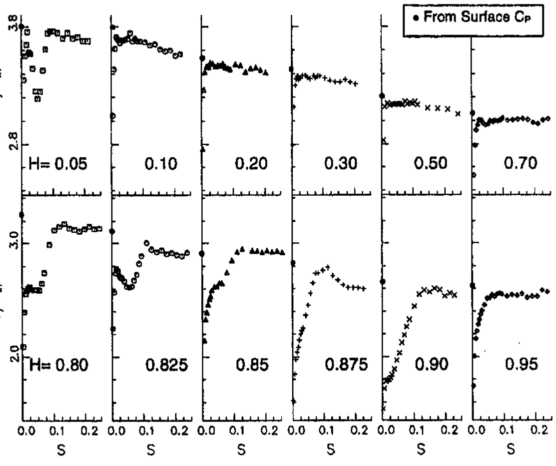

Fig. 2 Measured total velocity ($V = \sqrt{V_s^2 + V_r^2}$) on suction surface at $x/c_m = 0.85$

The measured free-stream total velocity V decreases gradually from a maximum in the hub region to a minimum near the casing region due to the presence of the radial pressure gradient (Fig. 2). The flow is inviscid over most of the vane passage ($H = 0.1$ through 0.7) with a very thin boundary layer region (2 percent of blade spacing). The calculated inviscid surface velocity derived from the measured static pressure distribution compares well with the extrapolated hot-wire data in the free stream for $H = 0.05$–0.7 as shown in Fig. 2. Appreciable boundary layer growth and deviation from typical vane boundary layer profiles occurs in regions close to the endwalls ($H > 0.8$) and this is caused by the secondary flow. These interaction regions are near the hub ($H < 0.05$) and from $H = 0.8$ to 0.95 near the casing. It is interesting to note that the velocities derived from the blade pressure distribution and the extrapolated values from the hot-wire data tend to deviate. This is due to the fact that the boundary layer assumption (normal pressure gradient is zero near the wall) is no longer valid.

The influence of the secondary flow at $H = 0.05$ results in a large increase in the radial velocity near the surface (same order of magnitude as the inlet axial velocity), indicating strong radial outward flow along the blade suction surface (Fig. 3). The existence of a dip in the measured total velocity profile close to the surface (Fig. 2) is an indication of the hub-suction passage vortex. This is also confirmed by a similar feature in the radial velocity at $H = 0.05$ location. The boundary layer profiles are not influenced by the wall from $H = 0.1$ to 0.8. Some typical profiles are plotted in boundary layer coordinates and compared with predictions in Fig. 4. The prediction of both the streamwise velocity and cross flow velocity components from the boundary layer code (Fig. 4) are in excellent agreement with the data. The boundary layer thickness is also predicted accurately. The predictions are not good in the secondary flow regions (Ristic, 1995).

In the casing suction corner, the data shown in Figs. 2 and 3 indicate that the passage vortex region extends from $H = 0.8$ to the $H = 0.95$, where the secondary flow, vane, and casing boundary layer interaction occurs. The total and axial velocity decrease in the region influenced by the secondary flow and this is evident from "wake" like profiles observed from $S = 0.02$ to 0.10 (Fig. 2). The strongest influence is in the region $H = 0.8$ to 0.95 location as indicated in the next section. The location closest to the casing endwall surface ($H = 0.95$) is completely within the viscous layer of the endwall surface (indicated by an increase in turbulence intensity discussed later) and the profiles are rather well behaved at this radial location.

The flow inside the suction surface boundary layer is radially inward over most of the blade surface, extending from $H = 0.3$ to the tip of the blade (Figs. 3 and 4), with maxima occurring at $H = 0.80$ where the maximum radial velocity is of the same order as the inlet axial velocity. The result is consistent with the flow visualization experiments indicating that the radial pressure gradient dominates the flow field along the suction surface at the trailing edge location. The three dimensionality in the boundary layer is dominant only in the secondary flow region located in the casing corner ($H = 0.8$ to 0.95) and in the hub region at $H = 0.05$. The boundary layers are representative of pressure driven three-dimensional boundary layers over most of the blade surface from $H = 0.1$ to 0.8.

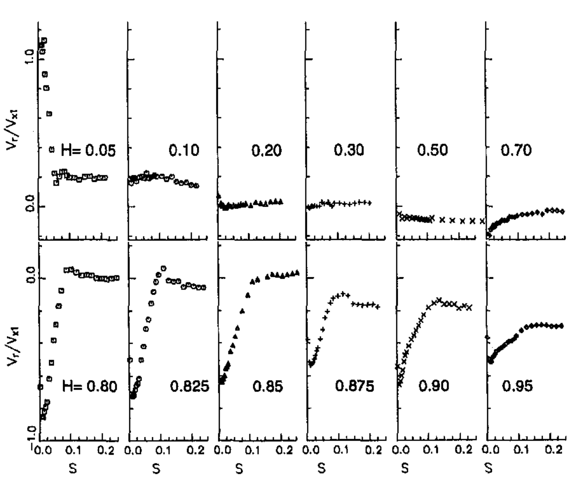

Fig. 3 Measured radial velocity (V_r) on suction surface at $x/c_m = 0.85$. Positive V_r is radially outward.

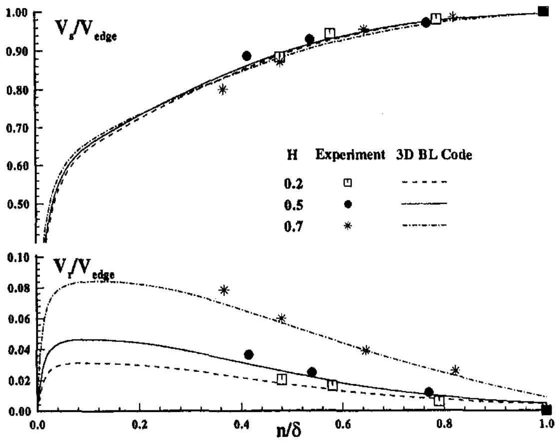

Fig. 4 Predicted and measured boundary layer velocity profiles on suction surface at $x/c_m = 0.85$. Radial (V_r/V_{edge}) and stream wise (V_s/V_{edge}) velocity profiles away from the endwall surfaces.

The data clearly reveal the effect of interaction between the casing boundary layer with the secondary flow. The secondary flow region produces a defect in total, axial, and tangential velocity resulting in a wake type of velocity profile in the buffer region of the boundary layer. The maximum defect in total velocity caused by the secondary vortex and flow is found to be as high as 20 percent of the free stream velocity, indicating the presence of a passage vortex.

Casing Surface Boundary Layer ($x/c_m = 0.85$). Boundary layer data on the casing surface at $x/c_m = 0.85$ are shown in Figs. 5 and 6. The measurements were performed at nine locations across the passage, including the secondary flow region of the suction-casing corner. The total velocity in the inviscid region increases gradually toward the inner radius due to the presence of radial pressure gradient. Comparison between the calculated inviscid surface velocity, derived from the vane static pressure distribution, and the extrapolated velocities from the hot-wire data are in good agreement, especially beyond $S = 0.439$ (Fig. 5). The vane-to-vane pressure gradient is responsible for the decrease in the total velocity from the suction surface ($S = 0.0$) to the pressure surface. The total velocity profiles from $S = 0.065$ through 0.219 (the data at $S = 0.219$ can be found in Ristic, 1995) again indicate wake-like velocity profiles in the secondary flow region caused by the passage vortex and the boundary layer interaction.

The velocity decreases in the vicinity of passage vortex as explained earlier. The velocity profiles at $S = 0.132$ and $S = 0.175$ indicate the presence of a strong passage vortex. The passage or secondary vortex is centered around $S = 0.132$ and $H = 0.875$, and extends from $S = 0.065$ to 0.219 (Fig. 5) and $H = 0.8$ to 0.9 (Fig. 2). The vortex location is characterized by velocity defect and step changes in yaw angles (Fig. 6). The presence of two dips in the velocity and angle profiles at $S = 0.132$, one near $H = 0.875$ and a second one with a smaller defect near $H = 0.95$, indicates the presence of a strong passage vortex and sweeping of the end wall boundary layer by second-

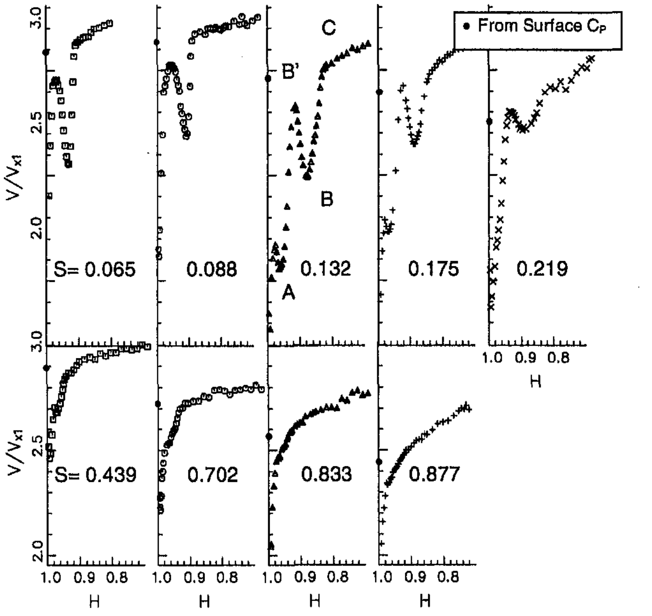

Fig. 5 Measured total velocity (V/V_{x1}) where $v = \sqrt{v_s^2 + v_c^2}$ on the casing surface at $x/c_m = 0.85$ ($S = 0.0$ is on the suction surface)

ary flow. The interaction of the boundary layer and the secondary flow combine to produce such an effect. Laser doppler measurements (Zaccaria et al., 1996) do not indicate the presence of a horseshoe vortex at $x/c_m = 0.56$.

The velocity profiles from the mid passage $S = 0.439$ to $S = 0.877$ exhibit conventional three-dimensional boundary layer characteristics. The boundary layer thickness is largest near the suction surface and decreases toward the pressure surface of the blade reaching a minimum at $S = 0.877$. Measurements closer to the pressure surface could not be accomplished due to accessibility problems.

The measured yaw angle (α), shown in Fig. 6, increases in the near wall region from approximately 62 deg in the free stream to a maximum of 72 deg at the $S = 0.439$ location. The increase is due to the turning of the boundary layers toward the suction surface caused by the strong transverse pressure gradient and the resulting secondary flow. The overturning decreases at locations closer to the pressure surface corner. The underturning caused by the passage vortex is as much as 6 deg at the $S = 0.132$ location. The influence of the passage vortex is dominant in the region $S = 0.065$ to 0.219 with maximum influence occurring near $S = 0.132$. The presence of both the overturning and the underturning of the flow in the secondary flow region indicate the presence of a passage vortex. But, the passage vortex has been transported inward. For example, at $S = 0.132$, it is located in the region $0.9 > H > 0.825$.

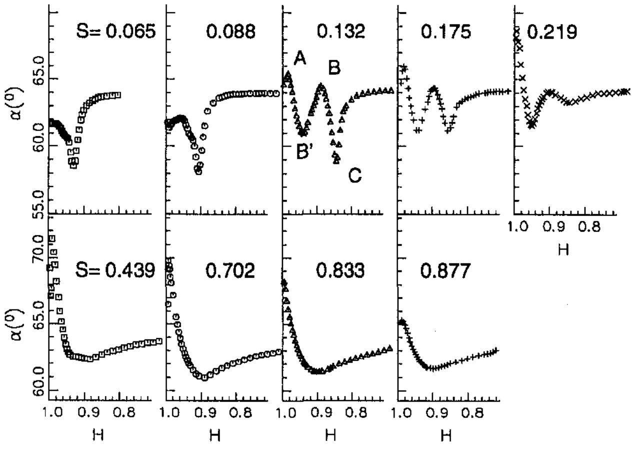

Fig. 6 Measured flow angle (α) on the casing surface at $x/c_m = 0.85$

The nature of velocity profiles and flow angles observed in the secondary vortex region needs additional interpretation. Away from the vortex region, $S \geq 0.439$, classical secondary flow is observed. The flow is overturned in the boundary layer region followed by underturning near the edge of the boundary layer. This is consistent with predictions from inviscid secondary flow theories. In the region $S = 0.065$ to 0.219, observed behavior indicates a very low velocity region (for example near $H = 0.9$ at $S = 0.132$) followed by an increase in velocity and flow angles on either side of this region (Figs. 5 and 6). Inside the vortex core, the axial velocity decreases and the flow angle increases. This is evident from Figs. 5 and 6. For example, at $S = 0.132$, the vortex is located at B, the velocity is minimum, and the flow angle is maximum (Fig. 6) at this location. The edge of the vortex is located at A (top leg) and C (bottom leg). Part of the outer leg of the vortex is immersed inside the boundary layer as indicated in AB' at $s = 0.132$ in Figs. 5 and 6. The velocity increases and the angle decreases in this region (from A to B') as in classical secondary flow theory. As the core is approached, from B' to B, the angle increases and the velocity decreases as indicated earlier. The velocity increases and angle decreases (underturning) in the outer leg of vortex from B to C. Thus the observed distribution is consistent with the boundary layer-vortex interaction mechanisms.

Hub Surface Boundary Layer ($x/c_m = 0.94$). Due to poor accessibility, measurements near the hub endwall surface were restricted to locations from $S = 0.416$ to $S = 0.924$, which are outside the secondary flow region. The measurements at $x/c_m = 0.94$ are shown in Fig. 7. Here again, the inviscid velocity derived from blade pressure is in excellent agreement with the measured velocity in the free stream. The measurements near the wall reveal the general features of three-dimensional boundary layers, with a very thin viscous region compared to those on the casing endwall surface. The boundary layer thickness decreases as the pressure surface ($S = 1.0$) is approached. The boundary layer thickness on the hub surface is much lower than that on the casing surface (more than 50 percent lower outside of the secondary flow region). The measured yaw angle (α) changes rapidly in the near wall region. The overturning angle near the hub wall is high in the mid-passage region (as

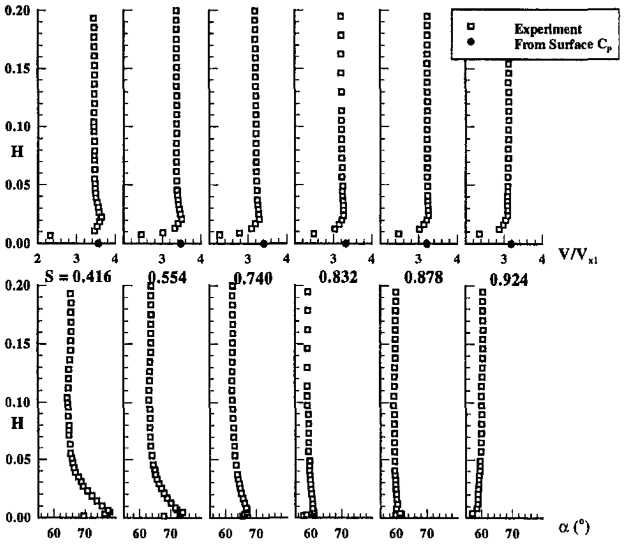

Fig. 7 Measured total velocity (V/V_{x1}) where $v = \sqrt{v_s^2 + v_c^2}$ and measured yaw angle (α) on hub surface at $x/c_m = 0.94$

much as 14 deg at $S = 0.416$) due to the high flow turning toward the hub-suction surface corner caused by the secondary flow. The overturning angle decreases as the pressure surface is approached. In general the hub endwall boundary layers are much thinner than the casing endwall boundary layers due to higher acceleration of the flow at this location.

Blade Pressure Surface Boundary Layers at $x/c_m = 0.945$. The measurements were taken at the trailing edge of the blade ($x/c_m = 0.945$) at seven radial stations on the blade pressure surface. The distribution of total and radial velocities are shown in Fig. 8. The inviscid surface velocity, based on the surface static pressure measurement, agree very well with the extrapolated hot-wire data. The boundary layer thickness is nearly constant from hub to tip. The measured radial velocity reveals inward radial flow inside the boundary layer, which is in agreement with the measurements by Zaccaria et al. (1993) acquired with a five-hole pneumatic probe. The free-stream radial velocity is negligible everywhere. Inside the boundary layers, the radial (inward) velocity increases toward the wall, especially in the blade tip region. The variation of radial velocity inside the boundary layer is especially strong in the tip region ($H =$ 0.9 and 0.95) due to large influence of the casing endwall surface boundary layer. The radial component of velocity is appreciable inside the boundary layer from $H = 0.10$ to 0.95. The maximum radial velocity, as expected in a three-dimensional boundary layer, occurs away from the surface and its magnitude is about 10 percent of the inlet axial velocity. The viscous region is very thin (less than 3 percent of the pitch); and as expected, the radial flow inside the boundary layer is inward, especially in the tip regions. The prediction of the pressure surface boundary layer profile from the boundary layer code is good in all regions.

Boundary Layer Integral Properties. The integral properties were calculated by fitting a fifth-order polynomial through the measured data points. From the flow visualization experiment, the boundary layers were determined to be laminar on the pressure surface at the measurement location, partially turbulent on the suction surface, and fully turbulent on hub and casing surfaces. The computed (boundary layer code) and measured integral properties of the boundary layers are presented in Figs. 9 and 10 for blade and wall surfaces, respectively. The shape factor H_{ss} is defined as the ratio of the displacement and momentum thicknesses ($H_{ss} = \delta_s^*/\theta_s$), all based on the streamwise component of velocity (Fig. 1).

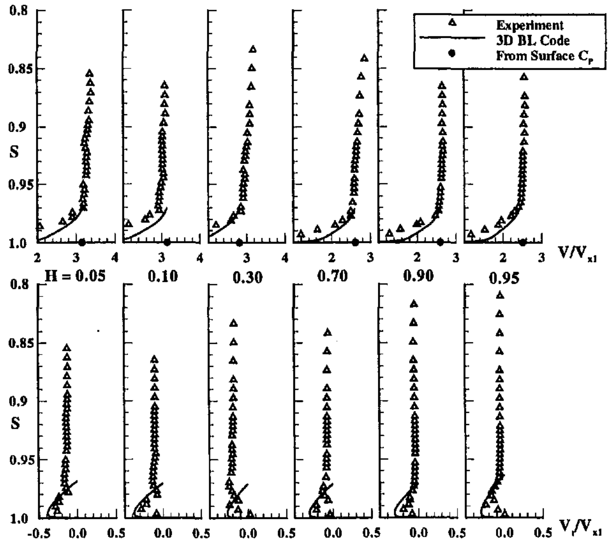

Fig. 8 Measured total velocity (V/V_{x1}) and radial velocity (V_r/V_{x1}) on pressure surface at $x/c_m = 0.945$

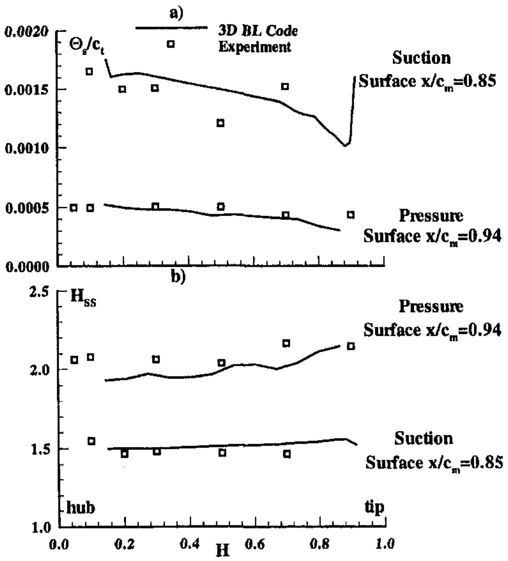

Fig. 9 Measured and computed integral properties of boundary layers. (*a*) Momentum thickness and (*b*) shape factor.

On the suction surface (Fig. 9(*a*)), the momentum thickness is nearly constant away from the endwalls. Close to the hub suction surface corner, the values increase rapidly due to the influence of the hub-wall boundary layer and secondary flow. Very good agreement between the measured and computed properties (from boundary layer code) is observed in the regions away from the endwalls and secondary flow regions ($H = 0.2$ to $H = 0.7$). In the casing suction corner, the passage vortex and casing boundary layer increases the momentum and displacement thicknesses substantially. The prediction from the boundary layer code is obviously inaccurate in this region. The measured shape factor H_{ss} (Fig. 9(*b*)) remained constant (around 1.5) indicating a turbulent boundary layer.

On the pressure surface, Fig. 9(*a*), the boundary layer integral properties computed from the boundary layer code are in

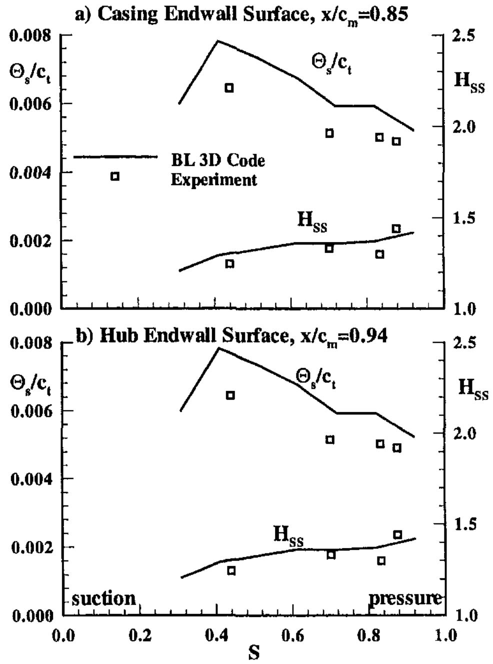

Fig. 10 Measured and computed integral properties of boundary layers. (*a*) Casing endwall surface and (*b*) hub endwall surface.

good agreement with the measured data in most of the regions away from the endwalls, where secondary flow effects are small. The three-dimensional boundary layer solution at $x/c_m = 0.94$ is fairly accurate in predicting the integral properties. The momentum thickness is very small, about 25–30 percent of those measured on the suction surface. The shape factor H_{ss} remains constant (Fig. 9(b)) with a value of two over the pressure surface indicating that the boundary layer is laminar.

Comparison of the predicted (boundary layer code) and the measured integral properties on the casing and hub endwall surface, shown in Fig. 10, indicate fairly good agreement away from the suction surface of the blade (from $S = 0.4$ toward the pressure surface). The momentum thicknesses decrease toward the pressure surface as expected. Near the mid pitch and close to the pressure surface regions, the prediction and measurement agree fairly well. The momentum thicknesses are much higher compared to those on the vane due to the presence of an upstream wall boundary layer, and the measured shape factor indicates accelerating turbulent boundary layer.

In the secondary flow region, the classical definition of the boundary layer integral properties are no longer applicable due to the difficulty in delineating the boundary between the viscous layer and the external flow. Hence, the data at these locations are not shown in Figs. 9 and 10. Outside the secondary flow region, the boundary layer approach is valid, requiring only an accurate prescription of the pressure distribution and is much simpler to implement.

Turbulence Properties. The turbulence intensity (Tu) is defined as follows:

$$\mathrm{Tu} = \frac{\sqrt{\overline{(v_s')^2} + \overline{(v_c')^2}}}{V} \qquad (1)$$

where v_c' is the cross flow velocity fluctuations for the wall (Fig. 1) and radial velocity fluctuations for the vane. It should be noted here that the third component (normal to the wall) was not measured. Hence, Tu is not the total turbulence intensity. Furthermore, the turbulence intensity as defined here is the total fluctuations, including both the random component (turbulence) and the deterministic component caused by the rotor potential interactions. The latter contribution is found to be about 1 percent of the mean velocity (Ristic, 1995). Hence, the dominant contribution to the unsteadiness inside the wall and vane boundary layers is due to random turbulence. Hence, the terminology "turbulence" is retained here. In most cases, the contribution to the free stream turbulence due to rotor potential interaction is about 1 percent.

The turbulence intensity for the suction surface of the nozzle blade at $x/c_m = 0.85$ is shown in Fig. 11. In the free stream, the average level of turbulence intensity was found to be 2.2 percent in the region from $H = 0.1$ to 0.7. Since the boundary layers are thin away from the casing and hub walls, the location and the magnitude of peak turbulence intensities in the near wall region could not be captured. Nevertheless, the data show increased intensities as the walls are approached. The free stream turbulence intensities increased near the casing suction surface corner to approximately 6 percent at $H = 0.95$, indicating that this measurement location is already within the casing boundary layer region. The measurement in the secondary flow region at the spanwise locations, $H = 0.8$ and 0.825, indicates the existence of a secondary peak in the passage vortex region. The turbulence intensity at $H = 0.8$ increases toward the location of the passage vortex reaching a maximum of 9 percent, then decreases and increases again toward the blade surface. The maximum turbulence intensity occurs at the $H = 0.90$ spanwise location reaching 18 percent. This is caused by the interaction of the blade surface and casing surface (corner flow) boundary layers. In the tip region, a decrease in turbulence intensities from location $H = 0.9$ to 0.95 is observed due to the reduced influence of the secondary flow and the passage vortex as the wall is approached.

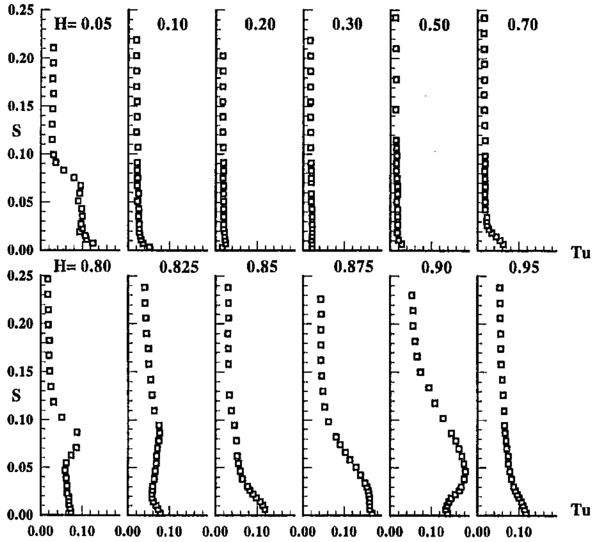

Fig. 11 Measured turbulence intensity (Tu) on suction surface at $x/c_m = 0.85$

Away from the endwalls, the components of the turbulence intensities in the stream wise (Tu_s) and cross wise (Tu_c) directions show similar levels (Ristic, 1995). This differs from conventional boundary layers, where the cross flow component is smaller than the streamwise component. The fact that the intensities are similar in magnitude indicates the influence of the radial inward flow and the secondary flow in amplifying the turbulence in the radial direction. The components of turbulence intensity differed only in the two extreme radial locations ($H = 0.05$ and 0.95) due to the merging of the wall and the blade boundary layers and their interaction with the secondary flow. In the passage vortex region, the relative levels of streamwise and radial components of turbulence remains similar.

The variation of turbulence intensities near the casing endwall surface is shown in Fig. 12. In the casing suction surface corner, the presence of double peak in the turbulence intensity profile is due to the presence of the passage vortex as described earlier. The increase in turbulence intensity close to the wall is due to the casing endwall boundary layer and the peak away from the surface is due to the passage vortex. The turbulence intensity (Fig. 12) increased from a free-stream value of 0.022 to 0.12 at $S = 0.132$ and $H = 0.84$. The turbulence intensity remains nearly constant in the passage vortex region, increasing again in the corner vortex region. The turbulence intensity increases toward the wall reaching a maximum value of 0.18. The overall levels of turbulence intensity in the cross flow direction is found to be larger than the level in the streamwise direction due to the high flow turning along the casing endwall. This clearly shows the need for anisotropic turbulence models in Navier-Stokes computation. Outside of the viscous and secondary flow regions, the unsteadiness in the mean flow is very low and is similar to measurements obtained at $x/c_m = 0.56$ location (Zaccaria et al., 1993).

In the hub region (see Ristic, 1995), the turbulence intensity is found to increase from a free-stream value of 2.1 percent to approximately 5 percent at the closest hub measurement location. The turbulence intensities decreases toward the pressure surface.

Composite Flow Field in the Casing Secondary Flow Region. The hot-wire data acquired on the vane and wall surfaces in the region $0.6 < H < 1.0$, and $0 < S \le 0.3$ is integrated and interpolated onto a uniform grid to provide a composite and comprehensive understanding of the viscous flow develop-

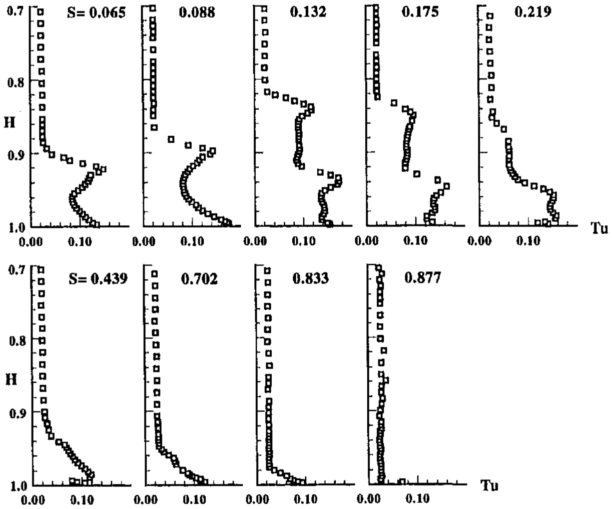

Fig. 12 Measured turbulence intensity on casing surface at $x/c_m = 0.85$

ment in the casing secondary flow/vortex region. The results are shown in Fig. 13. The total velocity normalized by V_{x1}, plotted in Fig. 13(*a*) indicates that minimum velocities occur close to the suction surface near $H \approx 0.9$, increasing gradually as the casing is approached and decreasing again near the wall. This low velocity region, caused by the presence of passage vortex, extends from 0.8 to 0.95 and covers nearly 7 to 8 percent of vane pitch, and its influence extends up to $H = 0.75$. In addition, the effect of sweeping of the boundary layer by the secondary flow vortex is evident near the suction surface corner, where high velocities are observed. This is caused by the duel effect of secondary vortex sweeping the endwall boundary layer and acceleration of the flow arising from the blockage effect of the secondary vortex. This region, even though small, has significantly higher velocity compared to other regions of the endwall flow.

The yaw angles, plotted in Fig. 13(*b*) indicate that the flow is overturned in the wall region and underturned away from the wall. High flow overturning (as much as 14 deg) occurs near the pressure surface, decreasing as the suction surface is approached. There are two underturning regions, one centered around $H = 0.95$ and the other one near $H = 0.840$. As explained earlier, this is caused by the secondary vortex and interaction of the outer leg of the secondary vortex with wall boundary layer. The second underturning region (near $H = 0.84$) is located away from the suction surface and represents the bottom leg of the passage vortex. The radial flow angle, shown in Fig. 13(*c*), indicates that the maximum radial inward velocity occurs in the same region as the minimum total velocity, with values as high as 45 deg, indicating that the radial velocity in this region (caused by secondary flow/vortex) is of the same order of magnitude as the inlet axial velocity. The flow is inward in the region extending from $H = 0.75$ to 0.97, and $S = 0$ to 0.2. The turbulence intensities are shown in Fig. 13(*d*). The high levels of turbulence intensity occur near the suction surface close to $H = 0.9$. Here again, the region of high turbulence intensity corresponds to a region of low total velocity, high inward radial angle, and the underturning region. This is mainly caused by the passage vortex and its interaction with the casing surface boundary layer.

Very close similarities in contours of Tu, ϕ, V/V_{x1}, α distributions should be noted. The maximum influence of the passage vortex is confined to 20 percent of the span from the casing and 10 percent of the blade spacing from the suction surface. The overall influence covers a much larger domain, extending all the way from the pressure to the suction surface in the outer 20 percent of span.

Concluding Remarks

It is evident from the results reported in this paper that boundary layers are very thin on blade surfaces, away from the endwall regions with the boundary layer thickness averaging about 0.5 and 3 percent of chord on the pressure and suction surfaces, respectively. In the endwall region, no noticeable growth (from inlet value) in boundary layer thickness is observed in regions away from the passage vortex regions. The interaction of the passage vortex and the casing boundary layer is observed in the casing region, resulting in an unconventional ''wake'' like outer layer in the casing boundary layer.

The vane surface boundary layers are three-dimensional with appreciable radial inward flow caused by the radial pressure gradient. The vane boundary layer thickness remained almost constant in the spanwise direction, on both of the vane surfaces, except in the secondary flow regions and close to the endwalls. The suction surface boundary layer is found to be transitional, with transition occurring between 70–80 percent chord.

On the casing surface, the velocity increases in the near wall region due to the interaction of the secondary flow, passage vortex, and the casing endwall boundary layer. The boundary layer thickness decreases as the pressure surface is approached. The secondary flow region in the suction surface-casing corner indicates the presence of a passage vortex detached from the vane and the casing surface. The radial inward flow along the suction surface in this region moves the passage vortex inward.

Boundary layer growth along the hub endwall was found to be much lower than that on the casing due to the higher acceleration at this location. The secondary flow is much stronger in the suction surface-casing corner due to the presence of strong transverse pressure gradient and thicker inlet boundary layer.

In general, the free-stream unsteadiness remained constant throughout the nozzle passage. The periodic unsteadiness due to the turbine rotor and the downstream fan accounts for approximately 1 percent of the free stream unsteadiness. The turbulence intensities are found to be high (as much as 18 percent) in the passage and the corner vortex region.

The three-dimensional boundary layer prediction shows good agreement with the data except in the regions of secondary flow and endwall boundary layer flow, where the conventional boundary layer assumptions are no longer valid. On the suction surface, the solution was accurate from $H = 0.1$ to $H = 0.7$ and is good agreement with the measured velocity profiles. On the nozzle vane pressure surface, the agreement was excellent

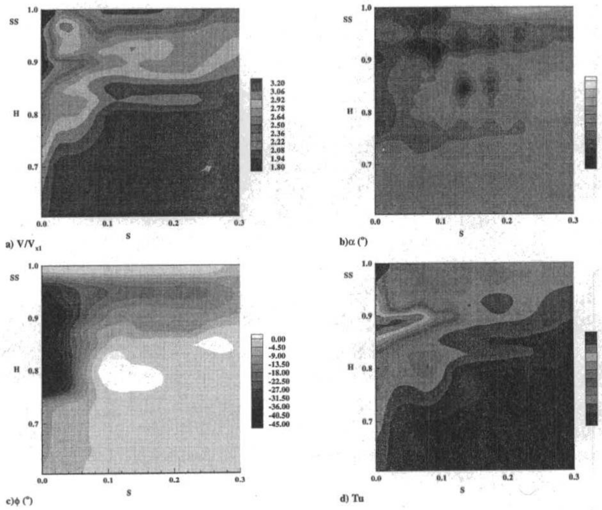

Fig. 13 Composite flow field in casing-suction surface corner at $x/c_m = 0.85$. (*a*) total velocity contours (V/V_{x1}), (*b*) yaw angle (α in degrees), (*c*) contours of measured radial angle (ϕ in degrees), (*d*) turbulence intensity (*Tu*) contour.

due to the smaller extent of the secondary flow region and the endwall boundary layers.

Acknowledgments

This work was supported by NASA through Grant NAG 3-555, with R. Boyle and K. Civinskas as technical monitors. The assistance of M. Zaccaria and L. Gourgeon in acquiring these data is gratefully acknowledged.

References

Anderson, O. L., 1985, "Assessment of a 3-D Boundary Layer Analysis to Predict Heat Transfer and Flow Field in Turbine Passage," NASA CR-174894 (Also see ASME *Journal of Fluids engineering,* Vol. 109, pp. 41–50).

Bammert, K., and Sandstede, H., 1980, "Measurement of the Boundary Layer Development along a Turbine Blade with Rough Surface," ASME Paper 80-GT-40.

Blanco, E., Ballesteros, R., and Santolaria, C., 1993, "Angular Range and Uncertainty Analysis of Non-Orthogonal Crossed Hot Wire Probes," ASME *Thermal Anemometry,* FED-Vol. 167.

Cebeci, T., and Smith, A. M. O., 1974, *Analysis of Turbulent Boundary Layers,* Academic Press, New York.

Gregory-Smith, D. G., et al., 1988, "Growth of Secondary Losses and Vorticity in an Axial Turbine Cascade," ASME *Journal of Turbomachinery,* Vol. 110, pp. 1–8.

Hodson, H. P., 1983, "The Development of Unsteady Boundary Layers on the Rotor of an Axial Flow Turbine," AGARD-CP-351.

Joslyn, D., and Dring, R. P., 1990, "Three-Dimensional Flow in an Axial Turbine," ASME papers 90-GT-56 and -57.

Lakshminarayana, B., et al., 1992, "Investigation of the Three-Dimensional flow Field in a Turbine Including Rotor/Stator Interaction, Part 1: Design, Development, and Performance of Turbine Facility," AIAA paper 92-3325.

Mee, D. J., Baines, N. C., and Oldfield, M. L. G., 1992, "Detailed Boundary Layer Measurements on a Transonic Turbine Cascade," ASME *Journal of Turbomachinery,* Vol. 114.

Radeztsky, R. H., Jr., et al., 1993, "Software Solution to Temperature-induced Hot Wire Voltage Drift," ASME *Thermal Anemometry,* FED Vol. 167.

Ristic, D., 1995, "Three-Dimensional Viscous Flow Field in an Axial Flow Turbine Nozzle Passage," M.S. thesis, Pennsylvania State University.

Sieverding, C. H., 1985, "Recent Progress in the Understanding of Basic Aspects of Secondary Flows in Turbine Blade Passages," ASME *Journal of Engineering for Gas Turbines and Power,* Vol. 107.

Zeschky, J., and Gallus, H. E., 1993, "Effect of Stator Wakes and Spanwise Non-uniform Inlet Conditions on the Rotor Flow of an Axial Turbine Stage," ASME *Journal of Turbomachinery,* Vol. 115, pp. 128–136.

Zaccaria, M., and Lakshminarayana, B., 1995, "Investigation of Three-Dimensional flow Field at the Exit of a Turbine Nozzle," *Journal of Propulsion and Power,* Vol. 11, pp. 55.

Zaccaria, M., Ristic, D., and Lakshminarayana, B., 1996, "Three Dimensional Flow Field in a Turbine Nozzle Passage," *Journal of Propulsion and Power,* Vol. 12, pp. 974–983.

DISCUSSION

E. S. Hall[1]

Allow me to separate this discussion into two parts: the first dealing with the computational aspects of this problem and the second dealing with the measurements in general. I must disagree with the authors' comments concerning the value of the three-dimensional boundary layer analysis. I concur that boundary layer predictions generally employ more discrete points and can be achieved more rapidly than a corresponding Navier-Stokes analysis. However, it cannot be ignored that the boundary layer analysis also requires the specification of the edge pressure which is not easy to develop without additional analyses. Elliptic effects resulting from aerodynamic blockage due to corner vorticies, etc. must be accounted for to adequately predict the edge pressure conditions. The computational cost of these additional analyses are often ignored when comparing boundary layer and Navier-Stokes solution times. The comparison also implies that the boundary layer predictions do not adequately match data in regions involving strong secondary flow. Modern highly-loaded turbine airfoils are often dominated by secondary flow effects, and again the three-dimensional boundary layer analysis is of limited use. Given the abundant computational resources available today, the only computational approach which makes sense for detailed 3-D turbine airfoil design is a Navier-Stokes code. At present, in my opinion, the only reasonable use of a 3-D boundary layer code is to predict turbine airfoil heat transfer given Navier-Stokes-derived edge conditions. Boundary layer codes have demonstrated somewhat better consistency predicting heat transfer compared to current Navier-Stokes codes with 2-equation turbulence models.

The authors' present detailed flow observations based on test measurements in the Penn State turbine rig. The data essentially confirms known secondary flow behavior in modern turbine blading. Two questions come immediately to mind as I ponder the utility of these data to enhance future designs. First, does detailed data taken at a freestream turbulence level of 1 percent have any validity for turbine airfoils operating in the engine environment, where freestream turbulence levels can be as high as 10 percent? At high freestream turbulence levels, regions of laminar/transitional/fully turbulence flow are non-distinct, and extrapolation of these results to the actual engine environment can be misleading. Second, how useful are the results from a single point of operation? Given the viscous nature of the fluid mechanics discussed, to be used effectively in design one would at least like to know the sensitivity to Reynolds number, airfoil loading distribution, angle distribution, etc. Industry research budgets are such that companies can no longer afford to generate fundamental design research data internally, and as an industry we rely on government agencies and academia to further this cause. Presentation of data based on a single observation is not in itself useful. What is useful is the trend of the data based on variations in operation. I believe that developing knowledge of the data trends should be the focus of this type of research effort.

Authors' Closure

The authors would like to thank Dr. Hall for his comments on our paper. We are not advocating use of the boundary layer code in all regions of the flowfield. The Navier-Stokes code is most useful in predicting the three-dimensional effects in the regions of secondary flow, endwall flow, and tip clearance effects. As mentioned by the reviewer, the heat transfer predictions are done much better with the boundary layer code and that is because the boundary layer properties, including the nearwall regions, are more accurately predicted by the boundary layer code. This is the point we were trying to make. If the interest lies in the three-dimensional boundary layer not affected by the endwall flows, the boundary layer code should provide better results in the prediction of the viscous effects, losses, and local properties, as well as the transition and the heat transfer when compared to a Navier-Stokes code. The Navier-Stokes code accuracy is affected by artificial dissipation and grid density. The edge conditions could be derived by simpler methods; but we are not advocating that the boundary layer code could be used in the entire hub-to-tip region. These are not useful in situations where the boundary layer interaction, compressibility effects, and shock waves are present. But in many applications, such as the hydraulic turbines and steam turbines, the boundary layer

---

[1] Staff Research Scientist, Allison Engine Co., P.O. Box 420, Indianapolis, IN 46206-0420.

due to the smaller extent of the secondary flow region and the endwall boundary layers.

Acknowledgments

This work was supported by NASA through Grant NAG 3-555, with R. Boyle and K. Civinskas as technical monitors. The assistance of M. Zaccaria and L. Gourgeon in acquiring these data is gratefully acknowledged.

References

Anderson, O. L., 1985, "Assessment of a 3-D Boundary Layer Analysis to Predict Heat Transfer and Flow Field in Turbine Passage," NASA CR-174894 (Also see ASME *Journal of Fluids engineering,* Vol. 109, pp. 41–50).

Bammert, K., and Sandstede, H., 1980, "Measurement of the Boundary Layer Development along a Turbine Blade with Rough Surface," ASME Paper 80-GT-40.

Blanco, E., Ballesteros, R., and Santolaria, C., 1993, "Angular Range and Uncertainty Analysis of Non-Orthogonal Crossed Hot Wire Probes," ASME *Thermal Anemometry,* FED-Vol. 167.

Cebeci, T., and Smith, A. M. O., 1974, *Analysis of Turbulent Boundary Layers,* Academic Press, New York.

Gregory-Smith, D. G., et al., 1988, "Growth of Secondary Losses and Vorticity in an Axial Turbine Cascade," ASME *Journal of Turbomachinery,* Vol. 110, pp. 1–8.

Hodson, H. P., 1983, "The Development of Unsteady Boundary Layers on the Rotor of an Axial Flow Turbine," AGARD-CP-351.

Joslyn, D., and Dring, R. P., 1990, "Three-Dimensional Flow in an Axial Turbine," ASME papers 90-GT-56 and -57.

Lakshminarayana, B., et al., 1992, "Investigation of the Three-Dimensional flow Field in a Turbine Including Rotor/Stator Interaction, Part 1: Design, Development, and Performance of Turbine Facility," AIAA paper 92-3325.

Mee, D. J., Baines, N. C., and Oldfield, M. L. G., 1992, "Detailed Boundary Layer Measurements on a Transonic Turbine Cascade," ASME *Journal of Turbomachinery,* Vol. 114.

Radeztsky, R. H., Jr., et al., 1993, "Software Solution to Temperature-induced Hot Wire Voltage Drift," ASME *Thermal Anemometry,* FED Vol. 167.

Ristic, D., 1995, "Three-Dimensional Viscous Flow Field in an Axial Flow Turbine Nozzle Passage," M.S. thesis, Pennsylvania State University.

Sieverding, C. H., 1985, "Recent Progress in the Understanding of Basic Aspects of Secondary Flows in Turbine Blade Passages," ASME *Journal of Engineering for Gas Turbines and Power,* Vol. 107.

Zeschky, J., and Gallus, H. E., 1993, "Effect of Stator Wakes and Spanwise Non-uniform Inlet Conditions on the Rotor Flow of an Axial Turbine Stage," ASME *Journal of Turbomachinery,* Vol. 115, pp. 128–136.

Zaccaria, M., and Lakshminarayana, B., 1995, "Investigation of Three-Dimensional flow Field at the Exit of a Turbine Nozzle," *Journal of Propulsion and Power,* Vol. 11, pp. 55.

Zaccaria, M., Ristic, D., and Lakshminarayana, B., 1996, "Three Dimensional Flow Field in a Turbine Nozzle Passage," *Journal of Propulsion and Power,* Vol. 12, pp. 974–983.

DISCUSSION

E. S. Hall[1]

Allow me to separate this discussion into two parts: the first dealing with the computational aspects of this problem and the second dealing with the measurements in general. I must disagree with the authors' comments concerning the value of the three-dimensional boundary layer analysis. I concur that boundary layer predictions generally employ more discrete points and can be achieved more rapidly than a corresponding Navier-Stokes analysis. However, it cannot be ignored that the boundary layer analysis also requires the specification of the edge pressure which is not easy to develop without additional analyses. Elliptic effects resulting from aerodynamic blockage due to corner vorticies, etc. must be accounted for to adequately predict the edge pressure conditions. The computational cost of these additional analyses are often ignored when comparing boundary layer and Navier-Stokes solution times. The comparison also implies that the boundary layer predictions do not adequately match data in regions involving strong secondary flow. Modern highly-loaded turbine airfoils are often dominated by secondary flow effects, and again the three-dimensional boundary layer analysis is of limited use. Given the abundant computational resources available today, the only computational approach which makes sense for detailed 3-D turbine airfoil design is a Navier-Stokes code. At present, in my opinion, the only reasonable use of a 3-D boundary layer code is to predict turbine airfoil heat transfer given Navier-Stokes-derived edge conditions. Boundary layer codes have demonstrated somewhat better consistency predicting heat transfer compared to current Navier-Stokes codes with 2-equation turbulence models.

The authors' present detailed flow observations based on test measurements in the Penn State turbine rig. The data essentially confirms known secondary flow behavior in modern turbine blading. Two questions come immediately to mind as I ponder the utility of these data to enhance future designs. First, does detailed data taken at a freestream turbulence level of 1 percent have any validity for turbine airfoils operating in the engine environment, where freestream turbulence levels can be as high as 10 percent? At high freestream turbulence levels, regions of laminar/transitional/fully turbulence flow are non-distinct, and extrapolation of these results to the actual engine environment can be misleading. Second, how useful are the results from a single point of operation? Given the viscous nature of the fluid mechanics discussed, to be used effectively in design one would at least like to know the sensitivity to Reynolds number, airfoil loading distribution, angle distribution, etc. Industry research budgets are such that companies can no longer afford to generate fundamental design research data internally, and as an industry we rely on government agencies and academia to further this cause. Presentation of data based on a single observation is not in itself useful. What is useful is the trend of the data based on variations in operation. I believe that developing knowledge of the data trends should be the focus of this type of research effort.

Authors' Closure

The authors would like to thank Dr. Hall for his comments on our paper. We are not advocating use of the boundary layer code in all regions of the flowfield. The Navier-Stokes code is most useful in predicting the three-dimensional effects in the regions of secondary flow, endwall flow, and tip clearance effects. As mentioned by the reviewer, the heat transfer predictions are done much better with the boundary layer code and that is because the boundary layer properties, including the nearwall regions, are more accurately predicted by the boundary layer code. This is the point we were trying to make. If the interest lies in the three-dimensional boundary layer not affected by the endwall flows, the boundary layer code should provide better results in the prediction of the viscous effects, losses, and local properties, as well as the transition and the heat transfer when compared to a Navier-Stokes code. The Navier-Stokes code accuracy is affected by artificial dissipation and grid density. The edge conditions could be derived by simpler methods; but we are not advocating that the boundary layer code could be used in the entire hub-to-tip region. These are not useful in situations where the boundary layer interaction, compressibility effects, and shock waves are present. But in many applications, such as the hydraulic turbines and steam turbines, the boundary layer

---

[1] Staff Research Scientist, Allison Engine Co., P.O. Box 420, Indianapolis, IN 46206-0420.

J. S. Shrimpton
Lecturer, Department of
Mechanical Engineering,
Imperial College of Science,
Technology and Medicine,
London, United Kingdom

A. J. Yule
Reader, Thermofluids Division,
Department of Mechanical Engineering,
UMIST,
Manchester, United Kingdom

Drop Size and Velocity Measurements in an Electrostatically Produced Hydrocarbon Spray

Liquid hydrocarbons are difficult to atomize electrostatically at practical flow rates due to their high resistivities and low concentration of charge carriers. However special "charge injection" techniques have been used in this investigation to produce combustible sprays of oils. An experimental investigation of the drop size and velocity distributions within a charged kerosine spray is presented, using a PDA system and photographic methods. Bimodal size distributions are found with a central core of larger drops or ligament formations near the nozzle surrounded by a sheath of smaller drops. Because of the bimodal character the concept of average diameter for the spray is difficult to apply so that there is little practical use defining a relationship between mean drop diameter and mean specific charge without a knowledge of a relationship between charge and size of individual drops. Examination of the velocity component distributions showed the processes which control the two-zone characteristics of the spray. The larger drops have a high inertia and were less deflected by the space charge force within the spray and it is argued that the larger drops possess a smaller specific charge compared with the smaller drops which reinforces the tendency for the large drops to remain along the spray centreline. For the smaller drops the converse is the case, to the extent that at low flow rates their trajectories have a negligible axial velocity component and recirculation toward the earthed injector body is observed.

Introduction

The process of liquid atomization may be enhanced by the use of electrostatic charge to impose an additional disruptive force on the liquid jet. For conducting and semi-conducting liquids charge transfer from electrode to liquid is accomplished by well-established contact or induction mechanisms (Law, 1978). Commercially viable systems (Bailey, 1986) using these principles are now in everyday use. Until recently it has been extremely difficult to charge, and hence electrostatically atomize, low conductivity liquids as characterized by hydrocarbon fuels. Such liquids had, until recently been electrostatically atomized at low flow rates (<50 mL/min) by using an antistatic additive to increase the electrical conductivity of the liquid to allow contact or induction charging methods to be feasible.

With the advent of the charge injection mechanism (Kelly, 1984; Turnbull, 1989) the electrical charging and purely electrostatic atomization of insulating liquids has now become a reality for practically useful flow rates. The mechanism relies on a submerged "field emission" electron gun, in this case a point electrode, which acts as a source of free excess charge with a typical charge mobility of 10^{-7} to 10^{-8} m^2/Vs in hydrocarbon oils. By immersing an electron gun directly into the liquid the problem of how to persuade charge to move off an electrode and into the liquid is solved by tailoring the velocity field, such that the charge carriers are extracted from the cathode surface. Free excess charge can be injected into the liquid without regard to its innate electrical conductivity or charge carrier density. The mechanism of charge transfer from electrode to hydrocarbon liquid is still currently under debate and there are few workers examining charged hydrocarbon spray dynamics with a view to applying the knowledge to a commercial system. Jido (1986, 1987) has examined the charging characteristics of kerosine/water emulsions. Bankston et al. (1988) noted qualitatively a dual zone spray when insulating fuel oils such as Jet-A and silicon oil were atomized; however, quantitative characterization of hydrocarbon oil sprays, produced "ab initio," electrostatically and without anti-static additives has not previously been reported.

At reasonable flow rates ($Q_L \geq 1$ mL/s) there has been some work (Yule et al., 1995) examining the drop size distribution within unadulterated charged hydrocarbon sprays but none regarding drop velocity as far as the authors are aware. Gomez and Tang (1991) have reported drop size distribution data in the range $1 \leq D \leq 40$ μm for heptane doped with an antistatic additive, effectively a semi-conducting liquid, at low flow rates. They noted a bimodal size distribution and that the drop size varied inversely with radial position. Dunn and Snarski (1992) and Grace and Dunn (1994) have made extensive studies of charged sprays of ethanol (a semi-conductor) in a series of papers. Their sprays were again in the $0 \leq D \leq 40$ μm size range at extremely high specific charge densities, up to $\rho_e = 210$ C/m^3, which acts to produce very high drop concentrations and the sprays more resembled aerosols with little penetration. Their drop diameter variations with radial position were less pronounced than reported by Gomez and Tang (1991).

The results in this paper are part of a study investigating the application of charge injection electrostatic atomizers for use in combustion systems of practically useful (>100 mL/min) flow rates. Drop size and velocity data are required to characterize the sprays, prior to combustion tests, and to provide an experimental data base for charged spray modeling, which can be used to optimize a combustion configuration.

Experimental

The description of the principles underlying the factors connecting nozzle design and electrical performance to flow rate

---

Contributed by the Fluids Engineering Division for publication in the JOURNAL OF FLUIDS ENGINEERING. Manuscript received by the Fluids Engineering Division November 14, 1996; revised manuscript received April 16, 1998. Associate Technical Editor: D. P. Telionis.

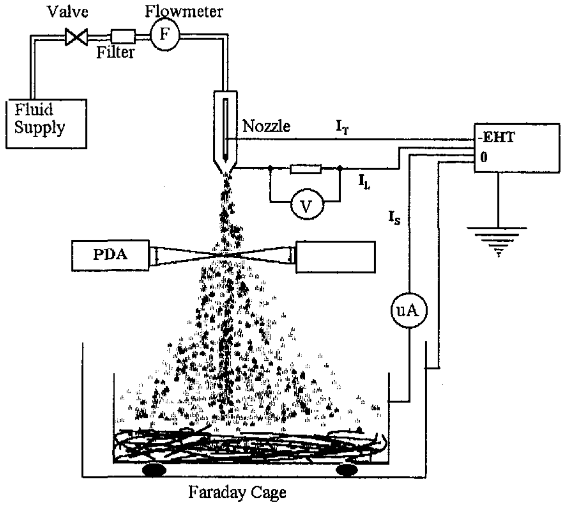

Fig. 1 Schematic of the apparatus

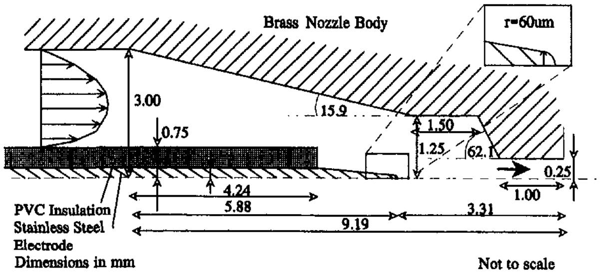

Fig. 2 Schematic of the atomizer nozzle

and liquid properties are covered elsewhere (Yule et al., 1995) as are the parameters controlling the maximum charge that may be carried by the spray (Shrimpton et al., 1995). These references also gave information regarding the design and performance of the nozzle used in the present work. A schematic of the experimental layout and electrical connections is given in Fig. 1 and a cross-section of the nozzle is shown in Fig. 2. The pipe work for the liquid supply was made of nylon with 6 mm inside diameter, and connections were also nylon snap-lock fittings to ensure effective electrical isolation of the nozzle from earth via the liquid feed. Liquid flow was produced using a reservoir, pressurised by compressed air, with a maximum safe working pressure of 0.6 MPa. The liquid flow was regulated by a standard needle valve. A Nupro 'F' Series in-line sintered metal filter was installed with a rated porosity of 7 μm. This served to reduce particulates and prevent small air bubbles from reaching the nozzle which could have been catalysts for electrical breakdown. No direct measurement was made of the total current (I_T) supplied to the cathode as it was considered unwise to "float" an instrument up to the required voltage. It was assumed that the liquid upstream of the nozzle acted as a perfect insulator and that the cathode and the anode (the nozzle body) were perfectly isolated from the rig supports and earth. It was therefore possible to calculate the total current (I_T) by summation of the two remaining current sinks. These were the current carried away by the spray (the spray current, I_S) and that which passed across the liquid inside the nozzle to the earthed inner surfaces of the nozzle body, the leakage current, I_L. The charged spray was captured by a metal drum, lined with wire wool to ensure a good, fast electrical response by keeping film thicknesses to an absolute minimum. In order to minimize errors arising from induced voltages the drum was mounted on PTFE blocks and surrounded by a Faraday cage. This was used to eliminate errors in the spray current from spurious induced voltages generated by external electric fields.

The results describe drop diameter, number, size distribution, and velocities for three flow rates, Q_L = 75, 120, and 180 mL/min. The magnitude of the mean spray specific charge, calculated from I_S/Q_L, for Q_L = 75 mL/min was ρ_e = 0.4 C/m^3, and for the two higher flow rates ρ_e = 0.5 C/m^3. The nozzle (Fig. 2) is loosely based on a design by Jido (1986) and has an orifice diameter of 0.5 mm. The liquid used is kerosine, in the form of a domestic heating fuel, marketed in the U.K. by Shell as "homeglow 28." It has a dynamic viscosity, μ_l $\approx$ 0.001 Ns/m^2, density, ρ_l = 780 kg/m^3 and surface tension, σ_T = 0.0235 N/m.

Measuring Technique. A Mie theory prediction code, STREU (INVENT), which assumes plane intensity beams was used to predict the optimal geometrical set up for the phase Doppler anemometer (PDA). As shown in Fig. 3, the linearity of the phase angle versus diameter for the Brewster angle position (70.6 deg off axis, for kerosine) was superior to the other off axis angles tested for $0 \le D \le 100$ μm. The 160 deg off-axis angle was examined since it was not known initially whether the larger drop diameter measurements ($D \approx 500$ μm) would be possible at the Brewster off axis angle. The erroneous phase jump in Fig. 3 for the 30 deg off-axis angle is due to the assumption of uniform, rather than Gaussian laser beam intensity profile within STREU. The phase angle versus diameter relationship was also found (not shown) to be linear for $100 \le D \le 527$ μm due to domination of 1st order refraction at the Brewster angle. Since there was no restriction on the optical access this configuration was adopted for all the results presented.

A DANTEC 3 detector, 1-D PDA system was used for all velocity and diameter measurements. The transmitting optics consisted of a 300 mW Argon ion laser of wavelength 514.5 nm stepped down to 100 mW. This was split by a DANTEC 55X modular LDA unit incorporating a Bragg cell, onto which a 600 mm focal length lens was mounted. This, using a beam separation of 40 mm gave a measuring volume diameter of 0.3 mm. The receiving optics consisted of the DANTEC 57X10 detector unit, again fitted with a 600 mm focal length lens. The separation of the detectors above and below the measurement volume was adjusted to allow a size range of $0 \le D \le 527$ μm to be measured. This coincides with drop size measurements of charged hydrocarbon sprays made previously (Yule et al., 1995) with a Malvern particle sizer. The authors are aware of the possible errors arising from Gaussian beam error and also the slit effect (Brenn et al., 1995). Due to the large size of many of the drops the frequency distributions of the large drop populations should be assessed qualitatively. Measurements were made assuming an axisymmetric jet, on a rectangular grid with $(z, r) = (0, 0)$ representing the atomizer orifice. Measure-

Nomenclature

D = drop diameter (μm)
D_{32} = sauter mean diameter (μm)
Q = drop charge (C)
Q_L = liquid flow rate (mL/min)
I_S = spray current (μA)
I_L = leakage current (μA)
I_T = total current (μA)
r = radial displacement (m)
u = axial drop velocity (m/s)
v = radial drop velocity (m/s)
z = axial displacement (m)
ρ_e = specific charge (C/m^3)
ρ_l = density (kg/m^3)
μ_l = dynamic viscosity (Ns/m^2)
σ_T = surface tension (N/m)

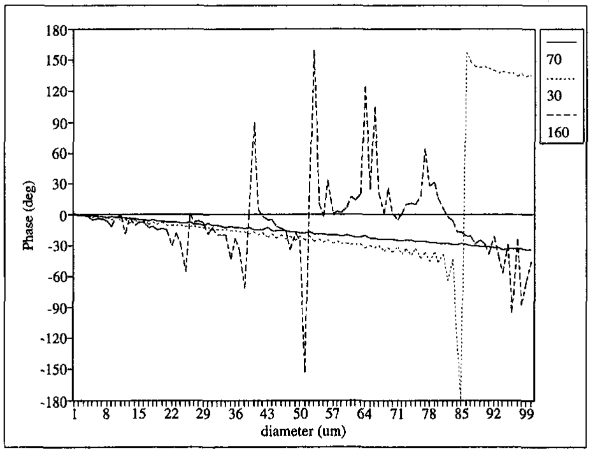

Fig. 3 Phase angle versus diameter for various off axis angles

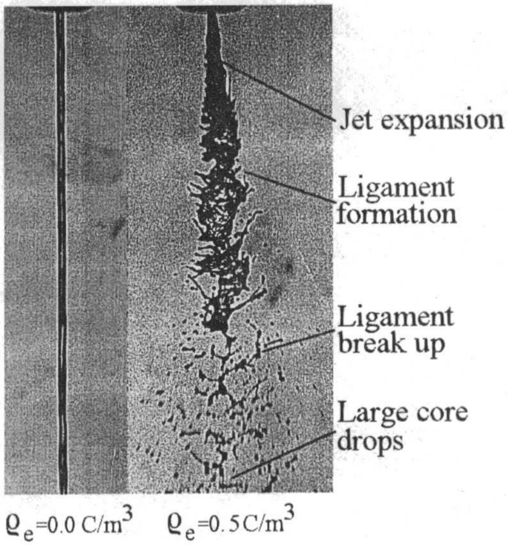

Fig. 4 Photograph of charged and uncharged hydrocarbon sprays, Q_L = 120 mL/min, d = 0.5 mm

ment locations of radial traverses were at 0.01 m intervals from the centreline up to 0.1 m and measurement planes were at 0.03 m axial intervals to 0.15 m downstream. The u component of the velocity was defined parallel to the spray centreline.

Due to the unavailability of the instrumentation required for measuring u and v velocity components simultaneously these components had to be measured separately. However, due to the narrowness of the size distributions and the extremely well-ordered nature of the drop trajectories in the spray repeatable correlation was obtained between diameter and u velocity. To measure the radial velocity components of the small drops the transmitter was rotated 90 deg so that the beams were in the horizontal plane and the polarization of the scattered light detected by the receiver was adjusted to 90 deg. For this arrangement the radial velocity components for the small drops could be easily extracted from the measurements since the large drops were low in number with respect to the small drops and their radial velocity components were small.

The validation limits in drop diameter were fixed for all measurements and typically gave a sample rejection rate which was approximately 20 to 30 percent of all samples obtained. The lack of sphericity was relatively common due to the combination of charge and relatively high viscosity, coupled with a relative velocity of the order of 10 m/s, which act to increase jet and droplet break-up time, and also the sphericity deviation that a drop in the process of breakup experiences.

Results: Droplet Diameter

Figure 4 shows the spray formation process which is peculiar to electrostatic atomization. The left-hand image shows an essentially unatomized kerosine jet from a 0.5 mm orifice at a flow rate Q_L = 120 mL/min with no electrostatic charge injection. The right-hand image shows the effect of a specific charge of 0.5 C/m^3 on the jet of the same flow rate. Clearly the atomization of the jet is wholly caused by the disruptive electrostatic forces. The PDA results can be interpreted in terms of three zones. These zones are (i), a central core of connected ligaments (which should not produce validated signals), (ii) large drops formed from the ligaments (which are measured only when a certain degree of sphericity is reached), and (iii) smaller drops which are dispersed more widely and which may be formed as satellites during ligament break up and/or from secondary break-up of the larger drops. Figures 5, 6, and 7 show the size distributions within the spray for Q_L = 75, 120 and 180 mL/min, at z = 0.15 m and r = 0. The distinctiveness and separation between two size classes of the bimodal distribution is profound and much more extreme than in the case of Gomez and Tang (1991), using doped heptane, or Dunn and Snarski (1991), using ethanol. This is thought to be due to the different electrical conductivity and charge mobility characteristics of the liquids. For conducting liquids, charge redistribution within the liquid is effectively instantaneous. This causes extremely short jet breakup lengths, spatially uniform sprays relative to the case presented here and $D \leq 50$ μm by virtue of high charge densities. In the case of insulating liquids, lower charge densities and slower moving charged species on the surface of the drops act to encourage the formation of bimodal sprays. It is argued that the charge cannot migrate rapidly enough to newly formed liquid surfaces during break up so that the central core drops, formed later during break-up are relatively lowly charged and thus larger. The character of the semi-conducting sprays of Gomez and Tang (1991) fall between these two extremes.

Not one data point was validated in the interval between the two size classes throughout the entire session for all flow rates and measurement positions. This remarkable fact would be unheard of for an uncharged spray, where a smooth, continuous Gaussian shaped frequency versus diameter curve would be expected. This highlights the fundamental effects that the charge exerts on jet and drop breakup in the case of liquid insulators. As shown in Fig. 4, photographic studies showed that the charged liquid jet radially expands as it emerges from the orifice and the jet surface quickly becomes distorted. The surface charge gives a localized increase in repulsive force between a protuberance and the rest of the jet and the protuberance is radially displaced away from the axial centreline to form a ligament. The dimensions and lengths of the radial ligaments should reduce for increase in surface tension, and reduction in viscosity. Many ligaments form and the surface area of the jet

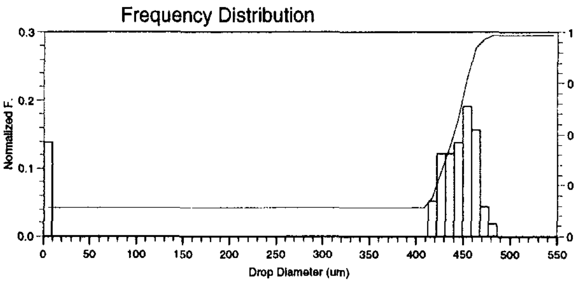

Fig. 5 Drop frequency distribution for Q_L = 75 mL/min, ρ_e = 0.4 C/m^3, z = 0.15 m, r = 0.00 m

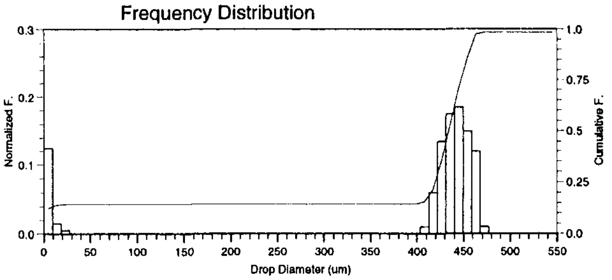

Fig. 6 Drop frequency distribution for Q_L = 120 mL/min, ρ_e = 0.5 C/m^3, z = 0.15 m, r = 0.00 m

is greatly increased. At this point the ligaments break up by symmetrical surface wave disturbances as predicted by Rayleigh (1879), assisted by surface charge which acts to reduce the surface tension. Clearly the PDA technique should not measure these ligaments. However, the drops formed from the ligaments will be measured when they have achieved a certain sphericity.

The Spray Central Core. The central core, as noted above was populated by two very different drop size ranges. One has a size range $0 \leq D \leq 50$ μm and the other a range $380 \leq D \leq 525$ μm. The invariance of the modal diameters was shown to be preserved under conditions of varying flow rate to a remarkable degree. The shape and positions of both distributions was found to be affected by the following factors.

1) At smaller axial displacements from the atomizer the number of large drops decreases due to an increase in the frequency of ligaments still present. This was detected by the PDA instrument by a sharp decrease in the validated samples for the large size class. The axial position for this decrease in the large drop population was also found to be a function of flow rate. At Q_L = 75 mL/min no large drops were detected for $z < 0.06$ m. However for Q_L = 180 mL/min the critical axial distance had increased to $z \leq 0.12$ m. This means that large "lumps" of liquid were too deformed, or still in the form of ligaments for measurement to be made near the nozzle.

2) Under conditions of increased flow rate the shape of the size distribution is modified and there are proportionally more smaller drops present relative to the large drop population in the central core. This accounts for the fact that an average diameter estimate, such as D_{32} reduces at larger specific charge as has been observed experimentally (Yule et al., 1995) using a Malvern particle sizer. Their data were obtained using Fraunhofer diffraction theory applied to light scattered from a cylindrical volume 9 mm in diameter and 40 mm in length. Unlike the PDA the Malvern instrument detects both ligaments and droplets but effectively represents the ligaments by numbers of drops with the same total projected area as the ligaments and gives diameters similar to the ligament diameters. As a result the gap in the PDA size distribution is filled with somewhat misleading data from the ligaments.

3) An additional factor regarding the average diameter estimation becomes relevant when the flow rate is increased. At Q_L = 75 mL/min the small drop size range is $0 \leq D \leq 10$ μm. At Q_L = 120 mL/min additional drops are reported at $D \approx 20$ μm. At Q_L = 180 mL/min the effect is more pronounced and a well-developed peak is evident centered around $D \approx 35$ μm. It is thought that the very small (satellite) drops ($D \approx 5$ μm) are the result of initial ligament disruption when the large drops are formed as noted above. The small drops of diameter $D \approx 35$ μm are thought to be the product of a charged drop disruption mechanism. Roth and Kelly (1983) have developed a charged drop disruption model for nonconducting liquids. It predicts that above a threshold specific charge a drop will break up in a nonrandom manner, defined by the conservation of energy between the initial (pre-break up) and final (post-break up) states. The post-breakup state consists of a large "residual" drop and a number of smaller "sibling" drops. The mass ratio of sibling to residual drops that Roth and Kelly (1983) found varies slightly with initial diameter and agrees with the results presented here and also with the experimental work of Taflin et al. (1989). The increased frequency of the (sibling) $D \approx 35$ μm drops at higher flow rates suggests that the increased drop deformation, due to aerodynamic effects, at higher injection velocities reduces the charged drop disruption threshold.

As the charge mobility of the liquid increases the difference between the maximum and minimum diameters of the droplet resulting from a particular charged drop break up should decrease. In the limit this could be a further reason for the different characterization of sprays of charged semi-conductors (weakly bimodal) and insulators (strongly bimodal). This is observed when the work of Grace and Dunn (1994), Gomez and Tang (1991), and the work presented here are compared.

The Spray Outer Sheath. The outer sheath was much more diffuse than the central core and in terms of the total liquid mass fraction essentially negligible relative to the central core. The data rates were extremely low near the periphery of the spray. Unlike the central core there was only one size distribution, which corresponded almost exactly to the small drop population within the central core. An extremely narrow size distribution was found for which $10 \leq D \leq 50$ μm in the outer sheath for all flow rates. The very small ($D \approx 5$ μm) satellite drops are not present in this region. This is thought to be due not to an absence of charge, but rather the high drag forces experienced by these drops quickly decelerates them and they tend to drift toward and terminate on the nearest earthed surface, the atomizer. Gomez and Tang (1991) report that their satellite drops (of mean size $D \approx 15$ μm) were deflected and form the outer sheath. They noted no evidence of charged drop break up however in further work (Gomez and Tang, 1994), charged drop disruption was deliberately triggered at drop charge levels comparable to those used in this work.

Results: Drop Velocity

The striking duality exhibited by the size analysis of charged hydrocarbon sprays was carried through into velocity measure-

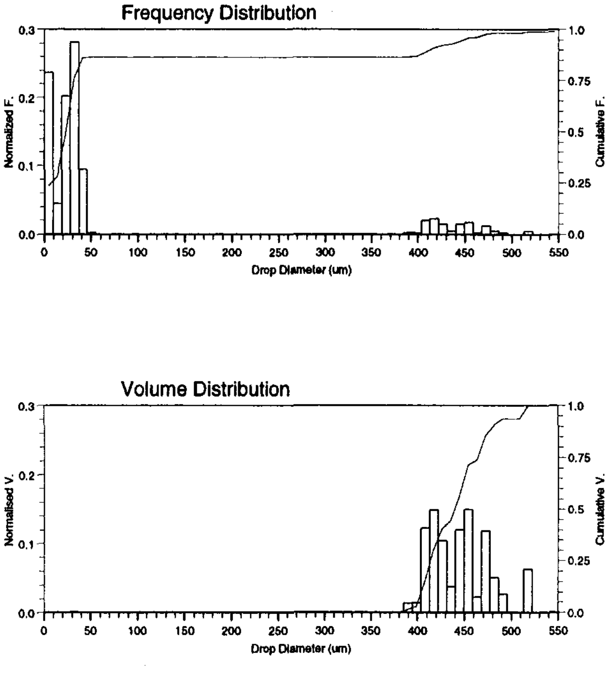

Fig. 7 Drop frequency distribution for Q_L = 180 mL/min, ρ_e = 0.5 C/m^3, z = 0.15 m, r = 0.00 m

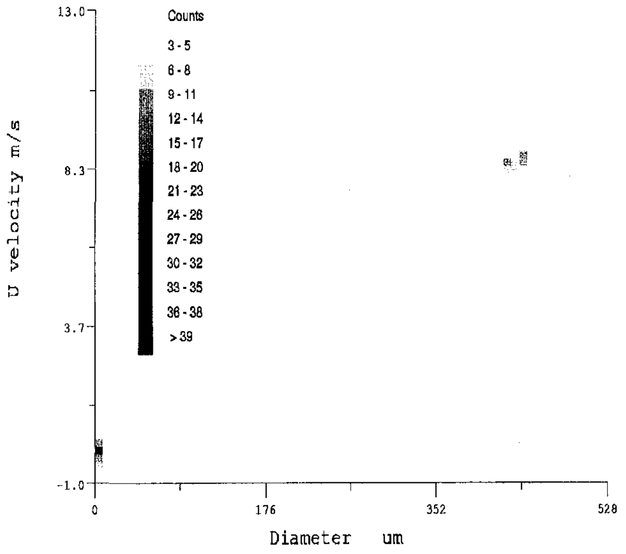

Fig. 8 Drop diameter versus axial velocity for Q_L = 120 mL/min, ρ_e = 0.5 C/m^3, z = 0.15 m, r = 0.03 m

ments using the PDA. This is shown in Fig. 8 where D and u are correlated for Q_L = 180 mL/min at z = 0.15 m and r = 0.03 m.

Velocity Correlation for 430 ≤ D ≤ 525 μm. The central core, possessing both large and small diameter drops shows some surprising results. The large drops exhibit axial velocity magnitudes in agreement with the average velocity in the liquid nozzle calculated from flow rate and orifice area. As noted above, the radial velocity component of the large drops was not recorded. An estimate may, however, be made from examining the maximum spray angle of the central core, defined by where large drop are detected. Results suggested that the spray angle, the boundary defined where no drops with D > 50 μm exist, is inversely proportional to flow rate and for Q_L = 75, 120 and 180 mL/min the central core spray angles are approximately 17, 9, and 6 deg, respectively. Comparison with an established (uncharged) spray plume correlation of Yokota and Matsuoka (Lefebvre, 1989) gives spray angles of 0.13, 0.16, and 0.20 deg for the same flow conditions. These values are much less than has been experimentally observed and highlights the degree of charged drop repulsion, even for the high inertia, low specific charge sprays considered here.

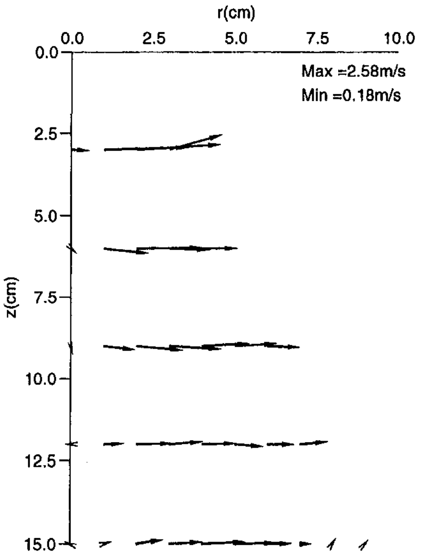

Fig. 9 Drop velocity vectors for 50 ≥ D ≥ 0 μm for Q_L = 75 mL/min, ρ_e = 0.4 C/m^3

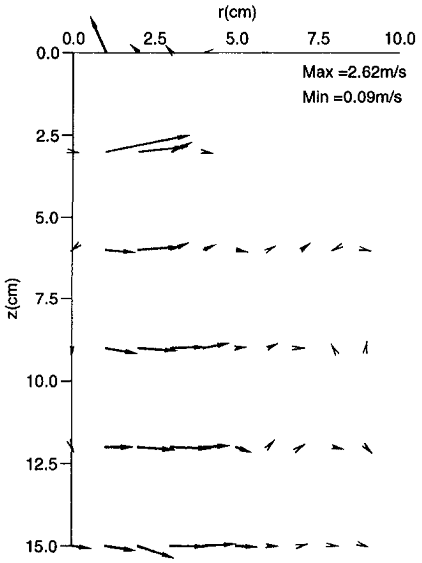

Fig. 10 Drop velocity vectors for 50 ≥ D ≥ 0 μm for Q_L = 120 mL/min, ρ_e = 0.5 C/m^3

Velocity Correlation for 0 ≤ D ≤ 50 μm. Figures 9, 10, and 11 show velocity vector plots for the smaller drops (0 ≤ D ≤ 50 μm) for Q_L = 75, 120 and 180 mL/min, respectively. It is noted that at Q_L = 75 mL/min the average radial velocity component of the drops in the central core along the spray centreline is zero. The axial component of all small drops at Q_L = 75 and 120 mL/min are relatively small throughout the spray. For these drops it is apparent that electrostatic forces completely dominate their trajectories and move the drops away from the charged central jet. At Q_L = 180 mL/min the axial velocity components of the drops in the vicinity of the central core become more significant. Figure 11 suggests that due to the larger drop number densities and higher drop momentum at the higher flow rate, more air is entrained, which in turn partially

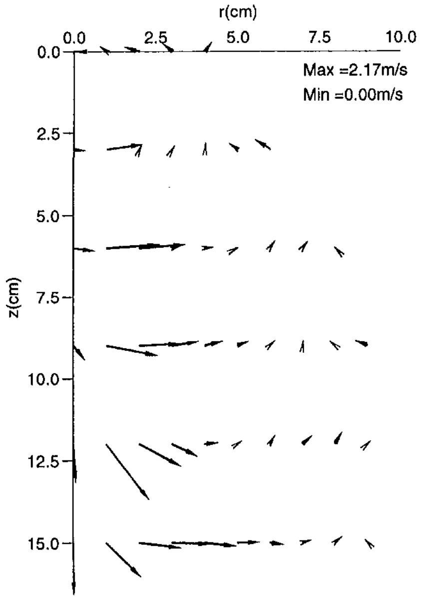

Fig. 11 Drop velocity vectors for 50 ≥ D ≥ 0 μm for Q_L = 180 mL/min, ρ_e = 0.5 C/m^3

entrains the smaller drops within the spray core. The largest radial components increase further away from the nozzle orifice at higher flow rates. This occurs because drops are created further downstream at higher flow rates. In the case of Q_L = 75 mL/min it can be seen that there is an initial burst of small drops created which undergo large accelerations and are recorded at $z = 0.03$ m and $z = 0.06$ m axial displacements. This is caused by the relatively high electric potential gradients in the vicinity of the earthed nozzle body due to high drop number, and hence charge, densities. At higher flow rates small drop formation occurs at larger axial distances and in regions of lower electric field gradient. A quantitative examination of the radial velocity components reveal that at all axial displacements the magnitudes tend to zero at $r = 0.0$ m and $r = 0.09$ m. Strong accelerations are observed in the interval from $r = 0.0$ m to the position of the peak radial component. The position of the peak radial component is a function of flow rate and varies from $r \approx 0.04$ m for $Q_L = 75$ mL/min to $r \approx 0.01$ m for $Q_L = 180$ ml/min.

Conclusions

The PDA instrument can be used to obtain sensible results on drop size from an electrostatically atomized hydrocarbon spray which undergoes a unique form of ligament disruption and break-up due the presence of electric charge on the jet surface.

The bimodal character of the size distribution is confirmed. One population has a size range $525 \geq D \geq 380$ μm and the other $50 \geq D \geq 0$ μm. This gives the spray a two zone character where both drop populations are present in a dense central core but only the latter is present in the surrounding diffuse sheath.

The striking difference exhibited by the size distributions with respect to an uncharged spray is carried into the velocity correlations. The large high inertia drops possess a high axial and low radial component. For the small drops the opposite is the case.

The results show the difficulties introduced when applying the PDA technique to sprays containing ligaments and non-spherical drops.

References

Bailey, A. G., 1986, "Theory and Practice of Electrostatic Spraying," *Atomization and Spray Technology,* Vol. 2, pp. 95–134.

Bankston, C. P., Back, L. H., Kwack, E. Y., and Kelly, A. J., 1988, "Experimental Investigation of Electrostatic Dispersion and Combustion of Diesel Fuel Jets," ASME *Journal of Engineering for Gas Turbines and Power,* Vol. 110, pp. 361–368.

Brenn, G., Domnick, J., Durst, F., Tropea, C., and Xu, T.-H., 1995, "Phase Doppler Arrangements with Minimized Gaussian Beam Effect and Slit Effect," *20th Anniversary of PDA Symposium,* 24th March, Universität Erlangen-Nürnberg, Erlangen, Germany.

Dunn, P. F., and Snarski, S. R., 1992, "Droplet Diameter, Flux and Total Current Measurements in an Electrohydrodynamic Spray," *Journal of Aerosol Physics,* Vol. 71, Part 1, pp. 80–84.

Gomez, A., and Tang, K., 1991, "Atomization of Quasi Mono-Disperse Electrostatic Sprays of Heptane," ICLASS-91, Gaithersburg, MD, USA, pp. 805–812.

Gomez, A., and Tang, K., 1994, "Charge and Fission of Droplets in Electrostatic Sprays," *Physics of Fluids A,* Vol. 6, pp. 404.

Grace, J. M., and Dunn, P. F., 1994, "Droplet Motion in an Electrohydrodynamic Fine Spray," *Proceedings of ICLASS-94,* Rouen, France, pp. 1001–1007.

Jido, M., 1986, "Study of Electrically Combined Droplet, Part 1," *Journal of Mechanical Engineering Laboratory,* Vol. 40, Part 5, pp. 224–233.

Jido, M., 1987, "Study of Electrically Combined Droplet, Part 2," *Journal of Mechanical Engineering Laboratory,* Vol. 4, Part 3, pp. 32–40.

Kelly, A. J., 1984, "The Electrostatic Atomization of Hydrocarbons," *Journal of the Institute of Energy,* pp. 312–320.

Law, S. E., 1978, "Embedded Electrode Electrostatic Spray Charging Nozzle," *Trans. ASME,* pp. 1096–1104.

Lefebvre, A. H., 1989, *Atomization and Sprays,* Hemisphere, New York, p. 296.

Rayleigh, Lord, 1879, "On the Capillary Phenomena of Jets," *Proceedings of the Royal Society,* Vol. 29, pp. 71–97.

Roth, D. G., and Kelly, A. J., 1983, "Analysis of the Disruption of Evaporating Charged Droplets," *IEEE Transactions of the Industrial Applications Society,* Vol. 1A-19, 5, pp. 771–775.

Shrimpton, J. S., Yule, A. J., Watkins, A. P., Balachandran, W., and Hu, D., 1995, "Partial Breakdown of Electrostatically Atomized Hydrocarbon Sprays," ILASS-95, Nurnberg, Germany, pp. 201–210.

Talfin, D. C., Ward, T. L., and Davis, E. J., 1989, "Electrified Drop Fission and the Rayleigh Limit," *Langmuir,* Vol. 5, pp. 376–384.

Turnbull, R. J., 1989, "Self Acceleration of a Charged Jet," *IEEE Transactions of the Industrial Applications Society,* Vol. 25, Part 4, pp. 699–704.

Yule, A. J., Shrimpton, J. S., Watkins, A. P., Balachandran, W., and Hu, D., 1995, "Electrostatically Atomized Hydrocarbon Sprays," *Fuel Journal,* Vol. 74, pp. 1094–1103.

Tatsuyuki Okamoto
Associate Professor.

Toshimi Takagi
Professor.

Department of Mechanical Engineering,
Faculty of Engineering, Osaka University,
2-1, Yamada-Oka, Suita, Osaka, 565, Japan

Toshikazu Kaji
Miyanodai Technology Development Center,
Fuji Photo Film Co., Ltd.,
798, Miyanodai, Kaisei-Machi,
Ashigarakami-gun, Kanagawa, 258 Japan

Katsunori Shimazaki
Maintenance Division,
All Nippon Airways Co., Ltd.,
3-2-5, Kasumigaseki, Chiyoda-ku, Tokyo,
100 Japan

Kenji Nakanishi
Printing and Reprographic Systems Group,
Sharp Corporation,
492, Minosho-cho, Yamato-Koriyama,
Nara, 639-11 Japan

Studies on the Behavior of Droplets and the Air Flow in a Hollow-Cone Spray

Experimental and numerical investigations are made on the behavior of droplets in a hollow-cone spray paying attention to the liquid sheet formed at the orifice of pressure-swirl atomizer. Simultaneous measurements of droplet sizes and velocities are made by phase-Doppler technique and numerical simulations are carried out based on the transient Eulerian equations for the gas and the Lagrangian equation for the droplets, taking account of the liquid sheet formed at the atomizer orifice. It is shown that the simulation gives good predictions by incorporating the existence of the liquid sheet. The predicted results indicate that the movement of the liquid sheet induces a strong air stream which acts as a strong side wind against the droplets immediately after breakup. This air stream selectively transports small droplets toward the central region and plays an essential role in the classification of droplets by size. Accordingly, the existence of the liquid sheet is significant for the characteristics of droplet dispersion and it should not be neglected in the prediction of hollow-cone spray flows. In addition, the shape of the liquid sheet is theoretically computed based on the simplified equations of motion. The comparison between the theoretical computation and the experimental result suggests that the surface tension of liquid is predominant in determining the shape of the liquid sheet.

1 Introduction

Dispersion of fuel droplets into the air has serious effects on the combustion characteristics of spray flames. Numerous studies (Lefebvre, 1989a; Bayvel and Orzechowski, 1993; Chigier, 1983; Chigier, 1991) have been made on the structure of atomizers, the fluid flow in nozzles, the mechanism of disintegration, and the spray characteristics. It is well known that the hollow-cone pressure-swirl atomizer fulfills fine atomization, and its radial liquid distribution is also preferable for combustion applications (Lefebvre, 1989b).

Near the orifice of the pressure-swirl atomizer, the conical liquid sheet persists over the practical range of the liquid injection pressure, though its shape varies through onion, tulip, and conical shape with a rise of the liquid injection pressure (Lefebvre, 1989b). Theoretical approaches have been made on the disintegration of conical liquid sheets (Eisenklam, 1976; York et al., 1953), but the actual conical liquid sheets break up at shorter distance than the theories predict, probably due to the destabilizing effect of the radius of curvature (Lefebvre, 1989c). The theory about the disintegration of the conical liquid sheet is not established. Consequently, there has been no numerical simulation of hollow-cone spray that incorporated the existence of the liquid sheet. In the numerical simulation of hollow-cone sprays, however, the neglect of the existence of the liquid sheets probably leads to an inadequate predictions of the air flow and the dispersion of droplets, because the existence of the liquid sheet must introduce complex air flow including recirculations and such air flows must influence the behavior of droplets.

El Banhawy and Whitelaw (1980) compared the predicted profiles of the time-mean velocity and temperature of the gas in a hollow-cone spray flame with the experimental results, and pointed out that the initial conditions of the spray seriously influenced the results of predictions. Nevertheless, the initial conditions were uncertain. It has been difficult in numerical simulations to give adequate initial conditions to the droplets in a hollow-cone spray. In recent years, however, advanced measuring instruments, phase-Doppler system for example, made it possible to provide valuable informations about the behavior and structure of sprays (Rosa et al., 1993; Presser et al., 1993; Li et al., 1992; McDonell et al., 1992; Edwards and Rudoff, 1990; Presser et al., 1990; McDonell and Samuelsen, 1988). Therefore, comparison between numerical simulations and experimental results can now be useful for the detailed evaluation of simulations and for the estimation of the initial conditions of the spray.

In this paper, the behavior of droplets in a hollow-cone spray is investigated experimentally together with the shape of the liquid sheet formed at the atomizer orifice. Subsequently, numerical simulations of this spray flow are carried out by incorporating the existence of the liquid sheet and these results are compared with the experimental results paying attention to the air flow and the dispersion of droplets. The results of simulations indicate that the air stream induced by the movement of the liquid sheet plays an essential role in the dispersion of droplets. The induced air stream promotes the classification of droplets by size.

Angle of the spray cone influences the dispersion of droplets into the air. Though a recent study (Chen et al., 1992) examined the factors affecting the spray angle of the hollow-cone spray, it did not include the effect of the surface tension of liquid. In addition, previous experiments (Giffen and Massey, 1950) and theoretical studies (Rizk and Lefebvre, 1985) showed that the surface tension hardly influenced the angle of the spray cone. On the other hand, it has been described in another book that the liquid sheet formed at the atomizer orifice displays the onion

---

Contributed by the Fluids Engineering Division for publication in the JOURNAL OF FLUIDS ENGINEERING. Manuscript received by the Fluids Engineering Division July 5, 1994; revised manuscript received April 10, 1996. Associate Technical Editor: M. W. Reeks.

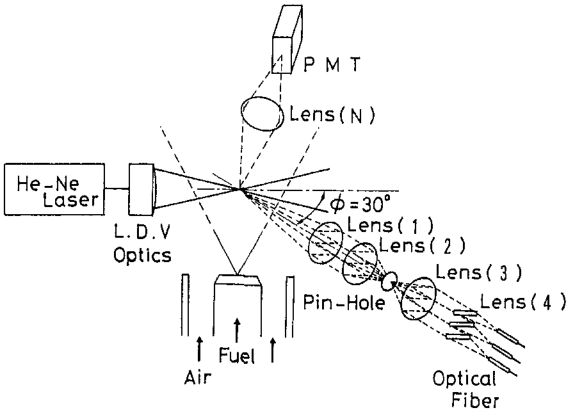

Fig. 1 Schematic diagram of the experimental apparatus

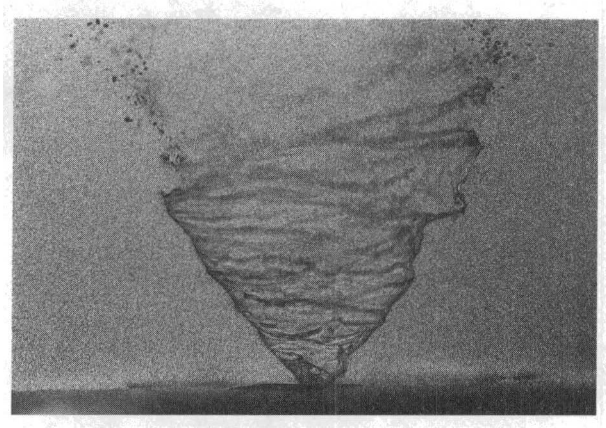

Fig. 2 An example of instantaneous shape of the liquid sheet formed at the orifice

shape due to the surface tension (Lefebvre, 1989b). In this paper, the effect of the surface tension and of the other factors affecting the shape of the liquid sheet is examined. The results suggest that the surface tension of liquid is predominant in determining the shape of the liquid sheet.

2 Spray Flow Field and Experiments

The outline of the experimental apparatus used in this study is shown in Fig. 1. A pressure-swirl atomizer (Delavan type-A, 0.5 GPH, 60 deg nominal spray angle) is set up vertically upward on the nozzle support (20 mm outer diameter). Water is injected from this atomizer. The liquid injection pressure is 0.686 MPa. This injection pressure is almost the same as the recommended value (100 psi). The flow rate of water is 4.5 $\times$ 10^{-7} m^3/s (27 cm^3/min). A free air jet having an almost flat velocity distribution (3.5 m/s) issues out through the coaxial air nozzle (40 mm inner diameter). The tip of the spray nozzle is flush with that of the air nozzle. Hereafter, x denotes the axial distance from the atomizer orifice and r denotes the radial distance from the axis of symmetry.

To investigate the behavior of the droplets, simultaneous measurements of size and velocity are made using a phase-Doppler anemometer. The light source is a He-Ne laser (35 mW light power). The throat diameter of laser beams at the measuring point is 300 μm. The receiving optics is at $\phi = 30$ deg of observing angle. The integrated lens (4) in the receiving optics forms the window array for three detectors methods. It is well known that good resolution and a wide dynamic range can be achieved with three detectors in a particle sizing system. In the present optical setting, the phase sensitivity against droplet diameter is approximately 7 deg/μm. The dynamic range of particle sizing sufficiently covers the minimum and maximum diameters found in the present experiment. Three Doppler signals from a droplet are digitized and stored in the memories, and then, the stored wave data are processed by a personal computer equipped with a DSP transputer. The time length of data transferred to the DSP is adjusted according to the frequency of Doppler signal. As a result, the dynamic range of velocity measurement is 0.03 m/s ~ 25 m/s. The lens (N) and the photo multiplier tube (PMT) behind that lens can count the frequency of droplets that pass through the measuring volume by detecting the light scattered by the droplets.

Figure 2 shows an example of the instantaneous shape of the liquid sheet found at the orifice of the pressure-swirl atomizer operating under the condition mentioned above. This photograph was taken with a flash of the Nd-YAG pulse laser. For determining the average shape of the liquid sheet, many similar photographs were taken. On each photograph, the radial position of the ridge of the liquid sheet was measured in several cross sections specified at regular interval of 0.5 mm. From the obtained data, the probability distribution of radial position of the liquid sheet in each cross section is deduced and is displayed as histogram in Fig. 3. The radial position is classified by the class width of 0.5 mm. The base line of each histogram corresponds to the axial location of the cross section and the height of each vertical bar is proportional to the probability. The round marks in Fig. 3 indicate the breakup points on the ridge of the liquid sheet. The curve in Fig. 3 indicates the average shape of the liquid sheet by smoothly connecting the average radial positions in different cross sections. The averaged location of the breakup point is inferred to be $x = 3$ mm and $r = 2.2$ mm. We define the angle of inclination of the liquid sheet as the angle from the vertically upward line. The angle of inclination of the averaged shape of the liquid sheet is 45 deg at the atomizer orifice, and the angle of inclination becomes small up to 20 deg at $x = 3$ mm.

3 Numerical Simulation Method

Various kinds of numerical simulation methods for predicting spray flows have been developed (Sirignano, 1993; Faeth, 1987). Here, we carry out numerical simulations and compare the predicted results with the experimental results. The fundamental equations are the transient Eulerian equations for the compressible gas in cylindrical coordinates and the Lagrangian equation for the droplets (O'Rourke, 1981). Evaporation is

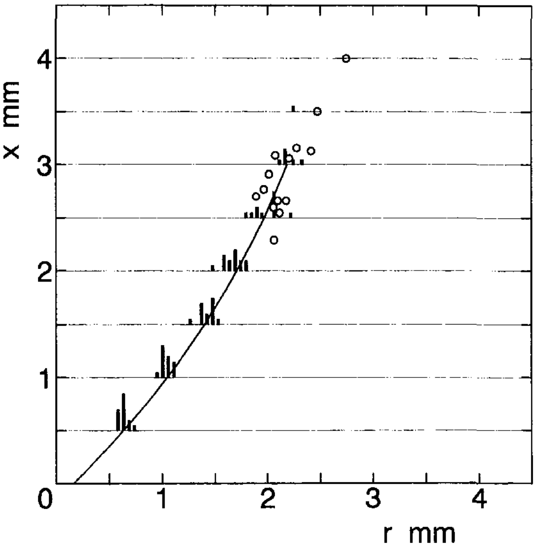

Fig. 3 Probability distribution of radial position of the ridge of the liquid sheet and the average shape of the liquid sheet

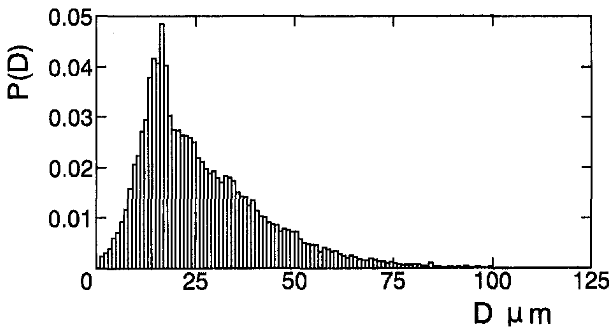

Fig. 4 Initial size distribution of droplets deduced from the measurements in a cross section of x = 15 mm

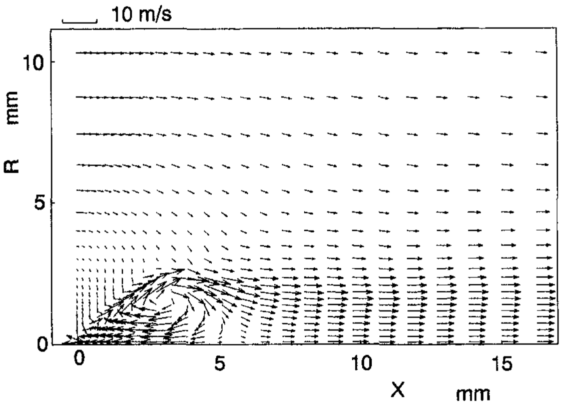

Fig. 5 Predicted velocity field of the air under the existence of liquid sheet and droplets

neglected in the present simulation. Therefore, the fundamental equations include (1) the conservation equations of mass, momentum, and energy for the gas, (2) the $k - \epsilon$ transport equations for turbulent kinetic energy and its dissipation rate, (3) the exchange rate of momentum between gas and droplets, and (4) the state equation of the gas.

Other auxiliary equations are (1) the equation to determine the drop collision frequency and the equation to determine the coalescence probability of droplets (O'Rourke, 1981) and (2) the equation to determine the secondary breakup of droplets.

All equations are solved in fully coupled form as a transient problem from the initiation of injection, until steady state is attained. After that, droplets are sampled numerically for collecting the information about velocity and size of the droplets that pass through the control volume.

The computer code is based on the computational method by O'Rourke (1981) and it has been confirmed that the code gives satisfactory predictions about transient sprays (Takagi, 1991). That computer code is extended in the present study to deal with the existence of the liquid sheet. The liquid sheet is treated as a moving thin wall. This wall prevents the air from passing through it as the realistic liquid sheet does. The average shape of the liquid sheet determined by experiments (refer to Fig. 3) is incorporated as given boundary conditions. The domain of computation was composed of numerous rectangular cells, in the original code (O'Rourke, 1981). To incorporate the liquid sheet easily into rectangular cell systems, cell size is adjusted so that the corners of the relevant cells coincide with the average shape of the liquid sheet. Therefore each relevant rectangular cell is divided into two right-angle triangles, for which conservation law is applied considering the fluxes on only two sides except the hypotenuse. The boundary conditions on the liquid sheet are handled with the wall function method. In that situation, a resultant velocity vector composed of two velocity components existing on two orthogonal sides of right-angle triangle is naturally parallel to the liquid sheet, due to the principle of continuation. Wall function method is applied by using this resultant velocity.

The speed of the liquid sheet is assumed to be 16 m/s and the initial conditions of droplets are assumed as follows. All droplets start from the tip of the liquid sheet, that is, x = 3 mm and r = 2.2 mm. The average value of the initial speed of droplets is 16 m/s and their probability distribution fit the normal distribution whose standard deviation is 2.5 m/s. The principal direction of the initial velocity of droplets is 20 deg in half cone angle. The initial direction of individual droplets fluctuates according to the normal distribution whose standard deviation is 10 deg. These values of average speed and principal direction and the standard deviations are estimated from the experiment. The initial size distribution of droplets was deduced from the measurements of size distribution and frequency of droplet passage at various radial locations in a cross section of x = 15 mm. Figure 4 illustrates the initial size distribution deduced in such way.

4 Behavior of Droplets

Figure 5 shows the predicted velocity field of the air under the existence of the liquid sheet and the spray droplets whose input conditions are as mentioned above. A recirculation zone is formed inside the cone of the liquid sheet. High velocity values are found on both sides of the liquid sheet. This indicates

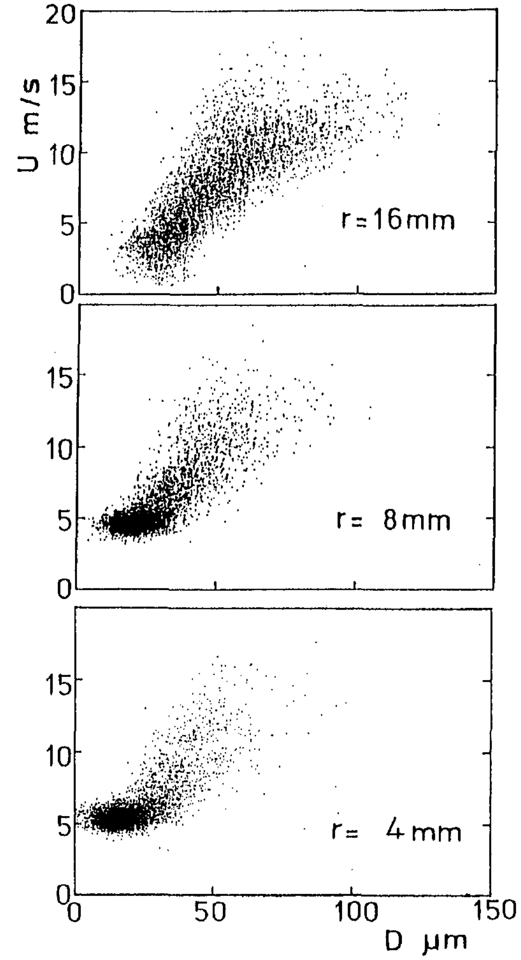

Fig. 6 Experimental correlation between particle diameter and axial velocity component of droplets that pass through the measuring points in a cross section of x = 30 mm

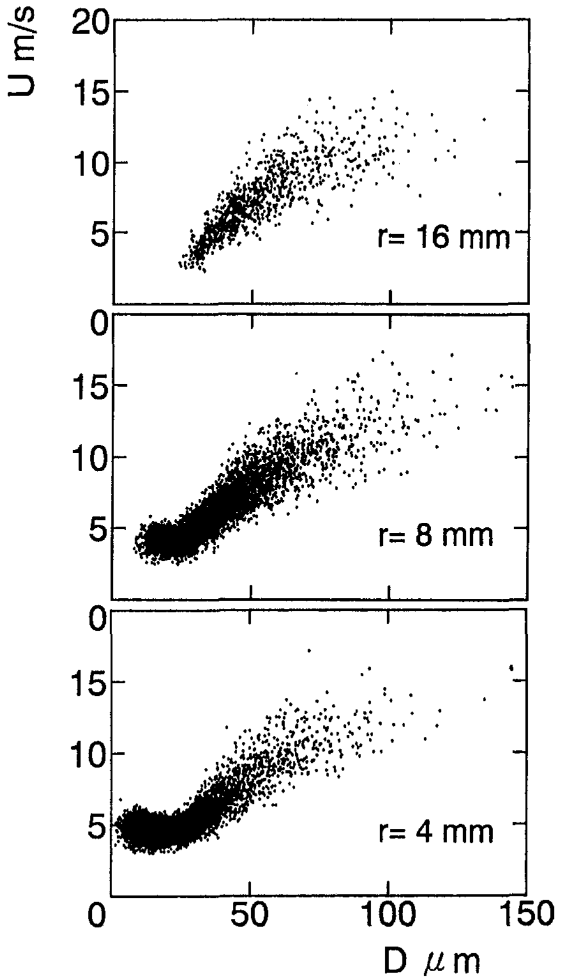

Fig. 7 Predicted correlation between particle diameter and axial velocity component of droplets, corresponding to Fig. 6

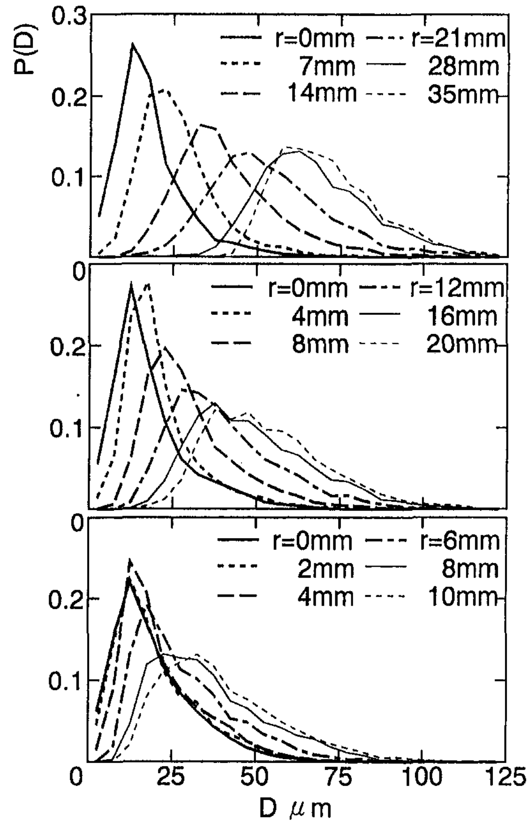

Fig. 8 Experimental size distribution of droplets that pass through the measuring points. Upper, middle, and lower parts correspond to the cross section of x = 15, 30, and 50 mm, respectively.

that the movement of the liquid sheet induces strong air stream on both sides of the liquid sheet. The air stream induced on the outside of the liquid sheet turns inward as it goes beyond the tip of the liquid sheet. Then, it flows into the rear of the recirculation zone. This air stream from the outside of the liquid sheet acts as a strong side wind for the droplets immediately after disintegration.

Figure 6 illustrates the experimental correlation between particle diameter and axial velocity component of the droplets that pass through the measuring points in a cross section of $x = 30$ mm. This figure contains the examples of correlation observed in the central ($r = 0$ mm), middle ($r = 8$ mm), and edge region ($r = 16$ mm) of the spray. These data are obtained using a phase-Doppler anemometer mentioned above. One dot on the figure corresponds to one droplet. Each measuring point contains 5000 size-velocity data pairs. These correlation data show the following tendencies. Size and axial velocity component of droplets are correlated fairly well. The larger droplets have higher axial velocity component and greater variance of axial velocity component than the smaller droplets. These tendencies are recognizable in all three positions referred to in Fig. 5, irrespective of radial distance from the central axis. On the central axis, small droplets (≤ 25 μm) represent a large proportion of the total number of droplets passing through that location, and the variance of velocity of such small droplets is comparatively small. As a result, a remarkably dense crowd of dots is found. On the other hand, such characteristics are not so obvious in the edge region of the spray. In addition, the above-mentioned tendencies can be noticed also in an upstream cross section of $x = 15$ mm, and also in several downstream cross sections up to $x = 70$ mm, though the data are not shown here.

Figure 7 shows the predicted correlation between size and axial velocity component of the droplets observed at the locations corresponding to Fig. 6. The above-mentioned tendency about the experimental correlation between droplet size and axial velocity component can be found also in these predicted results. For example, the larger droplets have the greater variance of axial velocity component as shown in Fig. 7.

The initial conditions of droplet velocity affect the relationship between droplet size and the variance of axial velocity component. If it is assumed that all droplets have the same initial velocity (both speed and direction) at the breakup, such trial computation gives greater variance of axial velocity component to small droplets than to large droplets. This tendency found in the prediction based on such very simple spray input condition is quite the opposite of the experimental results shown in Fig. 6. Consequently, it can be said that such simplified spray input condition is inadequate for predicting the relationship between droplet size and the variance of velocity.

Figure 8 shows the experimental size distributions of the droplets passing through each radial position. Droplets is classified by regular intervals of 5 μm and the size distributions are displayed in terms of number fraction. The positions of measurement are placed at regular intervals in each cross section. The most inner position is placed on the central axis and the most outer position approximately corresponds to the edge of the nominal spray cone angle in each cross section. The size distribution measured over three cross sections (x = 15, 30, and 50 mm) is displayed in Fig. 8.

Paying attention to the size distributions in the cross section of $x = 15$ mm, the size distribution on the central axis ($r = 0$ mm), and that in the edge region ($r = 8$ mm, for example)

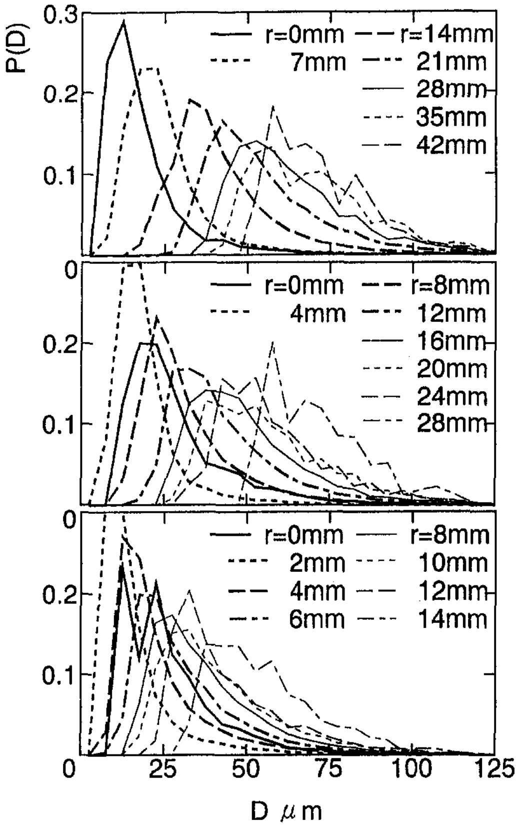

Fig. 9 Predicted size distribution of droplets, corresponding to Fig. 8

overlap each other over a fairly wide range of droplet size. On the other hand, in the cross section of x = 50 mm, the size distribution on the central axis (r = 0 mm) and that in the edge region (r = 28 mm) scarcely overlap each other. Thus, the difference in size distribution profile between the central and edge regions becomes more and more clear while the droplets penetrate toward the downstream cross section. In other words, classification of droplets by size proceeds with the distance from the atomizer.

Figure 9 shows the predicted size distribution at the locations corresponding to Fig. 8. We pay attention to the diameter at which probability takes the maximum value and the diameter at which probability starts to rise steeply. These characteristic diameters show almost the same value both in the experimental and numerical results. Thus, the numerical simulation can predict well the classification of droplets by size.

For examining the effect of the existence of the liquid sheet on droplet dispersion, trial computation is carried out, neglecting the existence of the liquid sheet. In this trial computation, the spray flow under the steady state is computed, as the first stage, based upon the assumption that injected liquid is already broken up into droplets at the atomizer orifice. In the next stage, the behavior of droplets is computed and the numerical sampling of droplets is carried out in the cross section of x = 15 mm. It is assumed for numerical sampling of droplets that the all droplets start from the average breakup point (x = 3 mm, r = 2.2 mm), and the initial conditions of droplets (size distribution, average velocity, and variance of velocity) are the same as the main computation.

Figure 10 shows the size distribution of droplets in the cross section of x = 15 mm obtained in this trial computation neglecting the liquid sheet. Comparing this result with the corresponding results obtained from the main computation incorporating the existence of the liquid sheet (the lowest part of Fig. 9) and the experimental result (the lowest part of Fig. 8), the classification of droplets by size is much more retarded in this trial computation than in the experimental results or in the main computation.

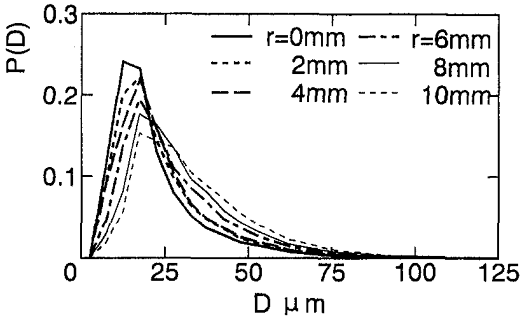

Fig. 10 Size distribution of droplets in a cross section of x = 15 mm obtained in the trial computation neglecting the liquid sheet

The air flow field predicted in this trial computation indicates that the air flows inwardly through the opening among droplets even at the vicinity of the atomizer orifice where the liquid sheet would exist in the realistic situation. This air entrained at the vicinity of the atomizer orifice flows along the central axis. Therefore, the air flowing near the starting point of droplets (x = 3 mm, r = 2.2 mm) does not go up to the vicinity of the central axis. As a result, the side wind near the starting point of droplets is much weaker than the case incorporating the existence of the liquid sheet as illustrated in Fig. 4. Tracing the predicted locus of droplets of various sizes about both computations considering or neglecting the liquid sheet, it is noticed that the strong air stream induced by the movement of the liquid sheet selectively carries smaller droplets into the vicinity of the central axis and plays an important role in the classification of droplets by size. Consequently, it can be said that the classification of droplets by size, especially near the starting point of droplets, is not properly predicted if the existence of the liquid sheet is neglected.

Figure 11 shows the radial profiles of the size-classified mean axial velocity of droplets. The experimental results indicate the following tendency. The averaged axial velocity of small droplets takes the maximum value at the central axis and decays monotonously toward the outer region. This tendency can be found in all cross sections. Even large droplets show similar tendency in downstream cross section. The larger droplets have

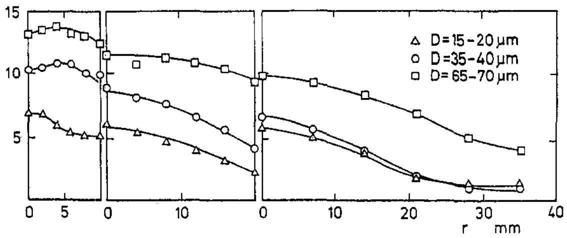

Fig. 11(*a*) Experimental data

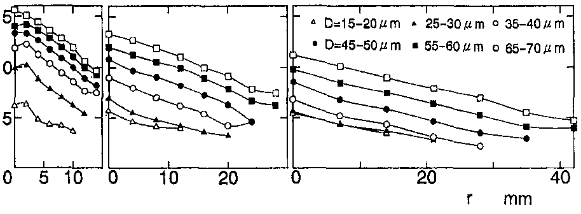

Fig. 11(*b*) Predicted results

Fig. 11 Radial profiles of the size-classified mean axial velocity of droplets. Left, middle, and right parts correspond to the cross section of x = 15, 30 and 50 mm, respectively.

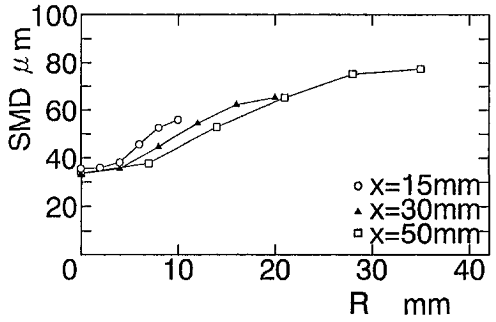

Fig. 12(*a*) Experimental data

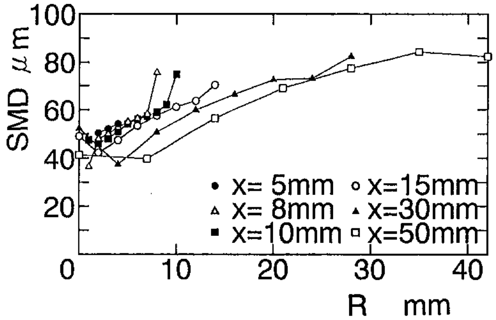

Fig. 12(*b*) Predicted results

Fig. 12 Spatial distributions of Sauter mean diameter of the droplets that pass through the measuring points

higher velocity than the smaller droplets. In a cross section of $x = 50$ mm, droplets belonging to two size classes of $D = 35 \sim 40$ μm and $D = 65 \sim 70$ μm have almost the same value of mean axial velocity. The corresponding numerical results show the same tendency and are in quantitative agreement with the experimental results.

Figure 12 shows the spatial distributions of Sauter mean diameter of the droplets that pass through the each location. Sauter mean diameter increases with the radial distance from the central axis. This tendency can be noticed in every cross section. The predicted results correspond closely with the experimental results.

5 Shape of Liquid Sheet

As shown in Fig. 3, the ridge of the averaged shape of the hollow liquid sheet is not straight and the cone angle of the liquid sheet decreases with the distance from the atomizer orifice. The reason for the decrease in cone angel can probably be attributed to the effects of (1) the surface tension of liquid, (2) the static pressure applied on both sides of the liquid sheet, and (3) the deceleration of the liquid sheet due to the shear stress exerted from the adjacent air. Though it is hardly possible to measure the static pressure applied on the inner surface of the liquid sheet and the shear stress on the liquid sheet surface exerted from the adjacent air, the numerical simulations carried out in this study let us know the distributions of such pressure and shear stress.

Here, the theoretical shape of the liquid sheet is calculated incorporating these three effects. At the beginning of the theoretical approach, it is assumed for simplicity that the shape of the liquid sheet is symmetrical with respect to the central axis. Then, the motion of a fluid element is discussed within the plane of symmetry.

The equation of motion for a fluid element is deduced as follows. The theory of strength of materials applied to a conical thin shell vessel gives the relationship between the tensional stress of shell material in tangential direction (hoop stress) and the net internal pressure applied on the conical shell.

$$\sigma = \frac{P\cdot R}{h\cdot\cos\theta} \tag{1}$$

Here, σ is the hoop stress, P is the net internal pressure of the vessel, R is the radial distance from the central axis to the shell, h is the thickness of the shell, and θ is the half cone angle of the vessel. Although the tensional stress never appears in the liquid, the effect of surface tension of a conical thin liquid sheet is similar to that of the hoop stress of a conical thin shell vessel. Therefore, it is convenient to covert the surface tension to an imaginary hoop stress. As the surface tension appears on both sides of the liquid sheet, the surface tension on the liquid sheet σ_s is related to imaginary hoop stress σ_{im} as follows.

$$2\sigma_s = h\cdot\sigma_{im} \tag{2}$$

Substituting σ in Eq. (1) by σ_{im} in Eq. (2), the effect of surface tension σ_s can be converted to an internal pressure as follows.

$$P = \frac{2\sigma_s\cdot\cos\theta}{R} \tag{3}$$

This internal pressure, however, is the imaginary pressure that would balance with the effect of surface tension. In actuality, the effect of surface tension acts like an external pressure and gives the fluid element inward acceleration perpendicular to the liquid sheet. Also, the difference of the static pressure on both sides of the liquid sheet leads to the acceleration in the same direction. Denoting the density of the liquid by ρ and the static pressure applied on the outer and inner surface by P_{out} and P_{in}, respectively, the inward acceleration perpendicular to the liquid sheet α_n is given by

$$\alpha_n = \frac{1}{\rho\cdot h}\left(\frac{2\sigma_s\cdot\cos\theta}{R} + P_{out} - P_{in}\right) \tag{4}$$

Second, the shear stresses exerted from the adjacent air give the fluid element the acceleration parallel to the tangent line. Internal stress due to the liquid viscosity also induces acceleration in the same direction. Denoting the distance along the liquid sheet by s, time by t, the shear stress exerted in the direction of positive s by τ and the speed of the fluid element by u, the acceleration along the liquid sheet α_s is given as follows,

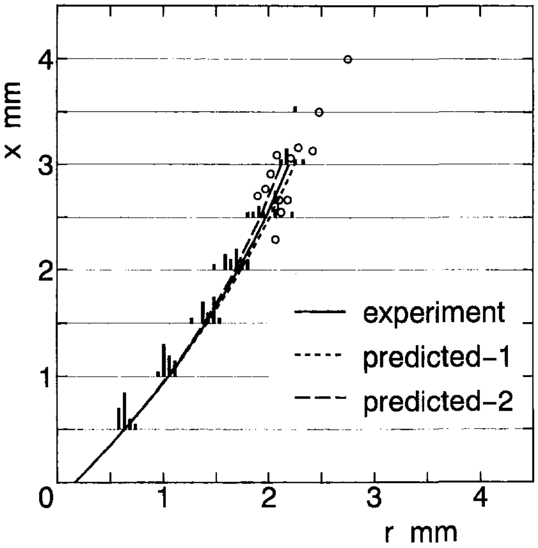

Fig. 13 Predicted shape of the liquid sheet, compared to the experimental average shape

$$\alpha_s = \frac{1}{\rho \cdot h} \cdot \left\{ \tau_{in} + \tau_{out} + \mu \frac{d^2u}{ds^2} \right\}$$

$$= \frac{1}{\rho \cdot h} \cdot \left\{ \tau_{in} + \tau_{out} + \frac{\mu}{u^2} \cdot \frac{d^2u}{dt^2} - \frac{\mu}{u^3} \left(\frac{du}{dt} \right)^2 \right\} \quad (5)$$

Here, μ denotes the laminar viscosity of the liquid, but the influence of the internal stress due to liquid viscosity is negligible.

Integrating Eqs. (4) and (5) in coupled form with respect to time t, velocity and locus of the liquid element can be calculated. The initial speed of the liquid sheet is assumed to be 16 m/s and the thickness of the liquid sheet h is determined on the way of calculation from the volumetric flow rate Q_V, speed of the liquid sheet u and the radius of the liquid sheet R as follows.

$$h = \frac{Q_V}{2\pi R u} \quad (6)$$

It is confirmed on the way of calculation, that the deceleration parallel to the liquid sheet due to shear stress is small and the effect on the shape of the liquid sheet is negligible. Figure 13 shows the predicted shape of the liquid sheet together with experimental results (Fig. 3). Predicted shape-1 includes only the effect of surface tension. Predicted shape-2 includes the effect of surface tension and the static pressure. Predicted shape-1 agrees well with the averaged shape acquired from the experiment. In addition, the effect of static pressure is much smaller than that of surface tension. Therefore, it can be said the surface tension of liquid is predominant in determining the shape of the liquid sheet.

6 Summary

Experimental and numerical investigations were made on the behavior of droplets in a hollow-cone spray paying attention to the liquid sheet formed at the atomizer orifice. Comparisons between experiments and simulations and the theoretical evaluation of the liquid sheet shape suggest the following.

(1) The movement of the liquid sheet induces strong air stream on both sides of it. The air stream induced on the outside of the liquid sheet flows inwardly into the rear of the recirculation zone that is formed because of the existence of the liquid sheet.

(2) This inward air stream induced by the liquid sheet acts as a strong side wind against the droplets immediately after the breakup of the liquid sheet. This stream transfers selectively small droplets into central region and plays an essential role in the progress of the classification of droplets by size.

(3) The numerical simulation predicts well the behavior of the droplets such as velocity, size distribution, and correlation between size and velocity in the hollow-cone spray by considering the existence of the liquid sheet.

(4) The shape of the hollow-cone liquid sheet is predominated by surface tension of liquid. The influence of the static pressure applied on the surface is much smaller.

References

Bayvel, L., and Orzechowski, Z., 1993, *Liquid Atomization, Combustion: An International Series*, Chigier, N., ed., Taylor & Francis.

Chen, S. K., Lefebvre, A. H., and Rollbuhler, J., 1992, "Factors Influencing the Effective Spray Cone Angle of Pressure-Swirl Atomizers," ASME *Journal of Engineering for Gas Turbines and Power*, Vol. 114, pp. 97–103.

Chigier, N., 1983, "Drop Size and Velocity Instrumentation," *Progress in Energy and Combustion Science*, Vol. 9, pp. 155–177.

Chigier, N., 1991, "Optical Imaging of Sprays," *Progress in Energy and Combustion Science*, Vol. 17, pp. 211–262.

Edwards, C. F., and Rudoff, R. C., 1990, "Structure of Swirl-Stabilized Spray Flame by Imaging, Laser Doppler Velocimetry and Phase Doppler Anemometry," *Twenty-Third Symposium* (International) *on Combustion*, The Combustion Institute, pp. 1353–1359.

Eisenklam, P., 1976, "Recent Research and Development Work on Liquid Atomization in Europe and the U.S.A.," 5th Conference on Liquid Atomization, Tokyo.

El Banhawy, Y., and Whitelaw, J. H., 1980, "Calculation of the Flow Properties of a Confined Kerosene-Spray Flame," *AIAA Journal*, Vol. 18, pp. 1503–1510.

Faeth, G. M., 1987, "Mixing Transport and Combustion in Sprays," *Progress in Energy and Combustion Science*, Vol. 13, pp. 293–345.

Giffen, E., and Massey, B. S., 1950, Report 1950/5, Motor Industry Research Association, England.

Lefebvre, A. H., 1989a, *Atomization and Sprays, Combustion: An International Series*, Chigier, N. ed., Hemisphere, Taylor & Francis Group.

Lefebvre, A. H., 1989b, *Atomization and Sprays, Combustion: An International Series*, Chigier, N. ed., Hemisphere, Taylor & Francis Group, pp. 112–113.

Lefebvre, A. H., 1989c, *Atomization and Sprays, Combustion: An International Series*, Chigier, N. ed., Hemisphere, Taylor & Francis Group, pp. 68–70.

Li, S. C., Libby, P. A., and Williams, F. A., 1992, "Experimental and Theoretical Studies of Counterflow Spray Diffusion Flames," *Twenty-Fourth Symposium (International) on Combustion*, The Combustion Institute, pp. 1503–1512.

McDonell, V. G., and Samuelsen, G. S., 1988, "Application of Two-Component Phase Doppler Interferometry to the Measurement of Particle Size, Mass Flux, and Velocities in Two-Phase Flows," *Twenty-Second Symposium (International) on Combustion*, The Combustion Institute, pp. 1961–1971.

McDonell, V. G., Adachi, M., and Samuelsen, G. S., 1992, "Structure of Reacting and Non-Reacting Swirling Air-Assisted Sprays," *Combustion Science and Technology*, Vol. 82, pp. 225–248.

O'Rourke, P. J., 1981, "Collective Drop Effects on Vaporizing Liquid Sprays," Ph.D. thesis, Princeton University.

Presser, C., Gupta, A. K., Avedisian, C. T., and Semerjian, H. G., 1990, "Fuel Property Effects on the Structure of Spray Flames," *Twenty-Third Symposium (International) on Combustion*, The Combustion Institute, pp. 1361–1367.

Presser, C., Gupta, A. K., and Semerjian, H. G., 1993, "Aerodynamic Characteristics of Swirling Spray Flames: Pressure Jet Atomizer," *Combustion and Flame*, Vol. 92, pp. 25–44.

Rizk, N. K., and Lefebvre, A. H., 1985, "Prediction of Velocity Coefficient and Spray Cone Angle for Simplex Swirl Atomizers," 3rd International Conference on Liquid Atomization and Spray Systems, London, Vol. 111C/2, pp. 1–16.

Rosa, A. B., Sankar, S. V., Wang, G., and Bachalo, W. D., 1993, "Particle Diagnostics and Turbulence Measurements in a Confined Isothermal Spray," ASME *Journal of Engineering for Gas Turbines and Power*, Vol. 115, pp. 499–506.

Sirignano, W. A., 1993, "Fluid Dynamics of Sprays—1992 Freeman Scholar Lecture," ASME JOURNAL OF FLUIDS ENGINEERING, Vol. 115, pp. 345–378.

Takagi, T., Fang, C. Y., Kamimoto, T., and Okamoto, T., 1991, "Numerical Simulation of Evaporation, Ignition and Combustion of Transient Sprays," *Combustion Science and Technology*, Vol. 75, pp. 1–12.

York, J. L., Stubbs, H. F., and Tek, M. R., 1953, "The Mechanism of Disintegration of Liquid Sheets," *Trans. ASME*, Vol. 75, pp. 1279–1286.

Haitao Xu
Ph.D. Student.

Yongchang Liu
Professor.

Department of Naval Architecture &
Ocean Engineering,
Huazhong University of Science and
Technology,
Wuhan, Hubei, 430074 P.R. China

Ping He
Assistant Professor.

Haiqing Wang
Assistant Professor.

Department of Mechanical &
Electrical Engineering,
Shenzhen Polytechnic,
Shenzhen, Guangdong, 518055 P.R. China

The TAR Model for Calculation of Droplet/Wall Impingement

In this paper, we present a new model, called the TAR model, for calculation of droplet/wall impingement. Using this model, we find that the critical Weber number for rebound is not a constant. It varies with the droplet radius. For large drops, the critical Weber numbers and rebound velocities predicted by the TAR model agree with experimental results very well. Whereas, the predicted hydrodynamic behavior of small droplets is very different from that of large drops. This conclusion is significant for modeling engine spray/wall interaction.

1 Introduction

At present, as engines become compact and the combustion chamber cavity in the piston becomes correspondingly small, spray/wall impact is inevitable. Because liquid fuel is introduced into the combustion chamber as a spray of droplets, more and more researchers are attracted to drop-wall interaction. Wachters and Westerling (1966) carried out an experimental study of drop-wall interaction, in which water drops (about 1 mm in radius) impinging on a hot polished metal surface (~400°C) were photographed using a stroboscope. It was observed that a droplet would either rebound or breakup depending on the approaching Weber number. They found that for different liquids, the critical value of Weber number, We_{cr}, is a constant around 40. This was confirmed by other researchers, (e.g., Akao et al., 1980, Araki and Moriyama, 1982). In recent years, Naber and Reitz (1988), Naber et al. (1988), Shih and Assanis (1991), Wang and Watkins (1993), and Park and Watkins (1996) published their models for spray/wall impingement, which are based on these experimental results and have been incorporated in multidimensional computer codes. But these models suffer from two major drawbacks. First, the experiments noted above were carried out with large drops (about 1 mm in radius), but in a diesel engine, the Sauter mean radius of spray droplets is very small (about 5 ~ 30 μm). Evidence is not sufficient for extending this conclusion to small droplets. Second, the effects of liquid viscosity are not considered. Thus the relationship between departure velocity and arrival velocity is uncertain. Therefore, these models are adjusted more or less to achieve a reasonable agreement with experiments. For example, Shih and Assanis (1991) let We_{cr} vary from 200 to 800 in their model, and they noted that when $\mathrm{We}_{cr} = 370$, modeling result is satisfactory. In the model proposed by Naber et al. (1988), a normal velocity component of 0–34 percent (randomly chosen) of the arrival velocity was imposed on the departure droplets.

The purpose of this paper is to present a theoretical model for droplet/wall impingement. The model is based on an analogy suggested by Taylor. We call this model the TAR (Taylor Analogy Rebound) model. The TAR model has several advantages over previous models. First, it predicts that there is not a constant critical Weber number for rebound. The Weber number is only a dimensionless measure of the relative importance of inertia force which distorts a drop to the surface tension force which restores sphericity. Whether or not a drop rebounds from the wall depends on the process of its deformation on the wall. Second, the effects of liquid viscosity are considered. Although these effects are negligible for large drops, liquid viscosity can significantly affect the deformation of small droplets. Third, for large drops, the model gives critical Weber numbers which agree well with experiments, and predicts the normal velocity component of a rebounding droplet after impingement and the residual time on the wall.

In following sections we present the equations used in the TAR model. These equations contain two dimensionless parameters which are determined by theoretical and experimental results. It is shown next how the model predicts the departure Weber number, the critical Weber number, and the residual time. For large drops, the model gives similar critical Weber numbers with experiments, but the residual time is different. We give some possible reasons for the discrepancy.

2 The TAR Model Equations

Taylor (1963) has suggested an analogy between an oscillating and distorting droplet and a spring-mass system. Based on this suggestion, O'Rourke and Amsden (1987) proposed the TAB (Taylor Analogy Breakup) model for calculation of spray droplet breakup, which was successfully incorporated in the KIVA-II code. We extend the Taylor analogy to the process of droplet/wall impingement. The dynamic behavior of a droplet impinging on a wall is assumed to be similar to the motion of a spring-mass system impinging on the wall. Bai and Gosman (1995) identify seven regimes for the droplet/wall impact. Generally, the seven regimes can be divided into three types (Wang and Watkins, 1993, see Fig. 1), namely,

---

Contributed by the Fluids Engineering Division for publication in the JOURNAL OF FLUIDS ENGINEERING. Manuscript received by the Fluids Engineering Division January 11, 1997; revised manuscript received March 3, 1998. Associate Technical Editor: F. Giralt.

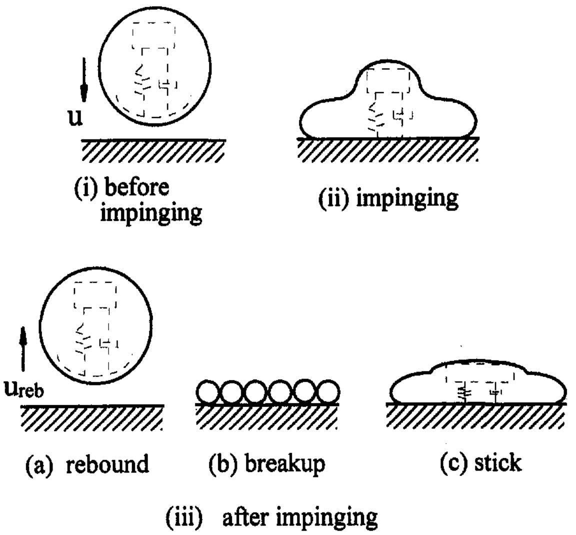

(i) before impinging (ii) impinging

(a) rebound (b) breakup (c) stick

(iii) after impinging

Fig. 1 The process of droplet/wall impingement is analogous to the motion of a spring-mass system impinging on the wall

(*a*) Rebound, in which an incident droplet bounces off the wall after impingement, which is similar to a spring-mass system rebounds from the wall;

(*b*) Breakup, in which an impinging drop breaks up and shatters into some smaller drops, which corresponds to the case that strong impaction causes the spring to break;

(*c*) Stick, in which an arrival droplet sticks to the wall and spreads out to form a wall film, as a spring-mass system in over-damped case.

The equation of a damped spring-mass system is

$$m\ddot{x} + c\dot{x} + kx = F \qquad (1)$$

where we take x to be the displacement of the top point of a droplet from its equilibrium position. In this paper, we only consider the case that the wall temperature is above the liquid's Leidenfrost temperature. As demonstrated by Chandra and Avedisian (1991), and Anders et al. (1993), at such high surface temperature, liquid evaporates so fast that the vapor generated between the impinging droplet and the hot wall can prevent droplet/wall contact. Therefore, the gravity and the wetting forces are negligible in this case, i.e.,

$$F = 0. \qquad (2)$$

In accordance with the Taylor analogy, the restoring force of the spring is analogous to the surface tension forces, thus,

$$\frac{k}{m} = C_k \frac{\sigma}{\rho r^3}, \qquad (3)$$

where σ is the gas-liquid surface tension coefficient, ρ is liquid density, r is the droplet radius, and C_k is a dimensionless parameter. Lamb (1932) gave

$$C_k = 8. \qquad (4)$$

The damping force is caused by liquid viscosity and is estimated through a simple model used by Chandra and Avedisian (1991), who presented that after impingement, when the droplet is flattened out in the shape of a disk (see Fig. 2), the dissipated energy E_d, can be determined as,

$$E_d = \int_0^{t_e}\int_V \phi\, dV dt \approx \phi V t_e. \qquad (5)$$

The dissipation per unit volume of the fluid is given by

$$\phi \approx \mu(u/h)^2, \qquad (6)$$

where μ is the liquid viscosity, u is the normal component of incident velocity, h represents the height of the disk, and t_e, the time for deformation is estimated by $t_e \approx 2r/u$. When the droplet is flattened out in the shape of a disk, the volume of the fluid, V, is

$$V = \pi R^2 h, \qquad (7)$$

where R is the radius of the disc.

Combining Eqs. (5)–(7), introducing $\beta = R/r$, the dissipated energy is obtained,

$$E_d = 3\pi\mu u \beta^4 r^2. \qquad (8)$$

In the TAR model, after considering droplet deformation, the dissipated energy is

$$E_d = \int_0^{\beta} c\dot{x}dx \approx cu\beta r. \qquad (9)$$

In conjunction Eq. (8) with (9), one obtains

$$\frac{c}{m} = \frac{9}{4}\beta^3 \frac{\mu}{\rho r^2}. \qquad (10)$$

Akao et al. (1980) gave a correlation of β,

$$\beta = 0.612(2\mathrm{We}_{in})^{0.38}, \qquad (11)$$

where $\mathrm{We}_{in} = \rho r u^2/\sigma$, is the incident Weber number. However, Stow and Hadfield (1981) argued that the relation between β and We_{in} is very weak. Therefore, within experimental resolution, β is considered to be proportional to $(\mathrm{We}_{\mathrm{in}})^{1/3}$

$$\beta = 0.612(2\mathrm{We}_{\mathrm{in}})^{1/3}. \qquad (12)$$

Substituting Eq. (12) into Eq. (10) gives

$$\frac{c}{m} = C_d \frac{\mu \mathrm{We}_{in}}{\rho r^2}, \qquad (13)$$

where $C_d = 1.03$, is a dimensionless parameter.

Obviously, the impinging droplet breaks up if and only if $x > 2r$. Before solving Eq. (1), we nondimensionalize x by $2r$. Letting $y = x/2r$, and using Eqs. (2), (3) and (13) in (1) gives

$$\ddot{y} + C_d \frac{\mu \mathrm{We}_{in}}{\rho r^2}\dot{y} + C_k \frac{\sigma}{\rho r^3} y = 0, \qquad (14)$$

with breakup occurring if and only if $y > 1$. This is the equation we use in our model. For a certain incident velocity, u, the initial conditions of Eq. (14) are

$$y(0) = 0, \quad \text{and} \quad \dot{y}(0) = \frac{u}{2r}. \qquad (15)$$

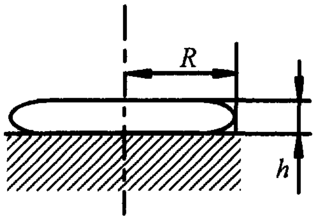

Fig. 2 Flattened droplet

The solution to Eq. (14) is

$$y(t) = \frac{u}{2\omega r} e^{-t/t_d} \sin \omega t, \qquad (16)$$

where

$$\frac{1}{t_d} = \frac{C_d}{2} \cdot \frac{\mu \mathrm{We}_{in}}{\rho r^2},$$

$$\omega^2 = \frac{C_k \sigma}{\rho r^3} - \frac{1}{t_d^2}. \qquad (17)$$

This completes the derivation of the TAR model. In next section, an application of the model is demonstrated and the shortcomings are discussed.

3 Application of the TAR Model

3.1 Calculation of the Rebounding Weber Number. If the droplet bounces, the rebounding time is $t_r = \pi/\omega$, and the rebounding velocity of the droplet apex, u_t, is

$$u_t = 2r \cdot \dot{y}(t_r) = u \cdot e^{-(\pi/\omega t_d)}. \qquad (18)$$

Note that u_t doesn't equal to u_{reb}, the departure velocity. By means of experimental data (Wachters and Westerling, 1966), the ratios of rebounding Weber numbers to the predicted droplet apex Weber numbers are calculated and plotted as open circles in Fig. 3. The curve fit of these data is

$$\frac{\mathrm{We}_{\mathrm{reb}}}{\mathrm{We}_t} = e^{-C_s \mathrm{We}_{in}} = e^{-0.1 \mathrm{We}_{in}} \qquad (19)$$

Combining Eq. (19) with (18) gives

$$\mathrm{We}_{\mathrm{reb}} = \mathrm{We}_{in} \cdot e^{-2\pi/\omega t_d} \cdot e^{-C_s \mathrm{We}_{in}}, \qquad (20)$$

which is plotted in Fig. 4. Fairly good agreement is obtained. In range of low We_{in} (5–15), the overestimation may be attributed partly to Eq. (12), which is regressed for high We_{in} (>15, see Akao et al., 1980), and partly to the nonlinear effects of viscosity on damping forces. Another deficiency is that Eq. (19) is obtained through curve fit of experimental data, $C_s = 0.1$, and may be not generally adaptable. Theoretical validation is needed here.

3.2 Prediction of Critical Weber Number. The TAR model predicts a critical velocity below which an incident droplet would rebound from the wall. There are two cases for a drop to deposit on the wall. One is the over damped case, i.e., $\omega^2 \le 0$; another is drop breakup, that is, $y_{\max} > 1$. Correspondingly, there are two limiting velocities.

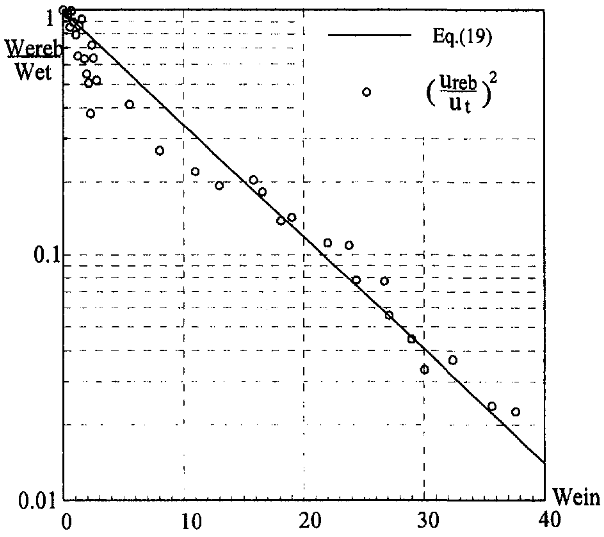

Fig. 3 Relationship between $\mathrm{We}_{\mathrm{reb}}/\mathrm{We}_t$ and We_{in}

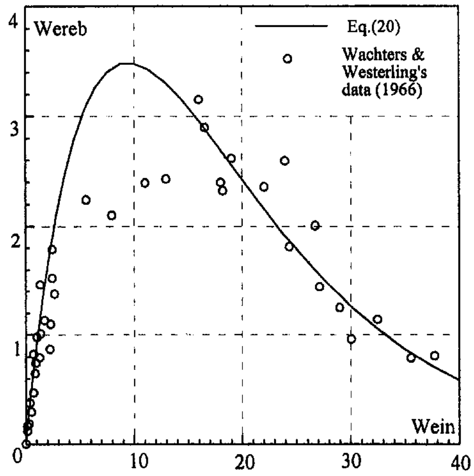

Fig. 4 Relationship between incident Weber number and departure Weber number

The over damped limiting velocity, u_{od}, and the limiting Weber number, We_{od}, are determined by $\omega^2 \le 0$:

$$u_{od} = \left(\frac{2\sqrt{C_k}}{C_d}\right)^{1/2} \cdot (\mathrm{Oh})^{1/2} \cdot \frac{\sigma}{\mu}, \qquad (21)$$

and

$$\mathrm{We}_{od} = \frac{2\sqrt{C_k}}{C_d \cdot \mathrm{Oh}}, \qquad (22)$$

where $\mathrm{Oh} = \mu/\sqrt{\rho r \sigma}$ is the Ohnesorge number. A droplet with a certain size (i.e., a certain Oh) will be over-damped and stick on the wall if its incident Weber number is higher than the We_{od} corresponding to its Oh.

When $\omega t = \pi/2$, Eq. (16) gives

$$y(t) = y_{\max} = \frac{u}{2\omega r} \cdot e^{-\pi/2\omega t_d}. \qquad (23)$$

According to limiting condition $y_{\max} > 1$, the breakup limiting parameters are

$$u_{br} = 2\sqrt{\frac{C_k \sigma}{\rho r}} \cdot \sqrt{1 - \zeta^2} \cdot e^{\zeta \pi / 2\sqrt{1 - \zeta^2}}. \qquad (24)$$

and

$$\mathrm{We}_{br} = 4C_k \cdot (1 - \zeta^2) \cdot e^{\zeta \pi / \sqrt{1 - \zeta^2}}. \qquad (25)$$

where

$$\zeta = \frac{C_d}{2\sqrt{C_k}} \cdot \mathrm{We}_{in} \cdot \mathrm{Oh}. \qquad (26)$$

A droplet will break up after impingement if its We_{in} exceeds We_{br}.

Therefore, the critical parameters for rebound are

$$u_{cr} = \min(u_{od}, u_{br}), \qquad (27)$$

and

$$\mathrm{We}_{cr} = \min(\mathrm{We}_{od}, \mathrm{We}_{br}). \tag{28}$$

Because ζ depends on u, or We_{in} (see Eq. (26)), Eq. (24) and (25) are transcendent functions for u_{br} and We_{br}. The relationship between the critical parameters (We_{cr}, u_{cr}), and the droplet radius, r (or its Ohnesorge number), can not be represented by simple correlation's. In figure 5, the curve shows the predicted We_{cr}, and the open circles represent the measurements of Wachters and Westerling (1966). In Fig. 5, it is clearly shown that for large drops (low Oh), the We_{cr} vary very slowly, and the predictions agree well with experiments. In fact, for low Oh, $\zeta \to 0$, and Eq. (25) gives

$$\mathrm{We}_{cr} = \mathrm{We}_{br} \approx 4C_k = 32. \tag{29}$$

That is to say, for large drops, the critical Weber number is about a constant, 32, which is independent of the liquid properties (due to the effects of viscosity, the predictions of We_{cr} is 34, but is still about a constant, as shown in Fig. 4). This is in good agreement with experiments (Wachters and Westerling, 1966; Akao et al., 1980; and Araki and Moriyama, 1982), in which the critical Weber number for several liquids is about 40.

When droplet radius, r, decreases, the liquid viscosity significantly affects the hydrodynamic behavior of small droplets, and the critical Weber number is no longer a constant. When $r \le r_0$, the over damped case occurs. Therefore, for large and small drops, the reasons that droplets deposit on the wall are different. When $r > r_0$, drop breakup is caused by inertia force. When $r \le r_0$, droplets stick on the wall because of the effects of liquid viscosity. Thus the conclusion that the critical Weber number is a constant, which is drawn from experiments carried out with large drops, can not be used to small incident droplets.

From Eqs. (23) and (25), it can be concluded that the Weber number alone cannot describe the impinging process. Because of the effects of the liquid viscosity, the Ohnesorge number must be considered, or other dimensionless groups, e.g., the Reynolds number Re (Akao et al., 1980), and the Laplace number La (Bai and Gosman, 1995), could be used to substitute Oh through $\mathrm{Oh} = \sqrt{\mathrm{We}}/\mathrm{Re}$ and $\mathrm{Oh} = \mathrm{La}^{-1/2}$.

In Fig. 6, the solution of Eq. (28) is plotted in the We-Oh plane. If Eq. (12) is generally appropriate, this curve is independent to liquid properties. It is shown in figure 6 that the transition Oh is about 0.02, which corresponds to 0.5 mm of radius for fuel droplet, and the critical Weber number is about 250. As mentioned earlier, Shih and Assanis (1991) let We_{cr} varies from 200 to 800 in their model, and they noted that when $\mathrm{We}_{cr} = 370$, the modeling result is satisfactory. It is evident that the critical Weber number cannot be fixed as 40 in engine spray/wall impingement modeling.

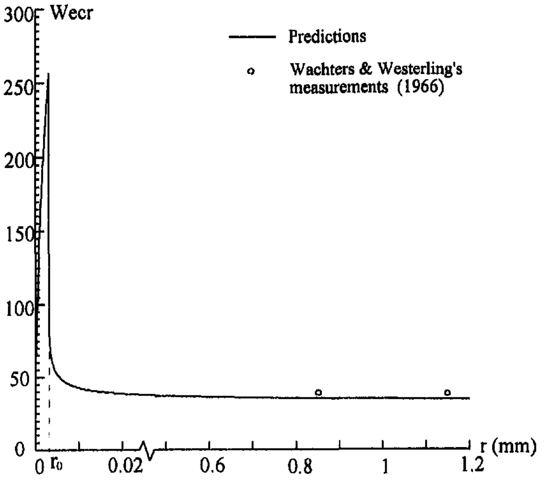

Fig. 5 Relationship between critical Weber number and droplet radius

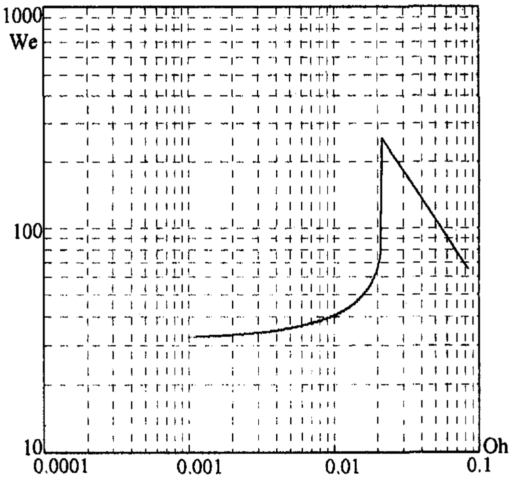

Fig. 6 Relationship between critical Weber number and Ohnesorge number

It must be pointed out that the quantitative results of the TAR model are derived on condition that the wall temperature is above the liquid Leidenfrost temperature, which is called the nonwetting regime by Naber and Farrell (1994). But the engine-like conditions are in the wetting or transition regimes (Naber and Farrell, 1994). Therefore, the quantitative data of the model are inadequate to be used in a engine spray/wall impingement modeling, although these data seem plausible when compared with Shih and Assanis' model (1991). In wetting or transition regimes, the wetting forces should be important to the hydrodynamic behavior of the impinging droplet, and a dimensionless parameter to measure the relative importance of the wetting forces must be incorporated in the model.

3.3 Prediction of Residual Time. When $\omega t = \pi$, the droplet rebounds from the wall, the residual time of drop on the wall is

$$t_r = \frac{\pi}{\omega} = \frac{\pi}{\sqrt{\dfrac{C_k\sigma}{\rho r^3} - \dfrac{1}{t_d^2}}}. \tag{29}$$

For large drops, $1/t_d \approx 0$. From Eq. (26),

$$t_r \approx \pi\sqrt{\frac{\rho r^3}{C_k\sigma}} = \pi\sqrt{\frac{\rho r^3}{8\sigma}}. \tag{30}$$

Wachters and Westerling (1966) gave

$$t_r = \pi\sqrt{\frac{\rho r^3}{2\sigma}}. \tag{31}$$

which is measured as the departure time of the bottom of the water droplet with radius of about 1 mm.

The prediction of the TAR model is only half of the experiment. This is caused by the definition that x is the displacement of the top point of a droplet. When the top point arrives its equilibrium position, the bottom of the droplet is still on the wall because of deformation. Therefore, the prediction of t_r is less than experiment, and the relationship between the half period of the droplet apex and the departure time of the droplet bottom needs further examination.

4 Conclusion

Based on the analogy suggested by Taylor, the TAR model for calculation of droplet/wall impingement is presented, in which, the effects of liquid viscosity are considered. According to the calculation of the model, the following conclusions can be drawn.

(1) The Weber number alone is inadequate to determine rebound/breakup boundary of droplet/wall impact. Due to the effects of the liquid viscosity, the Ohnesorge number (or Reynolds number) should be considered.

(2) For large drops (little Ohnesorge numbers), the model gives fairly good predictions of the critical Weber numbers. For small droplets, the model indicates that the critical Weber numbers are much higher than large ones, which needs experimental validations.

(3) The model is derived from the condition that the surface temperature is above the liquid's Leidenfrost temperature, which rarely happened in an IC engine (Naber and Farrell, 1993, and Nagaoka et al., 1994). It is arbitrary to use its predictions to engine-like conditions. But the hydrodynamics of impinging droplets is similar in any condition, the conclusions (1) and (2) are still instructive for modeling engine spray/wall impingement. Further theoretical and experimental investigations, such as the effects of the wetting forces, the relationship between departure velocity of a whole droplet and the velocity of the top point, and the pattern of breakup after impingement, are needed to refine the model for adaptability in more conditions.

Acknowledgment

The authors wish to express their grateful appreciation to Professor G. D. Jin for his helpful comments.

References

Akao, F., Araki, K., Mori, S., and Moriyama, A., 1980, "Deformation Behaviour of a Liquid Droplet Impinging onto a Hot Metal Surface," *Transactions of Iron and Steel Institute of Japan,* Vol. 21, pp. 737–743.

Anders, K., Rath, N., and Frohn, A., 1993, "The Velocity Change of Ethanol Droplets during Collision with a Wall Analyzed by Image Processing," *Experiment of Fluids,* Vol. 15, pp. 91–96.

Araki, K., and Moriyama, A., 1982, "Deformation Behaviour of a Liquid Droplet Impinging on a Hot Metal Surface," *International Conference on Liquid Atomization and Spray Systems (ICLASS-82),* University of Wisconsin.

Bai, C., and Gosman, A. D., 1995, "Development of Methodology for Spray Impingement Simulation," *SAE Journal of Engines,* Vol. 104, pp. 550–568.

Chandra, S., and Avedisian, C. T. 1991, "On the Collision of a Droplet with a Solid Surface," *Proceedings of Royal Society (London),* Series A432, pp. 13–41.

Lamb, H., 1932, *Hydrodynamics,* Dover Publication, New York.

Naber, J. D., and Reitz, R. D., 1988, "Modeling Engine Spray/Wall Impingement," *SAE Journal of Engines,* Vol. 97, pp. 118–140.

Naber, J., Enright, B., and Farrell, P. V. 1988, "Fuel Impingement in a direct Injection Diesel Engine," *SAE journal of Fuels and Lubricants,* Vol. 97, pp. 430–443.

Naber, J. D., and Farrel, P. V. 1993, "Hydrodynamics of Droplet Impingement on a Heated Surface," *SAE Journal of Engines,* Vol. 102, pp. 1346–1361.

Nagaoka, M., Kawazoe, H., and Nomura, N., "Modelling Fuel Spray Impingement on a Hot Wall for Gasoline Engines," *SAE Journal of Engines,* Vol. 103, pp. 878–896.

O'Rourke, P. J., and Amsden, A. A., 1987, "The Tab Method for Numerical Calculation of Spray Droplet Breakup," *Society of Automotive Engineers Paper,* No. 872089.

Park, K., and Watkins, A. P., 1996, "Comparison of Wall Spray Impaction Models with Experimental Data on Drop Velocities and Sizes," *International Journal of Heat and Fluid Flow,* Vol. 17, pp. 424–438.

Shih, L. K., and Assanis, D. N., 1991, "Implementation of a Fuel Spray Wall Interaction Model in KIVA-II," *SAE Journal of Engines,* Vol. 100, pp. 1498–1512.

Stow, C. D., and Hadfield, M. G., 1981, "An Experimental Investigation of Fluid Flow Resulting from the Impact of a Water Drop with an Unyielding Dry Surface," *Proceedings of Royal Society* (London), Series A373, pp. 419–441.

Taylor, G. I. 1963, "The Shape and Acceleration of a Drop in a High Speed Air Stream," *The Scientific Papers of G. I. Taylor,* G. K. Batchelor, ed., Vol. III, University Press, Cambridge.

Wachters, L. H. J., and Westerling, N. A. J., 1989, "The Heat Transfer from a Hot Wall to Impinging Water Drops in the Spheroidal State," *Chemical Engineering Science,* Vol. 21, pp. 1047–1056.

Wang, D. M., and Watkins, A. P., 1993, "Numerical Modeling of Diesel Spray Wall Impaction Phenomena," *International Journal of Heat and Fluid Flow,* Vol. 14, No. 3, pp. 301–312.

Chi-Chuan Hwang
Professor,
Department of Mechanical Engineering,
Chung Yuan University,
Chung-Li, Taiwan 32023

Chaur-Kie Lin
Associate Professor,
Department of Mechanical Engineering,
Chien Hsin College of Technology
and Commerce,
Chung-Li, Taiwan

Da-Chih Hou
Department of Electronic Engineering,
Chung Yuan University,
Chung-Li, Taiwan 32023

Wu-Yih Uen
Associate Professor,
Department of Electronic Engineering,
Chung Yuan University,
Chung-Li Taiwan 32023

Jenn-Sen Lin
Associate Professor,
Department of Mechanical Engineering,
Lien Ho College of Technology
and Commerce,
Miai-Li, Taiwan 360

Nonlinear Rupture Theory of a Thin Liquid Film With Insoluble Surfactant

Effects of insoluble surfactant on the dynamic rupture of a thin liquid film coated on a flat plate are studied. The strong nonlinear evolution equations derived by the integral method are solved by numerical method. The results show that enhancing (weakening) the Marangoni effect (the surface diffusion effect) will delay the rupture process. Furthermore, the rupture time predicted by the integral theory is shorter than that predicted by the long-wave expansion method. In addition, the quantitative difference in the rupture time predicted by two models enlarges with the increase of Marangoni effect, however, without obvious change as the diffusion effect increases.

1 Introduction

Much attention has been paid to the hydrodynamic stability of thin liquid films for their widespread applications in mechanical, chemical, and biomedical engineering, and so on. When the thickness of a liquid film is thinner than 1000 Å, the film will be unstable due to the van der Waals potential (VDWP) (Sheludko, 1967) and show a tendency to rupture. To study this rupture process, Ruckenstein and Jain (1974) have applied a linear stability analysis to a system composed of a thin liquid film coated on a plate. However, a linear analysis failed to follow the dynamics of the instability of a thin film with finite amplitude. Subsequently, a nonlinear method that is based on the long wave instability theory (William and Davis, 1982; Sharma and Ruckenstein, 1986; Hwang et al., 1993) was presented with the nonlinear evolution equations being derived asymptotically from the Navier-Stokes equations. Furthermore, Burelbach et al. (1988) showed that the rupture time is reduced by 25 percent over the Williams and Davis result if a finer computational grid is used. While, in the nonlinear analysis, two effects were reported to influence the rupture process, i.e., the nonlinearity in both the surface tension and VDWP that would accelerate the rupture process. Additionally, the inertia could increase the instability of the thin films, while the other high-order dissipation terms decrease it (Chen and Hwang, 1994; Hwang et al., 1996).

In addition, there have also been some research concerning the spreading of surfactants added to the thin films (Borgas and Grotberg, 1988; Gaver III and Grotberg, 1990; Troian et al., 1990; Jensen and Grotberg, 1992; Jensen and Grotberg, 1993; Gaver III and Grotberg, 1992). When nonuniformly distributed surfactants are deposited as a monolayer on the surface of a thin film, the resulting gradients of the surface tension make liquid flow and consequently induce the surfactants to spread. Effects of insoluble surfactant on the nonlinear rupture process of a free film and a coating film on a plate have been studied by De Wit et al. (1994), who extended the formulation and the methodology used by Erneux and Davis (1993).

In some research (Brogas and Grotberg, 1988; De Wit et al., 1994), the order of the magnitude of the dimensionless parameters (e.g., the dimensionless surface tension and the dimensionless Hamaker constant related to the strength of VDWP, etc.) are estimated to be large for retaining the main physical effects in the leading-order nonlinear evolution equations. However, the magnitude of those dimensionless parameters for real materials (such as water and ethanol) is small. Therefore, some high-order terms (including inertia terms and viscous dissipation terms (Hwang et al., 1996)) of the governing equations and boundary conditions, in which the above-mentioned parameters should be involved in, are usually neglected in those research. Hence, in the present work, first, the order of magnitude of each variable and parameter is adopted by considering the long-wave nature of the response and the small magnitude of the parameters themselves (William and Davis, 1982). Then, the simplified equations of motions and pertinent boundary conditions are formulated. Also, the high-order nonlinear contributions in the governing equations are considered. Finally, the integral method (Prokopiou et al., 1991; Alekseenko et al., 1991; Hwang et al., 1996) is applied with a specific velocity profile to derive the nonlinear evolution equations. This velocity profile includes an

---

Contributed by the Fluids Engineering Division for publication in the JOURNAL OF FLUIDS ENGINEERING. Manuscript received by the Fluids Engineering Division March 17, 1997; revised manuscript received April 10, 1998. Associate Technical Editor: F. Giralt.

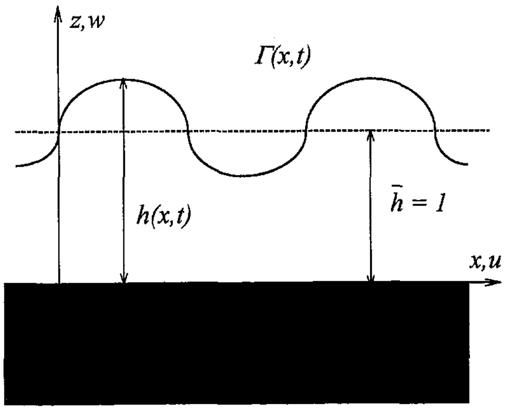

Fig. 1 A schematic cross-sectional view of a liquid film coated on a flat plate

unknown function to correlate shear-stress balance boundary condition at the interface. In this study, the evolution equations are used to simulate the nonlinear rupture processes and the numerical analysis results obtained from the present model will be systematically compared with those derived by using long-wave model.

2 Formulation

The physical model for the present study is shown in Fig. 1. The liquid is a Newtonian viscous fluid having kinematic viscosity ν and constant density ρ. In addition, we use the equilibrium value Γ_0 as a measuring unit for the concentration of the surfactant. Here, the gravity effect is neglected and only the effect of VDWP is investigated since a film that is thin to the degree of a micron is considered. Scaling the coordinate by the equilibrium thickness h_0, time by h_0^2/ν, velocity by ν/h_0, pressure by $\rho\nu^2/h_0^2$, and concentration of the surfactant by Γ_0, we have the resulting modified Navier-Stokes equations given by

$$u_t + uu_x + wu_z = -p_x - \phi_x + u_{xx} + u_{zz} \tag{1}$$

$$w_t + uw_x + ww_z = -p_z - \phi_z + w_{xx} + w_{zz} \tag{2}$$

together with the continuity equation

$$u_x + w_z = 0 \tag{3}$$

where u, w, and p are the surface diffusion coefficient of the surfactant, the dimensionless x-component velocity, the z-component velocity and pressure, respectively. All the subscripts present in the equations given above denote partial derivatives. The VDWP, expressed by the potential function ϕ which depends on the film thickness, can be given by (De Wit et al., 1994; Erneux and Davis, 1993)

$$\phi = A(h)^{-3} \tag{4}$$

where A is the dimensionaless Hamaker constant, $A = A'/(6\pi h_0\rho\nu^2)$.

The boundary conditions:
at $z = 0$,

$$u = w = 0 \tag{5}$$

at free surface, $z = h(x, t)$,

$$(u_z + w_x)(1 - h_x^2) - 4u_xh_x(1 + h_x^2)^{-1} = -M\Sigma_x(1 + h_x^2)^{1/2} \tag{6}$$

$$-p + 2[(1 - h_x^2)u_x - h_x(u_z + w_x)](1 + h_x^2)^{-1} = \Sigma h_{xx}(1 + h_x^2)^{-3/2} \tag{7}$$

$$\Gamma_t + [(u\Gamma)_x + h_x(w\Gamma)_x](1 + h_x^2)^{-1} = D_s\nabla_s^2\Gamma \tag{8}$$

Equations (6) and (7) are shear and normal stress balance conditions at the free surface, respectively. Equation (8) is a conservation equation for the concentration of the surface active substance.
where

$$\Sigma = T - M\Gamma, \quad M = -[\Gamma_0h_0/(\rho\nu^2)](\partial\sigma/\partial\Gamma)$$

$$T = \sigma_0h_0/(\rho\nu^2) \quad \text{and} \quad D_s = D_s'/\nu$$

Σ is the dimensionless surface tension, T is the dimensionless surface tension for the constant part of the tension σ_0 at equilibrium concentration Γ_0 and M is the dimensionless Marangoni number for the variation $\partial\sigma/\partial\Gamma$. of the dimensionless tension σ versus the dimensionless concentration Γ. It should be noted that the second term in the left side of Eq. (8) represents the rate of change of the concentration due to the dilatation of the free surface and the convection of the surfactant. D_s is the reciprocal of the dimensionless Schmidt number and D_s' is the surface diffusion coefficient of the surfactant.
where the surface gradient ∇_s is defined as

$$\nabla_s = \begin{bmatrix} \dfrac{1}{1 + h_x^2}\dfrac{\partial}{\partial x} \\ \dfrac{h_x^2}{1 + h_x^2}\dfrac{\partial}{\partial x} \end{bmatrix}$$

Simultaneously, the kinematic condition at the free surface is given by

$$h_t + uh_x = w \tag{9}$$

After solving the exact linear stability problem of Eqs. (1)–(9), one can find that the neutral state of the system is present at the cut-off wave number given by

$$k_c = \left(\frac{3A}{T - M}\right)^{1/2} \tag{10}$$

In order to retain the effects of van der Waals interaction, surface tension, Maragoni and surface diffusion, the order of the magnitude of A, T, M, and D_s are assumed as

$$A = O(\epsilon^4), \quad T = O(1), \quad M = O(\epsilon),$$
$$\text{and} \quad D_s = O(\epsilon) \tag{11}$$

where ϵ is a rather small parameter. By introducing Eq. (11) into Eq. (10), one can represent the order of magnitude of unstable wave number k as

$$k = O(\epsilon^2) \tag{12}$$

The order of other dimensionless variables are given as

$$u = O(1), \quad w = O(k), \quad p = O(k^{-1})$$
$$u = O(k^{-1}), \quad z = O(1), \quad t = O(k^{-1}) \tag{13}$$

Introducing Eqs. (11)–(13) into Eqs. (1)–(9) and neglecting the terms higher than $O(\epsilon^6)$, we can formulate the following simplified system:

$$\underline{u_t + uu_x + wu_z} = -p_x - \phi_x + u_{xx} + \underline{u_{zz}} \tag{14}$$

$$\underline{w_t + uw_x + ww_z} = -p_z + \underline{w_{zz}} \tag{15}$$

$$u_x + w_z = 0 \tag{16}$$

at $z = 0$

$$u = w = 0 \tag{17}$$

and at the interface, $z = h(x, t)$

$$u_z = \underline{4u_x h_x - w_x} - M\Gamma_x(1 + \underline{\tfrac{3}{2}h_x^2}) \quad (18)$$

$$-p = \underline{2u_x + 2u_z h_x} + (T - M\Gamma)h_{xx} \quad (19)$$

$$\Gamma_t + (u\Gamma)_x - D_s\Gamma_{xx} = \underline{h_x^2(u\Gamma)_x - h_x(w\Gamma)_x - D_s(h_x^2\Gamma_{xx} + h_x h_{xx}\Gamma_x)} \quad (20)$$

$$h_t + uh_x = w \quad (21)$$

The main differences between the integral theory and the long-wave theory can be presented from above equations. From Eqs. (14) and (15), obviously, the inertia terms (marked with underline in the left side of both equations) and shear stress terms (marked with underline in the right side of both equations) included in the momentum equations of the integral theory are excluded in those of the long-wave theory. Also, the terms representing the interfacial shear, normal stress, and surfactant distribution (marked with underline in Eqs. (18) (19), and (20), respectively) considered in the integral theory are not included in the long-wave theory.

The mass balance relationship is obtained by rewriting Eq. (21) as

$$h_t + q_x = 0 \quad (22)$$

where q is the local flow rate and can be expressed as

$$q = \int_0^h u dz$$

A specific profile must now be imposed in the integral method. For highly turbulent flow, a flat profile is usually assumed. However, for the flow of interest here, it has been experimentally established that a parabolic profile is more appropriate (Alekseenko et al., 1991). Therefore, we introduce the following second-order self-similar profile of u

$$u = \frac{3q}{h}\left[\left(\frac{z}{h}\right) - \frac{1}{2}\left(\frac{z}{h}\right)^2\right] - \frac{fh}{2}\left[\left(\frac{z}{h}\right) - \frac{3}{2}\left(\frac{z}{h}\right)^2\right]$$

where $f(x, t)$ is an unknown correlating function. This velocity profile satisfies the no-slip condition at the liquid-solid boundary and $u_z = f(x, t)$ at the free surface. Using the continuity equation Eqs. (16) and (18), the shear-stress balance boundary condition at the free surface can be given by the following form

$$f = \tfrac{1}{3}G_{xx}h^3 + \tfrac{1}{2}L_{xx}h^2 + 4G_x h^2 h_x + 4L_x hh_x - M\Gamma_x(1 + \tfrac{3}{2}h_x^2) \quad (23)$$

where

$$G(x, t) = \tfrac{3}{4}fh^{-1} - \tfrac{3}{2}qh^{-3}$$

$$L(x, t) = 3qh^{-2} - \tfrac{1}{2}f$$

Equation (23) represents the nonlinear shear-stress equilibrium relation at the interface and the unknown function f is correlated to h and q in the rupture process. Furthermore, integrating Eq. (14) over the whole film thickness and applying Eq. (15) with boundary conditions Eqs. (18) and (19), one can obtain the averaged x-momentum equation:

$$\begin{aligned} q_t + (\tfrac{1}{5}G^2h^5 + \tfrac{1}{2}GLh^4 + \tfrac{1}{3}L^2h^3)_x &= 3Ah^{-3}h_x + \tfrac{1}{3}G_{xx}h^3 \\ &+ f - L + \tfrac{1}{2}L_{xx}h^2 - 2fh_x^2 - 2h_x(G_x h^2 - L_x h) \\ &- (T - M\Gamma)h_x h_{xx} - \{\tfrac{1}{2}L_x h^2 + \tfrac{2}{3}G_x h^3 - \tfrac{1}{8}L_{xt}h^4 \\ &- \tfrac{1}{30}[2G_{xt} + 3LL_{xx} - 3L_x^2] - \tfrac{1}{36}[3GL_{xx} + 2G_{xx}L \\ &- 5G_x L_x]h^6 - \tfrac{1}{21}(GG_{xx} - G_x^2)h^7 - (T - M\Gamma)hh_{xx} \\ &- 2fhh_x - 2(G_x h^3 + L_x h^2)\}_x \end{aligned} \quad (24)$$

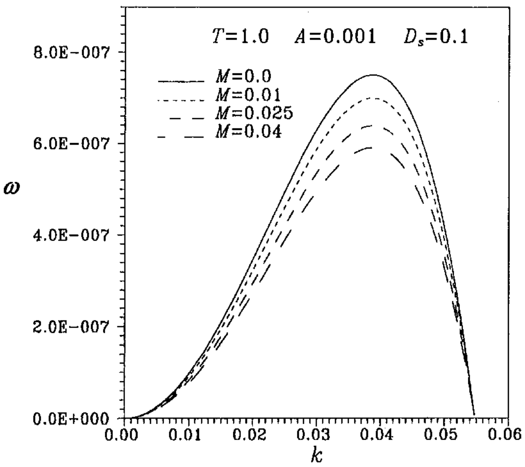

Fig. 2 The variation of perturbation growth rate ω as a function of wave number k for various M's

Finally, substituting the interface velocities (i.e., the value of u and w at $z = h$) into Eq. (20), we can rewrite the convection diffusion equation of insoluble surfactant as

$$\Gamma_t + (1 - h_x^2)(G\Gamma h^2 + L\Gamma h)_x - \tfrac{1}{6}(2G_x\Gamma h^3 + 3L_x\Gamma h^2)_x = D_s[(1 - h_x^2)\Gamma_{xx} - \Gamma_x h_x h_{xx}] \quad (25)$$

Equations (22)–(25) form a nonlinear evolution system involving the film thickness h, the local flow rate q, the correlating function f, and the concentration Γ. If the function f and the high-order terms in the diffusion equation are neglected, the evolution system is equivalent to that derived by De Wit et al. (1994).

3 Linear Rupture Theory

We perturb the basic state solution by small perturbations, i.e., $h = 1 + h'$, $q = q'$, $f = f'$ and $\Gamma = 1 + \Gamma'$. By inserting these terms into Eqs. (22)–(25), we can achieve a linearized problem admitting solutions of the form

$$(h', q', f', \Gamma') = (h_0', q_0', f_0', \Gamma_0')\exp(\omega t + ikx)$$

where $(h_0', q_0', f_0', \Gamma_0')$ are small initial disturbance amplitude, ω is the growth rate, and k is the wave number of perturbation, respectively. Then, we can derive the characteristic equation for the growth rate as follows:

$$\begin{aligned} &4(-\tfrac{1}{80}k^4 - \tfrac{11}{40}k^2 - 1)\omega^3 + [\tfrac{1}{80}Mk^4(k^2 - 6) + 4(\tfrac{1}{4}k^4 - 3k^2 \\ &- 3) + k^2(-\tfrac{1}{80}k^4 - \tfrac{11}{40}k^2 - 1)(M + 4D_s)]\omega^2 \\ &+ [Mk^2(k - 6)(-\tfrac{1}{4}k^2 + \tfrac{3}{2}) + k^2(\tfrac{1}{4}k^4 - 3k^2 - 3)(M \\ &+ 4D_s) - 4k^4(T - M) + 12Ak^2]\omega \\ &+ k^4(M + 4D_s)[3A - k^2(T - M)] = 0 \end{aligned} \quad (26)$$

Equation (26) admits a zero of ω if the last term is equal to zero. This leads the cut-off wave number k_c to be

$$k_c = \left(\frac{3A}{T - M}\right)^{1/2} \quad (27)$$

which agrees well with the exact linear results. The solutions to the characteristic equation for various M's are shown in Fig. 2. The peak of each $\omega - k$ curve denotes the maximum growth

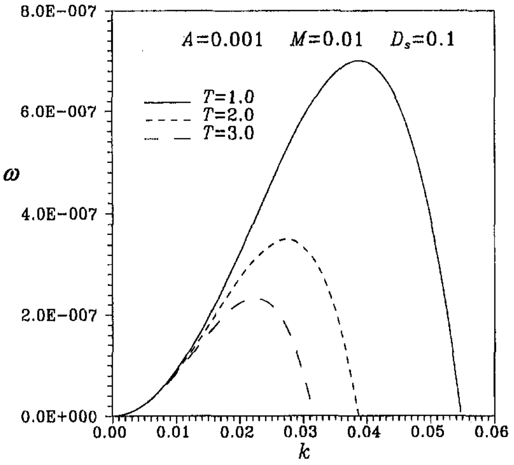

Fig. 3 The variation of perturbation growth rate as a function of wave number *k* for various *T*'s

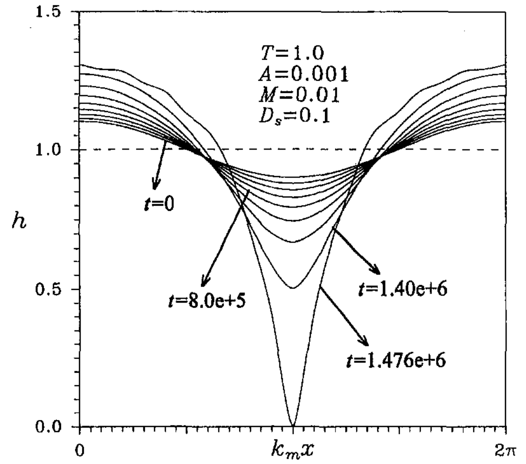

Fig. 4 Time variations of the profile of a liquid film thickness predicted by the nonlinear rupture theory

rate ω_m and the corresponding wave number k_m. It is clear that an increase in M results in a decrease in the maximum growth rate ω_m which is inversely proportional to the rupture time of the free film as addressed before (Williams and Davis, 1982; Sharma and Ruckenstein, 1986; Hwang et al., 1993; Chen and Hwang, 1994). This means that the film will become more stable as we increase the concentration Γ_0 of surfactants in the film or the rate $(-\partial\sigma/\partial\Gamma)$ and consequently increase the Marangoni number. If we increase the surface tension T, then the cutoff wave number k_c will decrease as shown in Fig. 3. The film is thus more stable as the domain of the most unstable wave number shrinks. It is obvious that as ω_m decreases, the rupture time of the film will be postponed. This result is in agreement with the fact that films with a higher interfacial tension are more stable.

4 Nonlinear Rupture Theory

The nonlinear rupture process of the film is revealed by solving Eqs. (22)–(25) numerically. Equations are discretized by using the finite-difference method. Central differences are employed in space while the midpoint rule is used for time. The calculation domain is fixed in the range $0 \le x \le 2\pi/k_m$. The periodic boundary conditions are considered. The initial conditions are

$$h(x, 0) = 1.0 + H_0 \cos k_m x$$

$$q(x, 0) = -\frac{\omega_m}{k_m} H_0 \sin k_m x$$

$$f(x, 0) = -\omega_m k_m H_0 \sin k_m x$$

$$\Gamma(x, 0) = 1.0$$

where H_0 is the initial disturbance. In all numerical results mentioned below, the initial disturbance is assumed to be 0.1. The Newton-Raphson iteration scheme is introduced to calculate the difference equations and the convergent tolerance is set to be 10^{-5}.

To realize the effect of adding surfactants to the liquid film on the rupture mechanism in a plate system, we first investigate qualitatively the flowing behavior of the liquid film after it is perturbed. Here, it is convenient to use a streamwise flow rate distribution: $Q = \int_0^h u dz$ to represent the kinetic tendency for the fluid and define the related flow rates Q_I, Q_L, Q_H, Q_V, and Q_M (see the details in the Appendix) as various flow rates due to the integral method, the long wave theory, the high-order viscous dissipation terms, the inertia terms and the Marangoni effect, respectively. Figure 4 shows nonlinear ripple behavior of the liquid film during the rupture process, where the center point given at $k_m x = \pi$ indicates the bottom of the ripple, while both side points denoted by $k_m x = 0$ and $k_m x = 2\pi$ show the peak of it. It is obvious that the variation of the film thickness is gentle near the peak regions and becomes steeper and steeper down along the peak regions. And finally a violent decrease in the film thickness appears at the bottom of the ripple. Figure 5 displays the distribution of all flow rates along the $k_m x$ axis. The corresponding ripple waveform can be referred to those depicted in Fig. 4. Note that if the Q-value to the left (right) side of the bottom of the ripple is negative, then this represents the fluid flowing from the bottom to the peak of the ripple. Otherwise, if the Q-value to the left (right) side of the bottom is positive, then the fluid is flowing in the reverse direction. First, it can be understood from the distribution of Q_L that the long-range molecular force caused by the van der Walls force will induce the fluid to flow from the bottom to the peak of the ripple on the film surface. This effect will thin the local film at the ripple bottom and to its extreme result in the rupture of the liquid film. Therefore, it is an unstable factor for the liquid film system. Next, it is evident from the distribution of Q_V that the effect caused by the inertial force will induce the fluid to flow in the same way as that of the van der Waals effect, that is, it is also an unstable factor for the liquid film system (Chen and Hwang, 1994). If the inertial terms are additionally considered in the long-wave theory, the flow rate of the fluid flowing from

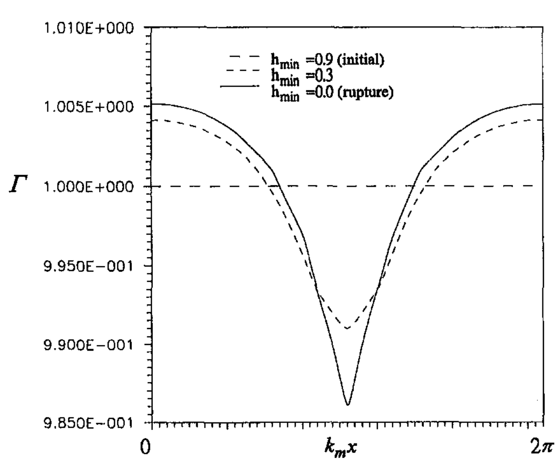

Fig. 5 The flow rate profiles for Q_I, Q_L, Q_H, Q_V. The values of parameters are A = 0.001, T = 1.0, M = 0.025, and D_s = 0.1.

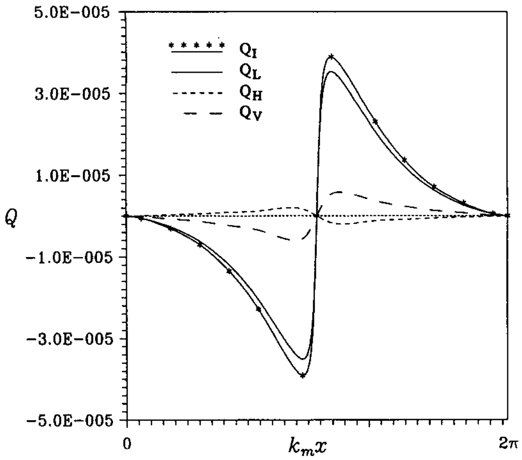

Fig. 6 The variation of surface concentration as a function of the position $k_m x$ with the process. The values of parameters are $A = 0.001$, $T = 1.0$, $M = 0.025$, and $D_s = 0.1$.

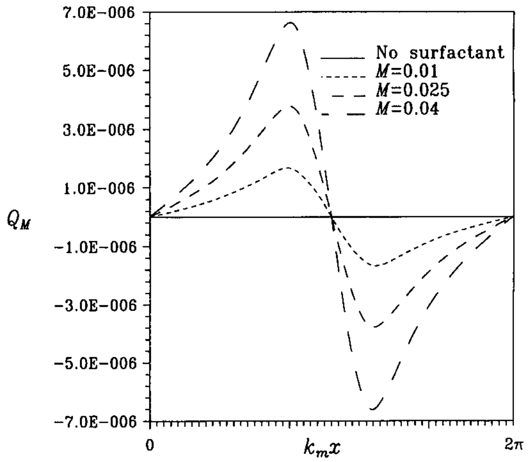

Fig. 7 The flow rate profiles for various Q_M's. The values of parameters are $A = 0.001$, $T = 1.0$, and $D_s = 0.1$.

the bottom to the peak of the ripple will increase. Consequently, the system will become more unstable and the rupture process is accelerated.

The effect of the high-order viscous dissipation terms on the flowing phenomenon of liquid film is also investigated. It can be known from the Q_H-distribution that the high-order viscous dissipation terms will induce the liquid to flow from the peak to the bottom of the surface ripple and exhibit a stabilization factor for the film system (Hwang et al., 1996). The high-order viscous dissipation terms in the momentum equation exhibit the effect of consuming part of the energy that is used to make the film rupture. This effect would weaken the perturbation phenomenon and increase the rupture time. From the Q_I-distribution, the flow rate predicted by the integral method which includes both inertial terms and high-order viscous dissipation terms is larger than that predicted by the long-wave theory. This is the reason the rupture time predicted by the former is shorter than that predicted by the latter and the former is much more unstable than the latter.

The following is a discussion on the influence of the Marangoni effect on the flowing phenomenon of liquid film. In general, some surfactants will be removed when the liquid is flowing from the bottom to the peak of the surface ripple. This causes the surfactant concentration to decrease near the bottom region but to increase near the peak region. The evolution of the surfactant concentration distribution on thin liquid films from initial disturbance to the final state is shown in Fig. 6 which exhibits a similar profile to Fig. 4. Note that the concentration is the highest near the peak while the lowest near the valley. This local variation of surfactant concentration will result in a concentration gradient, and further, present a stress (refer to the last term $-M\Gamma_x(1 + (3/2)h_x^2)$ in Eq. (23)) on the free surface that is perturbed. The stress is therefore to hinder the evolution of the perturbation. As shown in Fig. 7, the distribution of Q_M due to the Marangoni effect, has the function for stabilizing the liquid film system. Also, Fig. 7 demonstrates that the larger the M-value, the stronger the Marangoni effect. This induces the liquid to flow faster in a direction from the peak region to the bottom region of the ripple than in the reverse direction, and consequently makes the whole system more stable.

From the above analyses, it can be concluded that high-order viscous dissipation terms and the Marangoni effect are the stable factors for the liquid film system, while inertia terms are the unstable factors for that system.

The influences of various parameters M, T, and A on the rupture time are demonstrated in Fig. 8, Fig. 9, and Fig. 10, respectively. These results show that if one either adds surfactant (M increases) or chooses a fluid with higher surface tension T or lower the value of van der Waals attraction A, the film will rupture more slowly. This is because the redistribution of surfactant at the free surface makes the concentration of surfactant at the peak region become larger than that of the bottom region. Accordingly, the larger the M-value, the stronger the

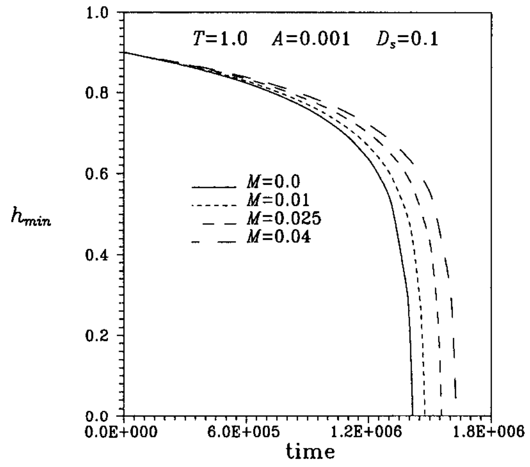

Fig. 8 The variation of h_{min} as a function of rupture time for various M's

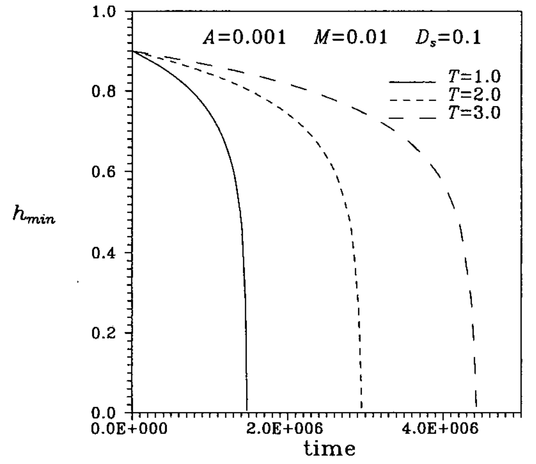

Fig. 9 The variation of h_{min} as a function of rupture time for various T's

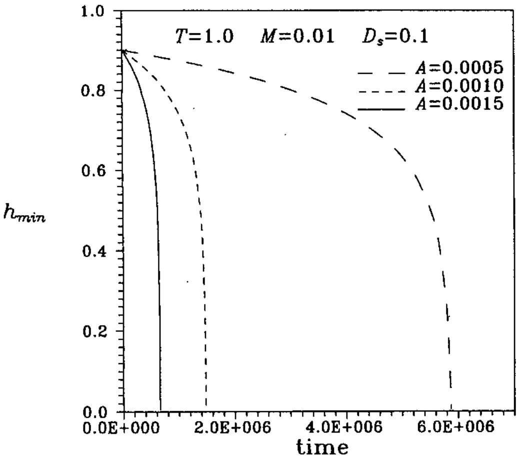

Fig. 10 The variation of h_{min} as a function of rupture time for various A's

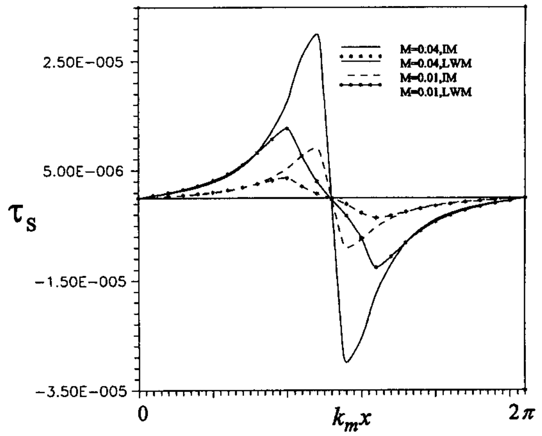

Fig. 12 The variation of surface shear attraction τ_S as a function of position $k_m x$ for $M = 0.01$ and $M = 0.04$. The values of parameters are $A = 0.001$, $T = 1.0$, $M = 0.01$, and $D_s = 0.1$ ($\tau_S = -M\Gamma_x$ for LWM, $\tau_S = -M\Gamma_x(1 + (3/2)h_x^2)$ for IM)).

Marangoni effect, which induces the liquid to flow faster from the peak region to the bottom region of the ripple and makes the liquid film system behave more stably. However, the flow generated by the VDWP, which is in a direction opposite to that of the Marangoni flow, makes the film unstable.

In the following, we compare the rupture behavior predicted by the long-wave method with that predicted by the integral method. Figure 11 shows the variation of nonlinear rupture time as a function of M-value predicted by the two methods. It is obvious that both methods predicted the nonlinear rupture time to increase following the M-value. It should be noted that the long-wave method always predicts the longer rupture time over the full range of M-value. In particular, the balance between two different rupture times enlarges following the M-value as can be seen from Fig. 11, the balance is about 2.6 percent at $M = 0$ but enlarges dramatically to 9.5 percent at $M = 0.04$. The results described above can be explained sequentially as follows. First, for the difference in rupture times demonstrated at $M = 0$ (denotes the system without surfactant), the overall effect of the unstable factor of inertia and the stable factor of high-order viscous dissipation terms involved in the integral method is to destabilize the thin film system, and thus enhance the rupture behavior to shorten the rupture time (Hwang et al., 1996). On the other hand, both the factors mentioned above are excluded in the long-wave expansion method, which gives a longer rupture time. Second, the different rupture behavior displayed when $M > 0$ (denotes the system with surfactant), can be understood by referring to Fig. 12, which shows the variation of surface shear attraction τ_S as a function of position $k_m x$ for $M = 0.01$ and $M = 0.04$, where LWM and IM denote the long-wave method and integral method, respectively. Obviously, a weaker shear attraction demonstrated by the integral method causes a stronger liquid flow toward the peak of the film undulation and consequently accelerates the rupture process. Moreover, when $M = 0.01$, the difference in the shear attraction predicted by both methods is small, while the difference increases evidently when $M = 0.04$. Therefore, the enlargement of the difference in the rupture time predicted by two methods is essentially due to an increasing difference shown in the two predicted shear attraction following the increases of M-value. In addition, as shown in Fig. 13, the nonlinear rupture time predicted by two models vary with the value of D_s. The difference in the rupture time predicted by two model decreases from 4.5 to 3.9 percent as the value of D_s increases from 0.1 to 0.5. It can be expected that the high-order effects, especially the high-order viscous dissipation terms in the shear-stress balance condition and the surfactant diffusion equation, will accelerate the rupture of the film.

5 Conclusion

The effect of insoluble surfactants on the instability of a liquid film on a flat plane is studied. The order of the magnitude

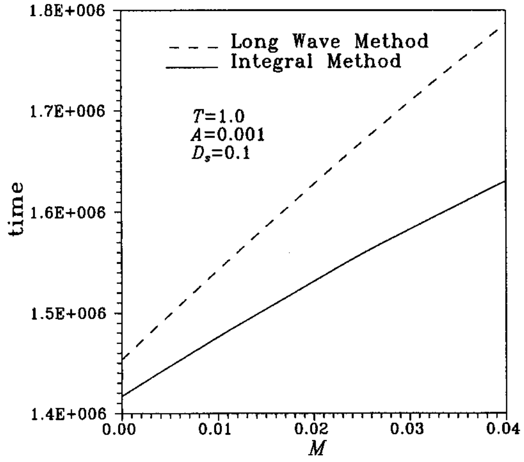

Fig. 11 The variation of rupture time as a function of the Marangoni number M predicted by two models (IM: Integral Method, LWM: Long-Wave Method)

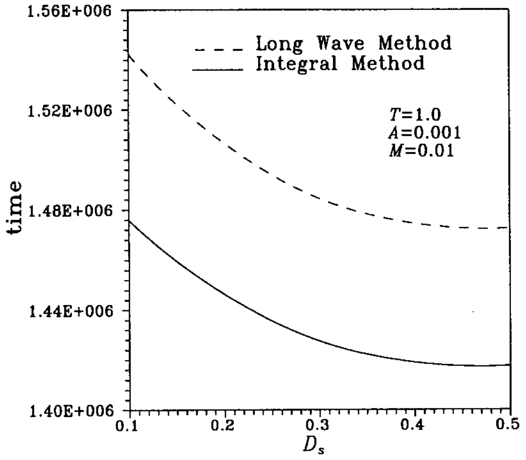

Fig. 13 The variation of rupture time as a function of diffusion coefficient D_s predicted by two models

of the dimensionless parameters are given to modify the Navier-Stokes' equations and the corresponding boundary conditions. Furthermore, the strong nonlinear evolution equations are derived by the integral method. And the numerical method is used to solve nonlinear evolution system for studying rupture process. The results show that the Marangoni effect and the effect of surface tension will delay the rupture process, while the effects of van der Waals and surface diffusion will enhance the rupture process. Comparing with the analysis results obtained from a liquid film bounded by two free surfaces, it is shown that the rupture time of the film coated on a flat plate is much longer than that of the former. In addition, the rupture time predicted by the integral method is shorter than that predicted by the long wave theory. This is because a destabilizing effect from the inertial term in the x-momentum equation is induced by the integral method. On the other hand, the quantitative difference in the rupture time predicated by two models enlarges when the Marangoni effect is enhanced, but does not vary obviously with the diffusion effect.

Acknowledgments

The authors gratefully acknowledge the financial support from the National Science Council under contract NSC 85-2212-E033-008.

References

Alekseenko, S. V., Narkoryakov, V. Ye., and Pokusaev, B. G., 1991, ''Wave Formation on a Vertical Falling Liquid Film,'' *AIChE Journal,* Vol. 31, pp. 1446–1460.

Borgas, M. S., and Grotberg, J. B., 1988, ''Monolayer Flow on a Thin Film,'' *Journal of Fluid Mechanics,* Vol. 193, pp. 151–176.

Burelbach, J. P., Bankoff, S. G., and Davis, S. H., 1988, ''Nonlinear Stability of Vaporizing/condensing Liquid Films,'' *Journal of Fluid Mechanics,* Vol. 195, pp. 463–494.

Chen, J. L., and Hwang, C. C., 1994, ''Effects on Inertia on the Process of a Thin Liquid Film,'' *Journal of Sciences Colloid Interface,* Vol. 167, pp. 214–216.

De Wit, A., Gallez, D., and Christov, C. I., 1994, ''Nonlinear Evolution Equation for Thin Liquid Films with Insoluble Surfactant,'' *Physics of Fluids,* Vol. 6, pp. 3256–3266.

Erneux, T., and Davis, S. H., 1993, ''Nonlinear Rupture of Free Films,'' *Physics of Fluids A,* Vol. 5, p. 1117.

Gaver III, D. P., and Grotberg, J. B., 1990, ''The Dynamics of a Localized Surfactant on a Thin Film,'' *Journal of Fluid Mechanics,* Vol. 213, pp. 127–148.

Gaver III, D. P., and Grotberg, J. B., 1992, ''Droplet Spreading on a Thin Viscous Film,'' *Journal of Fluid Mechanics,* Vol. 235, pp. 399–414.

Hwang, C. C., Chang, S. H. and Chen, J. L., 1993, ''On the Rupture Process of Thin Liquid Film,'' *Journal of Sciences Colloid Interface,* Vol. 159, pp. 184–216.

Hwang, C. C., Chen, J. L., and Shen, L. F., 1996, ''Strong Nonlinear Dynamic Rupture Theory of Thin Liquid Film,'' *Physics Review E,* Vol. 54, pp. 3013–3016.

Hwang, C. C., Chen, J. L., and Shen, L. F., 1996, ''Nonlinear Rupture Theory of a Thin Free Liquid Film with Insoluble Surfactant,'' *Journal of Physical Society Japan,* Vol. 65, pp. 2494–2501.

Jensen, O. E., and Grotberg, J. B., 1992, ''Insoluble Surfactant Spreading on a Thin Viscous Film: Shock Evolution and Film Rupture,'' *Journal of Fluid Mechanics,* Vol. 240, pp. 259–288.

Jensen, O. E. and Grotberg, J. B., 1993, ''The Spreading of Heat or Soluble Surfactant Along a Thin Liquid Film,'' *Physics of Fluids A,* Vol. 5, pp. 58–68.

Prokopiou, Th., Cheng, M., and Chang, H. C., 1991, ''Long waves on inclined films at high Reynolds number,'' *Journal of Fluid Mechanics,* Vol. 222, pp. 665–691.

Ruckemstein, E. and Jain, R. K., 1974, ''Spontaneous rupture of thin liquid film,'' *Journal of Chemical Society Far. Transactions II,* Vol. 70, pp. 132–147.

Sheludko, A., 1967, ''Thin liquid film,'' *Advanced Sciences Colloid Interface,* Vol. 1, pp. 391–494.

Troian, S. M., Herbolzheimer, E. and Safra, S. A., 1990, ''Model for the Fingering Instability Spreading Surfactant Drops,'' *Physics Review Letters,* Vol. 65, pp. 333–336.

Williams, M. B., and Davis, S. H., 1982, ''Nonlinear Theory of Film Rupture,'' *Journal of Sciences Colloid Interface,* Vol. 90, pp. 220–228.

APPENDIX

$$Q_V = \tfrac{1}{5}G^2h^5 + \tfrac{1}{2}GLh^4 + \tfrac{1}{3}L^2h^3$$

$$Q_H = \tfrac{1}{3}G_{xx}h^3 + f - L + \tfrac{1}{2}L_{xx}h^2 + \tfrac{1}{2}L_xh^2 + \tfrac{2}{3}G_xh^3$$

$$Q_M = -M\Gamma_x hh_{xx} - M\Gamma hh_{xxx}$$

$$Q_L = Thh_{xxx} + 3Ah^{-3}h_x$$

$$Q_I = Q_L + Q_H + Q_V$$

I. G. Hassan
Ph.D. Student.

H. M. Soliman
Professor. Mem. ASME

G. E. Sims
Professor.

Department of Mechanical
and Industrial Engineering,
University of Manitoba,
Winnipeg, Manitoba,
Canada R3T 5V6

J. E. Kowalski
Research Scientist,
Safety Thermalhydraulics Branch,
AECL Research,
Pinawa, Manitoba,
Canada R0E 1L0

Two-Phase Flow From a Stratified Region Through a Small Side Branch

(Data Bank Contribution)*

Experimental data are presented for the mass flow rate and quality of two-phase (air-water) discharge through a small branch (6.35 mm i.d.) located on the side of a large reservoir under stratified conditions. These data correspond to different values of the interface level between the onsets of gas and liquid entrainments for test-section pressures ranging from 316 to 517 kPa, test-section-to-separator pressure differences ranging from 40 to 235 kPa, and different hydraulic resistances of the line connecting the test section and separator. Influences of these independent variables on the mass flow rate and quality are discussed and normalized plots are presented showing that the data can be collapsed for a wide range of conditions. Comparisons are made with previous investigations and new empirical correlations are formulated and shown to be capable of predicting the present data with good accuracy.

1 Introduction

Studies of two-phase flow through small breaks in horizontal pipes under stratified-flow conditions have gained importance due to their relevance to many engineering applications (e.g., nuclear reactor safety during postulated loss-of-coolant accidents). Zuber (1980) pointed out that during such flows two distinct phenomena may occur, depending on the location of the gas-liquid interface relative to the break. If the interface is located above the break, gas can be entrained (by vortex or vortex-free motion) into the predominantly liquid flow through the break. On the other hand, if the interface is located below the break, liquid may be entrained into the predominantly gas flow. Accurate determination of the conditions at the onsets of these two phenomena, as well as the mass flow rate and quality of the two-phase flow discharging through the break at different locations of the interface are obviously relevant to engineering applications such as the development of safety codes for the nuclear industry. Zuber gives an excellent review of the early literature, including correlations for these phenomena.

The importance of this problem has motivated significant research, conducted mostly during the past ten years. Smoglie and Reimann (1986) performed experiments using stratified air-water flow at 200 to 500 kPa in a horizontal pipe (20.6 cm in diameter) with different break sizes (d = 6, 8, 12 and 20 mm) and different orientations for each break. The breaks were simulated by pipe stubs (0.055 m in length) with sharp-edged entrances and the flow through the break was controlled by a throttle valve. These results indicate an insignificant effect of the break size on the onsets of gas and liquid entrainment and the quality at the break. The onsets of entrainment were detected by the noise in the differential-pressure signals across the break. Empirical correlations were developed for the onsets of entrainment and branch quality in terms of normalized parameters.

Schrock et al. (1986) performed experiments using both air-water and steam-water as the working fluids. The experiments were performed at system pressures up to 1.07 MPa in a horizontal pipe (10.2 cm in diameter) with different break sizes (d = 4, 6 and 10 mm) and different orientations for each break. The breaks were simulated by tubes 123 mm in length. Viewing windows were placed at the break section and in the pipe just upstream and downstream of the break to allow visual observation of the flow phenomena. They concluded that the onset of gas entrainment (side and bottom orientations) was affected by surface tension and viscosity in addition to Froude number. The onset-of-gas-entrainment data for side orientation did not agree with the data of Smoglie and Reimann (1986). No explanation was given for this disagreement. Their data on the quality entering the branch, together with data from other studies, were correlated in terms of a normalized interface level.

Anderson (1987) presented experimental results for the onsets of liquid and vapor entrainment, as well as the flow quality into the branch for steam-water flows at high pressures (up to 6.2 MPa) using a 284-mm I.D. horizontal main pipe and a 34-mm I.D. branch line. Two orientations were used for the branch; horizontal and vertical downward. The onsets of entrainment were detected by the noise in the differential-pressure signal across the branch. Anderson (1987) reported good agreement between his experimental data and correlations of the same form as those proposed by Smoglie and Reimann (1986).

Yonomoto and Tasaka (1988) constructed a simple physical model to analyze two-phase flow through small breaks. Air-water experiments at a maximum pressure of 700 kPa were also conducted. A horizontal, square duct (19 cm × 19 cm) was used in the experiments instead of a round pipe. The break was simulated by a sharp-edged orifice (d = 10 and 20 mm). The onset conditions of gas and liquid entrainment were determined by visual observation. Good agreement was obtained between their model and their experimental data for discharge quality on the liquid-entrainment side and an empirical constant was incorporated in the model on the gas-entrainment side. A modified mathematical model was developed later by Yonomoto and Tasaka (1991), which improved the agreement with the experimental data.

Micaelli and Memponteil (1989) performed experiments using steam-water mixtures. A wide range of parameters was covered (system pressures of 2 to 7 MPa, main pipe diameters

---

* Data have been deposited to the JFE Data Bank. To access the file for the paper, see instructions on p. 652 of this issue.

Contributed by the Fluids Engineering Division for publication in the JOURNAL OF FLUIDS ENGINEERING. Manuscript received by the Fluids Engineering Division January 27, 1997; revised manuscript received February 24, 1998. Associate Technical Editor: M. Sommerfeld.

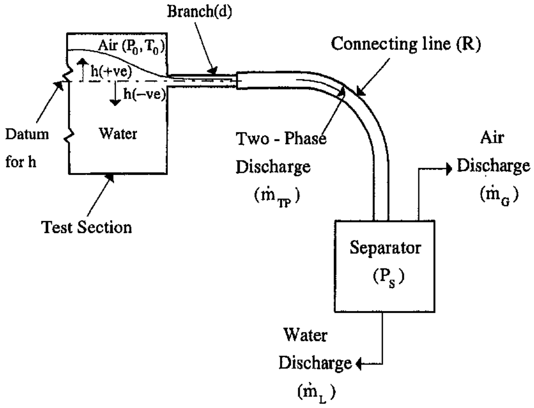

Fig. 1 Relevant experimental parameters

of 80 and 135 mm, and break diameters of 12 and 20 mm). The correlations for the beginning of liquid and gas entrainments were based on their experimental data as well as those of Smoglie and Reimann (1986), and Schrock et al. (1986). A semi-empirical correlation was developed for the break quality based on simple theoretical approaches adjusted by their own experimental data as well as other experimental data in the literature.

Experimental data and correlations were also developed for the onset of gas entrainment (Parrott et al., 1991) and the onset of liquid entrainment (Armstrong et al., 1992) during single and dual discharges from large reservoirs through small side branches (d = 6.35 mm). These experiments were conducted with air-water mixtures at pressures of 310 and 510 kPa. Both onsets were determined by visual observation.

This paper reports the results (onsets and mass flow rates of the two phases) of an experiment with a new geometry. The independent parameters were varied systematically in order to determine the effect of each. The results are correlated using new dimensionless parameters which may prove useful for universal correlation when the differences in geometry and measuring techniques among the various experimental investigations can be properly accommodated.

2 Experimental Investigation

2.1 Experimental Parameters. The independent parameters relevant to the present experiment are shown on the schematic diagram in Fig. 1. A branch of diameter d simulating a small break is placed in the side of a large reservoir containing stratified layers of air and water at a pressure P_o. The height of the flat air-water interface above the centreline of the branch is h. Thus, h is positive when the interface is above the branch centreline and negative when the interface is below the branch centreline. Discharging flow through the branch is directed (via a connecting line) to a separator where the pressure is maintained at P_s.

For the condition of fixed P_o and P_s, let us consider the dependence of the flow discharge on h. At high (positive) values of h, the flow discharge will be in the form of single-phase liquid and the flow rate, $\dot{m}_L$, would be essentially independent of h for the large values of ΔP considered in this experiment, where

$$\Delta P = P_o - P_s. \tag{1}$$

Decreasing h, a critical value is reached where gas begins being entrained in the predominantly liquid flow. This condition is called the onset or beginning of gas entrainment at which $h = h_{\mathrm{BGE}}$ and $\dot{m}_L = \dot{m}_{L,\mathrm{BGE}}$. For $h \gtrsim h_{\mathrm{BGE}}$, the value of $\dot{m}_L$ is essentially constant and equal to $\dot{m}_{L,\mathrm{BGE}}$. In the present experiment, the value of $\dot{m}_{L,\mathrm{BGE}}$ is dependent on ΔP and the hydraulic resistance of the connecting line, R, where

$$R = \sqrt{\Delta P}/\dot{m}_{L,\mathrm{BGE}}. \tag{2}$$

A further decrease in h results in a two-phase discharge, $\dot{m}_{\mathrm{TP}}$, which can be split in the separator into liquid and gas components with flow rates $\dot{m}_L$ and $\dot{m}_G$, respectively, where

$$\dot{m}_{\mathrm{TP}} = \dot{m}_L + \dot{m}_G; \tag{3}$$

the discharge quality, x, is given by

$$x = \dot{m}_G/\dot{m}_{\mathrm{TP}}. \tag{4}$$

It is reasonable to expect a decrease in $\dot{m}_{\mathrm{TP}}$ and an increase in x as h decreases. This trend continues until another critical value is reached (the onset of liquid entrainment), at which $h = h_{\mathrm{BLE}}$, $\dot{m}_G = \dot{m}_{G,\mathrm{BLE}}$, and the discharge quality equals one (although on lowering the interface level, at this point the flow changes from there being liquid entrained in the branch to there being no liquid entrained in the branch, the term "onset" or "beginning" is used rather than "end," in keeping with the existing literature). For $h \le h_{\mathrm{BLE}}$, the discharge will be in the form of single-phase gas and the flow rate, $\dot{m}_G$, remains essentially constant and equal to $\dot{m}_{G,\mathrm{BLE}}$. The value of $\dot{m}_{G,\mathrm{BLE}}$ is dependent on P_o, ΔP, and R.

The objective of this study is to focus on the two-phase discharge region corresponding to $h_{\mathrm{BLE}} \le h \le h_{\mathrm{BGE}}$ and to investigate the behavior of the mass flow rate, $\dot{m}_{\mathrm{TP}}$, and quality, x, within this region. Both of these dependent parameters are expected to be a function of the independent parameters P_o, ΔP, R, and h. It will be seen later that ΔP and R together act through their effect on $\dot{m}_{L,\mathrm{BGE}}$ and $\dot{m}_{G,\mathrm{BLE}}$, which really characterize the system, together with P_o and h.

2.2 Experimental Test Facility. A schematic diagram of the flow loop is shown in Fig. 2. An immersion-type circulating pump was used to supply distilled water to the test section at a rate adjusted by a bypass line. The inflow of water was fed into a disperser connected to the bottom flange of the test section. The disperser is basically a vertical copper tube (25.4 mm in diameter) closed at the top with twelve 12.7-mm holes distributed over its lateral surface. Thus, the inflow of water was dispersed into twelve horizontal streams to prevent the

Nomenclature

d = branch diameter
Fr = Froude number, given by Eqs. (7) and (8)
g = gravitational acceleration
H = normalized liquid level, given by Eq. (5)
h = liquid level
M = normalized mass flow rate, given by Eq. (6)

$\dot{m}$ = mass flow rate
P = pressure
R = hydraulic resistance, given by Eq. (2)
T = temperature
x = quality
$\delta(\ )$ = uncertainty in ( )
ρ = density

Subscripts

BGE = beginning of gas entrainment
BLE = beginning of liquid entrainment
G = gas phase
L = liquid phase
o = test-section condition
s = separator condition
TP = two phase

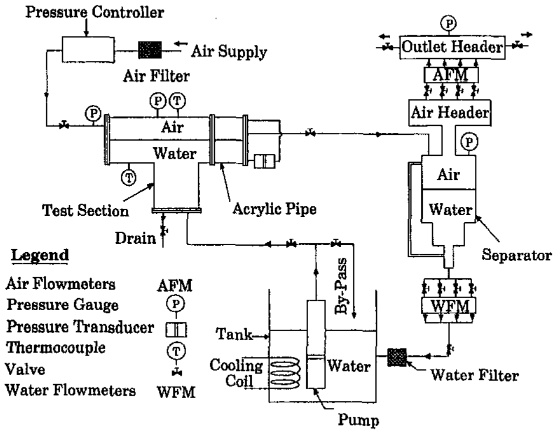

Fig. 2 Schematic diagram of the experimental test facility

gas-liquid interface from swelling. The attainment of a smooth interface was essential for an accurate measurement of the liquid height in the test section. The temperature of the water was held steady during the experiment by a cooling coil, as shown in Fig. 2. The test section was connected to an air supply equipped with a feedback pressure controller which maintained a steady pressure P_o in the test section throughout the experiment.

Details of the geometrical design of the test section were reported by Parrott et al. (1991). Basically, the test section is a large reservoir manufactured from type 304 stainless-steel sections, except for a clear acrylic pipe section near the outlet flange for visual observation of the flow phenomena. The outer diameter of this clear acrylic pipe (305 mm) was large enough to prevent significant visual distortion. The discharge branch was a hole, 6.35 mm in diameter, machined in a 127-mm-long brass block bolted to the outlet flange. Thus the branch had a straight length of 20 diameters within the brass block; there was then a straight 60-mm length of 6.35-mm-i.d. copper tubing and a 6.35-mm ($\frac{1}{4}$ in.) ball valve, onto which was fixed 12.7-mm-i.d. Tygon tubing running to the separator. The centerline of the outlet branch was located 28.4 mm from the centerline of the acrylic pipe (280-mm i.d.). A surveying transit was used to ensure that the faces of the outlet flange and the brass block were vertical, thus proving horizontality of the branch centerline. Two pressure taps, one on the air side and the other on the water side, were installed on the outlet flange and connected to a differential pressure transducer in order to measure the liquid height in the test section from which the value of h was determined. The air and water were basically stagnant near these pressure taps and therefore, the dynamic pressure effects on the liquid level measurement were insignificant.

The two-phase mixture leaving the test section through the side branch was directed to a separator where the air and water were split by centrifugal action. The flow rates of air and water were each measured by a bank of four variable-area-type flow meters with overlapping ranges. These flow-measuring stations covered the range of 15 cm^3/min to 0.0415 m^3/min on the water side and 198 cm^3/min to 1.3 m^3/min at standard conditions on the air side.

The temperature and pressure within the test section, as well as other locations within the loop, were recorded during the experiment. All flowmeters, thermocouples, and pressure gauges were calibrated before testing began.

2.3 Experimental Procedure. Fourteen sets of experimental data were collected in this investigation. Each set contains 17 to 30 data points covering the range $h_{\mathrm{BLE}} \leq h \leq h_{\mathrm{BGE}}$ with the values of P_o, ΔP, and R held constant. Values of P_o, ΔP, and R were varied among the data sets in such a manner so as to allow individual assessment of the influence of each independent parameter on $\dot{m}_{\mathrm{TP}}$ and x. The following procedure was followed in collecting the data for each set:

1. The conditions at the onset of gas entrainment (h_{BGE} and $\dot{m}_{L,\mathrm{BGE}}$) were established first. The air-water interface location (height) was set at a high value and was reduced in small steps, at which the liquid flow rate was measured under steady conditions. As the onset of gas entrainment was approached, the liquid level was further slowly lowered until gas was suddenly entrained at the branch; this onset was observed visually through the transparent part of the test section. The steady-state flow rate just before the onset gave $\dot{m}_{L,\mathrm{BGE}}$ and the reading of the pressure transducer immediately following the onset gave h_{BGE}.
2. Knowing from previous experience that the magnitudes of h_{BLE} and h_{BGE} are roughly the same, the distance between h_{BLE} and h_{BGE} was divided into a number (in the range of 17 to 30) of nearly equal intervals. The experiment was then conducted at decreasing values of h. At each h, the liquid level was held constant for a sufficient period of time that allowed the accurate measurement of gas and liquid flow rates leaving the separator, $\dot{m}_G$ and $\dot{m}_L$, respectively.
3. The value of h was continually decreased in steps until the exact values of h_{BLE} and $\dot{m}_{G,\mathrm{BLE}}$ were established. For conditions where $\dot{m}_L$ was finite and the interface was below the branch, a stream of water was pulled up from the interface through the branch. Decreasing the level caused this water stream to become thinner until it suddenly disappeared. This incidence (detected visually) marked the "onset" of liquid entrainment and the appropriate readings were immediately recorded for determining h_{BLE} and $\dot{m}_{G,\mathrm{BLE}}$.

2.4 Experimental Uncertainty. An estimate of the uncertainties in the independent and dependent variables was made in the fashion described by Moffat (1988) and Kline and McClintock (1953). All uncertainties quoted here are at "odds" (as used by these authors) of 20 to 1. The uncertainties are meant to accommodate: the accuracy of the calibrating device, the error in fitting an equation (for computer data reduction) to the calibration data, discrimination uncertainties in the measuring instruments, and unsteadiness in the process. Pressure gauges were calibrated using a deadweight tester, thermocouples using a standard mercury-in-glass thermometer, gas rotameters using wet test meters and venturi meters (in turn the calibrations of which were traceable to NIST standards) and liquid rotameters using a weigh-and-time method. The pressure transmitter used for measuring h was calibrated against a micromanometer and the digital voltmeter used in the calibration was subsequently used in the normal running of the experiments; for both calibration and subsequent experiments the sensitivity was approximately 35 mV per mm of water; the discrimination on the digital voltmeter was ±1 mV.

The results of the uncertainty analysis follow. The uncertainty in P_o (absolute pressure) was ±0.9 percent; the uncertainty in ΔP for data set no. 3 ($\Delta P = 40$ kPa, the smallest ΔP) was ±7.8 percent, while for the other data sets (higher ΔP) it was ±3.8 percent or less. The maximum uncertainty in the flow rates $\dot{m}_G$, $\dot{m}_L$, and $\dot{m}_{\mathrm{TP}}$ was ±4.0, ±2.4, and ±4.7 percent, respectively. The uncertainty in temperature measurements was ±0.25°C. The maximum uncertainty in the quality x was ±4.6 percent. The maximum uncertainty in R was ±4.7 percent. The absolute uncertainties in h, h_{BGE}, and h_{BLE} were ±0.13 mm, ±0.16 mm and ±0.16 mm, respectively; the uncertainty in h amounted to approximately 0.56 percent of $(h_{\mathrm{BGE}} - h_{\mathrm{BLE}})$. For the dimensionless quantity H (defined later and having a range of 0 to 1), the uncertainty δH was a maximum of ±0.007; in the range $0.1 \leq H \leq 1$ the maximum uncertainty in $\delta H/H$ was

Table 1 Nominal operating conditions*

Data set no.	P_o (kPa)	ΔP (kPa)	R $(\mathrm{kg}\cdot\mathrm{m})^{-1/2}$
1	316	123	1000
2		82	
3		40	
4	517	235	
5		166	
6		97	
7	316	127	
8	378		
9	448		
10	517		
11	316	123	1660
12			3000
13	517	235	1660
14			3000

* All tests were performed near room temperature.

±6 percent; the uncertainty in $\delta H/H$ increased with decreasing H and at the smallest finite H was ±13 percent. For the dimensionless quantity M (defined later and having a range of 0 to 1), δM varied between approximately ±0.003 and ±0.037, smaller values being associated with small M and larger values being associated with large M; in the range of $0.1 \le M \le 1$ the maximum uncertainty in $\delta M/M$ was ±5 percent; the uncertainty in $\delta M/M$ increased with decreasing M, was ±8 percent at $M = 0.05$ and increased to large values as M approached zero.

3 Results and Discussion

3.1 Presentation of Data and Trends. The operating conditions for the fourteen sets of experimental data generated in this investigation are listed in Table 1. Set nos. 1–3 and set nos. 4–6 explore the effect of ΔP at fixed values of P_o and R. The influence of R at fixed values of P_o and ΔP can be examined using set nos. 1, 11, and 12, or set nos. 4, 13, and 14. Finally, the influence of P_o at fixed values of ΔP and R can be examined from set nos. 7–10. A complete tabulation of all experimental data can be obtained either from the recent paper by Hassan et al. (1994), or the JFE Data Bank.

The intent of the experiments was to generate data for subcritical discharge. In order to confirm that choking conditions did not occur in the present experiments, the data for $\dot{m}_{TP}$ were compared with critical flow rates as obtained from two models. The models were the "homogeneous frozen flow model" (Whalley, 1987) and that by Henry and Fauske (1971). The results of the comparison, using the present data set no. 4 (largest flow rates), are shown in Fig. 3. Here, and with other data sets, for fixed P_o, ΔP, and R, the value at a given x, of the ratio of the actual $\dot{m}_{TP}$ to the predicted critical mass flow rate at any x never exceeded 0.8. An experimental check was also conducted for the limiting case of single-phase air flow by increasing ΔP beyond the maximum value otherwise used in the experiments and no choking occurred.

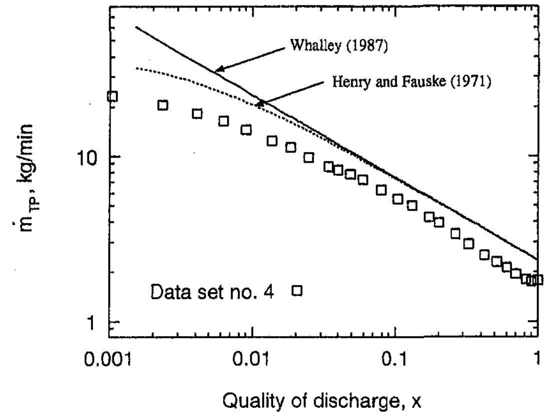

Fig. 3 Comparison of predicted critical mass flow rates with actual $\dot{m}_{TP}$ for data set no. 4. The maximum uncertainties in x and $\dot{m}_{TP}$ are ±4.6 percent and ±4.7 percent, respectively.

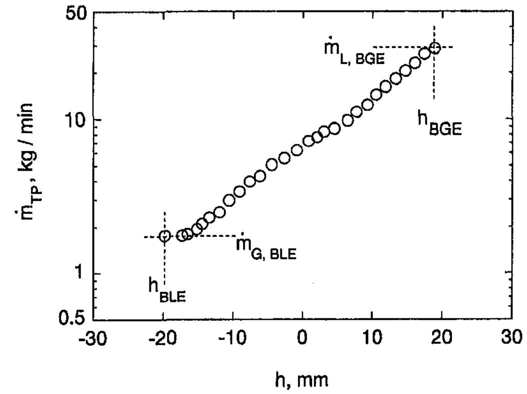

Fig. 4 Two-phase mass flow rate for data set no. 4. The uncertainty in h is ±0.13 mm, in $\dot{m}_{TP}$ is ±4.7 percent (max.), in h_{BLE} and h_{BGE} is ±0.16 mm, and in $\dot{m}_{G,BLE}$ and $\dot{m}_{L,BGE}$ is ±4.0 percent (max.) and ±2.4 percent (max.), respectively.

Figures 4 and 5 show typical results for $\dot{m}_{TP}$ and x, respectively. Within each data set (fixed P_o, ΔP, and R), $\dot{m}_{TP}$ decreases from $\dot{m}_{L,BGE}$ to $\dot{m}_{G,BLE}$ and x increases from 0 to 1 as h decreases from h_{BGE} to h_{BLE}. As the independent parameters P_o, ΔP, and R were varied during the experimental program, significant effects were noted on the measured dependent parameters. Increasing R at the same P_o and ΔP caused $\dot{m}_{L,BGE}$, $\dot{m}_{G,BLE}$, h_{BGE}, and $|h_{BLE}|$ to decrease, as shown in Fig. 6. Similar trends were produced by decreasing ΔP at the same P_o and R. Increasing P_o at the same ΔP and R had essentially no effect on h_{BGE} and $\dot{m}_{L,BGE}$ while $\dot{m}_{G,BLE}$ and $|h_{BLE}|$ increased, as shown in Fig. 7.

Normalized plots are shown in Figs. 8–13 using the following definitions for the normalized liquid level and the normalized mass flow rate, respectively:

$$H = (h - h_{BLE})/(h_{BGE} - h_{BLE}), \tag{5}$$

and

$$M = (\dot{m}_{TP} - \dot{m}_{G,BLE})/(\dot{m}_{L,BGE} - \dot{m}_{G,BLE}). \tag{6}$$

Figures 8–13 show that when the present data are plotted in terms of M versus H and x versus H, the effects of P_o, ΔP,

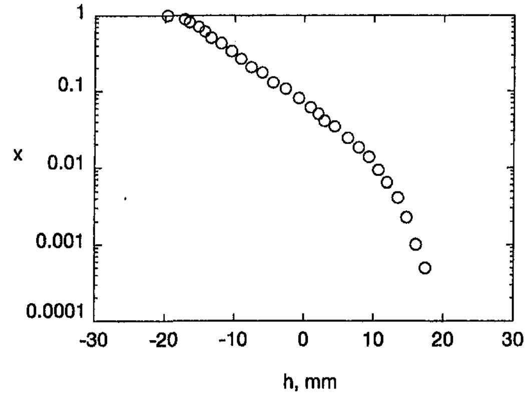

Fig. 5 Discharge quality for data set no. 4. The uncertainty in h is ±0.13 mm and in x is ±4.6 percent (max).

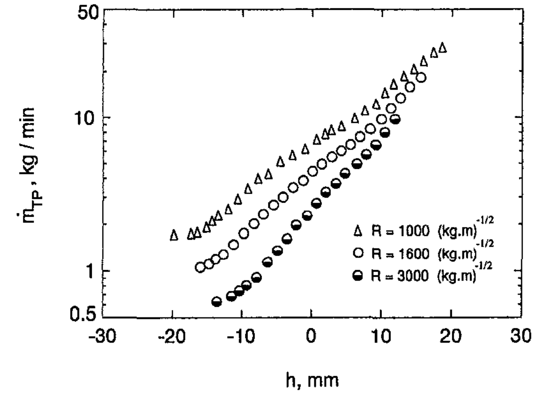

Fig. 6 Effect of R on $\dot{m}_{TP}$ from data set nos. 4, 13, and 14. The uncertainty in h is ±0.13 mm and in $\dot{m}_{TP}$ is ±4.7 percent (max.).

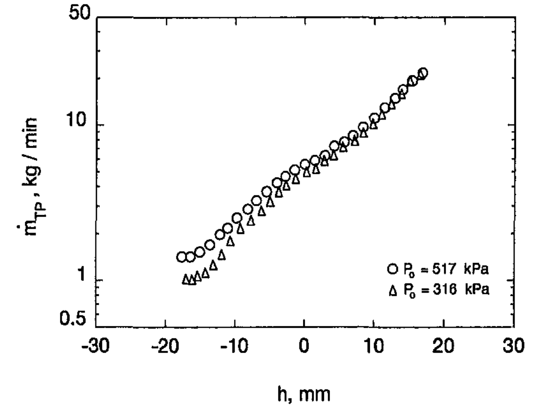

Fig. 7 Effect of P_o on $\dot{m}_{TP}$ from data set nos. 7 and 10. The uncertainty in h is ±0.13 mm and in $\dot{m}_{TP}$ is ±4.7 percent (max).

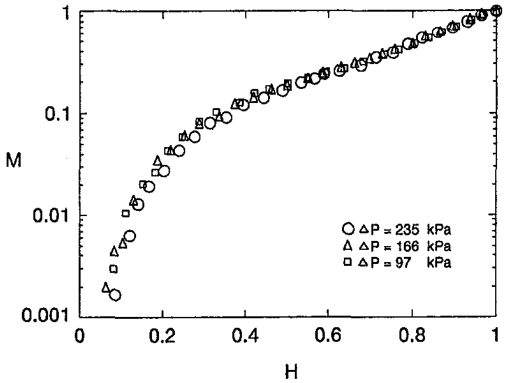

Fig. 8 Values of M for different ΔP using data set nos. 4–6. The uncertainty in H is ±0.007 (max) and in M varied between ~±0.003 and ±0.037; see Section 2.4 for more detail.

and R are largely absorbed within the present tested range of parameters. This observation is based on experimental data corresponding to a finite range of parameters and thus, should not be extended outside the present range without considerable thought. For example, Fig. 13 suggests a very small but consistent effect of P_o on x. This effect may become more visible if the range of P_o is considerably widened.

3.2 Comparisons With Existing Correlations. Comparisons were conducted between the present results and those of previous investigations. Figures 14 and 15 relate to the height of the interface at the onsets of gas and liquid entrainment, respectively. These results are correlated in terms of their respective Froude numbers, given by

$$\mathrm{Fr}_{\mathrm{BGE}} = (4/\pi)\dot{m}_{L,\mathrm{BGE}}/\sqrt{gd^5\rho_L(\rho_L - \rho_G)} \tag{7}$$

and

$$\mathrm{Fr}_{\mathrm{BLE}} = (4/\pi)\dot{m}_{G,\mathrm{BLE}}/\sqrt{gd^5\rho_G(\rho_L - \rho_G)}\,. \tag{8}$$

Deviations can be seen among different results for the case of h_{BGE} in Fig. 14, where the present results appear to be closest to those of Micaelli and Memponteil (1989) and Parrott et al. (1991). The correlation by Schrock et al. (1986) includes

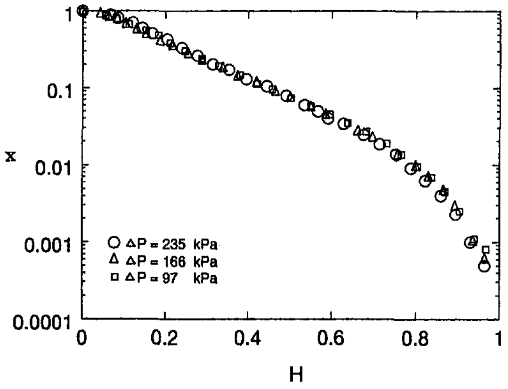

Fig. 9 Values of x for different ΔP using data set nos. 4–6. The maximum uncertainties in H and x are ±0.007 and ±4.6 percent, respectively.

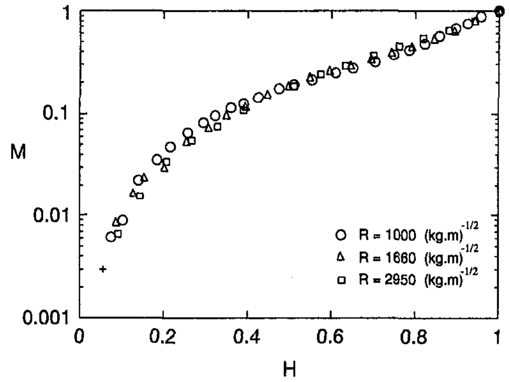

Fig. 10 Values of M for different R using data set nos. 1, 11 and 12. The uncertainty in H is ±0.007 (max.) and in M varied between ~±0.003 and ±0.037; see Section 2.4 for more detail.

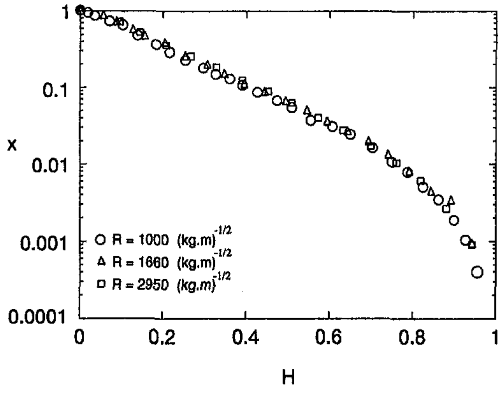

Fig. 11 Values of x for different R using data set nos. 1, 11, and 12. The maximum uncertainties in H and x are ±0.007 and ±4.6 percent, respectively.

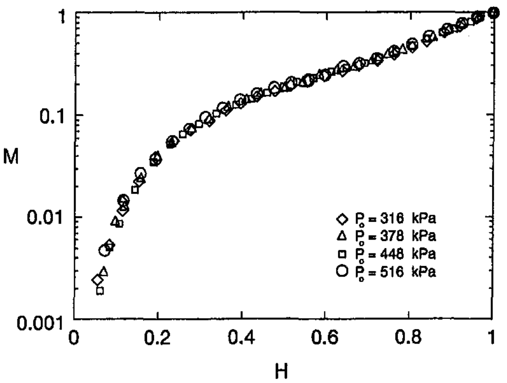

Fig. 12 Values of *M* for different P_o using data set nos. 7–10. The uncertainty in *H* is ±0.007 (max.) and in *M* varied between ~±0.003 and ±0.037; *see Section 2.4 for more detail.*

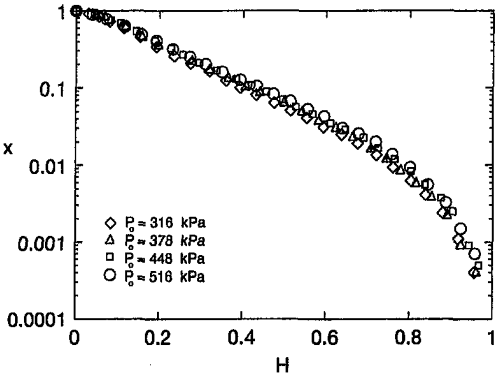

Fig. 13 Values of *x* for different P_o using data set nos. 7–10. The maximum uncertainties in *H* and *x* are ±0.007 and ±4.6 percent, respectively.

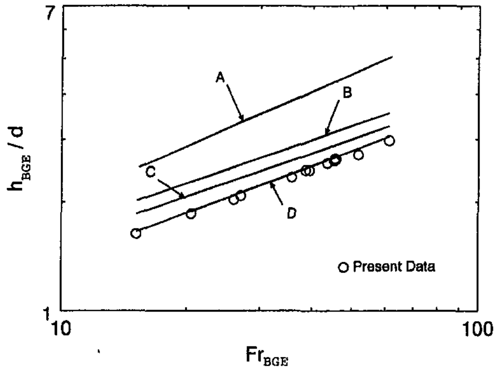

Fig. 14 Interface level at onset of gas entrainment [A—Schrock et al. (1986), B—Smoglie and Reimann (1986) and Yonomoto and Tasaka (1988), C—Micaelli and Memponteil (1989), and D—Parrott et al. (1991)]. The maximum uncertainties in Fr_{BGE} and in h_{BGE}/d are ±4.7 percent and ±2.2 percent, respectively.

viscosity and Bond numbers (in addition to Froude number) which were evaluated at the present experimental conditions. These deviations are not surprising in view of the different measuring and/or detection techniques for the onsets and the differences in geometry and flow conditions.

The deviations in the h_{BLE} results (Fig. 15) are not very significant. The manner by which the experiment is conducted can influence h_{BLE}. In the present experiment, all values of h_{BLE} were measured with a slowly decreasing liquid level whereby the area of the metal face between the interface and the branch was wet. Additional results were obtained with a slowly rising

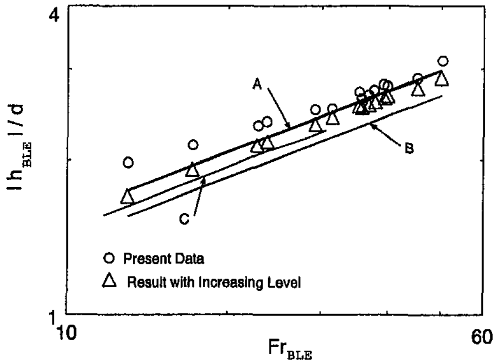

Fig. 15 Interface level at onset of liquid entrainment [A—Schrock et al. (1986), Smoglie and Reimann (1986) and Micaelli and Memponteil (1989), B—Yonomoto and Tasaka (1988), and C—Armstrong et al. (1991)]. The maximum uncertainties in Fr_{BLE} and $|h_{BLE}|/d$ are ±7.5 percent and ±2.2 percent, respectively.

liquid level (i.e., dry metal face) and they are shown in Fig. 15. Some deviation appears between the two sets of experimental results; however, these deviations are small, as well as the deviations among the different correlations for h_{BLE}. Considering Figs. 14 and 15 together, most certainly the correlating parameters used capture the essence of the phenomena.

The present values of *x* were compared with existing correlations from the literature (e.g., Smoglie and Reimann, 1986; Schrock et al., 1986; Yonomoto and Tasaka, 1988; Micaelli and Memponteil, 1989) and the results of these comparisons are given in Hassan (1995). The best agreement was obtained with the correlation of Micaelli and Mempontiel (1989) which has used the widest data base among existing correlations. In this correlation, the quality *x* was given as a function of h/h_b over the whole range $h_{BLE} \le h \le h_{BGE}$, where

$$h_b = 0.69[\dot{m}_{TP}^2/\{g\rho_m(\rho_L - \rho_G)\}]^{0.2} \qquad (9)$$

and ρ_m is the homogeneous density, given by

$$\rho_m = [x/\rho_G + (1 - x)/\rho_L]^{-1}. \qquad (10)$$

Figure 16 shows good agreement between data set no. 4 and the correlation of Micaelli and Memponteil throughout the whole range of *x*. This was typical of the other data sets (root-mean-square deviation between the correlation and all the data taken together was 22.6 percent).

The correlation of Micaelli and Memponteil (1989) is not in a suitable form for predicting *x*. This is because of the dependence on h_b, which in turn, requires a knowledge of $\dot{m}_{TP}$, a quantity not known a priori. Rather than requiring $\dot{m}_{TP}$ for the

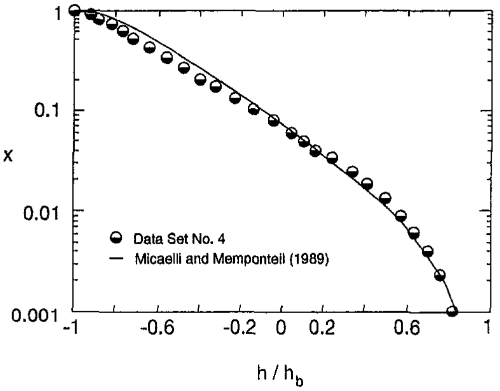

Fig. 16 Comparison between data set no. 4 and the correlation of Micaelli and Memponteil (1989). The uncertainty in *x* is ±4.6 percent (max.) and in *h* is ±0.13 mm.

determination of x, it would be useful to provide separate correlations for determining $\dot{m}_{TP}$ and x independently. The correlating parameters introduced in this paper (M and H), and used below to correlate the present data, may prove to be useful in developing universal correlations once the effects of the different geometries and measuring techniques have been determined (it is understood that one or more dimensionless fluid-property groups will no doubt appear as well).

3.3 Correlation of Present Data. Correlations were developed based on the present experimental data. They consist of the following relations:

$$h_{\mathrm{BGE}}/d = 0.57\mathrm{Fr}_{\mathrm{BGE}}^{0.4}, \tag{11}$$

$$|h_{\mathrm{BLE}}|/d = 0.87\mathrm{Fr}_{\mathrm{BLE}}^{0.31}, \tag{12}$$

$$x = 0.2\exp[6H(1 - 11.67H)/(1 - H)] + 0.8(1 - H^2)^{1.3}[-0.0122 + 0.42/(1 + \sqrt{\rho_L/\rho_G})]^H, \tag{13}$$

and

$$M = H^2\exp[-1.84H^2(1 - H^2)^{1.318}]. \tag{14}$$

For given values of ρ_L, ρ_G, d, h, $\dot{m}_{L,\mathrm{BGE}}$, and $\dot{m}_{G,\mathrm{BLE}}$, the corresponding values of $\dot{m}_{\mathrm{TP}}$ and x can be easily determined from the above relations (although ΔP and R were treated as independent variables in this experiment, their effect together is reflected in $\dot{m}_{L,\mathrm{BGE}}$ and $\dot{m}_{G,\mathrm{BLE}}$, as seen in the correlating equations for onsets, x and $\dot{m}_{\mathrm{TP}}$).

Equation (11) correlates the present data of h_{BGE} within ±five percent and its predictions are very close to those of Parrott et al. (1991), as can be seen in Fig. 14. Equation (12) correlates the present data of h_{BLE} (for decreasing liquid level) within ±five percent and its predictions are close to those of existing correlations, as shown in Fig. 15. Equations (13) and (14) converge to the appropriate limits at $H = 0$ and 1. They are consistent with the trends shown in Figs. 8–13, whereby x and M are functions of H with a slight dependence of x on P_o (or ρ_L/ρ_G).

Figures 17 and 18 show comparisons between all the present data and the correlating equations for x and M, respectively. Very good agreement can be seen in these figures. Quantitatively, the experimental values of x were predicted with a root-mean-square error of 8.1 percent over the range $0.001 \leq x \leq 1$. As well, the experimental values of M were predicted with a root-mean-square error of 13.2 percent over the range $0.001 \leq M \leq 1.0$ and a root-mean-square error of 8.2 percent over the range $0.01 \leq M \leq 1.0$. It should be emphasized that these correlating equations are empirical and thus, their accuracy can only be assured within the range of conditions covered in this investigation.

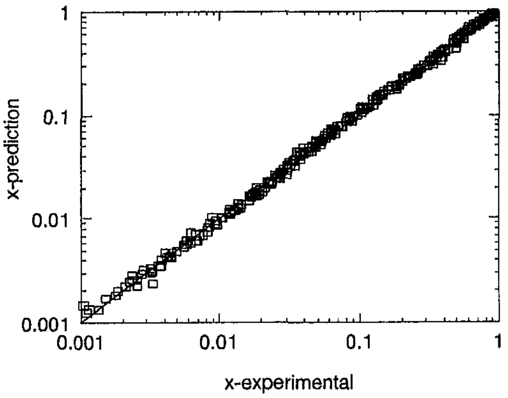

Fig. 17 Comparison between the present data for *x* and the proposed correlation. The maximum uncertainty in the experimental *x* is ±4.6 percent.

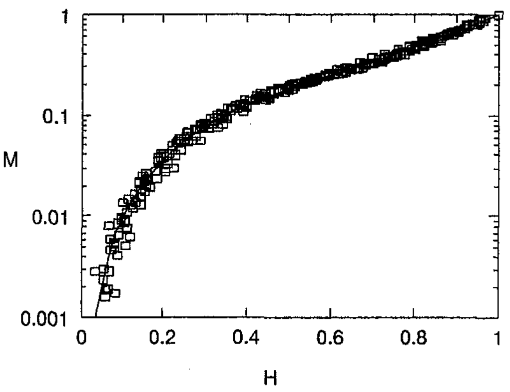

Fig. 18 Comparison between the present data for *M* and the proposed correlation. The uncertainty in *H* is ±0.007 (max) and in *M* varied between ~±0.003 and ±0.037; see Section 2.4 for more detail.

4 Concluding Remarks

New experimental data are reported on the onsets of gas and liquid entrainment, mass flow rate, and quality during two-phase discharge from a large reservoir through a small ($d = 6.35$ mm) side branch under stratified conditions. These data cover the ranges of $316 \leq P_o \leq 517$ kPa, $40 \leq \Delta P \leq 235$ kPa, and $1{,}000 \leq R \leq 3{,}000\ (\mathrm{kg}\cdot\mathrm{m})^{-1/2}$.

Influences of the independent parameters on the two-phase mass flow rate and quality were considered separately. These influences are shown to be significant when presented in terms of dimensional physical variables. However, these influences were largely absorbed when normalized parameters introduced in this study were used in presenting the data.

Comparisons were made between the present experimental data and existing empirical correlations. Good agreement is shown between the present values of x and the correlation of Micaelli and Memponteil (1989). Empirical relations were developed for the prediction of the two-phase mass flow rate and quality using the present normalized parameters. These relations agree very well with the experimental data. The new normalized parameters may prove useful in developing universal correlations once the effects of different geometries and measuring techniques have been determined.

JFE Data Bank Contribution

The experimental data generated in this investigation have been deposited in the JFE Data Bank. The data are listed in fourteen groups, each corresponding to one of the data sets of Table 1.

Acknowledgments

This research was carried out as a collaboration between the University of Manitoba and the Whiteshell Laboratories of AECL Research. The financial assistance provided by the Natural Sciences and Engineering Research Council of Canada and the CANDU Owners Group (COG) is gratefully acknowledged.

References

Anderson, J. L., 1987, "Entrainment and Pull-Through Phenomena at a Tee Junction," presented at the 1987 American Institute of Chemical Engineers Annual Meeting, New York, NY.

Armstrong, K. F., Parrott, S. D., Sims, G. E., Soliman, H. M., and Krishnan, V. S., 1992, "Theoretical and Experimental Study of the Onset of Liquid Entrainment During Dual Discharge from Large Reservoirs," *International Journal of Multiphase Flow,* Vol. 18, pp. 217–227.

Hassan, I. G., Soliman, H. M., Sims, G. E., and Kowalski, J. E., 1994, "Two-Phase Flow from a Large Reservoir Through a Small Side Orifice," *Experimental and Computational Aspects of Validation of Multiphase Flow CFD Codes,* FED-Vol. 180, pp. 47–58, ASME Fluids Engineering Division Summer Meeting, Lake Tahoe, Nevada.

Hassan, I. G., 1995, "Single, Dual and Triple Discharge from a Large, Stratified, Two-Phase Region Through Small Branches," Ph.D. thesis, University of Manitoba.

Henry, R. E., and Fauske, H. K., 1971, "The Two-Phase Critical Heat Flow of One-Component Mixtures in Nozzles, Orifices and Short Tubes," ASME *Journal of Heat Transfer,* Vol. 93, pp. 179–187.

Kline, S. J., and McClintock, F. A., 1953, "Describing the Uncertainties in Single-Sample Experiments," *Mechanical Engineering,* Vol. 75, pp. 3–8.

Micaelli, J. C., and Memponteil, A., 1989, "Two Phase Flow Behaviour in a Tee-Junction: the CATHARE Model," *Proceedings of the 4th International Topical Meeting on Nuclear Reactor Thermal-Hydraulics,* Vol. 2, pp. 1024–1030, Karlsruhe, Germany.

Moffat, R. J., 1988, "Describing the Uncertainties in Experimental Results," *Experimental Thermal and Fluid Science,* Vol. 1, pp. 3–17.

Parrott, S. D., Soliman, H. M., Sims, G. E., and Krishnan, V. S., 1991, "Experiments on the Onset of Gas Pull-Through During Dual Discharge from a Reservoir," *International Journal of Multiphase Flow,* Vol. 17, pp. 119–129.

Schrock, V. E., Revankar, S. T., Mannheimer, R., Wang, C. H., and Jia, D., 1986, "Steam-Water Critical Flow Through Small Pipes from Stratified Upstream Regions," *Proceedings of the 8th International Heat Transfer Conference,* pp. 2307–2311, San Francisco, CA.

Smoglie, C., and Reimann, J., 1986, "Two-Phase Flow Through Small Branches in a Horizontal Pipe with Stratified Flow," *International Journal of Multiphase Flow,* Vol. 12, pp. 609–625.

Whalley, P. B., 1987, *Boiling, Condensation and Gas-Liquid Flow,* Oxford University Press, Oxford, U.K., pp. 68–77.

Yonomoto, T., and Tasaka, K., 1988, "New Theoretical Model for Two-Phase Flow Discharged from Stratified Two-Phase Region Through Small Break," *Journal of Nuclear Science and Technology,* Vol. 25, pp. 441–455.

Yonomoto, T., and Tasaka, K., 1991, "Liquid and Gas Entrainment to a Small Break Hole from a Stratified Two-Phase Region," *International Journal of Multiphase Flow,* Vol. 17, pp. 745–765.

Zuber, N., 1980, "Problems in Modeling of Small Break LOCA," Nuclear Regulatory Commission Report NUREG-0724.

Transport of Heavy Particles in a Three-Dimensional Mixing Layer

Qunzhen Wang
Principal Engineer,
Thiokol Corp.,
Box 707, M/S 252,
Brigham City, UT 84302

Kyle D. Squires
Associate Professor,
Mechanical and Aerospace
Engineering Department,
Box 876106,
Arizona State University,
Tempe, AZ 85287-6106

Particle transport in a three-dimensional, temporally evolving mixing layer has been calculated using large eddy simulation of the incompressible Navier-Stokes equations. The initial fluid velocity field was obtained from a separate simulation of fully developed turbulent channel flow. The momentum thickness Reynolds number ranged from 710 in the initial field to 4460 at the end of the calculation. Following a short development period, the layer evolves nearly self-similarly. Fluid velocity statistics are in good agreement with both the direct numerical simulation results of Rogers and Moser (1994) and experimental measurements of Bell and Mehta (1990). Particles were treated in a Lagrangian manner by solving the equation of motion for an ensemble of 20,000 particles. The particles have the same material properties as in the experiments of Hishida et al. (1992), i.e., glass beads with diameters of 42, 72, and 135 μm. Particle motion is governed by drag and gravity, particle-particle collisions are neglected, and the coupling is from fluid to particles only. In general, the mean and fluctuating particle velocities are in reasonable agreement with the experimental measurements of Hishida et al. (1992). Consistent with previous studies, the Stokes number (St) corresponding to maximum dispersion increases as the flow evolves when defined using a fixed fluid timescale. Definition of the Stokes number using the time-dependent vorticity thickness, however, shows a maximum in dispersion throughout the simulation for St ≈ 1.

1 Introduction

Particle transport in free shear flows has been the subject of numerous studies owing to the relevance of these flows to engineering and scientific applications (e.g., see Crowe et al., 1985; Chein and Chung, 1987; Samimy and Lele, 1991; Lazaro and Lasheras, 1992a, b; Hishida et al., 1992; Wen et al., 1992; Martin and Meiburg, 1994; Raju and Meiburg, 1995; Kiger and Lasheras, 1995; Marcu and Meiburg, 1996; Crowe et al., 1996). Consequently, various features of particle-laden free shear flows are now reasonably well known. Perhaps the most well known being that the large-scale vortical rollers often observed in these flows dominate particle transport. Particles with relaxation times comparable to the roller timescale, i.e., possessing Stokes numbers near unity, can exhibit larger lateral dispersion than fluid elements (e.g., see Crowe et al., 1993, 1996).

Though the influence of large-scale organized motions on particle transport is known, most engineering models do not yield accurate predictions of particle transport in free shear flows. Most models rely on Reynolds averaging in which the governing equations are averaged over time or ensembles in order to produce transport equations for mean quantities. Application of Reynolds-averaged methods to free shear flows is problematic since the time-dependent organized structures which have the greatest effect on transport are lost as a consequence of the averaging process. Therefore, techniques capable of representing structural interactions are required in order to accurately predict particle transport in turbulent free shear flows.

A powerful approach for prediction of three-dimensional particle-laden free shear flows is large eddy simulation (LES). In LES the large scales of motion are computed directly while the effect of the smallest (subgrid) scales are modeled. The primary advantage of LES over direct numerical simulation (DNS), in which the Navier-Stokes equations are solved without recourse to modeling at any scale, is that calculations at higher Reynolds numbers are possible. Furthermore, since the small scales are more universal than the large scales, it is possible to use simpler models of the subgrid-scale (SGS) stress than are required to model the turbulent stresses in Reynolds-averaged techniques. One of the main improvements advancing LES as a viable tool for complex flows has been the development of dynamic subgrid modeling (Germano et al., 1991). Dynamic SGS models are especially attractive for computation of particle-laden flows since predictions of particle transport should be expected to be significantly improved by more accurate parameterizations of the turbulence. Therefore, the principal aim of the present study is application of LES and dynamic SGS models to the calculation of a three-dimensional, particle-laden turbulent mixing layer. The reader is referred to Sirignano (1992), Stock (1994), Simonin et al. (1995), and Wang and Squires (1996a) for further discussion of other applications of LES to calculation of gas-phase turbulent flows laden with heavy particles.

Of principal interest in this work is examination of particle transport in a high Reynolds number mixing layer evolving from fully developed turbulent initial conditions. In the majority of numerical simulations of free shear flows, perturbations are imposed on a well-defined initial velocity profile in order to initiate roll up and pairing. This approach is useful for examining the interactions between particles and large-scale rollers since the enhanced dispersion for particles with St ≈ 1 observed in previous work is a result of the strong interactions between the particles and large-scale coherent structures (e.g., see Crowe et al., 1996). It is worthwhile to point out, however, that the influence and universality of large-scale coherent motions in fully developed turbulent mixing layers has been a subject of study (e.g., see Hussain, 1983; Rogers and Moser, 1994). Rogers and Moser (1994) found, for example, that in a self-similar flow, growth of the mixing layer occurred without classical vortex pairings. It is then possible that the transport of heavy particles will differ in a mixing layer which does not possess a clearly identifiable large-scale structure, implying a possibly different Stokes number scaling at high Reynolds numbers. Therefore, it is also of interest to examine the Stokes number dependence of particle dispersion in a turbulent mixing layer

---

Contributed by the Fluids Engineering Division for publication in the JOURNAL OF FLUIDS ENGINEERING. Manuscript received by the Fluids Engineering Division May 31, 1996; revised manuscript received June 9, 1997. Associate Technical Editor: D. P. Telionis.

evolving from a fully developed initial condition in which there are no preferred disturbances imposed on the velocity field.

Calculation of a mixing layer from fully developed initial conditions was first performed by Rogers and Moser (1994). In their work two realizations from the DNS of a flat-plate turbulent boundary layer were merged to form the mixing layer. Self-similar evolution of the flow was obtained for calculations in which no additional disturbances were imposed on the initial velocity field as well as a second case in which the initially two-dimensional disturbances were relatively weak. A similar approach has been adopted in the present study which models experimental conditions in which the boundary layers merging from the splitter plate are turbulent.

The temporally evolving mixing layer is considered in this paper because of the considerable computational simplifications as compared to the spatially developing case, e.g., two homogeneous directions over which to accumulate statistics as well as no requirement for specification of turbulent inflow/outflow conditions. The experimental measurements of the particle-laden mixing layer considered by Hishida et al. (1992) serve as a baseline for evaluation of LES predictions. The particles used in the experiment were 42, 72, and 135 μm diameter glass beads. Mean and root-mean-square (rms) velocity fluctuations of both the fluid and particles were measured at several streamwise stations extending 250 mm downstream of the splitter plate. An overview of the numerical approach and treatment of the dispersed phase, as well as the statistical evolution of the fluid velocity field are discussed in Section 2. In Section 3.1 LES predictions of the particle velocity field are compared with the experimental measurements of Hishida et al. (1992) and in Section 3.2 the dependence of particle dispersion on Stokes number is discussed. The conclusions are summarized in Section 4.

2 Simulation Overview

2.1 LES of a 3D Temporally Evolving Mixing Layer. A three-dimensional temporally evolving mixing layer was calculated using LES of the incompressible Navier-Stokes equations. An eddy viscosity hypothesis was invoked to model the subgrid-scale stress in the fluid. The Lagrangian dynamic model developed by Meneveau et al. (1996) was used to compute the model coefficient (see also Germano et al., 1991). Since the main focus of the present study is on particle transport, the carrier flow was assumed unmodified by the presence of the dispersed phase, i.e., the coupling was from fluid to particles only. The equations governing conservation of mass and momentum for the fluid were solved using the fractional step method on a staggered grid (e.g., see Kim and Moin, 1985; Perot, 1993; Wu et al., 1995). Second-order Adams-Bashforth was used for advancement of the convective terms and part of the SGS term while the Crank-Nicholson method was applied for update of the viscous terms and a portion of the SGS stress. The Poisson equation for pressure was solved using Fourier series expansions in the streamwise and spanwise directions together with tridiagonal matrix inversion.

The initial condition for the velocity field is from a separate LES calculation of turbulent channel flow at Reynolds number based on friction velocity and channel half-width of 180 (see Wang et al., 1995; Wang and Squires, 1996a for details). Note that for the temporal layer considered in this work, statistically homogeneous initial conditions are appropriate (in the streamwise and spanwise directions). In the (spatially developing) experiment of Hishida et al. (1992), the properties of the splitter-plate boundary layers were not reported. Consequently, the initial conditions used in the LES are an approximation to the upstream conditions in Hishida et al. (1992). The Reynolds number based on the initial momentum thickness θ_0 and velocity difference ΔU is $\mathrm{Re} = \Delta U \theta_0/\nu = 710$. The Reynolds number based on the free stream velocity and boundary layer thickness on one side of the layer is 177. This value from the LES is smaller than the measured value of 200 in the high speed side of the experiment by Hishida et al. (1992) and larger than that in the low speed side of the experiments.

The size of the computational domain in the streamwise direction, $L_x = 116\theta_0$, and in the spanwise direction, $L_z = 39\theta_0$, are the same as the domain size in the channel flow of Wang and Squires (1996a). The domain size in the cross-stream direction was increased to $L_y = 233\theta_0$ in order to minimize any adverse effects of the cross-stream boundary condition on the evolution of the layer. For most of the results reported in the next section, the fluid flow was resolved using $64 \times 65 \times 128$ grid points in the x, y, and z directions, respectively. While a uniform mesh was used in the streamwise and spanwise directions, a stretched grid was used in the cross-stream direction with a clustering of grid points near the centerplane. For the temporally evolving layer periodic boundary conditions are appropriate for the streamwise and spanwise directions. No-stress boundary conditions were applied in the cross-stream direction along the top and bottom surfaces of the computational domain, i.e., $\bar{u}_2 = \partial \bar{u}_1/\partial x_2 = 0$ where $\bar{u}_1$ and $\bar{u}_2$ are the streamwise and cross-stream velocity, respectively.

2.2 Evolution of the Eulerian Velocity Field. Shown in Fig. 1(*a*) is the evolution of the momentum thickness along with the DNS results of Rogers and Moser (1994) for their unforced case. For a self-similar mixing layer the momentum thickness should increase linearly in a temporally evolving flow (downstream location in a spatially evolving layer). It is evident that the momentum thickness increases linearly after $\tau \equiv t\Delta U/\theta_0 \approx 50$. The dimensionless layer growth rate is about 0.017, which is slightly larger than the value of 0.014 from Rogers and Moser (1994). The range of r in the experiments quoted by Dimotakis (1991) is 0.014–0.022. Thus, the growth rate from the LES agrees very well with the experimental data. Figure 1(*a*) also shows that the momentum thickness increases by a factor of about 6 from $\tau = 0$ to $\tau = 330$, indicating that the Reynolds number based on the momentum thickness θ and the velocity difference ΔU increased from 710 to 4,460.

In the self-similar region the ratio of the vorticity thickness to the momentum thickness in the LES is about 4.5, close to the value of 4.8 obtained by Rogers and Moser (1994). This ratio is 4.44 for an error function mean velocity profile and 4.0 for a hyperbolic tangent velocity profile. The Reynolds number based on vorticity thickness increased to over 20,000 in the LES, high enough such that the current simulations produce fully developed turbulence (Rogers and Moser, 1994). In comparison with experiments on particle-laden mixing layers this value is larger than the range of $\mathrm{Re}_\omega \sim 1{,}000 - 4{,}500$ in Wen et al. (1992) and $\mathrm{Re}_\theta \sim 2{,}700$ in Hishida et al. (1992), while it is about half the value $\mathrm{Re}_\theta \sim 9{,}700$ in Lazaro and Lasheras (1992a, b) and Kiger and Lasheras (1995).

The evolution of the dissipation rate of turbulent kinetic energy,

$$\varepsilon = \int_{-\infty}^{\infty} \langle (\nu + \nu_T) |S|^2 \rangle_{xz} dy, \qquad (1)$$

is shown in Fig. 1(*b*), along with the results from Rogers and Moser (1994) ($\langle\,\rangle_{xz}$ denotes an average in the homogeneous x-z plane). Also shown in the figure is the molecular dissipation $\int_{-\infty}^{\infty} \nu \langle |S|^2 \rangle_{xz} dy$ and SGS contribution $\int_{-\infty}^{\infty} \langle \nu_T |S|^2 \rangle_{xz} dy$. It is interesting to note that the magnitude of the total dissipation in the LES is close to that of Rogers and Moser (1994) for $\tau > 50$. For a self-similar mixing layer, the total dissipation rate should be a constant. At large τ, the dissipation rates from both LES and DNS decrease, suggesting that self-similarity does not hold at later times. The self-similar region, as indicated by the region of constant dissipation, in the LES is roughly from $140 < \tau < 280$. Also interesting is that Fig. 1(*b*) shows the SGS

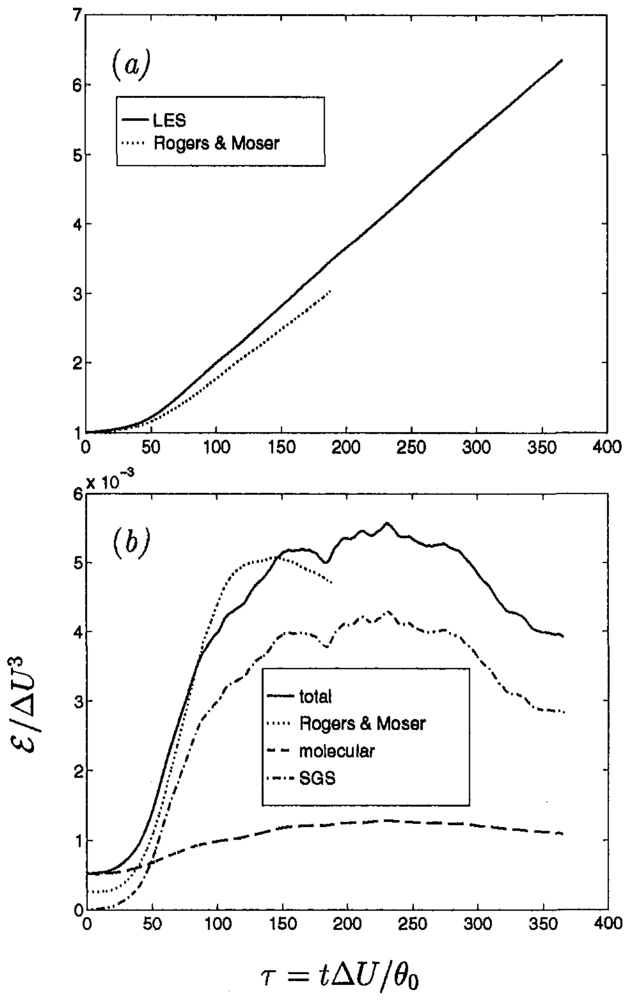

Fig. 1 Temporal evolution of momentum thickness θ and dissipation rate ε. (*a*) Momentum thickness; (*b*) dissipation rate.

dissipation is substantially larger than the molecular value in the self-similar region.

The mean velocity profiles at four times in the self-similar region are shown in Fig. 2(*a*) along with those from Rogers and Moser (1994) and the experimental measurements of Bell and Mehta (1990). It is clear that the collapse of the scaled mean profile is excellent and in good agreement with both DNS results and experimental data. A representative component of the resolved Reynolds stress tensor, $\langle u_2'' u_2'' \rangle$, where $u_i'' = \bar{u}_i - \langle \bar{u}_i \rangle_{xz}$ is shown in Fig. 2(*b*). The cross-stream fluctuations exhibit a reasonably good collapse and also agree well with the DNS and experiments. The effect of grid resolution on the cross-stream fluctuations is shown in Fig. 3. The cross-stream fluctuations shown in the figure are the most sensitive to changes in resolution (compared to the other normal stresses) and therefore provide an appropriate diagnostic for examining the effect of grid refinement on LES predictions. Compared to Fig. 2, the streamwise and spanwise resolution in Fig. 3 have been coarsened by 50 percent, the cross-stream grid spacings have been increased by as much as a factor of two. For the coarsest resolution (Fig. 3(*a*)), there is a relatively large discrepancy between LES predictions of $\langle u_2'' u_2'' \rangle$ and experimental measurements. Refining the cross-stream resolution (Fig. 3(*b*)) improves both the collapse of the profiles and agreement with Rogers and Moser (1994) and Bell and Mehta (1990). Further refining the grid in each coordinate direction (Fig. 3(*b*) to Fig. 2) shows a substantially smaller change in LES predictions with respect to changes in grid spacing. It is important to point out that in calculations in which there is not a large separation between the filter width and grid spacing, as in the present work, there will not be an absolute invariance of statistics to changes in grid refinement. Thus, the primary effect of changing grid spacing is to determine a range of resolutions where LES predictions are relatively insensitive to further changes in grid refinement. With that in mind, Figs. 2 and 3 demonstrate the flow is both adequately and accurately resolved.

2.3 Treatment of the Dispersed Phase. The particle equation of motion used in the simulations describes the motion of particles with densities substantially larger than that of the surrounding fluid and diameters small compared to the Kolmogorov scale:

$$\frac{dv_i}{dt} = -\frac{\rho_f}{\rho_p}\frac{3}{4}\frac{C_D}{d}|\mathbf{v} - \mathbf{u}|(v_i - u_i) + g\delta_{i1}, \qquad (2)$$

where v_i is the velocity of the particle, u_i is the velocity of the fluid at the particle position, and g is the acceleration of gravity. In the results shown in this paper, the fluid velocity u_i in (2) is the resolved component. The body force acts along the (positive) streamwise direction corresponding to the vertical configuration of Hishida et al. (1992). The fluid and particle densities in (2) are denoted ρ_f and ρ_p, respectively, and d is the particle diameter. An empirical relation for C_D given by Clift et al. (1978) was employed, i.e., $C_D = 24[1 + 0.15\,\mathrm{Re}_p^{0.687}]/\mathrm{Re}_p$ where the particle Reynolds number $\mathrm{Re}_p = |\mathbf{v} - \mathbf{u}|d/\nu$. It should also be noted that (2) neglects the influence of virtual mass, buoyancy, and the Basset history force. For particles with material densities large compared to the fluid these forces are

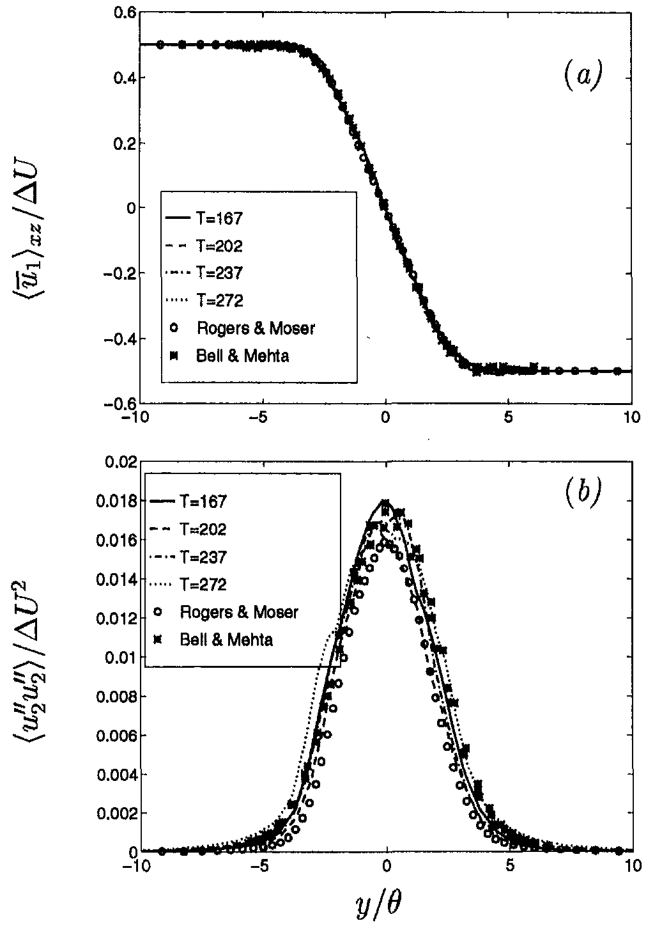

Fig. 2 Fluid streamwise mean velocity and cross-stream Reynolds stress. Calculations obtained using a grid resolution of 64 × 129 × 64. (*a*) Mean velocity; (*b*) $\langle u_2'' u_2'' \rangle/\Delta U^2$.

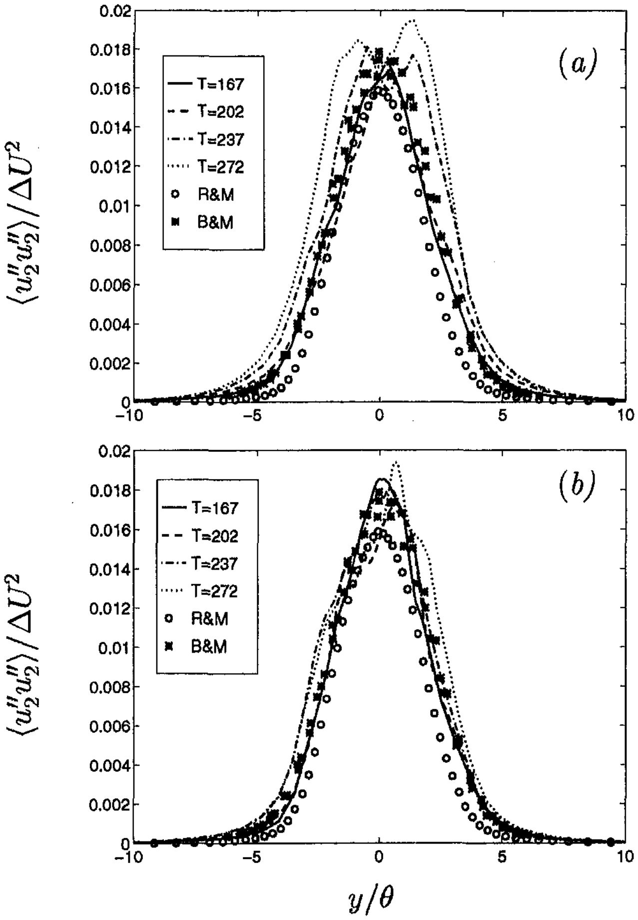

Fig. 3 Effect of grid resolution on Reynolds stresses. (*a*) Grid size: 48 × 65 × 48; (*b*) grid size: 48 × 97 × 48.

negligible compared to the drag. Previous investigations have shown that the effect of shear-induced lift, while relevant to problems of particle deposition, is less significant to this work and therefore has been neglected (see McLaughlin, 1989).

From computation of an Eulerian velocity field, (2) was integrated in time using second-order Adams-Bashforth. Since it is only by chance that a particle is located at a grid point where the Eulerian velocity field is available, fourth-order Lagrange polynomials were used to interpolate the fluid velocity to the particle position (see Wang et al., 1995 and references therein for discussion of interpolation errors). Particle displacements were also integrated using the second-order Adams-Bashforth method. Periodic boundary conditions were used to reintroduce particles which moved out of the computational domain in the streamwise or spanwise directions. The cross-stream dimension L_y was large enough such that no particle exits the computational domain.

Properties of the dispersed phase were obtained by following the trajectories of 20,000 particles. The particles used in the simulations possess material characteristics identical to those in the experiments of Hishida et al. (1992): 42, 72, and 135 μm diameter glass beads; the particle response time, which is defined as $\tau_p = \rho_p d^2/(18\rho_f \nu)$ is 0.014, 0.041, and 0.144s, respectively. For these diameters and sample sizes the dispersed phase volume fraction varies from 10^{-5} for the smaller particles to 10^{-4} for the 135 μm beads. For volume fractions in this range particle collisions are thought to be relatively less important (e.g., Crowe et al., 1996). However, in the central part of the layer, where particles were injected in the experiment and initially seeded in the computations, local values of the volume fraction may be large enough such that collisions are significant. The reader is referred to the work of Sommerfeld (1995) and Laviéville et al. (1995) for additional discussion of particle collisions.

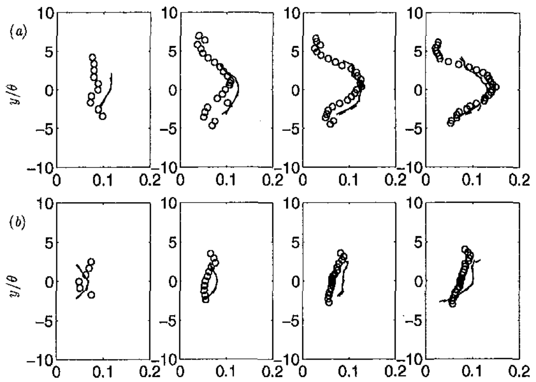

Fig. 4 Streamwise particle velocity fluctuations. (*a*) 42 μm glass beads; (*b*) 72 μm glass beads; first column: X = 100 mm (τ = 168); second column: X = 150 mm (τ = 236); third column: X = 200 mm (τ = 300); fourth column: X = 250 mm (τ = 362). —— LES (20,000 particles); ---- LES (10,000 particles); ○ Hishida et al. (1992).

In the experiments of Hishida et al. (1992), particles were injected from a nozzle near the splitter plate. In the calculations particles are initially (randomly) distributed in x-z planes $-0.5D \le y \le 0.5D$, where $D = 0.57$ mm is the nozzle diameter. The three groups of particles have the same initial distribution and same initial velocity. The initial particle velocities are designed to match those of the 135 μm particles in the experiment (injection velocities for other particle sizes were not measured). LES predictions in the temporally evolving flow are compared to the spatially developing experimental results by first using the convection velocity in the experiment (8.5 m/s) to transform from downstream evolution to time. LES predictions are then compared to the experimental results at equivalent times made dimensionless using the local momentum thickness and velocity difference ΔU.

3 Results

3.1 Comparison of LES Predictions to Experimental Measurements.

LES predictions of the streamwise particle fluctuating velocity and shear stress, $\langle v_1''v_2''\rangle$, are compared to the measurements from Hishida et al. (1992) in Figs. 4 and 5 ($v_i'' = v_i - \langle v_i \rangle$ is the particle velocity fluctuation). To compare

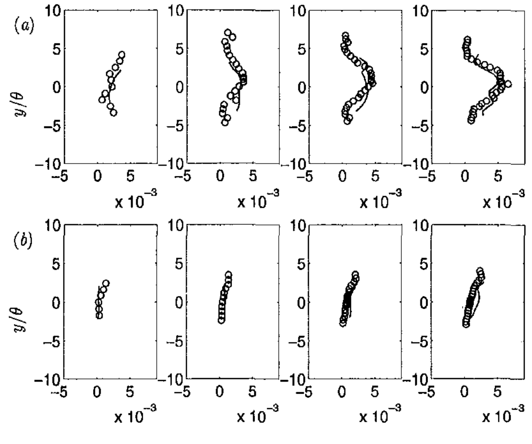

Fig. 5 Particle shear stress. (*a*) 42 μm particle; (*b*) 72 μm particle; first column: X = 100 mm (τ = 168); second column: X = 150 mm (τ = 236); third column: X = 200 mm (τ = 300); fourth column: X = 250 mm (τ = 362). —— LES; ○ Hishida et al. (1992).

with the experimental measurements, LES statistics of the particle velocities were sub-divided into x-z planes, mean and fluctuating velocities were then computed using ensemble averages in order to present statistical measures in the same manner as measured by Hishida et al. (1992). LES predictions are in reasonable agreement with the experiment and better than can be obtained using Reynolds-averaged methods (e.g., see Sommerfeld, 1992). LES predictions for the 135 μm particles (not shown) are also in good agreement with measurements. It is apparent from both figures that the streamwise fluctuations and shear stress decrease with increasing values of the diameter (or Stokes number). Note also that the effect of particle sample size on statistics is shown in Fig. 4. As evident in the figure, statistics obtained using 10,000 particles are nearly indistinguishable from those obtained in simulations where the sample size was doubled.

Though not shown here, the cross-stream fluctuations are significantly smaller than the streamwise values. Some insight into the behavior of the statistics in Figs. 4 and 5 can be gained through consideration of the transport equation for the particle kinetic stresses. As shown by Simonin et al. (1995), the transport equation for the fluctuating quantity $\langle v_i'' v_j'' \rangle$ can be obtained from the particle equation of motion (2)

$$\left[\frac{\partial}{\partial t} + V_m \frac{\partial}{\partial x_m}\right]\langle v_i'' v_j'' \rangle = P_{ij} + T_{ij} + \Pi_{ij}, \qquad (3)$$

where the mean particle velocity $V_i = \langle v_i \rangle$. The first term on the right-hand side, P_{ij}, represents production via the mean gradient of the particle velocity and does not require a model in a second-order closure. The triple correlation term, T_{ij}, represents transport by the particle velocity fluctuations and the last term, Π_{ij}, represents the momentum transfer rate from the fluid turbulence. If the fluid turbulence is modulated by the particles, Π_{ij} would appear in the fluid momentum equations to account for the effect of particles on the fluid momentum. In the present case in which particle volume fractions are small, there is negligible effect of the particles on the fluid.

For the temporally evolving mixing layer, the production term is non-zero in the streamwise direction. As shown in Fig. 5, the particle shear stress decreases with increasing diameter. Since the cross-stream gradient of the mean flow (not shown) is similar for the three particle sizes, production of streamwise fluctuations through interaction with the mean flow will also decrease with increasing diameter, which is one effect contributing to the decreasing streamwise fluctuation level for increasing diameter particles. It should also be noted that the particle kinetic stress can be produced by the momentum transfer from fluid turbulence through Π_{ij}. The momentum transfer term is inversely proportional to the mean particle relaxation time. Since the relaxation time is proportional to the square of the diameter, the magnitude of kinetic stress production through Π_{ij} will be expected to decrease with increases in diameter (for the same density ρ_p). However, whether Π_{11} is a source or sink for the streamwise fluctuations depends on the value of $\langle u_1'' v_1'' \rangle$ relative to $\langle v_1'' v_1'' \rangle$.

Overall, the agreement between the LES and experiments is reasonable. It is difficult to precisely capture the streamwise development of the layer in the experiment, i.e., the different initial conditions in the simulation and experiment will contribute to the discrepancies between LES predictions and measurements. In the LES, the layer evolves from the boundary layers on either side of a fully developed channel flow. The conditions of the splitter plate boundary layers in the experiment are not reported in Hishida et al. (1992). The velocity profile slightly downstream of the splitter tip in the experiment exhibits a slight wake component, an aspect also not replicated in the calculations. Hishida et al.'s (1992) measurements indicate that after the momentum thickness has increased by about a factor of seven the layer is relatively independent of the conditions near the splitter tip (i.e., at the station $X = 100$ mm in the experiment). The LES attains a nearly self-similar behavior after the momentum thickness has increased by less than a factor of three. All of these factors contribute to differences observed between LES predictions and experimental measurements. Slight differences in the initial particle velocities between simulation and experiment will also lead to a different evolution of the statistics (e.g., see Martin and Meiburg, 1994). An additional source of error in LES predictions is due to the neglect of particle transport by SGS velocity fluctuations. Though not shown here, modeling the contribution of fluid subgrid velocity fluctuations yields a negligible change in statistics of the particle velocity field, consistent with the well-resolved nature of the calculations and strong filtering of small-scale/high-frequency motions by particle inertia (see also Wang and Squires, 1996a).

3.2 Stokes Number Dependence of Particle Dispersion. Both experiments and computations have shown that particle dispersion in free shear flows is largest for particles with relaxation times comparable to the timescale of the large-scale coherent motions typically observed in these flows. The dispersion of particles with Stokes numbers around unity may be larger than that of fluid elements because of their 'history' and ability to maintain large inertia (see e.g., Crowe et al., 1985, 1996; Chein and Chung, 1987). However, as previously discussed, the Stokes number scaling in a fully-developed turbulent mixing layer, not evolving from well-defined initial conditions, has not been investigated. A series of calculations were performed for glass beads with diameters ranging from 1.5 μm to 135 μm. For each diameter, the trajectories of 20,000 particles were tracked in the simulations. Particles were initially located along the centerplane of the layer $y = 0$ and their velocity was initially zero. The particles are characterized by their Stokes number St $= \tau_p/\tau_f$, where τ_f is the large eddy time scale (see Crowe et al., 1985, 1988, 1996). The flow time scale is defined using a length scale and the velocity difference between the upper and lower streams.

Figure 6 shows the particle mean-square dispersion in the cross-stream direction, $\langle Y^2 \rangle(t) = \langle (y(t) - y_0)^2 \rangle = \langle y^2(t) \rangle$, where $y_0 = 0$ is the initial location and $\langle\ \rangle$ denotes an ensemble average over all particles with the same Stokes number. It is clear that the smallest particles (1.5 μm) follow the flow while the dispersion of larger particles can lead or lag the fluid, lagging at earlier times, leading at longer times in the evolution. It is also interesting to note the change in the dispersion beginning around $\tau \approx 200$, corresponding to a "pairing" of the layer.

In order to quantify the dispersion of finite-inertia particles relative to fluid elements, several quantities were examined: (1) the ratio of $\langle Y^2 \rangle$ for particles to that of fluid elements, $\langle Y^2 \rangle_p / \langle Y^2 \rangle_f$, where $\langle\ \rangle_p$ denotes an average over finite-inertia particles with the same St and $\langle\ \rangle_f$ an average over fluid elements; (2) the ratio of eddy diffusivity $\epsilon = d\langle Y^2 \rangle / dt/2$ of particles to fluid elements, ϵ_p/ϵ_f; (3) the ratio of maximum displacement before a specific time of particles to fluid elements, $\langle |Y|_{\max} \rangle_p / \langle |Y|_{\max} \rangle_f$; (4) the ratio of particle displacement at a specific time (averaged over all particles) to fluid elements, $\langle |Y| \rangle_p / \langle |Y| \rangle_f$. The quantity $\langle Y^2 \rangle_p / \langle Y^2 \rangle_f$ is the most

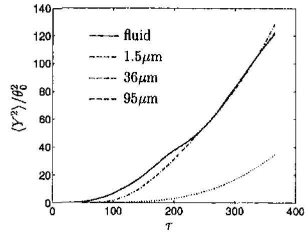

Fig. 6 Mean-square dispersion

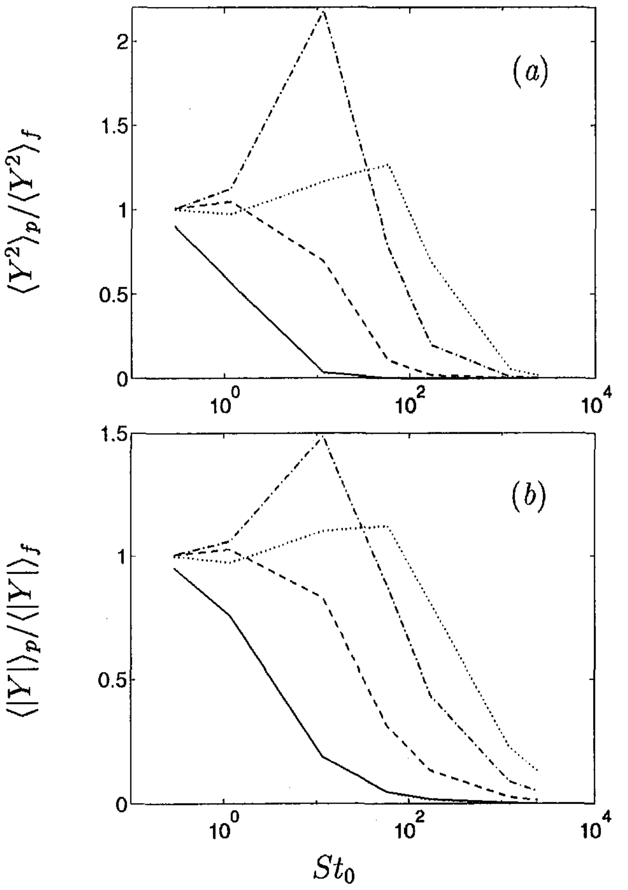

Fig. 7 Measures of particle dispersion with Stokes number defined using initial vorticity thickness. —— $\tau = 8$; ---- $\tau = 50$; – · – $\tau = 91$; -------- $\tau = 166$

common measure and has been used by several investigators in the study of particle dispersion in free shear flows (e.g., see Chein and Chung, 1988; Uthuppan et al., 1994; Wang and Squires, 1996b). The ratio of eddy diffusivities was used by Hishida et al. (1992) but it is important to note the measure used in their work (and in the present simulations) is strictly applicable to homogeneous turbulence. The quantity $\langle|Y|_{\max}\rangle_p/\langle|Y|_{\max}\rangle_f$ was used by Chein and Chung (1987) in simulations of a mixing layer in which one of their interests was on the effect of vortex pairing on dispersion. For flows in which pairing strongly influences the dispersion process, $\langle|Y|_{\max}\rangle_p/\langle|Y|_{\max}\rangle_f$ is a relevant measure since it reflects the history of particle motion and the fact that dispersion can exhibit a wavy trend in response to the pairing process (Chein and Chung, 1987). The fourth, $\langle|Y|\rangle_p/\langle|Y|\rangle_f$, depends on the particle position at a specific time, rather than on its history as does $\langle|Y|_{\max}\rangle_p/\langle|Y|_{\max}\rangle_f$. It should also be noted that other measures of dispersion can be obtained from profiles of the particle concentration but require a larger sample size than considered in this study (see Martin and Meiburg, 1994; Raju and Meiburg, 1995 for further discussion).

In the present case, each of the measures of dispersion described above exhibit similar behavior. Figure 7 shows the evolution of two of these measures as a function of the Stokes number defined using the initial vorticity thickness $\mathrm{St}_0 = \tau_p/\delta_{\omega 0}/\Delta U$. At early times, the ratios shown in the figure are smaller than unity and their values decrease for larger St_0 due to increasing particle inertia. For increasing time (e.g., $\tau = 91$ in the figure) there is a peak, larger than unity, around $\mathrm{St}_0 = 10$, indicating particle dispersion for this Stokes number is larger than those for both smaller and larger St_0. As time increases further the peak moves to larger Stokes numbers. Martin and Meiburg (1994) and Raju and Meiburg (1995) found similar behavior in two-dimensional mixing layers evolving from an initial condition in which disturbances were superimposed on the initial profile. The fact that the Stokes number corresponding to maximum dispersion increases with time is also consistent with the mean-square dispersion shown in Fig. 6, where $\langle Y^2\rangle$ is largest for the larger particles at longer evolution times.

Because of the time-dependent nature observed in quantities measuring dispersion such as those shown in Fig. 7, it is perhaps more appropriate to define an effective Stokes number which reflects the time-dependent evolution of the flow. A time-dependent Stokes number can be defined using a local lengthscale; in particular, the local vorticity thickness, resulting in $\mathrm{St} = \tau_p/\delta_\omega/\Delta U$. The same ratios from Fig. 7 have been replotted in Fig. 8 as a function of the time-dependent St. It is interesting to note the relatively good collapse of the curves, with the exception of the values at the earliest time $\tau = 108$. Furthermore, the maximum values occur near $\mathrm{St} = 1$ at all times, consistent with the usual notion that dispersion is maximized for Stokes numbers near unity. For smaller St the particles behave similarly to fluid elements and have nearly identical dispersion while the dispersion of particles with larger St is much smaller than the fluid. More importantly, the results in Fig. 8 show that to obtain maximum dispersion for $\mathrm{St} = 1$, the appropriate length scale is the vorticity thickness. It is interesting to note that definition of the Stokes number using the vorticity thickness is approximately the same as defining St using the dominant frequency of the layer, as suggested by Aggarwal (1994) (see also Wang and Squires, 1996b). It can be shown, for example, that if the mixing layer evolves self-similarly from a well-defined mean velocity profile (e.g., hyperbolic-tangent), the ratio between St defined using the fundamental frequency

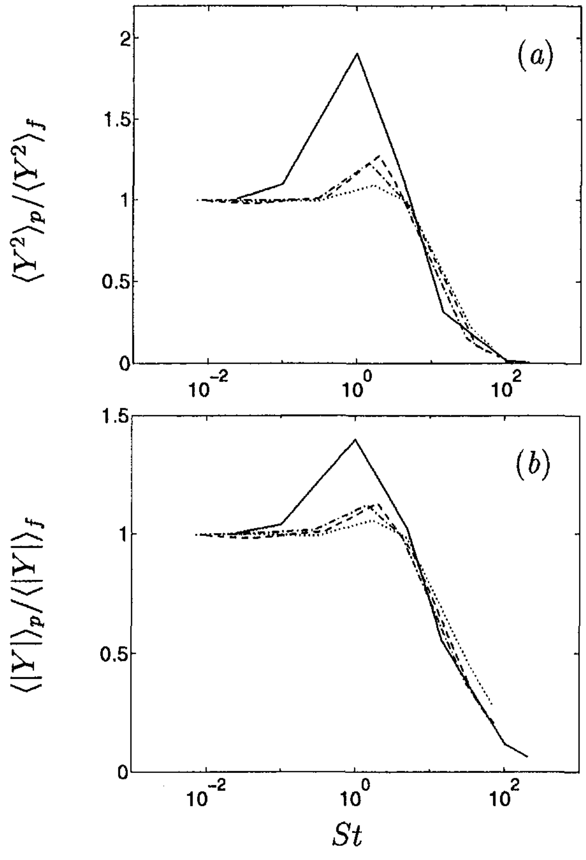

Fig. 8 Measures of particle dispersion with Stokes number defined using local vorticity thickness. —— $\tau = 108$; ---- $\tau = 216$; – · – $\tau = 257$; -------- $\tau = 315$

of the time-dependent mean velocity and that defined using the local vorticity thickness is near unity (≈ 1.125). Thus, LES results indicate that the peak in dispersion for St ≈ 1 is linked to the dominant frequency of the layer and that the vorticity thickness is the appropriate lengthscale for defining the Stokes number.

It should also be noted that since the lengthscales in a self-similar mixing layer grow linearly in time, other definitions of the Stokes number will yield results similar to Fig. 8 with appropriate shifts in the horizontal axis. For example, defining the Stokes numbers using the time-dependent momentum thickness would result in maximums in the ratio of the mean-square dispersion occurring around a Stokes number of 4.5, which is the ratio of the vorticity thickness to the momentum thickness in the LES.

4 Summary

Large eddy simulation of the fluid turbulence along with a Lagrangian treatment of the dispersed phase were used to model a particle-laden, temporally evolving turbulent mixing layer. The layer is formed by merging the fluid velocities on either side of a fully-developed channel flow with particles initially seeded along a narrow band near the centerplane. LES predictions of fluid velocity statistics are in good agreement with both DNS results and experimental measurements, yielding a growth rate in excellent agreement with previous measurements and an extended region of self-similar evolution.

LES predictions of particle velocity fluctuations were compared to the experimental measurements of Hishida et al. (1992). The level of agreement between the LES and measurements is quite good considering differences between simulation and experiment, i.e., the temporal flow in the LES vs. spatially-developing experiment, differences in initial conditions, etc. Particle inertia introduces additional "history" into particle-laden free shear flows, making them even more sensitive to initial conditions than their single-phase counterparts. Thus, even relatively small differences in factors such as initial/injection conditions should be expected to have a greater impact in subsequent evolution of the layer. A related issue is that while the behavior of the particle kinetic stressese can be analyzed using their transport equation, an important effect not yet considered in detail is that of initial conditions.

As also discussed, because the temporally-evolving flow was considered in the present investigation, translation of experimental measurements to the temporally evolving frame was accomplished using the convection velocity of the layer. The validity of this transformation for comparing predictions of the temporal flow to the spatially evolving layer is reasonably well established for single-phase mixing layers. For the particle-laden flow, this transformation is less accurate in the present case since the average injection velocity was about 10% of the layer convection velocity. Though not shown here, estimating convection velocities appropriate for a give particle size does improve comparison of LES predictions to measurements of the mean flow. Considering these and other differences it is noteworthy that the LES yields, overall, an accurate description of the flow, e.g., accurately reproducing the particle shear stress and capturing the strong anisotropy of the normal stresses.

Measures of particle dispersion were qualitatively similar to that previously observed in mixing layers evolving from initial conditions with specific disturbances used to initiate roll up and pairing. Because the initial conditions of the flow were fully developed, the Reynolds number range achieved in the present study is substantially higher than other calculations, as well as some experiments. In the fully developed flow in which there is a range of energetic modes, the resulting larger-scale structure continues to strongly influence bulk transport. Also important is the temporal dependence of the Stokes number on dispersion. Particle Stokes numbers corresponding to the maximum dispersion increases with time when defined using a fixed length scale, consistent with the fact that the flow timescale increases with evolution of the layer. Definition of St using the time-dependent vorticity thickness effectively scales the dispersion such that it is maximized for Stokes numbers near unity throughout the evolution of the flow, an interesting result in light of the dependence of the flow to upstream conditions. Further studies focusing on the spectral response of the flow will help to shed light on this finding.

Finally, it should also be remarked the present work helps to establish the validity of LES for prediction of dilute gas-solid flows. LES provides a detailed description of both phases and serves not only to provide insight into the underlying structural features of the flow, but is also well suited for development and validation of two-phase flow models for engineering applications. For more complex configurations with two-way coupling, phase change, etc., Reynolds-averaged models are computationally more viable, especially for engineering applications, but require significantly more empiricism than in LES. LES calculations provide sufficient detail concerning both phases that closure assumptions invoked in engineering models can be clearly evaluated. Accounting for the additional important phenomena occurring in two-phase flows will further increase the range of problems LES may make significant impact.

Acknowledgment

The authors are grateful to Dr. Michael Rogers for supplying the DNS and experimental results as well as providing helpful comments during the course of this study. This work is supported by the National Institute of Occupational Safety and Health (Grant Number OH03052-03). Computer time for the simulations was supplied by the National Center for Supercomputing Applications.

References

Aggarwal, S. K., 1994, "Relationship Between Stokes Number and Intrinsic Frequencies in Particle-Laden Flows," *AIAA Journal*, Vol. 32, pp. 1323–1325.

Bell, J. H., and Mehta, R. D., 1990, "Development of a Two-Stream Mixing Layer From Tripped and Untripped Boundary Layers," *AIAA Journal*, Vol. 8, pp. 2034–2042.

Chein, R., and Chung, J. N., 1987, "Effects of Vortex Pairing on Particle Dispersion in Turbulent Shear Flows," *International Journal of Multiphase Flow*, Vol. 13, pp. 785–802.

Chein, R., and Chung, J. N., 1988, "Simulation of Particle Dispersion in a Two-Dimensional Mixing Layer," *AIChE Journal*, Vol. 34, pp. 946–954.

Clift, R., Grace, J. R., and Weber, M. E., 1978, *Bubbles, Drops and Particles*, Academic Press, New York.

Crowe, C. T., Chung, J. N., and Troutt, T. R., 1988, "Particle Mixing in Free Shear Flows," *Progress in Energy and Combustion Science*, Vol. 14, pp. 171–194.

Crowe, C. T., Gore, R. A., and Troutt, T. R., 1985, "Particle Dispersion by Coherent Structures in Free Shear Flows," *Particulate Science and Technology*, Vol. 3, pp. 149–158.

Crowe, C. T., Chung, J. N., and Troutt, T. R., 1993, "Particle Dispersion by Organized Turbulent Structures," *Particulate Two-Phase Flow*, Roco, M. C., ed., Butterworth-Heinemann, Boston, pp. 627–669.

Crowe, C. T., Troutt, T. R., and Chung, J. N., 1996, "Numerical Models for Two-Phase Turbulent Flows," *Annual Reviews of Fluid Mechanics*, Vol. 28, pp. 11–43.

Dimotakis, P. E., 1991, "Turbulent Free Shear Layer Mixing and Combustion," *High-Speed-Flight Propulsion Systems, Progress in Astronautics and Aeronautics*, Murthy, S. N. B. and Curran, E. T., eds., pp. 265–340.

Germano, M., Piomelli, U., Moin, P., and Cabot, W. H., 1991, "A Dynamic Subgrid-Scale Eddy Viscosity Model," *Physics of Fluids*, Vol. 3(7), pp. 1760–1765.

Hishida, K., Ando, A., and Maeda, M., 1992, "Experiments on Particle Dispersion in a Turbulent Mixing Layer," *International Journal of Multiphase Flow*, Vol. 18, pp. 181–194.

Hussain, A. K. M. F., 1983, "Coherent Structures-Reality and Myth," *Physics of Fluids A*, Vol. 26, pp. 2816–2850.

Kiger, K. T., and Lasheras, J. C., 1995, "The Effect of Vortex Pairing on Particle Dispersion and Kinetic Energy Transfer in a Two-Phase Turbulent Shear Layer," *Journal of Fluid Mechanics*, Vol. 302, pp. 149–178.

Kim, J., and Moin, P., 1985, "Application of a Fractional-Step Method to Incompressible Navier-Stokes Equations," *Journal of Computational Physics*, Vol. 59, pp. 308–323.

Laviéville, J., Deutsch, E., and Simonin, O., 1995, "Large Eddy Simulation of Interactions Between Colliding Particles and a Homogeneous Isotropic Turbulence Field," *Gas-Particle Flows,* FED-Vol. 228, pp. 347–357.

Lazaro, B. J., and Lasheras, J. C., 1992a, "Particle Dispersion in the Developing Free Shear Layer, Part 1. Unforced Flow," *Journal of Fluid Mechanics,* Vol. 235, pp. 143–178.

Lazaro, B. J., and Lasheras, J. C., 1992b, "Particle Dispersion in the Developing Free Shear Layer. Part 2. Forced Flow," *Journal of Fluid Mechanics,* Vol. 235, pp. 179–221.

Marcu, J. E., and Meiburg, E., 1996, "Three-Dimensional Features of Particle Dispersion in a Nominally Plane Mixing Layer," *Physics of Fluids,* Vol. 8(9), p. 2266.

Martin, J. E., and Meiburg, E., 1994, "The Accumulation and Dispersion of Heavy Particles in Forced Two-Dimensional Mixing Layer. I. The Fundamental and Subharmonic Cases," *Physics of Fluids,* Vol. 6, pp. 1116–1132.

Meneveau, C., Lund, T. S., and Cabot, W., 1996, "A Lagrangian Dynamic Subgrid-Scale Model of Turbulence," *Journal of Fluid Mechanics,* Vol. 319, pp. 353–385.

Perot, J. B., 1993, "An Analysis of the Fractional Step Method," *Journal of Computational Physics,* Vol. 108, pp. 51–58.

Raju, N., and Meiburg, E., 1995, "The Accumulation and Dispersion of Heavy Particles in Forced Two-Dimensional Mixing Layer. Part 2: The Effect of Gravity," *Physics of Fluids,* Vol. 7, pp. 1241–1264.

Rogers, M. M., and Moser, R. D., 1994, "Direct Simulation of a Self-Similar Turbulent Mixing Layer," *Physics of Fluids,* Vol. 6(2), pp. 903–923.

Samimy, M., and Lele, S. K., 1991, "Motion of Particles With Inertia in a Compressible Free Shear Layer," *Physics of Fluids,* Vol. 3, pp. 1915–1923.

Simonin, O., Deutsch, E., and Boivin, M., 1995, "Large Eddy Simulation and Second-Moment Closure Model of Particle Fluctuating Motion in Two-Phase Turbulent Shear Flows," in *Turbulent Shear Flow 9,* F. Durst, N. Kasagi, B. E. Launder, F. W. Schmidt, J. H. Whitelaw, eds., Springer-Verlag (Heidelberg), pp. 85–115.

Sommerfeld, 1992, *Sixth Workshop on Two-Phase Flow Predictions,* Erlangen, Germany.

Sommerfeld, 1995, "The Importance of Inter-Particle Collisions in Horizontal Gas-Solid Channel Flows," *Gas-Particle Flows,* FED-Vol. 228, pp. 335–345.

Uthuppan, J., Aggarwal, S. K., Grinstein, F. F., and Kailasanath, K., 1994, "Particle Dispersion in a Transitional Axisymmetric Jet: A Numerical Simulation," *AIAA Journal,* Vol. 32, pp. 2004–2014.

Wang, Q., and Squires, K. D., 1996a, "Large Eddy Simulation of Particle-Laden Turbulent Channel Flows," *Physics of Fluids,* Vol. 8(5), pp. 1207–1223.

Wang, Q., and Squires, K. D., 1996b, "Particle Transport in a Nonuniformly Seeded Mixing Layer," *AIAA paper* 96-0683, pp. 1–11.

Wang, Q., Squires, K. D., and Wu, X., 1995, "Lagrangian Statistics in Turbulent Channel Flow," *Atmospheric Environment,* Vol. 29, pp. 2417–2427.

Wen, F., Kamalu, N., Chung, J. N., Crowe, C. T., and Troutt, T. R., 1992, "Particle Dispersion by Vortex Structures in Plane Mixing Layers," ASME JOURNAL OF FLUIDS ENGINEERING, Vol. 114, pp. 657–666.

Wu, X., Squires, K. D., and Wang, Q., 1995, "On Extension of the Fractional Step Method to General Curvilinear Coordinate Systems," *Numerical Heat Transfer,* Vol. 27, pp. 175–194.

On the Choking of the Flow of Piezoviscous Liquids

Scott Bair
Principal Research Engineer,
G. W. Woodruff School
of Mechanical Engineering,
Georgia Institute of Technology,
Atlanta, GA 30332-0405

M. M. Khonsari
Professor and Chair,
Department of Mechanical Engineering,
Southern Illinois University at Carbondale,
Carbondale, IL 62901-6603

Experimental evidence for choking of a piezoviscous fluid in a capillary tube is presented. It is shown that under a nearly isothermal condition, it is possible for the flow to experience choking whereby increasing the inlet pressure ceases to affect the flow rate. The occurrence of this phenomenon can be predicted by noting a singularity in the flowrate equation in a capillary tube under typical conditions encountered in injection molding (cf. Denn, 1981). Further examination of the general equations governing the shear flow of laminar, incompressible, linearly viscous (Newtonian) liquids under high pressures reveals a singularity in the solution for the pressure gradient. This apparently unreported phenomenon is shown to occur in liquids whose viscosity, μ*, increases exponentially with pressure, p, as* $\mu = \mu_0 e^{\alpha p}$*, where* α *denotes the pressure-viscosity coefficient. For a two-dimensional configuration with the shearing action taking place in the x direction and with* $p = p(x, y)$*, the singularity is shown to take place when:* $\tau_{yx} = \pm(1/\alpha)\sqrt{1 + \alpha^2 \tau_{xx}\tau_{yy}}$*, at which case both* $\partial p/\partial x$ *and* $\partial p/\partial y \rightarrow \infty$*. The occurrence of such a singularity in the pressure gradient may have an important physical implication in lubrication flows particularly in concentrated contacts such as elastohydrodynamic lubrication of rolling element bearings and gears.*

1 Introduction

A liquid is termed piezoviscous when its viscosity rises with pressure. This is typical of lubricating oils in nonconformal conjunctions such as rolling element bearings and gears.

It is known that pressure-driven (Poiseuille) flow of a piezoviscous liquid in a duct with a sufficiently long length gives rise to a pressure singularity upstream. If the entrance to the duct is placed at the singularity, the flowrate will be the maximum possible. That is, increasing the pressure at the inlet does not affect the flow rate so that flow is "choked." Denn (1981) with interest in the behavior of a high pressure flow in injection modeling analyzed the flow of a piezoviscous liquid in a capillary tube and went on to show that for an adiabatic flow, viscous heating combines with thermal softening to prevent choking altogether.

A singularity in a flow may manifest itself in the form of localization. Shear localization giving rise to the formation of shear bands has been observed experimentally in the plane Couette shear of highly viscous liquids operating under high-pressure and high-shear stress. There are two distinctly different physical mechanisms responsible for the formation of these shear bands: (1) Shear bands, as first reported by Bair et al. (1994a), can result from thermal run-away in a stress controlled experiment at a high Brinkman number. The theoretical analysis of adiabatic shear localization with an idealized inertialess liquid whose viscosity decreases exponentially with temperature predicts the occurrence of a shear band at the mid-plane where the temperature grows without bound. (2) Shear bands can result from mechanical failure of the liquid which has been modeled according to the Mohr-Columb criteria (Bair and Winer, 1994b). Slip occurs on a plane for which the ratio of shear stress to compressive normal stress attains the value of the material friction coefficient. We show in this paper that when the product of the shear stress in a piezoviscous liquid and the pressure-viscosity coefficient is unity, a pressure gradient singularity must exist for any departure from homogeneous shear. This singularity may be the initiator of mechanical shear bands.

In this paper, we first experimentally verify the occurrence of a choked flow in a tube and then concentrate on the governing equations of a general, two-dimensional flow of an incompressible piezoviscous liquid. The equations predict a singularity in the pressure gradients. The occurrence of such a singularity may have an important physical implication in lubrication flows particularly in concentrated contacts such as elastohydrodynamic lubrication of rolling element bearings and gears.

2 Capillary Flow of Piezoviscous Liquids

For very thin ducts or capillaries, the adiabatic idealization may be inappropriate and one might expect to approach a choked flow condition or to experience conditions under which the flow is insensitive to an increase in the inlet pressure. We experimentally investigate the capillary flow of two piezoviscous liquids: polyphenyl ether, 5P4E, and polyalphaolefin, SHF1001. The viscosity, μ, of these liquids has been measured to pressures of 0.8 GPa using a falling body viscometer at temperatures T = 0°C to 227°C and fitted to the Yasutomi Free Volume Model (Yasutomi et al., 1984; Bair and Winer, 1995). See Fig. 1 for the pressure viscosity behavior at 22°C calculated from the Free Volume Model. The statistical details of curve-fitting may be found in Yasutomi et al. (1984). It is convenient for the analysis to express the piezoviscous relation by the Barus equation

$$\mu = \mu_o e^{\alpha P} \tag{1}$$

where α is the pressure-viscosity coefficient, although it is apparent from Fig. 1 that the variation of viscosity with pressure is more complex than Eq. (1) implies. Setting

$$\alpha_0 = \left. \frac{\partial \ln \mu}{\partial p} \right|_{p=0} \tag{2}$$

we find that α_o = 61 and 31 Gpa^{-1} for 5P4E and SHF1001, respectively. For isoviscous flow, Q, through a capillary of circular cross section with internal radius, R, the Hagen-Poise-

---

Contributed by the Fluids Engineering Division for publication in the JOURNAL OF FLUIDS ENGINEERING. Manuscript received by the Fluids Engineering Division June 25, 1997; revised manuscript received January 12, 1998. Associate Technical Editor: M. S. Cramer.

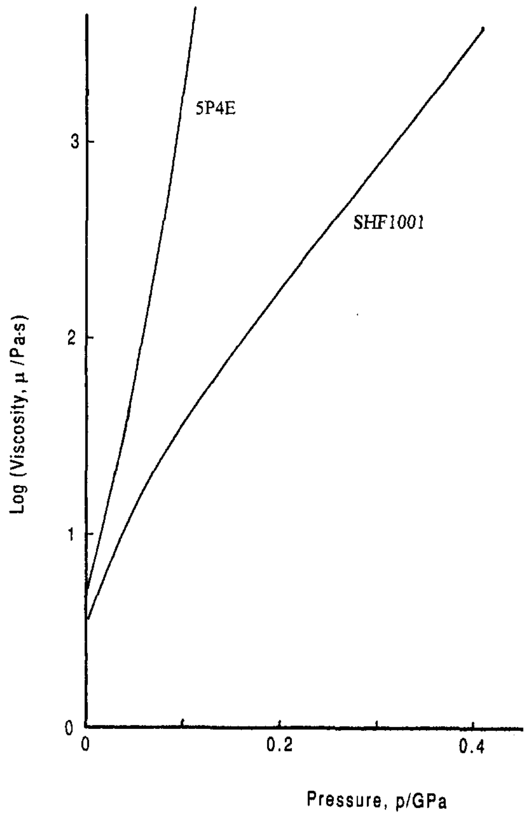

Fig. 1 *The variation of viscosity with pressure at 22°C for a polyphenyl ether, 5P4E and polyalphaolefin, SHF1001*

uille equation applies. The pressure at a distance L from the outlet at pressure zero is:

$$p = \frac{8\mu_o QL}{\pi R^4} \equiv p_{iv} \tag{3}$$

Penwell et al. (1971) derived the corresponding pressure for an isothermal, piezoviscous liquid as

$$p = -\frac{1}{\alpha} \ln (1 - ap_{iv}) \tag{4}$$

by neglecting the radial pressure variation.

Clearly, Eq. (4) yields a singularity for $p_{iv} = 1/\alpha$ which is located at $L = \pi R^4/8\alpha\mu_o Q$. Penwell et al. found experimental verification of Eq. (4); however, their pressure was always less than $1/\alpha$. Denn (1981) derived the inlet pressure, p_i, for piezoviscous, adiabatic capillary flow given implicitly by

$$\left(\alpha + \frac{\beta}{\rho c_v}\right) p_{iv} = e^{\beta p_i/\rho c_v} - e^{-p_i\alpha} \tag{5}$$

and concluded that choking does not occur when viscous heating is taken into account. Here, β is the temperature-viscosity coefficient, $-\partial(\ln \mu)/\partial T$, which we take to be 0.16 and 0.085°C^{-1} for 5P4E and SHF1001, respectively. P_{iv} is evaluated at the capillary inlet and ρc_v is the volumetric heat capacity of the liquid, which is about 1.9 M J/m^3°C.

Figure 2 shows experimental results as data points for a stainless-steel capillary with an inside diameter of 267 μm ($\pm$10 μm) and length of 7.45 cm. Pressure was measured with a Bourdon tube gauge ($\pm$0.7 MPa). Flow rate was determined to $\pm$3 percent by timing the change of the liquid level in a pipette. The curves marked 1, 2, and 3 are computed from Eqs. (3), (4), and (5), respectively. As is customary, we have used $\alpha = \alpha_o$ in Fig. 2. Curve 3 represents an adiabatic, piezoviscous flow and offers poor agreement with the experimental data. The isoviscous solution (curve 1) is inaccurate for the inlet pressure greater than $1/\alpha$. The isothermal, piezoviscous solution (curve 2) overestimates the pressure presumably because of viscous heating.

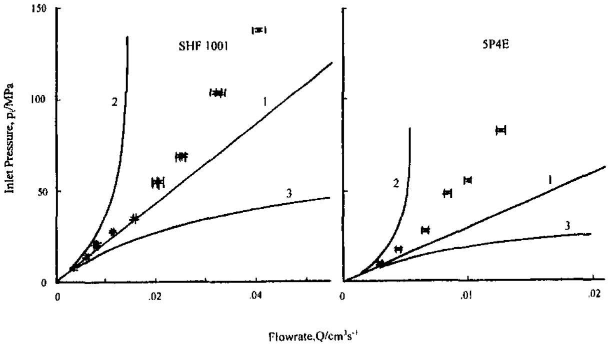

Fig. 2 Capillary inlet pressure versus flowrate (L/R = 560). Curve 1-isoviscous; 2-isothermal, piezoviscous; 3-adiabatic piezoviscous.

A new capillary was prepared from stainless-steel surgical tubing with 178 $\pm$ 10 μm inside diameter and 330 μm outside diameter with a length of 61 $\pm$ 0.2 cm. The capillary was coiled into a water bath and one end was brazed to a high-pressure fitting. All but 10 cm of the capillary length was submerged. Results for SHF1001 are shown in Fig. 3 for two runs. Apparently, this configuration approximates the isothermal ideal since choking is evident for a flowrate of about 0.58 mm^3/s. The two isothermal, piezoviscous curves represent $\alpha = \alpha_o$ for the solid curve and $\alpha = \alpha^*$ for the broken curve. Here,

$$\alpha^* = \left[\int_0^\infty \frac{\mu_o}{\mu(p)}\, dp\right]^{-1} \tag{6}$$

and is termed the reciprocal asymptotic isoviscous pressure in

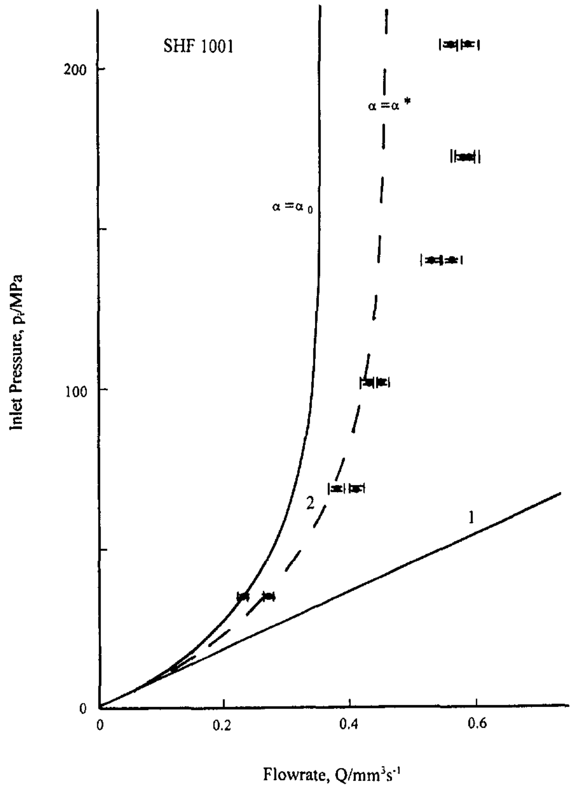

Fig. 3 Capillary inlet pressure versus flowrate (L/R = 6850)

elastohydrodynamics. It has been utilized as the pressure-viscosity coefficient for the general piezoviscous liquid and is 24 Gpa^{-1} for SHF1001. The choking flowrate is still greater than predicted using the improved α and this may be due to expansion of the capillary bore under pressure and viscous heating in the unsubmerged length.

The significance of α^* can be appreciated from substitution of dq/μ_0 for $dp/\mu(p)$ in the differential form of the Hagen-Poiseuille equation:

$$\frac{dp}{\mu(p)} = \frac{8Qdx}{\pi R^4} \tag{6a}$$

Substitution and integration along the length of the capillary yields

$$q = \frac{8Q\mu_o L}{\pi R^4} = p_{iv} \tag{6b}$$

where $q = \int_o^p (\mu_o/(\mu(p)))dp$. The pressure is unbounded for $q(\infty) = P_{iv}$, which is equivalent to $p_{iv} = 1/\alpha^*$.

3 Mathematical Development

In this section, we focus on the two-dimensional, inertialess, incompressible flow equations for a linearly viscous flow (Newtonian) in the absence of thermal effects. We will show the existence of a singularity of a somewhat different nature where the pressure is bounded but the pressure gradient are not.

The *equilibrium* equations written in the Cartesian coordinate system are:

$$\frac{\partial p}{\partial x} = \frac{\partial \tau_{xx}}{\partial x} + \frac{\partial \tau_{yx}}{\partial y} \tag{7}$$

$$\frac{\partial p}{\partial y} = \frac{\partial \tau_{yx}}{\partial x} + \frac{\partial \tau_{yy}}{\partial y} \tag{8}$$

where the deviatoric stresses, τ_{ij}, are defined as:

$$\tau_{xx} = 2\mu \frac{\partial u}{\partial x}\ ; \quad \tau_{yx} = \mu\left(\frac{\partial v}{\partial x} + \frac{\partial u}{\partial y}\right)\ ; \quad \tau_{yy} = 2\mu \frac{\partial v}{\partial y} \tag{9}$$

The *conservation of mass* (continuity) equation reads

$$\frac{\partial u}{\partial x} + \frac{\partial v}{\partial y} = 0 \tag{10}$$

The viscosity of the liquid, μ, is assumed to increase with exponentially with pressure as prescribed by Eq. (1).
Substituting Eqs. (1) and (9) into the equilibrium Eqs. (7), and (8) yields:

$$\frac{\partial p}{\partial x} = 2\mu \frac{\partial^2 u}{\partial x^2} + 2\left(\frac{\partial \mu}{\partial x}\right)\frac{\partial u}{\partial x} + \mu \frac{\partial v}{\partial x \partial y} + \mu \frac{\partial^2 u}{\partial y^2} + \left(\frac{\partial \mu}{\partial y}\right)\frac{\partial v}{\partial x} + \left(\frac{\partial \mu}{\partial y}\right)\frac{\partial u}{\partial y} \tag{11}$$

$$\frac{\partial p}{\partial y} = 2\mu \frac{\partial^2 v}{\partial y^2} + 2\left(\frac{\partial \mu}{\partial y}\right)\frac{\partial v}{\partial y} + \mu \frac{\partial u}{\partial x \partial y} + \mu \frac{\partial^2 v}{\partial x^2} + \left(\frac{\partial \mu}{\partial x}\right)\frac{\partial v}{\partial x} + \left(\frac{\partial \mu}{\partial x}\right)\frac{\partial u}{\partial y} \tag{12}$$

The above equations can be rewritten in the following form:

$$p_x = \mu(u_{xx} + u_{yy}) + 2\mu_x u_x + \mu_y v_x + \mu_y u_y \tag{13}$$

$$p_y = \mu(v_{xx} + v_{yy}) + 2\mu_y v_y + \mu_x v_x + \mu_x u_y \tag{14}$$

where the subscripts represent partial derivatives and we have made use of the continuity equation (10) to replace $v_{xy} = -u_{xx}$ and $u_{xy} = -v_{yy}$.

Further manipulation of (13) and (14) yields the following equations:

$$p_x = \mu\nabla^2 u + 2\alpha\mu u_x p_x + \mu\alpha(u_y + v_x)p_y \tag{15}$$

$$p_y = \mu\nabla^2 v + 2\alpha\mu v_y p_y + \mu\alpha(u_y + v_x)p_x \tag{16}$$

where $\nabla^2 u = u_{xx} + u_{yy}$.

Simultaneous solution of Eqs. (15) and (16) for pressure gradients, p_x and p_y gives

$$p_x = \frac{\mu[1 - 2\alpha\mu v_y]\nabla^2 u + \alpha\mu^2[v_x + u_y]\nabla^2 v}{D} \tag{17}$$

$$p_y = \frac{\mu[1 - 2\alpha\mu u_x]\nabla^2 v + \alpha\mu^2[v_x + u_y]\nabla^2 u}{D} \tag{18}$$

where $D = [1 - 2\alpha\mu u_x][1 - 2\alpha\mu v_y] - \alpha^2\mu^2[v_x + u_y]^2$.

If the expressions appearing in the numerator of Eqs. (17) and (18) are finite and nonzero, then when the denominator $D \rightarrow 0$, the pressure gradients become singular. To examine the necessary condition for this singularity to take place, rewrite the denominator in the following form:

$$\frac{D}{\alpha^2\mu^2} = \left(\frac{1}{\alpha\mu}\right)^2 + 4u_x v_y - (v_x + u_y)^2 = 0 \tag{19}$$

where we have made use of the continuity Eq. (10).
Alternatively, Eq. (19) can be written as

$$\frac{D}{\alpha^2\mu^2} = \left(\frac{1}{\alpha\mu}\right)^2 + \dot{\gamma}_{xx}\dot{\gamma}_{yy} - (\dot{\gamma}_{xx})^2 \tag{20}$$

where we have made use of the relationships: $\dot{\gamma}_{xx} = 2u_x$; $\dot{\gamma}_{yy} = 2v_y$; $\dot{\gamma}_{yx} = v_x + u_y$.
Finally, Eq. (2) be put in terms of the shear stresses as shown below:

$$\frac{D}{\alpha^2} = \frac{1}{\alpha^2} - \tau_{xy}^2 + \tau_{xx}\tau_{yy} = 0 \tag{21}$$

This implies that where

$$\tau_{yx} = \pm\frac{1}{\alpha}\sqrt{1 + \alpha^2\tau_{xx}\tau_{yy}}\ , \tag{22}$$

$\partial p/\partial x$ and $\partial p/\partial y \rightarrow \infty$. This is equivalent to the principal shear stress being $1/\alpha$.

Note that in deriving the above equations the usual lubrication assumption—commonly referred to as the thin-film flow was not invoked. As a special case, Eq. (22) reduces to $\tau_{yx} = \pm 1/\alpha$ when τ_{xx} or τ_{yy} is identically zero. It can be shown that when the component of the velocity in the y direction $v = 0$, the singularity condition is identical to $\tau_{yx} = \pm 1/\alpha$. This particular case, which we shall take up next, pertains to the flow in a slit.

3.1 Two-Dimensional, Inertialess, Incompressible, Flow Between Parallel Planes.

The radial component of the velocity, v_r, of a flow through a capillary with $\alpha = 0$ is nil if the no-slip boundary condition holds. Denn (1981) showed that $v_r = 0$ even when the viscosity varies with pressure according to Eq. (1). Following Denn's result for capillaries, we shall assume $v = 0$ for flow between parallel planes (slit flow). When $v = 0$, $\partial v/\partial x = \partial v/\partial y = \nabla^2 v = 0$ and from Eq. (10) we have $\partial u/\partial x = 0$ so that $\nabla^2 u = \partial^2 u/\partial y^2$. Also, from Eq. (9) it follows that

$\tau_{xx} = \tau_{yy} = 0$. Therefore, Eqs. (18) and (19) reduce to the following.

$$p_x = \frac{\mu u_{yy}}{1 - (\alpha \mu u_y)^2} \tag{23}$$

$$p_y = \frac{\alpha \mu^2 u_y}{1 - (\alpha \mu u_y)^2} u_{yy} \tag{24}$$

3.1.1 Plane Poiseuille Flow. To evaluate an expression for pressure, it is necessary to determine the velocity gradients. Let $u(y)$ be identical to the isoviscous velocity profile which, assuming that the no-slip boundary condition holds, takes on the following form:

$$u(y) = u_o\left(1 - \frac{4}{h^2} y^2\right) \tag{25}$$

where $u_o (u_o < 0)$ denotes the centerline velocity where $y = 0$ and the full gap size is h. The exit is at $x = 0$ and $u \leq 0$ so that pressure increases with x. Integration of Eq. (25) across the gap yields the volumetric flow rate per unit width, q, given below:

$$q = \tfrac{2}{3} u_o h \tag{26}$$

The velocity gradients in terms of the flow rate are:

$$\frac{\partial u}{\partial y} = -12 \frac{q}{h^3} y \quad \text{and} \quad \frac{\partial^2 u}{\partial y^2} = -\frac{12q}{h^3}. \tag{27}$$

Substitution of Eqs. (27) in (23) yields

$$\frac{\partial p}{\partial x} = \frac{p'_{iv} e^{\alpha p}}{[1 - (y \alpha p'_{iv} e^{\alpha p})^2]} \tag{28}$$

where the isoviscous pressure gradient $p'_{iv} = 12 q \mu_o / h^3$.

At the gap mid-plane ($y = 0$), the pressure gradient is:

$$\left.\frac{\partial p}{\partial x}\right|_{y=0} = p'_{iv} e^{\alpha p|_{y=0}} \tag{29}$$

Integrating (29) upstream from inlet, $x = 0$, gives

$$e^{-\alpha p|_{y=0}} = 1 - \alpha p'_{iv} x \tag{30}$$

or

$$p|_{y=0} = -\frac{1}{\alpha} \ln(1 - \alpha p_{iv}) \tag{31}$$

where $p_{iv} = p'_{iv} x$ which is p for isoviscous flow. Therefore, the midplane pressure is the same as that given by Eq. (4). Hence, the centerline pressure grows without bound when $p_{iv} = 1/\alpha$. We re-emphasize that the above analysis assumes that no secondary flow occurs and $v = 0$. Furthermore, it can be shown that while in a capillary tube the cross-flow velocity $v_r = 0$, the same does not hold for a piezoviscous liquid flow in a slit. See Appendix A and Bair et al. (1997) for details.

4 Closure

Experimental measurements of flow rate in a capillary tube under high inlet pressures presented in this paper attest to the existence of a choking phenomenon whereby flow ceases to respond to upstream pressure variation. This phenomenon, which has been predicted in the published literature, is said to occur for liquids whose viscosity vary with pressure and under isothermal conditions (Denn, 1981). The origin of the choking prediction is in a form of a singularity in the flow equation as derived by Penwell et al. (1971). To the authors' best knowledge, however, the present paper shows the first experimental evidence for this phenomenon. A parallel mathematical development for pressure-dependent liquids in a two-dimensional Cartesian coordinate system reported in this paper shows the existence of a somewhat different nature. It is shown that if the shear stress, τ_{xy}, satisfies Eq. (22), the pressure gradients $\partial p / \partial x$ and $\partial p / \partial y \to \infty$. The concept of this singularity may prove to play a role in elastohydrodynamic lubrication; although the analysis provided here is general and does not invoke the so-called thin-film assumption. Further, it is possible that the nucleation of mechanical shear bands in liquids may be explained by such singularities.

References

Bair, S., Qureshi, F., and Khonsari, M. M., 1994a, "Adiabatic Shear Localization in a Liquid Lubricant Under Pressure," ASME *Journal of Tribology*, Vol. 116, No. 4, pp. 705–708.

Bair, S., and Winer, W. O., 1994b, "A Rheological Basis for Concentrated Contact Friction," 20th Leeds-Lyon Symposium on Tribology, *Dissipative Processes in Tribology*, Tribology Series D. Dowson, ed., 27, pp. 37–44.

Bair, S., and Winer, W. O., 1995, "Application of the Yasutomi Free Volume to Various Liquid Lubricants," *Proc. Intern. Symp. Tribology*, Yokohama, Japan.

Bair, S., Winer, W. O., and Khonsari, M. M., 1997, "High Pressure Rheology of Lubricants and Limitations of the Reynolds Equation," *New Directions in Tribology*, World Tribology Congress in London, Hutchungs, I. M., ed., pp. 21–38.

Denn, M. M., 1981, "Pressure Drop-Flow Rate Equation for Adiabatic Capillary Flow with a Pressure and Temperature Dependent Viscosity," *Polymer Engr. Sci.*, Vol. 21, 2, pp. 65–68.

Penwell, R. C., Porter, R. S., and Middleman, S., 1971, "Determination of the Pressure Coefficient and Pressure Effects in Capillary Flow," *Journal of Polymer Science*, Part A2, Vol. 9, p. 736.

Yasutomi, S., Bair, S., and Winer, W. O., 1984, "An Application of a Free Volume Model to Lubricant Rheology," ASME *Journal of Tribology*, Vol. 106, No. 2, p. 298.

APPENDIX A

Secondary Flows in Piezoviscous Liquids Flowing Between Parallel Plates

In the analysis presented in Section 3.1 it was assumed that for flow between parallel plates the component of the velocity normal to the boundary, v, is nil. This is true for isoviscous flows and can be easily verified. For Piezoviscous flows, this assumption allows great simplification of the Navier-Stokes equations and is analogous to the result obtained by Denn (1981) for cylindrical Poiseuille flow. However, neglecting the cross-film velocity component in a flow of a piezoviscous fluid between parallel plates results in inconsistent cross-derivatives of pressure and is indicative of formation of secondary flows.

Let us begin by assuming that

$$u = u(y) \quad \text{and} \quad v \equiv 0. \tag{A-1}$$

Recall that the pressure gradients are given by (23) and (24) when $v \equiv 0$.

$$\frac{\partial p}{\partial x} = \frac{\mu u_{yy}}{1 - (\alpha \mu u_y)^2} \tag{A-2}$$

$$\frac{\partial p}{\partial y} = \frac{\alpha \mu^2 u_y u_{yy}}{1 - (\alpha \mu u_y)^2} = \alpha \mu u_y \frac{\partial p}{\partial x} \tag{A-3}$$

Differentiating (A-2) with respect to x and (A-3) with respect to y yields after much manipulation,

$$\frac{\partial}{\partial y}\left(\frac{\partial p}{\partial x}\right) = 3\alpha \frac{\partial p}{\partial y}\frac{\partial p}{\partial x} + \frac{u_{yyy}}{u_{yy}}\frac{\partial p}{\partial x} + 2\alpha^2 \frac{u_y}{u_{yy}}\left(\frac{\partial p}{\partial y}\right)^2 \frac{\partial p}{\partial x} \tag{A-4}$$

$$\frac{\partial}{\partial x}\left(\frac{\partial p}{\partial y}\right) = 2\alpha \frac{\partial p}{\partial y}\frac{\partial p}{\partial x} + \frac{2\alpha^2 u_y}{u_{yy}}\left(\frac{\partial p}{\partial y}\right)^2 \frac{\partial p}{\partial x} \tag{A-5}$$

Equating the RHS of (A-4) and (A-5) reveals properties of the admissible form of $u(y)$ when $v \equiv 0$.

$$u_{yyy} = -\alpha u_{yy} \frac{\partial p}{\partial y} = -\alpha^2 \mu u_y u_{yy} \frac{\partial p}{\partial x} \tag{A-6}$$

Equation (A-6) implies that the parabolic form of the velocity is inappropriate for $\alpha \neq 0$.

Additional information can be extracted by considering that $\partial u_{yyy}/\partial x = 0$, since $v \equiv 0$. Now,

$$-\alpha^2 u_y u_{yy} \left[\alpha\mu \left(\frac{\partial p}{\partial x} \right)^2 + \mu \frac{\partial^2 p}{\partial x^2} \right] = 0 \tag{A-7}$$

So that

$$\alpha \left(\frac{\partial p}{\partial x} \right)^2 = \frac{-\partial^2 p}{\partial x^2} \tag{A-8}$$

Differentiating Eq. (A-2) with respect to x gives

$$\frac{\partial}{\partial x} \left(\frac{\partial p}{\partial x} \right) = \alpha \left(\frac{\partial p}{\partial x} \right)^2 + 2\alpha^3 \mu \frac{u_y^2}{u_{yy}} \left(\frac{\partial p}{\partial x} \right)^3 \tag{A-9}$$

Substituting (A-9) into (A-8) yields

$$u_{yy} = -\alpha^2 \mu u_y^2 \frac{\partial p}{\partial x} \tag{A-10}$$

which must be satisfied for $v \equiv 0$. Substituting the expression for $\partial p/\partial x$ from (A-2) into (A-10) yields:

$$1 - \alpha^2 \mu^2 u_y^2 = -\alpha^2 \mu^2 u_y^2 \tag{A-11}$$

which is, of course, a contradiction. Therefore, $v \not\equiv 0$, and a secondary flow must occur for $\alpha \neq 0$ when a Poiseuille component exists.

Journal of Fluids Engineering
Technical Briefs

Boundary-Layer Control by Electric Fields

R. Vilela Mendes[1] **and J. A. Dente**[2]

1 Boundary Layers and Boundary Layer Control

In turbulent boundary layers, near-wall streamwise vortices are responsible for the high skin friction drag. Therefore, most recent attempts (Sirovich and Karlsson, 1997; Lee, et al., 1997) to reduce the skin friction drag concentrate on the control of the interactions between the vortices and the wall. However, because of the very large ratio between laminar and turbulent skin friction drag, it also makes sense to devote some effort to delay the transition. The control techniques that have been proposed include suction of slow-moving fluid through slots or a porous surface, use of compliant walls and wall cooling (or wall heating for liquids). Another class of techniques for boundary-layer control consists in acting on the flow by means of electromagnetic forces. Here different techniques should be envisaged according to whether the fluid is weakly conducting (an electrolyte like seawater or an ionized gas) or a good conductor (like a liquid metal). Proposals for boundary-layer control by electromagnetic forces trace its origin to the papers of Gailitis and Lielausis (1961), Tsinober and Shtern (1967), and Moffat (1967). Interest in these techniques has revived in recent years and some more accurate calculations and experimental verifications have been carried out, mostly in the context of electrolyte fluids (Tsinober, 1990; Henoch and Stace, 1995).

In this note we are concerned with the flow of air along an airfoil when a layer of ionized gas is created on the boundary-layer region. Local ionization of the air along the airfoil not being practical from the technological point of view, we will assume that a stream of ionized air (or other ionized gas) is injected through a backwards facing slot placed slightly behind the stagnation point (Fig. 1). The body force that we consider to be acting in the ionized fluid is a streamwise electric field created by a series of plate electrodes transversal to the flow on the airfoil surface.

In addition to numerical calculations, we obtain scaling solutions and analytical design formulas. Here we simply report the main results. More detail may be obtained from a full report available as an electronic preprint [physics/9705020 at xxx.lanl.gov]. The conclusion is that, by itself or in conjunction with other methods, this technique may be useful in delaying the transition.

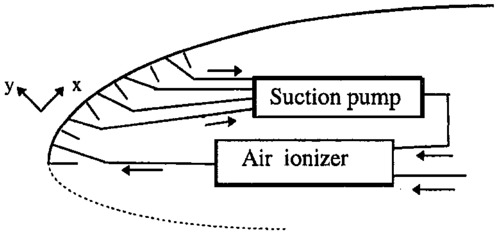

Fig. 1 Airfoil transversal cut showing ionized air injection, suction pump and plate electrodes

2 Ionized Boundary Layers With Electric Fields

The Boundary-Layer Equations. We use orthogonal curvilinear coordinates, with $\tilde{x}$ parallel to the surface along the flow, $\tilde{y}$ normal to the surface and assume that $\kappa\delta$ is small (κ being the curvature and δ the boundary layer thickness). Translational symmetry along the spanwise $\tilde{z}$-direction is assumed. Denote by $\tilde{u}$ and $\tilde{v}$ the components of the fluid velocity along the $\tilde{x}$ and $\tilde{y}$ directions. $\tilde{\rho}_m$ is the mass density, $\tilde{\sigma}_e$ the electric charge density and $\tilde{E}$ an applied electric field. The tilde denotes quantities in physical dimensions to be distinguished from the adimensional quantities defined below. Consider typical reference values L_r, δ_r, U_r, ρ_r, ν_r, σ_r, E_r for the airfoil width, the boundary layer thickness, the fluid velocity, the fluid mass density, the kinematic viscosity, the fluid charge density and the electric field. Then we define the adimensional quantities

$$t = \tilde{t}\frac{U_r}{L_r}, \quad x = \frac{\tilde{x}}{L_r}, \quad y = \frac{\tilde{y}}{\delta_r},$$

$$u = \frac{\tilde{u}}{U_r}, \quad v = \frac{\tilde{v}L_r}{U_r\delta_r}, \quad \rho_m = \frac{\tilde{\rho}_m}{\rho_r}$$

$$p = \frac{\tilde{p}}{\rho_r U_r^2}, \quad R_L = \frac{U_r L_r}{\nu_r},$$

$$\nu = \frac{\tilde{\nu}}{\nu_r}, \quad \sigma = \frac{\tilde{\sigma}}{\sigma_r}, \quad E = \frac{\tilde{E}}{E_r} \qquad (1)$$

In general, $R_L \gg 1$. We neglect terms of order $1/R_L$ and δ_r^2/L_r^2 and also notice that the y-component of the electric field is suppressed by the factor δ_r/L_r.
Defining $u_e = u\ (y = \infty)$, *a stream function* ψ *and a change of variables*

---

[1] Researcher, Grupo de Física-Matemática, Complexo II, Universidade de Lisboa, Av. Gama Pinto 2, 1699 Lisboa Codex, Portugal.

[2] Full Professor, Laboratório de Mecatrónica, DEEC, Instituto Superior Técnico, Av. Rovisco Pais, 1096 Lisboa Codex, Portugal.

Contributed by the Fluids Engineering Division of THE AMERICAN SOCIETY OF MECHANICAL ENGINEERS. Manuscript received by the Fluids Engineering Division December 16, 1996; revised manuscript received January 3, 1998. Associate Technical Editor: P. R. Bandyopadhyay.

$$\eta = \left(\frac{u_e}{\nu\omega}\right)^{1/2} \frac{y}{\xi(x)}, \quad \psi = (u_e \nu\omega)^{1/2}\xi(x)f(x,\eta) \quad (2)$$

with $\omega = L_r^2/\delta_r^2 R_L = L_r\nu_r/\delta_r^2 U_r$, $\gamma = L_r\sigma_r E_r/U_r^2\rho_r$, $u = \partial\psi/\partial y$ and $\upsilon = -(\partial\psi/\partial x)$, we obtain, for stationary solutions

$$\frac{\partial}{\partial\eta}\left(\frac{\partial^2 f}{\partial\eta^2}\right) + \xi\frac{\partial\xi}{\partial x} f \frac{\partial^2 f}{\partial\eta^2} + \frac{\xi^2}{u_e}\frac{\partial u_e}{\partial x}$$

$$+ \xi^2\left(\frac{\partial^2 f}{\partial\eta^2}\frac{\partial f}{\partial x} - \frac{\partial f}{\partial\eta}\frac{\partial^2 f}{\partial\eta\partial x}\right)$$

$$= -\frac{\gamma}{u_e^2\rho_m}\xi^2(x)\sigma(x,\eta)E_x(x,\eta) \quad (3)$$

Scaling Solutions. With plate electrodes transversal to the fluid flow the mean electric field in the x-direction may be parametrized by

$$\bar{E}_x = g(x)\frac{l(x)}{l^2(x) + y^2} \quad (4)$$

$E_0 = g(x)/l(x)$ is the field at $y = 0$ and $l(x)$ is of the order of the electrode spacing. For thin boundary layers the field E_x may with good approximation be considered to be independent of y throughout the boundary layer thickness. Ionized gas is injected through a slot near the leading edge of the airfoil, being then carried along the airfoil surface by the flow. The steady-state charge distribution in the boundary layer is obtained from the continuity equation

$$\sigma(x,y) = \sigma_0(1 - d_1\psi(x,y))\theta(1 - d_1\psi(x,y))\theta(x - x_0) \quad (5)$$

where σ_0 is the injection intensity, d_1 the rate of depletion, ψ the stream function and x_0 the coordinate of the injection slot. The dynamically-dependent charge density profile may also be parametrized by the simpler formula

$$\sigma(x,y) = \sigma_0\left(1 - \frac{u}{u_e}\right) \quad (6)$$

A scaling solution is one for which f is a function of η only. Equation (3) becomes

$$(f'')' + \xi\dot{\xi}ff'' + \frac{\xi^2}{u_e}\frac{\partial u_e}{\partial x}$$

$$= -\frac{\gamma}{\mathrm{u}_e\rho_m}\xi^2(x)\sigma_0(1 - f')g(x)\frac{l(x)}{u_e l^2(x) + \omega\nu\xi^2(x)\eta^2} \quad (7)$$

with boundary conditions $f(0) = f'(0) = 0, f'(\infty) = 1$. We have denoted $f' \equiv \partial f/\partial\eta$ and $\dot{\xi} = \partial\xi/\partial x$. With the pressure approximately constant for length scales L of the order of the airfoil $\partial u_e/\partial x \approx 0$. The factorized nature of Eq. (7) implies that solutions exist only if

$$\xi^{-2}(x) = \frac{2}{c_1}\frac{\dot{\xi}(x)}{\xi(x)} = \frac{1}{c_3}\frac{g(x)}{\xi(x)} = c_4 l^{-2}(x) \quad (8)$$

c_1, c_3 and c_4 being constants. Therefore

$$\xi(x) = \sqrt{c_1 x + c_2}, \quad g(x) = \frac{c_3}{\xi(x)},$$

$$l(x) = \sqrt{c_4}\xi(x) \quad (9)$$

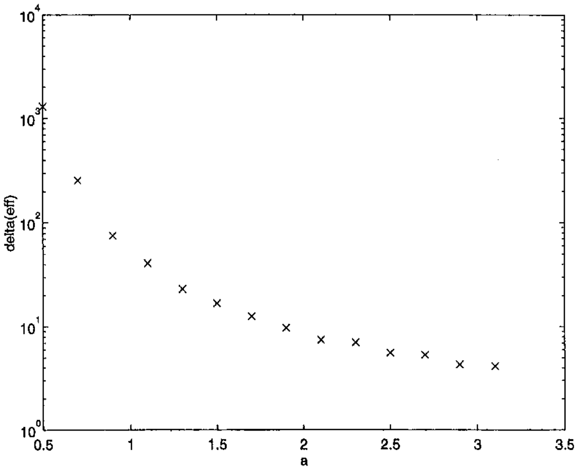

Fig. 2 Effective boundary layer thickness δ^* ($f'(\delta^*) = u/u_e = 0.95$) for the constant thickness scaling solution

There are two interesting situations. The one with $c_1 \neq 0$ $c_2 = 0$ and the one with $c_1 = 0$ $c_2 \neq 0$. The first one corresponds to a boundary layer starting at $x = 0$ and growing with $x^{1/2}$ and the second to a constant thickness boundary layer. In the first case one chooses $c_2 = 0$ to obtain a boundary layer starting at $x = 0$. The scaling hypothesis requires then an electric field that is singular at $x = 0$, $y = 0$ ($E_x \sim x^{-1}$). In any case this electric field solution is not very interesting for our purposes because it leads to a boundary layer growth of $x^{1/2}$, as in the free force Blasius solution. In the second case the equation is

$$f'''(\eta) + (1 - f'(\eta))\frac{a}{b^2 + \eta^2} = 0 \quad (10)$$

with $c_1 = 0$, $c_2 \neq 0$, $a = \gamma\sigma_0 c_3\sqrt{c_4}/u_e\beta\rho_m\nu\omega$, $b = \sqrt{u_e c_4/\nu\omega}$. With the replacement $\phi(\eta) = 1 - f'(\eta)$ and choosing $c_4 = \nu\omega/u_e$, which is a simple rescaling of ξ, Eq. (10) becomes the zero-eigenvalue problem for a Schrödinger equation in the potential $a/(1 + \eta^2)$. Using the WKB approximation we obtain

$$f'(\eta) = 1 - \frac{(1 + \eta^2)^{1/4}}{(\eta + \sqrt{1 + \eta^2})^{\sqrt{a}}} \quad (11)$$

which is a very good approximation to the exact solution for $a \geq 1$. Figure 2 shows the effective boundary layer thickness as a function of a. The effective boundary-layer thickness δ^* is defined here as the value of η at which the velocity u reaches 0.95 of its asymptotic value u_e. A very fast thinning of the boundary layer is obtained (several orders of magnitude) for a relatively short range of the a parameter. Figure 2 shows the variation of δ^* for small a. For large a (and small δ^*) one has the asymptotic formula

$$\delta^* \simeq \frac{2.9957}{\sqrt{a}}$$

If the longitudinal electric field E_x is assumed to be a constant (E_0) throughout the boundary-layer thickness, with the same charge profile, the solution is even simpler, namely

$$f'(\eta) = 1 - e^{-\eta\sqrt{h}} \quad (12)$$

with $\xi = \sqrt{c_2}$ and $h = \gamma c_2\sigma_0 E_0/\beta u_e^2\rho_m$.

For reference values of the physical quantities in Eqs. (1) we take

$$U_r = 100 \text{ m s}^{-1}, \quad L_r = 1 \text{ m},$$

$$\delta_r = 10^{-3} \text{ m}, \quad \rho_r = 1.2 \text{ Kg m}^{-3}$$

$$E_r = 500 \text{ V cm}^{-1}, \quad \sigma_r = 15\ \mu\text{C cm}^{-3},$$

$$\nu_r = 1.5 \times 10^{-5} \text{ m}^2 \text{ s}^{-1} \quad (13)$$

For these reference values, the adimensional constants ω and γ are $\omega = 0.15$ and $\gamma = 62.499$.

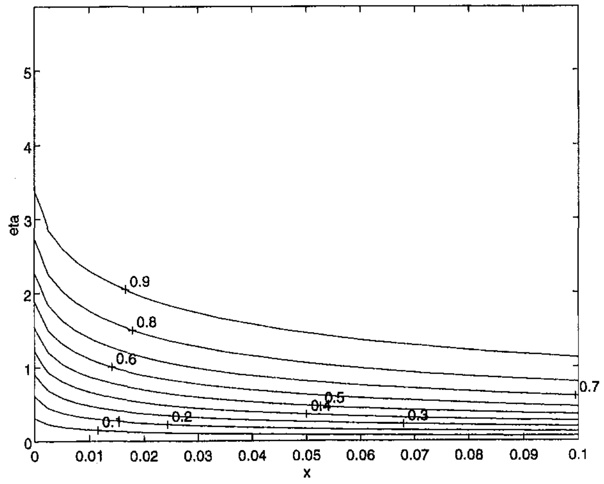

Fig. 3 Contour plot of $f'(x, \eta)$ for $S = 0.6$

Let y^* be the point at which $u/u_e = 0.95$. If stability of a laminar boundary layer cannot safely be guaranteed for local Reynold numbers $R_S = \tilde{u}_e\tilde{y}^*/\tilde{\nu}$ greater than about 10^3, we obtain for the classical force-free Blasius solution, and these reference parameters, that $\tilde{y}^* \simeq 0.15$ mm and, without control, the laminar region would be of the order of 1 cm, a tiny portion of a typical wing.

From the scaling solutions we may obtain an estimate of the controlling effect of a streamwise electric field on the boundary layer profile. The result is that a constant thickness boundary layer with local Reynolds number $R_S = 10^3$ is obtained for a charge density, in physical units, equal to $\tilde{\sigma}_0 = \sigma_0\sigma_r = 14.36$ μC cm^{-3}.

The above estimate is obtained using the reference values for the kinematic variables. For other values we have the following designing formula (in normalized units)

$$\sigma_0 E_0 = 0.957 \frac{u_e^3 \rho_m}{10^{-6} R_S^2 \nu} \tag{14}$$

For design purposes, another important estimate concerns the total current I of the injected ionized gas, which determines the required ionization power. Integrating (6) over the boundary layer one obtains

$$\tilde{I} = 0.03675 L \sqrt{\frac{\sigma_0 \nu \rho_m u_e^3}{E_0}} \tag{15}$$

with the current in physical MKS units and all terms in the right-hand side being adimensional quantities normalized by the reference values.

3 Numerical Results

For the numerical solution of Eq. (3), with σ given by Eq. (6), we use an implicit finite-difference technique (Blottner, 1970; Davis, 1970; Hamilton et al., 1992). The electric field is parametrized as in Eq. (4), namely

$$E_x = E_0 \frac{\dfrac{u_e l^2}{\nu\omega}}{\dfrac{u_e l^2}{\nu\omega} + \xi^2(x)\eta^2}$$

with $u_e l^2/\omega = 666.66$ which corresponds to $l = 10$, $u_e = 1$ and $\nu\omega = 0.15$. For these parameters the electric field has only a small variation throughout the boundary layer region. For the scaling function we take $\xi(x) = \sqrt{x}$. Then all results depend only on the variable S

$$S = \frac{1}{62.499} \frac{\gamma}{u_e^2 \rho_m} \sigma_0 E_0$$

($S = 1$ when all quantities take the reference values). In Fig. 3 we show a contour plot of the numerical solution for $f'(x, \eta)$ ($=u/u_e$) when $S = 0.6$. From the x-dependence of the numerical solutions we may compute the effect of the electric field in extending the laminar part of the boundary layer. By defining, as in Section 2, the length of the laminar part as the x-coordinate corresponding to a local Reynolds number of 10^3 and denoting by x_0 ($u/u_e = 0.95$) the force-free value we have obtained for the ratio $R = x/x_0$ the results shown in Fig. 4. For $S = 0$ we obtain the Blasius solution and as we approach $S = 0.957$, corresponding to the scaling solution, the ratio diverges. The matching of the results in the force-free and scaling limits is a good check of the numerical algorithm. A clear indication of the results in Fig. 4 is that not much improvement is obtained unless one is able to obtain ionization charge densities of the order of the reference value σ_r.

4 Remarks

1 In this paper we have concentrated on controlling the profile of the boundary layer. The profile has a direct effect on the laminar or turbulent nature of the flow which, in a simplified manner, we estimated by a local Reynolds number $R_S = \tilde{u}_e\tilde{y}^*/\nu$) defined as a function of the effective thickness $\tilde{y}^*$. Another relevant aspect, of course, is the active control of the transition instabilities that can be achieved by electromagnetic body forces on the charged fluid. A simplified treatment of the Tollmien-Schlichting fluctuations leads to the conclusion that a space-time modulation of the electric field, with the appropriate phase, is equivalent to an effective viscous damping effect which delays the growth of the transition region instability. For this to be effective one needs to detect the phase of the wave instabilities by electromagnetic probes. Absolute synchronization of the feedback electric modulation is, however, not so critical as in acoustic noise cancelation, because here the objective is only to obtain an effective damping effect. The effective damping gives an intuitive understanding of why a feedback electric modulation might work. A more rigorous treatment requires the solution of an integro-differential eigenvalue problem. For details refer to Vilela Mendes (1997).

2 Because of the perturbation induced by the injection method, it seems advisable to use this method in conjunction with suction and passive control in the rear part of the airfoil.

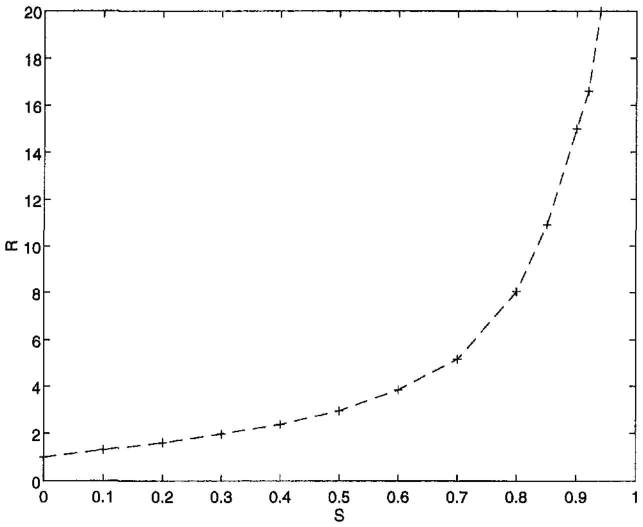

Fig. 4 Ratio of boundary layer laminar regions with and without electric field control

Even if a fully laminar boundary layer may never be completely achieved, any small improvement will become, in the long run, quite significant in terms of fuel consumption.

References

Blottner, F. G., 1970, "Finite Difference Methods of Solution of the Boundary-Layer Equations," *AIAA Journal*, Vol. 8, pp. 193–205.

Davis, R. T. 1970, "Numerical Solution of the Hypersonic Viscous Shock-Layer Equations," *AIAA Journal*, Vol. 8, pp. 843–851.

Gailitis, A. K., and Lielausis, O. A. 1961, "On the Possibility of Drag Reduction of a Flat Plate in an Electrolyte," *Appl. Magnetohydrodynamics*, Trudy Inst. Fis. AN Latv. SSR, Vol. 12, pp. 143–146.

Hamilton II, H. H., Millman, D. R., and Greendyke, R. B. 1992, "Finite-Difference Solution for Laminar or Turbulent Boundary Layer Flow Over Axisymmetric Bodies with Ideal Gas, CF4 or Equilibrium Air Chemistry," NASA Langley Research Center report no. L-17102.

Henoch, C., and Stace, J. 1995, "Experimental Investigation of a Salt Water Turbulent Boundary Layer Modified by an Applied Streamwise Magnetohydrodynamic Body Force," *Physics of Fluids*, Vol. 7, pp. 1371–1383.

Lee, C., Kim, J., Babcock, D., and Goodman, R. 1997, "Application of Neural Networks to Turbulence Control for Drag Reduction," *Physics of Fluids*, Vol. 9, pp. 1740–1747.

Moffat, H. K. 1967, "On the Suppression of Turbulence by a Uniform Magnetic Field," *Journal of Fluid Mechanics*, Vol. 28, pp. 571–592.

Sirovich, L. and Karlsson, S. 1997; "Turbulent Drag Reduction by Passive Mechanisms," *Nature*, Vol. 388, pp. 753–755.

Tsinober, A. B. and Shtern, A. G. 1967, "Possibility of Increasing the Flow Stability in a Boundary Layer by Means of Crossed Electric and Magnetic Fields," *Magnetohydrodynamics*, Vol. 3, pp. 103–105.

Tsinober, A. B. 1990, "MHD Flow Drag Reduction," *Viscous Drag Reduction in Boundary Layers*, Bushnell, D. M. and Hefner, J. N., *Progress in Astronautics and Aeronautics*, Vol. 123, American Institute of Aeronautics and Astronautics, Washington, pp. 327–349.

Vilela Mendes, R. 1997, "Active Control of Ionized Boundary Layers," LANL chao-dyn/9705017, to appear in *Int. Journal of Bifurcation and Chaos* (1998).

Analytical Solution to Flux Enhancement in Laminar Concentrically Stratified Pipe Flow of Bingham and Newtonian Fluids

C. D. Buchanan,[1] **C. Kleinstreuer,**[1] **and P. W. Longest**[1]

Introduction

Of interest is the efficient pipe flow of industrial fluids such as pastes, paints, food stuff, slurries, and dense particle suspensions which can be well represented by the Bingham fluid model. A simple Bingham fluid model consists of a fixed yield stress, below which the material moves like a solid, and a linear function between the deviatoric stress in excess to the yield stress and the shear rate. The ratio of the yield stress and the viscous stress is referred to as the Bingham number. For a given pressure gradient, the flow rate of such highly viscous non-Newtonian fluids can be enhanced when a low-viscosity immiscible Newtonian fluid layer, coating the inner pipe wall, is employed as a lubrication film. Related applications of stratified immiscible fluid flows in pipes include drag reduction in arterial blood flow with a cell-free wall plasma layer (Oka, 1981), two-phase flow in a tubular polymerizer (Kleinstreuer and Agarwal, 1987), fluid displacement by another in oil drilling (Bakhtiyarov and Siginer, 1996), two-layered fluid flow enhancement in a pipe employing oscillatory pressure gradients (Mai and Davis, 1996), and water-lubricated transport of heavy oils (Joseph et al., 1997).

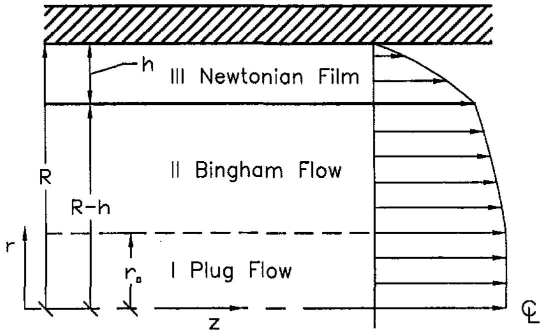

Fig. 1 System schematic and representative velocity profile

There are two stability aspects to be considered for these types of engineering applications, i.e., the transition to turbulent pipe flow and the possible instability at the interface between the two fluids. Frigaard et al. (1994) analyzed the stability of plane Poiseuille flow of a Bingham fluid and showed that the transitional Reynolds number Re_{tr} increases almost linearly with the Bingham number B. Interface instability is mainly associated with the viscosity jump assuming that density stratification is stabilizing. Hooper and Grimshaw (1985) developed an amplitude evolution equation for shear flow of two layered fluids in a horizontal channel. They formed a critical parameter $k^2s/d \lesssim 1$, i.e., wave amplification or decay, where k is the wave number of the disturbance, s represents the stabilizing effect of surface tension, and d is the growth rate of the linear disturbance. Published theoretical investigations which focus on flux enhancement stayed below such critical flow parameter values in order to avoid these types of instabilities.

The present study provides an analytical solution, not found in the open literature, to the idealized problem of flux enhancement for a Bingham fluid transported in a horizontal pipe with a constant smooth lubricating film of a low-viscosity Newtonian fluid (Buchanan, 1996). The model can be readily used for parametric sensitivity analyses, as shown in the present paper, as well as for stability investigations and as a benchmark for more comprehensive numerical models.

Theory

Bingham Flow Equations. Assuming steady laminar axisymmetric fully-developed flow of a Bingham fluid surrounded by a constant layer of a low-viscosity Newtonian fluid (cf. Fig. 1), the reduced continuity and momentum equations (Kleinstreuer, 1997) with $\partial p/\partial z \approx \Delta p/L =$ constant and

$$\tau_{rz} = \begin{cases} \tau_0 - \mu_0 \partial v_z/\partial r \quad \text{for} \quad \tau > \tau_0 \quad \text{(Bingham fluid)} \\ \text{indeterminate for} \quad \tau \le \tau_0 \quad \text{(Bingham fluid)} \\ -\mu \partial v_z/\partial r \quad \text{for} \quad \text{all } \tau \quad \text{(Newtonian fluid)} \end{cases} \tag{1a–c}$$

can be directly integrated. The results are for the shear stress:

$$\tau_{rz} = \frac{\Delta p}{2L} r \tag{2}$$

for the Newtonian film of region I:

---

[1] Graduate Student, Professor, and Graduate Student, respectively, Department of Mechanical and Aerospace Engineering, North Carolina State University, Raleigh, NC 27695-7910.

Contributed by the Fluids Engineering Division of THE AMERICAN SOCIETY OF MECHANICAL ENGINEERS. Manuscript received by the Fluids Engineering Division August 21, 1997; revised manuscript received February 24, 1998. Associate Technical Editor: M. N. Dhaubhadel.

Even if a fully laminar boundary layer may never be completely achieved, any small improvement will become, in the long run, quite significant in terms of fuel consumption.

References

Blottner, F. G., 1970, "Finite Difference Methods of Solution of the Boundary-Layer Equations," *AIAA Journal*, Vol. 8, pp. 193–205.

Davis, R. T. 1970, "Numerical Solution of the Hypersonic Viscous Shock-Layer Equations," *AIAA Journal*, Vol. 8, pp. 843–851.

Gailitis, A. K., and Lielausis, O. A. 1961, "On the Possibility of Drag Reduction of a Flat Plate in an Electrolyte," *Appl. Magnetohydrodynamics*, Trudy Inst. Fis. AN Latv. SSR, Vol. 12, pp. 143–146.

Hamilton II, H. H., Millman, D. R., and Greendyke, R. B. 1992, "Finite-Difference Solution for Laminar or Turbulent Boundary Layer Flow Over Axisymmetric Bodies with Ideal Gas, CF4 or Equilibrium Air Chemistry," NASA Langley Research Center report no. L-17102.

Henoch, C., and Stace, J. 1995, "Experimental Investigation of a Salt Water Turbulent Boundary Layer Modified by an Applied Streamwise Magnetohydrodynamic Body Force," *Physics of Fluids*, Vol. 7, pp. 1371–1383.

Lee, C., Kim, J., Babcock, D., and Goodman, R. 1997, "Application of Neural Networks to Turbulence Control for Drag Reduction," *Physics of Fluids*, Vol. 9, pp. 1740–1747.

Moffat, H. K. 1967, "On the Suppression of Turbulence by a Uniform Magnetic Field," *Journal of Fluid Mechanics*, Vol. 28, pp. 571–592.

Sirovich, L. and Karlsson, S. 1997; "Turbulent Drag Reduction by Passive Mechanisms," *Nature*, Vol. 388, pp. 753–755.

Tsinober, A. B. and Shtern, A. G. 1967, "Possibility of Increasing the Flow Stability in a Boundary Layer by Means of Crossed Electric and Magnetic Fields," *Magnetohydrodynamics*, Vol. 3, pp. 103–105.

Tsinober, A. B. 1990, "MHD Flow Drag Reduction," *Viscous Drag Reduction in Boundary Layers*, Bushnell, D. M. and Hefner, J. N., *Progress in Astronautics and Aeronautics*, Vol. 123, American Institute of Aeronautics and Astronautics, Washington, pp. 327–349.

Vilela Mendes, R. 1997, "Active Control of Ionized Boundary Layers," LANL chao-dyn/9705017, to appear in *Int. Journal of Bifurcation and Chaos* (1998).

Analytical Solution to Flux Enhancement in Laminar Concentrically Stratified Pipe Flow of Bingham and Newtonian Fluids

C. D. Buchanan,[1] C. Kleinstreuer,[1] and P. W. Longest[1]

Introduction

Of interest is the efficient pipe flow of industrial fluids such as pastes, paints, food stuff, slurries, and dense particle suspensions which can be well represented by the Bingham fluid model. A simple Bingham fluid model consists of a fixed yield stress, below which the material moves like a solid, and a linear function between the deviatoric stress in excess to the yield stress and the shear rate. The ratio of the yield stress and the viscous stress is referred to as the Bingham number. For a given pressure gradient, the flow rate of such highly viscous non-Newtonian fluids can be enhanced when a low-viscosity immiscible Newtonian fluid layer, coating the inner pipe wall, is employed as a lubrication film. Related applications of stratified immiscible fluid flows in pipes include drag reduction in arterial blood flow with a cell-free wall plasma layer (Oka, 1981), two-phase flow in a tubular polymerizer (Kleinstreuer and Agarwal, 1987), fluid displacement by another in oil drilling (Bakhtiyarov and Siginer, 1996), two-layered fluid flow enhancement in a pipe employing oscillatory pressure gradients (Mai and Davis, 1996), and water-lubricated transport of heavy oils (Joseph et al., 1997).

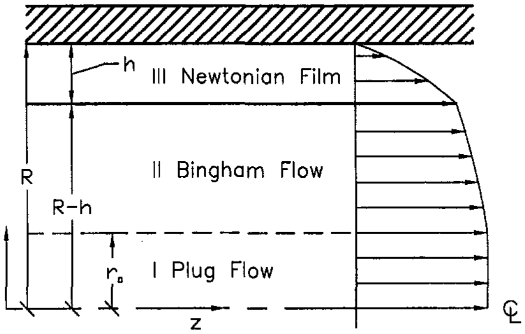

Fig. 1 System schematic and representative velocity profile

There are two stability aspects to be considered for these types of engineering applications, i.e., the transition to turbulent pipe flow and the possible instability at the interface between the two fluids. Frigaard et al. (1994) analyzed the stability of plane Poiseuille flow of a Bingham fluid and showed that the transitional Reynolds number Re_{tr} increases almost linearly with the Bingham number B. Interface instability is mainly associated with the viscosity jump assuming that density stratification is stabilizing. Hooper and Grimshaw (1985) developed an amplitude evolution equation for shear flow of two layered fluids in a horizontal channel. They formed a critical parameter $k^2 s/d \lesssim 1$, i.e., wave amplification or decay, where k is the wave number of the disturbance, s represents the stabilizing effect of surface tension, and d is the growth rate of the linear disturbance. Published theoretical investigations which focus on flux enhancement stayed below such critical flow parameter values in order to avoid these types of instabilities.

The present study provides an analytical solution, not found in the open literature, to the idealized problem of flux enhancement for a Bingham fluid transported in a horizontal pipe with a constant smooth lubricating film of a low-viscosity Newtonian fluid (Buchanan, 1996). The model can be readily used for parametric sensitivity analyses, as shown in the present paper, as well as for stability investigations and as a benchmark for more comprehensive numerical models.

Theory

Bingham Flow Equations. Assuming steady laminar axisymmetric fully-developed flow of a Bingham fluid surrounded by a constant layer of a low-viscosity Newtonian fluid (cf. Fig. 1), the reduced continuity and momentum equations (Kleinstreuer, 1997) with $\partial p/\partial z \approx \Delta p/L =$ constant and

$$\tau_{rz} = \begin{cases} \tau_0 - \mu_0 \partial v_z/\partial r & \text{for} \quad \tau > \tau_0 \quad \text{(Bingham fluid)} \\ \text{indeterminate for} & \tau \le \tau_0 \quad \text{(Bingham fluid)} \\ -\mu \partial v_z/\partial r & \text{for} \quad \text{all } \tau \quad \text{(Newtonian fluid)} \end{cases} \tag{1a–c}$$

can be directly integrated. The results are for the shear stress:

$$\tau_{rz} = \frac{\Delta p}{2L} r \tag{2}$$

for the Newtonian film of region I:

---

[1] Graduate Student, Professor, and Graduate Student, respectively, Department of Mechanical and Aerospace Engineering, North Carolina State University, Raleigh, NC 27695-7910.

Contributed by the Fluids Engineering Division of THE AMERICAN SOCIETY OF MECHANICAL ENGINEERS. Manuscript received by the Fluids Engineering Division August 21, 1997; revised manuscript received February 24, 1998. Associate Technical Editor: M. N. Dhaubhadel.

$$\frac{v_z^N}{\phi} = \frac{\mu_o}{\mu}\left[1 - \left(\frac{r}{R}\right)^2\right] \quad \text{for} \quad R - h \le r \le R \qquad (3a)$$

and for the Bingham fluid of regions II and III:

$$\frac{v_z^B}{\phi} = \begin{cases} 1 - \left(\frac{r}{R}\right)^2 - \frac{2\tau_0}{\tau_R}\left(1 - \frac{r}{R}\right) & \text{for} \quad r_0 \le r \le R \\ \left(1 - \frac{\tau_0}{\tau_R}\right)^2 = \text{const} & \text{for} \quad r \le r_0 \end{cases} \qquad (3b, c)$$

where τ_0 is the yield stress, τ_R is the wall shear stress, and $\phi \equiv \Delta p R^2/4\mu_0 L$.

The analysis implies that the interface at $r = R - h$ is smooth, that surface tension effects can be ignored, and that the shear stress is finite at $r = 0$. Clearly, the Bingham fluid exhibits uniform flow for $0 \le r \le r_0$, where

$$r_0 = \frac{2\tau_0 L}{\Delta p} \qquad (4)$$

is the "plug flow" radius. Integration of Eqs. (3*b*, *c*) across the tube's circular area yields the Buckingham-Reiner equation (Bird et al., 1960), i.e.,

$$Q_B = \frac{\pi \Delta p R^4}{8\mu_0 L}\left[1 - \frac{4}{3}\frac{\tau_0}{\tau_R} + \frac{1}{3}\left(\frac{\tau_0}{\tau_R}\right)^4\right] \qquad (5)$$

Lubricated Bingham Flow Solution. If the flow rate of the Bingham fluid is to be enhanced via a constant Newtonian lubrication film, three zones have to be considered (cf. Fig. 1). For the core region I, uniform velocity or plug flow remain, while in region II, shear effects determine the Bingham fluid velocity which merges at the interface of regions II and III with the Newtonian fluid velocity profile, viz,

$$\underline{\text{at } r = R - h}: \quad v_z^B = v_z^N \quad \text{and} \quad \tau_{rz}^B = \tau_{rz}^N \qquad (6a, b)$$

Matching Eq. (3*a*) with the velocity profile for the Newtonian layer at the interface $r = R - h$, and employing the conditions (6*a* and 6*b*) leads, after integration from $r = 0$ to $r = R - h$, to an expression for the volumetric flow rate of a lubricated Bingham fluid (Buchanan, 1996).

$$Q_{LB} = \frac{\pi \Delta p R^4}{8\mu_0 L}\left[2M\eta(2 - \eta)(1 - \eta)^2 + (1 - \eta)^4 - \frac{4}{3}(1 - \eta)^3 \frac{\tau_0}{\tau_R} + \frac{1}{3}\left(\frac{\tau_0}{\tau_R}\right)^4\right] \qquad (7)$$

where for practical purposes

$$M = \frac{\mu_0}{\mu} > 1, \quad \eta = \frac{h}{R} \ll 1 \quad \text{and}$$

$$\frac{\tau_0}{\tau_R} = \frac{r_0}{R} \equiv \kappa < 1 \qquad (8a\text{–}c)$$

A flow rate ratio $\hat{Q} \equiv Q_{LB}/Q_B$ is formed with Eqs. (5) and (7) resulting in

$$\hat{Q} \equiv \frac{Q_{LB}}{Q_B} = \frac{6M\eta(2-\eta)(1-\eta)^2 + 3(1-\eta)^4 - 4(1-\eta)^3\kappa + \kappa^4}{3 - 4\kappa + \kappa^4} \qquad (9)$$

where for flux enhancement purposes $\hat{Q}(M, \eta, \kappa) > 1$.

Flux Enhancement Equations. To express Eq. (9) in an expedient form for flux enhancement evaluations and parametric sensitivity analyses, a dimensionless combination of the system parameters M, η and κ was sought while maintaining reasonable value ranges, i.e.,

$$2 \le M \le 10, \quad 0.01 \le \eta \le 0.2, \quad 0.2 \le \kappa \le 0.6 \qquad (10a\text{–}c)$$

The dimensionless group, termed flux enhancement parameter or FEP, was determined employing least squares regression analysis, i.e.,

$$\Sigma[\hat{Q}(M, \kappa, \eta) - FEP]^2 = \min \qquad (11)$$

resulting in

$$FEP = M^{0.67}(\kappa\eta)^{0.1} \qquad (12)$$

with an average coefficient of multiple determination of $\zeta^2 = 0.983$ indicating that 98.3 percent of the observed variation of $\hat{Q}$, given FEP, can be predicted. The dimensionless group FEP collapses the expression for flux enhancement $\hat{Q} = \hat{Q}(FEP)$ to a curvilinear relationship if one of the three variables is held constant. The increase in $\hat{Q}$ within the given range (cf. Eq. 10*a*–*c*) is limited by a point where an increase in η, and hence an increase in FEP, results in a decrease in $\hat{Q}$. The restriction of $\hat{Q}$ by η is due to diminishing cross-sectional area available for the Bingham fluid core.

Results and Discussion

The forgoing analytic solutions are used to examine the tubular flow fields of two separated, Newtonian/non-Newtonian fluids as well as flow enhancement conditions for various system parameters, i.e., M, η, and κ.

Velocity Profiles. For characteristic values of η and κ, the lubricated Bingham fluid flow field is depicted with a series of dimensionless velocity profiles for representative viscosity ratio values, i.e., $M = 2$ (cf. Fig. 2(*a*)), $M = 6$ (cf. Fig. 2(*b*)) and $M = 10$ (cf. Fig. 2(*c*)). The lubricating film characteristics in terms of thickness $h = \eta \cdot R$ and viscosity $\mu = \mu_o/M$ appear to have the strongest influence on the velocity profiles and ultimately on flux enhancement. The combination of very low Newtonian viscosities and relatively thick lubrication layers generates fast moving, almost uniform Bingham fluid cores (cf. Fig. 2(*c*) versus Fig. 2(*a*)).

Flow Rate Enhancement. Flux enhancement with the goal of flow rate maximization, within the given parameter constraints (cf. Eq. (10*a*–*c*)), is evaluated with Eq. (9). The combined effects of the system parameters M and κ on the flux enhancement function $\hat{Q}(FEP)$ are given in Fig. 3 in the form of a flow enhancement map. For a given M and κ value, the contour line intersections represent specific $\hat{Q}_{\max}$-values corresponding to $\eta \approx 0.2$. Linear interpolation allows to obtain quick $\hat{Q}_{\max}$ results for any combination of M and κ, once the flow enhancement parameter is known.

Conclusions

An analytic solution for flux enhancement of a Bingham-type fluid has been obtained considering steady laminar fully-developed pipe flow. The Bingham fluid is lubricated by a concentric low-viscosity Newtonian wall layer of constant thickness h. Implementation of a smooth uniform lubrication layer, ideally, $h \le 0.2R$, would be most challenging. Nevertheless, the closed-form solution provided is most valuable for complex numerical model validations, two-fluid stability investigations, and parametric sensitivity analyses.

For the latter task (PSA), the dependence of enhanced Bingham flow rates, in terms of the ratio $\hat{Q} = Q_{\text{lubricated B.f.}}/$

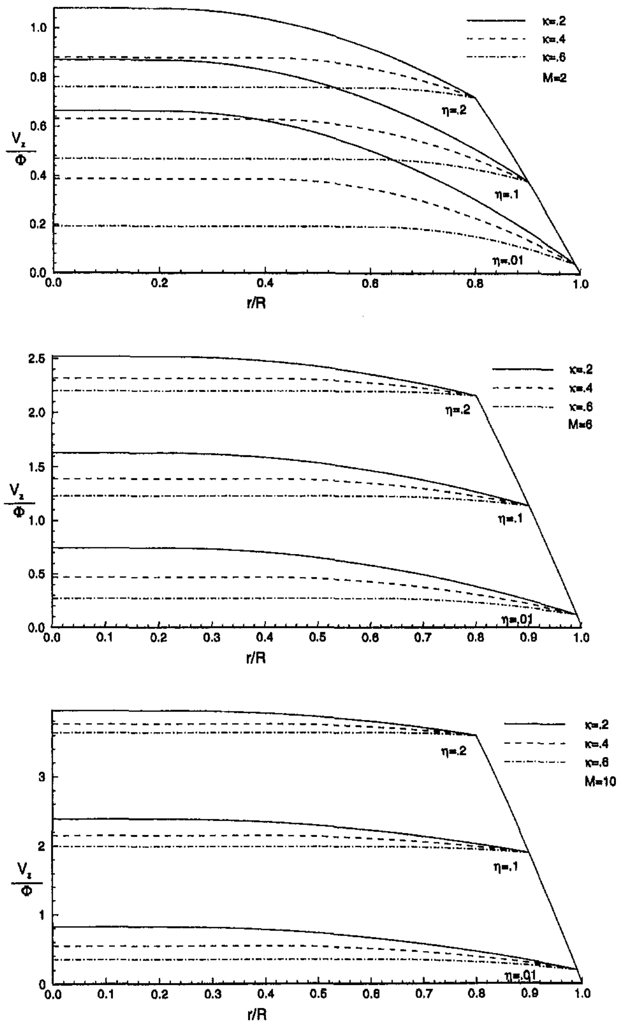

Fig. 2 Dimensionless axial velocity profiles for different Bingham yield stresses, i.e., $0.2 \le \kappa \le 0.6$ and Newtonian film thicknesses, i.e., $0.01 \le \eta \le 0.2$: (*a*) viscosity ratio $M \equiv \mu_o/\mu = 2$; (*b*) $M = 6$; and (*c*) $M = 10$

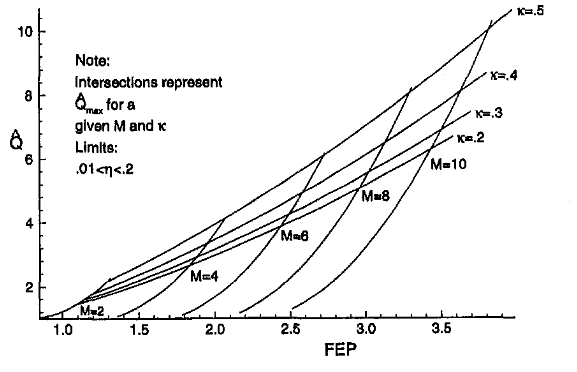

Fig. 3 Flow enhancement map for $\hat{Q} = \hat{Q}(FEP, M, \kappa)$

$Q_{\text{Bingham fluid only}}$, has been evaluated as a function of viscosity ratio $M = \mu_o/\mu$, dimensionless film thickness $\eta = h/R$, and Bingham yield stress $\kappa = \tau_o/\tau_R = r_o/R$. The function for the flow rate ratio, $\hat{Q} = \hat{Q}(M, \eta, \kappa)$, is graphically simplified for practical applications as $\hat{Q} = \hat{Q}(FEP)$ in order to elucidate the effects of M and κ. Crucial for flux enhancement is a low viscosity and substantial thickness of the Newtonian fluid layer. The reason is that the two-fluid interfacial shear decreases with lower viscosities as well as lower interfacial velocity gradients. That is achieved with high M-values and relatively large η-values, where $\eta \approx 0.2$ is the upper bound at which $\hat{Q} = \hat{Q}_{\max}$. For $\eta > 0.2$, the flow rate ratio declines because insufficient cross-sectional area is available for lubricated Bingham fluid flow.

References

Bakhtiyarov, S., and Siginer, D. A., 1996, "Displacement of a Fluid by Another in Tubes," AMD-Vol. 217, *Rheology and Fluid Mechanics of Nonlinear Materials,* ASME, New York.

Bird, R. B., Stewart, W. E., and Lightfoot, E. N., 1960, *Transport Phenomena,* Wiley, New York.

Buchanan, C. D., 1996, *Investigation of Lubricated Bingham Tube Flow,* Research Report MAE 557, N.C. State University, Raleigh NC.

Frigaard, I. A., Howison, S. D., and Sobey, I. J., 1994, "On the Stability of Poiseuille Flow of a Bingham Fluid," *Journal of Fluid Mechanics,* Vol. 263, pp. 133–139.

Hopper, A. P., and Grimshaw, R., 1985, "Nonlinear Instability at the Interface Between Two Viscous Fluids," *Physics of Fluids,* Vol. 28, No. 1, pp. 37–45.

Joseph, D. D., Bai, R., Chen, K. P., and Renardy, Y. Y., 1997, "Core-Annular Flows," *Annual Review of Fluid Mechanics,* Vol. 29, pp. 65–90; Annual Reviews Inc., Palo Alto, CA.

Kleinstreuer, C., 1997, *Engineering Fluid Dynamics—An Interdisciplinary Systems Approach,* Cambridge University Press, New York.

Kleinstreuer, C., and Agarwal, S., 1987, "Fluid Dynamics of a Tubular Polymerizer Largely Determined by Coupled Heat and Mass Transfer Processes," *International Journal of Engineering Science,* Vol. 25, No. 5, pp. 597–607.

Mai, T. Z., and Davis, A. M. J., 1996, "Laminar Pulsatile Two-Phase non-Newtonian Flow Through a Pipe," *Computers and Fluids,* Vol. 25, No. 1, pp. 77–93.

Oka, S., 1981, *Cardiovascular Hemorheology,* Cambridge University Press, New York.

Axial Pressure Distribution in the Entrance Region of Packed Beds of Spheres

J. D. McWhirter,[1] M. E. Crawford,[2] and D. E. Klein[2]

Nomenclature

Δp = pressure difference
Re$'$ = Reynolds number as modified by hydraulic radius theory
ϵ = porosity

Introduction

There are a number of reasons why the entrance length in randomly packed beds of spheres has yet to be measured. First, one may argue on physical grounds that it cannot be significantly greater than one sphere diameter because the tortuous, contracting and expanding flow through the pores rapidly (in a spatial sense) disconnects the downstream velocity profiles from upstream influences. Second, for most packed bed experiments, any errors due to entrance effects are usually negligible in comparison to the overall packed bed pressure drop. Third, any experiments for measuring the entrance length would be

---

[1] Assistant Professor, Idaho State University, Box 8060, Pocatello, Idaho 83209.

[2] Professor and Associate Vice Chancellor for Special Engineering Programs, respectively, The University of Texas System, Austin, TX 78712.

Contributed by the Fluids Engineering Division of THE AMERICAN SOCIETY OF MECHANICAL ENGINEERS. Manuscript received by the Fluids Engineering Division December 13, 1996; revised manuscript received May 4, 1998. Associate Technical Editor: F. Giralt.

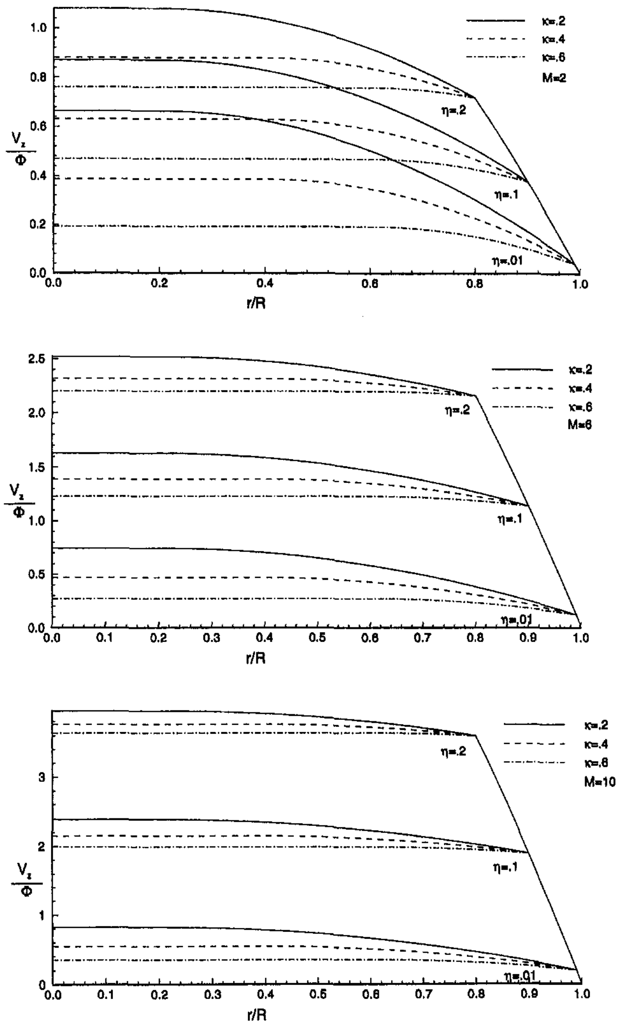

Fig. 2 Dimensionless axial velocity profiles for different Bingham yield stresses, i.e., $0.2 \le \kappa \le 0.6$ and Newtonian film thicknesses, i.e., $0.01 \le \eta \le 0.2$: (*a*) viscosity ratio $M \equiv \mu_o/\mu = 2$; (*b*) $M = 6$; and (*c*) $M = 10$

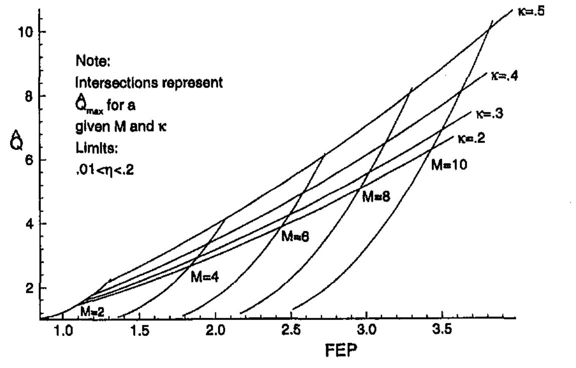

Fig. 3 Flow enhancement map for $\hat{Q} = \hat{Q}(FEP, M, \kappa)$

$Q_{\text{Bingham fluid only}}$, has been evaluated as a function of viscosity ratio $M = \mu_o/\mu$, dimensionless film thickness $\eta = h/R$, and Bingham yield stress $\kappa = \tau_o/\tau_R = r_o/R$. The function for the flow rate ratio, $\hat{Q} = \hat{Q}(M, \eta, \kappa)$, is graphically simplified for practical applications as $\hat{Q} = \hat{Q}(FEP)$ in order to elucidate the effects of M and κ. Crucial for flux enhancement is a low viscosity and substantial thickness of the Newtonian fluid layer. The reason is that the two-fluid interfacial shear decreases with lower viscosities as well as lower interfacial velocity gradients. That is achieved with high M-values and relatively large η-values, where $\eta \approx 0.2$ is the upper bound at which $\hat{Q} = \hat{Q}_{\max}$. For $\eta > 0.2$, the flow rate ratio declines because insufficient cross-sectional area is available for lubricated Bingham fluid flow.

References

Bakhtiyarov, S., and Siginer, D. A., 1996, "Displacement of a Fluid by Another in Tubes," AMD-Vol. 217, *Rheology and Fluid Mechanics of Nonlinear Materials,* ASME, New York.

Bird, R. B., Stewart, W. E., and Lightfoot, E. N., 1960, *Transport Phenomena,* Wiley, New York.

Buchanan, C. D., 1996, *Investigation of Lubricated Bingham Tube Flow,* Research Report MAE 557, N.C. State University, Raleigh NC.

Frigaard, I. A., Howison, S. D., and Sobey, I. J., 1994, "On the Stability of Poiseuille Flow of a Bingham Fluid," *Journal of Fluid Mechanics,* Vol. 263, pp. 133–139.

Hopper, A. P., and Grimshaw, R., 1985, "Nonlinear Instability at the Interface Between Two Viscous Fluids," *Physics of Fluids,* Vol. 28, No. 1, pp. 37–45.

Joseph, D. D., Bai, R., Chen, K. P., and Renardy, Y. Y., 1997, "Core-Annular Flows," *Annual Review of Fluid Mechanics,* Vol. 29, pp. 65–90; Annual Reviews Inc., Palo Alto, CA.

Kleinstreuer, C., 1997, *Engineering Fluid Dynamics—An Interdisciplinary Systems Approach,* Cambridge University Press, New York.

Kleinstreuer, C., and Agarwal, S., 1987, "Fluid Dynamics of a Tubular Polymerizer Largely Determined by Coupled Heat and Mass Transfer Processes," *International Journal of Engineering Science,* Vol. 25, No. 5, pp. 597–607.

Mai, T. Z., and Davis, A. M. J., 1996, "Laminar Pulsatile Two-Phase non-Newtonian Flow Through a Pipe," *Computers and Fluids,* Vol. 25, No. 1, pp. 77–93.

Oka, S., 1981, *Cardiovascular Hemorheology,* Cambridge University Press, New York.

Axial Pressure Distribution in the Entrance Region of Packed Beds of Spheres

J. D. McWhirter,[1] M. E. Crawford,[2] and D. E. Klein[2]

Nomenclature

Δp = pressure difference
Re′ = Reynolds number as modified by hydraulic radius theory
ϵ = porosity

Introduction

There are a number of reasons why the entrance length in randomly packed beds of spheres has yet to be measured. First, one may argue on physical grounds that it cannot be significantly greater than one sphere diameter because the tortuous, contracting and expanding flow through the pores rapidly (in a spatial sense) disconnects the downstream velocity profiles from upstream influences. Second, for most packed bed experiments, any errors due to entrance effects are usually negligible in comparison to the overall packed bed pressure drop. Third, any experiments for measuring the entrance length would be

---

[1] Assistant Professor, Idaho State University, Box 8060, Pocatello, Idaho 83209.

[2] Professor and Associate Vice Chancellor for Special Engineering Programs, respectively, The University of Texas System, Austin, TX 78712.

Contributed by the Fluids Engineering Division of The American Society of Mechanical Engineers. Manuscript received by the Fluids Engineering Division December 13, 1996; revised manuscript received May 4, 1998. Associate Technical Editor: F. Giralt.

difficult to perform because of the extremely small axial spatial resolution required (at least less than one half of a sphere diameter) for the pressure measurements, the circumferential pressure variation at the wall (McWhirter, 1995), and the small pressure difference between adjacent measurements for most feasible experiments. Fourth, the local packed bed porosity, which is largely responsible for entrance effects, converges to the packed bed average porosity within approximately one-half to one sphere diameter.

A confluence of constraints upon an experiment for measuring the liquid metal magnetohydrodynamic pressure drop in a packed bed suggested the benefit of determining the entrance length in a packed bed of spheres. One constraint was an expansion upstream and a contraction downstream of the liquid metal test section in order to transition from the loop pipe size to the test section pipe size. Another was the limited length of the homogeneous region of the magnetic flux density. It was necessary to obtain the pressure difference measurement confidently within the constant pressure gradient region of the fluid flow since the effect of a uniform magnetic field is to reduce the entrance length when compared to the magnetic-field free case (Lunsford and Walker, 1976). But, a large pressure difference was desirable from instrumentation considerations. Hence, an experimental investigation of the approximate entrance length in packed beds was undertaken.

For fluid flow in pipes the entrance length signifies the onset of a fully developed velocity profile, as well as the onset of a constant pressure gradient (Fox and McDonald, 1978). For randomly-packed beds of spheres, however, there is no similar concept of a fully developed velocity profile. The overall fluid mechanics are determined by the bed structure at the sub-pore level. However it is well known that the overall average packed bed properties are well characterized by a single parameter, the average packed bed porosity, ϵ. That is, although the packed bed geometry at the subpore level undergoes significant variation throughout the packed bed, the aggregate, macroscopic behavior is described by a relatively well known function of the average porosity of the packed bed and the fluid properties and flow rate (Fand et al., 1987).

If the packed bed entrance is formed, say, by spheres in contact with a rigid screen, the porosity in the plane parallel to the screen would be expected to behave similarly to that of the porosity of a bed of spheres in contact with a flat wall. For spheres in contact with a wall, the porosity, ϵ, is unity at the wall, reaches a minimum of around 0.2 at approximately one half a sphere diameter (normal distance) from the wall, and reaches the bed average porosity value in an damped oscillatory manner within a few sphere diameters as reported and discussed by Benenati and Brosilow (1962), Ridgeway and Tarbuck (1968), Haughey and Beveridge (1969), and Schneider and Rippin (1988). For a packed bed formed in this way the fluid dynamics would not be expected to provide a constant pressure gradient until the local porosity was relatively steady. Even if the porosity as a function of position were known explicitly, identifying a precise, experimentally verifiable location for the onset of an essentially constant pressure gradient would be difficult. Hence, it is concluded that the only realistic experimental technique for determining the entrance length in randomly packed beds of spheres is by measuring the packed bed wall pressure distribution with very high spatial resolution.

The only other known work concerning the entrance length in a packed bed of spheres is that of Dybbs and Edwards (1982). They conducted their entrance length work on a regular, not random, sphere packing and measured the intra-pore velocity profile in the Forchheimer flow regime. Their results showed that the entrance length was less than three ball diameters from the inlet. However, their work did not involve any pressure gradient measurements. No known entrance length work has been performed for the case of randomly packed spheres. Heil and Tels (1983) mention the wall pressure distribution in spout-bed reactors but no indication of entrance length is provided.

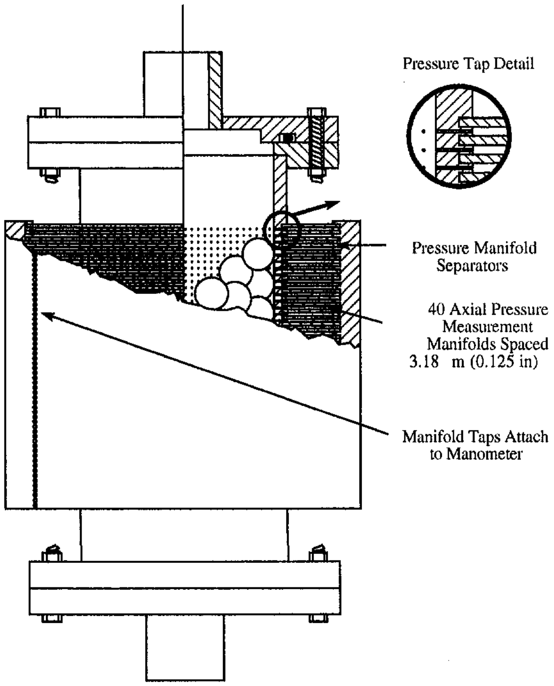

Fig. 1 **Acrylic test section used for measuring axial pressure distribution**

Experimental Apparatus

An acrylic tube, 10.16 cm (4 in) in diameter and 6.35 mm (0.25 in) thick was used for this experiment. Based upon the considerations mentioned above a spatial resolution of five axial measurements per sphere diameter was chosen resulting in an axial spacing between pressure taps of 3.17 mm (0.125 in). The circumferential pressure variation was averaged out by making 90 equally spaced holes around the circumference of the tube at each axial location. Figure 1 shows the test section, pressure manifold arrangement, and hole placement. A total of 40 axial pressure measurements were selected, resulting in a total axial coverage of 12.7 cm (5.0 in). The 3600 holes each have a diameter of 0.91 mm (0.036 in).

Four different expansion angles were studied: 0, 30, 60, and 90 degrees. The nonzero expansions were formed of machined acrylic plugs placed into the test section. Two sets of "O"-ring seals prevented bypass around the plugs. The 30 and 60 degree plugs had a 2.54 cm (1.0 in) inlet. The 90 degree plug had a 3.18 cm (1.25 in) inlet in order to allow two spheres to be inserted across the inside diameter of the plug. Details of these plugs are shown in Fig. 2. For the straight inlet, or 0 degree expansion, the water had to transition very rapidly from the tube diameter of the flow loop piping to the inside diameter of the test section, a radius ratio of ~2.3. A tapered plug with vanes was formed to serve the dual function of flow distributor and packed bed containment. In order to ensure an approximately uniform inlet velocity profile for the 0 degree expansion, a flow smoothing section was in contact with the tapered plug-and-vane flow distributor on the upstream side and an aluminum "honeycomb" flow straightener on the downstream side. The flow smoothing section was comprised of a three-deep layer of 4.76 mm (0.19 in) spheres contained by screens.

The average porosity of the packed bed was determined by subtracting from unity the ratio of the total volume of the spheres (found by counting the spheres during loading and knowing the sphere size) and the empty test section volume (computed from measuring the inside length and diameter).

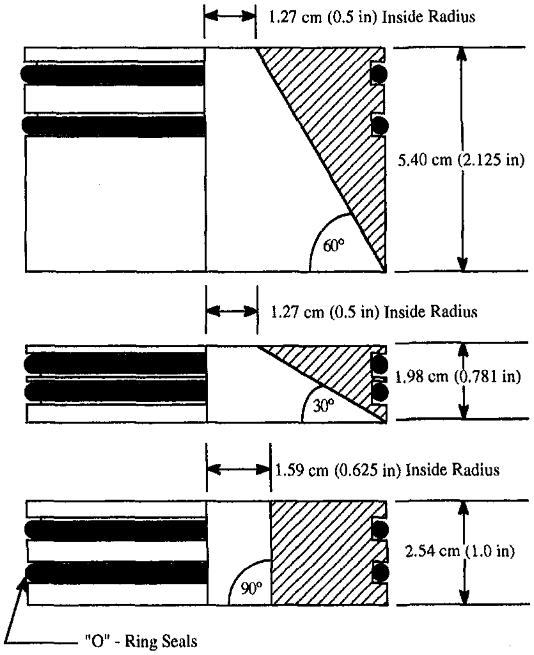

Fig. 2 30, 60, and 90 degree expansion details

Because the spheres and sphere packing techniques were common to all cases, the average porosity for all cases was approximately 0.5.

Results

The axial pressure distribution versus Re′ data for the four inlet geometries tested are shown in Figs. 3 through 6. The uncertainty in the Re′ at 20:1 odds is calculated to be 12 percent. The uncertainty in the pressure shown in the figures is based upon both resolution errors and bias errors. The pressures at zero Re′ (no flow) were used to estimate the magnitude of the bias errors.

For the case of the 0 degree expansion, shown in Fig. 3, at the higher Reynolds numbers, there is an initial rise in the pressure, followed by a mostly steady negative pressure gradient. The degree of the initial rise correlates relatively well with increasing flowrate. Also, there appears to be a deviation from linearity occurring in the vicinity of about six sphere diameters from the inlet for Re′ = 2321 and an inconsistent pressure reading at four sphere diameters from the inlet for Re′ = 1036, 1272 and 1488 which disappears at the higher Reynolds numbers. On aggregate any consistent deviations from linearity appear to be insignificant beyond one sphere diameter from the inlet. Hence, it is concluded that the entrance length for this case is approximately one sphere diameter.

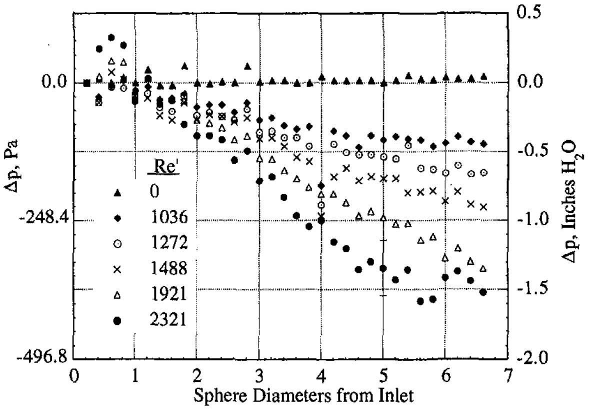

Fig. 3 Axial pressure distribution, zero degree expansion. The resolution uncertainty is ±8 percent of reading and the bias uncertainty is taken as the maximum zero-flow pressure difference.

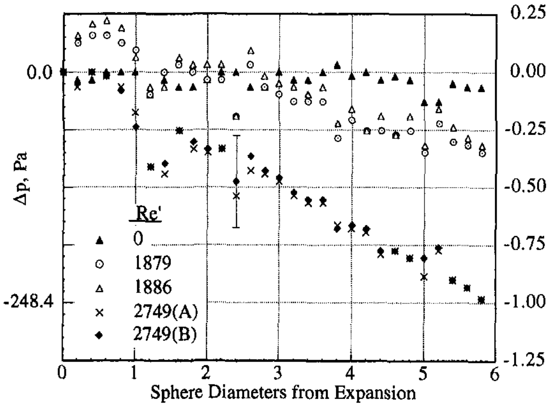

Fig. 4 Axial pressure distribution, 30 degree expansion. The resolution uncertainty is ±8 percent of reading and the bias uncertainty is taken as the maximum zero-flow pressure difference.

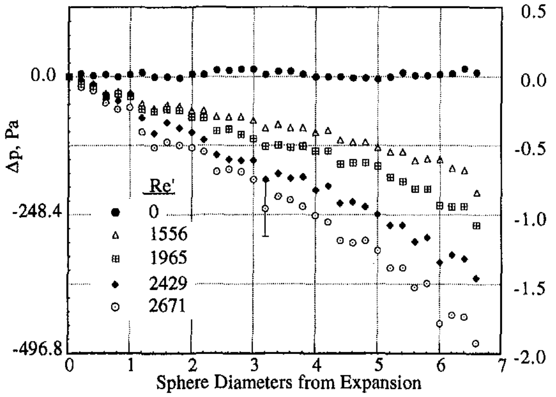

Fig. 5 Axial pressure distribution, 60 degree expansion. The resolution uncertainty is ±8 percent of reading and the bias uncertainty is taken as the maximum zero-flow pressure difference.

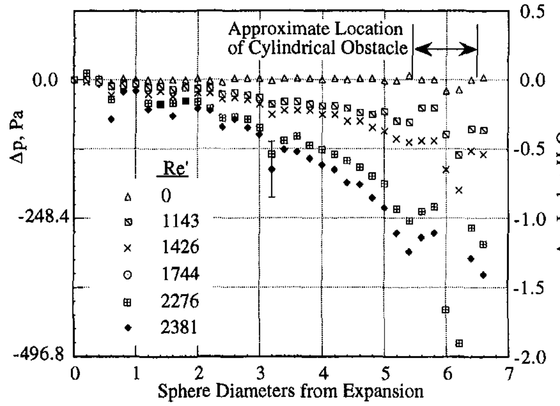

Fig. 6 Axial pressure distribution, 90 degree expansion. The resolution uncertainty is ±8 percent of reading and the bias uncertainty is taken as the maximum zero-flow pressure difference.

For the 30 degree expansion data shown in Fig. 4 there is considerable scatter in the results for Re′ = 1879 and 1886 as well as an initial rise in the pressure within a sphere diameter from the expansion. For Re′ = 2749 (A) and (B) there is an anomaly just beyond one sphere diameter from the expansion along with a relatively flat pressure distribution within a sphere diameter from the expansion. An approximately constant pressure gradient appears to be established after around one and one half sphere diameters. The data for the 60 degree expansion (Fig. 5), show substantially less scatter than the 0 degree and 30 degree expansion data. An approximately constant pressure gradient exists from the expansion to about five sphere diameters. It appears that the pressure gradient increases in the vicinity of five to seven sphere diameters from the expansion.

For the 90 degree expansion (Fig. 6) a cylindrical obstacle with diameter equal to one sphere diameter, cut to fit straight across the inside of the test section, was placed perpendicular to the flow direction in the vicinity of six sphere diameters from the expansion. This obstacle was placed in the packed bed in an attempt to assess the effects of a thermocouple placed just beyond the expansion in liquid metal test section (McWhirter, 1995). The pressure distributions show a small anomaly at about 0.6 and 3.2 sphere diameters from the expansion. Also, the pressure gradient seems to increase throughout the axial range of measurement. A brief rise and then rapid drop in the pressure occurs for all Reynolds numbers in the neighborhood of the cylindrical obstacle. The large pressure drop in the vicinity of the obstacle is expected, since the object causes about a fifty percent reduction in flow area at the thickest part of the obstacle and the flow must accelerate upon approach to and decelerate upon departure from the obstacle.

A number of phenomena may be observed from the results presented. Particularly noteworthy is the initial pressure rise at the beginning of the packed bed for the 0 degree and 30 degree expansions and near the transverse cylindrical obstacle in the case of the 90 degree expansion. For the 0 degree expansion one might expect to see an initially large pressure drop as the flow accelerates into the pores of the packed bed. However, this is not what is observed. A similar effect is seen for the 30 degree expansion but more data scatter exists for this case and the presence and magnitude of the rise does not correlate well with increasing flowrate. However, such an initial rise is also clearly seen for the case of the flow around the cylindrical obstacle with the 90 degree expansion. These initial pressure jumps are a characteristic for moderate Reynolds numbers where inertia, pressure forces and viscous forces are all significant contributors to the flow physics. Perhaps a qualitative analogy can be drawn between a uniform freestream flow entering a cascade of plates, as discussed in Panton (1984), and a uniform flow entering a packed bed of spheres. For flow entering a cascade of plates at moderate Reynolds number the presence of plates decelerates the fluid near the plates and viscous and pressure forces accelerate the flow between the plates to maintain continuity. The pressures along the stagnation streamline and at the wall initially increase as the flow enters the plates. On the other hand, the pressure along a channel centerline decreases as one would expect from inviscid flow theory for an accelerating flow. However, for this case of flow entering a cascade of plates, the net flow areas upstream and downstream from the plate cascade entrance are essentially equal.

For flow entering a packed bed of spheres the total flow area decreases by a factor of approximately 2 within a distance on the order of one half a sphere diameter from the inlet (Benenati and Brosilow, 1962). The extra acceleration required because of the reduction in flow area must come from viscous and pressure forces. The pressures measured at the wall of the packed bed indicate that the pressure increases to accelerate the flow and then decreases due to viscous losses in the packed bed with this transition occurring within about one and one half sphere diameters from the inlet. A similar explanation is plausible for the case of the flow around the cylindrical obstacle: the acceleration of the fluid around the obstacle requires an increase in pressure very near the leading edge of the obstacle.

For the 60 and 90 degree expansions, the pressure gradient appears to increase slightly for the 60 degree expansion, more so for the 90 degree expansion. An explanation for this behavior is that the flow pattern near the expansion inlet has some free jet characteristics and the flow must penetrate into the bed some distance before the flow fully covers the entire bed cross section. Hence, the velocity within the jet decelerates and tends to increase the pressure within the packed bed with diminishing effect as the flow spreads throughout the entire bed. When the viscous pressure drop is considered the result will be a flatter pressure gradient near the expansion and an increasing gradient as the flow spreads out across the bed. This same effect could also explain the anomaly of the initial rise in the pressure for the 30 degree expansion at lower flowrates but a flat pressure gradient at higher flowrates if the flow matched the expansion contour at these lower flowrates but retained some free jet characteristics at higher flowrates.

Conclusion

The axial pressure distribution near the inlet of a randomly packed bed of spheres at Reynolds numbers between 1036–2749 was measured for inlet geometries of 0, 30, 60, and 90 degrees. For the two smaller inlet geometry angles (0 and 30 degrees), an essentially constant pressure gradient was established within approximately one and one half sphere diameters. Hence it is concluded that the entrance length is of this same order for these cases. This compares well with the only other known previous investigation, under three sphere diameters, for a non-random packed bed in the Forchheimer flow regime. For the larger expansion angles, non-constant pressure gradients were observed.

References

Benenati, R. F., and C. B. Brosilow, 1962, "Void Fraction Distribution in Beds of Spheres," *AIChE Journal,* Vol. 8, No. 3, pp. 359–361.

Dybbs, A., and R. V. Edwards, 1982, "A New Look at Porous Media Fluid Mechanics, Darcy to Turbulent," *Proceedings of the NATO Advanced Study Institute on Mechanics of Fluids in Porous Media,* July 18–27, Newark, DE, pp. 201–256.

Fand, R. M., B. Y. K. Kim, A. C. C. Lam, and R. T. Phan, 1987, "Resistance to the Flow of Fluids Through Simple and Complex Porous Media Whose Matrices Are Composed of Randomly Packed Spheres," ASME JOURNAL OF FLUIDS ENGINEERING, Vol. 109, pp. 268–274.

Fox, R. W., and A. T. McDonald, 1978, *Introduction to Fluid Mechanics,* 2nd ed., Wiley, New York.

Haughey, D. P., and G. S. G. Beveridge, 1969, "Structural Properties of Packed Beds—A Review," *The Canadian Journal of Chemical Engineering,* Vol. 47, pp. 130–139.

Heil, C., and M Tels, 1983, "Pressure Distribution in Spout-Fluid Bed Reactors," *Canadian Journal of Chemical Engineering,* Vol. 61 no. 3, pp. 331–342.

Lunsford, G. S. S., and J. S. Walker, 1976, "On Establishing Fully-Developed Duct Flow in Strong Magnetic Fields," *Proceedings of the Bat-Sheva International Seminar,* pp. 7–14.

McWhirter, J. D., 1995, "Measurement of the Pressure Drop of a Liquid Metal Flowing Through a Packed Bed of Uniform Sized Conducting Spheres with Transverse Magnetic Field," Ph.D. dissertation, The University of Texas at Austin, Austin, TX.

Panton, R. L., 1984, *Incompressible Flow,* Wiley, New York.

Ridgeway, K., and K. J. Tarbuck, 1968, "Voidage Fluctuations in Randomly-Packed Beds of Spheres Adjacent to a Containing Wall," *Chemical Engineering Science,* Vol. 23, pp. 1147–1155.

Schneider, F. A., and D. W. T. Rippin, 1988, "Determination of the Local Voidage Distribution in Random Packed Beds of Complex Geometry," *Industrial Engineering Chemical Research,* Vol. 27, pp. 1936–1941.

Journal of Fluids Engineering

Discussion

Uncertainties and CFD Code Validation[1]

Patrick J. Roache.[2] The paper by Coleman and Stern (1997) proposes a new approach to CFD code validation that gives consideration to both experimental and simulation uncertainties. It is a valuable and thought-provoking contribution. Two criticisms follow.

(1) Hypothetical data-simulation comparisons are given in Figure 1 (see also Coleman, 1996), without and with experimental uncertainty bars (parts a and b, respectively). The authors state that one might interpret part a to indicate that Model 1 is superior to Model 2 since it seems to "capture the trend of the data." In contrast, when the experimental uncertainty is considered in part b, "it is obvious that arguing for one method over another based on comparison with the experimental data is wasted effort since the predictions from both methods fall well within the data uncertainty."

This negative evaluation would be true if and only if the uncertainty distribution within the plotted range of experimental uncertainty (commonly called "error bars") was flat, i.e. a step function. (For example, if the "error bar" covered the data value D to ±10%, this flat distribution would give equal probability that the true value was at D +1%, D −3%, D +9%, etc. or at D itself.) In such a case, our probabilistic knowledge is indifferent to any values within the range of the "error bar" and therefore to the relative merits of Model 1 and 2, and the authors' argument holds. Of course, we do not know what the appropriate probability distribution is, but most physical experiments have some preference for the data values reported, and the default model of probability is a Gaussian distribution. If, in the judgment of the reader, this is the more likely distribution, then there is probably a trend in the true values, and Model 1 does indeed "capture the trend of the data." One could readily express this quantitatively as a weighted integral over the assumed probability distributions within the "error bars," but qualitatively, I believe that the naive preference for Model 1 is justifiable.

(2) The principal thrust of the paper is that the validation uncertainty U_V should be the key metric in the validation process. They define the "validation uncertainty U_V as the combination of all uncertainties that we know how to estimate," which includes experimental and numerical uncertainties, the latter including lack of grid convergence. With the "comparison error" E defined as the difference between the experimental data set value the value produced by the simulation, they then interpret the condition $|E| < U_V$ to be the criteria for claiming that validation has been achieved at the U_V level.

The authors are well aware of a paradox inherent in this criterion, that increasing uncertainty of the experiments or the simulation (e.g., less convincing grid convergence tests) makes it easier to achieve validation. (The resolution of the paradox lies in the recognition that the validation level so achieved is less demanding, i.e. U_V is greater.) See more complete discussion in Coleman and Stern (1997) and in Roache (1998). However, besides the evident potential for misinterpretation in the use of U_V, a more basic problem exists with their proposal; it fails to account for an acceptable error tolerance in the Validation. This is easily demonstrated by the following "thought experiment."

Imagine a programmatic need for Validation with a 5% error tolerance (call it TOL_V). That is, the need is for a model/code that can predict physical reality to within 5%. Further imagine the limit of good experiments and calculations, i.e. vanishingly small experimental uncertainty and simulation uncertainty, so that their validation uncertainty U_V is also vanishingly small. Finally, imagine excellent agreement between experiment and simulation, say an observation error $|E| = 0.1$ percent. Then, their proposed criterion does not allow this to be considered a validation. No matter how good the agreement between experiment and simulation, nor how lax the programmatic needs, if the agreement is not as good as the combined uncertainties from experiment and simulation, it cannot be considered a validation, in this approach.

A modification of their validation criterion to include a programmatic validation tolerance TOL_V would avoid this difficulty.

$$|E| < U_V + TOL_V$$

However, the previously mentioned paradox remains, e.g. increasing experimental and/or numerical uncertainty still make it easier to achieve validation, at the level now defined by $U_V + TOL_V$. Further consideration by the simulation community will be required to determine whether or not this modification makes their proposal practical. See also further discussion in Roache (1998).

References

Coleman, H. W., 1996, "Uncertainty Consideration in Validating CFD Codes with Experimental Data," AIAA Paper 96-2027, 27th AIAA Fluid Dynamics Conference, June 17–20, 1996, New Orleans, LA.

Coleman, H. W., and Stern, F., 1997, "Uncertainties and CFD Code Validation," ASME JOURNAL OF FLUIDS ENGINEERING, Vol. 119, Dec., pp. 795–803.

Roache, P. J., 1998, *Verification and Validation in Computational Science and Engineering,* Hermosa Publishers, P. O. Box 9229, Albuquerque, NM 87119, Chapter 10.

Authors' Closure

We appreciate the thoughtful comments by Dr. Roache and the many contributions he has made in this field.

We do not accept his first point for a general case. If, for instance, the uncertainty bands plotted included a significant

---

[1] By H. W. Coleman and F. Stern published in the December 1997 issue of the JOURNAL OF FLUIDS ENGINEERING, Vol. 119, No. 4, pp. 795–803.

[2] Consultant, P.O. Box 9229, Albuquerque, N. Mex. 87119.

Journal of Fluids Engineering

Book Review

Applied Dimensional Analysis and Modeling, by Thomas Szirte, McGraw-Hill, NY, Dec. 1977.

REVIEWED BY SHELDON GREEN[1]

Applied Dimensional Analysis and Modeling is an extended (790 pages!) treatise on dimensional analysis and modeling. Although the intended audience of the book is never explicitly stated, one can reasonably assume, given the hundreds of example problems, that its intended audience is undergraduate students and researchers who have not previously been exposed to the power of dimensional analysis techniques.

The first chapter of the book covers some elementary matrix theory (determinants, matrix inversions, solutions of linear systems of equations, etc.), which is used subsequently in the development of mathematical results concerning dimensions in Chapters 2 through 10. Chapters 11 through 18 include numerous examples of the application of dimensional reasoning, to subjects as diverse as biomechanics, elasticity, electromagnetic radiation, and fluid mechanics.

Chapter 1 of the book (this chapter was written by Professor Rózsa) is a clear recapitulation of matrix theory. Although the chapter would have benefitted from some unworked review problems, the presentation of ideas is clear and at an appropriate pace. In contrast, this reviewer found most of Chapters 2 through 10 to be disappointingly pedantic. For example, surely any first year university student can convert Planck's constant from SI units to Imperial units. Likewise, does one need to explain that it is conventional to leave a gap in the expression "mass = 91 kg" between the "91" and the "kg?" Finally, does one really need a theorem stating that if one multiplies two variables, the result has dimensions equal to the product of the dimensions of the variables?

Chapters 11 to 18 represent a nice improvement from the preceding 9 chapters. In these chapters there are literally hundreds of examples of the application of dimensional analysis to physical problems. The author has found some excellent examples of situations (e.g., a sphere rolling down an inclined ramp) in which dimensional analysis can show that certain variables that one might intuit are important, are in fact physically irrelevant. He also gives nice examples of the application of physical reasoning to determine the form of relations between Π groups. Fluid mechanics specialists will note some unfortunate errors in the text. For example, when discussing the terminal velocity of a falling raindrop, the author neglects that air density could play a role in the process (i.e., he assumes the falling drop is in the Stokes flow regime), and thus deduces that the terminal velocity is proportional to the square of the droplet radius. Unless the rain is a fine mist, droplets will not be in the Stokes flow regime, and therefore do not have a terminal velocity proportional to the square of the droplet radius. As a further example, when discussing the power required to tow a barge, the author claims that model-scale measurements of drag force would be made by holding a model stationary in a moving stream. Although barge drag measurements could be made in this way, it is far more common to use a towing tank for the purpose. One can in fact use a dimensional analysis argument (along with a knowledge of the power requirements of wind tunnels) to show that the power required to operate an open water flume, of a size comparable to a reasonable model ship towing tank, is enormous, which is one of the reasons why towing tanks, not flumes, are used for barge drag measurements.

Without question, dimensional arguments can be very powerful. However, dimensional analysis is only effective if one identifies all physical variables that are important in a problem. The neglect, in the falling raindrop problem, of the role of air density is one example of such an omission. As a second example, the author uses dimensional arguments to conclude that all animals should be capable of leaping from rest to about the same height (of 2 m, according to the author). In fact, only a few select athletes can leap even 1 m vertically; professional high jumpers achieve extra height by converting kinetic energy (produced by a running start) into gravitational potential energy, and by rotating the body such that the lowest part of the body is near the center of mass. Similarly, a cat can leap significantly higher than a small dog owing to the cat's greater flexibility, which allows it to store more energy during the compression phase of a leap than can a dog. These three are very different physical mechanisms from those considered by the author. This example would therefore have been a good place for the author to have explicitly cautioned the reader about the hazards of relying on dimensional analysis when the underlying physics are not understood.

Given these shortcomings of the book, one might ask in what ways it is worthwhile. In view of its many diverse, interesting examples, taken from across the physical sciences, the reviewer believes that it serves a role as a compendium of dimensional analysis problems. As such, it would be a useful addition to the libraries of most universities, although few fluid mechanics specialists would want a copy specifically for a personal library.

---

[1] Professor, Department of Mechanical Engineering, The University of British Columbia, Vancouver, B.C. Canada V6T 1Z4.